International Journal on Advances in Telecommunications

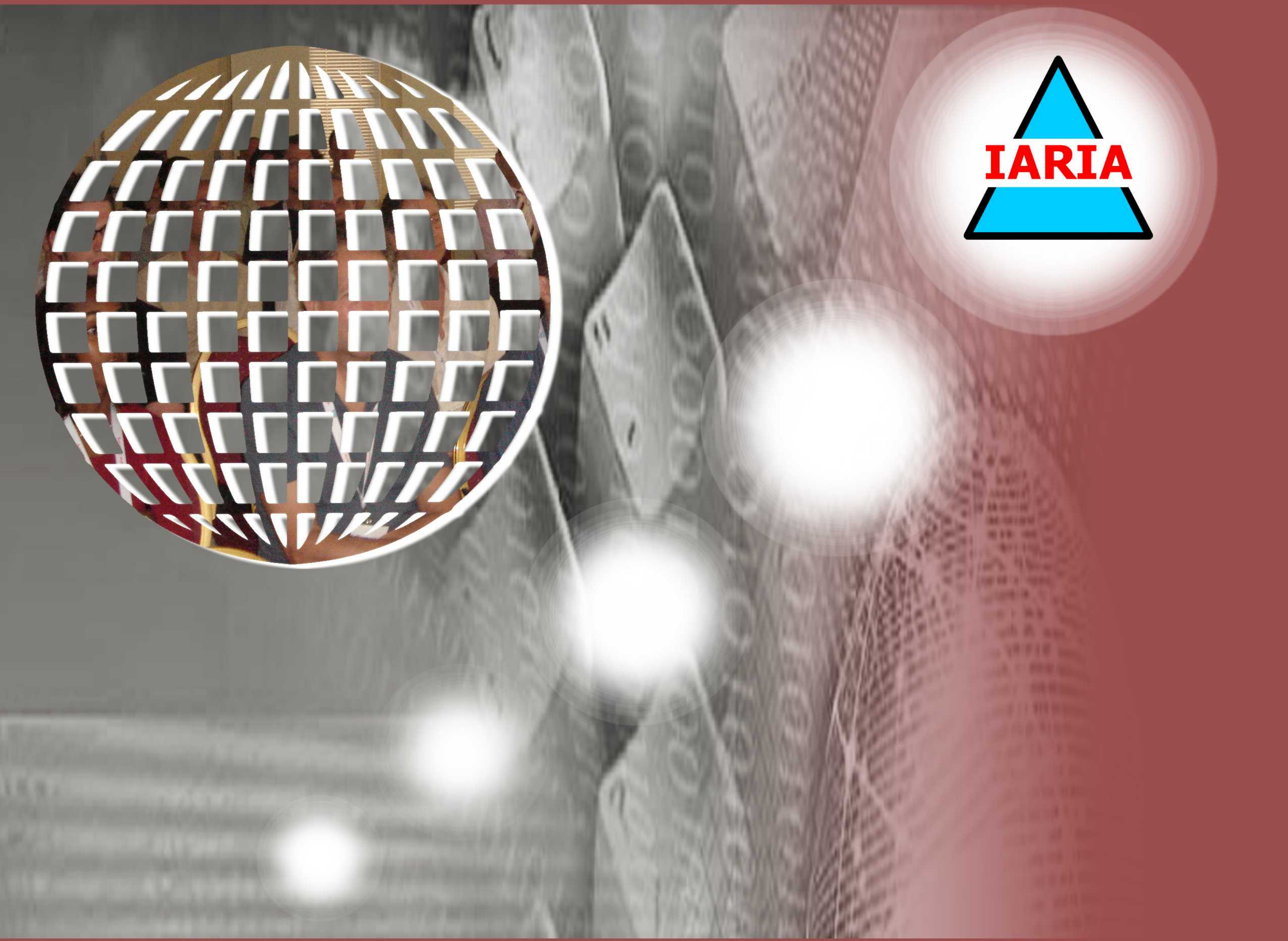

2011 vol. 4 nr. 1&2

The *International Journal on Advances in Telecommunications* is published by IARIA.
ISSN: 1942-2601
journals site: http://www.iariajournals.org
contact: petre@iaria.org

Sponsored by IARIA
www.iaria.org

International Journal on Advances in Telecommunications
Volume 4, Number 1 & 2, 2011

- Tulin Atmaca, IT/Telecom&Management SudParis, France
- Claus Bauer, Dolby Systems, USA
- Claude Chaudet, ENST, France
- Gerard Damm, Alcatel-Lucent, France
- Michael Grottke, Universitat Erlangen-Nurnberg, Germany
- Yuri Ivanov, Movidia Ltd. – Dublin, Ireland
- Ousmane Kone, UPPA - University of Bordeaux, France
- Wen-hsing Lai, National Kaohsiung First University of Science and Technology, Taiwan
- Pascal Lorenz, University of Haute Alsace, France
- Jan Lucenius, Helsinki University of Technology, Finland
- Dario Maggiorini, University of Milano, Italy
- Pubudu Pathirana, Deakin University, Australia
- Mei-Ling Shyu, University of Miami, USA

Communication Theory, QoS and Reliability

- Eugen Borcoci, University "Politehnica" of Bucharest (UPB), Romania
- Piotr Cholda, AGH University of Science and Technology - Krakow, Poland
- Michel Diaz, LAAS, France
- Ivan Gojmerac, Telecommunications Research Center Vienna (FTW), Austria
- Patrick Gratz, University of Luxembourg, Luxembourg
- Axel Kupper, Ludwig Maximilians University Munich, Germany
- Michael Menth, University of Wuerzburg, Germany
- Gianluca Reali, University of Perugia, Italy
- Joel Rodriques, University of Beira Interior, Portugal
- Zary Segall, University of Maryland, USA

Wireless and Mobile Communications

- Tommi Aihkisalo, VTT Technical Research Center of Finland - Oulu, Finland
- Zhiquan Bai, Shandong University - Jinan, P. R. China
- David Boyle, University of Limerick, Ireland
- Bezalel Gavish, Southern Methodist University - Dallas, USA
- Xiang Gui, Massey University-Palmerston North, New Zealand
- David Lozano, Telefonica Investigacion y Desarrollo (R&D), Spain
- D. Manivannan (Mani), University of Kentucky - Lexington, USA
- Himanshukumar Soni, G H Patel College of Engineering & Technology, India
- Radu Stoleru, Texas A&M University, USA
- Jose Villalon, University of Castilla La Mancha, Spain
- Natalija Vlajic, York University, Canada
- Xinbing Wang, Shanghai Jiaotong University, China
- Ossama Younis, Telcordia Technologies, USA

Systems and Network Communications

- Fernando Boronat, Integrated Management Coastal Research Institute, Spain
- Anne-Marie Bosneag, Ericsson Ireland Research Centre, Ireland

- Huaqun Guo, Institute for Infocomm Research, A*STAR, Singapore
- Jong-Hyouk Lee, INRIA, France
- Elizabeth I. Leonard, Naval Research Laboratory – Washington DC, USA
- Sjouke Mauw, University of Luxembourg, Luxembourg
- Reijo Savola, VTT, Finland

Multimedia

- Dumitru Dan Burdescu, University of Craiova, Romania
- Noel Crespi, Institut TELECOM SudParis-Evry, France
- Mislav Grgic, University of Zagreb, Croatia
- Christos Grecos, University of Central Lancashire, UK
- Atsushi Koike, Seikei University, Japan
- Polychronis Koutsakis, McMaster University, Canada
- Chung-Sheng Li, IBM Thomas J. Watson Research Center, USA
- Artur R. Lugmayr, Tampere University of Technology, Finland
- Parag S. Mogre, Technische Universitat Darmstadt, Germany
- Chong Wah Ngo, University of Hong Kong, Hong Kong
- Justin Zhan, Carnegie Mellon University, USA
- Yu Zheng, Microsoft Research Asia - Beijing, China

Space Communications

- Emmanuel Chaput, IRIT-CNRS, France
- Alban Duverdier, CNES (French Space Agency) Paris, France
- Istvan Frigyes, Budapest University of Technology and Economics, Hungary
- Michael Hadjitheodosiou ITT AES & University of Maryland, USA
- Mark A Johnson, The Aerospace Corporation, USA
- Massimiliano Laddomada, Texas A&M University-Texarkana, USA
- Haibin Liu, Aerospace Engineering Consultation Center-Beijing, China
- Elena-Simona Lohan, Tampere University of Technology, Finland
- Gerard Parr, University of Ulster-Coleraine, UK
- Cathryn Peoples, University of Ulster-Coleraine, UK
- Michael Sauer, Corning Incorporated/Corning R&D division, USA

Additional reviewers

- Vassilis Stylianakis, ECE, University of Patras, Greece

International Journal on Advances in Telecommunications
Volume 4, Numbers 1 & 2, 2011

CONTENTS

A Comparison of the Performance of Prediction Techniques in Curtailing Uplink Transmission and Energy Requirements in Mobile Free-Viewpoint Video Applications

Clifford De Raffaele and Carl James Debono
Department of Communications & Computer Engineering
University of Malta
Msida, MSD 2080, Malta
cderaffaele@ieee.org and c.debono@ieee.org

Abstract - **The rapid deployment of multimedia services on mobile networks together with the increase in consumer demand for immersive entertainment have paved the way for innovative video representations. Amongst these new applications is free-viewpoint video (FVV), whereby a scene is captured by an array of cameras distributed around a site to allow the user to alter the viewing perspective on demand, creating a three-dimensional (3D) effect. The implementation on mobile infrastructures is however still hindered by intrinsic wireless limitations, such as bandwidth constraints and limited battery power. To this effect, this paper presents a solution that reduces the number of uplink requests performed by the mobile terminal through view prediction techniques. The implementation and performance of four distinct prediction algorithms in anticipating the next viewpoint request by a mobile user in a typical FVV system are compared and contrasted. Additionally, each solution removes the jitter experienced by the user whilst moving from a view pattern to another by allowing some hysterisis in the convergence signal. Thus, this technique enhances the performance of all the algorithms by taking into consideration the fact that the user adapts to the presented views and will react accordingly. Simulation results illustrate that an uplink transmission reduction of up to 96.7% can be achieved in a conventional FVV simulation scenario. Therefore, the application of prediction schemes can drastically reduce the mobile terminal's power consumption and bandwidth resource requirements on the uplink channel.**

Keywords - Free-Viewpoint; Multiview video; Prediction algorithms; Wireless transmission.

I. INTRODUCTION

Video streaming solutions have experienced endless development in the course of time, from a relatively poor image quality, as far as the human senses are concerned, to forms of presentation which strive to present an increasingly better quality of experience [2], [3]. Driven by technological developments, the drastic reduction in the cost of imaging hardware equipment, together with the intensification of clientele expectations, the interest in interactive multiview services has augmented from academic and industrial perspectives alike [4]–[6]. Multiview video technologies provide the potential for innovative applications to be developed in order to facilitate and enhance the experience of scenes from a 3D perspective without the burden of restricting hardware [7], [8]. The latter feature, aids the commercial implementation of such a technology, especially in the end user entertainment market, by systems such as Free-Viewpoint television (FTV) [9].

Free-Viewpoint Video (FVV) provides the potential to expand the viewers experience far beyond what is presented by current conventional multimedia systems [10]. In such an innovative visual media technology, the user can observe a three-dimensional panoramic scene by freely changing perspective [11], [12]. Acquisition techniques for the realization of FVV entail a unique scene captured from multiple views via the deployment of a number of cameras distributed around the site, [13], as portrayed in Fig. 1. The hardware needed for multi-camera systems and for displays is rapidly developing, with new solutions being experimentally deployed [7], [9], [14], and [15].

Architectures that utilize a dense scene capturing framework can render a more complete FVV experience to the user. Nevertheless, feasibility constraints demand that the amount of scene sampling hardware employed is restricted [16], as this presents a linear increase in raw video data that necessitates processing [17]. In addition, spatial proximity of cameras must adhere to the physical limitations of the equipment [18]. Thus, the sole method for FVV viewers to observe a video stream of uninterrupted standpoints without being constrained to the actual camera locations is by the adoption of Video Based Rendering (VBR) techniques [19]. These methodologies apply computationally intensive Intermediate View Rendering (IVR) algorithms to synthesize virtual viewpoints between actual cameras as illustrated in Fig. 1. This process is therefore compulsory to provide gradual view changes in perspective from one actual camera location to another and its quality is directly responsible for the vividness of FVV experience [20].

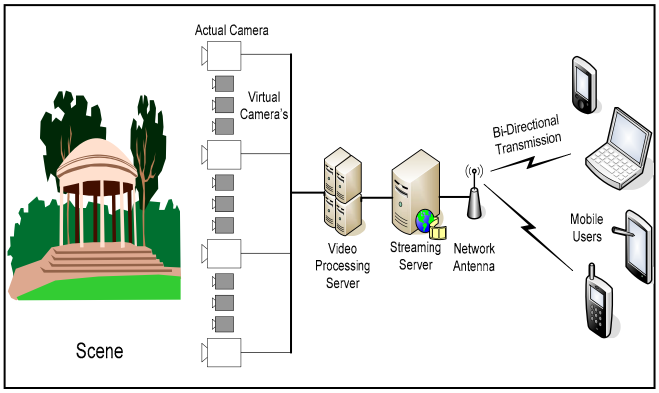

Figure 1. Block diagram of the entire system representing the scene being captured by multiple cameras, video-based rendering servers, the streaming server, and the wireless network.

Simultaneous to the advancements registered in multimedia, the field of mobile computing has witnessed a parallel growth rate. Nowadays, emerging mobile client devices are all fitted with a liquid crystal display screen and sufficient processing power to allow real-time presentation of multimedia information [21]. A similar trend is furthermore witnessed in the infrastructure of emerging and future wireless systems, which provide sufficient bit rates for the implementation of video communication applications [14]. Thus, this opens the way for motion video to become one of the major multimedia applications [6]. Nonetheless, this technology imparts a significant burden on the network infrastructure due to its strict latency requirements and wireless bandwidth restrictions. Furthermore, the harsh wireless transmission environment presents a supplementary range of peculiar technical challenges such as attenuation, fading, multi-user interference and spatio-temporal varying channel conditions [22]. Such issues, together with current business models in wireless systems, whereby the end-user's costs are proportional to the reserved bit-rate or the number of bits transmitted over a radio link [23], drive future multimedia network systems to provide a more efficient framework for the deployment of services.

A further impediment encountered in the implementation of FVV technology is intrinsic to mobile devices, since the latter are severely constrained in energy resources, storage capacity and processing power [24]. The combination of these obstacles makes the transmission of several views for virtual viewpoint rendering at the mobile terminal impractical under several perspectives. Thus, a sensible implementation for FVV is to implement real-time video-based rendering (VBR) techniques on customized processing architectures at the server's side and transmit only the required view to the mobile terminal [25], [26]. Inherently, this strategy demands the implementation of a feedback channel from the mobile device to request the required view perspective stipulated by the user. This necessitates that a request is made on the uplink channel at every video frame interval to request a perspective view. Alas, such a situation leads to substantial service delays, bandwidth usage and terminal power consumption.

This paper builds on [1] to present a solution which reduces the amount of feedback transmissions generated by the mobile terminal during free-viewpoint operation. Several prediction strategies are thoroughly investigated for adoption on the multimedia server to forecast the ensuing user's view request. The algorithms necessitate that feedback uplink packets are only sent when the received perspective does not match the users demand viewpoint. Hence, the server interprets the lack of feedback as a confirmation that the correct estimate was transmitted. If a feedback packet is received, the server is notified of the viewpoint prediction error, at which point the algorithm is retrained to converge to the new FVV pattern. Such a strategy presents the infrastructure with a reduced amount of transmission from the mobile terminals, which in turn preserves their battery power and reduces the uplink bandwidth utilization. The algorithms implemented also manage to minimize the round-trip delays incurred by the system due to the otherwise continuous transmissions on the uplink channel.

This paper is organized as follows; the prediction algorithms studied in this work are examined and discussed in Section II together with the details on the respective parameters employed. Section III discusses the implementation strategy adopted for each algorithm. Following this, Section IV presents the simulation results and highlights the curtailment in feedback transmission attained by each solution. To further aid understanding, this section also gives a quantitative measure description of the battery power saved. Finally, comments and conclusions are presented in Section V.

II. Viewpoint Prediction Algorithms

The successful implementation of prediction algorithms for system behavior estimation demands the utilization of a subset of the observed readings acquired previously from the system, to construct the original set of data within some pre-defined precision tolerance [27]. Viewpoint prediction is achieved by exploiting a combination of received data from the feedback channel, preceding data predictions, and a priori knowledge of the system's operation methodology. This work studies and compares the performance of the following four algorithms; Least Mean Squares, Kalman Filter, Recursive Mean Square, and Linear Regression, adopted specifically for FVV application in an effort to reduce uplink transmission requests and increase the battery lifetime of mobile terminals.

A. *Least Mean Square Algorithm*

Originally proposed in [28], the least mean square (LMS) algorithm consists of an iterative process of successive corrections on a weight vector which ultimately lead to the minimum square error between the received and derived signals. The algorithm provides several advantages for implementation in real-time scenarios particularly due to its low computational complexity. Furthermore, inherent to its iterative nature, the algorithm is suitable for slow time-varying environments since it exhibits a stable and robust performance [29].

The general function of the LMS algorithm is defined as:

$$\hat{x}(n) = \sum_{i=1}^{N} w_i(n) \times x(n-i) \qquad (1)$$

where $\hat{x}$ denotes the estimated input signal n, w_i represents the current system weight vector, and $x(n-i)$ corresponds to the set of delayed inputs.

In order to derive the prediction error, $e(n)$, the estimated value is subtracted from the real input value $x(n)$:

$$e(n) = x(n) - \hat{x}(n) \qquad (2)$$

The system weight vector is then modified using:

$$w(n+1) = w(n) + \mu x(n)e(n) \qquad (3)$$

As can be seen in (3), the rate of adaptation of the algorithm is directly dependent on the step size μ, which influences the speed of convergence, and on the order of the algorithm *N*. The computational complexity for executing each iteration can be summarized as $2N+1$ multiplications and $2N$ additions. After simulation trials, a value of five filter weights was deemed apt, as this was able to sufficiently restrain the processing load whilst still providing sufficient precision as to avoid excessive overshoots whilst the filter weight vectors were converging to the reference signal. The values for learning rate variable μ were determined through heuristic techniques. This parameter was furthermore adapted during run-time by initially assigning a large value to speed up convergence towards the reference signal, and then decrease it to a more temperate one, to reduce overshoot and allow more precise corrections as the weight vectors approach convergence.

B. Kalman Filter Algorithm

The Kalman Filter introduced in [30] is primarily a recursive algorithm notably suitable to address the estimation problem for linearly evolving systems [31]. Apart from its practical demands being apposite for real-time applications, a convergence to a stable steady state is guaranteed by the filter [32].

Prediction of the forward state is performed by multiplying the current system state x_k with the state transition matrix *A* as illustrated in (4):

$$\hat{x}_{k+1} = A \times x_k \qquad (4)$$

The Kalman filter also forecasts the predicted error covariance and makes use of this value together with an observation matrix *H* to compute the Kalman gain *K*. Following the acquisition of a measurement of the system output z_k, this is used to update the estimate value x_{k+1} using:

$$x_{k+1} = \hat{x}_{k+1} + K\left(z_k - H\hat{x}_{k+1}\right) \qquad (5)$$

The obtained positional measurement of the scene is compared with the previous value, and since the measurements are done within constant time intervals, the view change request rate can be calculated. This new value is employed to update the input vector x_{k+1}. Finally, the error covariance is amended for the next iteration.

C. Recursive Least Square Algorithm

The Recursive Least Square (RLS) algorithm aims at achieving the minimization of the sum of squares difference between the modeled filter output and the desired signal [33] by calculating the optimum filter weights. This is attained using an exponentially weighted estimate of the input autocorrelation and cross-correlation [34]. Owing to the prediction filter nature of the algorithm, the learning mode operation entails an iterative process whereby current weight vectors are used to generate data prediction in the future, and subsequently measurement data is considered as reference for updating the internal weight vectors.

An intrinsic property of the adapted RLS is the capability to pursue fast convergence in time-varying environments even in cases where the eigenvalue spread of an input signal correlation matrix is large [35]. Unfortunately, the latter benefit is achieved at the cost a substantial increase in complexity, which during implementation has an order of $\mathcal{O}(N^2)$ FLOPS per sample, with *N* being the filter length [36], and an increased sensitivity to mismatch is registered in comparison to the structurally similar least square algorithm [37]. When new samples of the incoming signal are received, the coefficient vector updates the solution for the least squares problem in recursive form using [38]:

$$\underline{w}(k+1) = \underline{w}(k) + \underline{g}(k)e(k), \qquad (6)$$

where $w(k)$ is the coefficient vector of the adaptive filter at time *k*, *N* is the length of the latter vector, $e(k)$ symbolizes the difference between the generated filter output and the desired signal, and $g(k)$ represents the Kalman gain. To render the algorithm feasible for real-time applications, and thus reduce the computational cost incurred by the RLS to execute the necessary matrix manipulations upon every epoch, the matrix inversion lemma technique [33] is applied to obtain a simple update for the inverse of the data input equation:

$$P^{-1}(k) = \frac{1}{\lambda}\left[P^{-1}(k-1) - \underline{g}(k)\underline{x}^T(k)P^{-1}(k-1)\right], \qquad (7)$$

where $x(k)$ is the input data vector, and $\lambda \in (0,1]$ is called the forgetting factor. This parameter has direct influence on the memory of the algorithm, with the upper bound value of unity assigned to imply infinite memory and is hence only suitable for statistically stationary systems. The algorithm contains no a priori information on the system at initialization, thus, an approximate initialization technique is employed for the covariance matrix by setting $P^{-1}=\delta I$, which is representative of a scaled version of the identity matrix [38].

D. Linear Regression Algorithm

The statistical method defined by the Linear Regression (LR) algorithm is capable of modeling the relationship between two or more variables, by deriving a linear equation to fit the observed data using a least squares metric [39]. The implementation of a linear model provides several advantages for a real-time system, particularly due to its computational simplicity and inherent ease of use [40]. The validity of this statistical technique is held under the assumption that the output has a linear dependence on the input [41], thus the system model can be composed in the form:

$$\hat{Y} = \beta_1 \times X + \beta_0 + \varepsilon, \quad (8)$$

where the output predicted value $\hat{Y}$ is expressed for a given dependent variable input X. The additional amount ε represents the residual error from the regression line, whilst the variables in the model function β_0 and β_1 are referred to as the model parameters and are estimated from a training set of n observations, in the form of $(X_1,Y_1),(X_2,Y_2),\ldots,(X_n,Y_n)$, using [42]:

$$\beta_1 = \frac{\sum_{i=1}^{n}(X_i - \overline{X})\times(Y_i - \overline{Y})}{\sum_{i=1}^{n}(X_i - \overline{X})^2}, \quad (9)$$

$$\beta_0 = \hat{Y} - b_1 \times \overline{X}, \quad (10)$$

where the statistical values $\overline{X}$ and $\overline{Y}$ represent the means of the respective variables.

Equations (9) and (10) are only computed whilst the algorithm is operating in the training phase so that the model functions converge. Once the aforementioned parameters are established, the algorithm operates in offline mode, and the computational load for executing the LR algorithm on the server, is only that of computing a single multiplication and two additions to derive the predicted output.

III. Implementation of the Prediction Algorithms

The prediction techniques studied attempt to reduce the amount of feedback transitions necessary on the uplink channel. This is performed by combining a priori information regarding the system implementation together with dynamic data of the user's previous viewing motion to forecast the user's future observation points.

The characteristics of each algorithm are scrutinized and their implementation for the specific scenario presented in FVV is analyzed. The various parameters demanded by either technique are optimized in respect of the unique features of the FVV structure by applying heuristic approaches or taking into consideration the intrinsic nature of the system.

A. Least-Mean Square Algorithm

The LMS algorithm was implemented in a dual topology configuration were two identical adaptation algorithms were executed simultaneously on the mobile terminal and server alike. Implementation of the system involved the adoption of the LMS algorithm to estimate the view required by the user. The prediction of the desired perspective is achieved from interpretation of the preceding readings as well as the adapted LMS weight coefficients. Via this implementation, both sides of the network are able to generate equivalent estimates that keep the system synchronized whilst adapting to the dynamic user perspective demands.

At the mobile terminal, a comparison between the local predicted and the actual input readings is executed iteratively yielding a dynamic error assessment. When the current error in prediction exceeds a pre-defined tolerance threshold, the mobile terminal interprets the situation as a change in the user's input pattern. Although, by adapting the learning rate parameter during execution, the system quickly re-aligns its weight vectors to the new input pattern, the inconsistencies of the weight vectors during the conversion still allow for a suitable error signal to be detected by a comparator; hence triggering a change in the state of the network. In this situation, the mobile terminal attempts to re-synchronize its LMS algorithm with that of the server by training both filters for twenty iterations. During this period of online operation, the current user input pattern is considered as the reference signal, and transmitted to the server such that the weight vectors of both LMS algorithms converge to the new pattern.

Subsequent to the elapse of the training phase, both systems are turned offline again, whereby the reference signal for the local LMS algorithm is taken to be the former predicted value. During this state, provided that no new feedback from the mobile terminal is received at the server, the server assumes that its estimate is correct and thus transmits the predicted view. Via this methodology, the server is capable of tracking the predictions done by the mobile terminal without the requirement of constant transmission requests to update the current viewpoint state.

B. Kalman Filter Algorithm

The Kalman Filter system topology involved the implementation of the algorithm solely on the network server. The filter toggles between an online state and a stand-alone mode during operation. Initially, the mobile terminal commences by transmitting on the uplink channel a training sequence in order to converge the filter's output, computed at the broadcasting server node, to the pattern being viewed by the user. Following this initialization epoch, the algorithm converts its operation mode to a stand-alone state. In this form, the Kalman filter computes the prediction algorithm by utilizing the previous state vector values and error covalence as the observed measurement. In this way, the server forecasts the view number that would be demanded by the user and transmits the respective video perspective to the mobile terminal.

A comparison between the predicted and the actual input reading is executed on the mobile terminal during every iteration, yielding a dynamic error assessment. The latter value determines the state in which the system will operate by reference to a threshold error value. When the error value exceeds this limit, the mobile terminal transmits the first packet of data on the uplink, and subsequently the system implemented on the server node moves to online mode. In this training condition, the Kalman filter receives a sequence of the current user inputs for the desired viewpoint sequence as its reference signal from the mobile terminal via the feedback channel. An array of fifteen values is needed by the Kalman filter to converge to the new pattern of views. When the pre-defined amount of training iterations elapses, the system is redirected to offline stand-alone mode, where no information is required from the mobile terminal, thus reducing the feedback transmissions. In this mode, unless a transmission is received at the server, the previous prediction is considered as correct, and this computed value adopted as the observed measurement for the following epoch.

C. *Recursive Least Square Algorithm*

Similar to the Kalman filter infrastructure, the RLS system involves the adaptation of the algorithm on the server node to track the user demands for FVV viewing. Each time a discrepancy between the received view and the user's demanded one is noted, a training set composed of eight samples is transmitted from the mobile terminal. Upon receiving the initial feedback packet, the server turns the RLS algorithm in online mode and commences a training routine. A recursive approach is utilized during this period by the algorithm to adapt to the new linear viewing pattern. Following the successful convergence, the RLS algorithm is turned back offline, and the server predicts the views that will be demanded by the user using the algorithm's compiled values.

D. *Linear Regression Algorithm*

To track the FVV viewpoint user demands, the linear regression algorithm was also implemented solely on the server node. Due to the inherent nature of the FVV system operation, the algorithm was limited to a linear first-order model, to reduced complexity whilst still providing reliable accuracy in the regression line generated. Since observations done at the mobile terminal are inputted directly by the user, there are no sources of error during the acquisition of information. This feature was exploited to curtail the training set of measurements used by the algorithm to only two samples, which is the minimum amount of observations required for the LR algorithm to produce a robust regression line.

After training, the mobile terminal simply checks whether the received view matches that demanded by the user. If the prediction is correct, the mobile terminal refrains from transmitting feedback, and the server assumes that the estimate it has calculated is correct. Otherwise, feedback view information is delivered to the server which will wait for the second data packet to be transmitted before restarting the execution of the algorithm.

IV. Simulation and Results

Free-Viewpoint Video systems provide the user with the ability to autonomously decide upon the perspective that is observed in a particular scene. This level of interactivity intrinsically implies that a substantial amount of information is exchanged between the user and the host of the system. In the mobile video applications scenario, such data requirements entail bi-directional communication between the mobile terminal and the network server on the wireless infrastructure. Establishing such an infrastructure, demands bandwidth utilization to support both the streaming video sequences on the downstream as well as viewpoint requests on the uplink channel.

A. *Simulation Overview*

To objectively simulate and analyze the employment of the free-viewpoint structure embedded by the prediction algorithms, a typical situation was modeled using the Maltab® platform for two separate FVV usage profiles. It is assumed that the FVV user is not consistently changing views at a fast rate. Such a scenario is not practical as the user will not be able to follow the content of the video. Thus, our system considers the feasible implementation whereby users alter viewing patterns at a practical rate. The FVV system considered consisted of a number of adjacent cameras, which allowed the rendering of nine distinct virtual views in between each actual capturing location. These virtual views were generated on the server node and provided to the users upon demand, to enhance the FVV experience attained when altering the viewpoint between two locations by providing a gradual transition. The mobile terminal employs its user interface to display the video streams as well as receive input from the client as regards the viewpoint request. The latter is considered to be in the form of a vertical slider which allows the user to shift his view perspective between a finite number of cameras with an unrestricted range of motion speed as illustrated in Fig. 2.

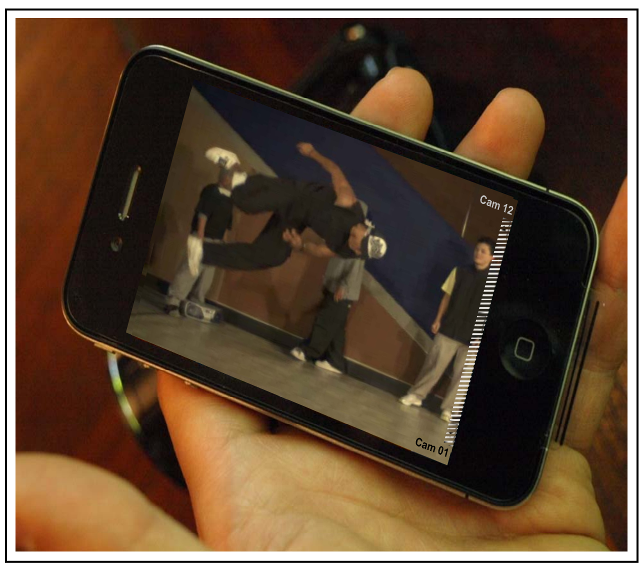

Figure 2. End-user mobile interface for free-viewpoint video streaming.

Figure 3. Linear free-viewpoint video motion from one perspective to another via consequent intermediate frames [43].

The simulated scenarios start with the user receiving a view from a single camera and not requesting any view changes. At an arbitrary point in time, the user starts changing the viewing angle at a particular velocity, thus performing free-viewpoint operation. Subsequently, this motion pattern will change casually, with each epoch having a different rate of change and duration of the varying FVV perspective. This results in a linear motion as illustrated in the video sequence shown in Fig. 3, whereby the change of perspective is gradual from one camera outlook to the next, and this can be modeled with lines of constant gradient [43].

The FVV simulated usage profiles can be described as: (i) pattern A which shows a velocity pattern in which free-viewpoint motion can be either static or else change with at least one virtual view per time step, and (ii) pattern B which shows a pattern whereby the user can scroll through views more leniently and hence take more than one time step to change from a virtual standpoint to a neighboring one. Due to the quantized nature by which view changes can be requested, the reference pattern generated by a user making requests similar to pattern B can introduce a jittered pattern of motion as depicted in Fig. 4. In this situation, the view will remain constant for a small period of time and then alter by the minimum quantized amount, giving the impression of a slow changing perspective. Thus, the speed for this scenario is proportional to the number of time steps in which the view remains constant between changes.

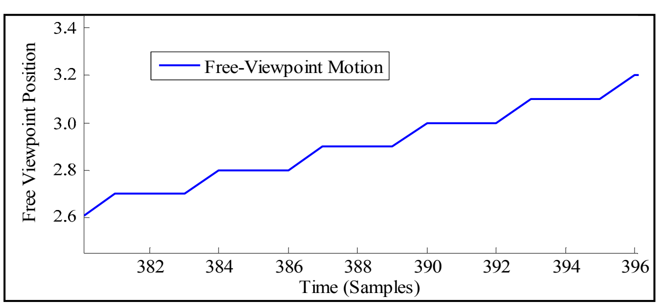

Figure 4. Free-viewpoint pattern which is slower than one virtual perspective per time frame

The performance evaluation of the proposed algorithms is compared to the system specifications described by the reference FVV architecture found in [25]. This reference methodology, whose view request profiles for patterns A and B are shown in Fig. 5(a) and Fig. 6(a) respectively, portrays the operation of an FVV system where the mobile terminal transmits to the server in each time step to demand the view being requested by the user. The server processes the requested viewpoint and transmits the perspective back to the terminal. The image from the modified outlook would then be viewed on the mobile terminal in the subsequent video time frame.

In order to further improve the FVV algorithms described in [1], a modified request pattern is employed at the server node for the prediction filters to converge too. This technique is adopted to eliminate the jitter experienced by the user during the first video-frame of a new FVV motion pattern. The utilized pattern achieves this by allowing some hysterisis on the signal, which results in delaying the user's request by a constant view separation. The latter is derived from the prediction errors generated by any of the algorithms upon motion pattern alteration, whereby for a particular time step, the received frame and that demanded by the user are not synchronized. With this enhanced approach, instead of converging directly to the user pattern, and hence yielding a nuisance jitter in FVV motion, the system, takes into consideration the video frames already viewed at the mobile terminal, and converges the algorithms to the modified signal, which directly reflects the same motion pattern evoked by the user's input. This amendment is able to significantly improve the quality of experience delivered to the client, by feasibly considering the implementation scenario and hence striving to smooth the free-viewpoint motion video received. Furthermore, the small delay registered is only of one video frame, usually 40 milliseconds, and thus goes unnoticed by the user who will naturally adapt to the viewed perspective pattern.

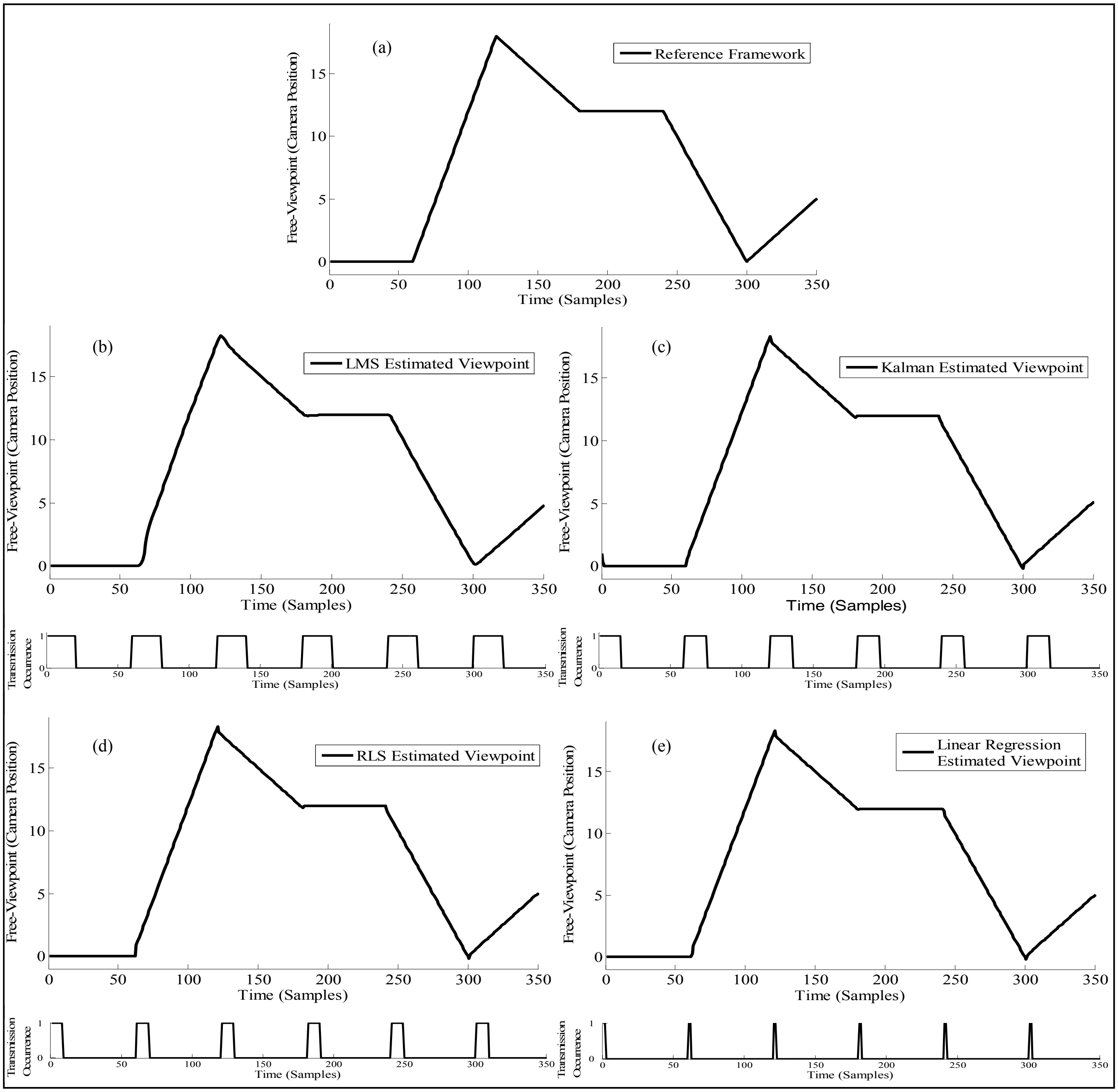

Figure 5. Simulation results and the associatae transmission occurrences comparing the proposed algorithms in a typical FVV scenario for pattern A: (a) reference user input, (b) Least Mean Squares, (c) Kalman Filter, (d) Recursive Least Squares, (e) Linear Regression.

B. *Analysis of Pattern A*

The simulation of the LMS for pattern A is presented in Figure 5(b). The inherent slow convergence speed of the algorithm is evident in the simulation results. The transmission occurrence signal, beneath the same figure, indicates that when the input view pattern was altered, the converged weights lost validity and hence yielded an error in the predicted viewpoint thereby re-initiating the training phase. Even though the learning rate parameter was adaptively modified in the initial stage of training, a certain amount of time steps have to elapse before the algorithm's internal memory buffers are occupied and all the weight vectors updated accordingly. Thus, the LMS algorithm necessitates the delay of an initial settling time before being employed successfully in FVV applications. Alas, the same compromise made on the parameter μ hinders the maximum frequency at which the system can alter the viewing pattern and the maximum change in gradient the system is able to adhere to.

With respect to the standard reference pattern, the LMS algorithm provides a considerable improvement in feedback transmission reduction. With a minimal increase on the computational resources of both the mobile terminal and the server, an average reduction of 65% in feedback transmissions is obtained. This technique thus reduces the traffic passed over the uplink channel from 350 transmissions to approximately 120 in the considered scenario.

The pattern A results for the Kalman Filter, illustrated in Fig 5(c), implicitly expose the benefits derived from the powerful adaptation of this algorithm. In comparison to the LMS technique, the initial convergence speed is greatly enhanced, drastically minimizing the necessary setup time. The Kalman filter algorithm, although inducing a significantly larger computational cost at the server, relieves the execution cost from the mobile terminal, which must only perform a comparison between the view perspectives received and those demanded by the viewer. The prediction properties of the latter methodology are also more robust requiring a set of only fifteen training samples to adapt to the new pattern with a significantly reduced error such that offline operation is sustained. This enables the system to sustain a higher frequency of change in view pattern in a stable manner. For the observed scenario, the Kalman filter solution results in an uplink transmission reduction of 74%.

Implementation of the Kalman filter on the server node is nonetheless a computationally complex task which poses imminent scalability issues. On the other hand, transmission occurrence was considerably reduced with respect to the LMS algorithm as this parameter inferred directly on the achievement of adopting prediction techniques. A compromise between these algorithms was found by the implementation of the RLS algorithm. The latter is able to adopt the advantages of the Kalman filter's convergence speed and robustness whilst attaining a reduction in implementation complexity.

The simulation results for the RLS algorithm on Fig. 5(d) illustrate that although the filter length was pruned to five as to conserve the memory footprint, convergence towards the desired output is still achieved at a satisfactory speed. In comparison to the LMS algorithm, the RLS implementation still requires a small number of training samples to be processed to fill the weight vector with relevant values of the new pattern. Nonetheless, the RLS algorithm can achieve a much quicker convergence to the reference signal as is evident from Fig. 5(d), where substantial convergence is achieved after the first couple of epochs. This benefit is mainly derived from the manipulation of the forgetting factor λ, which by means of adaptive variations can concentrate more heavily on the new input measurements whilst allocating less influence to the irrelevant values. The recursive nature of the algorithm also aids to provide a stable convergence, as was a principle advantage in the Kalman Filter. The same feature however, presents the need for an additional amount of samples to be computed prior to running the RLS algorithm in offline mode. Nevertheless, this technique allows the algorithm to converge successfully after processing only eight training samples. Over the considered typical input pattern scenario, the RLS is able to yield an efficiency gain of 87% over the standard architecture defined in [25], whilst requiring a notably reduced computational cost with respect to the Kalman Filter implementation.

The final investigated solution employs the Linear Regression algorithm on the server to predict the desired view sequences requested by the user. The results in Fig. 5(e) implicitly expose the benefits derived from the adaptation characteristics of this algorithm. Instead of attempting to predict the next viewpoint, this LR implementation predicts the velocity by which the viewpoints are changing between defined video time steps, thus generating a regression line which indicates the rate of change demanded by the user. When comparing the results of the LR algorithm to those attained by the previous filter algorithms for the pattern A, it is evident that the Linear Regression considerably outperforms the former. The algorithm converges faster than its counterparts to the desired signal output, since it takes direct advantage of the linear nature in which the FVV viewpoint is altered. Hence for the same scenario, the LR algorithm registered a decrease in the transmission requirements by the mobile terminal of 96.5% compared to the standard, and requires only 12 transmissions throughout the 350 time steps.

C. *Analysis of Pattern B*

Moreover, the performance enhancement of the LR algorithm is even further pronounced in the scenario expressed with input pattern B. This usage profile, visualized in the simulation results of Fig. 6, depicts the futile efforts performed by the LMS, Kalman Filter and RLS algorithms in Fig. 6(b), Fig. 6(c) and Fig. 6(d) respectively. The latter struggle to adapt to the stepped motion pattern of this scenario, resulting in a large amount of prediction failures and subsequent re-initiation of training epochs. The periodic gradient change presents the filters with an input sample incoherent with the previous stationary samples, yielding the algorithms to incorrectly update their weight vector.

The LR algorithm however, successfully manages to cope with the demand for slow free-viewpoint movement that is presented by pattern B. As evidenced in Fig. 6(e), when the algorithm detects a unitary gradient change subsequently followed by a stationary request, the implementation keeps track of the amount of time steps that the user spends on a fixed viewpoint between view changes by means of a dedicated counter. This information is used once an error is retransmitted by the mobile terminal, at which point the linear regression parameters are computed taking into account the new position and the previous samples. Since the system's FVV viewpoints are quantized in nature, the regression line generated performs well as the output is truncated to the resolution of the views. Hence, the algorithm is able to successfully predict any user's input pattern after a maximum of two error signals.

A consistent performance gain is also registered with the linear regression algorithm in the more flexible scenario represented by pattern B, were on average, the uplink transmission reduction achieved amounted to 92%.

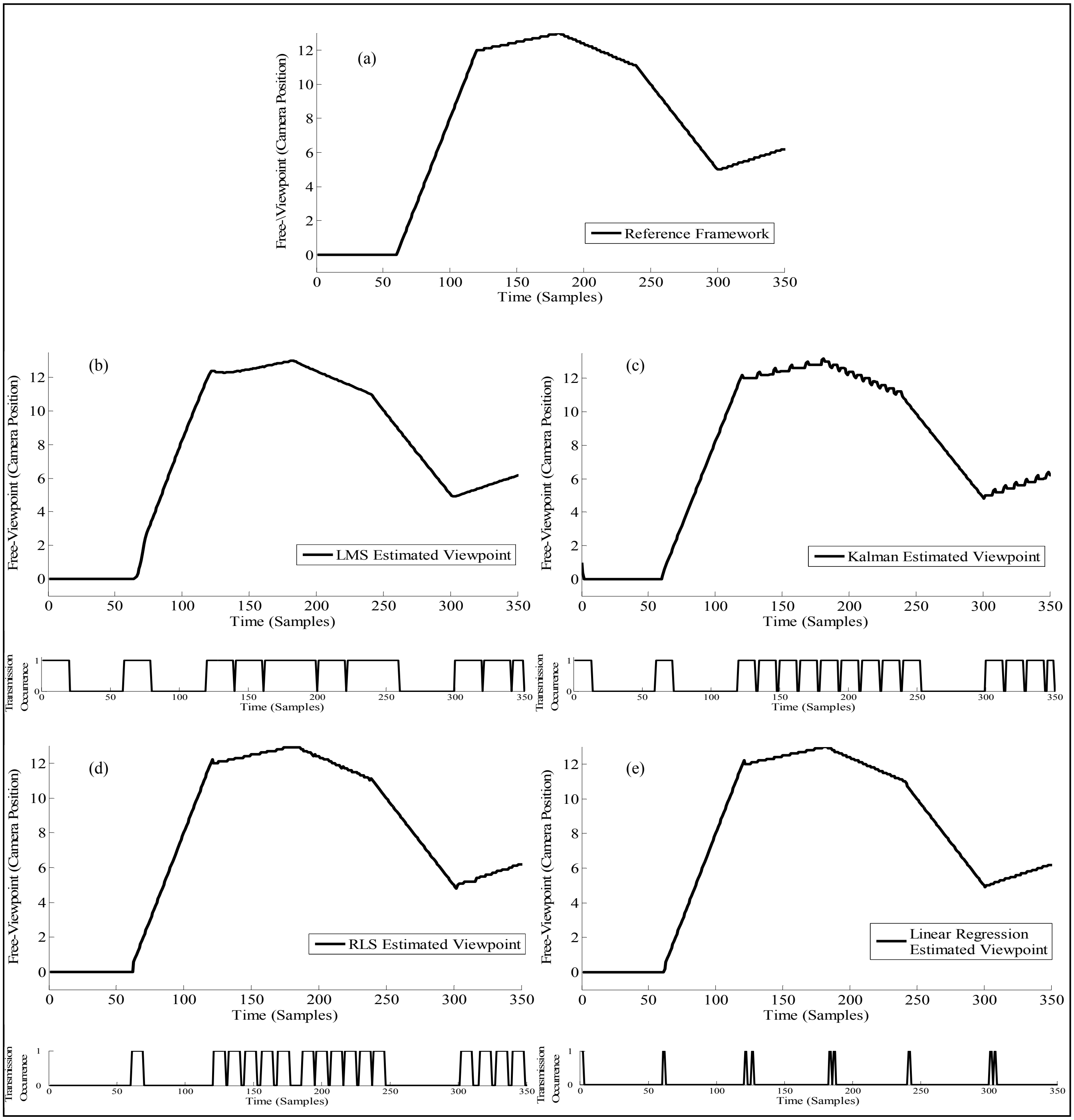

Figure 6. Simulation results and the associatae transmission occurrences comparing the proposed algorithms in a typical FVV scenario for Pattern B: (a) reference user input, (b) Least Mean Squares, (c) Kalman Filter, (d) Recursive Least Squares, (e) Linear Regression.

The small discrepancy between both scenarios adopting the LR algorithm is due to the additional transmissions required to cater for the slow movements in viewpoint patterns. Furthermore, since the LR algorithm necessitates only of a small amount of training samples to converge, this methodology is also able to better accommodate highly dynamic view pattern changes.

D. Battery Consumption Simulation

To obtain a quantitative analysis of the energy resources saved at the mobile terminal by the implementation of the proposed prediction algorithms, a simulation of the energy consumed by the transceiver operation of a mobile station employed only for FVV usage was performed. Although the proposed system is able to operate over any networking topology, a scenario involving a currently implemented wireless architecture was simulated so as to attain appreciation of the algorithm's performance.

The mobile device is considered to be equipped with a 1500mAh battery and consumes an average current of 25mA during transmission and an average current of 20mA during reception of data. The considered scenario is that of a terminal operating in a network employing HSPA technology with a downlink and uplink bandwidth of 7.2Mbits/s and 1.4Mbits/s respectively. The free-viewpoint operation requires a single packet of 50 bytes to send view requests and a mean of four 200 byte packets on the downlink channel. The transmitted data constitutes a continuous video stream in CIF standard resolution employing the H.264/AVC baseline profile.

The drastic reduction in the necessary transmissions on the uplink channel achieved by the employment of view prediction algorithms significantly reduces the battery power consumed by the mobile terminal during FVV operation, as shown in Fig. 7. Even though the amount of data which is transmitted on the uplink channel is much smaller than that of the received video, the energy saved is still significant for a resource limited device. This considerable drop in energy consumption occurs because the transmitter module is the most power hungry component of any mobile terminal. Furthermore, the prediction solutions enhance the Quality of Service (QoS) provided by the FVV system. This occurs because the algorithms offer a pro-active network implementation by predicting and providing the required view perspective to the user instantaneously, thus reducing the round-trip delays incurred by the reference method.

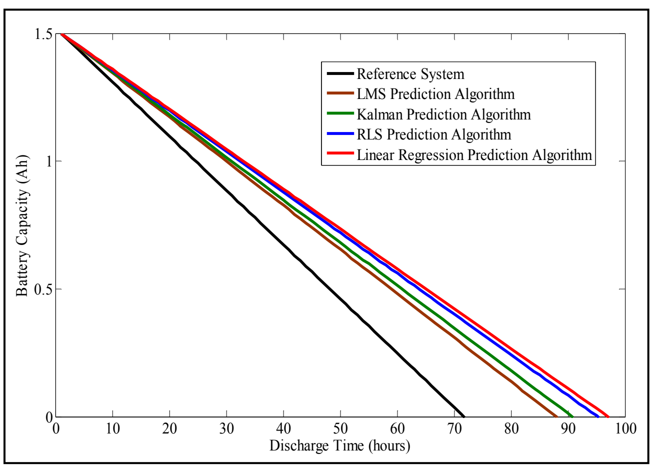

Figure 7. Comparison of the battery discharge time on a mobile terminal when adopting the prediction algorithms

V. Conclusion

This paper has presented a detailed study in the adaptation of prediction algorithms to free-viewpoint video technology to reduce the amount of uplink transmission. Four distinct algorithms were analyzed and implemented in several simulation scenarios representing typical FVV architectures. The minor increase in computational costs incurred at the server and/or mobile node are justified by a drastic reduction of up to 96.7% in the amount of feedback packets transmitted on the wireless uplink channel. The requests from the mobile client demanding a different perspective of the scene in a typical FVV usage profile are replaced by the server's predictions through one of the prediction algorithms. The benefits achieved from such systems enable a considerable gain in terms of power conservation for the multimedia mobile terminal as well as a reduced utilization of the uplink bandwidth. Moreover, hysterisis is introduced in the algorithm's converging pattern, making the real-time experience more pleasing and avoiding any video jitter being presented to the mobile client.

References

[1] C. De Raffaele and C.J. Debono, "Applying Prediction Techniques to Reduce Uplink Transmission and Energy Requirements in Mobile Free-Viewpoint Video Applications," in Proc. of the IARIA 2010 Second International Conference on Advances in Multimedia (MMEDIA 2010), pp. 55-60, Jun 2010.

[2] C. Fehn, P. Kauff, M. Op de Beeck, F. Ernst, W.I. Jsselsteijn, M. Pollefeys, L. Van Gool, E. Ofek, and I. Sexton, "An Evolutionary and Optimised Approach on 3D-TV," in Proc. of Int. Broadcast Conf., pp. 357–365, Amsterdam, Netherlands, 2002.

[3] J. Lim, J. Kim, K.N. Ngan, and K. Sohn, "Advanced Rate Control Technologies for 3D-HDTV," in IEEE Trans. on Consumer Electronics, vol. 49, no. 4, pp. 1498-1506, Nov. 2003.

[4] S.U. Kum, and K. Mayer-Patel, "Intra-Stream Encoding for Multiple Depth Streams," in Proc. of the 16th Int. Workshop on Network and Operating Systems Support for Digital Audio and Video, pp. 62–67, Newport, USA, May 2006.

[5] S. Tan, A. Aksay, C. Bilen, G.B. Akar, and E. Arikan, "Error Resilient Layered Stereoscopic Video Streaming," in Proc. of the Int. Conf. on True Vision Capture, Transmission and Display of 3D Video, pp. 1–4, Kos Island, Greece, May 2007.

[6] A. Kubotka, A. Smolic, M. Magnor, M. Tanimoto, T. Chen, and C. Zhang, "Multiview Imaging and 3DTV," in IEEE Signal Process Mag., vol. 24, no. 6, pp. 10–21, Nov. 2007.

[7] J. Konrad and M. Halle, "3-D Displays and Signal Processing," in IEEE Signal Processing Mag., vol. 24, no. 7, pp. 97–111, Nov. 2007.

[8] H. Kalva, L. Christodoulou, L. M. Mayron, O. Marques, and B. Furht, "Design and Evaluation of a 3D Video System Based on H.264 View Coding," in Int. Workshop on Network and Operating Systems Support for Digital Audio and Video (NOSSDAV), pp. 12–12, May 2006.

[9] T. Fujii, and M. Tanimoto, "Free-Viewpoint TV (FTV) System," in Proc. of Pacific Rim Conf. on Multimedia, pp. 497-504, Tokyo, 2004.

[10] A. Smolic, H. Kimata, and A. Vetro, "Development of MPEG Standards for 3D and Free Viewpoint Video," in Proc. of the SPIE Conf. Optics East 2005: Communications, Multimedia & Display Technologies, vol. 6014, pp. 262–273, Nov. 2005.

[11] M. Tanimoto, M.P. Tehrani, T. Fujii, and T. Yendo, "Free-Viewpoint TV," in IEEE Signal Process Mag., vol. 28, no. 1, pp. 67–76, Jan. 2011.

[12] X. Guo, Y. Lu, F. Wu, W. Gao, and S. Li, "Free Viewpoint Switching in Multi-View Video Streaming using Wyner-Ziv Video Coding," in Proc. of SPIE Visual Communications and Image Processing 2006, vol. 6077, pp. 298–305, California, USA, Jan. 2006.

[13] A. Smolic, and P. Kauff, "Interactive 3D Video Representation and Coding Technologies," in IEEE Special Issue on Advances in Video Coding and Delivery, vol. 93, no. 1, Jan. 2005.

[14] J. Berent and P. Luigi Dragotti, "Plenoptic Manifolds," in IEEE Signal Processing Mag., vol. 24, no. 7, pp. 34–44, Nov. 2007.

[15] A. Vetro, W. Matusik, H. Pfister, and J. Xin, "Coding Approaches for End-to-End 3D TV Systems," in Proc. of the 23rd Picture Coding Symposium (PCS '04), pp. 319–324, San Francisco, California, USA, Dec. 2004.

[16] C. Zhang, L. Huo, C. Xia, W. Zeng, and W. Gao, "A virtual view generation method for free-viewpoint video system," in Proc. of the 2007 Int. Symp. on Intelligent Signal Processing and Communication Systems, Xiamen, 2007, pp. 361–364.

[17] S.U. Yoon, E.K. Lee, S.Y. Kim, and Y.S.Ho, "A Framework for Multi-View Video Coding using Layered Depth Images," in Proc. of the Pacific Rim Conf. on Multimedia, pp. 431–442, Jeju Island, Korea, 2005.

[18] J. Carranza, C.M. Theobalt, M. Magnor, and H.P. Seidel, "Free-Viewpoint Video of Human Actors," in ACM Trans. on Graphics, vol. 22, no. 3, pp. 569–577, Jul. 2003.

[19] V. Nozick and H. Saito, "On-Line Free-Viewpoint Video: From Single to Multiple View Rendering," in Int. Journal of Automation and Computing, vol. 5, no. 3, pp. 257–267, Jul. 2008.

[20] J. Starck, J. Kilner and A. Hilton, "Objective Quality Assessment in Free-Viewpoint Video Production," in Proc. 3DTV Conf.: The True Vision – Capture, Transmission and Display of 3D Video, pp. 225–228, Istanbul, 2008.

[21] T. Stockhammer, and M.M. Hannuksela, "H.264/AVC Video for Wireless Transmission," in IEEE Trans. Wireless Communications, vol. 12, pp. 6–13, Aug. 2005.

[22] T. Stockhammer, M.M. Hannuksela, and T. Wiegand, "H.264/AVC in Wireless Environments," IEEE Trans. Circuits and Systems for Video Technology, vol. 13, pp. 657–673, Jul. 2003.

[23] T. Stockhammer, and T. Wiegand, "H.264/AVC for wireless applications," in Proc. of the IEEE Inter. Workshop on Mobile Multimedia Communications, Munich, 2003.

[24] H.K. Arachchi, and W.A.C. Fernando, "H.264/AVC in mobile environment: a review," SPIE Optical Engineering, vol. 44, pp. 097006.1–097006.7, Sep. 2005.

[25] J. Kwon, M. Kim, and C. Choi, "Multiview video service framework for 3D mobile devices," in Proc. of the Int. Conf. on Intelligent Information Hiding and Multimedia Signal Processing, pp. 1321–1234, Harbin, 2008.

[26] C.J. Debono and C. De Raffaele, "Minimizing Uplink Data in Wireless Free-Viewpoint Video Transmission Applications," in Proc. of the 2009 Third Int. Conf. on Next Generation Mobile Applications, Services and Technologies (NGMAST 2009), pp. 298-302, Cardiff, September 2009.

[27] C.J. Debono, and N.P. Borg, "The implementation of an adaptive data reduction technique for wireless sensor networks," in Proc. of the IEEE 8th Int. Symp. on Signal Processing and Information Technology, pp. 402–406, Sarajevo, 2008.

[28] B. Widrow, and M.E. Hoff, "Adaptive switch circuits," in IRE WESCON Convention Record, Vol. 55, part 4, pp. 96–104, New York, NY, USA, Aug. 1960.

[29] A. Zhang, and N. Gong, "A Novel Variable Step Size LMS Algorithm Based on Neural Network," in Proc. of the Int. Conf. on Intelligent Systems and Knowledge Engineering (ISKE 2007), Chengdu, China, Oct. 2007.

[30] R.E. Kalman, "A New Approach to Linear Filtering and Prediction Problems", in Trans. of the ASME- Journal of Basic Engineering, Vol. 82, pp. 35–45, Mar. 1960.

[31] S.S. Xiong, and Z.Y. Zhou, "Neural Filtering of Colored Noise Based on Kalman Filter Structure," in IEEE Trans. on Instrumentation and Measurement, vol. 52, no. 3, pp. 742–747, Jun. 2003.

[32] X. Huan, and S. Mannor, "A Kalman Filter Design Based on the Performance/Robustness Tradeoff," in Proc. of the 44th Annual Allerton Conf. on Communication, Control, and Computing, pp. 59–63, Sep. 2007.

[33] G.C. Goodwin, and R.L. Payne, Dynamic System Identification: Experiment Design and Data Analysis. Academic Press, New York, 1977.

[34] P.C. Wei, J.R. Zeidler, and W.H. Ku, "Adaptive recovery of a chirped signal using the RLS algorithm," IEEE Trans. Signal Processing. vol. 45, pp. 363–376, Feb. 1997.

[35] P.S.R. Diniz, Adaptive Filtering: Algorithms and Practical Implementation, 3rd ed. Springer Publishers, New York, 2008.

[36] Y.V. Zakharov, G.P. White, and J. Liu "Low-complexity RLS algorithms using dichotomous coordinate descent iterations," IEEE Trans. Signal Processing, vol. 56, pp. 3150–3161, Jul. 2008.

[37] Z. Tian, K.L. Bell, and H.L. Van Trees "A recursive least squares implementation for LCMP beamforming under quadratic constraint," IEEE Trans. Signal Processing. vol.49, pp. 1138–1145, Jun. 2001.

[38] S. Haykin, Adaptive Filter Theory 3rd ed. Prentice Hall, New Jersey, 1996.

[39] K.B. Song, S.K. Ha, J.W. Park, D.J. Kweon, and K.H. Kim, "Hybrid load forecasting method with analysis of temperature sensitivities," IEEE Trans. Power Systems, vol. 21, pp. 869–876, May 2006.

[40] M.R. Gupta, E.K. Garcia, and E. Chin, "Adaptive local linear regression with application to printer color management," IEEE Trans. Image Processing, vol. 17, pp. 936–945, Jun. 2008.

[41] A. Gu, and A. Zakhor, "Optical proximity correction with linear regression," IEEE Semiconductor Manufacturing, vol. 21, pp. 263–271, May 2008.

[42] N.R. Draper, and H. Smith, Applied Regression Analysis, 3rd ed. John Wiley & Sons Inc., New York, 1998.

[43] C. De Raffaele, "Efficient Transmission of Free-Viewpoint Video Services on Mobile Devices," *M.Sc. ICT Dissertation*, University of Malta, 2010.

Capacity Analysis and Simulation of 3-D Space-Time Correlated HAP-MIMO Channels

Emmanouel T. Michailidis and Athanasios G. Kanatas
Department of Digital Systems
University of Piraeus
Piraeus, Greece
{emichail, kanatas}@unipi.gr

***Abstract*—High-altitude platforms (HAPs) are one of the most promising alternative infrastructures for realizing next generation mobile communications networks. This paper utilizes a recently proposed three-dimensional (3-D) reference multiple-input multiple-output (MIMO) channel model for HAPs and investigates the capacity of spatially and temporally correlated HAP-MIMO channels. The effect of several parameters, such as the elevation angle of the platform, the configuration and displacement of the antenna arrays, the Doppler spread, and the 3-D non-uniform distribution of the local scatterers, on the capacity is studied. Based on the reference model, a 3-D sum-of-sinusoids (SoS) deterministic simulation model for HAP-MIMO channels is proposed. The results show that the simulation model is a good approximation of the reference model.**

Keywords-Capacity; 3-D scattering model; correlation; high-altitude platform (HAP); multiple-input multiple-output (MIMO) channel; Ricean fading; simulation

I. INTRODUCTION

Wireless communications services are traditionally provided by terrestrial and satellite systems. Terrestrial links are widely used to provide services in areas with complex propagation conditions, while satellite links are usually used to provide high-speed connections, where terrestrial infrastructure is not available. These systems represent two well established infrastructures that have been dominant in the telecommunications arena for years. Recently, an alternative wireless communications technology has emerged known as high-altitude platforms (HAPs) and has attracted considerable attention worldwide [1]-[6]. The term HAPs defines aerial platforms flying at an altitude of approximately 20 km above the ground, in the stratosphere. Among the frequency bands that the International Telecommunication Union (ITU) has licensed for communications through HAPs is the 2 GHz frequency band for mobile communications services [7].

The growing exigencies for spectral efficiency and higher data-rates have prompted the development of advanced physical layer techniques. Hence, it is crucial we apply and/or originate techniques in order to construct high-performance HAP-based systems. At these measures, the multiple-input multiple-output (MIMO) technology is a potential candidate, since it can significantly upgrade the performance of wireless communications networks and surpass the conventional single-input single-output (SISO) technology [8]-[11]. The performance of MIMO systems strongly depends on the channel characteristics, which are mainly determined by the antenna configuration and the richness of scattering. Therefore, the signals coming from HAPs to terrestrial stations are affected by the physical environment and the geometrical characteristics of the link.

Recently, the authors proposed a three-dimensional (3-D) geometry-based model for HAP-MIMO channels and justified its geometry [2]. In this paper, which is an extended and thorough version of [1], the reference model is utilized to analytically study the capacity of HAP-MIMO channels. Several parameters are considered, e.g., the elevation angle of the platform, the array configuration, the Doppler spread, and the 3-D non-isotropic distribution of the scatterers. The impact of each parameter on the capacity is separately examined and extensive numerical results are provided. The stratospheric winds may cause variations in the position of the platform [12][13]. Hence, this paper extends [1] and goes further to investigate the influence of any possible displacement of the HAP antennas on the channel capacity.

To the best of the authors' knowledge, there are no experimental data available in the literature to verify the theoretical results. However, simulation of fading channels in software is commonly used as opposed to field trials, because it allows for cost-effective and time-saving system analysis, design, test, and verification. The prime requirement of a simulation set-up is to capture the fading effects created by the radio channel and the goal of any simulation model is to properly reproduce the channel properties. Many different methods have been adopted for the simulation of fading channels. Among them, the sum-of-sinusoids (SoS) principle introduced by Rice [14] has been widely accepted by academia and industry as an adequate basis for the design of simulation models for cellular channels [15]-[17]. According to this principle, the overall channel waveform is the sum of several complex sinusoids having frequencies, amplitudes and phases that are appropriately selected to accurately approximate the desired statistical properties. Indeed, the complexity of the SoS-based models is typically reduced by cleverly choosing the model parameters to reduce the computation load. Furthermore, SoS-based models can be easily extended to develop simulation channel models for MIMO systems due to their explicit inclusion of spatial information, e.g., the multipath angles of arrival and departure.

Owing to these advantages, this paper proposes a 3-D deterministic SoS-based simulation model for HAP-MIMO channels. The deterministic models are easy to implement and have short simulation times. Specifically, they have fixed parameters for all simulation trials and converge to the desired properties in a single simulation trial leading to deterministic statistical properties [16]. The simulation results demonstrate the usefulness of the proposed simulation model.

The rest of the paper is organized as follows. Section II briefly reviews the 3-D reference model, while Section III describes the channel statistics. Section IV studies the HAP-MIMO channel capacity and provides numerical results. Section V details the deterministic simulation model and provides simulation results. Finally, concluding remarks are drawn in Section VI.

II. THE 3-D REFERENCE MODEL

This paper considers a downlink HAP-MIMO communication channel with n_T transmit and n_R receive omni-directional antenna elements at a quasi-stationary Stratospheric Base Station (SBS) and a Terrestrial Mobile Station (TMS), respectively. The antennas are numbered as $1 \le p \le q \le n_T$ and $1 \le l \le m \le n_R$, respectively. Frequencies well below 10 GHz are utilized. Hence, both line-of-sight (LoS) and non-line-of-sight (NLoS) links are considered, while rain effects are insignificant.

The geometrical characteristics of the reference model and the definition of the Cartesian coordinate system are discussed in Figures 1 and 2. Figure 1 shows the 3-D model for a 2×2 HAP-MIMO channel, while Figure 2 presents the projection of this model to the *x*-*y* plane. Based on this simple configuration, uniform linear arrays (ULAs) with an arbitrary number of antennas can be constructed. The *x*-axis is the line that connects coordinate origin O (centre of the projections of the SBS antenna elements to the *x*-*y* plane) and O' (lower center of the cylinder), while O_T and O_R represent the centers of the SBS and TMS arrays, respectively. The elevation angle of SBS relative to O_R is β_T and the heights of the SBS and TMS arrays are H_T and H_R, respectively. Then, the distance between O and O' is $D \approx H_T / \tan\beta_T$. The spacing between two adjacent antenna elements at the SBS and TMS is denoted by δ_T and δ_R, respectively, while a_{LoS}^{Rl} denotes the azimuth angle of arrival (AAoA) of the LoS paths. The angles θ_T and θ_R represent the orientation of the SBS and TMS antenna arrays respectively, and the angle ψ_R describes the elevation angle of the l^{th} TMS antenna element. Moreover, TMS is moving with speed v_R in the direction determined by the angle γ_R. It is assumed that $N \to \infty$ scatterers in the vicinity of the TMS are non-uniformly distributed within a cylinder of radius $R_{S,\max}$ and height $H_{S,\max}$ [2]. Then, the n^{th} scatterer is denoted by $S^{(n)}$, the distance between its projection to the *x*-*y* plane and O' is $R_S^{(n)} \in \left(0, R_{S,\max}\right]$, and its height is $H_S^{(n)} \in \left(0, H_{S,\max}\right]$. Finally, $a_T^{(n)}$ and $a_R^{(n)}$ denote the azimuth angle of departure (AAoD) of the waves that impinge on $S^{(n)}$ and the AAoA of the waves scattered from $S^{(n)}$, respectively.

The displacement due to the winds or pressure variations of the stratosphere is a major problem to be faced [12], [13]. In practice, there are 6 degrees of freedom to which HAPs are subjected. Specifically, HAPs may be displaced in any direction at a varying speed, and the displacements can be shifting along the *x*-, *y*-, and *z*-axes, as well as roll, pitch, and yaw. Considering that SBS antenna elements are installed along the SBS, rotation with respect to the *x*-axis corresponds to pitch, rotation on the *y*-axis corresponds to roll and rotation along *z*-axis corresponds to yaw (see Figure 1). Note that pitch corresponds to an elevation of the p^{th} SBS antenna element, which is described by the angle ψ_T. For ease of reference, the parameters of the reference model are summarized in Table I.

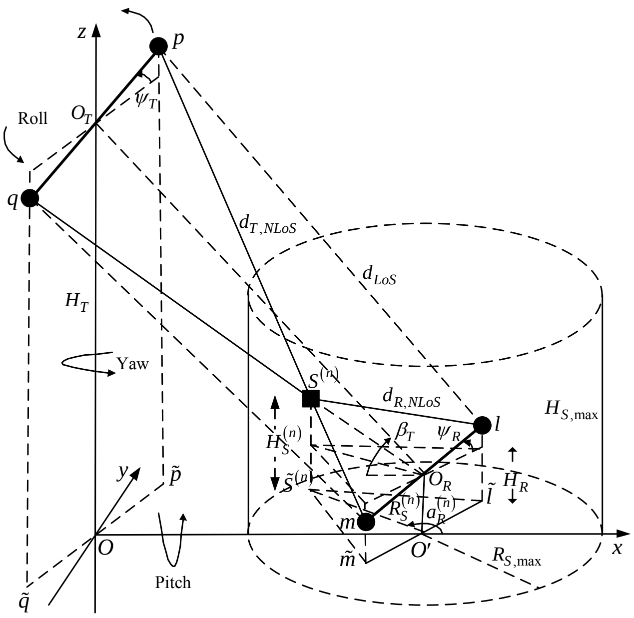

Figure 1. LoS and NLoS paths of the 3-D model for a 2×2 HAP-MIMO channel.

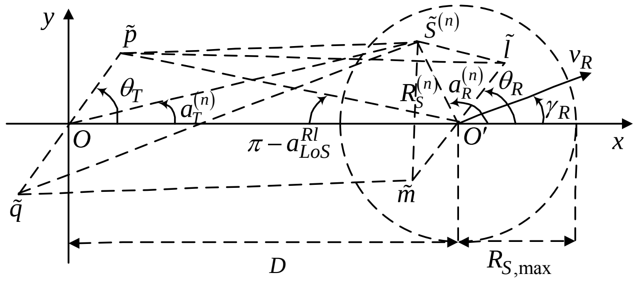

Figure 2. LoS and NLoS paths of the projection of the 3-D model to the x-y plane for a 2×2 HAP-MIMO channel.

TABLE I
DEFINITION OF THE MODEL PARAMETERS

D	The distance between the centre O of the projections of the SBS antenna elements to the x-y plane and the lower centre O' of the cylinder.
$R_{S,\max}$, $H_{S,\max}$	The radius and the height of the cylinder with the scatterers, respectively.
δ_T, δ_R	The spacing between two adjacent antenna elements at the SBS and TMS, respectively.
θ_T, θ_R	The orientation of the SBS and TMS antennas in the x-y plane (relative to the x-axis), respectively.
ψ_T, ψ_R	The elevation angle of the l^{th} TMS antenna element and the p^{th} SBS antenna element, respectively, relative to the x-y plane.
v_R	The velocity of the TMS.
γ_R	The moving direction of the TMS.
β_T	The elevation angle of the SBS relative to O_R.
H_T, H_R, $H_S^{(n)}$	The height of the SBS, the TMS, and the n^{th} scatterer, respectively.
a_{LoS}^{Rl}	The azimuth angle of arrival of the LoS paths.
$a_T^{(n)}$, $a_R^{(n)}$	The azimuth angle of arrival and the azimuth angle of departure at/from the n^{th} scatterer, respectively
$R_S^{(n)}$	The distance between O' and the projection of the n^{th} scatterer to the x-y plane.
$\varphi^{(n)}$	The random phase introduced by the n^{th} scatterer.
μ	The mean azimuth angle at which the scatterers are distributed in the x-y plane (von Mises distribution).
k	The spread of the scatterers around the mean azimuth angle (von Mises distribution).
a	The spread of the scatterers around the TMS (hyperbolic distribution).
$H_{S,\text{mean}}$	The mean of scatterer's height (log-normal distribution).
σ	The standard deviation of scatterer's height (log-normal distribution).

III. CHANNEL STATISTICS

A HAP-based communication channel is expected to be Ricean in its general form [3]. Hence, the impulse response $h_{pl}(t)$ of the sub-channel p-l is a superposition of the LoS and NLoS rays and is given by

$$h_{pl}(t) = \sqrt{\frac{K_{pl}}{K_{pl}+1}}h_{pl,LoS}(t) + \sqrt{\frac{1}{K_{pl}+1}}h_{pl,NLoS}(t), \quad (1)$$

where K_{pl} is the Ricean factor of the sub-channel p-l. The LoS and NLoS components of the impulse response, are expressed, respectively, as follows [2]

$$h_{pl,LoS}(t) = e^{-j\frac{2\pi}{\lambda}d_{LoS}} e^{-j2\pi t f_{R,\max}\cos\gamma_R}, \quad (2)$$

$$h_{pl,NLoS}(t) = \lim_{N\to\infty} \frac{1}{\sqrt{N}} \sum_{n=1}^{N} e^{-j\frac{2\pi}{\lambda}\left(d_{T,NLoS}+d_{R,NLoS}\right)}$$
$$\times e^{j\varphi^{(n)}} e^{j2\pi t f_{R,\max}\cos\left(a_R^{(n)}-\gamma_R\right)\cos\left[\arctan\left(H_S^{(n)}/R_S^{(n)}\right)\right]}, \quad (3)$$

where $f_{R,\max} = v_R/\lambda$ is the maximum Doppler frequency associated with TMS, λ is the carrier wavelength, and $\varphi^{(n)}$ is the random phase introduced by the n^{th} scatterer. Considering that $\left\{R_{S,\max},\delta_T\right\} \ll D$, $\delta_R \ll R_{S,\max}$, and $H_T \gg \left\{H_R, H_{S,\max}\right\}$, one can show that the distances d_{LoS}, $d_{T,NLoS}$, and $d_{R,NLoS}$ can be approximated as [2]

$$d_{LoS} \approx \frac{D}{\cos\beta_T} - \frac{0.5\left(n_T+1-2p\right)\delta_T\cos\theta_T\cos\psi_T}{\cos\beta_T} + \frac{0.5\left(n_R+1-2l\right)\delta_R\cos\theta_R\cos\psi_R}{\cos\beta_T}, \quad (4)$$

$$d_{T,NLoS} \approx \frac{D}{\cos\beta_T} - \frac{0.5\left(n_T+1-2p\right)\delta_T\cos\theta_T\cos\psi_T}{\cos\beta_T} - \frac{0.5\left(n_T+1-2p\right)\delta_T\sin\theta_T\cos\psi_T R_S^{(n)}\sin a_R^{(n)}}{D\cos\beta_T}, \quad (5)$$

$$d_{R,NLoS} \approx R^{(n)}/\cos\left[\arctan\left(H_S^{(n)}/R_S^{(n)}\right)\right] - 0.5\left(n_R+1-2l\right)$$
$$\times\delta_R\cos\psi_R\cos\left(\theta_R-\alpha_R^{(n)}\right)\cos\left[\arctan\left(H_S^{(n)}/R_S^{(n)}\right)\right]$$
$$-0.5\left(n_R+1-2l\right)\delta_R\sin\psi_R\sin\left[\arctan\left(H_S^{(n)}/R_S^{(n)}\right)\right]. \quad (6)$$

Since the number of local scatterers is infinite, central limit theorem implies that $h_{pl,NLoS}(t)$ is a lowpass zero-mean complex Gaussian process. Hence, the envelope $\left|h_{pl,NLoS}(t)\right|$ is Rayleigh distributed.

The space-time correlation function (STCF) between two arbitrary subchannels $h_{pl,NLoS}(t)$ and $h_{qm,NLoS}(t)$ is defined as

$$R_{pl,qm}^{NLoS}(\delta_T,\delta_R,\tau,t) = \mathrm{E}\left[h_{pl,NLoS}(t)\,h_{qm,NLoS}^{*}(t+\tau)\right], \quad (7)$$

where $(\cdot)^{*}$ denotes complex conjugate operation and $\mathrm{E}[\cdot]$ is the statistical expectation operator. The number of local scatterers in the reference model is infinite. Thus, the discrete variables $a_R^{(n)}$, $R_S^{(n)}$ and $H_S^{(n)}$ can be replaced with continuous random variables a_R, R_S and H_S with joint probability density function (pdf) $f(a_R,R_S,H_S)$. From Figure 1, the aforementioned variables are independent. Therefore, the joint pdf $f(a_R,R_S,H_S)$ can be decomposed to the product $f(a_R)\,f(R_S)\,f(H_S)$.

The experimentally verified von Mises pdf [18], [19] is used to characterize a_R and is defined as

$$f(a_R) = \frac{e^{k\cos(a_R-\mu)}}{2\pi I_0(k)},\ -\pi \le a_R \le \pi, \quad (8)$$

where $I_0(\cdot)$ is the zeroth-order modified Bessel function of the first kind, $\mu \in [-\pi,\pi]$ is the mean angle at which the scatterers are distributed in the *x*-*y* plane, and $k \ge 0$ controls the spread around μ. In addition, the experimentally verified hyperbolic pdf [20], [21] is used to characterize R_S and is defined as

$$f(R_S) = \frac{a}{\tanh(aR_{S,\max})\cosh^2(aR_S)},\ 0<R_S \le R_{S,\max}, \quad (9)$$

where $a \in (0,1)$ controls the spread of the scatterers around the TMS. Moreover, the experimentally verified log-normal pdf [22], [23] is used to characterize H_S and is defined as

$$f(H_S) = \frac{e^{-\frac{1}{2\sigma^2}\ln^2\left(\frac{H_S}{H_{S,\text{mean}}}\right)}}{H_S\sigma\sqrt{2\pi}},\ 0<H_S \le H_{S,\max}, \quad (10)$$

where $H_{S,\text{mean}}$ and σ are the mean and standard deviation of H_S, respectively. Finally, using (3) and (5)-(10), and the equality $\int_{-\pi}^{\pi} e^{a\sin(c)+b\cos(c)}dc = 2\pi I_0\left(\sqrt{a^2+b^2}\right)$ [24, eq.3.338-4], the STCF of the NLoS component is derived as follows

$$R_{pl,qm}^{NLoS} = \int_0^{H_{S,\max}}\int_0^{R_{S,\max}} x_1 I_0\left(\sqrt{x_2^2+x_3^2}\right) dR_S\,dH_S, \quad (11)$$

where

$$x_1 = \frac{a\cdot e^{j\frac{2\pi(q-p)\delta_T\cos\theta_T\cos\psi_T}{\lambda\cos\beta_T}}}{\sigma\sqrt{2\pi}\tanh(aR_{S,\max})I_0(k)} \times \frac{e^{-\frac{1}{2\sigma^2}\ln^2\left(\frac{H_S}{H_{S,\text{mean}}}\right)} e^{j\frac{2\pi(m-l)\delta_R\sin\psi_R\sin[\arctan(H_S/R_S)]}{\lambda}}}{H_S\cosh^2(aR_S)}, \quad (12)$$

$$x_2 = j\frac{2\pi(q-p)\delta_T\sin\theta_T\cos\psi_T R_S}{\lambda D\cos\beta_T} + j\frac{2\pi(m-l)\delta_R\sin\theta_R\cos\psi_R\cos[\arctan(H_S/R_S)]}{\lambda} - j2\pi\tau f_{R,\max}\sin\gamma_R\cos[\arctan(H_S/R_S)] + k\sin\mu, \quad (13)$$

$$x_3 = j\frac{2\pi(m-l)\delta_R\cos\theta_R\cos\psi_R}{\lambda}\cos[\arctan(H_S/R_S)] - j2\pi\tau f_{R,\max}\cos\gamma_R\cos[\arctan(H_S/R_S)] + k\cos\mu. \quad (14)$$

The double integral in (11) has to be evaluated numerically, since there is no closed-form solution.

IV. CAPACITY ANALYSIS OF 3-D HAP-MIMO CHANNELS

In this section, the HAP-MIMO channel capacity is defined and the utility of the reference model is demonstrated. Numerical results are provided and the influence of the model parameters on the capacity is studied.

It is assumed that the channel is known to the TMS and unknown to the SBS. Then, the HAP-MIMO channel capacity can be obtained from [9]

$$C = \log_2\det\left(\mathbf{I}_{n_R} + \left(\frac{SNR}{n_T}\right)\mathbf{H}\mathbf{H}^H\right) bps/Hz, \quad (15)$$

where $\mathbf{H}$ is the $n_R \times n_T$ channel matrix, $\mathbf{I}_{n_R}$ is an identity matrix of size n_R, SNR corresponds to the average receive signal-to-noise ratio, $(\cdot)^H$ denotes the complex conjugate (Hermitian) transpose operator, and $\det(\cdot)$ denotes the matrix determinant. Throughout this paper, the notion of ergodic capacity is also employed, which corresponds to the expectation of the instantaneous channel capacity

$$C_{erg} = \mathrm{E}\left[\log_2\det\left(\mathbf{I}_{n_R} + \left(\frac{\text{SNR}}{n_T}\right)\mathbf{H}\mathbf{H}^H\right)\right] \text{bps/Hz}. \quad (16)$$

Since the channel is Ricean in general, $\mathbf{H}$ is given by

$$\mathbf{H} = \sqrt{\frac{K}{K+1}}\mathbf{H}_{LoS} + \sqrt{\frac{1}{K+1}}\mathbf{H}_{NLoS}, \quad (17)$$

where $\mathbf{H}_{LoS}$ is the $n_R \times n_T$ matrix containing the LoS responses among the antenna elements, $\mathbf{H}_{NLoS}$ is the $n_R \times n_T$ matrix containing the NLoS responses due to the scattered waves and K is the Ricean factor.

The elements of $\mathbf{H}_{LoS}$ can be obtained using (2) and (4) as follows

$$\mathbf{H}_{LoS} = \begin{bmatrix} h_{11,LoS} & \cdots & h_{1n_T,LoS} \\ \vdots & \ddots & \vdots \\ h_{n_R 1,LoS} & \cdots & h_{n_R n_T,LoS} \end{bmatrix}. \tag{18}$$

The matrix $\mathbf{H}_{NLoS}$ can be evaluated after a large number of channel realizations using the following equation [25]

$$\mathrm{vec}\left(\mathbf{H}_{NLoS}\right) = \mathbf{R}_{NLoS}^{1/2} \mathrm{vec}\left(\mathbf{H}_w\right), \tag{19}$$

where $\mathbf{R}_{NLoS}$ is the $n_R n_T \times n_R n_T$ correlation matrix associated with the NLoS component, $\mathbf{R}_{NLoS}^{1/2}$ is the square root of $\mathbf{R}_{NLoS}$ that satisfies $\mathbf{R}_{NLoS}^{1/2}\mathbf{R}_{NLoS}^{H/2} = \mathbf{R}_{NLoS}$, $\mathbf{H}_w$ is a $n_R \times n_T$ stochastic matrix with independent and identically distributed (i.i.d.) zero mean complex Gaussian entries, and $\mathrm{vec}(\cdot)$ denotes matrix vectorization[1]. Using (11)-(14), $\mathbf{R}_{NLoS}$ is given by

$$\mathbf{R}_{NLoS} = \begin{bmatrix} R_{11,11}^{NLoS} & R_{11,21}^{NLoS} & \cdots & R_{11,n_R n_T}^{NLoS} \\ R_{21,11}^{NLoS} & \ddots & & R_{21,n_R n_T}^{NLoS} \\ \vdots & & \ddots & \vdots \\ R_{n_R n_T,11}^{NLoS} & \cdots & & R_{n_R n_T,n_R n_T}^{NLoS} \end{bmatrix}. \tag{20}$$

Finally, the channel matrix is normalized so that the constraint

$$\mathrm{E}\left[\left\|\mathbf{H}\right\|_{\mathrm{F}}^2\right] = n_T n_R \tag{21}$$

is fulfilled, where $\|\cdot\|_{\mathrm{F}}$ represents the Frobenius norm of a matrix. This normalization corresponds to a system with perfect power control [26] and makes SNR independent of $\mathbf{H}$.

A. *Numerical Results*

This subsection investigates the effect of the model parameters on the capacity of space-time correlated HAP-MIMO channels. These parameters control the correlation between the subchannels [2]. In particular, the correlation depends on the degree of scattering in a specific propagation environment and the antenna inter-element spacing at both the transmitter and the receiver. Hence, dense scattering in the propagation environment in combination with adequate antenna spacing ensure decorrelation. Considering coherent diffuse components or sparse scattering and increased correlation, the rank of the channel matrix is deficient and the spectral efficiency is low. Therefore, the model parameters control the performance issues, i.e., the spatial multiplexing gain and the capacity enhancement. Unless indicated otherwise, the values of the model parameters used to obtain the curves are $H_T = 20$ km, $\beta_T = 60^\circ$, $\delta_T = 50\lambda$, $\delta_R = 0.5\lambda$, $\theta_T = \theta_R = 90^\circ$, $\psi_T = \psi_R = 0^\circ$, $k = 3$, $\mu = 0^\circ$, $a = 0.01$ (this value corresponds to a mean R_S of about 60 m [2]), $R_{S,\max} = 200$ m, $H_{S,\max} = 70$ m, $f_{R,\max} = 100$ Hz, $\gamma_R = 60^\circ$, $\mathrm{SNR} = 18$ dB, and $K_{pl} = K_{qm} = K = 3$ dB. A typical densely built-up district (London, U.K. [22]) is considered and we set $H_{S,\mathrm{mean}} = 17.6$ m and $\sigma = 0.31$, i.e., the surrounding buildings act as scatterers. Finally, a normalized Doppler frequency $f_n = f_{R,\max} T_s = 0.01$ is used, where T_s is the sampling period.

Figures 3 and 4 compare the ergodic capacity obtained using a HAP-MIMO, i.e., $n_T = n_R = 2$, and a HAP-SISO, i.e., $n_T = n_R = 1$, architecture by varying the Ricean factor and the received SNR. One observes that maximum capacity is obtained in an ideal HAP-MIMO Rayleigh channel scenario. Then, the capacity increases up to 10.6 bps/Hz compared to the capacity of a HAP-SISO channel. However, the potential MIMO gain drastically degrades with the strength of the LoS component, i.e., increasing the Ricean factor increases the correlation and decreases the capacity gain. Providing that the propagation conditions are characterized by rich multipath, e.g., in dense urban areas, the benefits of MIMO technology can be even more obvious. On the contrary, HAP-SISO channels take advantage of the existence of a strong LoS signal, i.e., increasing the Ricean factor drastically increases the capacity. Note that the difference in capacity between HAP-MIMO and HAP-SISO architectures increases, as the SNR increases. However, this difference is nullified, when the SNR is low. Then, the rank of the channel matrix plays an important role. In addition, the channel capacity achieved using both architectures is invariable for $K > 10$ dB.

Figures 5-9 investigate the effect of spatial correlation on the channel capacity. Figure 5 shows the ergodic capacity as a function of the spacing δ_T between SBS antenna elements for different SBS elevation angle β_T and $K = 0$. One observes that increasing δ_T beyond approximately 70λ, 50λ, and 30λ, when $\beta_T = 50^\circ$, $\beta_T = 60^\circ$ and $\beta_T = 70^\circ$, respectively, has a negligible effect on the channel

[1] The vectorization of a matrix is a linear transformation, which converts the matrix into a column vector. Specifically, the vectorization of a $m \times n$ matrix A, denoted by $\mathrm{vec}(A)$, is the $mn \times 1$ column vector obtained by stacking the columns of the matrix A on top of one another.

capacity. According to [3], [4], HAPs are either airships (up to 200 m in length) or aircrafts (up to 30 m in length). Considering 2.1 GHz carrier frequency [7], the wavelength is equal to approximately 0.14 m. Hence, Figure 5 implies that applying MIMO techniques to a single HAP offers considerable capacity gain, as soon as the Ricean is small.

Figure 6 depicts the complementary cumulative distribution function (CCDF) of the capacity and examines the effect of SBS antenna array orientation on the capacity. One observes that SBS broadside antenna arrays, i.e., $\theta_T = 90^\circ$, provide maximum capacity. Moreover, decreasing θ_T from 90° to 60° has a negligible effect on the capacity. However, further decrease of θ_T significantly decreases the capacity. The capacity also depends on the relative angle between the TMS antenna array and the local scatterers around the TMS, i.e., θ_R-μ, and is maximized when the difference between θ_R and μ is 90° [17].

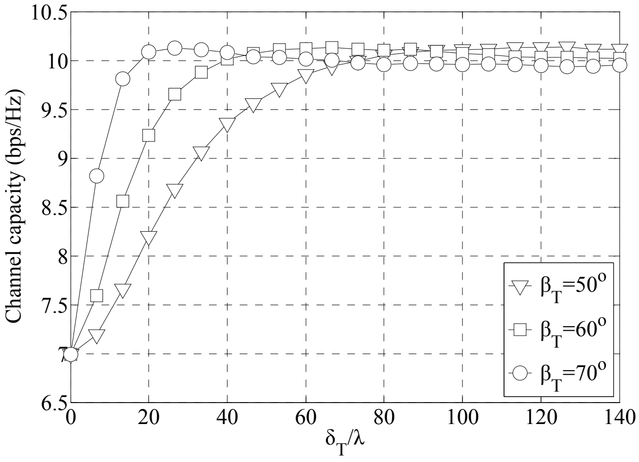

Figure 5. The ergodic capacity of a HAP-MIMO channel in terms of the spacing between the SBS antenna elements for different SBS elevation angle.

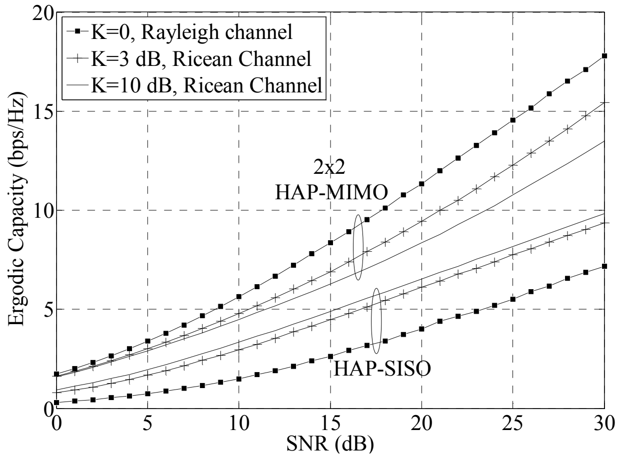

Figure 3. Comparison of the ergodic capacity obtained using the HAP-MIMO and HAP-SISO architectures as a function of the received SNR for different Ricean factor.

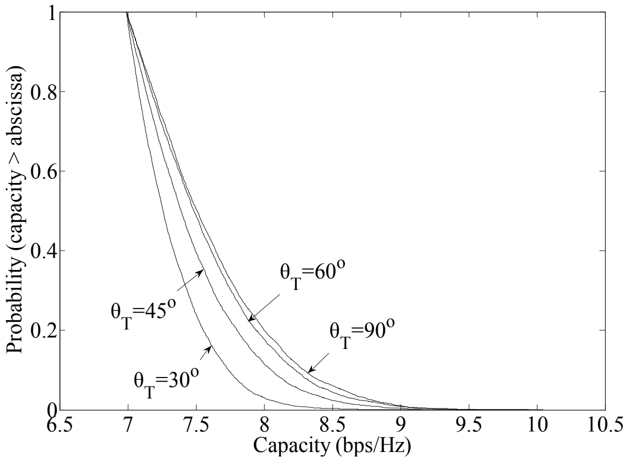

Figure 6. Contrasting complementary cumulative distribution function of the capacity of a HAP-MIMO channel for different antenna array orientation at the SBS.

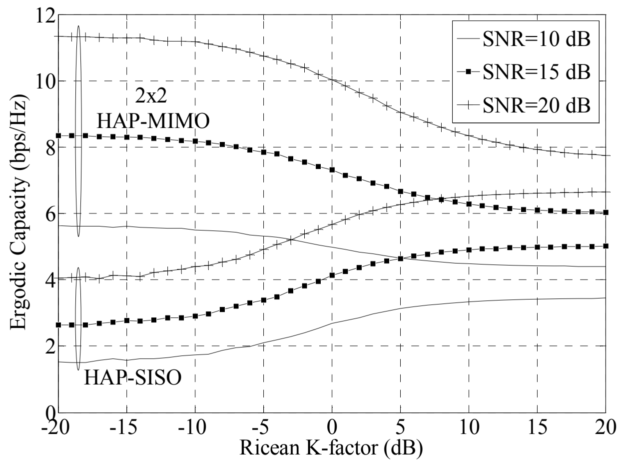

Figure 4. Comparison of the ergodic capacity obtained using the HAP-MIMO and HAP-SISO architectures as a function of the Ricean factor for different received SNR.

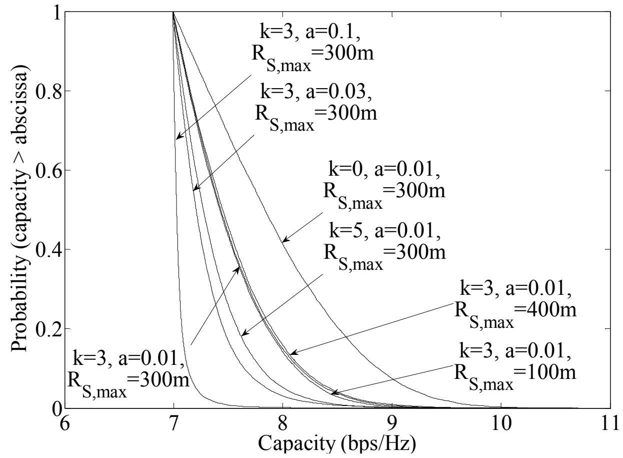

Figure 7. Contrasting complementary cumulative distribution function of the capacity of a HAP-MIMO channel for different degree of scattering, spread of scatterers, and maximum distance between TMS-scatterers.

Figure 7 depicts depicts the CCDF of the capacity and examines the influence of the parameters k, a, and $R_{S,\max}$ on the capacity, i.e., the influence of two-dimensional (2-D) scattering. The effect of each parameter is examined independently (keeping all other parameters fixed). Note that as k increases, the scattering becomes increasingly non-isotropic and the capacity decreases (due to the increase in spatial correlation [2]). Moreover, increasing a decreases the spread of scatterers and decreases the capacity (due to the increase in spatial correlation [2]). However, changing $R_{S,\max}$ has a negligible effect on the capacity and the spatial correlation [2].

Figure 8 shows the CCDF of the capacity, when the TMS antenna array is horizontally, i.e., $\psi_R = 0^\circ$, or vertically placed, i.e., $\psi_R = 90^\circ$, for different $H_{S,\text{mean}}$. Note that changing $H_{S,\text{mean}}$ has an insignificant influence on the capacity, when the TMS antenna array is horizontally placed. However, the capacity depends on the degree of urbanization, i.e., the heights of the scatterers, when the TMS antenna array is vertically placed. Then, increasing $H_{S,\text{mean}}$ increases the capacity. The difference between capacities of systems with horizontally and vertically placed TMS antenna array is nullified in highly urbanized areas. Figure 8 suggests that if the available area in the *x-y* plane is limited for antenna array realization, the TMS antenna array can be tilted without significant loss of capacity.

Figure 9 examines the effect of the temporal correlation by separately varying the normalized Doppler frequency f_n and the moving direction γ_R of the TMS. Observe that an increase in f_n results in an increase in channel capacity due to the decrease in temporal correlation. Furthermore, as γ_R increases (up to 180°), the TMS moves toward the SBS and the channel capacity increases.

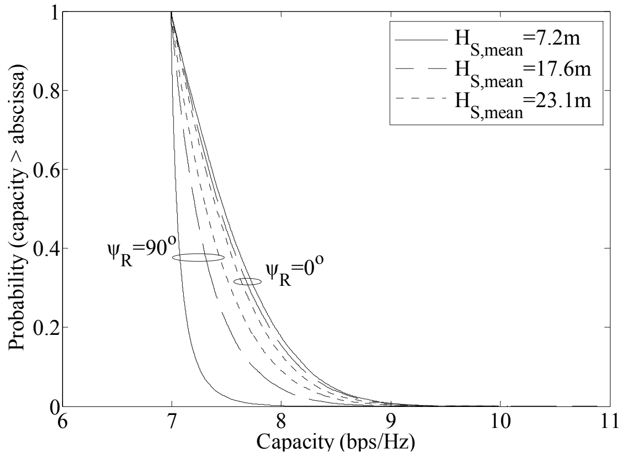

Figure 8. Contrasting complementary cumulative distribution function of the capacity of a HAP-MIMO channel for horizontally or vertically placed TMS antennas and different mean of the scatterer height.

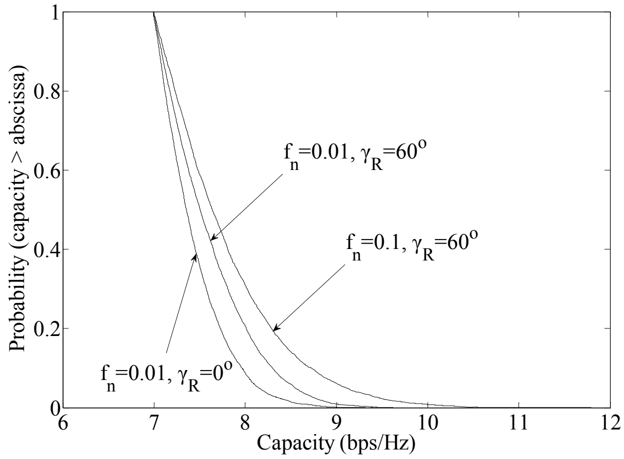

Figure 9. Contrasting complementary cumulative distribution function of the capacity of a HAP-MIMO channel for different normalized Doppler frequency and different moving direction at the TMS.

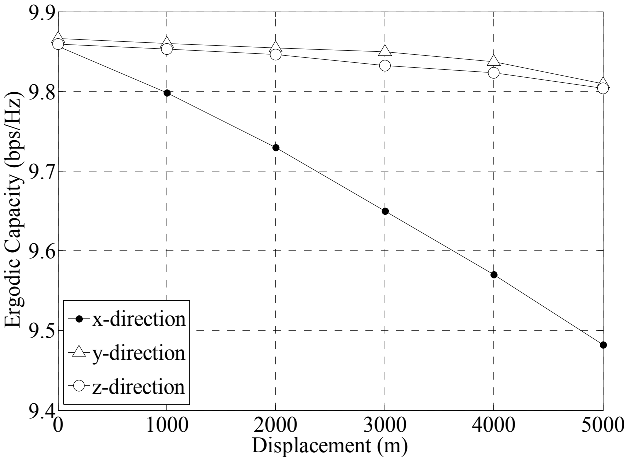

Figure 10. The ergodic capacity of a HAP-MIMO channel for different directions of SBS antenna displacement due to the stratospheric winds.

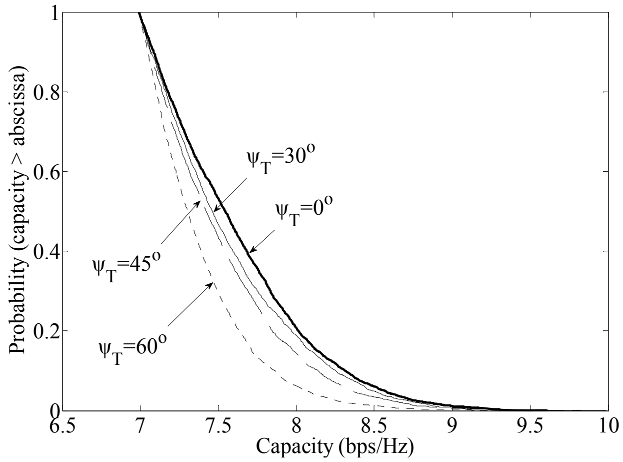

Figure 11. Contrasting complementary cumulative distribution function of the capacity of a HAP-MIMO channel for different elevation angle of the p^{th} SBS antenna element (pitch effect).

Figures 10 and 11 investigate the effect of HAP antenna displacement due to the stratospheric winds on the capacity of HAP-MIMO channels. The influence of each degree of freedom on the capacity is examined independently (keeping all other parameters fixed) in the following figures. Roll and pitch can be considered identical to each other, since both are based on similar principles. In addition, yaw corresponds to a change in the orientation of the SBS antenna array, which is described by the angle θ_T Therefore, Figure 6 represents also the yaw effect and the effect of only pitch and yaw on the capacity is studied.

Figure 10 demonstrates the influence of up to 5 km shifting along either x-, y- or z-axis on the capacity. One observes that the capacity is relatively insensitive to displacements along y- and z-axis. However, the capacity fairly decreases up to 0.5 bps/Hz or 4%, when the displacement takes place along x-axis.

Figure 11 depicts the effect of pitch on the capacity. Note that increasing ψ_T from 0° to 45° has a negligible effect on the capacity. However, further increase in ψ_T drastically decreases the capacity.

V. SIMULATION OF 3-D HAP-MIMO CHANNELS

The reference model assumes an infinite number of scatterers and prevents practical implementation. Hence, simulation models with finite number of scatterers are desirable. Under the framework of the reference model, a stochastic simulation model can be directly obtained by using a finite number N of scatterers. Then, considering a Ricean HAP-MIMO channel, the impulse response of the sub-channel p-l associated with the stochastic simulation model is given by

$$\hat{h}_{pl}(t) = \sqrt{\frac{K_{pl}}{K_{pl}+1}} h_{pl,LoS}(t) + \sqrt{\frac{1}{K_{pl}+1}} \hat{h}_{pl,NLoS}(t), \quad (22)$$

where

$$\hat{h}_{pl,NLoS}(t) = \frac{1}{\sqrt{N}} \sum_{n=1}^{N} e^{-j\frac{2\pi}{\lambda}\left(d_{T,NLoS}+d_{R,NLoS}\right)} e^{j\varphi^{(n)}} \times e^{j2\pi t f_{R,\max} \cos\left(a_R^{(n)}-\gamma_R\right) \cos\left[\arctan\left(H_S^{(n)}/R_S^{(n)}\right)\right]} \quad (23)$$

is the NLoS component of the impulse response, $h_{pl,LoS}(t)$ is defined in (2), "$\hat{\cdot}$" describes a stochastic process, and $d_{T,NLoS}$ and $d_{R,NLoS}$ are defined in (5) and (6), respectively. The random variables $a_R^{(n)}$, $R_S^{(n)}$, and $H_S^{(n)}$ can be generated utilizing the distributions defined in Section II, while $\varphi^{(n)}$ is generated as a random variable uniformly distributed in the interval $[-\pi, \pi)$. All other parameters of the simulation model are identical with those of the reference model. Specifically, $a_R^{(n)}$ is modeled using the von Mises pdf and can be generated as

$$a_R^{(n)} = F_{a_R}^{-1}(\delta), \quad (24)$$

where δ is a random variable uniformly distributed in the interval $(0,1)$. The function $F_{a_R}^{-1}(\cdot)$ denotes the inverse function of the von Mises cumulative distribution function (cdf) and can be evaluated using the numerical method presented in [27]. In addition, $R_S^{(n)}$ is modeled using the hyperbolic pdf and can be generated as

$$R_S^{(n)} = F_{R_S}^{-1}(\zeta), \quad (25)$$

where ζ is a random variable uniformly distributed in the interval $(0,1)$. The function $F_{R_S}(\cdot)$ denotes the hyperbolic cdf, which is given by

$$F_{R_S}(R_S) = \tanh(aR_S) / \tanh(aR_{S,\max}). \quad (26)$$

Finally, $H_S^{(n)}$ is modeled using the log-normal pdf and can be generated as

$$H_S^{(n)} = F_{H_S}^{-1}(\xi), \quad (27)$$

where ξ is a random variable uniformly distributed in the interval (0,1). The function $F_{H_S}(\cdot)$ denotes the log-normal cdf, which is given by

$$F_{H_S}(H_S) = \frac{1}{2} \operatorname{erfc}\left[-\frac{\ln(H_S) - \ln(H_{S,\mathrm{mean}})}{\sigma\sqrt{2}}\right], \quad (28)$$

where $\operatorname{erfc}(x) = \left(2/\sqrt{\pi}\right)\int_x^\infty e^{-u^2} du$ is the complementary error function.

To simulate a HAP-MIMO channel, this generic stochastic simulation model can be directly applied by generating the variables $a_R^{(n)}$, $R_S^{(n)}$, $H_S^{(n)}$, and $\varphi^{(n)}$. However, due to the high degree of randomness during the computation of these variables, an infinite number of simulation trials is required and the stochastic simulation model is still non-realizable and inefficient. Hence, one must otherwise determine the model parameters, in order to fully exploit the inherent advantages of the SoS principle. This procedure is called the parameter computation method and the type of a simulation model is directly related to this method.

A. A 3-D Deterministic Simulation Model

This subsection proposes a SoS-based deterministic simulation model for HAP-MIMO channels and derives the corresponding channel impulse response and the STCF for a 3-D non-isotropic scattering environment.

Since the location of each scatterer inside the cylinder can be fully described by $a_R^{(n)}$, $R_S^{(n)}$, and $H_S^{(n)}$, the entire scattering region is considered as a 3-D point lattice partitioned into three scattering sub-regions, which are individually associated with one of these random variables. In particular, it is considered that N_1 scattering points are non-uniformly placed around a ring, N_2 scattering points are non-uniformly placed along a radial line, and N_3 scattering points are non-uniformly placed along a vertical line. Then, $N = N_1 N_2 N_3$ is the total finite number of discrete local scatterers, a random scatterer is now designated by $S^{(n_1,n_2,n_3)}$ and its location is controlled by $a_R^{(n_1)}$, $R_S^{(n_2)}$, and $H_S^{(n_3)}$, where $n_1 \in \{1,...,N_1\}$, $n_2 \in \{1,...,N_2\}$, and $n_3 \in \{1,...,N_3\}$.

Under these considerations and based on [17], the impulse response of the sub-channel p-l can be written as

$$\tilde{h}_{pl}(t) = \sqrt{\frac{K_{pl}}{K_{pl}+1}} h_{pl,LoS}(t) + \sqrt{\frac{1}{K_{pl}+1}} \tilde{h}_{pl,NLoS}(t), \quad (29)$$

where

$$\tilde{h}_{pl,NLoS}(t) = \frac{1}{\sqrt{N_1 N_2 N_3}} \sum_{n_1=1}^{N_1} \sum_{n_2=1}^{N_2} \sum_{n_3=1}^{N_3} e^{j\varphi^{(n_1,n_2,n_3)}}$$
$$\times e^{j2\pi t f_{R,\max} \cos\left(a_R^{(n_1)} - \gamma_R\right) \cos\left[\arctan\left(H_S^{(n_3)}/R_S^{(n_2)}\right)\right]}$$
$$\times e^{-j\frac{2\pi}{\lambda}\left(d'_{T,NLoS} + d'_{R,NLoS}\right)} \quad (30)$$

is the NLoS component of the impulse response, $h_{pl,LoS}(t)$ is defined in (2) " $\sim$ " describes a deterministic time averaged quantity, and $d'_{T,NLoS}$ and $d'_{R,NLoS}$ are expressed, respectively, as

$$d'_{T,NLoS} \approx \frac{D}{\cos\beta_T} - \frac{0.5(n_T + 1 - 2p)\delta_T \cos\theta_T \cos\psi_T}{\cos\beta_T}$$
$$- \frac{0.5(n_T + 1 - 2p)\delta_T \sin\theta_T \cos\psi_T R_S^{(n_2)} \sin a_R^{(n_1)}}{D\cos\beta_T}, \quad (31)$$

$$d'_{R,NLoS} \approx R^{(n_2)} / \cos\left[\arctan\left(H_S^{(n_3)} / R_S^{(n_2)}\right)\right]$$
$$-0.5(n_R + 1 - 2l)\delta_R \cos\psi_R \cos\left(\theta_R - \alpha_R^{(n_1)}\right)$$
$$\times \cos\left[\arctan\left(H_S^{(n_3)} / R_S^{(n_2)}\right)\right] - 0.5(n_R + 1 - 2l)\delta_R \sin\psi_R$$
$$\times \sin\left[\arctan\left(H_S^{(n_3)} / R_S^{(n_2)}\right)\right]. \quad (32)$$

Providing that a sufficient large number of scatterers is used, i.e., $N = N_1 N_2 N_3 \geq 20$, central limit theorem implies that $\tilde{h}_{pl,NLoS}(t)$ is close to a low-pass zero-mean complex Gaussian process.

The STCF between two arbitrary subchannels $\tilde{h}_{pl,NLoS}(t)$ and $\tilde{h}_{qm,NLoS}(t)$ is defined as

$$\tilde{R}_{pl,qm}^{NLoS}(\delta_T, \delta_R, \tau) = \mathrm{E}\left[\tilde{h}_{pl,NLoS}(t)\tilde{h}^*_{qm,NLoS}(t+\tau)\right]$$
$$\approx \frac{(N_1 N_2 N_3)^{-1}}{\sqrt{(K_{pl}+1)(K_{qm}+1)}} \sum_{n_1=1}^{N_1} \sum_{n_2=1}^{N_2} \sum_{n_3=1}^{N_3} e^{j\frac{2\pi(q-p)\delta_T \cos\theta_T \cos\psi_T}{\lambda\cos\beta_T}}$$
$$\times e^{\frac{j2\pi(q-p)\delta_T \sin\theta_T \cos\psi_T R_S^{(n_2)} \sin a_R^{(n_1)}}{\lambda D \cos\beta_T}}$$
$$\times e^{\frac{j2\pi(m-l)\delta_R \sin\psi_R \sin\left[\arctan\left(H_S^{(n_3)}/R_S^{(n_2)}\right)\right]}{\lambda}}$$
$$\times e^{\frac{j2\pi(m-l)\delta_R \cos\theta_R \cos\psi_R \cos a_R^{(n_1)} \cos\left[\arctan\left(H_S^{(n_3)}/R_S^{(n_2)}\right)\right]}{\lambda}}$$
$$\times e^{\frac{j2\pi(m-l)\delta_R \sin\theta_R \cos\psi_R \sin a_R^{(n_1)} \cos\left[\arctan\left(H_S^{(n_3)}/R_S^{(n_2)}\right)\right]}{\lambda}}$$
$$\times e^{-j2\pi\tau f_{R,\max} \cos\left(a_R^{(n_1)} - \gamma_R\right) \cos\left[\arctan\left(H_S^{(n_3)}/R_S^{(n_2)}\right)\right]}. \quad (33)$$

From (33), it is obvious that $a_R^{(n_1)}$, $R_S^{(n_2)}$, and $H_S^{(n_3)}$ must be properly determined, such that the simulation model approximates the reference model. Note that no parameter computation method will be applied to the phases $\varphi^{(n_1,n_2,n_3)}$, since the STCF does not depend on them. Notwithstanding, the interest reader is referred to [28], where an efficient method to compute the phases is given. Following a similar approach to that proposed in [17], the aforementioned parameters are generated as follows

$$a_R^{(n_1)} = F_{a_R}^{-1}\left(\frac{n_1 - 0.5}{N_1}\right), \quad (34)$$

$$R_S^{(n_2)} = F_{R_S}^{-1}\left(\frac{n_2 - 0.5}{N_2}\right), \quad (35)$$

$$H_S^{(n_3)} = F_{H_S}^{-1}\left(\frac{n_3 - 0.5}{N_3}\right) \quad (36)$$

for $n_1 = 1,...,N_1$, $n_2 = 1,...,N_2$, and $n_3 = 1,...,N_3$. Hence, the proposed deterministic model computes constant values for the model parameters, needs a single run to obtain the desired statistical properties and hence has short simulation times. However, it is important to properly determine the number of scattering points, i.e., N_1, N_2, and N_3, needed to achieve a desired convergence level. Indeed, the complexity of the deterministic simulation model is controlled by N_1, N_2, and N_3. Thus, N_1, N_2, and N_3 should be carefully determined to reduce the computation load of the complete channel simulator and improve the efficiency and the reliability of the proposed model.

The MIMO channel models are generally classified into physical or non-physical (analytical) models based on the modeling philosophy [29]. Physical channel models depend on the characteristics of the propagation environment and allow for an accurate reproduction of the real channel. On the contrary, non-physical models synthesize the MIMO channel matrix in the context of system and algorithm development and verification and can be further subdivided into propagation-motivated models and correlation-based models.

Due to the different way of generation of $\mathbf{H}_{NLoS}$, the reference model is referred to as the non-physical model, while the deterministic model is referred to as the physical model. In particular, the reference model generates the elements of $\mathbf{H}_{NLoS}$ using (11)-(14), (19) and (20). On the contrary, the deterministic model generates the elements of $\mathbf{H}_{NLoS}$ using (30) and hence $\mathbf{H}_{NLoS}$ is given by

$$\mathbf{H}_{NLoS} = \begin{bmatrix} \tilde{h}_{11,NLoS} & \cdots & \tilde{h}_{1n_T,NLoS} \\ \vdots & \ddots & \vdots \\ \tilde{h}_{n_R1,NLoS} & \cdots & \tilde{h}_{n_Rn_T,NLoS} \end{bmatrix}. \tag{37}$$

B. Simulation Results

In this section, the performance of the deterministic simulation model is evaluated. The values of the model parameters used are $\mathrm{SNR} = 15$ dB, $K_{pl} = K_{qm} = K = 3$ dB, $H_T = 20$ km, $\beta_T = 60^\circ$, $\delta_T = 50\lambda$, $\delta_R = 0.5\lambda$, $\theta_T = 60^\circ$, $\theta_R = 30^\circ$, $\psi_T = 0^\circ$, $\psi_R = 30^\circ$, $k = 5$, $\mu = 60^\circ$, $a = 0.01$, $R_{S,\max} = 180$ m, $H_{S,\max} = 70$ m, $H_{S,\mathrm{mean}} = 17.6$ m, $\sigma = 0.31$, $f_{R,\max} = 100$ Hz, $\gamma_R = 30^\circ$, $N_1 = 30$, $N_2 = 20$, and $N_3 = 5$. Finally, a normalized sampling period $f_{R,\max}T_s = 0.02$ is used, where T_s is the sampling period.

The goal of any simulation model is to reproduce the channel's desired statistical properties. Figures 12 and 13 investigate the performance of the deterministic model for different complexity, i.e., different N_1, N_2, and N_3, in terms of the temporal correlation function (TCF), i.e., $n_T = n_R = 1$, for the time delay range $0\text{ s} \le \tau \le 0.1$ s, which is typically of interest for many communications systems, and the spatial correlation function (SCF), i.e., $\tau = 0$, for the ranges $0 \le \delta_T \le 200\lambda$ and $0 \le \delta_R \le 3\lambda$, respectively. As soon as the value of the Ricean factor is sufficiently small, the maximum values of the range of the inter-element distances chosen, i.e., 200λ and 3λ, ensure low spatial correlation in many propagation scenarios, as shown in [2]. The effect of the variation of each number of coordinates of scattering points is examined independently, provided that the other numbers are sufficiently large and do not affect the simulation results. The performance evaluation is realized in terms of the root mean square error (RMSE) between the absolute TCFs and SCFs of the simulation model and the reference model. According to Figures 12 and 13, the performance can be improved by increasing the number of the discrete local scatterers, i.e., N_1, N_2, and N_3, and thus the complexity of the proposed model. Figures 12 and 13 also suggest that reasonable values for N_1 (associated with a_R), N_2 (associated with R_S), and N_3 (associated with H_S) are in the order of 30, 20, and 5, respectively.

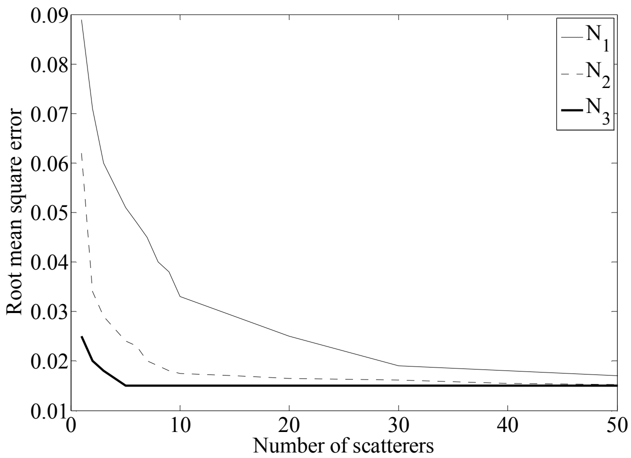

Figure 12. Performance evaluation of the deterministic simulation model in terms of the temporal correlation function.

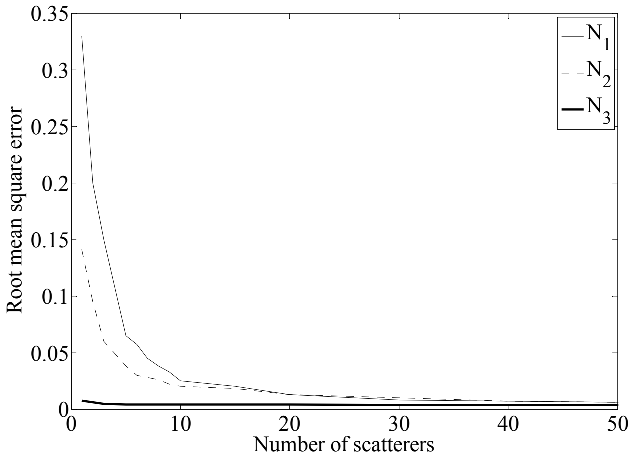

Figure 13. Performance evaluation of the deterministic simulation model in terms of the spatial correlation function.

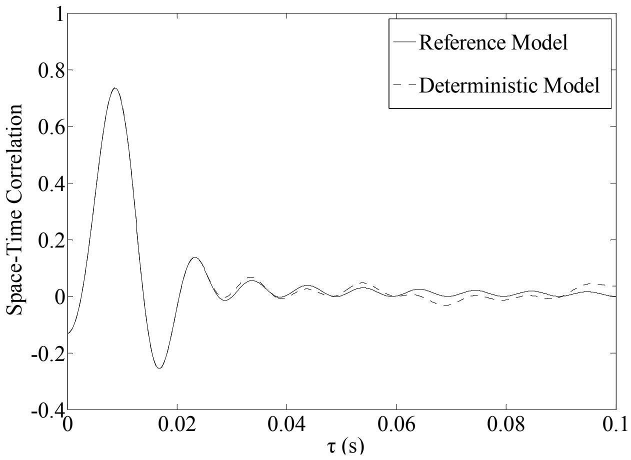

Figure 14. Real part of the STCFs of the NLoS component of the reference model and the deterministic model.

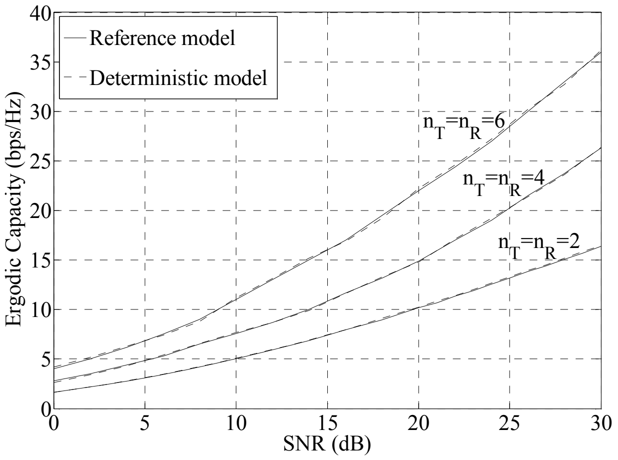

Figure 15. Comparison between the ergodic capacities obtained using the reference and the deterministic model for different number of antenna elements.

Figure 14 compares the real part of the STCFs of the NLoS component associated with the reference and the simulation model. One observes that the STCF of the deterministic model closely matches the reference one for the time delay range $0 \le \tau(\mathrm{s}) \le 0.1$. We also obtain that the RMSE between the absolute STCFs of the deterministic model and the reference model is 0.026 for $N_1 = 30$, $N_2 = 20$, and $N_3 = 5$, and 0.018 for $N_1 = 40$, $N_2 = 30$, and $N_3 = 10$. Hence, increasing the number of scatterers, enhances the performance of the deterministic model.

Finally, Figure 15 compares the ergodic capacity against SNR for different number of antenna elements ($n_T = n_R = 2$, $n_T = n_R = 4$, and $n_T = n_R = 6$) obtained using the reference and the deterministic models. The results show very good agreement between the non-physical and the physical models and verify the usefulness of the proposed simulation model. These results also show that increasing the number of antenna elements, increases the prospective MIMO capacity gain. Nevertheless, when multiple antenna elements are utilized, these antenna elements should be placed at significant distances from each other to ensure that the paths are really diverse. Hence, the HAP length should be adequate to accommodate two or more antenna elements.

VI. Conclusion and Future Work

In this paper, the channel capacity of a HAP-based communications system equipped with multi-element antennas at both sides has been defined and investigated. Specifically, the capacity has been studied taking into account a recently proposed 3-D reference model for HAP-MIMO channels. The numerical results have demonstrated that the MIMO architecture outperforms the conventional SISO architecture in terms of the channel capacity. These results have also shown that the capacity depends on the strength of the LoS signal and the received SNR. Specifically, increasing the Ricean factor decreases the capacity, while increasing the SNR and the number of antenna elements increases the capacity. Furthermore, the results have underlined the effects of spatial and temporal correlation on the capacity of ULAs and have suggested that applying MIMO techniques to a single HAP can effectively enhance the capacity, as soon as the Ricean factor is small. In particular, the influence of the elevation angle of the platform, the antenna configuration and displacement, the mobility of the terrestrial station, and the non-uniform distribution of the local scatterers on the capacity has been analyzed. It has been shown that increasing the elevation angle of the platform increases the capacity, while increasing the density of the scatterers in the vicinity of the user and the spacing between the antennas increases the capacity. Moreover, broadside HAP antennas maximize the capacity, while vertically placed antennas at the mobile terminal provide considerable capacity gain in highly urbanized areas. Finally, the results have underlined that changing the velocity and the moving direction of the user significantly affects the capacity. From the non-realizable reference model, a 3-D deterministic simulation model for HAP-MIMO mobile fading channels has been proposed. The simulation results have shown that the simulation model satisfactorily approximates the reference one in terms of the correlation properties and the channel capacity.

The capacity analysis and the proposed deterministic simulation model provide a convenient framework for the analysis, design, test, and optimization of future HAP-MIMO communications systems. Nevertheless, this work could be further improved or extended into different areas. Due to the lack of channel-sounding measurement campaigns, the contribution of this work has been limited to developing a simulation model for HAP-MIMO channels. However, it is important to verify the theoretical model in real-world propagation conditions. Specifically, HAPs could be emulated by using a helicopter, a small plane or a balloon containing two or more antennas sufficiently separated. However, access to a real HAP would be even more ideal. In addition, the analysis in this paper is restricted to HAP-MIMO systems employing ULAs at both sides of the communication link. The HAP-MIMO channel models can be modified to employ other antenna array geometries, such as uniform planar arrays (UPAs), uniform circular arrays (UCAs), and spherical antenna arrays (SAAs), or a combination of them. Apart from considering only single-bounce rays, this work can also be extended to additionally support double-bounce or multiple-bounce rays (due to multiple scattering, reflection or diffraction of the radiated energy). Then, more sophisticated and realistic channel models can be obtained. Finally, there is perhaps an opportunity to extend the material in the paper by taking into account the energy efficiency issues, i.e., investigating the impact of possible power constraints at the wireless devices on the available channel capacity of HAP-MIMO channels.

REFERENCES

[1] E. T. Michailidis and A. G. Kanatas, "On the Capacity of 3-D Space-Time Correlated HAP-MIMO Channels," in *Proc. 2nd International Conference on Advances in Satellite and Space Communications (SPACOMM) 2010*, Athens/Glyfada, Greece, pp. 87-92, 13-19 Jun. 2010.

[2] E. T. Michailidis and A. G. Kanatas, "Three Dimensional HAP-MIMO Channels: Modeling and Analysis of Space-Time Correlation," *IEEE Transactions on Vehicular Technology*, vol. 59, no. 5, pp. 2232-2242, Jun. 2010.

[3] A. Aragón-Zavala, J. L. Cuevas-Ruíz, and J. A. Delgado-Penín, *High-Altitude Platforms for Wireless Communications*, New York, USA: John Wiley & Sons, Dec. 2008.

[4] S. Karapantazis and F. Pavlidou, "Broadband communications via high-altitude platforms: A survey," *IEEE Communications Society Surveys & Tutorials*, vol. 7, no. 1, pp. 2-31, 2005.

[5] A. K. Widiawan and R. Tafazolli, "High Altitude Platform Station (HAPS): A Review of New Infrastructure Development for Future Wireless Communications," *Wireless Personal Communications*, vol. 42, no. 3, pp. 387-404, Aug. 2007.

[6] A. Mohammed and Z. Yang, "Broadband Communications and Applications from High Altitude Platforms," *International Journal of Recent Trends in Engineering*, vol. 1, no. 3, pp. 239-243, May 2009.

[7] "Minimum performance characteristics and operational conditions for high altitude platform stations providing IMT-2000 in the bands 1885–1980 MHz, 2010–2025 MHz and 2110–2170 MHz in region 1 and 3 and 1885–1980 MHz and 2110–2160 MHz in region 2," *International Telecommunication Union*, Geneva, Switzerland, ITU-R Recommendation F.1456, 2000.

[8] A. Paulraj, R. Nabar, and D. Gore, *Introduction to Space-Time Wireless Communications*, Cambridge, UK: Cambridge University Press, 2003.

[9] E. Telatar, "Capacity of multi-antenna Gaussian channels," *European Transactions on Telecommunications*, vol. 10, no. 6, pp. 585-595, 1999.

[10] G. J. Foschini and M. J. Gans, "On Limits of Wireless Communications in a Fading Environment when Using Multiple Antennas," *Wireless Personal Communications*, vol. 6, no. 3, pp. 311-335, 1998.

[11] P.-D. Arapoglou, E. T. Michailidis, A. D. Panagopoulos, A. G. Kanatas, and R. Prieto-Cerdeira, "The Land Mobile Earth-Space Channel: SISO to MIMO Modeling from L- to Ka-Bands," *IEEE Vehicular Technology Magazine, Special Issue on Trends in Mobile Radio Channels: Modeling, Analysis, and Simulation*, vol. 6, no. 2, pp. 44-53, Jun. 2011.

[12] D. I. Axiotis, M. E. Theologou, and E. D. Sykas, "The effect of platform instability on the system level performance of HAPS UMTS," *IEEE Communications Letters*, vol. 8, no. 2, pp. 111-113, Feb. 2004.

[13] K. Katzis, D. A. J. Pearce, and D. Grace, "Impact of high altitude platform movements on cellular handover," in *Proc. International Workshop on High Altitude Platform Systems,* Athens, Greece, Sep. 2005.

[14] S. O. Rice, "Mathematical analysis of random noise," *Bell Systems Technical Journal*, vol. 23, pp. 282-332, Jul. 1944.

[15] C. Xiao, Y. R. Zheng, and N. C. Beaulieu, "Novel sum-of-sinusoids simulation models for Rayleigh and Rician fading channels," *IEEE Transactions on Wireless Communications*, vol. 5, no. 12, pp. 3667-3679, Dec. 2006.

[16] C.-X. Wang, M. Patzold, and D. Yuan, "Accurate and efficient simulation of multiple uncorrelated Rayleigh fading waveforms," *IEEE Transactions on Wireless Communications*, vol.6, no.3, pp.833-839, Mar. 2007.

[17] A. G. Zajić, and G. L. Stüber, "Three-dimensional modeling, simulation, and capacity analysis of space-time correlated mobile-to-mobile channels," *IEEE Transactions on Vehicular Technology*, vol. 57, no. 4, pp. 2042-2054, Jul. 2008.

[18] A. Abdi and M. Kaveh, "A space-time correlation model for multielement antenna systems in mobile fading channels," *IEEE Journal on Selected Areas in Communications,* vol. 20, no. 3, pp. 550-560, Apr. 2002.

[19] A. Abdi, J. A. Barger, and M. Kaveh, "A parametric model for the distribution of the angle of arrival and the associated correlation function and power spectrum at the mobile station," *IEEE Transactions on Vehicular Technology*, vol. 51, no. 3, pp. 425-434, May 2002.

[20] S. S. Mahmoud, Z. M. Hussain, and P. O'Shea, "Space-time model for mobile radio channel with hyperbolically distributed scatterers," *IEEE Antennas and Wireless Propagation Letters*, vol. 1, pp. 211-214.

[21] S. S. Mahmoud, Z. M. Hussain, and P. O'Shea, "A geometrical-based microcell mobile radio channel model," *Wireless Networks*, vol. 12, no. 5, pp. 653-664, Sep. 2006.

[22] M. A. Vázquez-Castro, F. Perez-Fontan, and S. R. Saunders, "Shadowing correlation assessment and modeling for satellite diversity in urban environments," *International Journal of Satellite Communications*, vol. 20, no. 2, , pp. 151-166, March/April 2002.

[23] C. Tzaras, B. G. Evans, and S. R. Saunders, "Physical-statistical analysis of land mobile-satellite channel," *Electronics Letters*, vol. 34, no. 13, pp. 1355-1357, Jun. 1998.

[24] I. S. Gradshteyn and I. M. Ryzhik, *Table of Integrals, Series and Products*, 5th edition, Edited by A. Jeffrey, Academic Press, 1994.

[25] D.-S. Shiu, G. J. Foschini, M. J. Gans, and J. M. Kahn, "Fading correlation and its effect on the capacity of multielement antenna systems," *IEEE Transactions on Communications*, vol. 48, no. 3, pp. 502-513, Mar. 2000.

[26] R. U. Nabar, Ö. Oyman, H. Bolcskei, and A. J. Paulraj, "Capacity scaling laws in MIMO wireless networks," in *Proc. 41st Allerton Conference on Communication, Control, and Computing 2003*, pp. 378-389, Monticello-Illinois, USA, Oct. 2003.

[27] K. V. Mardia and P. E. Jupp, *Directional Statistics*, New York: Wiley, 1999.

[28] M. Pätzold, U. Killat, F. Laue, and Y. Li, "On the properties of deterministic simulation models for mobile fading channels," *IEEE Transactions on Vehicular Technology*, vol. 47, no. 1, pp. 254-269, Feb. 1998.

[29] P. Almers, E. Bonek, A. Burr, et al., "Survey of Channel and Radio Propagation Models for Wireless MIMO Systems," *EURASIP Journal on Wireless Communications and Networking*, vol. 2007, 2007.

Analytical evaluation of the role of estimation and quantization errors in downstream vectored VDSL systems

Marco Baldi, Franco Chiaraluce
Dip. Ing. Biomedica, Elettronica e Telecomunicazioni
Università Politecnica delle Marche
Ancona, Italy
{m.baldi, f.chiaraluce}@univpm.it

Roberto Garello
Dipartimento di Elettronica
Politecnico di Torino
Torino, Italy
garello@polito.it

Marco Polano
Telecom Italia
Torino, Italy
marco.polano@telecomitalia.it

Marcello Valentini
Torino, Italy
marcello.valentini@ieee.org

***Abstract*— We investigate the effect of non idealities in the diagonalizing precoder vectoring technique used for cancellation of the far-end crosstalk in downstream VDSL networks. By using analytical formulas, we estimate the average bit rate achievable as a function of both relative and absolute estimation errors. Several numerical examples are provided, in different scenarios and operation conditions. Results are presented covering an important aspect for practical applications: the transmitted power required to achieve a target bit rate, as a function of the line length. Finally, we provide some results on the impact of a smart quantization law, which limits the performance loss.**

Keywords-VDSL; vectoring; channel estimation errors; quantization errors

I. INTRODUCTION

A great amount of work has been done to improve the features of digital subscriber line (DSL) systems. Several papers appeared in past and recent literature for performance evaluation of such systems (see [1], [2], and the references therein). In this paper, our goal is to study and quantify the impact of some practical impairment parameters on the achievable bit rate and the other performance figures, under realistic scenarios. We mainly focus on the solutions adopted for overcoming the limitations imposed by far-end crosstalk (FEXT), which is a major problem in very high speed networks [3], [4]. Most of these solutions adopt user coordination techniques [5]; in particular, in the downstream direction, that will be considered in this paper, coordination is possible as the transmitting modems are co-located at the central office. So, FEXT can be completely canceled, at least in principle, through a pre-distortion to apply, tone by tone, at each modem's signal before its transmission. Using these discrete multi-tone (DMT) *vectored* transmission techniques, the achievable bit rates can be significantly increased with respect to non-vectored solutions. As a matter of fact, the recently issued ITU-T G.vector (G.993.5) [6] allows expanded use of 100 Mbps DSL. Additionally, a distinctive feature of the vectored VDSL systems is that its steady-state performance is more predictable than non-vectored systems [7]. In essence, the vectored systems become more stable, and this should encourage the adoption of analytical models for performance analysis and evaluation. Actually, such models are already available, and allow to forecasting easily the best performance achievable.

However, some problems exist, that can make difficult to reach this optimal behavior. The first problem is the effect of estimation errors. Pre-distortion requires the knowledge of the channel transfer function; this is rather easy to obtain for the direct channels, but becomes more difficult for the crosstalk channels. The latter are not yet completely described and, although suitable models have been proposed, they require in depth verification. As regards the coordination technique, in this paper we consider the adoption of the diagonalizing precoder (DP) proposed in [8], that has the advantage of an easy implementation and does not require modifications of the customer premise equipment. In [9] some analytical and simulation results were provided to study this technique in a low complexity implementation. In [1], [2] we developed a theoretical approach that permits to analytically determine the average bit rate achievable, as a function of the relative or the absolute estimation error. In this paper, we extend that theoretical analysis and we further support it by a number of simulations, that allow a more complete characterization of the random variables involved, for example by evaluation of the probability density function (p.d.f.). Moreover, we present new results characterizing the target bit rate and the transmitted power necessary to achieve it, that are two aspects of key importance for practical applications.

Another significant aspect concerns the need to take into account the effect of finite word length in the representation of the precoder variables, i.e., to measure the impact of quantization errors. This issue is extremely important, due to its influence on the performance complexity trade-off: on one hand, coarse quantization can imply intolerable rate loss but, on the other hand, a large number of quantization bits can yield high hardware complexity and a great amount of memory needed for the precoding process. In [10], it has been shown that to obtain a limited capacity loss, due to quantization errors, a 14 bits representation of the precoder entries may be necessary. On the other hand, in [2] we showed that, by adopting a suitable quantization law, the same loss can be ensured by using only 10 bits. A further study on such quantization technique is presented in this paper, focusing on different practical scenarios and confirming the performance gain.

In essence, the main contributions of this paper consist in facing the issues described above both in (simple) analytical terms and through an extensive numerical evaluation. Various realistic examples are considered. The statistical character of the variables involved is taken into account, which is not very common in previous literature. The results of the analysis are also used to discuss relevant aspects, like evaluation of the power required for achieving a target bit rate, which are of great importance in practical applications.

The organization of the paper is as follows. In Section II we introduce the system and its relevant performance parameters in ideal conditions. In Section III we describe the channel model adopted and the statistical issues it involves. In Section IV we discuss the effect of the estimation errors, through theoretical arguments and simulations. Section V describes the simulation environments and gives several numerical examples. In Section VI we present the impact of the quantization errors, and we discuss the quantization law that allows to reduce the number of quantization bits. Finally, Section VII concludes the paper.

II. IDEAL BEHAVIOR

We consider the VDSL 998 17 standard [11], characterized by 4096 tones with frequency separation Δ = 4312.5 Hz. For downstream, the Power Spectral Density (PSD) cannot exceed the mask described in Table I and depicted in Fig. 1 [11].

Denoting by s_k^{mask} the value of the PSD at the kth tone, the power transmitted on line n at tone k must satisfy the constraint $P_k^n \le s_k^{mask} \cdot \Delta$. On each line we consider a total power $P_T^n = \sum_{k=1}^{M} P_k^n$ equal to 14.5 dBm (a typical value for cabinet transmission), distributed by the water-filling algorithm (see [12], for example) on the M = 2454 tones allocated for downstream.

Let us consider Fig. 2, that refers to the kth downstream tone f_k. In the figure, $\mathbf{X}_k = [X_k^1, X_k^2, \ldots, X_k^L]^T$ is an L-component vector collecting the symbols transmitted by L users on as many lines. $\mathbf{H}_k$ is the $L\times L$ channel matrix; its (i, j)th element, H_k^{ij}, represents the channel from transmitter j to receiver i.

TABLE I. PSD MASK FOR VDSL 998 17 DOWNSTREAM

tone		PSD [dBm/Hz]	
from	to	from	to
32	256	–36.5	–36.5
256	376	–36.5	–46.5
376	512	–46.5	–48.0
512	870	–48.0	–51.2
1026	1971	–52.7	–54.8
3246	4096	–56.5	–56.5

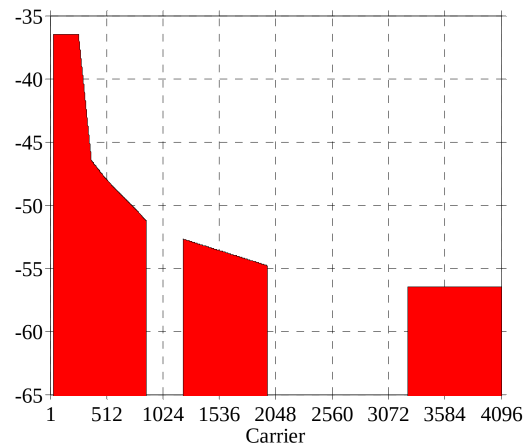

Figure 1. Graphic representation of the PSD mask for VDSL 998 17 downstream.

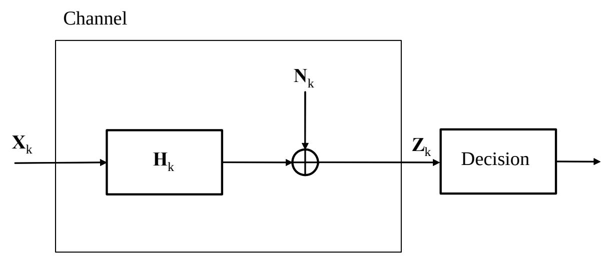

Figure 2. Schematic representation of the VDSL system.

The matrix $\mathbf{H}_k$ is row-wise diagonal dominant (RWDD); this means that, on each row of $\mathbf{H}_k$, the diagonal element has typically much larger magnitude than the off-diagonal elements (i.e., $\left|H_k^{ii}\right| \gg \left|H_k^{ij}\right|$, $\forall j \neq i$). Also shown in Fig. 2, $\mathbf{N}_k$ is the L-component vector describing the additive thermal noise.

If all the L lines of the binder are controlled by the same operator, and the line drivers are co-located (in the same cabinet or central office) then the vector of symbols $\mathbf{X}_k$ can be made available to an apparatus able to coordinate the L lines. Ideally, this knowledge can be used to completely eliminate the FEXT interference by applying a proper precoder. This idea was first presented in [5], where vectored DMT was introduced.

In the simplest form of precoding (from a conceptual viewpoint), the vector $\mathbf{X}_k$ is pre-multiplied by a matrix $\mathbf{P}_k = \left\{p_k^{ij}\right\}$, such that $\mathbf{P}_k = \alpha_k \mathbf{H}_k^{-1}$, which is able to completely remove the FEXT interference. This method requires:

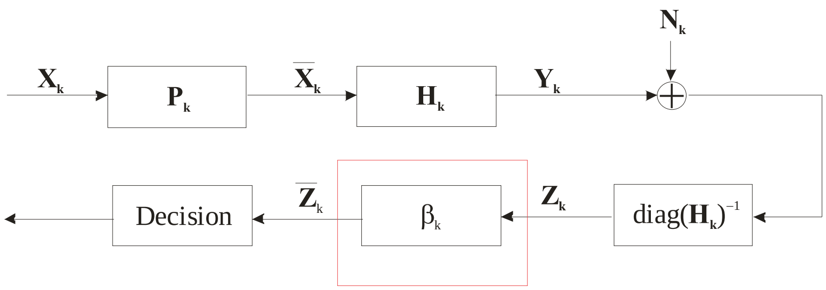

Figure 3. Schematic representation of the vectored system based on DP.

- The exact knowledge of the channel matrix $\mathbf{H}_k$ at the transmitter side.
- The use of a scaling factor α_k for not exceeding the PSD mask. The Tomlinson precoder was proposed to solve this problem in [5], but has a quite large complexity..

To overcome the complexity of the Tomlinson precoder, some alternative schemes have been considered. Among them, one of the most promising is the Diagonalizing Precoder (DP) [8]. The DP system at tone k is shown in Fig. 3; the precoding matrix $\mathbf{P}_k$ is now defined as:

$$\mathbf{P}_k = \beta_k^{-1}\mathbf{H}_k^{-1} \cdot \mathrm{diag}(\mathbf{H}_k)\,, \tag{1}$$

with $\beta_k \triangleq \max_i \left\| \left[\mathbf{H}_k^{-1} \cdot \mathrm{diag}(\mathbf{H}_k) \right]_{\text{row } i} \right\|$. In (1), diag($\mathbf{H}_k$) is the diagonal matrix having elements $H_k^{11}, \ldots, H_k^{LL}$.

In ideal conditions (i.e., perfectly compensated FEXT), the signal-to-noise ratio at the nth receiver and the kth tone is:

$$SNR_k^n = \frac{P_k^n \left| H_k^{nn} \right|^2}{\sigma_N^2} \tag{2}$$

where P_k^n is the transmitted power and σ_N^2 is the variance of the thermal noise, that is independent of k and n.

By using the well-known gap approximation, the number of bit/symbol of user n at tone k is given by:

$$c_k^n = \log_2\left\{1 + \frac{SNR_k^n}{\Gamma}\right\}, \tag{3}$$

where Γ is the transmission gap, and the achievable bit rate is:

$$C^n = R_S \sum_{k=1}^{M} c_k^n\,, \tag{4}$$

where R_S = 4000 symbol/s is the net symbol rate (which differs from Δ because of the cyclic prefix). Actually, in (3) and (4), the integer part of c_k^n must be assumed. To simplify the notation, however, this will be not explicitly indicated afterward (but will be used in the numerical evaluations).

III. CHANNEL MODEL

We describe the diagonal elements of matrix $\mathbf{H}_k$ (direct channel) through the well-known Marconi (MAR1) model [13]. As regards the FEXT, such model can be extended by using the following expression, that takes into account the statistical coupling dispersion with respect to the 1% worst case [14].

$$H_{FEXT}(f,d) = \left| H(f,d) \right| f \sqrt{d}\,\chi 10^{-X/20} e^{i\Phi}\,. \tag{5}$$

In (5), $H(f, d)$ is the direct channel at frequency f (in MHz) and distance d (in km), $\chi = 10^{-2.25}$ is a coupling coefficient, X is a Gaussian random variable with mean value (in dB) μ_X and standard deviation (in dB) σ_X, Φ is a uniform random variable $\in[0, 2\pi)$. For the subsequent analysis, it will be useful to compute the square modulus of (5). Because of the assumption on X, $10^{-X/10}$ is a log-normal variable whose mean value and variance are well known and can be expressed as functions of μ_X and σ_X. These expressions will be used in Section V, where several numerical examples will be discussed.

The values of μ_X and σ_X depend on the type of cable adopted. In the next numerical examples, we will set σ_X = 7.8 dB and $\mu_X = 2.33\times\sigma_X$ = 18.174 dB.

Eq. (5) is self-consistent in the case of lines with equal length and permits us to obtain the off-diagonal elements H_k^{nj}, with $n \neq j$. In a more practical scenario, where the lines within the cable have different lengths, say d_n and d_j, H_k^{nj} can be obtained through the following expression:

$$H_k^{nj} = \left| H_k^{nn} \right| f_k \sqrt{\min\left(d_j, d_n\right)}\,\chi 10^{-X/20} e^{i\Phi}\,, \tag{6}$$

as the FEXT contribution is limited to the common length, while it is further attenuated in the longest loop.

In previous literature, (5) has been often used neglecting the statistical issues and considering the maximum $\left| H_k^{nj} \right|$ value, that is obtained by setting X = 0. This represents a worst case situation, that rarely occurs in practice. Instead, by following the approach presented in

[1] and [2], we can face the problem in statistical terms, so deriving more significant values for the quantities involved. Examples will be given in Section IV.

Even assuming the worst case situation, the crosstalk channel H_k^{nj} from a disturber j into a victim n is always much weaker than H_k^{nn}. As mentioned above, this yields the RWDD character of the downstream VDSL channel matrix, that is known to be a key issue for the efficiency of the vectored system.

IV. Effect of Estimation Errors

An analytical approach to quantify the impact of estimation errors was developed in [2] and is reported here for paper completeness. In Section V, this approach will be used to produce a set of results, matched to practical applications, much more extended with respect to the scenarios considered in [2].

Let $\hat{\mathbf{H}}_k$ be the estimated channel matrix. If an estimation error is present, it is modeled through a matrix $\mathbf{E}_k$ such that:

$$\hat{\mathbf{H}}_k = \mathbf{H}_k + \mathbf{E}_k . \tag{7}$$

It is reasonable to assume that the direct channels are estimated correctly, so that $\mathbf{E}_k$ has zero diagonal elements. Moreover, for a given error percentage e, assumed constant for all the off-diagonal elements, we have $\hat{H}_k^{ij} = H_k^{ij}(1+e)$.

Matrix $\hat{\mathbf{H}}_k$ must replace, in (1), the actual matrix $\mathbf{H}_k$ and, looking at Fig. 3, through simple algebra, we find [2]:

$$\begin{aligned}\bar{\mathbf{Z}}_k &= \left\{\mathbf{I} - \left[\mathrm{diag}\left(\hat{\mathbf{H}}_k\right)\right]^{-1} \cdot \mathrm{diag}\left(\mathbf{E}_k \cdot \hat{\mathbf{H}}_k^{-1}\right) \cdot \mathrm{diag}\left(\hat{\mathbf{H}}_k\right)\right\} \cdot \mathbf{X}_k \\ &- \left[\mathrm{diag}\left(\hat{\mathbf{H}}_k\right)\right]^{-1} \cdot \left[\mathbf{E}_k \cdot \hat{\mathbf{H}}_k^{-1} - \mathrm{diag}\left(\mathbf{E}_k \cdot \hat{\mathbf{H}}_k^{-1}\right)\right] \cdot \mathrm{diag}\left(\hat{\mathbf{H}}_k\right) \cdot \mathbf{X}_k \\ &+ \beta_k \left[\mathrm{diag}\left(\hat{\mathbf{H}}_k\right)\right]^{-1} \cdot \mathbf{N}_k .\end{aligned} \tag{8}$$

Taking into account the RWDD character of the channel matrix, it is possible to verify that $\beta_k \approx 1$, $\hat{\mathbf{H}}_k^{-1} \cdot \mathrm{diag}\left(\hat{\mathbf{H}}_k\right) \approx \mathbf{I}$ and $\mathrm{diag}\left(\mathbf{E}_k \cdot \hat{\mathbf{H}}_k^{-1}\right) \approx 0$. Then, (8) becomes:

$$\bar{\mathbf{Z}}_k \approx \mathbf{X}_k - \left[\mathrm{diag}\left(\hat{\mathbf{H}}_k\right)\right]^{-1} \cdot \mathbf{E}_k \cdot \mathbf{X}_k + \left[\mathrm{diag}\left(\hat{\mathbf{H}}_k\right)\right]^{-1} \cdot \mathbf{N}_k . \tag{9}$$

So, by elaborating (9) to obtain the signal-to-noise ratio, the number of bit/symbol (3) results in:

$$c_k^n = \log_2 \left\{ 1 + \frac{P_k^n \left|H_k^{nn}\right|^2}{\left|e\right|^2 \sum_{\substack{j=1 \\ j \neq n}}^{L} \left|H_k^{nj}\right|^2 P_k^j + \sigma_N^2} \cdot \frac{1}{\Gamma} \right\} . \tag{10}$$

Because of the presence of the random variables H_k^{nj}, c_k^n is a random variable as well. In this paper, we consider two different approaches for estimating its mean $\left\langle c_k^n \right\rangle$; they are described next. From the knowledge of $\left\langle c_k^n \right\rangle$, the mean of C^n can be derived as well, by using (4).

Approximation 1: A first coarse approximation consists in replacing, in (10), the mean of $\left|H_k^{nj}\right|^2$, so that:

$$\left\langle c_k^n \right\rangle_1 = \log_2 \left\{ 1 + \frac{P_k^n \left|H_k^{nn}\right|^2}{\left|e\right|^2 \sum_{\substack{j=1 \\ j \neq n}}^{L} \left\langle \left|H_k^{nj}\right|^2 \right\rangle P_k^j + \sigma_N^2} \cdot \frac{1}{\Gamma} \right\} . \tag{11}$$

Based on the channel model described in Section III, it is possible to verify that:

$$\left\langle \left|H_k^{nj}\right|^2 \right\rangle = \left|H_k^{nn}\right|^2 f_k^2 \min\left(d_j, d_n\right) \chi^2 \mathrm{e}^{-\ln(10)/10\mu_X + [\ln(10)/10]^2 \sigma_X^2 / 2} . \tag{12}$$

Approximation 2: A more accurate analysis should consider c_k^n as a function of the random variable:

$$Y = \sum_{\substack{j=1 \\ j \neq n}}^{L} Y_j = \sum_{\substack{j=1 \\ j \neq n}}^{L} P_k^j \min\left(d_j, d_n\right) 10^{-X_j/10} , \tag{13}$$

and then obtain $\left\langle c_k^n \right\rangle$ accordingly. Once having fixed the scenario, P_k^j and $\min\left(d_j, d_n\right)$ are known, so that Y is the sum of properly scaled log-normal variables. With simple algebra we have (details are given in the Appendix):

$$\begin{aligned}\left\langle c_k^n \right\rangle_2 = \left\langle c_k^n \right\rangle_1 + \log_2 \Bigg[&\sqrt{\frac{\left(b\mu_Y + \sigma_N^2\right)^2 + b^2 \sigma_Y^2}{\left(b\mu_Y + a + \sigma_N^2\right)^2 + b^2 \sigma_Y^2}} \\ &\cdot \left(1 + \frac{a}{b\mu_Y + \sigma_N^2}\right) \Bigg] ,\end{aligned} \tag{14}$$

where μ_Y and σ_Y^2 are the mean value and variance of Y, and

$$a = \frac{P_k^n \left|H_k^{nn}\right|^2}{\Gamma} \quad , \quad b = |e|^2 \left|H_k^{nn}\right|^2 f_k^2 \chi^2 . \tag{15}$$

Some analytical methods are known for computing the statistical averages of Y, as required in (14). Among them: 1) Wilkinson's method is particularly simple and provides an explicit solution [15]; 2) Schwartz & Yeh's method is more accurate but requires a recursive approach [16].

By applying Wilkinson's method, we find the following expressions:

$$\mu_Y = e^{-\ln 10/10 \mu_X + (\ln 10/10)^2 \sigma_X^2 /2} \sum_{\substack{j=1 \\ j \neq n}}^{L} P_k^j \min\left(d_j, d_n\right),$$

$$\sigma_Y^2 = e^{-2\ln 10/10 \mu_X + (\ln 10/10)^2 \sigma_X^2} \left\{ e^{(\ln 10/10)^2 \sigma_X^2} \sum_{\substack{j=1 \\ j \neq n}}^{L} \left[P_k^j \min\left(d_j, d_n\right)\right]^2 \right.$$
$$\left. + \sum_{\substack{j=1 \\ j \neq n}}^{L} \sum_{\substack{m=1 \\ m \neq j,n}}^{L} \left[P_k^j \min\left(d_j, d_n\right)\right]\left[P_k^m \min\left(d_m, d_n\right)\right] \right\} - \mu_Y^2 . \tag{16}$$

Channel estimation is typically realized through Least Squares (LS) or Recursive Least Squares (RLS) algorithms [17] and it is based on the transmission of S training symbols with constant power level. The goodness of the estimate depends on the value of S and on the ratio P_k^n / σ_N^2 [10]. Following an analytical procedure similar to that reported in [18], it is easy to verify that the average number of bit/symbol for user n at tone k, in the case of using the LS algorithm, can be written as [2]:

$$\left\langle c_k^n \right\rangle = \log_2 \left\{ 1 + \frac{P_k^n \left|H_k^{nn}\right|^2}{\left(\frac{L-1}{S} + 1\right)\sigma_N^2} \cdot \frac{1}{\Gamma} \right\} . \tag{17}$$

Whilst (10), (11) and (14) refer to a fixed relative error percentage, (17) takes into account the variance of the estimation error, on the basis of the actual algorithm used for channel estimation. It also suggests the main method to limit the impact of the error, that consists, as obvious, in increasing the value of S. Numerical examples will be given in the following section.

V. NUMERICAL EXAMPLES AND SIMULATIONS

In our numerical examples we have used the PSD mask of the VDSL2 998 bandplan, up to 17 MHz, described in Section II. σ_N^2 has been computed on the basis of a background spectral density of –140 dBm/Hz. Moreover, we have assumed Γ = 9.75 dB and a maximum number of bit/carrier (bit clipping) equal to 15.

A. Considered scenarios

By varying the number and length of the interfering lines, a huge number of different scenarios can be analyzed. Among them, just for explicative purposes, we have focused on the following three scenarios, that extend a first series of cases already presented in [2].

Scenario 1: In the first scenario, we assume that the lines have four different lengths, all multiple of a minimum value Δd. The situation is schematically shown in Fig. 4 (where DSLAM means Digital Subscriber Line Access Multiplexer and CPE denotes the Customer-Premises Equipment). For each length we have L/4 lines, with L = 8 (Case 1.1) or L = 16 (Case 1.2). In the simulations that will be discussed next, we have considered Δd = 0.3 km.

Scenario 2: In the second scenario, the L/4 lines in the first group have length d, while those in the ith group, with i = 2, 3, 4, have length $d + (i - 1)\,\Delta d$. This scenario is schematically shown in Fig. 5. For each length we have L = 8 (Case 2.1) or L = 16 (Case 2.2). In the simulations that will be discussed next, in particular, we have assumed d = 0.9 km and Δd = 0.1 km. A case that this scenario is well suited to model is the one plotted in Fig. 6, in which a first long span arrives up to the cellar of a building and, from that, at regular intervals, L/4 lines are separated to cover different building floors.

Scenario 3: In the third scenario, we have L = 8 (Case 3.1) or L = 16 (Case 3.2) lines with equal length. This can be seen as a special case of Scenario 2, when Δd = 0 is assumed.

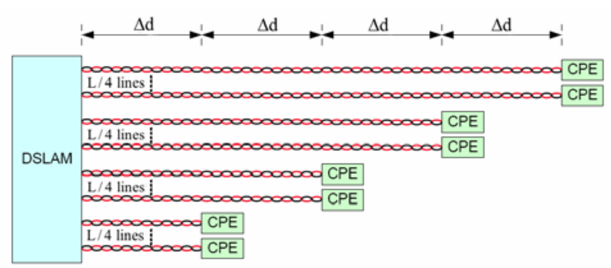

Figure 4. Schematic description of Scenario 1.

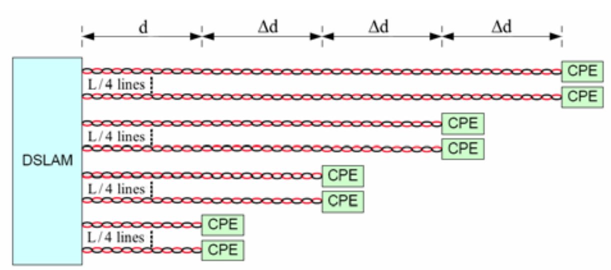

Figure 5. Schematic description of Scenario 2.

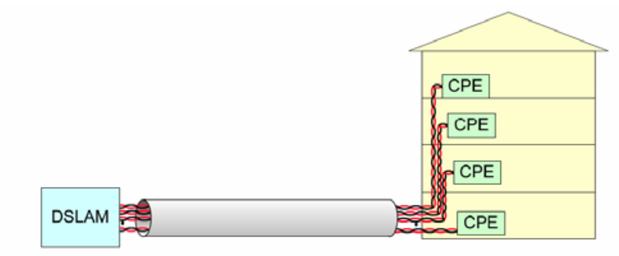

Figure 6. Example of application of the Scenario 2.

B. *Examples of average bit rates*

Tables II-V report some examples of computation of the average bit rates, for the Scenarios 1 and 2 introduced in Section V.A, by assuming the presence of an error percentage *e* in the evaluation of the channel matrix. Both the analytical approximations discussed in Section III have been considered.

TABLE II. EXAMPLES OF AVERAGE BIT RATES FOR CASE 1.1

Line length (km)	Simulation based on (9) (Mbps)	Simulation based on (8) (Mbps)	$\langle C^n \rangle_1$ (Mbps)	$\langle C^n \rangle_2$ (Mbps)
		e = 0.1		
0.3	140.56	140.53	136.29	140.44
0.6	99.93	99.86	100.05	100.41
0.9	63.25	63.24	63.25	63.28
1.2	40.91	40.91	40.90	40.90
		e = 0.5		
0.3	115.00	114.95	105.29	114.03
0.6	89.05	88.94	87.21	92.38
0.9	60.02	60.01	59.16	61.21
1.2	40.11	40.11	39.58	40.26

TABLE III. EXAMPLES OF AVERAGE BIT RATES FOR CASE 1.2

Line length (km)	Simulation based on (9) (Mbps)	Simulation based on (8) (Mbps)	$\langle C^n \rangle_1$ (Mbps)	$\langle C^n \rangle_2$ (Mbps)
		e = 0.1		
0.3	135.99	135.92	130.22	135.02
0.6	98.70	98.52	98.82	99.38
0.9	63.00	62.98	62.99	63.06
1.2	40.86	40.85	40.82	40.83
		e = 0.5		
0.3	102.28	102.19	95.76	101.19
0.6	82.25	82.01	80.83	84.68
0.9	57.20	57.16	56.16	58.10
1.2	39.13	39.12	38.27	39.08

TABLE IV. EXAMPLES OF AVERAGE BIT RATES FOR CASE 2.1

Line length (km)	Simulation based on (9) (Mbps)	Simulation based on (8) (Mbps)	$\langle C^n \rangle_1$ (Mbps)	$\langle C^n \rangle_2$ (Mbps)
		e = 0.1		
0.9	63.13	63.12	63.17	63.22
1.0	54.33	54.32	54.36	54.38
1.1	46.49	46.48	46.49	46.50
1.2	40.89	40.88	40.86	40.87
		e = 0.5		
0.9	58.65	58.62	58.06	60.28
1.0	51.22	51.20	50.90	52.52
1.1	44.44	44.42	43.99	45.19
1.2	39.59	39.58	39.01	39.89

TABLE V. EXAMPLES OF AVERAGE BIT RATES FOR CASE 2.2

Line length (km)	Simulation based on (9) (Mbps)	Simulation based on (8) (Mbps)	$\langle C^n \rangle_1$ (Mbps)	$\langle C^n \rangle_2$ (Mbps)
		e = 0.1		
0.9	62.77	62.72	62.83	62.93
1.0	54.10	54.06	54.14	54.19
1.1	46.35	46.33	46.34	46.37
1.2	40.80	40.79	40.76	40.78
		e = 0.5		
0.9	55.33	55.27	54.80	56.69
1.0	48.73	48.67	48.41	49.92
1.1	42.59	42.55	41.98	43.16
1.2	38.28	38.26	37.44	38.36

The reliability of the approximated average bit rates has been tested also through a comparison with the simulation results. For this purpose, the samples of $\left|H_k^{nj}\right|^2$ have been generated, according to their statistics, and used in (10). The confidence of the estimation can be made high by increasing the number of random extractions. The numerical elaboration has been managed through simple programs written in Matlab© and C++.

Simulations have been performed by considering either the exact expression (8) or the approximate expression (9). The results confirm that the use of (9) is quite acceptable, being related to the RWDD character of matrix $\mathbf{H}_k$.

We also observe that Approximation 2 is generally better for the case of short lengths, while, for longer lengths, the gap between the two approximations becomes less pronounced. In all the considered cases, the agreement between the simulated and the analytical results is good, thus proving the effectiveness of the proposed model.

On the other hand, simulations permit us to derive any statistical description of the random variable c_k^n . In Fig. 7, for example, we have plotted the estimated p.d.f. for *d* = 0.6 km and *e* = 0.5, in Case 1.1. Coherent with Table II, the calculated mean value of the p.d.f. is 88.94 Mbps; it is also noticeable the fact that the curve is very narrow around the mean, thus demonstrating a small variance of the achievable bit rates, that is another recognized property of the vectored systems [7], even in the presence of estimation errors.

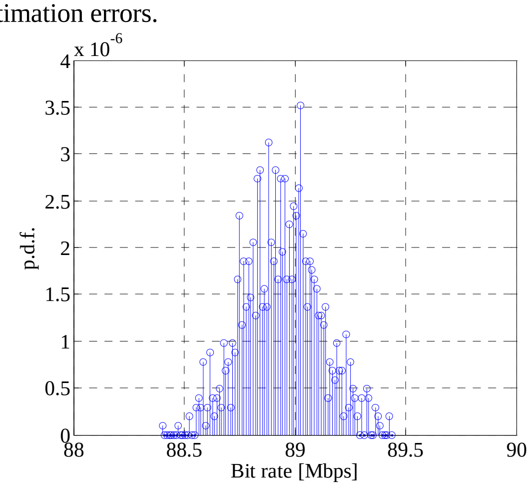

Figure 7. Estimated p.d.f. for *d* = 0.6 km and *e* = 0.5 in Case 1.1.

As stressed above, (17) also permits us to evaluate the impact of the estimation error induced by a limited number of training symbols. The achievable bit rate for different values of S, by considering the Scenarios 1 and 2 described in Section V.A, are reported in Tables VI-IX. For the non-vectored system, the results have been obtained by adopting the Approximation 2.

TABLE VI. AVERAGE BIT RATES AS A FUNCTION OF THE NUMBER OF TRAINING SYMBOLS FOR CASE 1.1

Line length (km)	Non-vector. (Mbps)	Vector. $S = 1$ (Mbps)	Vector. $S = 10$ (Mbps)	Vector. $.S = 100$ (Mbps)	Vector. $S = 1000$ (Mbps)	Vector. Ideal (Mbps)
0.3	96.79	133.88	141.97	144.41	144.66	144.69
0.6	82.14	79.32	95.86	100.23	100.88	100.96
0.9	57.11	48.08	59.71	63.01	63.41	63.46
1.2	38.80	30.95	38.31	40.60	40.92	40.96

TABLE VII. AVERAGE BIT RATES AS A FUNCTION OF THE NUMBER OF TRAINING SYMBOLS FOR CASE 1.2

Line length (km)	Non-vector. (Mbps)	Vector. $S = 1$ (Mbps)	Vector. $S = 10$ (Mbps)	Vector. $S = 100$ (Mbps)	Vector. $S = 1000$ (Mbps)	Vector. Ideal (Mbps)
0.3	83.10	127.90	139.91	143.96	144.63	144.69
0.6	71.77	71.92	91.96	99.58	100.80	100.96
0.9	51.82	42.82	56.84	62.49	63.36	63.46
1.2	36.07	27.78	36.42	40.24	40.88	40.96

TABLE VIII. AVERAGE BIT RATES AS A FUNCTION OF THE NUMBER OF TRAINING SYMBOLS FOR CASE 2.1

Line length (km)	Non-vector. (Mbps)	Vector. $S = 1$ (Mbps)	Vector. $S = 10$ (Mbps)	Vector. $S = 100$ (Mbps)	Vector. $S = 1000$ (Mbps)	Vector. Ideal (Mbps)
0.9	55.32	48.08	59.71	63.01	63.41	63.46
1.0	48.86	39.87	50.82	54.08	54.50	54.54
1.1	42.41	34.58	43.43	46.20	46.57	46.62
1.2	37.80	30.95	38.31	40.60	40.92	40.96

TABLE IX. AVERAGE BIT RATES AS A FUNCTION OF THE NUMBER OF TRAINING SYMBOLS FOR CASE 2.2

Line length (km)	Non-vector. (Mbps)	Vector. $S = 1$ (Mbps)	Vector. $S = 10$ (Mbps)	Vector. $S = 100$ (Mbps)	Vector. $S = 1000$ (Mbps)	Vector. Ideal (Mbps)
0.9	49.68	42.82	56.84	62.49	63.36	63.46
1.0	44.39	35.37	48.12	53.58	54.44	54.54
1.1	38.76	30.91	41.15	45.78	46.53	46.62
1.2	34.74	27.78	36.42	40.24	40.88	40.96

From the tables we see that, just by using $S = 100$ training symbols, the average bit rate is very close to the ideal result, thus providing the expected high gain with respect to the non-vectored system (also shown in the table for the sake of reference). We have developed a number of similar comparisons for different scenarios; when longer loops are considered, the requirement on S can become more stringent. Moreover, as clearly shown by (17), for an increasing number of lines, the value of S has to be increased as well. However, assuming $S = 1000$ symbols should guarantee a limited impact of the estimation errors for any VDSL2 scenario of practical interest.

From a different viewpoint, the designer can be interested to fix a value of the bit rate and to determine the maximum line length that is compatible with it, for a suitable total power. Obviously, this length depends on the number and length of the interfering lines. Some examples are shown in Table X, for "target" bit rates of 50, 75 and 100 Mbps. The Case 3.1 has been analyzed, and therefore the system consists of $L = 8$ lines of equal length; the value of S has been assumed high enough to make the impact of the absolute estimation errors negligible. The table shows the total power required for reaching the specified bit rates, as a function of the line length. Where the label "n.r." appears, this means that the target bit rate cannot be reached within a total power of 14.5 dBm that, in Section II, has been assumed as a typical value. Focusing attention on the bit rate of 100 Mbps, that is the expected value in the G.993.5 Standard, we see that the non-vectored system is unable to reach it even for the shortest lengths. On the contrary, by introducing vectored transmission, the 100 Mbps target can be reached up to distances longer than 600 m. Obviously, this conclusion holds for the specific scenario here considered (note, in particular, that the tagged line and all the interfering ones have the same length) but it can be easily extended, updating the limits, to other scenarios.

Another relevant aspect that results from the numerical analysis is that, depending on the line length, the desired bit rate can often be reached by using a total power P_T^n that is significantly smaller than the typical value of 14.5 dBm. This power saving is another merit of the vectored system, and it is seen with particular interest by the vendors, for the technological advantages it provides.

TABLE X. TOTAL POWER (IN dBm) REQUIRED FOR ACHIEVING THE TARGET BIT RATE IN CASE OF L = 8 LINES OF EQUAL LENGTH

Bit rate (Mbps)	Technique	Line length d (km)										
		0.2	0.3	0.4	0.5	0.6	0.7	0.8	0.9	1.0	1.1	1.2
50	Vectored	–35.2	–28.8	–22.8	–17.9	–13.2	–8.3	–3.3	1.9	7	12.2	n.r.
	Non-vectored	–30.2	–23.5	–17.1	–11.4	–6.3	–0.4	5.9	12.6	n.r.	n.r.	n.r.
75	Vectored	–27.3	–20.9	–14.4	–7.8	–1	5.6	11.6	n.r.	n.r.	n.r.	n.r.
	Non-vectored	–20.5	–13.4	–5.3	4.9	n.r.	n.r.	n.r.	n.r.	n.r.	n.r	n.r.
100	Vectored	–19.7	–13.1	–6.2	1.1	9	n.r.	n.r.	n.r.	n.r.	n.r	n.r.
	Non-vectored	n.r.	n.r.	n.r.	n.r.	n.r.	n.r	n.r	n.r	n.r	n.r.	n.r.

VI. Effect of Quantization Errors

The effect of quantization errors can be modeled in a way similar to that discussed in Section IV for the estimation errors. This analysis has been reported in [2], and is here repeated for the sake of completeness.

Let us suppose that matrix $\mathbf{P}_k$ is represented, in finite precision, as a matrix $\hat{\mathbf{P}}_k$, such that:

$$\hat{\mathbf{P}}_k = \mathbf{P}_k + \mathbf{E}_k \,, \tag{18}$$

where matrix $\mathbf{E}_k$ now expresses the quantization errors. The latter, in turn, can be related to a matrix $\mathbf{\Delta}_k$ as follows:

$$\mathbf{\Delta}_k = \mathbf{P}_k^{-1} \cdot \mathbf{E}_k \,. \tag{19}$$

In ideal conditions, we have $\mathbf{\Delta}_k = \mathbf{E}_k = \mathbf{0}$. Through simple algebra, the signal-to-noise ratio at the nth receiver and the kth tone, in the presence of quantization errors, is [10]:

$$S\bar{N}R_k^n = \frac{\left|H_k^{nn}\right|^2 \left|1+\Delta_k^{nn}\right|^2 P_k^n}{\left|H_k^{nn}\right|^2 \sum_{\substack{j=1 \\ j\neq n}}^{L} \left|\Delta_k^{nj}\right|^2 P_k^j + \sigma_N^2} \,, \tag{20}$$

being Δ_k^{nj} the (n, j)th element of $\mathbf{\Delta}_k$. Eq. (20) can be used to replace SNR_k^n in (3), thus reducing the achievable bit rate with respect to the ideal condition. By investigating the statistical properties of c_k^n in presence of quantization errors, it is possible to find the number of quantization bits needed to have a penalty smaller than a prefixed percentage. In this view, an important analytical work was done in [10], where a number of bounds were determined, and their reliability tested through simulations.

In that paper, however, the elements of $\mathbf{E}_k$ were modeled as random variables uniformly distributed in the range $[-2^{-v}, 2^{-v}]$, where v is the number of quantization bits. No specific quantization law was considered.

Noting by $\bar{c}_k^n$ the number of bit/symbol for user n at tone k in presence of quantization errors, and using (3) and (4), the effect on the bit rate is measured by the following parameter:

$$\frac{\langle L^n \rangle}{C^n} \cdot 100 = \frac{\sum_{k=1}^{M} \langle L_k^n \rangle}{C^n} \cdot 100 \,, \tag{21}$$

where $L_k^n = c_k^n - \bar{c}_k^n = \log_2 \left\{ \frac{1+\Gamma^{-1} SNR_k^n}{1+\Gamma^{-1} S\bar{N}R_k^n} \right\}$ has the meaning of transmission rate loss for the nth receiver at the kth tone [10]. Taking into account that the modulus of the diagonal elements of matrix $\mathbf{P}_k$ is about 1, a first choice consists in assuming a midtread quantization law between −1 and 1. Because of the RWDD property of matrix $\mathbf{H}_k$, however, the off-diagonal elements are very small. So, following this quantization law, most of the off-diagonal elements become zero after quantization, particularly in the case of small v and low frequencies.

Explicitly, this means that the vectoring procedure is made ineffective by quantization. In spite of this, for small values of v, the error due to the quantization is, on average, smaller than that resulting from the assumption of a uniform error. Tables XI and XII show the values of $\langle L^n \rangle / C^n \cdot 100$, in Case 3.2 (i.e., with L = 16 lines of equal length) as obtained by the model in [10] and by the midtread quantization law here considered, for various line lengths, namely: d = 0.3 km, d = 0.6 km, d = 0.9 km and d = 1.2 km. The difference between the two groups of results is evident for small v, while it almost disappears for large v. Both tables confirm that, wishing to have a rate loss below 4% for line lengths ≥ 0.3 km, v = 14 bits is almost always required. Though this value could be implemented on the basis of the current technology, it seems exaggeratedly high, and, in fact, it can be reduced by using a smarter quantization law.

The key point is the need to distinguish between the dynamics of the diagonal elements of $\mathbf{P}_k$, that are close to 1, and that of the off-diagonal elements, that are much smaller than 1. So, in [2] we proposed to adapt the midtread quantization law to such dynamics, by assuming different quantization thresholds for the two classes of data. This approach is further developed and assessed in the following. In practice, the 2^v quantization levels are distributed between $-T_{h1}$ and T_{h1} for the diagonal elements, and between $-T_{h2}$ and T_{h2} for the off-diagonal elements. The assumption of T_{h1} equal to 1 seems a natural choice. On the contrary, the choice of T_{h2} should take into account the dynamics of the off-diagonal elements. Fig. 8 shows an example of max and average values of $\left|P_k^{ij}\right|$, with $i \neq j$, for L = 16 and line length d = 0.3 km or d = 1.2 km.

While the maximum of $\left|P_k^{ij}\right|$ can be locally rather high, the average value is very small, and the assumption of T_{h2} = 0.05 is a reasonable choice, particularly for the short line lengths. So, our quantization law assumes a uniform distribution in the range [–1, +1], for the diagonal elements, and in the range [–0.05, +0.05], for the off-diagonal elements. It should be noted that the implementation of this quantization scheme does not require any additional processing, but only a selective management of the elements of the precoding matrix.

The results obtained by using the midtread quantization law with different thresholds are shown in Table XIII. In comparison with Tables XI and XII, we see a significant improvement for any value of v. In particular, the target of capacity loss below 4%, for d ≥ 0.3 km, can now be achieved by using only v = 10 bits (or even v = 8 bits, for the longest lines), with a significant saving with respect to the case of equal thresholds.

TABLE XI. $\langle L^n \rangle / C^n \cdot 100$ WITH UNIFORM GENERATION OF THE QUANTIZATION ERRORS FOR CASE 3.2

d (km)	$v = 6$	$v = 8$	$v = 10$	$v = 12$	$v = 14$
0.3	86.28	59.33	33.75	13.79	3.34
0.6	64.99	37.95	17.73	5.88	1.08
0.9	60.15	33.40	14.90	4.53	0.71
1.2	61.23	33.13	14.02	4.11	0.60

TABLE XII. $\langle L^n \rangle / C^n \cdot 100$ WITH MIDTREAD QUANTIZATION FOR CASE 3.2

d (km)	$v = 6$	$v = 8$	$v = 10$	$v = 12$	$v = 14$
0.3	61.69	50.84	31.85	13.59	3.37
0.6	38.56	29.24	16.00	5.77	1.13
0.9	28.76	22.85	12.75	4.36	0.72
1.2	24.27	20.03	11.37	3.92	0.61

Similar conclusions were drawn in [2], by considering different scenarios and parameter values, thus proving the effectiveness of the proposed quantization law under rather general conditions.

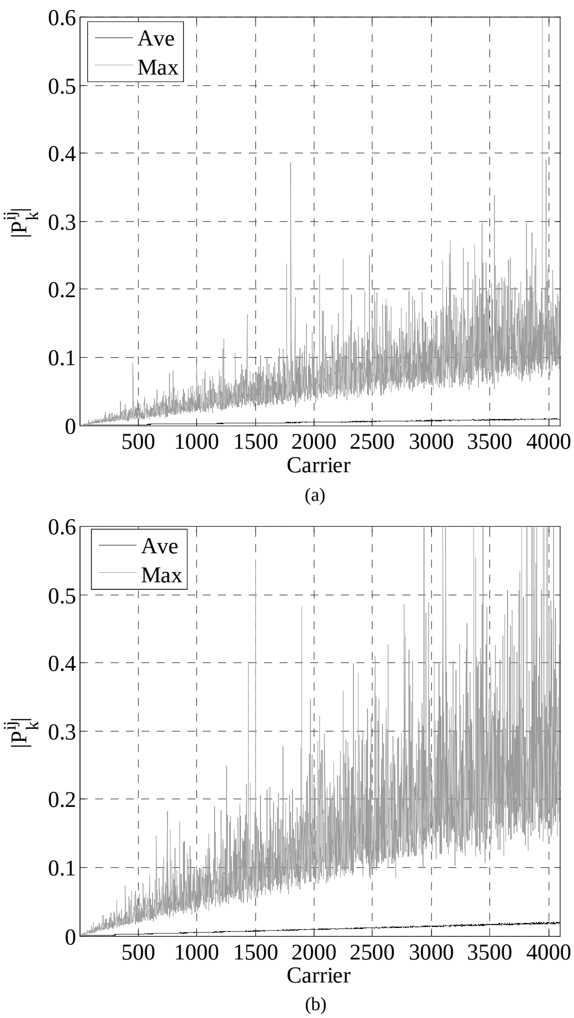

Figure 8. Simulated dynamics for the off-diagonal elements of the precoding matrix: (a) d = 0.3 km, (b) d = 1.2 km, in Case 3.2.

TABLE XIII. $\langle L^n \rangle / C^n \cdot 100$ WITH MIDTREAD QUANTIZATION ADOPTING DIFFERENT THRESHOLDS FOR CASE 3.2

d (km)	$v = 6$	$v = 8$	$v = 10$	$v = 12$	$v = 14$
0.3	29.79	12.66	3.85	1.65	1.48
0.6	15.03	5.17	1.21	0.54	0.49
0.9	11.41	3.58	0.59	0.11	0.07
1.2	10.17	3.14	0.45	0.05	0.03

VII. CONCLUSION

Estimation errors and quantization errors can severely limit the performance of vectored VDSL systems. The analysis of their effects must be performed by taking into account the statistical nature of the FEXT. In this paper, we have considered the case of a downstream VDSL link, where crosstalk is nominally canceled by using a diagonalizing precoder. Starting from analytical formulas for quantifying the effect of such impairments, we have performed a study on practical VDSL scenarios. We have verified that the impact of the estimation errors can be made negligible by using a number of training symbols in the order of S = 1000. Additionally, only 10 bits or fewer are required to maintain the capacity loss below 4% in the presence of quantization errors in the precoding matrix representation. The presented approach also allows to analytically determine the transmitted power that is necessary to achieve a target bit rate at a given distance, that is a key parameter for the design of VDSL systems.

The analysis has been focused on the VDSL2 17 MHz profiles, but it can be extended, for example, to the VDSL2 30 MHz profiles, whose adoption is planned for the near future.

ACKNOWLEDGMENT

Part of this work has been funded by Telecom Italia S.p.A. The authors wish to thank Marco Burzio and Paola Cinato, for helpful discussion and technical comments.

APPENDIX

Derivation of Approximation 2

Let us define:

$$SNR_k^n = \frac{P_k^n \left|H_k^{nn}\right|^2}{|e|^2 \sum_{\substack{j=1 \\ j \neq n}}^{L} \left|H_k^{nj}\right|^2 P_k^j + \sigma_N^2}, \tag{22}$$

the signal-to-noise ratio in the presence of the error percentage e. With the positions (13) and (15), we have:

$$\begin{aligned}\log_2\left(1+\frac{SNR_k^n}{\Gamma}\right) &= \log_2\left(1+\frac{a}{bY+\sigma_N^2}\right) \\ &= \log_2\left(Y+\frac{a+\sigma_N^2}{b}\right) - \log_2\left(Y+\frac{\sigma_N^2}{b}\right).\end{aligned} \tag{23}$$

Let us define:

$$W_1 = Y + \frac{a+\sigma_N^2}{b}, \quad W_2 = Y + \frac{\sigma_N^2}{b}. \tag{24}$$

Both W_1 and W_2 are log-normal variables, with mean value and variance:

$$\mu_{W_1} = \mu_Y + \frac{a+\sigma_N^2}{b}, \quad \mu_{W_2} = \mu_Y + \frac{\sigma_N^2}{b}, \tag{25}$$

$$\sigma_{W_1}^2 = \sigma_{W_2}^2 = \sigma_Y^2. \tag{26}$$

Consequently,

$$\Pi_1 = \log_2 W_1, \quad \Pi_2 = \log_2 W_2 \tag{27}$$

are Gaussian variables, with mean value

$$\langle \Pi_{1/2} \rangle = \log_2\left(\mu_{W_{1/2}}\right) - \frac{1}{2}\log_2\left(1 + \frac{\sigma_{W_{1/2}}^2}{\mu_{W_{1/2}}^2}\right). \tag{28}$$

So, through simple algebra, we obtain:

$$\langle \Pi_1 \rangle - \langle \Pi_2 \rangle = \log_2\left(\frac{\mu_{W_1}}{\mu_{W_2}}\right) + \frac{1}{2}\log_2\left(\frac{\langle W_2^2 \rangle}{\langle W_1^2 \rangle} + \frac{\mu_{W_1}^2}{\mu_{W_2}^2}\right) \tag{29}$$

where $\langle W_i^2 \rangle$, i =1, 2, is the average square value of W_i. Finally, by using the expressions above, (14) is derived.

REFERENCES

[1] M. Baldi, F. Chiaraluce, R. Garello, M. Polano, and M. Valentini, "On the Effect of Estimation and Quantization Errors in Downstream VDSL Systems", Proc. Third International Conference on Communication Theory, Reliability and Quality of Service, CTRQ 2010, Athens/Glyfada, Greece, 13 - 19 Jun. 2010, pp. 49-54.

[2] M. Baldi, F. Chiaraluce, R. Garello, M. Polano, and M. Valentini, "Simple Statistical Analysis of the Impact of Some Nonidealities in Downstream VDSL with Linear Precoding", Eurasip Journal on Advances in Signal Processing, Volume 2010, Article ID 454871, 14 pages, doi: 10.1155/2010/454871.

[3] J. Louveaux and A.-J. van der Veen, "Adaptive Precoding for Downstream Crosstalk Precancelation in DSL Systems Using Sign-Error Feedback", IEEE Transactions on Signal Processing, vol. 58, Jun. 2010, pp. 3173-3179.

[4] R. Y. Gilad, E. Domanovitz, A. Priebatch, I. Sharfer, A. Matza, and E. Tsur, "Vectored VDSL from a Practical Perspective,'" Proc. 2010 IEEE Sensor Array and Multichannel Signal Processing Workshop, Kibbutz Ma'ale Hahamisha, Israel, Oct. 2010, pp. 225-228.

[5] G. Ginis and J. M. Cioffi, "Vectored Transmission for Digital Subscriber Line Systems", IEEE Journal on Selected Areas in Communications, vol. 20, Jun. 2002, pp. 1085-1104.

[6] ITU-T Recommendation G.993.5, "Self-FEXT Cancellation (Vectoring) for Use with VDSL2 Transceivers," Apr. 2010.

[7] V. Oksman, et al., "The ITU-T's New G.vector Standard Proliferates 100 Mb/s DSL", IEEE Communications Magazine, vol. 48, Oct. 2010, pp. 140-148.

[8] R. Cendrillon, G. Ginis, E. Van den Bogaert, and M. Moonen, "A Near-Optimal Linear Crosstalk Precoder for Downstream VDSL", IEEE Transactions on Communications, vol. 55, May 2007, pp. 860-863.

[9] A. Leshem and L. Youming, "A Low Complexity Linear Precoding Technique for Next Generation VDSL Downstream over Copper", IEEE Transactions on Signal Processing, vol. 55, Nov. 2007, pp. 5527-5534.

[10] E. Sayag, A. Leshem, and N. D. Sidiropoulos, "Finite Word Length Effects on Transmission Rate in Zero Forcing Linear Precoding for Multichannel DSL," IEEE Transactions on Signal Processing, vol. 57, Apr. 2009, pp. 1469-1482.

[11] ITU-T Recommendation G.993.2, Amendment 1, ``VTU-R Limit PSD masks for band plan 998 (and its extensions)," Table B.6, Profile 998E17-M2x-NUS0, Apr. 2007.

[12] W. Yu, "Multiuser water-filling in the presence of crosstalk,'" Proc. IEEE Inf. Theory Appls. Workshop, San Diego, CA, 29 Jan.-2 Feb. 2007, pp. 414-420.

[13] J. Musson, "Maximum Likelihood Estimation of the Primary Parameters of Twisted Pair Cables," ETSI/STC TM6 981t08a1, Madrid, Spain, Jan. 1998.

[14] M. Sorbara, P. Duvaut, F. Shmulyian, S. Singh, and A. Mahadevan, "Construction of a DSL-MIMO Channel for Evaluation of FEXT Cancellation Systems in VDSL2," Proc. 2007 IEEE Sarnoff Symposium, Princeton, New Jersey, 30 Apr.-2 May 2007, pp. 1-6.

[15] P. Cardieri and T. S. Rappaport, "Statistics of the Sum of Log-normal Variables in Wireless Communications,'" Proc. 51st IEEE Vehicular Technology Conference (VTC'00), Tokyo, Japan, May 2000, pp. 1823-1827.

[16] S. C. Schwartz and Y. S. Yeh, "On the distribution function and moments of power sums with log-normal components", The Bell System Technical Journal, vol. 61, Sep. 1982, pp. 1441-1462.

[17] P. Turcza and T. Twardowski, "RLS Based MIMO Channel Identification for FEXT Compensation in Vectored xDSL System,'" Proc. European Conference on Circuit Theory and Design, Cork, Ireland, 29 Aug..-2 Sep. 2005, pp. 251-254.

[18] J. Le Masson, M. Ouzzif, and I. Wahibi, "Channel Estimation Using Data and Pilots for a Coordinated DSL System", Proc. IEEE Globecom 2007, Washington, DC, USA, 26 -30 Nov. 2007, pp. 2868-2872.

Signal Detection for 3GPP LTE Downlink: Algorithm and Implementation

Huan Xuan Nguyen
School of Engineering and Information Sciences
Middlesex University
The Burroughs, London, NW4 4BT, United Kingdom
Email: H.Nguyen@mdx.ac.uk

***Abstract*—In this paper[1], we investigate an efficient signal detection algorithm, which combines lattice reduction (LR) and list decoding (LD) techniques for the 3rd generation long term evolution (LTE) downlink systems. The resulting detector, called LRLD based detector, is carried out within the framework of successive interference cancellation (SIC), which takes full advantages of the reliable LR detection. We then extend our studies to the implementation possibility of the LRLD based detector and provide reference for the possible real silicon implementation. Simulation results show that the proposed detector provides a near maximum likelihood (ML) performance with a significantly reduced complexity.**

***Index Terms*—3GPP LTE downlink, signal detection, lattice reduction, successive interference cancellation, implementation study.**

I. Introduction

The 3rd generation partnership project (3GPP) [2] is in the process of defining the long-term evolution (LTE) and Advanced-LTE for 3G radio access, in order to maintain the future competitiveness of 3G technology. The main targets for this evolution concern increased data rates, improved spectrum efficiency, improved coverage, and reduced latency. The LTE downlink is based on orthogonal frequency division multiple access (OFDMA) that allows multiple access on the same channel [3]. This allows simple receivers in case of large bandwidth, frequency selective scheduling and adaptive modulation and coding. The LTE uplink is based on single carrier frequency division multiple access (SC-FDMA) technique [4].

In order to fulfill the requirements on coverage, capacity, and high data rates, novel multiple input multiple output (MIMO) schemes need to be supported as part of the long-term 3G evolution. Signal detection in MIMO systems have recently drawn significant attention. If the maximum likelihood (ML) detection is used, the complexity grows exponentially with the number of transmit antennas. Thus, various approaches are devised to reduce the complexity. The successive interference cancellation (SIC) approach is employed in [5]. The relation between the SIC based MIMO detection and the decision feedback equalizer (DFE) is exploited in [6]. A probabilistic data association (PDA) algorithm, which was devised for the multiuser detection in [7], is applied to the MIMO detection in [8]. In [9], the partial maximum a posteriori probability (MAP) principle is derived to discuss the optimality of the SIC based detection. List decoding (LD) based detectors are also considered for the MIMO detection to obtain soft-decision in [10] and [11]. In [12], a lattice reduction (LR) based MIMO detector used as a low complexity MIMO detector is first discussed. In [13], more LR based MIMO detectors are proposed. Following this trend, this paper considers the signal detection in the LTE downlink, where an efficient signal detection algorithm based on the LR and LD techniques is investigated. The resulting detector (called LRLD detector) produces a list in the LR domain, which results in a much more reliable list and thus is efficient in mitigating error propagation when the SIC based detection is employed. Simulation results show that the LRLD detector provides a near ML performance with a significantly reduced complexity.

However, the potential capacity of the MIMO channel can only be exploited if implementable hardware architecture is available. The main issue in implementing the MIMO detector is the latency incurred by preprocessing the channel matrices

[1]This work was partly presented at the 2010 International Conference on Digital Communications (see reference [1].)

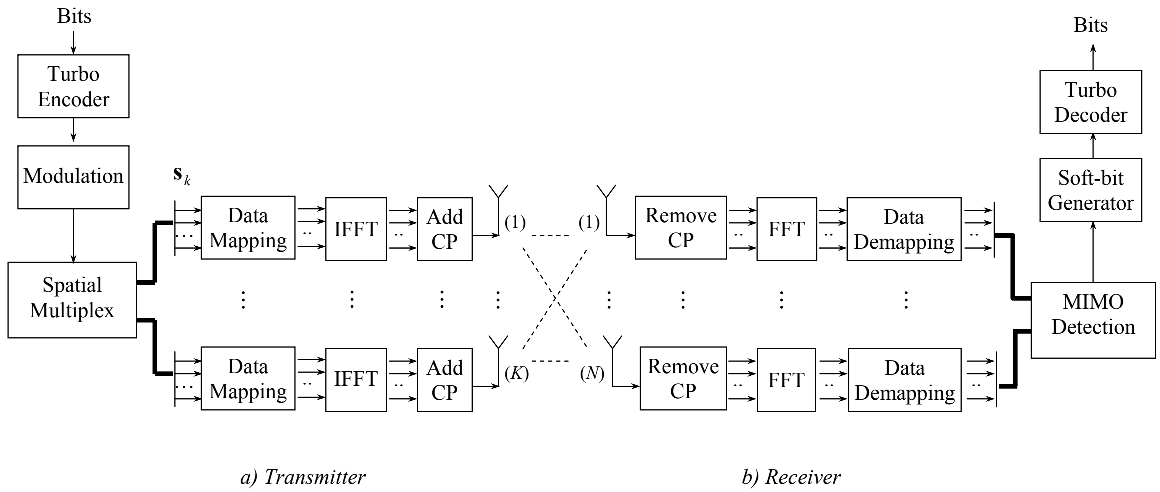

Fig. 1. Block diagram of a MIMO-OFDMA LTE downlink.

[14]. There have been extensive work on the implementation of the MIMO detection either with minimum mean square error-successive interference cancellation (MMSE-SIC) [15], vertical-Bell Laboratories layered space-time (V-BLAST) [16] or Maximum Likelihood (ML) receivers [17]-[22]. However, while the formers usually provide an inferior performance, the latter demandingly requires a large silicon complexity. Thus, finding a reasonable trade-off between an implementable architecture of the MIMO detector and a near ML performance is always a motivation. We therefore extend our studies to the implementation possibility of the proposed detector and then provide references for the possible real silicon implementation.

The rest of the paper is structured as follows. Section II describes the system and channel models. The signal detection algorithm is designed and discussed in Section III. Section IV studies the implementation possibility of the proposed detector. Section V provides simulation results and some concluding remarks are provided in Section VI.

Notation: Bold-face upper (lower) letters denote matrices (column vectors); $(\cdot)^*$, $(\cdot)^{\mathrm{T}}$ and $(\cdot)^{\mathrm{H}}$ denote complex conjugation, transpose and Hermitian transpose, respectively; $\mathbf{I}$ is the identity matrix; $\mathrm{E}[\cdot]$ denotes statistical expectation; $\mathrm{Diag}(\mathbf{x})$ denotes a matrix with vector $\mathbf{x}$ being its diagonal; $\mathcal{N}(\mu, \sigma^2)$ denotes Gaussian distribution with mean μ and variance σ^2; $\delta_{n,n'}$ denotes Kronecker delta; $J_0(\cdot)$ denotes zero-order Bessel function of the first kind; $|\cdot|$ denotes absolute value; and $\|\cdot\|$ denotes Frobenius norm.

II. System and Channel Models

The MIMO-OFDMA LTE system is a parallel of single-input single-output OFDMA (SISO-OFDMA) where blocks of K data symbols are mapped onto the spatial multiplexing (SM) module followed by the data mapping and inverse fast Fourier transform (IFFT) operations, as shown in Figure 1. Note that we do not consider MIMO encoding (e.g., space-time coding) in this work. The data mapping operation is used for subcarrier mapping (e.g., distributed or localized mapping in multiple access [4]). Reversed operations are carried out at the receiver, which are then followed by the signal detection and MIMO processing. Assume that there are K transmit antennas and N receive antennas. Let P and Q denote the number of subcarriers used in one orthogonal frequency division multiplexing (OFDM) symbol for the user of interest and the size of the IFFT, respectively. We denote

$$\mathbf{s}_{P,k} = [s_{1,k}, s_{2,k}, \cdots, s_{P,k}]^{\mathrm{T}} \tag{1}$$

as the transmitted signal vector from the kth transmit antenna. For convenience, it is assumed that $E[s_{p,k}s_{p,k}^*] = 1$ for $1 \leq p \leq P, 1 \leq k \leq K$.

Assuming that the guard interval (i.e., cyclic prefix (CP)) is longer than the maximum channel span, the received signal vector after removing CP and taking fast Fourier transform (FFT) at the nth receive antenna can be written as

$$\mathbf{r}_{P,n} \triangleq [r_{1,n}, r_{2,n}, \cdots, r_{P,n}]^{\mathrm{T}} \tag{2}$$

$$= \sum_{k=1}^{K} \mathrm{Diag}(\mathbf{h}_{n,k})\mathbf{s}_{P,k} + \mathbf{w}_n \tag{3}$$

where $\mathbf{h}_{n,k} = [h_{n,k}(i_1), h_{n,k}(i_2), \cdots, h_{n,k}(i_P)]^T$ is the frequency-domain channel vector from the kth transmit antenna to the nth receive antenna and $\mathbf{w}_n$ is a zero-mean complex Gaussian vector with variance σ_w^2. Here, $i_p = \mathcal{P}(p)$ where $\mathcal{P}(\cdot)$ is the subcarrier mapping function that maps a data symbol onto one of the Q subcarriers. Obviously, i_p is obtained depending on the subcarrier mapping pattern and $i_p \in \{1, 2, \cdots, Q\}$. Note that

$$h_{n,k}(i_p) = \sum_{l=1}^{L} g_{n,k}(l) e^{-\frac{2\pi j}{Q}(l-1)(i_p-1)}$$

where $g_{n,k}(l)$ is the lth tap of the fading channel from kth transmit antenna to the nth receive antenna and L is the number of paths. We can rewrite the received signal for each subcarrier as follow

$$\mathbf{r}_{p,N} = \mathbf{H}(i_p)\mathbf{s}_{p,K} + \mathbf{w}_p \tag{4}$$

where $\mathbf{r}_{p,N} = [r_{p,1}, r_{p,2}, ..., r_{p,N}]^T, p = 0, 1, ..., P-1$, is the signal vector at the i_pth subcarrier received through the N receive antennas. $\mathbf{s}_{p,K}$= $[s_{p,1}, s_{p,2}, ..., s_{p,K}]^T$ is the data symbol vector at the i_pth subcarrier transmitted through K transmit antennas. $\mathbf{w}_p$ is also the complex Gaussian noise vector. $\mathbf{H}(i_p)$ is the frequency-domain channel matrix at the i_pth subcarrier given as

$$\mathbf{H}(i_p) = \begin{pmatrix} h_{1,1}(i_p) & h_{1,2}(i_p) & \cdots & h_{1,K}(i_p) \\ h_{2,1}(i_p) & h_{2,2}(i_p) & \cdots & h_{2,K}(i_p) \\ \vdots & \vdots & \ddots & \vdots \\ h_{N,1}(i_p) & h_{N,2}(i_p) & \cdots & h_{N,K}(i_p) \end{pmatrix}. \tag{5}$$

We assume that the channel is unchanged during one OFDM symbol interval and $g_{n,k}(l)$ is independent and has identical Gaussian distribution $g_{n,k}(l) \sim \mathcal{N}(0, \sigma_l^2)$. Here, σ_l^2 is the normalized average power of each propagation path with

$$\sum_{l=0}^{L-1} \sigma_l^2 = 1. \tag{6}$$

Typical urban (TU) [23] and spatial channel model (SCM) [24] power delay profiles are used in this paper.

1) Typical Urban: We consider the time varying channel whose channel impulse response (CIR) is modeled by L propagation paths,

$$g(\tau, t) = \sum_{l=0}^{L-1} \gamma_l(t)\delta(\tau - \tau_l). \tag{7}$$

Assume that the channel is a wide-sense stationary uncorrelated scattering (WSSUS) Rayleigh fading and unchanged during one OFDM symbol interval. The maximum channel impulse span is also assumed to be within the guard interval. For convenience, let $\tau_l = lT_s$, $T_b = T + T_g$ where $T_s = T/Q$. Here, T, T_b and T_g denote the useful OFDM symbol interval, the whole OFDM symbol interval and the guard interval, respectively. Then, the channel impulse vector at each (OFDM symbol) time index n, denoted by $\mathbf{g}(t) = [g_0(t), g_1(t), ..., g_{L-1}(t)]^T$, can represent the discrete CIR. The autocorrelation function of $g_l(t) = g(lT_s, tT_b)$ is expressed as

$$E\{g_l(t)g_{l'}^*(t')\} = \sigma_l^2 J_0(2\pi f_D(t-t')T_b)\delta_{l,l'}, \tag{8}$$

where f_D is the maximum Doppler frequency and σ_l^2 is the normalized average power of each propagation tap with

$$\sum_{l=0}^{L-1} \sigma_l^2 = 1. \tag{9}$$

An typical urban (TU) power delay profile [23] is used to model $\{\sigma_l^2\}$.

2) Spatial Channel Model: SCM was proposed by the 3GPP for both link- and system-level simulations. The 3GPP SCM emulates the double-directional and clustering effects of small scale fading mechanisms in a variety of environments, such as suburban macrocell, urban macrocell, and urban microcell. It considers N clusters of scatterers. A cluster can be considered as a resolvable path. Within a resolvable path (cluster), there are M subpaths which are regarded as the unresolvable rays. A simplified plot of the SCM is given in Figure 2, where only one cluster of scatterers is shown as an example. Here, θ_v is the angle of the mobile station (MS) velocity vector with respect to the MS broadside, $\theta_{n,m,AoD}$ is the absolute angle of departure (AoD) for the mth ($m = 1, ..., M$) subpath of the nth ($n = 1, ..., N$) path at the base station (BS) with respect to the BS broadside, and $\theta_{n,m,AoA}$ is the absolute angle of arrival (AoA) for the mth subpath of the nth path at the MS with respect to the MS broadside. Details of the generation of SCM simulation parameters can be found in [24].

III. Signal Detection

For convenience, the indices in (4) are omitted. The $N \times 1$ received signal vector $\mathbf{r}_{p,N}$, now denoted by $\mathbf{r}$, is given by

$$\mathbf{r} = \mathbf{Hs} + \mathbf{w}, \tag{10}$$

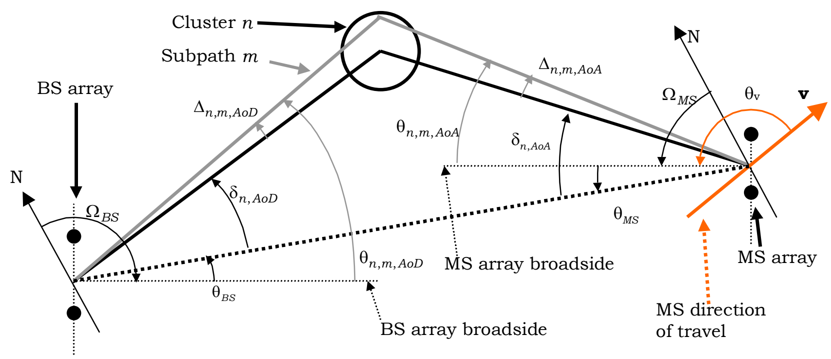

Fig. 2. BS and MS angle parameters in the 3GPP SCM with one cluster of scatterers [24].

where $\mathbf{H}$, $\mathbf{s}$, and $\mathbf{w}$ are the $N \times K$ channel matrix, the $K \times 1$ transmitted signal vector, and the $N \times 1$ noise vector, respectively. Let $\mathcal{S}$ denote the signal alphabet for symbols, i.e., $s_k \in \mathcal{S}$, where s_k denotes the kth element of $\mathbf{s}$, and its size is denoted by M, i.e., $M = |\mathcal{S}|$.

A. Conventional Detectors

We consider two conventional detection approaches: ML and MMSE.

1) ML Detection: The ML detection finds the data symbol vector that maximizes the likelihood function as follows:

$$\begin{aligned} \mathbf{s}_{\rm ml} &= \arg \max_{\mathbf{s} \in \mathcal{S}^K} f(\mathbf{r}|\mathbf{s}) \\ &= \arg \min_{\mathbf{s} \in \mathcal{S}^K} ||\mathbf{r} - \mathbf{H}\mathbf{s}||^2. \end{aligned} \tag{11}$$

To identify the ML vector, an exhaustive search is required. Because the number of candidate vectors for $\mathbf{s}$ is M^K, the complexity grows exponentially with K.

If the a priori probability of $\mathbf{s}$ is available, the maximum a posteriori (MAP) sequence detection can be formulated. Suppose that $\mathbf{b}$ is a bit-level symbol vector representation of $\mathbf{s}$. The elements of $\mathbf{b}$ are binary and the size of $\mathbf{b}$ is $(K \log_2 M) \times 1$. With the a priori probability of $\mathbf{b}$, the MAP vector (at the bit-level) becomes

$$\begin{aligned} \mathbf{b}_{\rm map} &= \arg \max_{\mathbf{b}} \Pr(\mathbf{b}|\mathbf{r}) \\ &= \arg \max_{\mathbf{b}} f(\mathbf{r}|\mathbf{b}) \Pr(\mathbf{b}), \end{aligned} \tag{12}$$

where $\Pr(\mathbf{b})$ denotes the a priori probability of $\mathbf{b}$. In addition, the a posteriori probability of each bit can be found by marginalization as

$$\begin{aligned} \Pr(b_i = +1|\mathbf{r}) &= \sum_{\mathbf{b} \in \mathcal{B}_i^+} \Pr(\mathbf{b}|\mathbf{r}) \\ \Pr(b_i = -1|\mathbf{r}) &= \sum_{\mathbf{b} \in \mathcal{B}_i^-} \Pr(\mathbf{b}|\mathbf{r}), \end{aligned} \tag{13}$$

where $\mathcal{B}_i^{\pm} = \{[b_1 \ b_2 \ \ldots \ b_{\bar{K}}]^{\rm T} \ | \ b_i = \pm 1, b_m \in \{+1, -1\}, \ \forall m \neq i\}$ and $\bar{K} = K \log_2 M$.

2) MMSE Detection: It is easy to perform the (linear) MMSE detection if the constraint on the symbol vector, $s_k \in \mathcal{S}$, $\forall k$, is not imposed. Using the orthogonality principle, the MMSE estimator for $\mathbf{s}$ can be found as

$$\begin{aligned} \mathbf{W}_{\rm mmse} &= \arg \min_{\mathbf{W}} E[||\mathbf{s} - \mathbf{W}^{\rm H}\mathbf{r}||^2] \\ &= \left(E[\mathbf{r}\mathbf{r}^{\rm H}]\right)^{-1} E[\mathbf{r}\mathbf{s}^{\rm H}]. \end{aligned} \tag{14}$$

We can show that

$$\begin{aligned} E[\mathbf{r}\mathbf{r}^{\rm H}] &= \mathbf{H}\mathbf{H}^{\rm H} + \sigma_w^2 \mathbf{I} \\ E[\mathbf{r}\mathbf{s}^{\rm H}] &= \mathbf{H}. \end{aligned}$$

It follows that

$$\mathbf{W}_{\rm mmse} = (\mathbf{H}\mathbf{H}^{\rm H} + \sigma_w^2 \mathbf{I})^{-1} \mathbf{H}$$

and

$$\begin{aligned} \hat{\mathbf{s}}_{\rm mmse} &= \mathbf{W}_{\rm mmse}^{\rm H} \mathbf{r} \\ &= \mathbf{H}^{\rm H}(\mathbf{H}\mathbf{H}^{\rm H} + \sigma_w^2 \mathbf{I})^{-1} \mathbf{r}. \end{aligned} \tag{15}$$

B. Proposed Detector

We assume that $N \geq K$ and consider the QR factorization of the channel matrix as $\mathbf{H} = \mathbf{Q}\mathbf{R}$, where $\mathbf{Q}$ is unitary and $\mathbf{R}$ is upper triangle. We have

$$\mathbf{x} = \mathbf{Q}^{\rm H}\mathbf{r} = \mathbf{R}\mathbf{s} + \mathbf{Q}^{\rm H}\mathbf{w}. \tag{16}$$

Since the statistical properties of $\mathbf{Q}^{\rm H}\mathbf{w}$ are identical to that of $\mathbf{w}$, $\mathbf{Q}^{\rm H}\mathbf{w}$ will be denoted by $\mathbf{w}$. If $N = K$, there is no zero rows in $\mathbf{R}$, otherwise the last $N - K$ rows would be zero. Thus, the last $N - K$ elements of $\mathbf{x}$ would be ignored for the detection if $N > K$. Accordingly, the first K rows of $\mathbf{R}$ would be considered. If there is no risk of confusion, hereafter, we assume that the sizes of $\mathbf{x}$, $\mathbf{R}$, and $\mathbf{w}$ are $K \times 1$, $K \times K$, and $K \times 1$, respectively.

The complexity of the conventional LR based detector can grows significantly with the number of basis vectors. To avoid this problem, we propose an LRLD based detection algorithm, which breaks a high dimensional MIMO detection problem into multiple lower dimensional MIMO sub-detection problems.

To perform the proposed LRLD based detection, we consider the partition of $\mathbf{x}$ as follows:

$$\begin{bmatrix} \mathbf{x}_1 \\ \mathbf{x}_2 \end{bmatrix} = \begin{bmatrix} \mathbf{R}_1 & \mathbf{R}_3 \\ \mathbf{0} & \mathbf{R}_2 \end{bmatrix} \begin{bmatrix} \mathbf{s}_1 \\ \mathbf{s}_2 \end{bmatrix} + \begin{bmatrix} \mathbf{w}_1 \\ \mathbf{w}_2 \end{bmatrix}, \tag{17}$$

where $\mathbf{x}_i$, $\mathbf{s}_i$, and $\mathbf{w}_i$ denote the $K_i \times 1$ ith subvectors of $\mathbf{x}$, $\mathbf{s}$, and $\mathbf{w}$, $i = 1, 2$, respectively. Note that $K_1 + K_2 = K$. From (17), we can have two lower dimensional MIMO sub-detection problems to detect $\mathbf{s}_1$ and $\mathbf{s}_2$. It is straightforward to extend the partition into more than two groups. However, for the sake of simplicity, we only consider the partition into two groups as in (17).

In the proposed LRLD based detection, the sub-detection of $\mathbf{s}_2$ is carried out first using the LR based detector. Then, a list of candidate vectors of $\mathbf{s}_2$ is generated. With the list of $\mathbf{s}_2$, the sub-detection of $\mathbf{s}_1$ is performed with the LR based detector. The candidate vector in the list is used for the SIC to mitigate the interference from $\mathbf{s}_2$. The algorithm steps (AS) of the proposed LRLD based detector is summarized as follows.

AS1) The LR based detection of $\mathbf{s}_2$ is performed with the received signal $\mathbf{x}_2$, i.e.,

$$\tilde{\mathbf{c}}_2 = \text{LRDet}(\mathbf{x}_2),$$

where LRDet$(\cdot)$ is the function of the LR detection operation (see Appendix A for details of the LR detection), and $\tilde{\mathbf{c}}_2$ is the estimated vector of $\mathbf{s}_2$ in the corresponding LR domain. Note that there is no interference from $\mathbf{s}_1$ in detecting $\mathbf{s}_2$.

AS2) A list of candidate vectors in the lattice-reduced domain is generated by

$$\mathcal{C}_2 = \text{List}(\tilde{\mathbf{c}}_2),$$

where List is a function that chooses the Q closest vectors to $\tilde{\mathbf{c}}_2 (1 \le Q \le M^{K_2})$ in the LR domain. The details of the list generation is discussed in Appendix B.

AS3) The list of candidates of $\mathbf{s}_2$, denoted by $\mathcal{S}_2$, can be converted from $\mathcal{C}_2$. For convenience, denote $\mathcal{S}_2 = \{\tilde{\mathbf{s}}_2^{(1)}, \tilde{\mathbf{s}}_2^{(2)}, \cdots, \tilde{\mathbf{s}}_2^{(Q)}\}$.

AS4) Once $\mathcal{S}_2$ is available, the LR-based detection of $\mathbf{s}_1$ can be carried out with SIC, i.e.,

$$\tilde{\mathbf{c}}_1^{(q)} = \text{LRDet}(\mathbf{x}_1 - \mathbf{R}_3 \tilde{\mathbf{s}}_2^{(q)}),$$

where $\tilde{\mathbf{s}}_2^{(q)}$ is the qth decision vector of $\mathbf{s}_2$ from list $\mathcal{S}_2$.

AS5) Let $\tilde{\mathbf{s}}_1^{(q)}$ denote the signal vector corresponding to $\tilde{\mathbf{c}}_1^{(q)}$ in the LR domain and $\tilde{\mathbf{s}}^{(q)} = [(\tilde{\mathbf{s}}_1^{(q)})^{\mathrm{T}} \ (\tilde{\mathbf{s}}_2^{(q)})^{\mathrm{T}}]^{\mathrm{T}}$, the final decision of $\mathbf{s}$ is found as

$$\tilde{\mathbf{s}} = \arg \min_{q=1,2,\cdots,Q} \left\| \mathbf{x} - \mathbf{R}\tilde{\mathbf{s}}^{(q)} \right\|^2 .$$

Softbit Generation: As we are using turbo code for channel coding, its inputs should be soft bits. The probability of the qth candidate $\hat{\mathbf{s}}^{(q)}$ in the list can be found as

$$P(\hat{\mathbf{s}}^{(q)}) = C_Q \exp\left(-\frac{1}{\sigma_w^2} ||\mathbf{x} - \mathbf{R}\hat{\mathbf{s}}^{(q)}||^2 \right), \tag{18}$$

where C_Q is the normalization constant, which is given by

$$C_Q = \frac{1}{\sum_{q=1,\cdots,Q} \exp\left(-\frac{1}{\sigma_w^2} ||\mathbf{x} - \mathbf{R}\hat{\mathbf{s}}^{(q)}||^2 \right)}.$$

Note that

$$\sum_{q=1,\cdots,Q} P(\hat{\mathbf{s}}^{(q)}) = 1. \tag{19}$$

Suppose that $\hat{\mathbf{b}}^{(q)}$ is a bit-level symbol vector representation of $\hat{\mathbf{s}}^{(q)}$, i.e., $\hat{\mathbf{s}}^{(q)} = \mathcal{M}(\hat{\mathbf{b}}^{(q)})$ where $\mathcal{M}(\cdot)$ denotes the mapping rule. The elements of $\hat{\mathbf{b}}^{(q)}$ are binary and the size of $\hat{\mathbf{b}}^{(q)}$ is $\bar{K} \times 1$ where $\bar{K} = K \log_2 M$. Correspondingly, the probability of $\hat{\mathbf{b}}^{(q)}$ can be written as

$$P(\hat{\mathbf{b}}^{(q)}) = C_Q \exp\left(-\frac{1}{\sigma_w^2} ||\mathbf{x} - \mathbf{R}\mathcal{M}(\hat{\mathbf{b}}^{(q)})||^2 \right), \tag{20}$$

The soft log-likelihood ratio (LLR) value of the ith bit b_i ($i = 1, 2, \cdots, \bar{K}$) can then be obtained as

$$\Lambda(b_i) = \log \frac{\sum_{\hat{\mathbf{b}}^{(q)} \in \mathcal{B}_i^+} P(\hat{\mathbf{b}}^{(q)})}{\sum_{\hat{\mathbf{b}}^{(q)} \in \mathcal{B}_i^-} P(\hat{\mathbf{b}}^{(q)})}, \tag{21}$$

where $\mathcal{B}_i^{\pm} = \{[b_1 \ b_2 \ \ldots \ b_{\bar{K}}]^{\mathrm{T}} \mid b_i = \pm 1, b_m \in \{+1, -1\}, \ \forall m \neq i\}$.

IV. Implementation Study of the Proposed Detector

In this section, we study the implementation possibility of the proposed LRLD detector. Note that some details of the proposed detector and definition of certain parameters, e.g., α, β, are presented in Appendix A and B.

A. Detector Structure

For convenience, we outline the implementation steps (IS) required for the proposed detector as follows.

IS1) *QR decomposition*:

$$\mathbf{H} = \mathbf{Q}\mathbf{R},$$

where

$$\mathbf{R} = \begin{bmatrix} \mathbf{R}_1 & \mathbf{R}_3 \\ \mathbf{0} & \mathbf{R}_2 \end{bmatrix}.$$

IS2) *Gaussian lattice reduction*:

$$\bar{\mathbf{R}}_1 = \mathbf{R}_1\mathbf{U}_1,$$

$$\bar{\mathbf{R}}_2 = \mathbf{R}_2\mathbf{U}_2.$$

IS3) *MMSE filtering weight matrices*:

$$\mathbf{W}_1 = (\mathbf{R}_1\mathbf{R}_1^{\mathrm{H}}\alpha^2 E_s + |\alpha|^2\sigma_w^2\mathbf{I})^{-1}\mathbf{R}_1\mathbf{U}_1^{-\mathrm{H}}\alpha^2 E_s,$$
$$\mathbf{W}_2 = (\mathbf{R}_2\mathbf{R}_2^{\mathrm{H}}\alpha^2 E_s + |\alpha|^2\sigma_w^2\mathbf{I})^{-1}\mathbf{R}_2\mathbf{U}_2^{-\mathrm{H}}\alpha^2 E_s.$$

IS4) *Unitary transformation*:

$$\mathbf{x} = \mathbf{Q}^{\mathrm{H}}\mathbf{r}$$
$$= \mathbf{R}\mathbf{s} + \mathbf{w},$$

or

$$\begin{bmatrix} \mathbf{x}_1 \\ \mathbf{x}_2 \end{bmatrix} = \begin{bmatrix} \mathbf{R}_1 & \mathbf{R}_3 \\ \mathbf{0} & \mathbf{R}_2 \end{bmatrix} \begin{bmatrix} \mathbf{s}_1 \\ \mathbf{s}_2 \end{bmatrix} + \begin{bmatrix} \mathbf{w}_1 \\ \mathbf{w}_2 \end{bmatrix}.$$

IS5) *Scaling/shifting*:

$$\mathbf{d}_2 = \alpha\mathbf{x}_2 + \beta\mathbf{R}_2\mathbf{1},$$
$$\mathbf{b}_2 = \alpha\mathbf{s}_2 + \beta\mathbf{1},$$
$$\mathbf{d}_1^{(q)} = \alpha(\mathbf{x}_1 - \mathbf{R}_3\hat{\mathbf{s}}_2^{(q)}) + \beta\mathbf{R}_1\mathbf{1},$$
$$\mathbf{b}_1 = \alpha\mathbf{s}_1 + \beta\mathbf{1}.$$

IS6) *LR based list detection*: This step includes three stages:

- one MMSE filtering operation to estimate $\mathbf{c}_2$ (i.e., signal vector $\mathbf{s}_2$ in the LR domain):

$$\tilde{\mathbf{c}}_2 = \mathbf{W}_2^H(\mathbf{d}_2 - \beta\mathbf{R}_2\mathbf{1}) + \mathbf{U}_2^{-1}\beta\mathbf{1}$$
$$= \alpha\mathbf{W}_2^H\mathbf{x}_2 + \mathbf{U}_2^{-1}\beta\mathbf{1}.$$

- sorting and storing the list of $\mathbf{c}_2$ (of length Q):

$$\mathcal{C}_2 = \{\mathbf{c}_2 \mid ||\tilde{\mathbf{c}}_2 - \mathbf{c}_2|| < r(Q)\}.$$

- Q parallel MMSE filtering operations to estimate $\mathbf{c}_1$ with respect to each candidate of the list of $\mathbf{c}_2$:

$$\tilde{\mathbf{c}}_1^{(q)} = \alpha\mathbf{W}_1^H(\mathbf{x}_1 - \mathbf{R}_3\hat{\mathbf{s}}_2^{(q)}) + \mathbf{U}_1^{-1}\beta\mathbf{1},$$

where $\mathbf{s}_2^{(q)} = (\mathbf{U}_2\mathbf{c}_2^{(q)} - \beta\mathbf{1})/\alpha$ and $\mathbf{c}_2^{(q)} \in \mathcal{C}_2$.

The implementation operations can be classified into two types: Pre-processing and detection processing.

Pre-processing: This is often referred to as channel-rate processing, in which all operations need to be carried out only when there is a new channel update. All steps from IS1) to IS3) belong to this type.

Detection Processing: This can be referred to as symbol-rate processing. This type of processing includes all operations that are carried out after each received signal vector arrives. In our proposed detector, the received data will be processed in a first in first out (FIFO) manner. The FIFO buffer is used to bridge the latency incurred among the received signals. All steps from IS4) to IS6) belong to this type.

Figure 3 shows a high-level structure of the proposed detector with respect to hardware implementation. We will describe each major operation next. Some operations such as unitary transformation, shifting/scaling and final decision are straightforward and thus ignored. Since memory is nowadays not a big issue in the hardware implementation, we assume that a certain amount of memory is available wherever needed.

B. Pre-Processing

In our proposed detector, there are three dominant components in the pre-processing stage – QR decomposition, Gaussian lattice reduction and matrix inversion operations. It is always desirable to have a low latency in preprocessing the channel matrices. Thus, selection of algorithm to be implemented for each of the three above operations may well decide the real silicon complexity. We will consider each operation in details next.

1) QR Decomposition: As shown in [25], QR decomposition is preferred to Cholesky decomposition due to the numerical stability. In our detection algorithm, although the QR operation is required only once for each channel update, it still provides a significant load of computations as the operation is carried out to the channel matrix of full size. We therefore study different algorithms in the literature for the QR decomposition.

Gram-Schmidt:

The Gram-Schmidt (GS) procedure finds the QR decomposition of a matrix $\mathbf{H}$ such that $\mathbf{H} = \mathbf{Q}\mathbf{R}$, where $\mathbf{Q}$ is unitary and $\mathbf{R}$ is upper triangular. An obvious drawback of

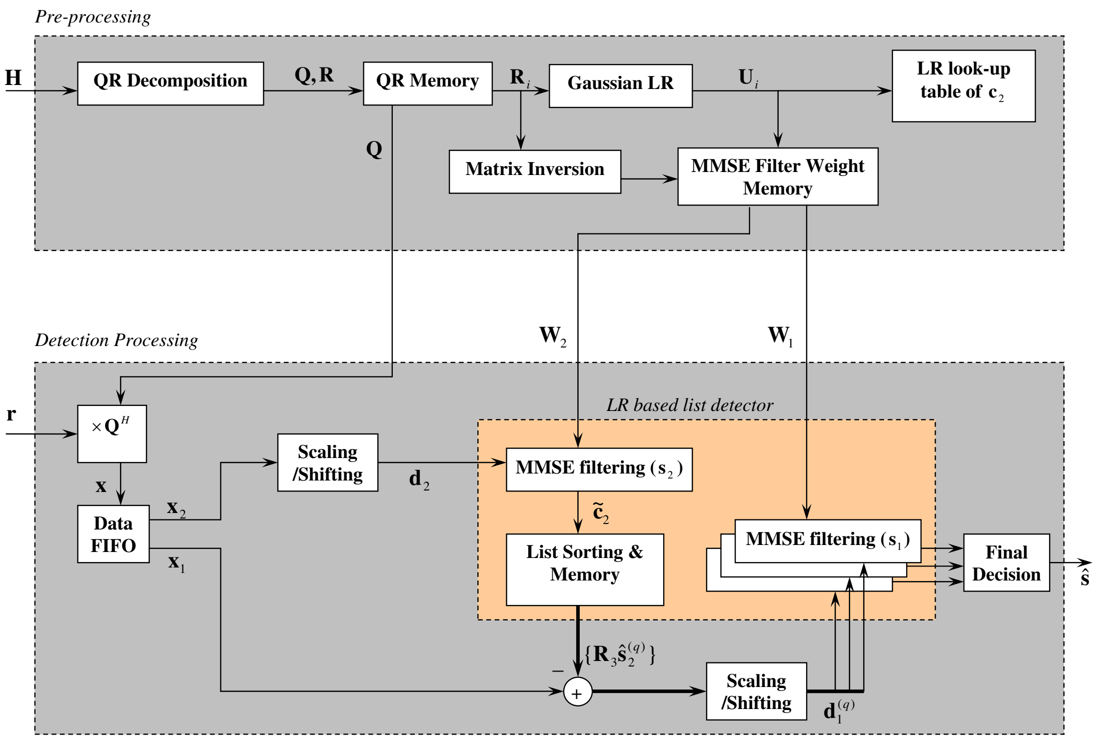

Fig. 3. High-level structure diagram of the implementation of the proposed LR based list detector.

the GS algorithm is the fact that it requires costly square-root and division operations and that the overall computational complexity is high. Thus, a modified version of the GS is presented (see [26]). The details of the modified GS are discussed in [27], [28]. The corresponding algorithm proceeds as follows.

Gram-Schmidt algorithm:

1) `initialize:` $\mathbf{Q} = \mathbf{H}, \mathbf{R} = \mathbf{0}$
2) `for` $k = 1$ `to` K
3) $\quad [\mathbf{R}]_{k,k} = \sqrt{\mathbf{q}_k^{\mathrm{H}}\mathbf{q}_k}$
4) $\quad \mathbf{q}_k = \mathbf{q}_k / [\mathbf{R}]_{k,k}$
5) $\quad$ `for` $i = k+1$ `to` K
6) $\quad\quad [\mathbf{R}]_{k,i} = \mathbf{q}_k^{\mathrm{H}}\mathbf{q}_i$
7) $\quad\quad \mathbf{q}_i = \mathbf{q}_i - [\mathbf{R}]_{k,i}\mathbf{q}_k$
8) $\quad$ `end for`
9) `end for`

Generally, the GS is accurate to the floating-point precision. For fixed-point arithmetic, the problem of quantization and round-off errors is not ignorable and therefore there is loss in accuracy (e.g., loss in the orthogonality of $\mathbf{Q}$) [27]. It was shown in [29] that the orthogonalization error (ϵ_o) in fixed-point version of the GS algorithm is bounded by the product of condition number $\kappa(\mathbf{H})$ of matrix $\mathbf{H}$ and machine precision ε, as follows

$$\begin{aligned}\epsilon_o &= \| \mathbf{I} - \mathbf{Q}^{\mathrm{H}}\mathbf{Q} \| \\ &\leq \zeta(K) \times \varepsilon \times \kappa(\mathbf{H}),\end{aligned}$$

where $\zeta(K)$ is a low degree polynomial in K depending only on details of computer arithmetic. This implies that for a well-conditioned matrix, fixed-point architecture for the GS is still accurate to the integer multiples of the machine precision ε. However, for ill-conditioned matrices, the computed $\mathbf{Q}$ can be very far from orthogonal. Thus, we can consider the numerically more favorable scheme, Householder Transformation, which is based on unitary transformation.

Householder Transformation:

The use of unitary transformations instead of the conventional methods is to alleviate the numerical problem such as requirement of high number precision, i.e., large silicon area in fixed-point very-large-scale integration (VLSI) implementation is required. The reason for this more favorable behavior is that unitary transformations do not alter the length of a vector and thus cannot lead to an excessive increase in dynamic range or to an enhancement of quantization noise. Two typical algorithms using unitary transformations are Householder Transformation and Givens Rotation. For illustrative purpose, we overview the Householder Reflection algorithm only.

The Householder Transformation algorithm recursively applies a sequence of unitary transformations $\mathbf{Q}_i^{\mathrm{H}}$ to matrix $\mathbf{H}$ as follows:

$$\mathbf{R}^{(k+1)} = \mathbf{Q}_k^{\mathrm{H}} \mathbf{R}^{(k)},$$

where $\mathbf{R}^{(1)} = \mathbf{H}$. Each transformation will eliminate more subdiagonal entries until finally $\mathbf{R} = \mathbf{R}^{(K-1)} = \mathbf{Q}_{K-1}^{\mathrm{H}} \cdots \mathbf{Q}_1^{\mathrm{H}} \mathbf{H}$. The unitary matrix $\mathbf{Q}^{\mathrm{H}}$ is readily obtained from

$$\mathbf{Q}^{\mathrm{H}} = \mathbf{Q}_{K-1}^{\mathrm{H}} \cdots \mathbf{Q}_1^{\mathrm{H}}.$$

The algorithm can be described in details as follows.

Householder Transformation algorithm:

1) `initialize:` $\mathbf{Q}^{(0)} = \mathbf{I}, \mathbf{R}^{(1)} = \mathbf{H}$
2) `for` $k = 1$ `to` $K-1$
3) $\quad\bar{\mathbf{q}}_k = \mathbf{r}_k + \parallel \mathbf{r}_k \parallel \mathbf{1}$
4) $\quad\bar{\mathbf{Q}}_k = \mathbf{I} - 2\frac{\bar{\mathbf{q}}_k \bar{\mathbf{q}}_k^{\mathrm{H}}}{\|\bar{\mathbf{q}}_k\|^2}$
5) $\quad\mathbf{P}_k = \begin{bmatrix} \mathbf{I}_{k-1} & \mathbf{0} \\ \mathbf{0} & \bar{\mathbf{Q}}_k \end{bmatrix}$
6) $\quad[\mathbf{R}]_{k+1}^{H} = \mathbf{P}_k \mathbf{R}^{(k)}$
7) $\quad\mathbf{Q}^{(k)} = \mathbf{P}_k \mathbf{Q}^{(k-1)}$
8) `end for`
9) $\mathbf{Q}^{\mathrm{H}} = \mathbf{Q}^{(K-1)}$

We compare the complexity of the two methods in Table I. The Householder Reflection algorithm provides a slightly lower number of complex multiplications (CMs), divisions and square root operations compared to the Gram-Schmidt algorithm. In addition, for fixed-point implementation, the Householder Reflection algorithm is supposed to be more stable.

Note that $(K^2 + K(K+1)/2)$ words of memory[2] are required to store matrices $\mathbf{Q}$ and $\mathbf{R}$ at the output of the QR decomposition operation.

2) Lattice Reduction Using Gaussian Method: In the proposed LR based list detector, the LR is applied to the subchannel matrix $\mathbf{R}_1$ and $\mathbf{R}_2$. For convenience, we consider these matrices of size 2×2 only. Thus, this basis-2 LR can be carried out using the simple Gaussian method. We can limit the maximum number of iterations in this Gaussian lattice reduction algorithm to a small number (e.g., 2 iterations is reasonable) while keeping the overall performance almost the same. For the implementation purpose, we can fix the maximum number of iterations to T, and the Gaussian LR algorithm is summarized as follows.

1) `Input` $(\mathbf{b}_1, \mathbf{b}_2, T)$
2) `Set` $\mathbf{J} = \begin{bmatrix} 0 & 1 \\ 1 & 0 \end{bmatrix}$ `and` $\mathbf{U} = \begin{bmatrix} 1 & 0 \\ 0 & 1 \end{bmatrix}$
3) i = 0
4) `do`
5) $\quad$`if` $||\mathbf{b}_1|| > ||\mathbf{b}_2||$
6) $\qquad$`swap` $\mathbf{b}_1$ `and` $\mathbf{b}_2$`, and` $\mathbf{U} = \mathbf{UJ}$
7) $\quad$`end if`
8) $\quad$`if` $|<\mathbf{b}_2, \mathbf{b}_1>| > 1/2$
9) $\qquad\hat{t} = \lfloor \frac{<\mathbf{b}_2, \mathbf{b}_1>}{||\mathbf{b}_1||^2} \rceil$
10) $\qquad\mathbf{b}_2 = \mathbf{b}_2 - \hat{t}\mathbf{b}_1$ and $\mathbf{U} = \mathbf{U} \begin{bmatrix} 1 & -t \\ 0 & 1 \end{bmatrix}$
11) $\quad$`end if`
12) $\quad i = i + 1$
13) `while` $(||\mathbf{b}_1|| < ||\mathbf{b}_2||) \&\& (i \leq T)$
14) `return` $(\mathbf{b}_1, \mathbf{b}_2, \mathbf{U})$

In the worst case where the Gaussian LR algorithm runs until the maximum iteration $i = T$, the number of CMs required for the Gaussian LR is $4T$. Six words of memory are required to store data of the unimodular matrix at the output.

3) Matrix Inversion: In our proposed detector, the dominant complexity component in obtaining the MMSE filtering weight matrices is the matrix inversion operations, $(\mathbf{R}_1\mathbf{R}_1^{\mathrm{H}}\alpha^2 E_s + |\alpha|^2\sigma_w^2\mathbf{I})^{-1}$ and $(\mathbf{R}_2\mathbf{R}_2^{\mathrm{H}}\alpha^2 E_s + |\alpha|^2\sigma_w^2\mathbf{I})^{-1}$. Fortunately, the fact that the size of these submatrices to be inverted is reasonably small leads to a reasonably low load of computations. For example, a 2×2 matrix $\mathbf{R} = \begin{bmatrix} r_{1,1} & r_{1,2} \\ r_{2,1} & r_{2,2} \end{bmatrix}$ can be simply inverted using adjoint method

$$\mathbf{R}^{-1} = \frac{1}{r_{1,2}r_{2,1} - r_{1,1}r_{1,1}} \begin{bmatrix} r_{2,2} & -r_{2,1} \\ -r_{1,2} & r_{1,1} \end{bmatrix},$$

which requires 1 division and 6 CMs.

In a general case of matrix $\mathbf{H}$ of size $K \times K$, the complexity of inversion operation may vary depending on implementation method. We overview some typical methods:

[2]The term 'word of memory' is referred to the amount of memory required to store one complex number. The number of bits in one word may vary depending on the dynamic range of the observing data. Thus, throughout the section, we use 'word' as a unit of memory.

TABLE I
COMPLEXITY COMPARISON OF THE TWO METHODS: GRAM-SCHMIDT (GS) AND HOUSEHOLDER REFLECTION (HR)

Algorithm	**Division**	**Square root**	**Complex multiplications (CMs)**	**CMs with $K=4$**
GS	K	K	$2K^2 + 2\sum_{k=1}^{K} K(K-k)$	80
HR	$K-1$	$K-1$	$2\sum_{k=1}^{K-1}(K-k+1)^2$	78

a) Adjoint Method:

$$\mathbf{H}^{-1} = \frac{\text{adj}(\mathbf{H})}{\det(\mathbf{H})}.$$

Unfortunately, for the matrix inversion using adjoint method, there is no generic expression for the number of CMs as it depends heavily on the dimension K. However, the approximated number of CMs can be of up to scale in 2^K as [30]

$$\mathcal{C}_m \approx a2^K + K^2 + K.$$

b) LR Decomposition: Matrix $\mathbf{H}$ is decomposed into a lower-triangular matrix $\mathbf{L}$ and a upper-triangular matrix $\mathbf{R}$, i.e., $\mathbf{H}^{-1} = \mathbf{R}^{-1}\mathbf{L}^{-1}$. The algorithm is as follows

1) `Initiate` $\mathbf{L} = \mathbf{H}, \mathbf{R} = \mathbf{I}$
2) `For` $i = 1$ `to` K
3) `For` $j = 1$ `to` K
4) $[\mathbf{R}]_{j,i} = [\mathbf{L}]_{j,i} - \sum_{k=1}^{j-1}[\mathbf{L}]_{j,k}[\mathbf{R}]_{k,j}$
5) $[\mathbf{L}]_{j,i} = \frac{[\mathbf{R}]_{j,i}}{[\mathbf{R}]_{i,i}}$
6) `end for`
7) `end for`

The number of CMs for matrix inversion using LR decomposition is $4(K^3 - K)/3$.

c) QR Decomposition: Matrix $\mathbf{H}$ can be inverted using QR decomposition as $\mathbf{H}^{-1} = \mathbf{R}^{-1}\mathbf{Q}^H$. If Gram-Schmidt algorithm is used for QR decomposition, the total number of CMs required for matrix inversion is $(9K^3 + 10K^2 - K)/6$.

In general, a major concern with matrix inversion algorithms is the need for a high number precision which gives rise to a large silicon area in fixed-point VLSI implementations. The two main reasons for these numerical requirements are: i) the use of costly operation such as square root and divisions, which leads to a significant increase of the dynamic range for some intermediate variables; and ii) the desire to replace repeated divisions by multiplications with the corresponding inverse in order to reduce the number of costly operations. Unfortunately, multiplications often results in an enhancement of the quantization noise and thus requires a high fixed point precision.

A VLSI architecture has therefore been proposed in [28] to deal with numerical problems for fixed-point implementation. It was based on the QR decomposition with modified Gram-Schmidt algorithm. The results showed that for typical 4×4 MIMO channel matrices, the architecture was able to achieve a clock rate of 277 MHz with a latency of 18 time units and area of 72K gates using $0.18 - \mu m$ CMOS technology, which is impressive compared to previously known architectures. In other direction, the architecture can be designed focusing on reducing number of matrix inversions, which is well-suited to the systems with multiple channels to be processed such as MIMO-OFDM systems [31], [30].

C. Detection Processing

This is where all operations are carried out when a new set of received signal symbols arrives. The resources required for the detection processing is in fact much less compared to the preprocessing stage. In addition, the hardware for preprocessing can be conveniently reused for the detection processing. As a result, the latency in the detection processing is reasonably low. Two operations will be discussed in this section: List sorting in the lattice domain and MMSE filtering to find the estimates of $\mathbf{s}_1$ and $\mathbf{s}_2$.

1) List Sorting in LR Domain: The list of candidate vectors in the LR domain is formed by

$$\mathcal{C}_2 = \{\mathbf{c}_2 \mid ||\tilde{\mathbf{c}}_2 - \mathbf{c}_2|| < r(Q)\}.$$

The problem is that the alphabet of signal in LR domain ($\mathbf{c}_2$) varies depending on channel. For example, while the alphabet of $\mathbf{s}_2$ is known, that of $\mathbf{c}_2 = \mathbf{U}_2^{-1}(\alpha\mathbf{s}_2 + \beta\mathbf{1})$ depends on $\mathbf{U}_2$. However, with Gaussian reduction method, $\mathbf{U}_2$ has always a form of

$$\mathbf{U}_2 = \begin{bmatrix} 1 & t \\ 0 & 1 \end{bmatrix},$$

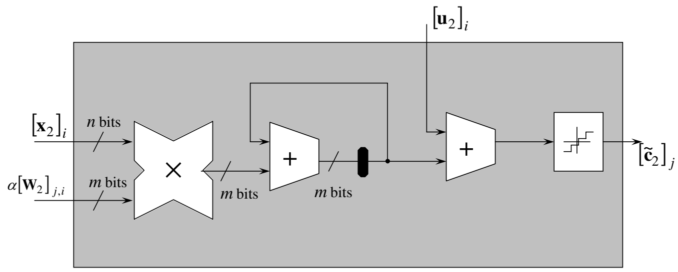

Fig. 4. Block diagram of the linear filtering operation: Inputs are $\mathbf{x}_2$, α, $\mathbf{W}_2$ and $\mathbf{u}_2$ while output is $\tilde{\mathbf{c}}_2$.

where t is an integer. As the maximum number of iterations in the Gaussian LR algorithm is limited to $T = 2$ or 3 only, we can easily obtain a known set of t (and accordingly $\mathbf{U}_2$). Thus, a look-up table can be formed for the alphabet of $\mathbf{c}_2$. This look-up table is formed in the pre-processing stage after the Gaussian LR algorithm is carried out to subchannel matrix $\mathbf{R}_2$. Memory is required to store this pre-calculated data. For example, it requires TM words of memory to store the alphabet of $\mathbf{c}_2$, where M is the size of alphabet of $\mathbf{s}_2$. In addition, $2Q$ words are required for storing $\mathcal{C}_2$.

2) MMSE filtering: This is a matrix-multiplication based operation. One MMSE filtering operation to estimate $\mathbf{c}_2$ is applied to received signal vector $\mathbf{x}_2$:

$$\tilde{\mathbf{c}}_2 = \alpha \mathbf{W}_2^H \mathbf{x}_2 + \mathbf{u}_2,$$

where $\mathbf{u}_2 = \mathbf{U}_2^{-1}\beta\mathbf{1}$. Q times of same operation are applied to received signal vector $\mathbf{x}_1$:

$$\tilde{\mathbf{c}}_1^{(q)} = \alpha \mathbf{W}_1^H \bar{\mathbf{x}}_1^{(q)} + \mathbf{u}_1, \tag{22}$$

where $\mathbf{u}_1 = \mathbf{U}_1^{-1}\beta\mathbf{1}$ and $\bar{\mathbf{x}}_1^{(q)} = \mathbf{x}_1 - \mathbf{R}_3\hat{\mathbf{s}}_2^{(q)}$. Note that Q operations in (22) can be carried out in parallel (see Figure 3). The parallel structure often allows low latency and high throughput. The most complex steps can then be processed in a single cycle, however, at the expense of large silicon area. In addition, with parallel structure, memories need to be implemented based on register files for sufficient access bandwidth. Thus, trade-off between latency/throughput and silicon area needs to be considered.

The weight matrices $\mathbf{W}_1$ and $\mathbf{W}_2$ are pre-calculated and stored in the pre-processing stage. Note that only 8 words of memory are needed for this storage requirement. A simple VLSI architecture for MMSE filtering of $\mathbf{x}_2$ is shown in Figure 4. Filtering operation for $\mathbf{x}_1^{(q)}$ can be carried out similarly. Due to different dynamic ranges, variables can be represented by different numbers of bits (e.g., n bits for $\mathbf{x}_2$ whereas m bits for $\mathbf{W}_2$). It is expected that $m > n$ as entries of $\mathbf{W}_2$ has a larger dynamic range, thus they should be presented with considerable number of bits for the accurate fixed-point implementation.

Memory-wise, there are $2Q$ words required to store the outputs $\{\tilde{\mathbf{c}}_1, \tilde{\mathbf{c}}_2, \cdots, \tilde{\mathbf{c}}_Q\}$.

D. Fixed-Point Considerations

A critical issue in fixed-point arithmetic is the difference in dynamic ranges of variables. Number of integer and fractional bits for each variable should be carefully determined to avoid overflows and, at the same time, not to waste hardware resources.

For example, entries of channel matrix $\mathbf{H}$ is usually assumed to be Gaussian distributed, thus has a infinite dynamic range. To deal with this problem, two common approaches can be employed:

- A sufficiently large number of integer bits is used for representing $\mathbf{H}$ to ensure that overflows occur only rarely. At the same time, the round-off error (i.e., accumulation of rounding errors during fixed point arithmetic operations) should be purely due to loss in fractional precision. In this case, it is shown in [27] that the error variance varies only with the number of fractional bits, η, in the form:

$$\sigma_e^2 = 2^{-2\eta}/3.$$

- Automatic gain control adjusts the data of $\mathbf{H}$ to the available number of integer bits with an appropriate scaling factor γ in which the new channel matrix become $\bar{\mathbf{H}} = \gamma\mathbf{H}$. γ can be chosen as

$$\gamma = \frac{1}{\max|[\mathbf{H}]_{i,j}|}.$$

Depending on hardware resources, each approach can be applied. However, practical systems tend to compromise between the two approaches.

V. Simulation Results

We run simulations for MIMO-OFDMA LTE downlink system with parameters being given in Table II.

Figures 5 and 6 show bit error rate (BER) performance of different detectors for TU and SCM channels. 4-QAM is

TABLE II
SIMULATION PARAMETERS

Parameter	Value
Center Frequency	3.5GHz
Bandwidth	10MHz
Subcarrier Spacing	15kHz
FFT size	1024
Number of usable subcarriers	601
Cyclic Prefix (CP)	FFT size / 8
Channel Model & Velocity	TU-30km/h and SCM-3km/h
Modulation	16-QAM, Gray Mapping
Channel Coding	Turbo Coding, Code Rate 1/2
Channel Estimation	Ideal
Data Mapping	Localized Subcarrier Pattern

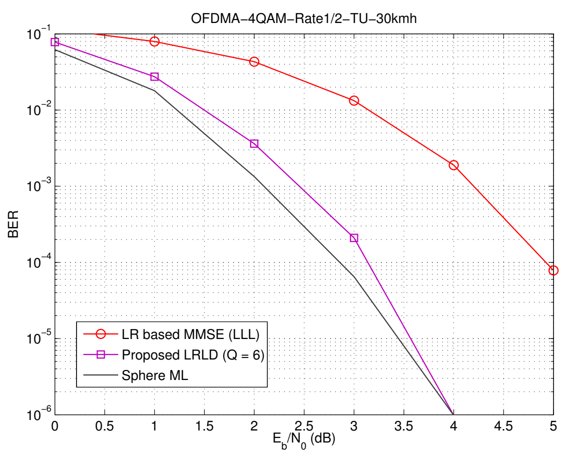

Fig. 5. BER performance comparison of different detectors with 4QAM modulation and TU channel (receiver velocity of 30kmh.)

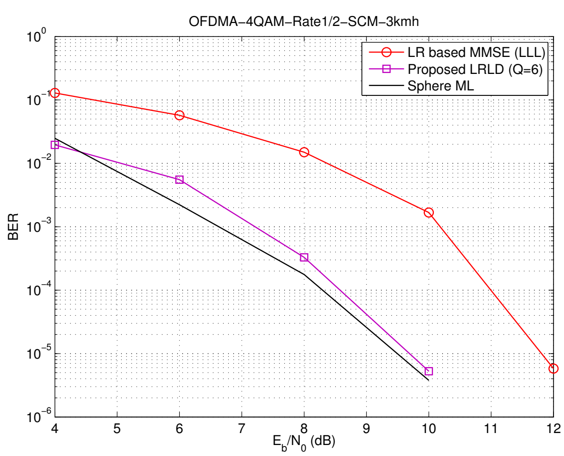

Fig. 6. BER performance comparison of different detectors 4QAM modulation and SCM channel (receiver velocity of 3kmh.)

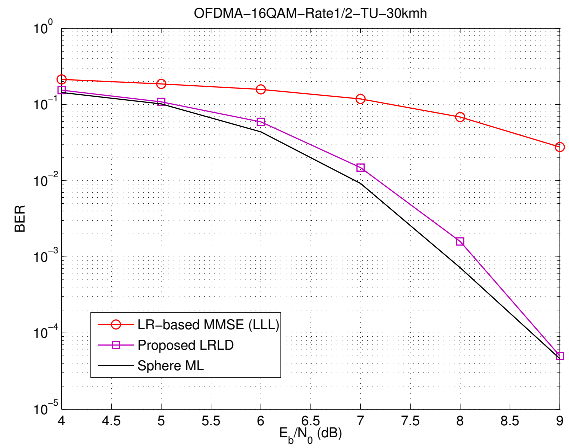

Fig. 7. BER performance comparison of different detectors with 16QAM modulation and TU channel (receiver velocity of 30kmh.)

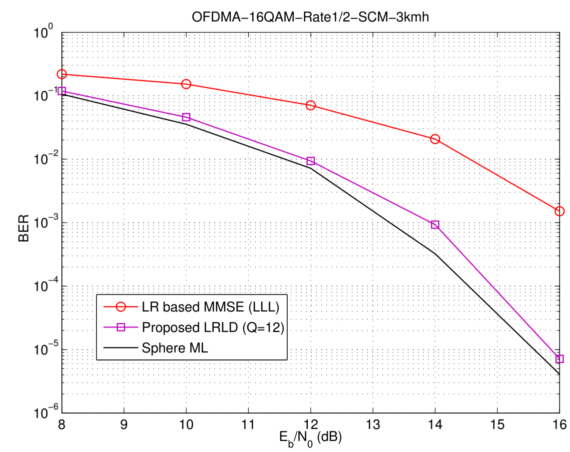

Fig. 8. BER performance comparison of different detectors with 16QAM modulation and SCM channel (receiver velocity of 3kmh.)

used for modulation. We compare the proposed LRLD based detector with the conventional LR based Minimum Mean Square Error (MMSE) detector that uses LenstraLenstraLovsz (LLL) algorithm [32] and the optimal sphere ML detector. It can be seen that the proposed detector provides a near ML performance and outperform the conventional LR based MMSE detector. The same behaviour is observed with 16-QAM modulation in Figures 7 and 8.

Complexity comparison: To fully examine the complexity of different detection methods, simulation is considered and results are shown in Figure 9 where the estimated flops using MATLAB execution time were obtained over all operations for each detector under the same environment. The execution time

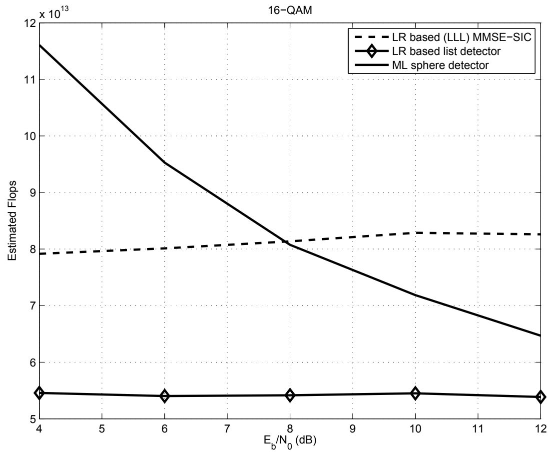

Fig. 9. Complexity comparison.

is averaged over hundreds of thousands of channel realizations. Note that Schnorr-Euchner algorithm [33] is used for sphere ML detector. The LLL-reduced algorithm with reduction factor $\delta = 3/4$ [32] is chosen for the LR based MMSE-SIC detector. No limitation on the number of iterations is imposed for any LR algorithm. The proposed LRLD based detector clearly requires the lowest number of flops. We can also see that the number of flops of the proposed detector is slightly higher than half of that of the LR based MMSE-SIC detector where the LLL-reduced algorithm is used.

VI. Conclusion

An efficient signal detector based on two techniques, namely LR and LD, has been investigated in this paper for the MIMO-OFDMA LTE downlink systems. By generating the list in LR domain, a more reliable list detection is obtained to facilitate SIC detection. As a result, the proposed detector outperforms conventional LR based detectors and provides a near ML performance with significantly reduced complexity. The implementation possibility was then studied to provide references for the real silicon implementation.

Appendix A
LR based Signal Detection

We describe the LR based detection that is used in Steps AS1 and AS4. Let $\mathbb{C}$ denote the set of complex integers or Gaussian integers, $\mathbb{C} = \mathbb{Z} + j\mathbb{Z}$, where $\mathbb{Z}$ denotes the set of integers and $j = \sqrt{-1}$. We assume that $\{\alpha s + \beta | s \in \mathcal{S}\} \subseteq \mathbb{C}$, where α and β are the scaling and shifting coefficients, respectively. For example, for M-QAM, if $M = 2^{2m}$, we have

$$\mathcal{S} = \{s = a + jb | a, b \in \{\pm A, \pm 3A, \ldots, \pm(2m-1)A\}\},$$

where $A = \sqrt{(3E_s/2(M-1))}$ and $E_s = E[|s|^2]$ denotes the symbol energy. Thus, $\alpha = 1/(2A)$ and $\beta = ((2m-1)/2)(1+j)$. Note that the pair of α and β is not uniquely decided.

TABLE III
Signals and parameters for the LR-based detection

Steps	$\mathbf{y}$	$\mathbf{A}$	$\mathbf{z}$	$\tilde{\mathbf{c}}$	K_i
AS1)	$\mathbf{x}_2$	$\mathbf{R}_2$	$\mathbf{s}_2$	$\tilde{\mathbf{c}}_2$	K_2
AS4)	$\mathbf{x}_1 - \mathbf{R}_2\hat{\mathbf{s}}_2^{(q)}$	$\mathbf{R}_1$	$\mathbf{s}_1$	$\tilde{\mathbf{c}}_1^{(q)}$	K_1

Consider the MIMO detection with the following signal:

$$\mathbf{y} = \mathbf{A}\mathbf{z} + \mathbf{v}, \tag{23}$$

where $\mathbf{A}$ is a MIMO channel matrix, $\mathbf{z} \in \mathcal{S}^{K_i}$ is the signal vector, and $\mathbf{v}$ is a zero-mean Gaussian noise with $E[\mathbf{v}\mathbf{v}^{\mathrm{H}}] = \sigma_w^2\mathbf{I}$. We scale and shift $\mathbf{y}$ as

$$\mathbf{d} = \alpha\mathbf{y} + \beta\mathbf{A}\mathbf{1} = \mathbf{A}(\alpha\mathbf{z} + \beta\mathbf{1}) + \alpha\mathbf{v} = \mathbf{A}\mathbf{b} + \alpha\mathbf{v}, \tag{24}$$

where $\mathbf{1} = [1\ 1\ \ldots\ 1]^{\mathrm{T}}$, and $\mathbf{b} = \alpha\mathbf{z} + \beta\mathbf{1} \in \mathbb{C}^{K_i}$. Let $\bar{\mathbf{A}} = \mathbf{A}\mathbf{U}$ where $\mathbf{U}$ is a unimodular matrix. Using any LR algorithm including LLL algorithm [32], we can find $\mathbf{U}$ that makes the column vectors of $\bar{\mathbf{A}}$ shorter. It follows that

$$\mathbf{d} = \mathbf{A}\mathbf{U}\mathbf{U}^{-1}\mathbf{b} + \alpha\mathbf{v} = \bar{\mathbf{A}}\mathbf{c} + \alpha\mathbf{v}, \tag{25}$$

where $\mathbf{c} = \mathbf{U}^{-1}\mathbf{b}$. The MMSE filter to estimate $\mathbf{c}$ is given by

$$\begin{aligned}\mathbf{W}_{\mathrm{mmse}} &= \min_{\mathbf{W}} E[||\mathbf{W}^{\mathrm{H}}(\mathbf{d} - \bar{\mathbf{d}}) - (\mathbf{c} - \bar{\mathbf{c}})||^2] \\ &= (\mathbf{A}\mathbf{A}^{\mathrm{H}}\alpha^2 E_s + |\alpha|^2\sigma_w^2\mathbf{I})^{-1}\mathbf{A}\mathbf{U}^{-\mathrm{H}}\alpha^2 E_s,\end{aligned} \tag{26}$$

where $\bar{\mathbf{d}} = E[\mathbf{d}] = \beta\mathbf{A}\mathbf{1}$, $\bar{\mathbf{c}} = E[\mathbf{c}] = \mathbf{U}^{-1}\beta\mathbf{1}$, and $\mathrm{Cov}(\mathbf{c}) = |\alpha|^2\mathbf{U}^{-1}\mathbf{U}^{-\mathrm{H}}E_s$. The estimate of $\mathbf{c}$ is given by:

$$\tilde{\mathbf{c}} = \bar{\mathbf{c}} + \mathbf{W}_{\mathrm{mmse}}^{\mathrm{H}}(\mathbf{d} - \bar{\mathbf{d}}).$$

In Table III, the signals and parameters for the LR based MMSE detection for each step are shown.

Appendix B
List Generation in the LR Domain

To avoid or mitigate the error propagation, the use of a list of candidate vectors of $\mathbf{s}_2$ in detecting $\mathbf{s}_1$ is crucial. Using the

ML metric, we can find the candidate vectors in the list, $\mathcal{S}_2$. Let

$$||\mathbf{r} - \mathbf{R}_2\hat{\mathbf{s}}_2^{(1)}||^2 \leq ||\mathbf{r} - \mathbf{R}_2\hat{\mathbf{s}}_2^{(2)}||^2 \leq \ldots \leq ||\mathbf{r} - \mathbf{R}_2\hat{\mathbf{s}}_2^{(M^{K_2})}||^2,$$

where $\hat{\mathbf{s}}_2^{(q)}$ denotes the symbol vector that corresponds to the qth largest likelihood. Therefore, an ideal list would be

$$\mathcal{S}_2 = \{\hat{\mathbf{s}}_2^{(1)}, \hat{\mathbf{s}}_2^{(2)}, \ldots, \hat{\mathbf{s}}_2^{(Q)}\}. \tag{27}$$

However, this requires an exhaustive search, which results in a high computational complexity due to computing of $\mathbf{R}_2\mathbf{s}_2$ for all $\mathbf{s}_2 \in \mathcal{S}^{K_2}$.

To avoid a high computational complexity, we can find a suboptimal list in the LR domain with low complexity. Consider (24). According to Table III, let $\mathbf{A} = \mathbf{R}_2$, $\mathbf{d} = \alpha\mathbf{x}_2 + \beta\mathbf{A}\mathbf{1}$, and $\mathbf{b} = \alpha\mathbf{s}_2 + \beta\mathbf{1}$. Then, since $\bar{\mathbf{A}} = \mathbf{A}\mathbf{U}$, we can see that the ML metric to construct the list is given by

$$||\mathbf{d} - \mathbf{A}\mathbf{b}|| = ||\mathbf{d} - \bar{\mathbf{A}}\mathbf{c}||. \tag{28}$$

It is noteworthy that the metric on the right hand side in (28) is defined in the LR domain. Let $\tilde{\mathbf{s}}_2$ be the signal vector in $\mathcal{S}^{K_2}$ corresponding to $\tilde{\mathbf{c}}_2$ and assume that $\tilde{\mathbf{s}}_2$ is sufficiently close to $\hat{\mathbf{s}}_2^{(1)}$. Then, we can have $\mathbf{d} \simeq \bar{\mathbf{A}}\tilde{\mathbf{c}}_2$. From this, the ML metric (ignoring a scaling factor) for constructing the list in the LR domain becomes

$$||\mathbf{d} - \bar{\mathbf{A}}\mathbf{c}|| = ||\bar{\mathbf{A}}\tilde{\mathbf{c}}_2 - \bar{\mathbf{A}}\mathbf{c}|| = ||\tilde{\mathbf{c}}_2 - \mathbf{c}||_{\bar{\mathbf{A}}^{\mathrm{H}}\bar{\mathbf{A}}}, \tag{29}$$

where $||\mathbf{x}||_{\mathbf{A}} = \sqrt{\mathbf{x}^{\mathrm{H}}\mathbf{A}\mathbf{x}}$ is a weighted norm. The list in the LR domain becomes

$$\mathcal{C}_2 = \{\mathbf{c} \mid ||\tilde{\mathbf{c}}_2 - \mathbf{c}||_{\bar{\mathbf{A}}^{\mathrm{H}}\bar{\mathbf{A}}} < r_{\bar{\mathbf{A}}}(Q)\}, \tag{30}$$

where $r_{\bar{\mathbf{A}}}(Q) > 0$ is the radius of an ellipsoid centered at $\tilde{\mathbf{c}}_2$, which contains Q elements in the LR domain. If the column vectors of $\bar{\mathbf{A}}$ or the basis vectors in the LR domain are orthogonal, $\bar{\mathbf{A}}^{\mathrm{H}}\bar{\mathbf{A}}$ becomes diagonal. Furthermore, if they have the same norm, $\bar{\mathbf{A}}^{\mathrm{H}}\bar{\mathbf{A}} \propto \mathbf{I}$. Thus, for nearly orthogonal basis vectors of almost equal norm, the list of $\mathbf{c}_2$ can be approximated as

$$\mathcal{C}_2 \simeq \{\mathbf{c} \mid ||\tilde{\mathbf{c}}_2 - \mathbf{c}|| < r(Q)\}, \tag{31}$$

where $r(Q) > 0$ is the radius of a sphere centered at $\tilde{\mathbf{c}}_2$, which contains Q elements. Since the LR provides a set of nearly orthogonal basis vectors for the LR based detection, we can see that the column vectors in $\bar{\mathbf{A}}$ are nearly orthogonal with a a two-basis system. Let $\mathcal{S}_2$ denotes the list in the original domain converted from $\mathcal{C}_2$ as in step AS3. Since no matrix-vector multiplications are required to generate $\mathcal{C}_2$ or $\mathcal{S}_2$, we can use $\mathcal{S}_2$ as the list in the proposed detector to reduce computational complexity. Note that the list generated in the LR domain is much more reliable than the list generated in the original domain (this list is different from $\mathcal{S}_2$).

REFERENCES

[1] H. X. Nguyen, "An efficient signal detection algorithm for 3GPP LTE downlink," in *Proc. IEEE International Conf. on Digital Telecommunications (ICDT 2010)*, Athens, Greece, Jun. 2010, pp. 77-81.

[2] 3rd Generation Partnership Project (3GPP) TR 25.814, "Technical specification group radio access network: Physical layer aspects for Evolved UTRA," *http://www.3gpp.org/ftp/Specs/html-info/25814.htm*.

[3] H. Ekstrom, A. Furuskar, J. Karlsson, M. Meyer, S. Parkvall, J. Torsner, and M. Wahlqvist, "Technical solutions for the 3G Long-Term Evolution," *IEEE Commun. Mag.*, vol. 44, pp. 38-45, Mar. 2006.

[4] H. G. Myung, J. Lim, and D. J. Goodman, "Single carrier FDMA for uplink wireless transmission," *IEEE Veh. Technol. Mag.*, vol. 1, pp. 30-38, Sep. 2006.

[5] G. J. Foschini, G. Golden, R. Valenzuela, and P. Wolniansky, "Simplified processing for wireless communication at high spectral efficiency," *IEEE J. Select. Areas Commun.*, no. 11, pp. 1841-1852, 1999.

[6] W. J. Choi, R. Negi, and J. Cioffi, "Combined ML and DFE decoding fo the V-BLAST system," in *Proc. IEEE International Conf. Communications*, New Orleans, LA, 2000, pp. 1243-1248.

[7] J. Luo, K. Pattipati, P. Willett, and F. Hasegawa, "Near optimal multiuser detection in synchronous CDMA using probabilistic data association," *IEEE Commun. Lett.*, vol. 5, pp. 361-363, Sep. 2001.

[8] D. Pham, K. R. Pattipati, P. K. Willett, and J. Luo "A generalized probabilistic data association detector for multiple antenna systems," *IEEE Commun. Lett.*, vol. 8, no. 4, April 2004.

[9] J. Choi, "On the partial MAP detection with applications to MIMO channels," *IEEE Trans. Signal Proc.*, vol.53, pp.158-167, Jan. 2005.

[10] D. J. Love, S. Hosur, A. Batra, and R. W. Heath, "Chase decoding for space-time codes," in *Proc. IEEE Vehicular Technology Conf.*, vol. 3, Nov. 2004, pp. 1663-1667.

[11] D. W. Waters and J. R. Barry, "The Chase family of detection algorithms for multiple-input multiple-output channels," *IEEE Trans. Signal Proc.*, vol. 56, No. 2, pp. 739-747, February 2008.

[12] H. Yao and G. W. Wornell, "Lattice-reduction-aided detectors for MIMO communication systems," in *Proc. IEEE Global Telecommunications Conf.*, Taiwan, Nov. 2002, pp. 424-428.

[13] D. Wubben, R. Bohnke, V. Kuhn and K. -D. Kammeyer, "Near-maximum-likelihood detection of MIMO systems using MMSE-based lattice reduction" in *Proc. IEEE International Conf. Communications*, vol. 2, Paris, Jun. 2004. pp. 798-802.

[14] H. Bolcskei, "MIMO-OFDM wireless systems: Basics, perspectives, and challenges," *IEEE Wireless Commmun.*, vol. 13, pp. 31-37, Aug. 2006.

[15] D. Perels, S. Haene, P. Luethi, A. Burg, N. Felber, W. Fichtner, and H. Bolcskei, "ASIC Implementation of a MIMO-OFDM Transceiver for 192 Mbps WLANs," *Proc. ESSCIRC*, Grenoble, France, 2005, pp. 215-218.

[16] Z. Guo and P. Nilsson, “A VLSI implementation of MIMO detection for future wireless communications,” in *Proc. 14th IEEE 2003 Int. Symp. Personal, Indoor and Mobile Radio Communication*, 2003, pp. 2852 - 2856.

[17] G. Knagge, L. Davis, G. Woodwar, S. R. Weller, “VLSI preprocessing techniques for MUD and MIMO sphere detection,” in *Proc. 6th Australian Communications Theory Workshop*, Feb. 2005, pp. 221 - 228.

[18] A. Burg, M. Borgmann, M. Wenk, M. Zellweger, W. Fichtner, and H. Bolcskei “VLSI implementation of MIMO detection using the sphere decoding algorithm,” *IEEE J. Solid-State Circuits*, vol. 40, pp. 1566 - 1577, Jul. 2005.

[19] A. Burg, M. Borgmann, M. Wenk, C. Studer, and H. Bolcskei, “Advanced receiver algorithms for MIMO wireless communications,” in *Proc. Design, Automation and Test in Europe (DATE ’06)*, vol. 1, Mar. 2006.

[20] C. Studer, A. Burg, and H. Bolcskei, “Soft-output sphere decoding: Algorithms and VLSI implementation,” submitted to *IEEE J. Select. Areas Commun.*, Apr. 2007.

[21] D. Garrett, L. Davis, S. ten Brink, B. Hochwald, and G. Knagge, “Silicon complexity for maximum likelihood MIMO detection using spherical decoding,” *IEEE J. Solid-State Circuits*, vol. 39, pp. 1544 - 1552, Sep. 2004.

[22] S. Chen, T. Zhang, and Y. Xin, “Relaxed K-Best MIMO signal detector design and VLSI implementation,” *IEEE Trans. VLSI Syst.*, vol. 15, pp. 328 - 337, Mar. 2007.

[23] R. Steele, *Mobile Radio Communications*, New York: IEEE Press, 1992.

[24] 3GPP, TR 25.996, “Spatial channel model for multiple input multiple output (MIMO) simulations (Rel. 6),” 2003.

[25] L. M. Davis, “Scaled and decoupled cholesky and QR decompositions with application to spherical MIMO detection,” in *Proc. IEEE Wireless Communications and Networking Conf.*, vol. 1, Mar. 2003, pp. 326-331.

[26] G. H. Golub and C. F. V. Loan, *Matrix computations*, 3rd ed. Baltimore, MD: John Hopkins University Press, 1996.

[27] C. K. Singh, S. H. Prasad, and P. T. Balsara, “A fixed-point implementation for QR Decomposition,” in *Proc. 2006 IEEE Dallas/CAS Workshop Design, Applications, Integration and Software*, Oct. 2006, pp. 75-78.

[28] C. K. Singh, S. H. Prasad, and P. T. Balsara, “VLSI architecture for matrix inversion using modified Gram-Schmidt based QR decomposition,” in *Proc. 20th IEEE Int. Conf. VLSI Design*, Jan. 2007, pp. 836-841.

[29] A. Bjorck, and C. Paige, “Loss and recapture of orthogonality in the modified gram-schmidt algorithm,” *SIAM J. Matrix Anal. Appl.*, vol. 13(1), pp. 176-190, 1992.

[30] M. Borgmann and H. Bolcskei, “Interpolation-based efficient matrix inversion for MIMO-OFDM receivers,” in *Proc. 38th Asilomar Conf. Signals, Systems, Computers*, vol. 2, Pacific Grove, CA, Nov. 2004, pp. 1941-1947.

[31] D. Cescato, M. Borgmann, H. Bolcskei, J. Hansen, and A. Burg, “Interpolation-based QR decomposition in MIMO-OFDM systems,” in *Proc. 6th IEEE Workshop Signal Processing Advances in Wireless Communications (SPAWC)*, New York, NY, Jun. 2005, pp. 945-949.

[32] A. K. Lenstra, J. H. W. Lenstra, and L. Lovasz, “Factorizing polynomials with rational coefficients,” *Math. Ann.*, vol. 261, pp. 515-534, 1982.

[33] C. P. Schnorr and M. Euchner, “Lattice basis reduction: Improved practical algorithms and solving subset sum problems,” *Math.Programming*, vol. 66, pp. 181-191, 1994.

Multiwavelets in the Context of Hierarchical Stereo Correspondence Matching Techniques

Pooneh Bagheri Zadeh and Cristian V. Serdean
Department of Engineering, Faculty of Technology,
De Montfort University
Leicester, UK
E-mail: pbz@dmu.ac.uk , cvs@dmu.ac.uk

***Abstract*—**This paper presents an evaluation of different types and families of multiwavelets in stereo correspondence matching. First, the paper introduces two hierarchical stereo matching techniques based on balanced and respectively unbalanced multiwavelet transforms, which employ normalized cross correlation to search for disparities. Different multiwavelet families, with different properties and filter types are evaluated, such as balanced versus unbalanced multiwavelets and symmetric-symmetric versus symmetric-antisymmetric multiwavelets. Each approximation subband carries a different spectral content of the original image and the information in the basebands of the multiwavelet transform is less sensitive to the shift variability of the multiwavelet transform. This can be exploited in order to improve the accuracy of the initial disparity map. As this initial disparity map is estimated at the lowest resolution, it needs to be progressively propagated to higher resolution levels. As a result, the search at high resolution levels is significantly reduced, thereby reducing the computational cost of the overall process and improving the reliability of the final disparity map. The evaluation of different types and families of multiwavelets shows that unbalanced multiwavelets produce a smoother disparity map with less mismatch errors compared to balanced multiwavelets. Finally, the paper introduces a third technique, which replaces normalized cross correlation with a better performing global error energy minimization algorithm operating based on a similar hierarchical technique. The results show that the multiwavelet techniques produce a smoother disparity map with less mismatch errors compared to applying a similar matching algorithm in either the spatial and/or the wavelet domains. The performance of the proposed algorithms is also compared against several state-of-the-art techniques from the Middlebury database.

Keywords- Multiwavelets, Correspondence matching, Disparity estimation, Stereo vision.

I. INTRODUCTION

Stereo correspondence is an issue of great importance in the field of computer vision and 3D reconstruction. It aims to find the closest possible match between the corresponding points of two images captured simultaneously by two cameras placed at slightly different spatial locations. The cameras are usually aligned in such a way that each scan line of the rectified images corresponds to the same line in the other image, hence searching for the best correspondence match is restricted to a horizontal search. A disparity map generated from the correspondence matching process, along with the stereo camera parameters are then used to calculate the depth map and produce a 3D view of the scene. Various constraints can be taken into account in order to improve the accuracy. Even so, the accuracy of the correspondence map, which is crucial in generating a precise 3D view of the scene, is limited due to a number of problems such as occlusion, ambiguity, illumination variation and radial distortion [2].

Area-based (local) and energy-based (global) correspondence matching algorithms are the two most common types of algorithms used in the literature to generate disparity maps. In area-based methods a disparity vector for each pixel within a window search area is calculated using a matching algorithm, while in energy-based methods, the disparity vector is determined using a global cost function minimization technique. Area-based methods are fast but produce descent results, while the global methods are time consuming and generating more accurate results.

Muhlman et al. [3] presented an area-based matching technique for RGB stereo images. This algorithm uses left to right consistency and uniqueness constrains to generate the initial disparity map. The resulting disparity map is then further smoothed by applying a median filter. Another area-based scheme was proposed by Stefano et al. [4]. Stefano's algorithm is based on uniqueness and constraint, but it relies on a left to right matching phase. Yoon et al. [5] introduced a local correlation based correspondence matching technique, which uses a refined implementation of the Sum of Absolute Differences (SAD) criteria and a left to right consistency check. This algorithm uses a variable correlation window size to reduce the errors in the areas containing blurring or mismatch errors. Yoon and Kweon [6] proposed another local based algorithm, which uses different supporting weights based on the colour similarity and the geometric distances of each pixel in the search area in order to reduce the amount of ambiguity errors.

Kim et al. [7] reported a global-based technique for stereo correspondence matching. This algorithm first generates a dense disparity map using a region dividing technique based on Canny edge detection. It then further refines the disparity map by minimizing the energy function using a Lagrangian optimization algorithm. Ogale and Aloimonos [8] proposed another global-based correspondence matching algorithm, which is independent of the contrast variation of the stereo images. This algorithm relies on multiple spatial frequency channels for local matching and a fast non-iterative left/right diffusion process for the global solution. An energy-based algorithm for stereo matching, which uses a belief propagation algorithm, was presented in [9]. This algorithm uses hierarchical belief propagation to iteratively optimize the smoothness of the disparity map. It delivers fast convergence by removing redundant computations. Choi and Jeong [10] proposed an energy-based stereo matching technique, which models the intensity differences between the two stereo images using a uniform local bias assumption. This local bias assumption is less sensitive to the intensity dissimilarity between the stereo images when using normalized crosscorrelation matching cost functions. The resulting information from the cost function is used in conjunction with a fast belief propagation algorithm to generate a smooth disparity map.

Over the past years much research has been done to improve the performance of the correspondence matching techniques. Multiresolution based stereo matching algorithms have received much attention due to the hierarchical and scale-space localization properties of the wavelets [11][13]. This allows for correspondence matching to be performed on a coarse-to-fine basis, resulting in decreased computational costs. Jiang and et al. proposed a wavelet based stereo image pair coding algorithm [14]. A wavelet transform decomposes the images into low and high frequency subbands and the disparity map is estimated using both the approximation and edge information. This is followed by a disparity compensation and subspace projection technique to improve the disparity map estimation. Caspary and Zeevi [15] presented another wavelet based stereo matching technique. This algorithm employs a differential operator in the wavelet domain to iteratively minimize a defined cost function. Sarkar and Bansal [13] presented a multiresolution based correspondence matching technique using a mutual information algorithm. They showed that the multiresolution technique produces significantly more accurate matching results compared to correlation based algorithms at much lower computational cost.

Research has shown that unlike scalar wavelets, multiwavelets can possess orthogonality (preserving length), symmetry (good performance at the boundaries via linear-phase), and a high approximation order at the same time [12], which could potentially increase the accuracy of correspondence matching techniques. Bhatti and Nahavandi [16] proposed a multiwavelet based stereo correspondence matching algorithm which makes use of the wavelet transform modulus maxima to generate a disparity map at the coarsest level. This is then followed by the coarse-to-fine strategy to refine the disparity map up to the finest level. Bagheri Zadeh and Serdean [1] proposed another multiwavelet based stereo correspondence matching technique. They used a global error energy minimization technique to find the best correspondence points between the same multiwavelet's lowest frequency subbands of the stereo pair, followed by a fuzzy algorithm to form a dense disparity map.

In spite of their highly desirable properties compared to scalar wavelets, literature surveys show that the application of multiwavelets in stereo correspondence matching has received relatively little attention so far.

This paper, investigates the application of different types and families of multiwavelets in the context of stereo correspondence matching. For this purpose, a multiwavelet is first applied to the input stereo images to decompose them into a number of subbands. Normalized cross correlation is used to generate a disparity map at the coarsest level. In the case of balanced multiwavelets, as the four low frequency subbands have similar spectral content, they can be shuffled to generate a single baseband, while in the case of unbalanced multiwavelets, the resulting basebands are used to form four disparity maps and then a Fuzzy algorithm is used to combine the four maps and generate a single disparity map. Furthermore, the paper also presents a novel hierarchical, multiwavelet based stereo correspondence matching algorithm, which employs a global error energy minimization algorithm to generate a disparity map for each of the four approximation subbands of the multiwavelet transformed input stereo pair. Again, a Fuzzy algorithm is used to combine the four disparity maps and generate an initial disparity map. As in the previous techniques, the initial estimated disparity map is then refined at higher resolution levels, taking advantage of the hierarchical, multiresolution nature of the multiwavelets to efficiently generate a more accurate final disparity map. This map is further smoothed with the aid of a median filter.

The rest of the paper is organized as it follows. Section II presents a brief review of the multiwavelet transform. An evaluation of different types and families of multiwavelets in the context of stereo correspondence matching is presented in Section III. The proposed hierarchical stereo matching technique based on global error energy minimization is introduced in Section IV. Experimental results are presented and discussed in Section V, while Section VI is dedicated to the conclusions.

II. MULTIWAVELET TRANSFORM

Multiwavelet transforms are in many ways similar to scalar wavelet transforms. Classical wavelet theory is based on the following refinement equations:

$$\begin{aligned} \phi(t) &= \sum_{k=-\infty}^{k=\infty} h_k \phi(m\,t-k) \\ \psi(t) &= \sum_{k=-\infty}^{k=\infty} g_k \psi(m\,t-k) \end{aligned} \tag{1}$$

where $\phi(t)$ is a scaling function, $\psi(t)$ is a wavelet function, h_k and g_k are scalar filters and m represents the subband number. In contrast to wavelet transforms, multiwavelets

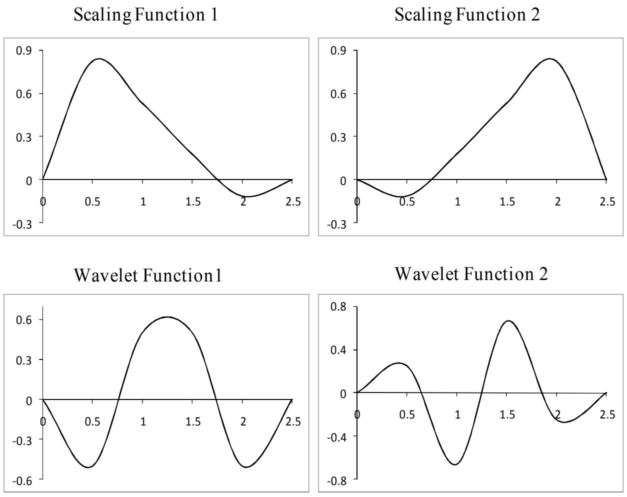

a) bat01 balanced multiwavelet

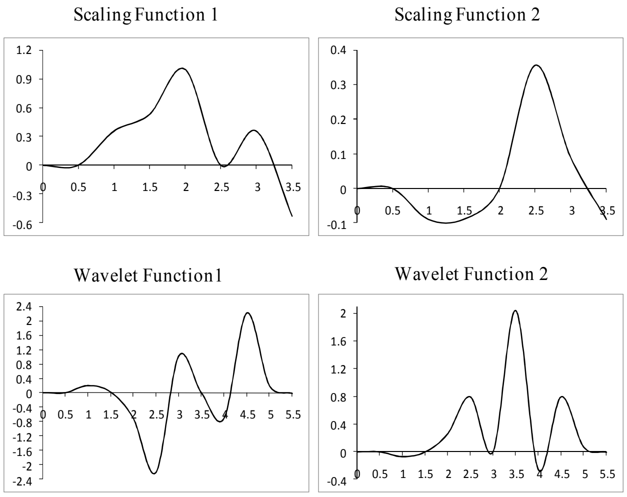

b) bih32s unbalanced multiwavelet

Figure 1. Multiwavelets basis functions, a) balanced, b) unbalanced.

have two or more scaling and respectively wavelet functions.

The set of scaling and wavelet functions of a multiwavelet in vector notation can be defined as:

$$\begin{aligned}\Phi(t) &\equiv [\phi_1(t) \quad \phi_2(t) \quad \phi_3(t) \quad \ldots \quad \phi_r(t)]^T \\ \Psi(t) &\equiv [\psi_1(t) \quad \psi_2(t) \quad \psi_3(t) \quad \ldots \quad \psi_r(t)]^T\end{aligned} \tag{2}$$

where $\Phi(t)$ and $\Psi(t)$ are the multiscaling and respectively multiwavelet functions, with r scaling- and wavelet functions. In the case of scalar wavelets $r=1$, while multiwavelets support $r \geq 2$. To date, most multiwavelets are restricted to $r=2$. Such multiwavelets possess two scaling and two wavelet functions and can be represented as [17]:

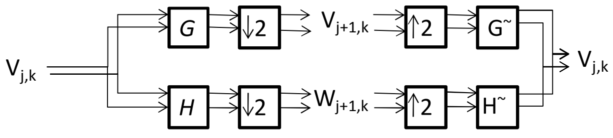

Figure 2. Analysis/synthesis stage of one level multiwavelet transform.

L_1L_1	L_1L_2	L_1H_1	L_1H_2
L_2L_1	L_2L_2	L_2H_1	L_2H_2
H_1L_1	H_1L_2	H_1H_1	H_1H_2
H_2L_1	H_2L_2	H_2H_1	H_2H_2

Figure 3. One level of 2D Multiwavelet decomposition.

$$\begin{aligned}\Phi(t) &= \sqrt{2}\sum_{k=-\infty}^{k=\infty} H_k \Phi(m\,t-k) \\ \Psi(t) &= \sqrt{2}\sum_{k=-\infty}^{k=\infty} G_k \Psi(m\,t-k)\end{aligned} \tag{3}$$

where H_k and G_k are $r \times r$ matrix filters and m is the subband number. Figure 1 shows an example of balanced and unbalanced multiwavelet basis functions.

Similar to wavelet transforms, multiwavelets can be implemented using Mallat's filter bank theory [11]. Figure 2 shows one level of analysis/synthesis for a 1D multiwavelet transform, where blocks G and H are low- and high-pass analysis filters and $G^{\sim}$ and $H^{\sim}$ are low- and high-pass synthesis filters. Due to its separability property, a 2D multiwavelet transform can be implemented via two 1D transforms. Therefore, for one level of decomposition, a 2D multiwavelet with multiplicity $r=2$ generates sixteen subbands, as shown in Figure 3. In Figure 3, L_xL_y represent the approximation subbands while L_xH_y , H_xL_y and H_xH_y are the detail subbands, with $x=\overline{1,2}$ and $y=\overline{1,2}$.

The major advantage of multiwavelets over scalar wavelets is their ability to possess symmetry, orthogonality and higher order of approximation simultaneously, which is impossible for scalar wavelets. Furthermore, the multichannel structure of the multiwavelet transform is a closer approximation of the human visual system than what wavelets offer. In the case of unbalanced multiwavelets, the resulting approximation subbands carry different spectral content of the original image (both high- and low-frequencies), while for balanced multiwavelets, the approximation subbands contain similar spectral content of the original image [19]. This feature of unbalanced multiwavelets has the potential to increase the accuracy of

(a)

(b)

(c)

Figure 4. Single level decomposition of Lena test image (a) Antonini 9/7 wavelet transform, (b) balanced bat01 multiwavelet transform and (c) unbalanced GHM multiwavelet transform.

the calculated disparity maps and reduce the number of erroneous matches compared to that of balanced multiwavelets.

A visual comparison of the resulting subbands for a 2D wavelet, balanced and respectively unbalanced multiwavelet decomposition is shown in Figure 4. Antonini 9/7 wavelet and, balanced bat01 and unbalanced GHM multiwavelets were applied to Lena test image and results are illustrated in Figures 4(a) to 4(c), respectively. As it can be seen from Figure 4, multiwavelets generate four subbands instead of each subband that wavelets create. The resulting unbalanced multiwavelet subbands carry different spectral content of the original Lena test image, while the balanced multiwavelet subbands produce similar spectral content of the original image. More information about the generation of multiwavelets, their properties and their applications can be found in [12], [17] and [18].

III. Evaluation of Multiwavelet Families in Stereo Correspondence Matching

The proposed stereo correspondence matching evaluation system is based on multiwavelets and normalized cross correlation. Figures 5(a) and 5(b) show the block diagrams of the proposed system for both balanced and respectively unbalanced multiwavelets. A pair of stereo images is input to the stereo matching system. The images are first rectified to suppress vertical displacement. A multiwavelet transform is then applied to each input stereo image. Different types and families of multiwavelets are evaluated. Since the information in the approximation subbands is less sensitive to the shift variability of the multiwavelets, these subbands are used in the correspondence matching process. In the case of balanced multiwavelets (Figure 5(a)), as their basebands contain similar spectral information, it is possible to use the shuffling technique proposed in [27] to rearrange the multiwavelet coefficients and generate a single low frequency subband. Figure 6 shows how four multiwavelet basebands are reshuffled to form a single baseband. Figure 6(a) shows the four multiwavelet basebands with eight pixels (two from each baseband) highlighted and given a unique numeric label. Figure 6(b) shows the same set of pixels after reshuffling, where coefficients corresponding to the same spatial locations in different basebands are placed together to generate a single baseband. Normalized cross correlation is then employed to find the best correspondence points between the two basebands of the stereo image pairs and a disparity map is generated.

Figure 5(b) shows the block diagram of the unbalanced multiwavelet based stereo matching system. While the shuffling technique works very well for balanced multiwavelets, it is not suitable for unbalanced multiwavelets due to the different spatio-frequency content of the four approximation subbands. The unbalanced multiwavelet basebands contain both high and low frequency information with L_1L_1 (top left baseband) containing most of the image energy. For correspondence matching purposes, the same basebands from the two views are input to the normalized cross correlation block, generating four disparity maps as a result. A Fuzzy algorithm is

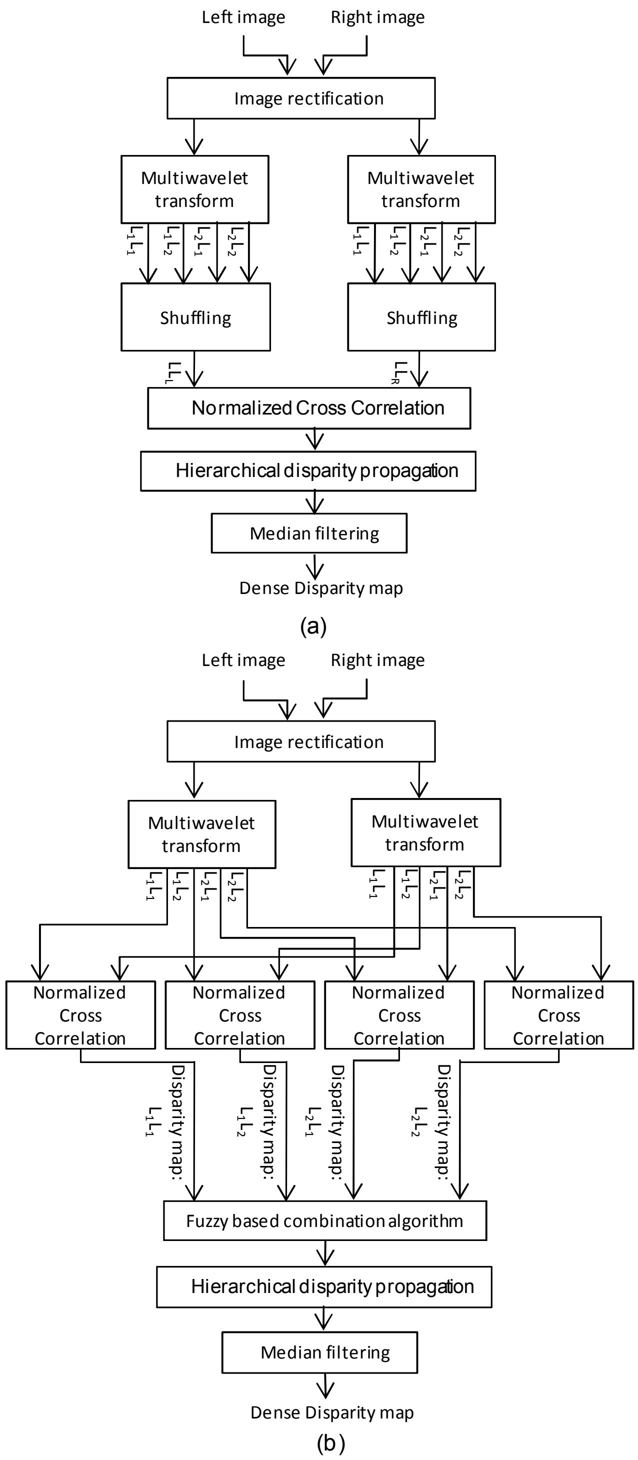

Figure 5. Block diagram of multiwavelet based stereo matching technique, for (a) balanced- and (b) unbalanced-multiwavelets.

employed to combine the four disparity maps. This algorithm gives a higher weight to the disparity values resulting from the L_1L_1 subbands. The disparity values in the other three disparity maps are used to refine the initial disparity map.

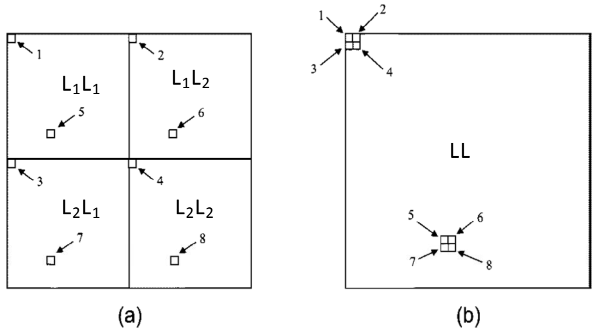

Figure 6. Shuffling method for multiwavelet baseband coefficients; selected pixels are numbered to indicate correspondence (a) before shuffling and (b) after shuffling.

These initial disparities generated at the lowest resolution for both unbalanced and balanced multiwavelets are passed on to higher resolution levels. This process is detailed in Section IV sub-section B. Finally a median filter is applied to the resulting disparity map to further smooth the resulting disparities and generate the final disparity map.

IV. Hierarchical Multiwavelet-based Stereo Correspondence Matchning

Figure 7 shows a block diagram of the proposed hierarchical multiwavelet-based stereo matching technique which employs a global error energy minimization algorithm. A pair of rectified stereo images is input to the system. An unbalanced multiwavelet transform is then applied to the stereo images to decorrelate them into their subbands. In this paper, an unbalanced multiwavelet with a multiplicity order $r=2$ is used, and as such the multiwavelet transform of each input image contains four basebands. The basebands of the unbalanced multiwavelets contain both high and low frequencies information, with L_1L_1 (top left baseband) containing most of the image energy. For correspondence matching purposes, the same basebands from the two views are input to a regional-based stereo matching block generating four disparity maps as a result [20]. This global error energy minimization technique is briefly described in sub-section A. The Fuzzy algorithm, which was discussed in Section III, is then employed to combine the four disparity maps. The initial disparity is estimated at the lowest resolution and the information needs to be progressively passed on to higher resolution levels. Hence, the search at high resolution levels is significantly reduced, thereby reducing the computational cost of the overall algorithm. This process is detailed in sub-section B. Finally a median filter is applied to the last processed disparity map to further smooth the final disparity map.

A. *Global Error Energy Minimization technique*

The Global Error Energy Minimization (GEEM) technique [20] employed in this paper calculates a disparity vector for each pixel. It searches for the best match for each pixel in the correspondence search area of the other image using an error minimization criterion. For RGB images, the error energy criteria can be defined as:

$$
\begin{aligned}
&Er_{en}(i,j,w_x,w_y) \;=\; \frac{1}{3}\sum_{k=1}^{3}\left(I_1(i+w_x, j+w_y, k) - I_2(i,j,k)\right)^2 \\
&-d_x \le w_x \le d_x \quad and \quad -d_y \le w_y \le d_y \\
&i \;=\; 1, \;\ldots\; m \quad and \quad j \;=\; 1, \;\cdots\; n
\end{aligned}
\tag{4}
$$

where I_1 and I_2 are the two input images, $Er_{en}(i,j,w_x,w_y)$ is the energy difference of the pixel $I_2(i,j)$ and pixel $I_1(i+w_x, j+w_y)$, d_x is the maximum displacement around the pixel in the x direction, d_y is the maximum displacement around the pixel in the y direction, m and n represent the image size and k represents the three components of an RGB image.

In order for the GEEM algorithm to determine the disparity vector for each pixel in the current view, it first calculates Er_{en} of each pixel with all the pixels from its search area in the corresponding image. For every disparity vector (w_x, w_y) in the disparity search area, the energy of the error is calculated using Equation 4 and placed into a matrix. Each of the resulting error energy matrices is first filtered using an average filter to decrease the number of incorrect matches [21]. The disparity index of each pixel is then determined by finding the disparity index from the matrix, which contains the minimum error energy for that pixel. In order to increase the reliability of the disparity vectors around the object boundaries, which is the result of object occlusion in images, the generated disparity map undergoes a thresholding procedure as it follows:

$$
\tilde{d}(i,j) = \begin{cases} d(i,j) & Er_{en}(i,j) \le \alpha \times Mean(Er_{en}) \\ 0 & Er_{en}(i,j) > \alpha \times Mean(Er_{en}) \end{cases} \tag{5}
$$

where $\tilde{d}(i,j)$ is the processed disparity map, $d(i,j)$ is the original disparity map, α is a tolerance reliability factor and $Er_{en}(i,j)$ is the minimum error energy of the pixel (i,j) calculated and selected in the previous stage. Finally a median filter is applied to the processed disparity map $\tilde{d}(i,j)$, to further smooth the resulting final disparity map.

B. Hierarchical disparity propagation

The information in the initial disparity map, generated at the coarsest level, needs to be refined by propagating it to the higher resolutions. Based on the wavelet theory, one point (x,y) of a coarse subband in the decomposition level $i+1$ corresponds to four points $(2x,2y)$, $(2x+1,2y)$, $(2x,2y+1)$ and $(2x+1,2y+1)$ of its finer subband at the decomposition level i. If (x,y) in the left image

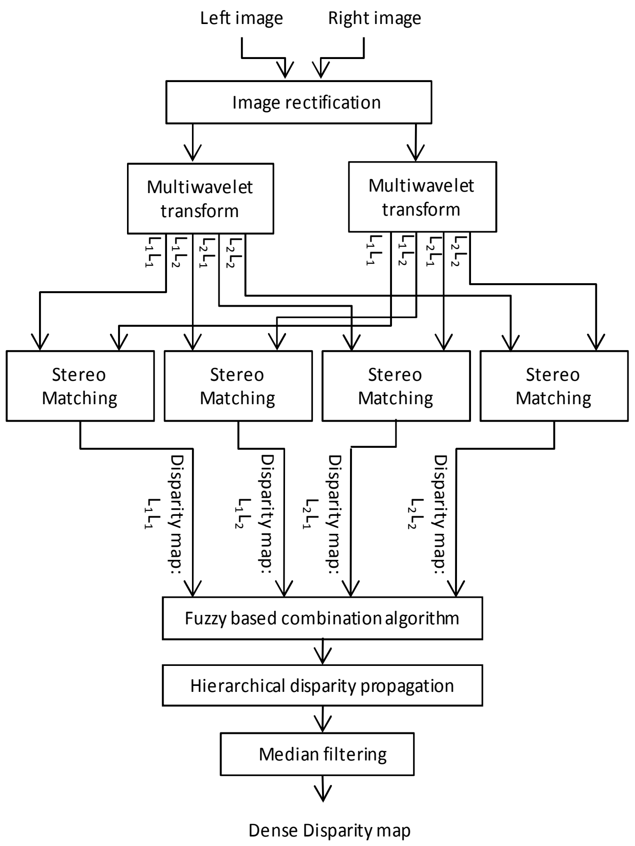

Figure 7. Block diagram of the hierarchical multiwavelet-based stereo matching technique using the global error energy minimization algorithm.

corresponds to (x', y') in the right image at level $i+1$, $(2x,2y)$ corresponds to one of the four points $(2x', 2y')$, $(2x'+1, 2y')$, $(2x', 2y'+1)$ and $(2x'+1, 2y'+1)$ from level i. Hence, the disparity in level $i+1$ can be propagated to the next finer level i by:

$$
D_i(2x,2y) = 2D_{i+1}(x,y) + \Delta d \tag{6}
$$

where Δd is one of $(0,0)$, $(1,0)$, $(0,1)$ and $(1,1)$, which minimizes the error of the matching metric. Disparities at the remaining points are interpolated from $D_i(2x,2y)$. A similar method has been employed in [13].

V. SIMULATION RESULTS

The performance of the proposed algorithms discussed in this paper has been assessed against the 'Cones', 'Tsukuba', 'Teddy' and 'Venus' standard stereo test images from the Middlebury stereo database [22]. Figure 8 shows the left image and the ground truth for these test images. The performance of different types and families of multiwavelets in the context of stereo correspondence matching has been evaluated using the 'Teddy' and 'Cones' stereo test images

(a) 'Cones'

(b) 'Teddy'

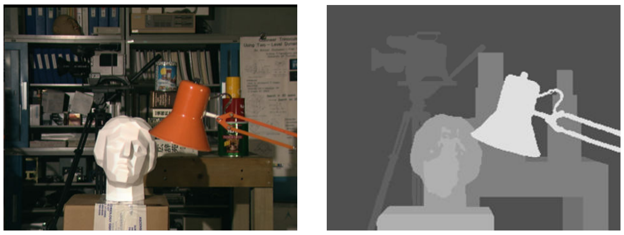

(c) 'Tsukuba'

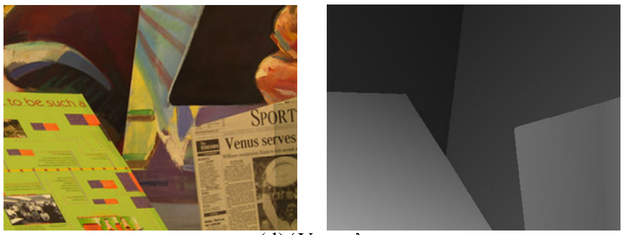

(d) 'Venus'

Figure 8. The left image and the ground truth of the (a) 'Cones', (b) 'Tsukuba', (c) 'Teddy' and (d) 'Venus' stereo test images.

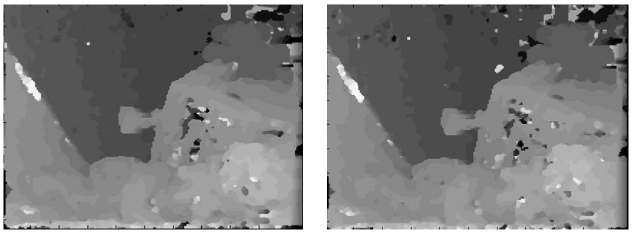

(a) (b)

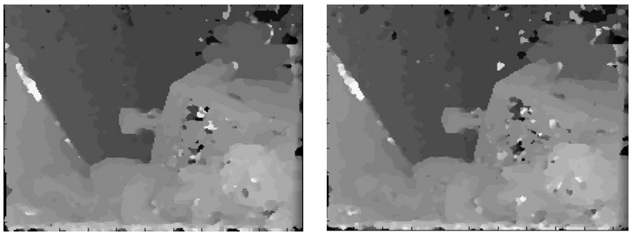

(c) (d)

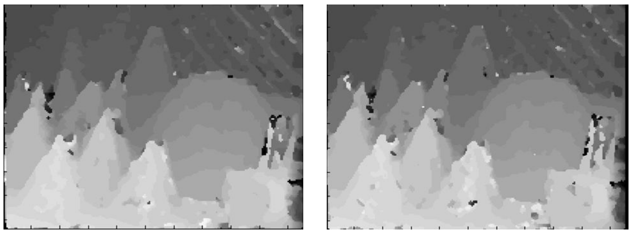

(e) (f)

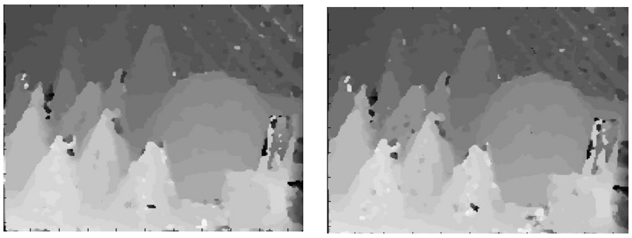

(g) (h)

Figure 9. Disparity maps obtained by using the multiwavelet basebands of the 'Teddy' stereo test image for subbands: a) L_1L_1 , b) L_1L_2 , c) L_2L_1 and d) L_2L_2 and respectively 'Cones' stereo test image for subbands: e) L_1L_1 , f) L_1L_2 , g) L_2L_1 and h) L_2L_2 .

based on the evaluation system discussed in Section III. Figures 9(a) to 9(h) give a visual comparison of the generated disparity maps for multiwavelet subbands L_1L_1 , L_1L_2 , L_2L_1 and L_2L_2 of the 'Teddy' and 'Cones' stereo test images. The experimental results were generated using a number of multiwavelet types, i.e., balanced versus unbalanced, and symmetric-symmetric (SYM - SYM) versus symmetric - antisymmetric (SYM - ASYM) multiwavelets (as listed in Table I). Table I shows the percentage of "bad pixels" at which the disparity error is larger than 1, for all regions (all). As it can be seen from the results presented in Table I, generally unbalanced multiwavelets give better results compared to the balanced multiwavelets. Furthermore, the symmetric-symmetric multiwavelets seem to produce slightly better results compared to symmetric-antisymmetric multiwavelets such as SA4. However, the symmetric - symmetric and symmetric-antisymmetric filter nature of multiwavelets doesn't seem to have a significant effect on the resulting disparity maps. The resulting disparity maps for balanced GHM and unbalanced BIGHM multiwavelets, applied to the 'Cones' and 'Teddy' test images are shown in Figures 10(a) and 10(b). From these figures, it is clear that the unbalanced multiwavelet based algorithm produces more accurate and smoother disparity maps compared to the balanced multiwavelet. This can be explained by the fact that the approximation subbands of the unbalanced multiwavelet carry different spectral content of the input images, which in turn enables the matching algorithm to generate more reliable matches.

TABLE I. EVALUATION RESULTS OF DIFFERENT MULTIWAVELETS IN STEREO CORRESPONDENCE MATCHING.

'TEDDY' (ALL)			
Balanced Multiwavelets		***Unbalanced Multiwavelets***	
CARDBAL2	9.78	BIH32S	8.82
CARDBAL 3	9.54	BIH52S (SYM-SYM)	9.06
BAT 01	9.98	BIH34N	8.82
BAT02	9.69	BIH54N (SYM-SYM)	9.24
GHM (SYM-SYM)	10.35	BIGHM	8.91
		SA4 (SYM-ASYM)	10.01
'CONES' (ALL)			
Balanced Multiwavelets		***Unbalanced Multiwavelets***	
CARDBAL2	9.82	BIH32S	9.65
CARDBAL 3	9.40	BIH52S (SYM-SYM)	9.73
BAT 01	10.23	BIH34N	9.65
BAT02	9.77	BIH54N (SYM-SYM)	9.76
GHM (SYM-SYM)	10.59	BIGHM	9.45
		SA4 (SYM-ASYM)	9.73

The performance of the proposed multiwavelet based GEEM technique has been evaluated against the 'Cones', 'Tsukuba', 'Teddy' and 'Venus' stereo test images. The performance of the proposed multiwavelet based GEEM algorithm is first benchmarked against similar GEEM algorithms operating in the spatial domain and respectively in the wavelet domain. A visual comparison of their performance is presented in Figure 11. The experimental results were generated using the GHM multiwavelet and the Antonini 9/7 scalar wavelet. The resulting disparity maps obtained using the proposed multiwavelet based algorithm, the wavelet based algorithm and respectively the GEEM technique applied to the original stereo views for the 'Teddy' and 'Cones' stereo pairs, are illustrated in Figures 11(a), 11(b) and 11(c) respectively. In these figures, areas with intensity zero represent occluded and unreliable disparities. As Figure 11 shows, the proposed multiwavelet based algorithm produces significantly more accurate and smoother disparity maps compared to both wavelet and spatial domain GEEM based algorithms. This can be explained by the multichannel structure of the multiwavelet transform, where the four resulting subbands carrying different spectral content of the input images, enable the global error energy minimization algorithm to generate more reliable matches. Operating on multiple channels with a narrower, more adaptive frequency spectrum split is certainly consistent with the structure of the human visual system itself, and from this point of view multiwavelets can be seen as a closer approximation of the human visual system than wavelets.

In order to give an objective quality comparison, the proposed algorithm is also evaluated against some well known techniques from the Middlebury database [22]. The results are presented in Table II. The chosen algorithms used for comparison are: AdaptingBP [23] (ranked second in the Middlebury database), DoubleBP [24] (ranked fourth in the Middlebury database), Graph Cut [25] and DP [26]. Table II shows the percentage of "bad pixels" at which the disparity error is bigger than 1. For each pair of images, the results in non-occluded regions (nonoc.), all regions (all) and depth discontinuity regions (disc.) are presented. From Table II, it

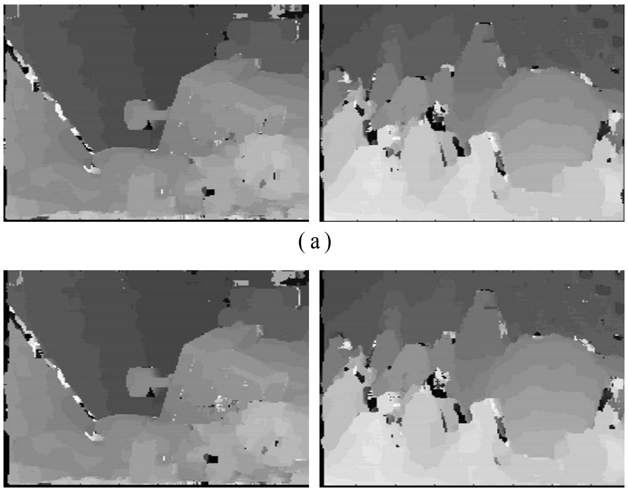

(a)

(b)

Figure 10. Disparity maps for 'Cones' and 'Teddy' stereo test image (a) unbalanced BIGHM and (b) balanced GHM multiwavelets.

can be seen that the multiwavelet based algorithm produces the second best results for 'Cones' and 'Teddy' stereo test images, while for 'Tsukuba' and 'Venus' it ranks third, and respectively third relative to the other four algorithms used for this comparison.

VI. CONCLUSIONS

This paper presented an investigation into the application of different types and families of multiwavelets in the context of stereo correspondence matching. The paper introduced a new multiwavelet-based stereo matching technique which employs a global error energy minimization algorithm. For evaluation purposes, two correspondence matching algorithms were designed to deal with both balanced and unbalanced multiwavelets. In the case of balanced multiwavelets, due to the similar frequency content of the four multiwavelet approximation subbands, they were re-shuffled to generate one baseband and then normalized cross correlation was employed to generate a disparity map. In the case of unbalanced multiwavelets, normalized cross correlation was applied to the four resulting basebands leading to four disparity maps. These maps were then combined using a Fuzzy algorithm to form a single disparity map. The initial disparity map was then refined by hierarchically propagating it to the finer levels. The results generated using Middlebury stereo test images show that unbalanced multiwavelets work better than balanced ones for stereo correspondence matching, while the symmetric-symmetric and symmetric-antisymmetric nature of the multiwavelets doesn't have a significant effect in reducing erroneous matches.

This paper also introduced a hierarchical stereo matching technique based on multiwavelet transform and global error energy minimization algorithms. For one level of decomposition, a multiwavelet transform with multiplicity of 2, decomposes the input stereo images into 16 subbands. The resulting four approximation subbands of the two views were

TABLE II. EVALUATION RESULTS BASED ON THE ONLINE MIDDLEBURY STEREO BENCHMARK SYSTEM.

ALGORITHM	'TSUKUBA'		
	NONOC.	ALL	DISC.
PROPOSED METHOD	0.89	1.39	5.9
ADAPTINGBP	1.11	1.37	5.79
DOUBLE BP	0.88	1.29	4.76
GRAPH CUT	1.27	1.99	6.48
DP	4.12	5.04	12
	'VENUS'		
PROPOSED METHOD	2.59	2.61	2.02
ADAPTINGBP	0.1	0.21	1.44
DOUBLE BP	0.13	0.45	1.87
GRAPH CUT	2.79	3.13	3.6
DP	10.1	11	21
	'TEDDY'		
PROPOSED METHOD	6.45	7.12	9.31
ADAPTINGBP	4.22	7.06	11.8
DOUBLE BP	5.53	8.30	9.63
GRAPH CUT	12	17.6	22
DP	14	21.6	20.6
	'CONES'		
PROPOSED METHOD	7.25	8.09	10.66
ADAPTINGBP	2.48	7.92	7.37
DOUBLE BP	2.90	8.78	7.79
GRAPH CUT	4.89	11.8	12.1
DP	10.5	19.1	21.1

then used to generate a set of four disparity maps using a global error energy minimization algorithm. The resulting four disparity maps were then combined using a Fuzzy algorithm. The output of the Fuzzy combination algorithm constitutes the initial disparity map, which was then refined by hierarchically propagating it to the finer levels. Results show that the proposed technique produces a disparity map with significantly less mismatch errors compared to the same global error energy minimization algorithm applied to the original image data or to the wavelet transformed image data. The performance of the proposed multiwavelet based algorithm has been compared to other well-known techniques benchmarked and published in the Middlebury database. The results show that the proposed multiwavelet based algorithm fares well against many well established algorithms ranked at top positions in the Middlebury database. The multichannel nature of the multiwavelets and the different spectral content of the resulting subbands allow for greater correspondence matching flexibility than in the case of wavelets, and explain why the multiwavelet based technique performs better than when similar global error energy algorithms were applied in the wavelet and respectively the spatial domain.

ACKNOWLEDGMENT

This work was supported by EPSRC under the EP/G029423/1 grant.

REFERENCES

[1] P. Bagheri Zadeh and C. Serdean, “Stereo Correspondence Matching using Multi-Wavelets”, 2010 Fifth International Conference on Digital Telecommunications (ICDT2010), Athens, Greece, pp. 153-157, June 2010.

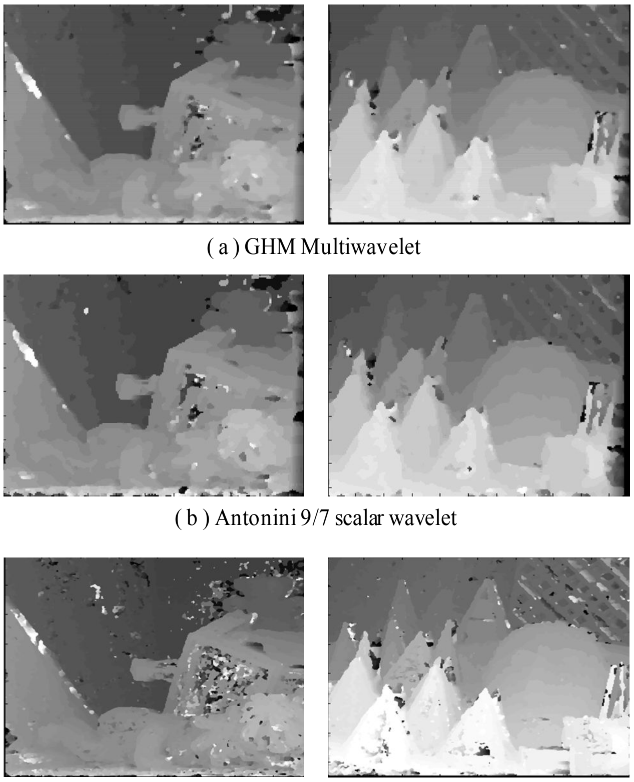

(a) GHM Multiwavelet

(b) Antonini 9/7 scalar wavelet

(c) spatial domain

Figure 11. Disparity maps for 'Teddy' stereo test image (left) and 'Cones' stereo test image (right), using a) the proposed multiwavelet-based global energy minimization algorithm, b) the wavelet-based global energy minimization algorithm and c) global energy minimization algorithm in spatial domain.

[2] D. Scharstein and R. Szeliski, “A Taxonomy and Evaluation of Dense Two-Frame Stereo Correspondence Algorithms,” International Journal of Computer Vision, vol. 47, pp. 7-42, April 2002.

[3] K. Muhlmann, D. Maier, R. Hesser, and R. Manner, “Calculating dense disparity maps from color stereo images, an efficient implementation,” Proc. IEEE Workshop on Stereo and Multi-Baseline Vision (SMBV 2001), 2001, pp. 30-36 , doi: 10.1109/SMBV.2001.988760.

[4] L. Di Stefano, M. Marchionni, S. Mattoccia, and G. Neri, “A Fast Area-Based Stereo Matching Algorithm,” Image and Vision Computing, vol. 22, pp. 983-1005, March 2004.

[5] S. Yoon, S. K. Park, S. Kang, and Y. Keun Kwak, “Fast correlation-based stereo matching with the reduction of systematic errors,”Pattern Recognition Letters, vol. 26 , pp. 2221-2231, October 2005.

[6] K.J. Yoon and I. S. Kweon, “ Adaptive support-weight approach for correspondence search,” IEEE Transactions on Pattern Analysis and Machine Intelligence, vol. 28, pp. 650-656, April 2006.

[7] H. Kim, S. Yang, and K. Sohn, “ 3D reconstruction of stereo images for interaction between real and virtual worlds,” Proc. IEEE International Conference on Mixed and Augmented Reality, October 2003.

[8] A.S. Ogale and Y. Aloimonos, “Robust Contrast Invariant Stereo Correspondence,” Proc. IEEE International Conference on Robotics and Automation, ICRA 2005, pp. 819-824, April 2005.

[9] Q. Yang, L. Wang, R. Yang, S Wang, M. Liao, and D. Nister, “Real-time global stereo matching using hierarchical belief propagation", In Proceedings of the British Machine Vision Conference (BMVC), 2006.

[10] I. Choi and H. Jeong, “Fast Belief Propagation for Real-time Stereo Matching,” International Conference on Advanced Communication Tech., ICACT 2009, pp. 1175-1179, Feburary 2009.

[11] S. Mallat, A Wavelet Tour of Signal Processing, Academic Press, 1999.

[12] V. Strela and A.T. Walden, “Signal and image denoising via wavelet thresholding: orthogonal and biorthogonal, scalar and multiple wavelet transforms,” In. Nonlinear and Nonstationary Signal Processing, pp. 124-157, 1998.

[13] I. Sarkar and M. Bansal, “A wavelet-based multiresolution approch to solve the stereo correspondence problem using mutual information,” IEEE Transaction on System, Man, and Cybernetics, vol. 37, pp. 1009-1014, August 2007.

[14] Q. Jiang, J. J. Lee, and M.H. Hayes, “A wavelet based stereo image coding algorithm,” IEEE International Conference on Acoustics, Speech, and Signal Processing (ICASSP 99), vol.6, pp. 3157 - 3160, March 1999.

[15] G. Caspary and Y. Zeevi, “Wavelet-based multiresolution stereo vision,” Proc. IEEE International Conference on Pattern Recognition (ICPR 2002), pp. 680- 683 , December 2002.

[16] A. Bhatti and S. Nahvandi, “Depth estimation using multi-wavelet analysis based stereo vision approach,” International Journal of Wavelets, Multiresolution and Information Processing, vol. 6, pp. 481-497, 2008.

[17] V. Strela, “Multiwavelets: threory and applications,” PhD thesis, MIT, 1996.

[18] J. Lian and C. K. Chui, “Balanced Multiwavelets With Short Filters,” IEEE Signal Processing Letters, vol. 11, no. 2, pp. 75-78, Feb. 2004.

[19] L. Ghouti, A. Bouridane, M. K. Ibrahim, and S. Boussakta, “Digital Image Watermarking Using Balanced Multiwavelets,” IEEE Trans. on Signal Pro. , Vol. 54, no. 4, pp. 1519-1536, 2006.

[20] B. B. Alagoz, “Obtaning depth maps from colour images by region based stereo matching algorithms,” OncuBilim Algorithm and System Labs, vol. 08, Art.No:04, 2008.

[21] R.C. Gonzalez, R.E. Woods, and S.L. Eddins, Digital Image Processing second edition, Prentice Hall, pp. 75-142, 2002.

[22] http://vision.middlebury.edu/stereo/, last accessed June 2010.

[23] A. Klaus, M. Sormann, and K. Karner, “Segment-based stereo matching using belief propagation and a self-adapting dissimilarity measure,” Proceedings of the 18th International Conference on Pattern Recognition (ICPR 2006), vol. 3, pp. 15-18, August 2006.

[24] Q. Yang, L. Wang, R. Yang, H. Stewenius, and D. Nister, “Stereo Matching with Color-Weighted Correlation, Hierarchical Belief Propagation, and Occlusion Handling,” IEEE Transaction on Pattern Analysis and Machine Intelligence,” Vol. 31, pp.1-13, March 2009.

[25] V. Kolmogorov and R. Zabih , “Multi-camera scene reconstruction via graph cuts,” 7th European Conference on Computer Vision (ECCV 2002), pp. 8-40, May 2002.

[26] D. Scharstein and R. Szeliski, “A taxonomy and evaluation of dense two-frame stereo correspondence algorithms,” International Journal of Computer Vision (IJCV 2002), Vol. 47, pp. 7-42 , April 2002.

[27] M.B. Martin, and A.E. Bell, “New image compression techniques multiwavelets and multiwavelet packets,” IEEE Trans. Image Process. Vol. 10, no. 4, pp. 500–510, 2001.

UAV-based Sensor Networks for Future Force Warriors

Jorma Jormakka
Department of Military Technology
National Defence University
Helsinki, Finland
jorma.o.jormakka@kolumbus.fi

Tapio Saarelainen
Department of Military Technology
National Defence University
Helsinki, Finland
tapio.saarelainen@mil.fi

Abstract **- The Future Battlefield Commander relies on Command, Control, Communications, Computers, Information, Intelligence (C^4I^2) tools to perform optimally in his given tasks in versatile and hostile environments. The concept of war has changed from traditional wars to the asymmetric wars. This article presents a new networking concept for sensor networks, the Wireless Polling Sensor Network (WPSN) for the Dismounted Future Warrior. The WPSN comprises a small ad hoc network of mobile Unmanned Vehicles (UVs), and a fixed set of sensor nodes that continuously survey the area. The UVs move along pre-planned routes and poll the sensors. The article briefly describes the Future Warrior system, presents the WPSN solution, and explains the main use cases of the WPSN concept: road-side bomb detection, location service in built-up areas, and marking a target by Special Operations units. An evaluation of the advantages and disadvantages of the proposed WPSN concept is given; and a provably computationally secure crypto-protocol between base stations and other nodes, such as UAVs, is presented. The main output of the paper offers WPSN solutions together with SCPAs and UVs to attain the maximum performance at all warrior levels.**

Keywords - Wireless Sensor Network; Future Warrior; Situation Awareness, UAV, cryptology, One-Time Pad (OTP).

I. INTRODUCTION

This article describes a new concept called the Wireless Polling Sensor Network (WPSN) to be used in the Future Warrior gear. It comprises sensor nodes that are not networked with each other but communicate with a mobile ad hoc network of a small number of Unmanned Air Vehicles (UAVs), also called drones. The article presents the motivation and some applications of the concept. The article is an extended version of a paper [1] presented in the ICDT conference in 2010 and in addition to material from [1], it includes an evaluation of the basic concept of the proposed UAV-sensor network solution, and presents a new crypto-protocol based on exchanging One-Time Pads, used between base stations and other nodes of the proposed system. The crypto-protocol has appeared earlier in the departmental preprint series [2] but has not been published.

The main setting of the WPSN is the Future Warrior system. A warrior's electronic skeleton, shown in Fig. 1, is a backbone and a platform for implementing required electronic solutions to be used in modern warfare. The Wireless Polling Sensor Network is a part of a larger system of communication, navigation and positioning systems.

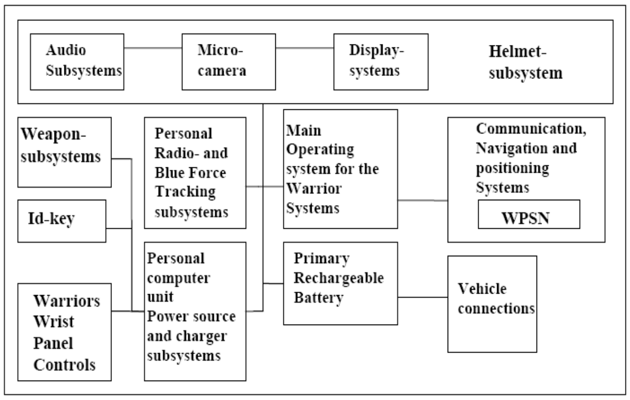

Figure 1. A Warrior's electronic skeleton.

Militaries search advantage in the future battlefield through novel solutions utilizing existing technologies and communication network systems and thereby enhancing the warrior efficiency. The main objective of these networks and technical solutions is to improve Situational Awareness (SA) [3] at all of the warrior levels in the decision-making process. Blue Force Tracking-systems (BFT) are an essential part of SA. They provide vital information for commanders in helping them to make better decisions and to avoid fratricide. Troops need to be constantly precisely located. It is crucial to improve the efficiency of dismounted operations with smaller and more capable units. The units require a great degree of flexibility and reliability in order to obtain their goals.

Future Warrior systems apply several levels of warriors from the least trained to the experienced commanders or the professionals of the Special Forces. Table 1 shows examples of different technical solutions that are needed at different warrior levels. Demands for the solutions are derived from the needs of the warriors at different levels according to their performance and tasks. The WPSN-system applications must be implemented into Future Warrior systems taking into account the different warrior levels.

One of the most important constraints imposed by the Future Warrior system is the maximum weight of any equipment in the warrior gear. For instance if a ground-based fixed sensor node has a mass can reach up to 10 kg the nodes can be transported to the site by the Special Forces. The UGVs present a better payload platform, but they are significantly slower, and their control and communication systems need to be improved.

TABLE I. DIFFERENT WARRIOR LEVELS.

Warrior level	Basic Warrior	Squad / Platoon leader	The Company Commander	Special Force Soldier
Range for the systems (comms.)	up to 3 miles, WLAN / LAN, PTT-radio	up to 5 miles, WLAN / LAN, PTT-radio	up to 10 miles, WLAN / LAN, PTT-radio, SATCOM	up to 100 miles, WLAN / LAN, PTT-radio, SATCOM
Duties tasked	Defensive, offensive, reconnaissance	Defensive, offensive, reconnaissance + C4I2	Defensive, offensive, reconnaissance + C4I2	According to task
Demands for used solutions	Basic gear	Advanced gear and lightened C4I2	Gear for C4I2	According to task
Duration of operations	up to 72 hrs	up to 72 hrs	up to 72 hrs	up to 120 hrs
Military Operations in the woods	Yes	Yes	Yes	Yes
Military Operations in Urban Territory (MOUT)	Yes	Yes	Yes	Yes
Military Operations behind enemy lines	No	No	No	All
Hostage Missions	No	No	No	All
Rescue Missions	No	No	No	All
Need for fire support	No	No	YES	YES
Need for emergency evacuation in hostile territory	No	No	YES	YES

In order to motivate the WPSN concept, let us recall the typical structure of a Wireless Sensor Network (WSN). A WSN usually contains an ad hoc network of sensor nodes, a gateway node, and a control station. This results in problems with energy, security and in military applications of survivability. This type of a WSN loses connectivity when a sufficient number of nodes is removed or destroyed. It may also be too easily detected, and its life-time may be short and unpredictable. There are only few civilian applications available for ad hoc WSNs, such as applications for monitoring seismic and environmental changes. A more traditionally structured WSN comprises a base station and sensor nodes connected by wireless links.

Another motivation for WPSN we get from the present UAV systems for dismounted soldiers. UAVs bring a significant edge in the C^4I^2 environment as a new sensor and a relay platform but the present solutions are far from perfect. These systems have a base controller, a line-of-sight data link to the UAV and a relatively small UAV, typically equipped with a camera (Infra-Red or visual). Because of the line-of-sight requirement, they have a limited range and cannot be easily used in urban areas. Additionally, the camera does not see anything else than what is happening at the moment the UAV's camera surveys the area. A single small UAV has also a very small payload on the range of pounds [4].

The Wireless Polling Sensor Network (WPSN) is proposed as a solution to the problems of both the WSN and the small UAV systems. WPSN comprises a mobile ad hoc network of UAVs or UGVs with *1-n* nodes, *n* being a small number, and a set of fixed ground-based sensors. The network of UAV can operate as a multi-hop ad-hoc network in case it is motivated, for instance, by multi-sensor co-operation, or by a lack of a line-of-sight connection. A control station has a data link to a selected node of this mobile network. More than one node improves survivability in applications where nodes can be destroyed. The sensor nodes do not form a network but they are polled by a selected node of the mobile network. A possibility for this is created by adding a random-access event channel.

The WPSN solution has many advantages over the traditional WSNs: Polling can use sensor specific codes and security issues become easy. The fixed sensor nodes do not lose connectivity even if a high number of nodes are removed. The WPSN is a part of mobile mesh network systems operating in an environment of harsh propagation of channels and interference, frequent and rapid changes of network topology [5].

The need for a special gateway node, typical to a WSN, is removed: the fixed sensor nodes use directional antennas that only emit in the upward direction and an UAV polls them. The signal strength remains sufficient for a UAV on reasonable altitudes and the fixed sensor nodes are difficult to locate by ground-based measurements. The transmit antenna selection is a practical technique for achieving significant power gain, even with commodity hardware and without changes to the 802.11 protocols [6]. For example, field experiments have been conducted in which the network was based on the frequencies of 2,4 and 5,8 GHz, and also the 900 MHz frequency was used for the point to point mode [7]. The detection methods are based on motion, either seismic, or acoustic etc. The WPSN concept can use also in Unmanned Ground Vehicles (UGVs) instead of UAVs. In a UGV application, the fixed sensor nodes can, for example, be GPS pseudolites that an UGV installs [8]. The composition of this paper is as follows: Section 2 reviews the background work. Section 3 presents applications of UAV-based sensor networks and the overall evaluation of the concept. Section 4 concentrates on a provably computationally secure protocol between base stations and other nodes. Finally, Section 5 concludes the paper.

II. RELATED WORK

Several Future Soldier Programs are currently underway in various militaries, including the Finnish Army definition work contributing to its Future Warrior (Future Force Warrior, FFW) and its demands. The result involves defining the gear for each level of a Future Warrior. The critical solutions involve communicating, Situational Awareness (SA) and Command and Control (C2) information among highly dispersed battlefield units in a dynamic environment [3][9]. In fact, the US Army is fielding its new SA system known as Force XXI Battle Command and Brigade and Below (FBCB2) [9]. An extension of this is the Deep Green.

The need for UV-based sensor systems is clear. There are strict constraints on the weight and dimensions of equipment carried by a soldier and therefore it is essential for the Future Force Warrior (FFW) to be networked and to use external systems based on new innovations. One way of networking a soldier installing a high-bandwidth conformal antenna into the soldier's helmet with the coverage of over 750 MHz through a 2,7 GHz frequency band [10].

Systems that are very similar to the proposed WPSN, comprising a network of UVs and a fixed set of sensors, do not seem to exist yet. Presently UAVs are directly connected to a base station [11]. There are some experimental UAV networks [11][12]. UGV networks seem to be non-existing, while single UGVs are widely used e.g. by police forces. However, all technical elements of the WPSN solution are available. The novelty of the WPSN solution is not in technical elements but in the realization that the solution can fill certain currently critical military needs.

The WPSN system uses a mobile network of UVs. It can be considered as a Mobile Backbone Network (MBN) of a sensor network. A typical layout of a MBN is based on the Backbone network (Bnet), access nets (Anets) and regular (flat) ad hoc network(s) [13]. A Mobile Backbone Network Routing with the Flow Control (MBNR-FC) method is a known method to improve network throughput as well as the packet delay, the delay jitter and the loss ratio performance [14].

Possible solutions for tracking and location service have been searched from satellite positioning systems, like the Global Positioning System (GPS). With Differential Global Positioning Systems (DGPS) the errors of GPS can be corrected to the acceptable level of few meters [14] [7] [22]. However, GPS cannot always be relied on and especially militaries that do not own positioning satellites are constantly in search of alternative methods.

There are many existing MAC protocols and some of them can provide sufficient Quality of Service in a MANET. The mobile ad hoc network between the UAVs in the WPSN uses a MAC protocol called ISMA/RA (Inhibit Sense Multiple Access/with Reservation for Ad hoc networks) presented in [26]. It was developed in 2004 by the first author and Marko Ahvenainen [27] for military ad hoc networks, and has been implemented as a simulation model. ISMA/RA can be considered as a modification of ISMA/P [15]. The idea in ISMA/RA, as well as in ISMA/P and PRMA [16], is to guarantee bandwidth in multiple hops by a combination of random access and polling protocols, and by dividing the time axis into slots. The behavior of ISMA/P is analyzed in [17] and well understood. The TDMA approach for ad hoc WLAN networks is also used in HiperLAN/2, but the solution and performance issues (like in [18]) in HiperLAN are quite different from those of ISMA/RA. This paper offers a provably computationally secure protocol between base stations and other nodes combined with the introduced use cases of the WPSN. The introduced secure protocol combined with use cases of the WPSN enables the maximum performance at all warrior levels.

III. Applications of UAV-based sensor networks

The article describes three scenarios in which the WPSN can be utilized to maintain the initiative; namely, on the road, in built-up areas, including inside buildings, and, finally, how the Special Forces can utilize these systems [19].

A. *Road side bomb detection*

Increased Overseas Operations present road side bombs as a serious concern for the friendly troops due to the road side bombs' efficiency related to their unpredicted location. By using a solution based on the Wireless Polling Sensor Network, road side bombs can be detected using this new technology based on novel sensor data collection techniques. The detection procedure involves the following phases.

Firstly, the new concept of Wireless Polling Sensor Network comprises fixed sensor nodes, which do not communicate with each other. These nodes answer to mobile polling if they have something to report. The mobile polling nodes are a swarm of pre-programmed UAVs equipped with homing devices.

Secondly, the fixed nodes detect activity at the road-side, such as humans or large objects moving. The detection is based on a significant change in the electromagnetic spectrum, such as thermal, magnetic, or seismic change of the monitored area. The UAV patrols the area regularly, for instance, once an hour. Finally, as bombs are typically placed on the sites hours or days in advance, the WPSN application does not require real-time reporting to match the needs.

The fixed sensor nodes do not emit electromagnetic radiation except when the UAV sends a polling request with a specific code. The static nodes use directional antennas and communicate directly above (in a certain angle). A Wireless Polling Sensor Network has an edge over a traditional Wireless Sensor Network, for the system will remain functional even if some sensor nodes have been destroyed. A swarm of UAVs as polling devices gives an edge to the system resulting in reliable data gathering as seen in Fig. 2, and the arrows indicate the data transmission between the entities, the UAVs and the sensor nodes.

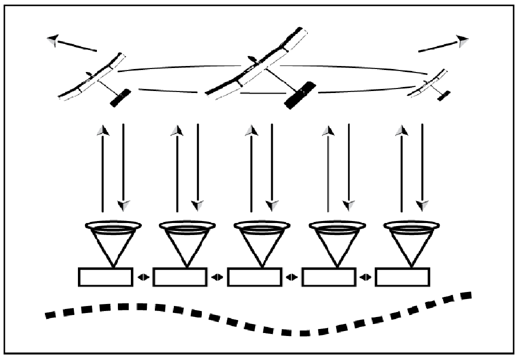

Figure 2. The structure of the WPSN with the swarm of UAVs.

Energy consumption in a multi-hop sensor network is higher than in the proposed solution since messages from other nodes must be relayed, and this depends on the placement of the nodes relative to the control point. The detection of the sensor nodes by the opponent is also much easier in a fixed multi-hop network. The WPSN has lower energy consumption together with better protection against detection, resulting in increased survivability of the network.

The polling procedure begins with mutual authentication of the UAV and the sensor. After authentication stage information is sent in encrypted from the sensor to the UAV. Since the transmitting power of a sensor is low, directional antennas are used for securing the transmission towards the

UAV. This enures the safety and QoS of transmission. The jamming of the system is made difficult by directional antennas. The system is battle-proof and answers only the UAV after a defined and pre-programmed identification protocol.

As the signal propagation time and the message forwarding delay are 10 ms and 15 ms, respectively, the communication delay can be understood to be on an accepted level when a swarm of UAVs is used to collect the accrued sensor data [29]. Since currently neither a test-laboratory nor UAVs can be utilized for testing purposes, the information referred to in this particular section of the paper is based on a relevant study [29]. As explained in Section III on page 3, the UAVs are used in swarms of three or four in order to ensure maximized data gathering and the validity of the sensor data. Moreover, as described in Section III, reliable communication between a single UAV and sensors takes only fragments of seconds after the identification procedures. In this case, the altitude of the swarm of UAVs is 400 meters. This altitude indicates that, once the angle of the transmitting sensor is from 5 to 7 degrees, the communication area at the altitude of 400 meters is at least 33,3 meters in diameter and in maximum 46,7 meters in diameter. In this example the speed of a single UAV is 80 km/h and 22 m/s allowing a UAV to receive a signal from a sensor for longer than a second. And again, as explained in [29], the signal propagation time and the message forwarding delay are 10 ms and 15 ms, which gives enough time for a single UAV to communicate with each sensor in a swarm of UAVs. And in case a single UAV fails to communicate with a sensor, another member of a swarm of UAVs can replace this function. When all the collected data are verified, these accrued data can be merged.

The topology of network systems has to be correctly coordinated (i.e., managing spectrum usage with group mobility patterns). The hierarchy of a network has to support this. This can be achieved by hierarchical design where devices are only to interact with their peers from the same group [19]. This means the swarm of UAVs communicates in the same intra-group while the UAVs and multi-sensors are in an inter-group with the UAVs. This ensures the QoS and proper maintenance of networks. Improved network performance can be obtained by using more channels, aggregation of more packets per frame and appropriate channel assignment [20]. A UAV can be used as a platform to provide the needed services, for example, Digital Video Broadcast – Terrestrial [DVB-T) and Digital Video Broadcast –Handheld (DVB-H) [21].

B. *Location services in urban areas*

Another interesting application of the WPSN is related to positioning and location services, especially in urban warfare. This solution is based on the Ground Positioning System (GPS) and the GPS-Pseudolite, better known as the Self-Calibrating Pseudolite Array (SCPA) [22] [8]. Studies indicate that the SCPA provides an effective means of acquiring a satellite-based Carrier-phase Differential GPS-type (CDGPS) centimeter-level positioning in locations without access to the GPS satellite constellation [8].

An Army tactical warfighter needs network services both On-The-Move (OTM) and At-The-Halt (ATH) [23]. One of the lessons learned from Iraq and Afghanistan was the need for a more robust Beyond-Line-Of-Sight (BLOS) communication capacity between the lower Army echelon Land Warriors, from Squad Leaders to Battalion Commanders [23].

The SCPA technique is used in Mars Rover Navigation [8]. The application can be as follows: The warrior polls the SCPA stationed on the urban battlefield (roof-tops, perimeters of buildings). The warrior acts as a polling UAV as described in Fig. 3, and the arrows indicate the data transmission between the entities and the triangle-shaped objects represent the SCPA.

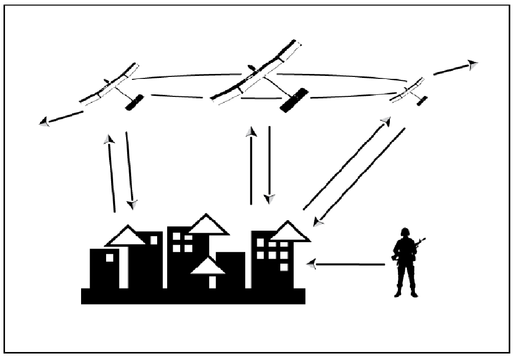

Figure 3. The WPSN presented in the urban infrastructure.

The proposed and described solutions have to be based on novel, generic and robust battlefield-proven solutions in order to meet the given needs, and this in turn involves addressing the topology of the network system carefully.

The novel sensor data collection techniques include: 1) the Development of a new networking concept: Wireless Polling Sensor Network, 2) A mobile ad hoc sensor network that can support near real-time streams, and 3) Generic SOA-interfaces for sensors and sensor platform control. One of these is the medium access control (MAC) algorithm and protocol for ad-hoc wireless networks that employs power control spatial-reuse scheduling techniques [24]. The Networks inside the WPSN solutions have to be functional and communicate as seen in Fig. 4, and the arrows indicate the data transmission between the entities, the UAVs and the sensor nodes.

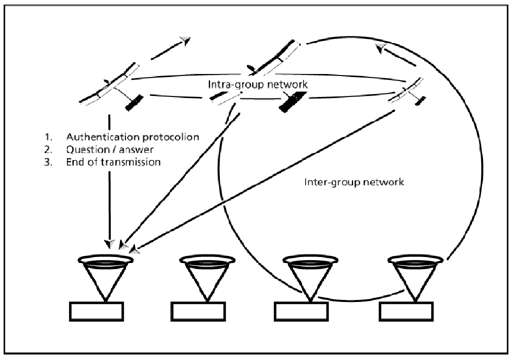

Figure 4. The principle of the network topology.

Since the power production and power consumption will remain as a challenge, certain actions need to be addressed. Thus when defining the network design, it has to be emphasized that network coding enables a more efficient, scalable and reliable wireless network [25].

The multi-sensor system comprises (Fig. 5): 1) a control unit (CU) that is placed on the operational centre, 2) a number of sensor control units (SCUs) that form a mobile ad hoc sensor network capable of near real-time data transfer, 3) sensor platforms, such as unmanned air or land vehicles, 4) different types of sensors, and 5) new algorithms for multi-sensor collaboration.

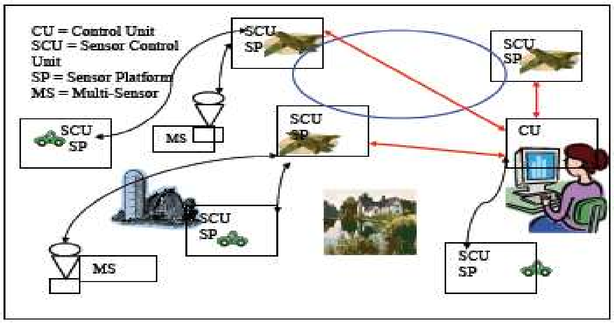

Figure 5. The network system of the WPSN.

Another application in an urban environment is a multi-hop mobile sensor network consisting of UGVs for investigation of buildings or placing SCPAs on a site. A network of a small number of such UGVs does not present technical problems as a small mobile ad hoc network, but it removes the need for a line-of-sight connection. The main new advantage is the addition of location mechanisms and pre-planned routes that are manually assisted when needed.

C. *Solution for the special forces*

The Special Forces need a precise location of a target to have it destroyed. Let us assume that in this example the selected target is heavily fortified, guarded and built of concrete, or buried deep in soil. The power of conventional weapons used by the Special Forces is not enough to destroy the target. Therefore, the target has to be marked for the bombs or guided missiles. This idea utilizes the possibilities of the Wireless Polling Sensor Network (WPSN), and the solution is based on the use of the SCPA. The idea is to set the SCPAs close to the selected target and measure the distance and direction from this specific spot at the target. This way the place of each SCPA is very precisely measured in relation to other SCPAs and the target. Once this has been done to each SCPA, a swarm of UAVs can be sent on their way to poll the SCPAs and collect the data to be transmitted to the destruction device for preparation purposes, if needed. The SCPAs do not form a network between each other, thus not transmitting, and they do not have a specific ground station. Pseudolites only answer the UAVs according to the communication protocol described earlier in Section III, B. In Fig. 6 below the arrows indicate the data transmission between the entities, and the question mark indicates the target to be destroyed.

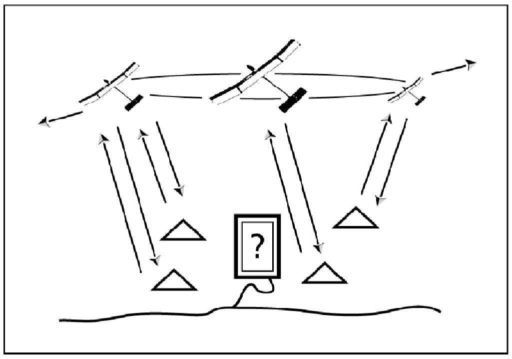

Figure 6. An example of the SCPA in the use of the Special Forces.

Once the pseudolites are set on their positions, the selected destruction device (in this case a fighter with an intelligent bomb) approaches the target at the selected moment and drops the bomb and dismisses the area. The destruction device polls the SCPAs while heading towards the target and, based on the collected data, the destruction device is being guided at its target. This protocol deletes the need to depend on GPS-satellites and thus gives an edge to gain the goals in rough and mountainous terrain, where GPS-satellites cannot be seen all the time. Jamming the SCPAs is not easy, for they transmit the encrypted data only once in a very narrow angle (5 – 7 degrees) straight upwards and after the bomb has the data, it is locked to its target.

In this paper the altitude for a swarm of UAVs has been defined to be 400 meters because a UAV is hard to detect or destroy from that altitude. Furthermore, the distance between the UAVs and ground-based sensors ensure reliable means of communication. Besides, small UAVs are relatively inexpensive and easy to replace which makes them an invaluable asset in military operations.

D. *Evaluation of the concept*

As the UAV sensor network is still on the design stage and no implementations can be tested, evaluation of the whole solution can only be based on looking at the basic ideas of the concept and finding its strengths and weaknesses. We go through some typical issues that should be considered for any sensor network solution.

Offered service: The proposed WPSN solution provides location and targeting service, and in the road side bomb application continuous sensor data collection from the area. In the last application the solution does not give reliable alarms of intrusion, unlike e.g. burglar alarm systems. Therefore the information is likely to include many false positives and a rapid reaction to each sensor data item that might indicate an effort to plant a bomb would be superfluous. It is sufficient to poll the sensor nodes after a relatively long period of time immediately before a patrol tour. The solution does not assist in fast response but can mitigate the effects and provide sensor data for demonstrating that an incidence was planned, and possibly an identification of the attacker if voice sensors are used.

Coverage issues: The proposed system is suitable for areas so large that they cannot be easily covered by a fixed wireless base station, or by a WSN, and the set of sensors can be formed of disconnected parts, unlike in WSN. The use of a network of several UAVs is a clear improvement to the present applications where one UAV is controlled by a ground station and a line-of-sight connection is required. This limits the operational range of UAVs to roughly ten kilometers in open areas and prevents the use of UAVs in urban areas. A networked set of UAVs can increase the range by multi-hop routing. If one UAV has a line-of-sight connection to a ground station, it can forward messages to and from other UAVs. This requires that the MAC protocol supports real-time traffic. Controlling a UAV (and especially a number of them) through multi-hop connections is difficult but in the presented solution it is made possible by the sensor nodes: the UAVs have a pre-planned route and feedback information from the sensor nodes allows the UAVs to make corrections to their positions and to stay at the planned route. It is also expected that a ground based pilot can control the swarm of networked UAVs by steering only one of them and relying on suitable control protocols that keep the UAVs of the swarm in a fixed formation. Connectivity issues for an *n*-node UAV/UGV network can appear but they are typical to any mobile ad hoc network (MANET). In the case of WPSN, connectivity problems of the MANET are minor since the UAV/UGV nodes follow pre-assigned paths and the number *n* of nodes is small. Connectivity issues between the UAV/UGV and sensor nodes determine how strictly the UAV/UGV must follow the pre-assigned path but this restriction can be avoided by increasing the altitude of the UAV. From a sufficient altitude the UAV can receive data from all ground sensors.

Operational limitations: The most important restriction to the system is caused by weather conditions, which do not always allow the use of UAVs but this limitation is not seen as a major argument against the solution. The polling device could of course also be a ground-based vehicle avoiding the weather dependence. There is an advantage in using an UAV since camera picture from an UAV can often give a probable reason e.g. why a sensor node is not communicating. The solution requires usage of planned routes. There can naturally be many alternative planned routes. The concept does not in any way require that all sensor nodes must be polled in any specific order.

Performance issues: Performance evaluation of the whole system is not presented in this article since there are no real-life experiments so far. We can describe the main performance issues. Traffic congestion problems cannot appear in the system: the UAV/UGV makes the round e.g. every hour and collects sensor data from a relatively small number of sensors.

Dependability issues: The WSPN network cannot be easily disabled by removal or blocking of some nodes, as is the case for a WSN in essentially one-dimensional areas, such as a road where one parked truck may disconnect the WSN. A problem of a malicious network node unwilling to transfer data of other nodes does not occur since the sensor nodes communicate only with the polling network, which can be assumed secure. Unauthorized removal of sensor nodes is interpreted as a signal of undesired activity. There are ways to protect the sensor nodes against efforts to break the security algorithms protecting their communication with the polling nodes, e.g. by self-destruction, even if there is physical access to the sensor nodes. The sensor nodes should be difficult to find, otherwise they may be stolen. The communication mode of replying only to the polling node request makes the nodes difficult to find by electro-magnetic sensors.

Energy issues: Polling is in general considered a less efficient communication method than generating events from incidences, since many nodes have nothing to report. In the road-side bomb application there are some factors that change this conclusion. It is desirable to get a stay-alive announcement from each sensor in any case; therefore it is not sufficient to generate events only if something suspicious happens. The time to poll the sensor nodes is negligible compared to the time the polling UAV needs for the round trip for physical reasons, so polling is not slower in this case. The energy constraints in the UAV are not a limiting factor. It is of course possible to create a hierarchical sensor node structure where only some nodes communicate with the polling nodes while the other nodes report events to the communicating node. However, some robustness is lost in the hierarchical model. The polling network concept has a clear advantage in networks that are essentially one-dimensional, like a road side: a WSN node must pass messages created by other nodes; consequently its energy usage cannot be well predicted. In the WSPN solution energy usage can be well estimated and it is more important to have a good estimate of the battery life-time than a maximal prolongation of sensor operational time between battery recharge. The same patrol routes are not used for years, nor do the sensor nodes need to last for years without recharging. The energy needed to communicate with the polling node is not negligible, but especially as the communication is in free space, it is not assumed to be a limiting factor for the sensor node batteries. Sufficiency of energy in ground-based sensors and in UAV/UGV nodes is a limitation but the sensor nodes do not need to be especially small in this application.

Technology development: A proposed technological solution should have characteristics that make it more future-proof. The WSPN solution is open to development of sensor techniques. It may be possible in the near future to detect threats better from sensor data, e.g., to distinguish between a deer and a walking human. Applications of unmanned vehicles to military and crisis management situations are also a fast developing area. Ad hoc sensor networks have on the other hand met with certain scalability problems. A simple polling network concept seems to give future promises. A military system should be flexible enough to have a range of usages. While the WSPN concept has been created for the current need in road-side bomb detection, the system has other applications e.g. in location finding and in targeting.

Possible applications: The road side bomb detection is the main application. There is a current need for it and the existing methods, i.e., disabling communication to an IED by jamming, and surveillance by UAVs, are inadequate. The use of WPSN for targeting instead of GPS has some advantages and disadvantages. It is vulnerable to ground-based jamming but on the other hand, the frequency can be selected from a wider range. Location service in urban area is a much studied but difficult issue. The proposed system may be a partial solution.

IV. A Provably Computationally Secure Protocol between Base Stations and other Nodes

In the case of UAVs and other easily captured nodes there is a special disadvantage in using ordinary crypto algorithms requiring stored key. There is also no time and no computing power for asymmetric algorithms. We will give a solution to this problem by novel idea of exchanging One-Time Pads and encrypting data with one of the OTPs. The other OTP must be discarded for security reasons.

A. Basic idea of the crypto-algorithm

One-time pad (OTP), or Vernam's cipher, is a crypto algorithm where the key is as long as the plain text. The modern version of the algorithm simply takes a bitwise exclusive or of the key and the plain text. Denoting exclusive or by $\otimes$, the key K by a sequence of symbols $K=(K_i)_i$, and plaintext by $A=(A_i)_i$, the cryptotext in OTP is $X = A\otimes K = (A_i \otimes K_i)_i$. OTP has perfect security because even if all keys are tried, it is not possible to break OTP: for any plain text there always exists a key that encrypts the plain text to the observed crypto text. OTP has only one problem, as the keys are very long, there is no convenient way to transfer keys to the sides in communication.

In this article we describe a simple method of exchanging OTP keys in such a way that we obtain a method with provable computational security. We will briefly explain the method. If A and B are two users and A wants to send data A to B, let us first assume that A and B have exchanged their OTP keys K_A and K_B in such a way that an attacker can see $K_A \otimes K_B$. If A sends $K_A \otimes A$, the attacker can only get

$$(K_A \otimes K_B)\otimes(K_A \otimes A) = K_B \otimes A$$

and cannot open the plain text A. This method would have perfect security, but we cannot exchange the OTP keys quite as well as here. The proposed method shows to the attacker $(K_{A,i} \otimes K_{B,i})_i$ and $(K_{A,i} \otimes K_{B,i+k})_i$

for some fixed k. Using this relation the attacker can guess one symbol $K_{A,i}$ and calculate the symbol $K_{A,i+k}$. Thus, we have only computational complexity. However, if the attacker can only guess half of the bits in one symbol, he does not gain any information of the next symbol. Indeed, let $K_{A,i}$ be divided into two disjoint sets of bits C and D and C is guessed, D is unknown. We can try to guess a set E of bits from $K_{A,i+k}$. The remaining set of bits in $K_{A,i+k}$ is denoted by F. The set C has at most half of the bits in a symbol and we cannot obtain more bits to E than there are in C. It turns out that the bits of E can be assigned any values and there always exist D and F such that E has the assigned values. Thus, guessing E in this way is not possible. There is another way to proceed: when C is guessed we can open a part of plain text A_i. If the plain text has internal correlations between bits, then we can try to guess the bits D. The proposed solution is that A is cryptotext of a conventional symmetric cipher which hides statistical correlation. This cipher cannot be broken because the cryptotext of the cipher is not seen. The attacker only sees the cryptotext xored by the OTP. The attacker can go through all keys of the symmetric cipher and guess the plain text, but this can be made harder than directly guessing the OTP symbol. This leaves guessing at least half of the OTP symbol as the only effective approach. The actual method is a bit more complicated than this simple idea and will be described later.

The proposed method requires sending three times as much data as a conventional symmetric cipher: exchanging the OTPs is necessary. Computation time is not necessarily increased and xoring is a fast operation. While there today exist good ciphers for which there are no effective attacks, there are reasons for searching for algorithms based on OTP exchange. One reason is that currently there are very few good crypto-algorithms, second is that algorithms based on hard mathematical problems invite mathematicians to try to break them and we do not know how long the algorithms stand. The third reason is that symmetric ciphers require storing the keys, so if a node holding a key is lost, security can be broken.

B. Related work

Exchanging OTPs as a method of provable computational security has not been proposed earlier to the author's best knowledge. There is no direct related work but the idea has been taken from Simon Singh's popular science book [28], on page 282 Singh mentions an algorithm, which we have drawn in Figure 1. Singh attributes it to an unknown inventor. To the authors' knowledge it has not been discussed in scientific literature, which is odd since the algorithm is quite interesting: only B needs to know the one-time pad. Let us look at it and later fix the problem it has.

Let r be a prime and we will use integers modulo r, i.e., not bits, as symbols in the following crypto algorithms.

Let $t \geq 1$ be an integer. A one-time pad (OTP) is a crypto algorithm that encodes the plain text

$$D(1), D(2), D(3), \ldots \quad (1)$$

with a key

$$K(1), K(2), K(3), \ldots \quad (2)$$

by taking the bit-wise exclusive or $\oplus$, thus the crypto text is

$$K(1) \oplus D(1), K(2) \oplus D(2), K(3) \oplus D(3), \ldots \quad (3)$$

The task is to get the key to both sides. Let us first consider an algorithm where A sends data $D(t)$ to B over a two-way additive channel. A sends the data in plain text and B sends a one-time pad $K(t)$ to A. Let us assume that the end-to-end delay is T symbols, see Figure 7.

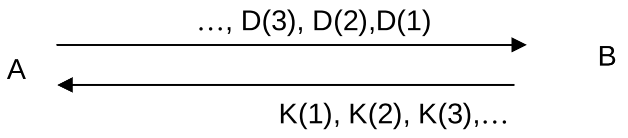

Figure 7. Interesting but insecure.

Let an eaves-dropper be located at a place that is j symbol transmission times from the place of A, or he can use directional antennas. He can read encrypted data

$$E(t) = D(1+t-j) + K(t-T+j)\beta_j. \quad (4)$$

The real number $\beta_j > 0$ gives the difference in signal strength of the signal from A and from B at the place j of the eaves-dropper. The fault of the protocol is that if the eaves-dropper listens in two places, j and i, and in two times t_1, t_2, he can subtract the signals and get the data. Let the times be chosen such that

$$t_1 + j = t_2 + i = a. \quad (5)$$

Then

$$\beta_i E(t_1) - \beta_j E(t_2) = (\beta_i - \beta_j) D(1+a). \quad (6)$$

Thus, the algorithm in Figure 1 has a serious flaw. However, to some extent the problem can be removed: in order to get a secure algorithm A must send both the data and the key. As a way to get the key to A let us first think of sending it in plain text in a channel consisting of separate up-link and down-link channels as in Figure 8.

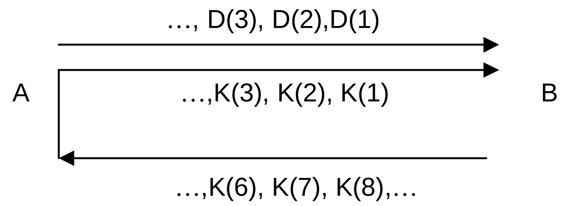

Figure 8. Better, but the key goes in plain text.

A echoes the OTP from B back to B. Now A learns the one-time pad of B. On the down-link we have the OTP, so it is secure. Let us secure the up-link by another one-time pad, this pad is created by A. For clarity, let us denote the OTP created by B by

$$K_B(1), K_B(2), K_B(3), \ldots \quad (7)$$

and the OTP created by A by

$$K_A(1), K_A(2), K_A(3), \ldots \quad (8)$$

There is no place to send any data, so let us forget sending the data and we shall only send the one-time pads as in Figure 9.

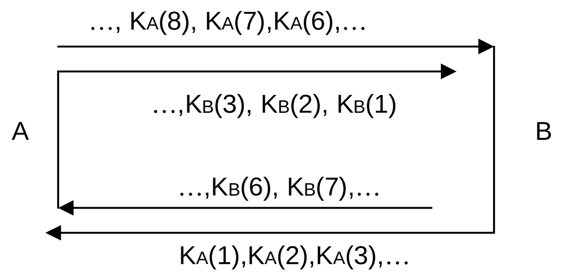

Figure 9. The basic idea of OTP exchange.

Let us denote by $g: Z_r \times Z_r \rightarrow Z_r$ a mapping used by A for encrypting $K_A(t)$ by $K_B(t-T)$. B applies the same function g for encrypting $K_B(t)$ by $K_A(t-T)$. The function g is known to both A and B and does not contain any secret parameters. We assume that B can obtain $K_A(t)$ from knowing

$$K_B(t-T) \text{ and } g(K_A(t), K_B(t-T)). \tag{9}$$

Likewise, we assume that A can obtain $K_B(t)$ from knowing

$$K_A(t-T) \text{ and } g(K_B(t), K_A(t-T)). \tag{10}$$

The algorithm in Figure 3 is the proposed OTP exchange. Next e will analyze it.

C. Analysis

Let us assume that the eaves-dropper follows data both from the up-link and the down-link. Let us assume that he is j symbol transmission times from the place of A. On the down-link he hears

$$E_{down}(t) = g(K_A(1+t-j), K_B(1+t-j-T)) \tag{11}$$

On the up-link he hears

$$E_{up}(t) = g(K_B(t-T+j), K_A(t+j-2T)). \tag{12}$$

He cannot gain anything from listening in two places as signal strengths attenuate in the same way for the two parameters of the function g, it suffices to look at different times he reads data. Here we also do not need to assume that the channel is additive. The channel adds noise and distortion, but these issues are not of concern to us now. We focus on the cryptographic algorithm and assume that the channel has not errors or distortion. The eaves-dropper can read the up-link and the down-link in different times and try to solve the keys recursively. Let

$$t_2 = t_1 + 1 - 2j \tag{13}$$

and let us write

$$x_1 = K_B(t_1 - T + j) = K_B(1 + t_2 - j - T), \tag{14}$$
$$y_1 = K_A(t_1 + j - 2T), \; y_2 = K_A(1 + t_2 - j).$$

Then

$$E_{up}(t_1) = g(x_1, y_1), \; E_{down}(t_2) = g(y_2, x_1). \tag{15}$$

By guessing y_1 the eaves-dropper can solve x_1 from the first (up) equation because A can also do it. Having obtained x_1 the eaves-dropper can solve y_2 from the second (down) equation since B can also solve the equation. This can be continued to the next key symbols

$$E_{up}(t_3) = g(x_2, y_2), \; E_{up}(t_4) = g(y_2, x_3). \tag{16}$$

Thus, if there are unique solutions x_k, y_k, the eaves-dropper can obtain the whole one-time pads.

Let us firstly notice that values x_k, y_k that agree with what the eaves-dropper is listening can be computed for every guess y_1. As the algorithm treats all x_k, y_k in the same way, the eaves-dropper might just as well start from guessing any x_k or y_k. The important thing is that he does not get any more information from this OTP exchange protocol. If he wants to know if his guess is correct, he must compute some values x_k, $k = 1,2,\ldots$ and check if he can open data encrypted by B. B encrypts data

$$D_B(1), D_B(2), D_B(3), \ldots \tag{17}$$

in the usual way as

$$K_B(1) \oplus D_B(1), K_B(2) \oplus D_B(2), K_B(3) \oplus D_B(3), \ldots$$

Perfect security of OTP does not any more hold. The first symbol may decode to anything depending on the guess of $K_B(1)$ but already at the second symbol the eaves-dropper may notice that data does not decode to some sensible data. The important question is if the eaves-dropper has any better way than guessing one key symbol or a large part of it. We can naturally select the symbol length in bits in such a way that guessing one symbol or a large part of it by brute force is sufficiently difficult.

If any faster way for the eaves-dropper exists depends largely on the function g. Let us select the function as

$$g(y, x) = x + y 2^{n/2} \bmod r \tag{18}$$

where $n = \lceil \log_2 r \rceil$ is the number of bits in the prime r. Let

$$x = x_a + x_b \text{ and } y = y_a + y_b \tag{19}$$

be representations where x and y have been split into two parts that do not have any bits in common in their binary representations. For instance, x_a can be the low bits and x_b give the high bits, but we allow any kind of a split of bits into x_a and x_b. The eaves-dropper can check if the bits in x_a are decoded into sensible data in the data sent by B. As B encrypts with OTP, there exists key bits x_a that decode the encrypted data into any selected data. The eaves-dropper must try to compute y by solving

$$e = g(y, x) . \tag{20}$$

After obtaining the key symbol y the eaves-dropper can decrypt data encoded by A. If also some bits of data encrypted by A are sensible the eaves-dropper may try to conclude that he has made the correct guess of the bits x_a. If he can obtain all bits of x in this way, he has a method of effective crypto-analysis, but if he must guess a large part of x before he can conclude that the guess is correct, he needs a good guess before (15)-(16) can be used. Let us show that the latter case is true. The following theorem says that more than half of bits in a symbol x must be guessed before it is possible to test if the guess is correct.

Theorem 1. *Let* $e \in Z_r$ *be a fixed number. Let* $x = x_a + x_b$ *and* $y = y_a + y_b$ *be representations where* x *and* y *have been split into two parts that do not have any bits in common in their binary representations. Let* x_a *and* y_a *have maximum* $\frac{n}{2}$ *valid bits (i.e., the length of* x_a *and* y_a *can be* n *bits but only at most half of the bits are determined by* x_a *and* y_a*, the rest are determined by* x_b *and* y_b*). For any* x_a *and* y_a *there almost always exists* x_b *and* y_b *such that* $e = g(y, x)$. *Almost always here means with probability on the range of* $1 - 2^{-n}$.

Proof: Let us consider the first order congruence

$$g(y, x) - x_a - y_a 2^{n/2} \equiv x_b + y_b 2^{n/2} (\mathrm{mod}\, r) . \tag{21}$$

As r is a prime, the number

$$z = x_b + y_b 2^{n/2} (\mathrm{mod}\, r) \tag{22}$$

gets 2^n (possibly not different) values when x_b and y_b range over the numbers in $Z_{n/2}$. Different values (x_b, y_b) and (x_b', y_b') yield the same z only if

$$x_b + y_b 2^{n/2} - x_b' + y_b' 2^{n/2} \equiv 0 \quad (\mathrm{mod}\, r) \tag{23}$$

The number $x_b + y_b 2^{n/2} - x_b' + y_b' 2^{n/2}$ has typically about $2n$ bits and r has n bits. The probability that the number is divisible by r is about 2^{-n}. We can say that almost always z values from two (x_b, y_b) and (x_b', y_b') are different since there are 2^n possibilities for (x_b, y_b) and the probability 2^{-n} means that in average one z may not be obtained. The probability 2^{-n} is very small compared to the probability $2^{-n/2}$ of guessing x_a by brute force. Thus,

$$g(y, x) - x_a - y_a 2^{n/2} \equiv z \quad (\mathrm{mod}\, r) \tag{24}$$

can be satisfied for almost any selection of x_a and y_a.

From Theorem l we notice that unless the eaves-dropper can guess more than half of the bits in a symbol he cannot conclude anything by checking decrypted data. Even if the bits decrypted by x_a and y_a make sense, it does not mean anything at all. Just as in OTP, any sensible data for these bits can be obtained from some selection of x_a and y_a. Only if the eaves-dropper can guess more than half of the bits of a symbol, then x_b and y_b have only a limited range and z in the proof of Theorem 1 cannot be found. Then the equation $e = g(y, x)$ is usually not satisfied for any selected x_a and such y_a, that the data sent by A makes sense. We conclude that the algorithm has in a certain sense provable computational complexity of $2^{n/2}$ trials.

A provable lower bound of $2^{n/2}$ trials by brute force would be much better than the situation with conventional stream ciphers. While there has been recent progress in stream cipher design, new crypto-analytic methods can still be developed. The reason why the OTP exchange protocol could be better than modern stream ciphers is partly due to the fact that an algorithm encrypting real data must remove the structure of the data. The OTP exchange protocol is encrypting random keys that do not have a structure. Partly the reason is that real data is encrypted with one-time pads that do not try to remove the structure from the data: they simply make every possible decoding of the data equally probable.

However, Theorem 1 does not quite say that there is a lower bound of $2^{n/2}$ trials by brute force. There are two possible ways of attack. In the first way the attacker may try to guess the correct x_a and check it by decrypting data encrypted by OTP. As every key symbol is randomly selected, the correct x_a is random and by Theorem 1 there is practically no chance that the attacker can gain anything unless x_a has more than half of the bits in a symbol. The only choice in this attack is to guess x_a by brute force.

The second way is that the attacker guesses data encrypted by OTP and computes the key symbols from the guessed data and the encrypted data. Then he checks if (15)-(16) is satisfied. This attack works well if plain text is encrypted. For instance, if any part of a text that has been encrypted by OTP is revealed and the encrypted data of the corresponding key exchange is obtained, it is a simple matter to open all text that has been encrypted with the OTP. Possible attacks include searching for published documents that have been encrypted by OTP. This is similar to the way the Japanese diplomat cipher was broken in the Second World War. The attack does not break the OTP system, but all other texts that are encrypted by the same OTP are broken. Another attack is searching for common long phrases. If the symbol length is 256 bits, the phrase must be longer than 128 bits, i.e., 16 bytes. Such are relatively long phrases, but not impossible to find in text. Then the attacker must search for the correct starting place, which is relatively easy. Such old style attacks work against OTP since OTP does not use diffusion and confusion: if plain text and encrypted text pairs are obtained, the key is immediately revealed. It is of no concern in OTP as keys are not reused but the dependences (15)-(16) of the OTP exchange make the property extremely dangerous.

The correction seems to be to encrypt plain text first with some good symmetric cipher and then use OTP. The symmetric cipher must be so good that guessing what crypto text some plain text produces is very difficult. The OTP hides all information of the crypto text produced by the symmetric cipher, thus the attacker does not have crypto text. The relations (15)-(16) do not mean that there are relations between the parts of the OTP. The OTP is a completely valid OTP where no symbols have any correlations with each other or with the text that they encrypt. Without any information of crypto text he does not have any information that has a relation to the key of the symmetric cipher, thus he cannot recover the key. We conclude that the attack of guessing the plain text is not possible for information theoretical reasons. The only remaining attack is to guess x_a by brute force. This is naturally much less than the original perfect security but it is quite good for a more practical system than plain OTP.

D. Possible modifications

Let us look briefly at another possibility. We may allow non-unique values for x_k, y_k. It does not make decoding data especially harder, the decoder must at each stage select from two values. As an example of such a possibility let us select

$$g(x,y) = x^i + xy + y^2 \bmod r \, , \tag{25}$$

where i >1 is some integer. The quadratic equation

$$e = y^2 \bmod r \tag{26}$$

has two solutions z and $r - z$ if e is a quadratic residue and no solutions if it is not. We can always complete (25) into a quadratic form as

$$(y + 2^{-1}x)^2 \equiv y^2 + xy - x^2 \bmod r \, , \tag{27}$$

thus

$$(y + 2^{-1}x)^2 \equiv g(x,y) - x^2 + x^i \bmod r \, . \tag{28}$$

The quadratic equation can be rather fast solved by the Shank-Tonelli Algorithm. (A rather fast free C-language implementation of the Shank-Tonelli Algorithm is in the *msieve* factorization software by J. Papadopoulos.)

The eaves-dropper must solve the values x_k, y_k recursively and he may have to keep trace of all paths for a small number of steps before he can decide if data can be decoded. This method may be suitable for an application where the symbol is small and the eaves-dropper cannot decide from a small umber of symbols if he has found the solution. We will not study this possibility further. There are several complications, such as quadratic non-residues, but it may be worth the mention the possibility of non-unique keys.

OTP exchange provides provably secure communications with some cost, i.e., bandwidth demands are increased. A conventional way to provide secure communication is e.g. by using the Diffie-Hellmann key exchange protocol for establishing a shared encryption key, and then encrypting data with a conventional symmetric algorithm. The gain of using OTP exchange is that it cannot be eavesdropped as it is provably computationally secure, and we can better estimate when and if it can be broken. Experiences from real wars, for instance with Enigma in the WWII, has shown that militaries should not trust conventional wisdom of how difficult encryption algorithms are to break.

D. Initializing OTP exchange

The protocol in Figure 3 must be started in some way so that key symbols are not revealed to an eaves-dropper at the start. A simple solution is that before A has obtained any part of the B's OTP, it encrypts data with A's credentials that must be known to B. The credentials must be long enough for encrypting T first symbols from A's OTP, a time stamp and a sequence number. The latter fields are needed to prevent replay of the start of communication. In a similar way, B also needs credentials known to A. Notice that (15)-(16) can be used backwards. If OTP encrypts plain text that can be guessed, user credentials are revealed. Therefore, plain text encrypted with OTP must be first encrypted with a conventional cipher.

E. Comments on error coding

OTP has good error propagation characteristics: one erroneous bit in crypto text only causes one erroneous bit in the plain text. Error coding data before encrypting is a possible solution because of small error propagation. OTP exchange has more worries from errors. If any error occurs in transmission from A to B, B gets a wrong key symbol $K_A(t)$ and consequently encrypts its own key symbols with wrong $K_A(t)$. Consequently, A obtains wrong $K_B(t)$ and uses it to encrypt key symbols. Neither side notices anything wrong while A and B obtain quite different versions of $K_A(t)$ and $K_B(t)$. As a result, data cannot be decrypted. Adding error codes to key symbols leads to dependences between key symbols and should be avoided. Therefore $E_{up}(t)$ and $E_{down}(t)$ must be extended by error coding. It is not necessarily best to use forward error coding since there is the return channel.

F. The issue of synchronization

The OTP exchange protocol needs the time T. Time synchronization in the protocol does not need any external protocol for synchronizing clocks. Both sides receive the OTP that they have sent and can synchronize to it with the ordinary HUNT mode, i.e., looking for the known bit sequence. This ability of the protocol can be used by other mechanisms. It directly gives the roundtrip delay from A to B. The round-trip delay can give location information e.g. if one of the sides is in a known place and the communication is through a communication satellite that does not add a time stamp.

G. Generation of key sequences

It might appear that one-time pads do not have any great advantage over ordinary stream ciphers since OTPs are usually generated by pseudo-random number generators. This is a wrong view. A typical stream cipher is essentially a pseudo random number generator but it has finite data as keys and possible other agreed parameters. Because this data is finite, the pseudo random sequence is finite. If an attacker collects enough data and keys are not changed often enough, he can take advantage of this periodicity. In the proposed method the OTP is not periodic. The OTPs of A and B are independent and created by A and B respectively. The other side learns the OTP through the OTP exchange. Even though the key symbols in the OTPs are probably created by pseudo random number generators, their parameters can be modified over time without the need of agreeing on them. Thus, the data is not finite as it must be in conventional stream ciphers.

V. CONCLUSIONS

This article suggests that viable methods exist, which improve the C^4I^2 of a warrior at all the levels. The examples covered are based on use cases of WPSN-solutions. They indicate that a warrior can obtain more critical information on the battlefield by using the presented WPSN solutions. This improves the general efficiency of a warrior at all levels. The platforms used today on the battlefield are not efficient. This is because they are based on a single sensor and they do not collect data in a way that would allow collaboration of multiple sensors. The proposed solution makes use of multi-sensor collaboration for improved location information and better situation awareness.

A warrior has to be functional and his gear needs to be planned according to the task. A key factor is the efficiency of a warrior, which can be gained via an improved Situational Awareness (SA), Blue Force Tracking (BFT) and Command and Control systems (C^4I^2). A warrior has to maintain his or her agility and stay active on the battlefield; all the gear cannot be attached.

Thus the warrior skeleton and its communication systems need to be carefully defined and built at each level due to the task requirements. Currently, the present solutions seen in active use are cumbersome and lack integration. The WPSN-solutions are unseen in these platforms. The maximum potential remains unreachable without sensor and data fusion. Militaries are moving towards smaller units while the demands keep increasing. At the same time troops are created for dismounted operations where a greater degree of flexibility and reliability of battle-proof and robust systems are needed.

The article discusses typical scenarios in which the WPSN can be invaluable. The effect of roadside bombs can be avoided once their precise location is known early and precisely enough. The increased knowledge at the basic warrior level in the form of location information gained from the SCPA on the battlefield improves the warrior's ability to carry out the task. Roadside bombs can be detected early enough and dismantled or destroyed before own or allied forces arrive at the spot. The Special Forces utilize the same output of the SCPA while conducting their ultimate tasks. Since the nodes of the WPSN do not communicate with each other, the system remains concealed, yet active. The WPSN node communicates with the UAV through encrypted messages. Thus the WPSN responds only after the UAV has submitted a polling request with a specific code. Utilizing swarms of UAVs and UGVs has to be emphasized. The routes of Unmanned Vehicles (UVs) can be fed into the systems early enough to gain the needed information from the designated areas.

The WPSN-solution features many advantages over those of the traditional WSNs. This is, polling can use sensor specific codes and thereby security issues become easier to tackle. Moreover, energy consumption of the nodes in the fixed network is more equal since multi-hop data transmission is removed. The fixed sensor nodes do not lose connectivity even if a large number of nodes are removed.

As demonstrated via the presented use cases, WPSN solutions together with SCPAs and UVs can be utilized to reach the maximum performance at all warrior levels. Planning the warrior's gear requires a deep understanding of the environment and the demands set on a warrior. The warrior's niche and the nature of his or her missions have to be thoroughly understood. The keys to success can be found in precise planning based on the needs of warrior systems and subsystems from bottom to top.

REFERENCES

[1] T. Saarelainen, J. Jormakka, C4I2-Tools for future battlefield warriors, *Proceedings of the Fifth Telecommunication Conference on Digital Telecommunications IDCT '10*, 16.-19. June 2010, Athens, pp. 224-233, doi 10.1109/ICDT.2010.15.

[2] J. Jormakka, A Cyptoprotocol for Exchanging One time Pads," in *User's view on battlespace systems*, National Defence University, Department of Military Technology, Series 3, no 9, ISBN 978-951-25-1993-4, Edita, Helsinki 2009, pp. 137-147.

[3] G. Jakobson, J. Buford and L. Lewis, A Framework of Cognitive Situation Modelling and Recognition, Proceedings of the IEEE Symposium on Military Communications Conference, 2006. MILCOM 2006. IEEE Press, Oct. 2006, pp. 1 – 7, doi:10.1109/MILCOM.2006.302076.

[4] D. Hague, H.T. Kung, and B. Suter, Field Experimentation of Cots-based UAV Networking, Proceedings of the IEEE Symposium on Military Communications Conference, 2006. MILCOM 2006. IEEE Press, Oct. 2006, pp. 1 – 7, doi:10.1109/MILCOM.2006.302070.

[5] A. Blair, T. Brown, and M. Johnson, Tactical Mobile Mesh Network System Design, Proceedings of the IEEE Symposium on Military Communications Conference, 2007. MILCOM 2007. IEEE Press, Oct. 2007, pp. 1 – 7, doi:10.1109/MILCOM.2007.4454980.

[6] C-M. Cheng, P-H. Hsiao, H. T. Kung, and D. Vlah, Transmit Antenna Selection Based on Link-layer Channel Probing, Proceedings on the IEEE Symposium on World of Wireless, Mobile and Multimedia Networks, 2007. WoWMoM 2007. IEEE Press, Jun. 2007, pp. 1 – 6, doi:10.1109/WOWMOM.2007.4351703.

[7] O. Kosut, A. Turovsky, J. Sun, M. Ezovski, L. Tong, and G. Whipps, Integrated Mobile and Static Sensing for Target Tracking, Proceedings of the IEEE Symposium on Military Communications Conference, 2007. MILCOM 2007. IEEE Press, Oct. 2007, pp. 1 – 7, doi:10.1109/MILCOM.2007.4454968.

[8] M. Matsuoka, S.M. Rock, and M. G. Bualat, Autonomous Deployment of a Self-Calibrating Pseudolite Array for Mars Rover Navigation, Proceedings of the IEEE Symposium on Position Location and Navigation Symposium, 2004. (PLANS 2004) IEEE Press, Apr. 2004, pp. 733 – 739, INSPEC Accession Number: 7972394.

[9] K. R. Chevli, P.Y. Kim, A.A. Kagel, D.W. Moy, R.S.Pattay, R.A. Nichols, and A.D. Goldfinger, Blue Force Tracking Network Modeling and Simulation, Proceedings of the IEEE Symposium on Military Communications Conference, 2006. MILCOM 2006. IEEE press, Oct. 2006, pp. 1 – 7, doi:10.1109/MILCOM.2006.302050.

[10] D. Herold, L. Griffiths, and T.Y. Fung, Lightweight, High-Bandwidth Conformal Antenna System for Ballistic Helmets, Proceedings of the IEEE Symposium on Military Communications Conference, 2007. MILCOM 2007. IEEE Press, Oct. 2007, pp. 1 – 6, doi:10.1109/ MILCOM. 2007.4455055.

[11] P-J, Park, S-M, Choi, D-H, Lee, and B-S, Lee, Performance of UAV (Unmanned Aerial Vehicle) Communication System Adapting WiBro with Array Antenna, Proceedings of the IEEE Symposium on Advanced Communication Technology, 2009. ICACT 2009. IEEE Press, Feb. 2009, vol 2, pp. 1233 – 1237, INSPEC Accession Number: 10571377.

[12] A, Ruangwiset, Path Generation for Ground Target Tracking of Airplane-typed UAV, Proceedings of the IEEE Symposium on Robotics and Biomimetics, 2008. ROBIO 2008. IEEE Press, Feb. 2009, pp. 1354 – 1358, doi:10.1109/ROBIO.2009.4913197.

[13] I. Rubin, A. Behzad, Z. Runhe, L. Huiyu, and E. Caballero, TBONE: A Mobile-backbone Protocol for Ad-hoc Wireless Networks, Proceedings of the IEEE Symposium on Aerospace, 2002. IEEE Press, vol 6, pp. 6-2727 - 6-2740 vol.6, doi:10.1109/AERO.2002.1036113.

[14] H. Zheng, J. Shi, and L. Cao, Group-Mobility-Aware Spectrum Management for Future Digital Battlefields**,** Proceedings of the IEEE Symposium on Military Communications Conference, 2006. MILCOM 2006. IEEE Press, Oct. 2006, pp. 1 – 7, doi:10.1109/MILCOM.2006.302052.

[15] S. S. Chakraborty and S. Wager, A New Approach for Medium-Access Control for Data Traffic and Its Adaptation to the GSM General Packet Radio Services, *IEEE Transactions on Vehicular Technology*, Volume: 481, Jan. 1999, pp. 240 – 248.

[16] D. Googman, R.A. Valenzuela, K.T. Gayliard, and B. Ramamurthi, Packet Reservation Multiple Access for Local Wireless Communications, *IEEE Transactions on Communications*, vol. 37, issue 8, pp. 885 – 890, Aug. 1989, doi: 10.1109/26.31190.

[17] J. Jormakka, Performance Analysis of ISMA/P, *Transactions of Vehicular Technology*, vol.52, no. 1, January 2003, pp. 254 – 259.

[18] J. Habeta, R. Dutar and J, Wiegert, Performance Evaluation of HiperLAN/2 Multihop Ad Hoc Networks, *European Wireless 2002*, Feb. 2002.

[19] D. Al-Abri and J. McNair, Improving Localization Accuracy in Wireless Sensor Networks Using Location Verification Feedback, Proceedings of the IEEE Symposium on Military Communications Conference, 2007. MILCOM 2007. IEEE Press, Oct. 2007, pp. 1 – 7, doi:10.1109/ MILCOM.2007.4454844.

[20] O. Villavicencio, K. Lu, H. Zhu, and S. Kota, Performance of IEEE 802.11n in Multi-channel Multi-radio Wireless ad Hoc Network, MILCOM 2007, Proceedings of the IEEE Symposium on Military Communications Conference, 2007. MILCOM 2007. IEEE Press, Oct. 2007, pp. 1 – 6, doi:10.1109/MILCOM.2007.4454755.

[21] B. Bennett, P. Hemmings, and B. A. Hamilton, Operational Considerations of Deploying Wimax Technology as a Last-mile Tactical Communication System, Proceedings of the IEEE Symposium on Military Communications Conference, 2006. MILCOM 2006. IEEE Press, Oct. 2006, pp. 1 – 7, doi:10.1109/MILCOM.2006.302298.

[22] W. Wang, Z. Liu, and R. Xie, INS/GPS/Pseudolite Integrated Navigation for Land Vehicle in Urban Canyon Environments, Proceedings of the IEEE Symposium on Cybernetics and Intelligent Systems, 2004 IEEE Press, vol 2, pp. 1183 – 1186, doi:10.1109/ICCIS.2004.1460758.

[23] S. R. Ali, R.S. Wexler, and R. Hoffmann, Soldier Network Extension (SNE) On-The-Move Satellite Communications (SATCOM) for Army Tactical Battalion-level Network Healing and Thickening, Proceedings of the IEEE Symposium on Military Communications Conference, 2007. MILCOM 2007. IEEE Press, Oct. 2007, pp. 1 – 5, doi:10.1109/MILCOM.2007.4455035.

[24] A. Behzad, I. Rubin, and A. Mojibi-Yazdi, Distributed Power Controlled Medium Access Control for Ad-hoc Wireless Networks, Proceedings of the IEEE Symposium on Computer Communications, 2003. CCW 2003. Proceedings. 2003 IEEE Press, Oct. 2003, doi:10.1109/CCW. 2003.1240789.

[25] C. Fragouli, D. Katabi, A. Markopoulou, M. Rahul, and R. Hariharan, Wireless Network Coding: Opportunities & Challenges, Proceedings of the IEEE Sympoisum on Military Communications Conference, 2007. MILCOM 2007. IEEE Press, Oct. 2007, pp. 1 – 8, doi:10.1109/MILCOM 2007. 4454988.

[26] J. Jormakka, A TDMA-based MAC protocol for Ad Hoc Networks, *IUP Journal of Telecommunications*, in press, to appear Dec 2010.

[27] J. Jormakka and S. Ahvenainen, On Military Applications of IP-based Ad Hoc Networks, in *Technical Aspects of Network Centric Warfare*, National Defence College, Dept. of Techn., Series 1, No 17, Helsinki 2004, pp. 115 – 131.

[28] S. Singh, *The Code Book*, Fourth Estate, 2000, accessed on 22.12.2010 at 23:15.

[29] E. Haque, F. Wei, Y. Fukunaga, T. Gouda, X. Lu, and K. Mori, Autonomous Background Coordination Technology for Timely Sensor Connection in Wireless Sensor Networks, Proceedings of the IEEE International Symposium on Autonomous Decentralized Systems, 2011, pp. 10 – 16, doi 10.1109/ISADS.2011.8.

Managing Quality of Experience on a Commercial Mobile TV Platform

Vlado Menkovski, Georgios Exarchakos, Antonio Liotta

Electrical Engineering Department
Eindhoven University of Technology
Eindhoven, The Netherlands
{v.menkovski, g.exarchakos, a.liotta}@tue.nl

Antonio Cuadra-Sánchez

Indra
Parque Tecnologico de Boecillo
47151 Valladolid, Spain
acuadra@indra.es

***Abstract* – The user perceived quality or Quality of Experience (QoE) is of significant importance to multimedia service providers because of its relevance for efficient management of provided services. However, due to its subjective nature, QoE is difficult to estimate. Subjective methods are costly and impractical, while objective methods do not correlate precisely with the subjective perception. In addition to the challenges in estimating QoE, further challenges are presented in determining the means of managing the QoE in today's complex and varied multimedia distribution systems. As a result of the high number of components and parameters that affect the perceived quality, from content creation to delivery and presentation, the QoE aware management in these highly versatile environments becomes increasingly difficult. We present a method that uses limited initial subjective tests to develop prediction models for QoE as perceived by the viewers. This minimizes the complexities associated with subjective methods while maintaining the accuracy. Further we present a method of calculating the QoE remedies for managing the QoE per stream, based on the QoE prediction models.**

Keywords - Quality of Experience, QoE, Machine Learning, Subjective Testing, Monitoring, QoE management

I. INTRODUCTION

Multimedia content broadcasting is commonly implemented in a highly diverse and varying environment. In addition to the diversity, the lack of standards for quality assessment in this domain makes estimation of the perceived service quality particularly difficult. The challenges with the estimation of the quality of experience (QoE) make it hard to know whether the delivered service meets the customers' expectations and brings user satisfaction.

The variability of the system is particularly high on the end-user terminal devices. The screen sizes, mode of use and computing capabilities of these devices highly affect the end user QoE. However, due to the technical difficulties and the lack of understanding of the QoE the common approach with service providers is to to use an 'average' setup with regards to the multimedia parameters; that is a trade-off between the power of the average device and the quality of the parameters. In addition to this, the service providers need to take into account dimensioning of their own resources in a way that will deliver a functioning service while still being commercially viable.

The down side to the 'average' (or one-size-fits-all) approach is two faceted: i) the service provider remains in the dark regarding the value of the service to its customers and ii) its resources are not optimally used. These two are usually in competition; any management technique should target the balance of that trade-off. This, however, would imply understanding of the customers' QoE.

The providers are not completely oblivious to the factors that affect the QoE, on the contrary they have access to a plethora of parameters that affect the QoE. Some of which are the QoS parameters, such as network conditions and performance, also the content encoding parameters and characteristics. Nevertheless, a gap exists between all these factors and the QoE itself. This gap is the major motivation of this work. The overall goal reached by this work is to develop a methodology that will bridge this gap and deliver accurate information about the perceived user experience looking at the application QoS (AQoS) and network QoS (NQoS) parameters.

Part of this work has been published in the MMEDIA 2010 conference [1], which focuses on building QoE models for a commercial IPTV platform. In this paper we have extended this work to include calculating the remedies for the QoE per stream that enable QoE management decisions.

In the following sections, we present a methodology and an implementation of a QoE assessment platform developed for a service provider. The designed platform estimates QoE of mobile TV services based on existing QoS monitoring data using QoE prediction models. The prediction models are built using Machine Learning (ML) techniques from subjective data acquired by a limited-size initial subjective test. The work here provides evidence for the efficiency of this methodology and elaborates on the QoE software platform. The QoE value produced by that platform enriches the system's monitoring tools [2] and will be further used for managing the service and dimensioning the resources.

To provide for QoE enabled management a remedies algorithm [3] is described and implemented, which calculates the parameters and amounts that need to be changed to reach the desired QoE in particular streams. The remedies algorithm is in a way extension of the QoE assessment method because it derives the remedies based on the QoE prediction models.

The paper continues with Section II discussing related work that deals with estimation of perceived quality of multimedia. In Section III, we present an overall description of the mobile TV probe-based monitoring solution that measures the QoS of the system and the QoE prediction platform that delivers QoE values. Section IV discusses the method used for the QoE prediction platform, expanding to the subjective tests and machine learning algorithms. The results from the subjective tests and the ML prediction models are analysed in Section V. Section VI presents the remedies algorithm used to improve the QoE per multimedia stream. Section VII presents results from the remedies used in the particular IPTV platform. Finally, Section VIII sums up with the conclusions and future work.

II. Related Work

Perception of quality for streaming video has been a lively field of research. There are many efforts mostly looking into objective methodologies. Some have also executed subjective tests either to estimate quality or to compare the accuracy of different objective approaches.

Due to a wide diversification of models, it is difficult to select the best model for video quality. In [4] the International Telecommunication Union (ITU) presents a classification of the different objective quality assessment models. Its authors have classified the models into media layer, parametric, bit-stream and hybrid models. This classification is based on the model's focus. The media layer models focus on the media signal and they use knowledge of the Human Visual System (HVS) to predict the subjective quality of video. The parametric ones look at the protocol information and statistics through non intrusive probes to predict the quality. The bit-stream models derive the quality via analysing content characteristics collected from the coded bit-stream information. In [5], a survey of different video quality methods is presented. The paper concludes that there are many different methods and algorithms for video quality estimation; thus, there is need for a standardized way to compare them. There are different international standardization bodies working in this area and they have delivered progress, as given in [4]. However, there is still lack of a comprehensive method for comparing the video quality assessment models with a subjective database that can bring a common reference point. The Peak Signal to Noise Ratio (PSNR) and Mean Squared Error (MSE) are purely computational metrics for comparison of models used by many publications in this research field. However, PSNR and MSE deliver unsatisfactory results as they lack of understanding of the HVS [6]. Therefore, as a common practice, a wide variety of published work in video quality uses subjective tests as a relevant comparison method, much of which follows the standard for subjective studies as given in [7].

As we have seen from the ITU standardization of the models, some models focus on the content, some on encoding and other on the transport of the multimedia content.

The authors of [8] give an analysis of the dependency of the perceived quality on the values of the video frame rate and encoding quantization. They have concluded that traditional encoding schemes for frame-rate and quantization step are not optimal from the perspective of perceived quality. Keeping the frame rate at a lower value allows for higher budget of bits per picture for coding and produces higher quality overall.

The authors of [9] have developed a utility function for each of the following network QoS parameters: delay, jitter, packet loss rate and bandwidth of the video stream. They used generic utility functions for the parameters and derived the constants from results of executed subjective tests. They claim that managing the multimedia streams with the utility function approach is more effective than reservation protocols in today's converged network environments. Their work is still limited because of the fact that they have not considered the interdependency between the NQoS parameters but considered them independently.

On the perception of loss of data during transport, the work done in [10] presents a methodology that focuses on the stream, to determine the effects of loss on the video. First they estimate the artefacts in the video due to the loss of data. Then, they try to study the visibility of those artefacts and their correlation with the perceived quality. The paper discusses a comprehensive analysis of the error handling schemes of H.264 video codec in order to predict the video artefacts. Then it continues to analyse the artefacts from the point of view of magnitude (spatial inconsistency and special extent), special priority (region of interest) and temporal duration. The results show that this approach can sometimes follow the trend of Mean Opinion Score (MOS) of the subjective study better than the PSNR values but the method is still not accurate sometimes even less than PSNR

The methods so far are all looking at particular factors that affect the QoE but none of them takes a holistic approach and look at all of the factors. The concept of quality does not have a single dimension but more than one [11], such as qualitative, emotional, and communicative. QoE also encompasses the expectations that the viewers have. So, for accurate assessment, subjective feedback is necessary.

The work done in [12] builds on subjective tests and delivers prediction models using discriminant analysis. Furthermore, in [13] and [14], improvements to the accuracy of the prediction models are given. The work here shows the multiple benefits of optimizing the QoE instead of targeting specific QoS metrics.

Understanding the significance of QoE in determining the value of the service and establishing the optimal balance between resources and quality we propose this method that builds up on previous work done in the area. More particularly we are focused on QoE models induced from subjective tests using ML techniques as an optimal balance between the complexities of subjective studies and accuracy of ML subjective models.

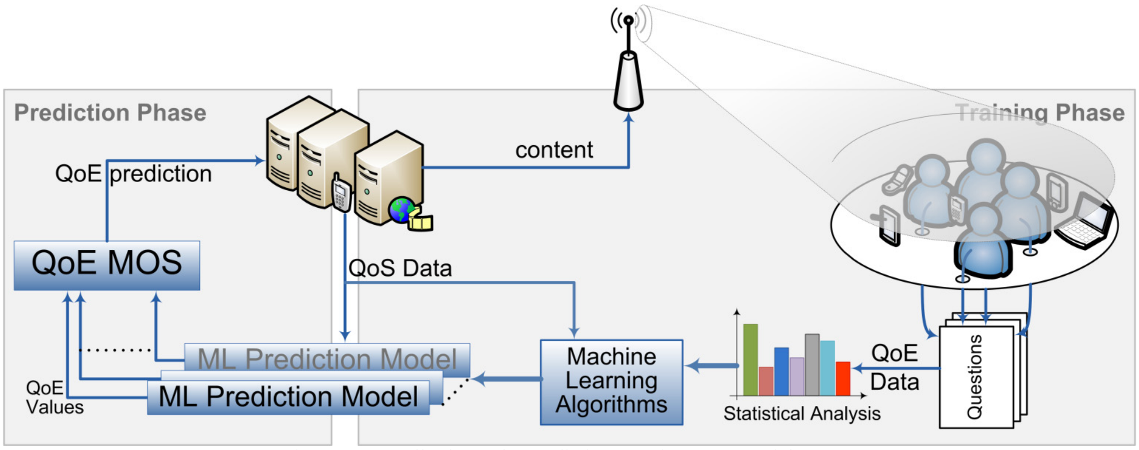

Figure 1: Overall schema for predicting QoE in a commercial system

III. Bridging the QoS to QoE Gap

Mobile TV is a service for mobile devices where customers can experience video-streaming content. They can select a set of available multicast channels or video contents with fixed quality settings. Some services might offer different streams for the same channel with different quality settings or adapted to specific devices. Offering multilayer video is not common due to the computational complexity. Many providers find it more efficient to maintain more than one stream with different qualities than a single multilayer stream due to compatibility issues with end user devices. In order to monitor the service quality, a probe-based network monitoring system is in place gathering information from the MobileTV content distribution platform. The probes collect information for each stream such as type of device, name of channel, stream, duration of the connection; these are captured in an Internet Protocol Detailed Record (IPDR) format [15]. In addition to this information, using RTCP in conjunction with RTSP helps the collection of QoS statistical values including: number of packets, packet loss ratio for audio, packet loss ratio for video, average delay, maximum delay, and jitter. In a nutshell, there is a deployed system fetching the AQoS and NQoS data from the system in real-time [2]. The AQoS involves application level QoS parameters as Video and Audio Bitrate and Video Frame Rate. The NQoS represents the network QoS parameters some of which are Packet loss, Jitter, and Delay.

The deployed system gives a good overview of the network conditions providing useful information for dimensioning the resources and managing the parameters of the content encoding. However, it cannot give any information as to how the service is perceived by the end-user. The metric QoE is a conglomerate of all the conditions that affect the perception of quality including the AQoS and NQoS as well as external factors such as the terminal type, the content itself and the expectations of the viewers. As QoE is directly linked with the value that the customers perceive it is useful for a service provider to be aware of the QoE instead of only looking at QoS.

The methodology developed here presents a mechanism for mapping QoS to QoE by executing limited initial subjective studies. It relies on Machine Learning techniques to build prediction models that accurately estimate the value of QoE based on the AQoS and NQoS parameters. The method is executed in two phases (Figure 1). The training phase uses input data from IPDR records of QoS parameters and QoE values as captured by surveys on customers' opinions. Its output is a set of prediction models for each question of the survey. In the prediction phase, these models fed with IPDR records and combined with a weighting scheme can predict the final overall QoE of a service. The weighting scheme is implemented using a SVM Regression Model [16].

During the subjective studies, the system records the IPDR values for the specific content provision used in the studies. Then, each queried customer fills in a questionnaire. All these values from the surveys are aligned with the IPDR records by selecting the ones that correspond to each content provision only. After this one-to-one mapping of QoS and QoE values, the Machine Learning algorithms build models that know how to predict the latter from the former; there is one model per question. As long as there is no radical change to the environment (e.g. new device or user group) these models are expected to perform accurate predictions of a subset of QoE values.

The QoE prediction models are plugged in a QoE prediction platform for online use. A statistical analysis on the results of the subjective study about the QoE of a service shows how the service, as a whole, is perceived from the perspective of its quality. Putting more emphasis on specific content attributes, via a different analysis, we can draw conclusions e.g. on a per content type basis. Correlating the subjective test data with the data from the network probes (AQoS and NQoS) we can create a set of training data for the ML algorithms of the prediction models. These ML algorithms, in a supervised learning mode, can develop classifiers (prediction models), which will be further used to predict the QoE on unobserved cases in the production environment.

In the prediction phase, these models get as input the IPDR values and produce the QoE ones for each question. The statistical analysis of the subjective study results also gives a set of weights for each question. These weights are used to produce the Mean Opinion Score (overall QoE) out of the predicted values via appropriately weighting the output of each model.

IV. Subjective Studies

Dealing with subjective metrics, such as QoE, requires subjective studies mostly because it is hard to identify the impact of objective metrics, such as QoS, on the perceived quality. In addition, the QoE evaluation will also demonstrate the level of expectations that the customers have.

Subjective studies by themselves pose a number of challenges as they rely on user sampling and their results need to reflect the real preferences of the whole user group. The more representative this sample and controlled the testing conditions are the more accurate the subjective studies are. Meeting all these constraints adds to the expenses and complexities associated with executing subjective studies. We have designed a targeted subjective study with typical users of the service to establish their preferences for quality and measure their QoE for the varied services.

A. *The questionnaire*

We carried out these subjective studies with the use of a questionnaire. Instead of asking a simple question where people rate the perceived quality from 1 to 5, we devised a questionnaire of ten different questions each of them bringing more subtle differences of the perceived quality of the viewers (Figure 2).

Question 1:	What is the type of content viewed?
Question 2:	Amount of delay before the video started?
Question 3:	Frozen images or interruptions?
Question 4:	Interruptions in the audio
Question 5:	Pixelation artifacts in the video
Question 6:	Noise or distortions in the audio
Question 7:	Audio and video synchronization
Question 8:	Quality of colours
Question 9:	Sharpness of video
Question 10:	Overall quality

Figure 2: Questions of the subjective study given to customers

The first question characterizes the content in seven different categories: News, Music Videos, Entertainment, Documentary, Movie or TV Series, Cartoon and Sports. This question is important because we want to observe i) the different expectations of quality for the different types of content ii) the different user expectations for different type of content [17] and iii) how the dynamics in the video affect the compression ratio also associated to the type.

Questions from two to nine are all of subjective nature with the given four levels of perceived problems from ‘none’ to ‘excessive’. The last question is the overall perception of the QoE. Instead of only asking the last question we have now more information from the previous questions and can map different network and application QoS conditions to answers given the questions Q2 to Q9. While Q1 answers is mapped to the name of the channel in the IPDR records.

B. *Statistical Analysis*

The results from the subjective study are captured in Figure 3 and Figure 4 and give a clear view as to how users perceive the quality. While the former gives the number of customers per content type the latter presents their opinion per question.

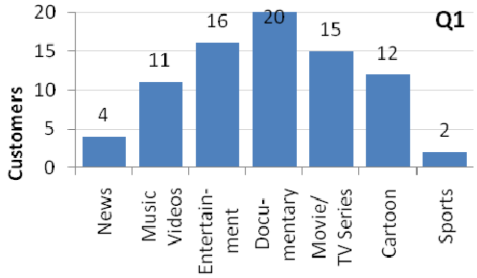

Figure 3: Distribution of queried users (customers) over the different types of viewed content.

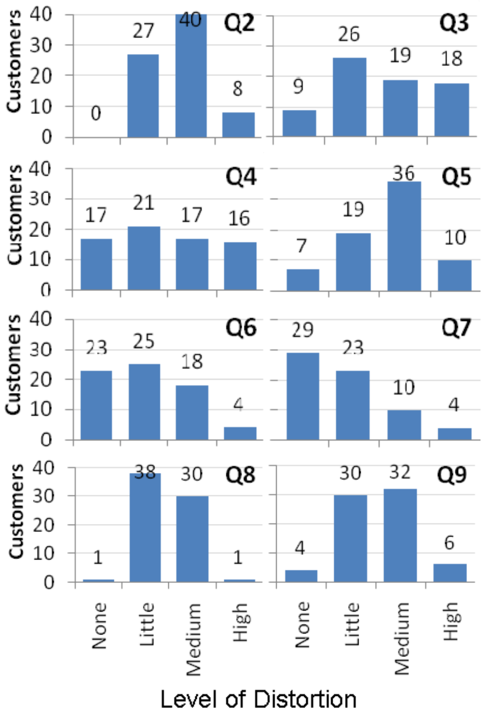

Figure 4: Distribution of queried users based on their answers to questions 2-9.

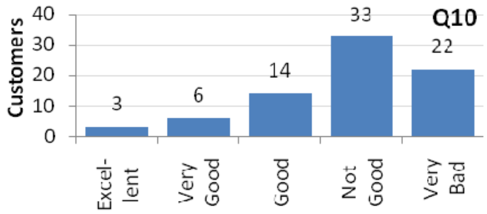

Figure 5: Overall quality as perceived by the users and captured through questionnaires.

Customers' opinion on the overall quality appears in Figure 5. This figure presents the distribution of the queried users over the different levels of perceived quality with high concentration in mediocre or lower quality levels.

A clearer view on the overall user perception of the content quality appears in Figure 6, which presents 8 pie charts each presenting the percentages of users with the same opinion per content type.

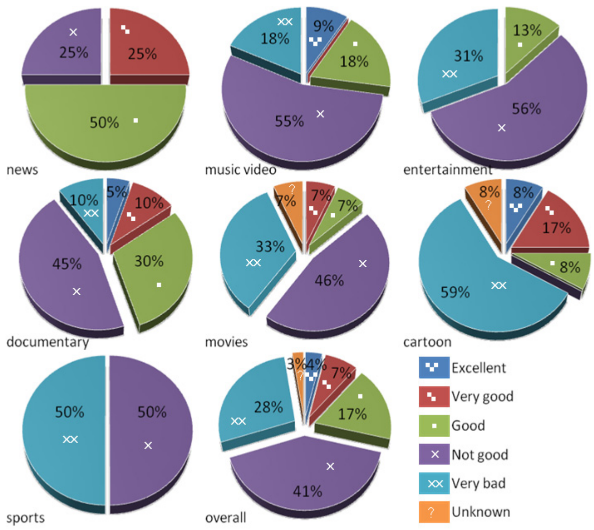

Figure 6: Customers' opinion as distributed per content type

V. Prediction Models

The first step into building prediction models is to prepare the training data. This data is the input to the prediction models and consists of two sets: the objective data (NQoS and AQoS) from the network monitoring system and the subjective ones from the questionnaires. The role of the devised prediction models is to map the objective to subjective values. In other words, based on the viewing conditions we want to predict the perceived quality.

Initially, we built a prediction model for each question (one through nine) to estimate the QoE value from the subjective questionnaires. In a final step, we built a final prediction model that correlates the answers of questions one through nine in a final answer for question ten. In addition, we provide the confidence of the classification based on errors during the training phase.

Related work that explores ML techniques with subjective data results shows that decision tree (DT) algorithms [13] achieve particularly good results with subjective datasets. In this work, we used decision trees induction algorithm C4.5 implementation (J48) part of the Weka ML platform [18] in combination with an ensemble classifier.

We have developed nine prediction models, one per each question. For the final one we used SVM regression [16] to build a regression model that combines all predictions from the previous questions with different weights to produce the final QoE value (see Figure 7and Figure 8). The weights are application and system specific and administrators are supposed to set them as parameters of their network.

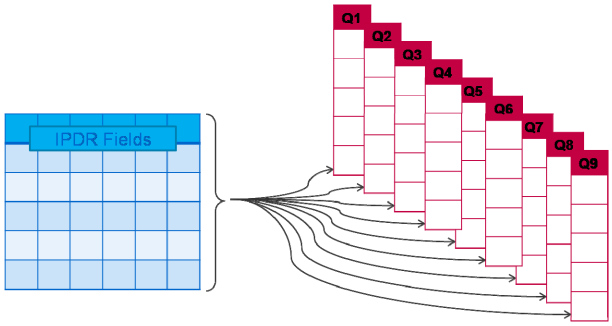

Figure 7: Correlation of QoS metrics from IPDR fields with customers' opinion from the subjective studies

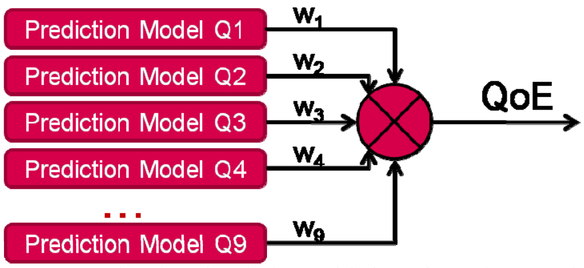

Figure 8: Combination of prediction models for each question to produce final QoE predicted value

The SVM Regression algorithm develops a regression function trained on the mapping of Q1 to Q9 with the QoE value. The results from the prediction models are given in Figure 9. The accuracy of the prediction models is calculated using 10-fold cross-validation [19].

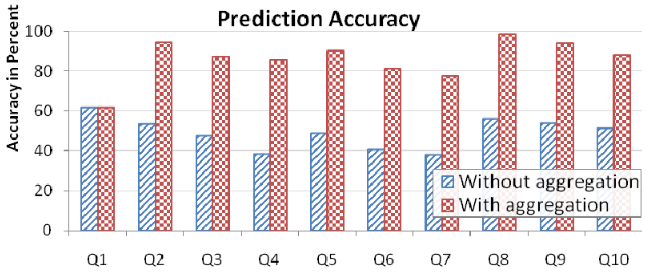

Figure 9: Prediction accuracy with and without output aggregation

The DT classifier uses categorical labels or outputs, which make them easy for humans to read and understand, for example “Excellent” or “Not Good”. But from a ML point of view these labels are not ordered, they are considered the same as we would consider the labels “Red” and “Blue”. So when we are calculating the prediction accuracy, only the exact predictions are taken into account. We do not know how many near misses we have. Most of these near misses would provide for good management tips. For instance, a prediction of “Very Bad” and “Not Good” might lead to the same management decision since both cases are not satisfactory. If we take this into account and also tolerate a small error rate for the output, such as errors with a distance of one or less from the actual value, the accuracy of the models significantly increases. For graphical representation we can look at the confusion matrix in Figure 10; the main diagonal represents the accurate cases (actual value row and predicted value column). If we add the values in the two adjacent diagonals, we can get the new accuracy with tolerance of ±1 and thus get a higher effective accuracy of our classifier (Figure 9).

a	b	c	d	<-- classified
0	0	0	0	a = None
0	0	25	2	b = Little
0	0	40	0	c = Medium
0	2	6	0	d = High

Figure 10: Confusion Matrix for high accuracy with tolerance ±1

For the final value of the QoE, as mentioned before, we use the weights from the regression model. The QoE is calculated as a sum of the Q_1-Q_9 answers each multiplied by its weight (w_1-w_9). As Q_1 is categorical, w_1 has different value for each type of content. We can look at these weights as a metric of the influence/importance of each question on the final answer (Figure 11). Question 3 has the most significant influence on QoE, based on the weights from the figure followed by 7 and 9. This information can be useful in improving the service as well as improving the subjective studies for feature iterations.

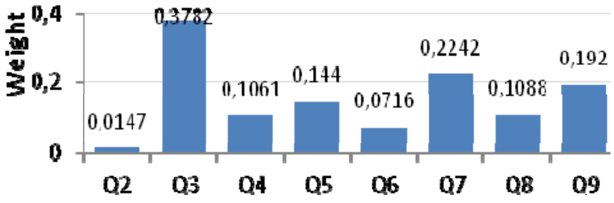

Figure 11: Question weights on the final overall QoE

The models built from the training data are now part of a QoE prediction platform built around them. This platform can load QoS data and feed it into the prediction models, thus, producing the QoE as a final result.

VI. Improving QoE

Estimating the QoE is a crucial step in QoE-aware network management. However for a complete implementation of the management loop we need to be able to maintain a target QoE value for each stream. Maintaining a target QoE involves determining the desired conditions that need to be achieved or the needed changes to the parameters the will achieve the target QoE. To accomplish this task we use an algorithm [3] that based on the QoE prediction model estimates the minimum needed changes in the measured stream parameters to improve the QoE.

This technique is enabled by the DT prediction models we use for estimating the QoE. One of the strengths of DT compared to other ML prediction models is their intelligibility. A DT in a way represents a set of rules stacked in a hierarchical way. Simple decision trees commonly define just a few rules that are deduced from the data and used for classification, but when the number of rules grows the size of the DT also grows, and with that, it loses its intelligibility. This algorithm represents a QoE prediction DT model in the geometric space, defined by the dataset parameters. It considers each of the dataset parameters as a dimension in a hyperspace. Each of the datapoints from the dataset can be represented as a point in this hyperspace. The DT is represented by hyper regions formed by the leaves of the DT (Figure 112). Each node of the DT represents a binary split (for binary trees) that maps into a hyperplane in data hyperspace. At the bottom, the leaves of the tree, carve out hyper regions. These hyper regions, according to the appropriate leaf are associated with a class label membership. Every datapoint in the dataset falls on a leaf from the DT, therefore each corresponding point in the hyperspace falls into one of the hyper regions, and as such is classified with the corresponding class label. In our particular case the hyper regions are associated class labels that are the QoE estimates.

The algorithm (Figure 13) that represents the DT in the hyperspace as follows:

This algorithm implements the DT representation in the dataset’s hyperspace by generating a set of hyper regions that represent the tree leaves. Each hyper region contains a set of split rules that define the hyper-surface, which carves out the hyper region. The split rules are either representing an inequality of the type *Parameter1 >= Value1* or of the type *Parameter1 = Value1* depending on whether *Parameter1* is continual or categorical. If the leaf is on the left side of a continual *Parameter1* split then the split inequality will be ‘more than or equal to’, if it is on the right side the split inequality will be ‘less than’.

Having a list of *HyperRegion*-s we can easily determine where each datapoint from the dataset belongs to, by testing the datapoint on the split rules of each hyper region. The hyper region is associated with the same class label as the leaf it represents, so all datapoints that belong to that region are classified as such.

In order to improve the QoE estimation of a particular stream, we need to look at the datapoint that was generated by the monitoring system for that stream. If the datapoint is

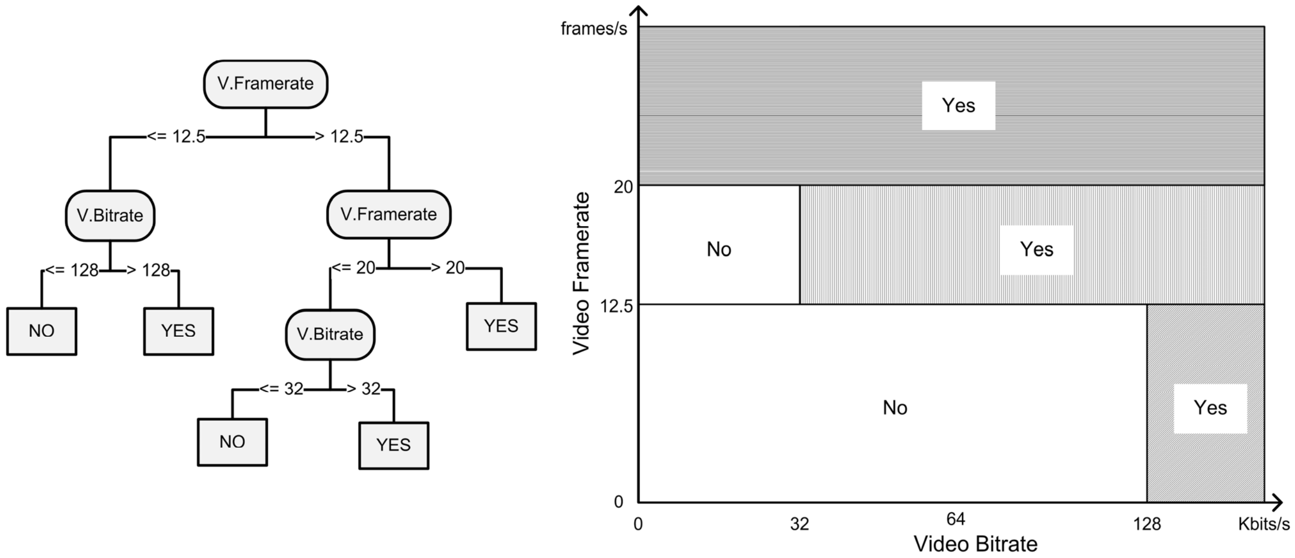

Figure 112. Simple decision tree in 2D space

classified with a QoE value that is not satisfactory, we look at the distance to a set of hyper regions $\overline{\Phi}$ that are associated with a satisfactory QoE value. The distance to each of the desired regions is the difference in parameter values that are needed in order to move the datapoint to the desired regions.

> Start from the root node and call a recursive method `FindLeaves`
>
> `FindLeaves:`
>
> 1) If the node has children
>   a) Call `FindLeaves` on each child
>   b) Add the SplitRule on each of the Hyper Regions ($\overline{\Phi}$) that are returned
>   i) If the leaf split is categorical add a Split Rule: Attribute = 'value'
>   ii) If the leaf split is continual add on the leaves from the left side SplitRule: Attribute < value, and on the leaves from the right side Attribute > value
>   c) Return the set of Hyper Regions ($\overline{\Phi}$)
> 2) Else, you are in a leaf
>   a) Create an Hyper Region object
>   i) Assign the class of the leaf to the Φ
>   ii) Return Φ

Figure 13. DT to Hyper Region algorithm

The output of the algorithm is a set of distance vectors, which define the parameters that need to be changed and their change values.

To illustrate the matter better we can take an example from the laptop dataset from [13]. The prediction model built from this dataset is given in Figure 112. If we look at the datapoint given in Table 1 we can see that this datapoint will be classified by the model as QoE = No ('Not Acceptable'). Since the V. Framerate is less than 12.5 and the V.Bitrate is less than 32 the datapoint reaches a leaf with 'Not Acceptable' class associated with it.

Now, what is the best way to improve the QoE of this stream?

First of all there are parameters that characterize the type of the content such as the Video SI and the Video TI and cannot be changed. In this dataset structure we are looking into increasing the V.Bitrate and V.Framerate. If we increase the V.Bitrate for this particular datapoint by one step to 64kbits/s we can see that the datapoint goes now down the DT to one of the bottom leaves, but it is still classified as QoE Acceptable = No. On another hand if we increase the V.Framerate to 15f/s we can see that the datapoint is classified as QoE Acceptable = Yes without adding more bandwidth.

TABLE I. EXAMPLE DATAPOINT

Video SI	Video TI	V. Bitrate	V. Framerate
67	70	32	10

We can deduce a rule from the model that a video with these characteristics needs to have higher V.Framerate for it to be perceived with high quality. However, this rule is not easily evident from only looking at the model. We can also imagine a system with large number of attributes that we can change where tuning this attributes the right way becomes an increasing problem. Further down this line of reasoning, if we want to make a system-wise improvement that will increase the QoE of most streams we cannot easily derive which parameters are best to be increased and by how much.

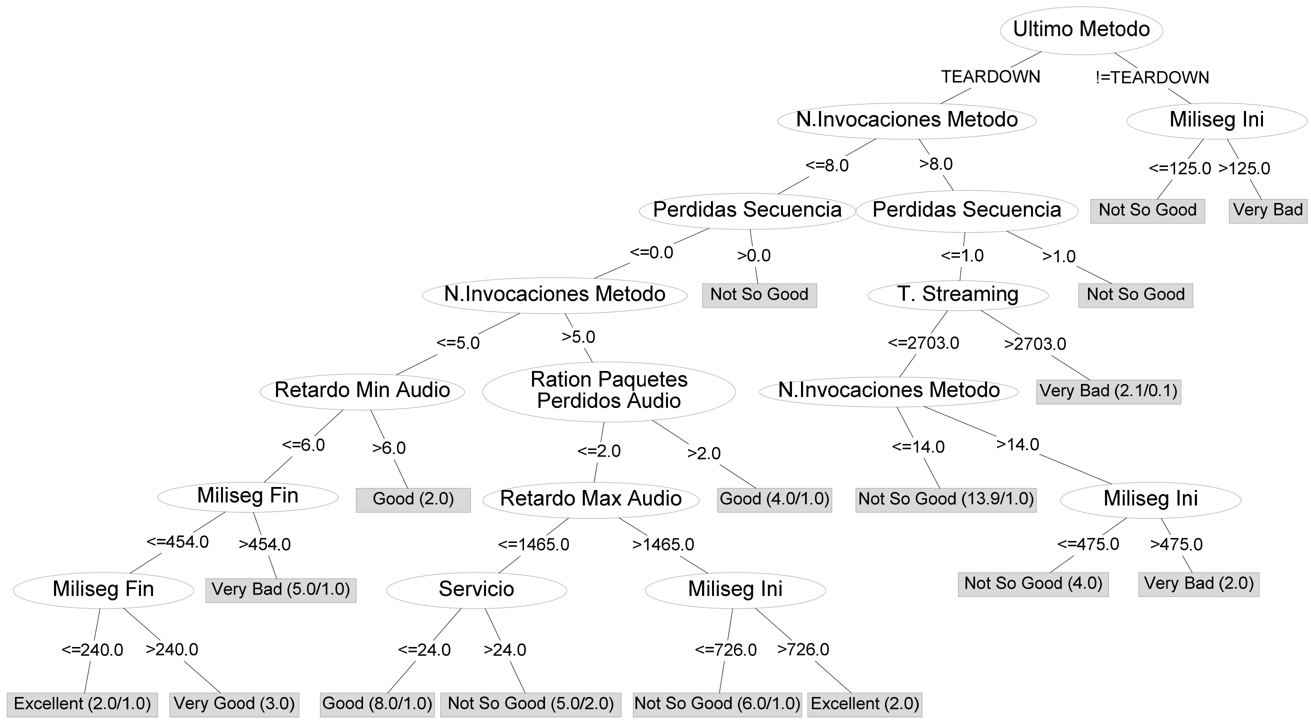

Figure 14. Simple decision tree in 2D space

In the case of the example datapoint the algorithm returns the two possible paths:

- Increasing the Framerate to above 12.5f/s
- Increasing the V. Bitrate to above 32kbits/s and the Video TI to above 87

Since we know that increasing the Video TI is not an option, because this is defining the type of content we can see, then the only option is to increase the frame rate. In a general case, there can be many different paths to a hyper region with the desired class.

To automate the process we can assign cost functions to the change of the attribute values and automatically calculate the cheapest way to reach the desired QoE. In this manner attributes that are not changeable, such as the Video TI, can have infinite value of the cost function.

Given a datapoint and a target label the algorithm produces a set of change vectors. Each of the change vectors applied to the datapoint moves the datapoint to a hyper-region classified with the target label. In other words, each change vector is one possible fix for the datapoint.

$$\overline{\Phi} = FindLeaves(DT, QoE) \quad (1)$$

$$\overline{\Delta\varphi_i} = Distance(\Phi_i, \overline{d}) \quad (2)$$

$$\Delta\varphi_{optimum} = \min_i \left(Cost(\Delta\varphi_i \right) \quad (3)$$

In (1), $\overline{\Phi}$ is a set of regions with a targeted QoE value. The distance function in (2) calculates the vector of distances for each attribute to the target region in $\overline{\Delta\varphi}$. The optimal distance vector is the one with minimal cost (3) for the given input datapoint $\overline{d}$. The *Cost* function in (3) is dependent on the application. Each system has explicit and implicit costs associated with changes of specific parameters.

VII. Application of the Remedies in mobile IPTV

The remedies algorithm has been implemented by extending the Weka [20] platform, so that algorithms like J48 [21] that induce decision trees can be used to calculate the hyper regions. Furthermore, we can now measure the distance of any datapoint classified by the DT to the desired hyper-region.

The decision tree built from the data of the subjective study is given in Fig. 14. The boxed nodes represent the leaves and map to the hyper-regions as we have seen in Fig. 2. There are 17 hyper-regions, out of which, only two are with excellent QoE value. The algorithm generates the remedy output specific for each particular broadcasting system. A target QoE values needs to be defined, and a specific cost for changing a parameter needs to be given as well. If the target value if excellent QoE the algorithm will calculate the minimum cost of changing specific parameters so that the datapoint falls in one of the two Excellent hyper-regions. Of course some parameters are not changeable, such as the type of video. For these an infinite cost is assigned so that the algorithm does not propose these absurd remedies.

A more elaborate QoE improvement is also possible where not all datapoints are targeted for the excellent regions, but the management is executed based on the utility of improving a QoE of a stream in regards to the costs. Then multiple levels of remedies can be suggested by the algorithm with varying costs, and the provider can chose to apply mechanisms to implement the remedies based on their utility to the customers.

VIII. Conclusions and Future works

We have presented a method for estimating the QoE which circumvents some pitfalls of exhaustive subjective testing while still resulting in accurate estimation on QoE. We have discussed the importance of QoE as a metric to define the value of a multimedia service provided to the customers. We also presented an algorithm that can generate suggested remedies per multimedia stream for streams with a lower than desired QoE. To implement this method we relied on ML techniques that were successful in building prediction models that accurately predict the QoE from a small training dataset of the subjective tests. We also presented a QoE platform that makes use of the prediction models to bring QoE estimations in real-time based on data from network probes. This platform is currently part of a mobile TV system where it estimates the QoE of the streaming multimedia content and proposes remedies for different streams. The necessity for this kind of platform arises from the need for multimedia service providers to estimate the experienced quality by their customers, to diagnose the reasons for lowers than desired QoE and for the remedies that they can implement.

In conclusion this methodology presents a pragmatic solution for estimating and maintaining QoE with a wide range of applicability. Its success and usability depends on the quality of the prediction models, while as architecture it is flexible enough to be used in many different environments. To make use of its full potential a more elaborate subjective study in better controlled conditions will yield in more precise prediction models and better effectiveness overall.

This platform can be extended with Online Learning techniques that will provide continuous improvements in the prediction models and further reduce the load of the initial subjective tests. The online learning approach will also provide the ability of the system to adapt the models to the ever changing conditions of the production environment, such as introduction of new content, new terminal devices etc. In addition to Online Learning techniques, some Active Learning approaches will be of benefit to improve the gain of asking the customer for feedback intelligently as opposed to randomly selecting for feedback.

Acknowledgments

The work included in this article has been supported by Telefonica R&D and Indra (Spain). The authors thank María del Mar Cutanda, head of division at Indra, for providing guidance and feedback.

References

[1] V. Menkovski, G. Exarchakos, A. Liotta, and A. Sánchez, "Measuring Quality of Experience on a Commercial Mobile TV Platform," in *Advances in Multimedia (MMEDIA), 2010 Second International Conferences on*, pp. 33-38, 2010.

[2] A. Cuadra-Sanchez and C. Casas-Caballero, "End-to-End Quality of Service Monitoring in Convergent IPTV Platforms," in *Proceedings of the 2009 Third International Conference on Next Generation Mobile Applications, Services and Technologies*, pp. 303–308, 2009.

[3] V. Menkovski, G. Exarchakos, A. Liotta, and A. Sanchez, "Estimations and Remedies for Quality of Experience in Multimedia Streaming," in *Advances in Human-Oriented and Personalized Mechanisms, Technologies and Services (CENTRIC), 2010 Third International Conference on*, pp. 11-15, 2010.

[4] A. Takahashi, D. Hands, and V. Barriac, "Standardization activities in the ITU for a QoE assessment of IPTV," *Communications Magazine, IEEE*, vol. 46, no. 2, pp. 78-84, 2008.

[5] S. Winkler, "Video Quality Measurement Standards - Current Status and Trends," in *Proceedings of ICICS 2009*, 2009.

[6] S. Winkler, *Video Quality and Beyond.* Symmetricom, 2007.

[7] R. I. ITU-T, "910," *Subjective video quality assessment methods for multimedia applications*, 1999.

[8] Quan Huynh-Thu and M. Ghanbari, "Temporal Aspect of Perceived Quality in Mobile Video Broadcasting," *Broadcasting, IEEE Transactions on*, vol. 54, no. 3, pp. 641-651, 2008.

[9] Mu Mu, A. Mauthe, and F. Garcia, "A Utility-Based QoS Model for Emerging Multimedia Applications," in *Next Generation Mobile Applications, Services and Technologies, 2008. NGMAST '08. The Second International Conference on*, pp. 521-528, 2008.

[10] M. Mu, R. Gostner, A. Mauthe, G. Tyson, and F. Garcia, "Visibility of Individual Packet Loss on H. 264 Encoded Video Stream–A User Study on the Impact of Packet Loss on Perceived Video Quality," *Annual Multimedia Computing and Networking, San Jose, USA*, 2009.

[11] M. T. Virtanen, N. Gleiss, and M. Goldstein, "On the use of evaluative category scales in telecommunications," in *Proceedings of Human Factors in Telecommunications*, vol. 95, 1995.

[12] F. Agboma and A. Liotta, "QoE-aware QoS management," in *Proceedings of the 6th International Conference on Advances in Mobile Computing and Multimedia*, pp. 111-116, 2008.

[13] V. Menkovski, A. Oredope, A. Liotta, and A. Cuadra Sánchez, "Predicting Quality of Experience in Multimedia Streaming," in *Proceedings of the 7th International Conference on Advances in Mobile Computing and Multimedia*, pp. 52-59, 2009.

[14] V. Menkovski, A. Oredope, A. Liotta, and A. Cuadra Sánchez, "Optimized online learning for QoE prediction," in *Proceedings of the 21st Benelux Conferece on Artificial Intelligence*, 2009.

[15] "TM Forum - TM Forum IPDR Program." [Online]. Available: http://www.tmforum.org/ipdr. [Accessed: 23-Mar-2010].

[16] A. J. Smola and B. Sch\ölkopf, "A tutorial on support vector regression," *Statistics and Computing*, vol. 14, no. 3, pp. 199–222, 2004.

[17] F. Agboma and A. Liotta, "Addressing user expectations in mobile content delivery," *Mobile Information Systems*, vol. 3, no. 3, pp. 153-164, Jan. 2007.

[18] I. H. Witten and E. Frank, *Data mining*. Morgan Kaufmann, 2005.

[19] R. Kohavi, "A Study of Cross-Validation and Bootstrap for Accuracy Estimation and Model Selection," in *IJCAI*, pp. 1137–1145, 1995.

[20] "Weka 3 - Data Mining with Open Source Machine Learning Software in Java." [Online]. Available: http://www.cs.waikato.ac.nz/ml/weka/. [Accessed: 02-Jun-2009].

[21] S. L. Salzberg, "C4.5: Programs for Machine Learning by J. Ross Quinlan. Morgan Kaufmann Publishers, Inc., 1993," *Machine Learning*, vol. 16, no. 3, pp. 235-240, 1994.

SIP Server Implementation and Performance on a Bare PC

A. Alexander, R. Yasinovskyy, A. L. Wijesinha, and R. Karne
Department of Computer & Information Sciences
Towson University
Towson, MD 21252
USA

***Abstract*—We describe the implementation and performance of a bare PC SIP server that runs without the support of an operating system (OS) or kernel. A bare PC SIP server provides immunity against OS vulnerabilities and yields performance gains due to the elimination of OS overhead. We discuss server design focusing on its novel architectural features and illustrate key implementation aspects by examining relevant task and method invocations for SIP request processing. We also study bare PC SIP server performance by comparing its latency and throughput against two conventional OS-based SIP servers running on equivalent hardware: OpenSER on Linux and Brekeke on Windows. Furthermore, we measure internal bare PC SIP server performance by providing internal timings for the most significant operations associated with registration and proxy services. Additionally, we study performance under increasing server load by obtaining the execution time spent in the bare PC SIP handler method and the total processing time including network protocol processing overhead when processing SIP requests and responses. The results show that the bare PC server performs better than the OS-based servers in most cases and that its internal processing times are small as would be expected due to the elimination of OS overhead. The design and implementation details of the bare PC SIP server presented here give insight into understanding SIP server performance on a bare machine.**

***Keywords*-SIP server, implementation, performance, internal timings, bare machine computing, operating systems.**

I. Introduction

Bare PC or bare machine systems run on the hardware without the need for an operating system (OS) or kernel. In [1], the performance of a bare PC SIP server running on an ordinary desktop was studied. It was shown that in most cases the server performs better than two conventional (OS-based) SIP servers running on identical non-server machines. This paper is an extended version of [1] that gives details underlying the implementation of the bare PC SIP server and new internal timings for key server operations. Material relevant to server design and implementation is taken from [2]. However, it is supplemented with details concerning tasking and method invocations that were omitted in [2]. Additionally, the new internal timings under increasing server load given here are more accurate than the approximate timings initially reported in [1]. The implementation specifics and new timing results provide further insight into bare PC SIP server operation and performance.

Previous studies on bare PC email and Web servers show that they significantly outperform their counterparts running on conventional OS-based systems [3] [4]. Bare PC applications and servers also have inherent immunity to attacks that target vulnerabilities of a given OS. Many studies have dealt with the design and performance of network and security protocols in a bare PC. For example, the performance of SRTP for bare PC VoIP is evaluated in [5], and peer-to-peer communication among bare PC VoIP clients is discussed in [6]. However, there have been no studies of SIP (Session Initiation Protocol) on a bare PC. SIP is the most frequently used protocol today for initiating VoIP calls and for media session support with a variety of other applications including video streaming, instant messaging, gaming, and IPTV. For example, most SIP servers can provide voice, video, instant messaging, and presence services.

In general, SIP servers locate and register clients, provide proxy services for forwarding SIP messages, or redirect SIP requests to other servers. An optimized SIP server can thus help improve the overall performance of audio or video applications by supporting audio or multimedia sessions (although it is typically not directly involved in the actual transmission of audio or video). The throughput and latency of the SIP server when responding to requests from SIP user agent clients and other SIP servers are often used as measures in evaluating its performance.

We use a popular open source SIP workload generator to evaluate the performance of the bare PC SIP server by measuring its throughput and latency for registration, proxying, and redirection, with and without authentication, for increasing workloads. We compare performance of the bare PC server with popular OS-based (Linux and Windows) servers for the same workloads when running on compatible hardware. Our results show that the bare PC SIP server has higher or equal throughput to the Linux server and higher throughput than the Windows server, except in case of redirection, when its throughput is less than that of the Linux server. The latency performance of the bare PC server is also shown in general to be better than or equal to that of Linux server and better than that of the Windows server, except for invite with authentication and invite-not-found without authentication. We also provide internal timings measured on the bare PC SIP server.

The performance results of the server are better understood by examining its design and implementation details. To this end, we describe the bare PC SIP server components within the self-supporting application object (AO) that runs directly on the PC hardware. In particular, we examine SIP packet processing for requests and their responses. In addition, tasking is discussed and examples of method invocations are given to highlight protocol intertwining and other novel implementation characteristics in the bare PC SIP server.

Our contributions in this paper include: 1) results characterizing the performance of a bare PC SIP server running on an ordinary desktop; 2) internal timings for SIP-related operations on a bare PC SIP server; 3) comparisons of the throughput and latency for a bare PC SIP server, Linux and Windows servers running on identical machines; and 4) design and implementation details of the bare PC SIP server.

The rest of this paper is organized as follows. In Section II, we summarize related work. In Section III, we describe the design of the bare PC SIP server and relevant optimizations. In Section IV, we provide implementation details of the server. In Section V, we give the experimental setup and discuss the results of the performance study. In Section V, we present the conclusion.

II. Related Work

There are many commercial and open source servers implementing SIP and its companion protocol SDP. While a SIP server usually runs over UDP and in some cases over TCP, the use of SCTP as a transport protocol for SIP has also been studied [7]. An early study on SIP server performance [8] found that the overhead on a Java SIP server due to security mechanisms such as authentication and TLS was negligible. However, the study in [9], which measured throughput and latency in a dedicated gigabit Ethernet for stateless and stateful proxies over UDP and TCP, showed that authentication, TCP, or the operation/server configuration can significantly change SIP server performance. Their experiments were conducted using a 3.06 GHz server class machine, and only the performance of a single SIP server (OpenSER on Linux) was evaluated. In [10], SIP server performance for several stateful SIP proxies over UDP was evaluated. The authors concluded that the overhead due to string processing operations and memory management could consume significant processing time and that performance varied considerably depending on the proxy. Recent work on SIP servers has dealt with performance under overload conditions [11], scalability issues [12] [13], load balancing [14], and the impact of transport protocols on performance [15].

The main difference between previous performance studies and the performance studies in this paper is that we study the performance of a bare PC SIP server and compare it with the performance of two OS-based SIP servers using ordinary desktop (non-server) machines. Also, in addition to evaluating performance for the usual register, invite, and redirect operations, we also evaluate SIP server performance for the register update, register logout, and invite-not-found operations likely to be encountered in practice. Internal timings for key operations measured on the bare PC SIP server are also reported. We only consider SIP over UDP with stateless proxying, which is the most common configuration when setting up VoIP calls.

Previous work describing the design and implementation of SIP servers that require an OS. For example, in [16], a SIP server is implemented on top of an existing SIP stack, and in [17], SIP servers are implemented on the Solaris 8 OS. These studies focus primarily on the high-level SIP implementation on a conventional system, whereas the design and implementation of the bare PC SIP server is based on the underlying bare computing paradigm and architecture.

III. Design

This section describes key design details of the bare PC SIP server. We begin by briefly outlining bare application characteristics in general and then give an overview of the bare PC server.

A. *Bare PC Applications*

Any bare PC or bare machine computing application, including the bare PC SIP server, is encapsulated in an application object (AO) [18]. Since there is no OS, minimal code for the application to directly run on the PC hardware is contained in the AO. This means that the AO contains the code for the bootable self-executing application itself, any required network interface drivers, handlers for protocols used by the application, and memory and task management mechanisms to facilitate concurrency and scheduling [19]. Real memory is used since there is no hard disk, and application code is intertwined with protocol code to eliminate redundancy and improve efficiency as in the case of bare PC Web and email servers [4] [20].

B. *SIP Server Overview*

The bare PC SIP server AO implements a lean version of SIP that provides essential functionality only. Additional features such as those needed to support load balancing and media stream security are not included. Although a bare PC SIP server that can operate over TCP or UDP has been implemented, this paper only considers SIP over UDP since the majority of SIP servers employed in practice use UDP.

The SIP server AO consists of several objects. In addition to the Ethernet, IP, UDP, and SIP objects, the DHCP and trivial FTP (TFTP) objects provide lean implementations of these protocols and are used as needed (for example, at server start-up) as described in the next section. An MD5 object is used to provide support for user authentication via standard SIP authentication (i.e., HTTP-Authentication) when authentication is enabled for registration and proxying.

An incoming UDP packet containing a SIP message is placed in the Ethernet buffer, where the bare PC SIP application can directly access it i.e., real mode is used and there is no notion of user space or kernel space since there is no OS. The Ethernet handler processes the packet, determines that the packet is for IP, and the IP handler in turn processes the packet and invokes the UDP handler, which verifies the UDP checksum (if this feature is enabled) and the port number. In case of the SIP server, the port number is 5060 and the packet is finally processed by the SIP handler. To send a response, the SIP, the UDP, IP and Ethernet handlers add the respective headers before the packet is transmitted by the network interface hardware. Data copying is minimized in the bare PC SIP server since there is a single copy of the message and headers are added and removed as in a conventional system by manipulating pointers.

In addition to the usual Main and Receive (Rcv) CPU tasks, which are used in all bare PC systems, the bare PC SIP server has a SIP task to handle each SIP request. This task design strategy simplifies task management, minimizes context (task) switching, and increases efficiency. The Main task runs upon start-up and whenever the Rcv task or a SIP task terminates. It activates the Rcv task whenever a packet arrives in the Ethernet buffer. It also activates a SIP task for processing after it is determined that the packet is for SIP. This SIP task runs until SIP processing is complete and the response is sent. Once the SIP task terminates, the Main task runs again. Thus, when the SIP Server AO's Rcv task is activated by the Main task upon the arrival of a SIP request in the Ethernet buffer, a single thread of execution handles the request all the way from the Ethernet level through the IP and UDP handlers. Then the SIP task runs as described above. This simple task design approach reduces the processing overhead.

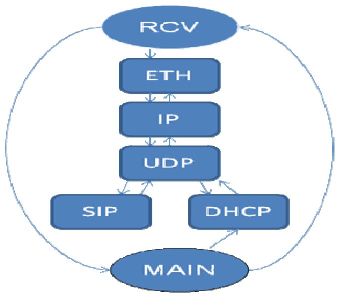

Figure 1. SIP server protocol/task relationships.

As described in [2] and shown in Figure 1, it is possible to use only two CPU tasks in the SIP server AO: a receive (Rcv) task that processes a received packet all the way from its arrival in the Ethernet buffer until a response is sent, and a Main task that runs whenever a Rcv task completes (and also when the system is booted or the system is idle). For example, for a register message, the Rcv task itself could manage the lookup and update operations and send the response to the client. However, it is more convenient and efficient (as in the present version of the SIP server) to use a separate SIP task for each request as discussed above. In case of the invite message for example, a new SIP task is activated to handle the request. Since there may be a delay in contacting the peer (callee), the SIP task could be suspended and resumed when the response arrives. In general, since a typical workload involves a mix of requests for different services, bare PC SIP server performance is improved by the concurrent handling of requests. This strategy of allowing a CPU task to run to completion unless it has to wait for an event such as a response enables the CPU to be kept busy doing useful work. Simple task management and the disabling of timer interrupts on bare PC servers also reduce context switching (compared to conventional OS-based servers) and improve performance.

IV. Implementation

The section examines the key aspects of bare PC SIP server implementation. Details of processing steps and method invocations are included to illustrate novel characteristics of the implementation. The current implementation supports registrar, redirector, and proxy modes with or without authentication. Since the bare PC SIP server implementation is lean, only specific content from an incoming SIP packet is parsed. Although the server code consists of a single monolithic executable, the implementation itself is modular allowing for updates and implementation of new features. The bare PC SIP server AO contains about 2000 lines of code.

A. Boot Sequence

The bare PC SIP server is booted by directly loading its AO from a USB flash drive. The bare PC SIP Server boot sequence begins when the Main task invokes the DHCP handler to send a DHCP request for an IP address (unless the server has been preconfigured to use a specific IP address). When a response arrives, the Rcv task is activated to process it. Next, a file containing username and password combinations of authorized users is transferred from another host on the network using an adaptation of trivial FTP. As discussed later, multiple data structures to facilitate server operations such as user lookup, username and password lookup, and state lookup are then created in memory. The last step in the boot process is to display the user interface for administering the server.

B. User Database Lookup

After the usernames and passwords from the file are read into memory, the bare PC SIP server runs the sipservergetdb() function to store them in the USER_DATABASE structure:

```
Struct USER_DATABASE {
char username [20];
int username_size;
int username_hash;
char Password [20];
int Password_size;
};
```

The data structures HASH_TABLE and SORTED_TABLE shown below are also used.

```
Struct HASH_TABLE {
int hash_hit;
int hash_reg_db_loc[HASH_REG_DB_SIZE];
int hash_hit_size
};
Struct SORTED_TABLE {
int hash;
int hash_link;
};
```

In essence, the hash of each username serves as an index into HASH_TABLE, which is used together with SORTED_TABLE to facilitate looking up the user in the USER_DATABASE structure, and to retrieve information when making or receiving calls, or registering a user. The HASH_TABLE structure links back to the SORTED_TABLE and USER_DATABASE structures. The details are as follows. First, the hash values are stored in a SORTED_TABLE array (which allows for efficient searching for a given hash value), and each position in the sorted array is linked to the specific HASH_TABLE array corresponding to that hash value. In turn, each position in the HASH_TABLE array corresponds to a user that hashed to that value and contains a link back to the USER_DATABASE entry for that user. The HASH_TABLE structure links the index in the USER_DATABASE structure to the hash value of the SORTED_TABLE as shown in Figure 2.

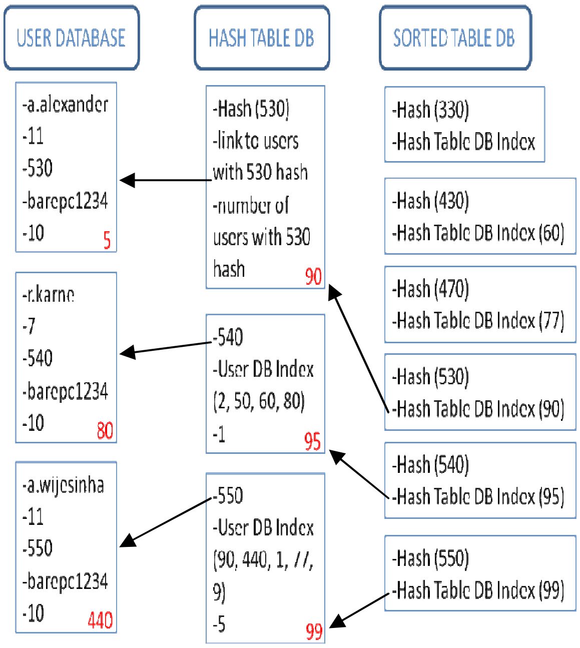

Figure 2. Database and hash table relationships.

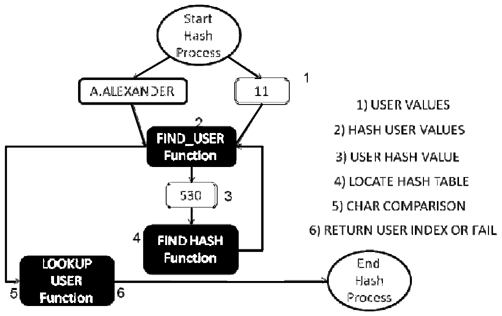

Figure 3. User lookup process.

The user lookup process in Figure 3 is done by using two functions: the find_hash_hit() function, which is based on a particular hash value, and the find_user() function that is based on the username and size. In performance tests, this search operation was found to be a likely bottleneck because of the username comparisons triggered by collisions on a single hash value. The find_user() function takes a username and username size as input. It then hashes the username and passes the value to the find_hash_hit() function, which finds the corresponding hash table containing all the users with that same hash value. The hash table is passed back to the find_user() function, which calls the lookup_user() function. The latter goes through each user in that specific hash table and first compares the sizes of the usernames; if they match, it looks for a second match on the full username. If the user is found, the location containing the user's information in the database, including the IP Address and port, is returned. To improve performance, future bare PC SIP server implementations will use adaptations of data structures and search techniques used by popular Linux SIP servers.

C. SIP Message Processing

The siphandler() function manages the processing of received SIP messages. This function, which is called directly by the udp_handler() function after verifying the SIP port in the UDP header, is the key element in the bare PC SIP server. The siphandler() function calls the parse_headers() function. The latter goes through the SIP packet and parses out specific identifiers to identify the type of message (for example, REGISTER, INVITE, ACK, BYE, 180 Ringing, 200 OK and 100 Trying). Within the parse_headers() function are specific functions built to handle the following SIP tags: Header, Via, From, To, Expires, Authorization, Proxy Authorization, CallId, CSeq, Contact, and Content Length. In keeping with the lean SIP implementation, only the indicated tags are parsed to expedite the processing of SIP packets (other tags are bypassed). Once the tags are parsed and the relevant data from the packet is stored, control returns to the siphandler() function. Further processing is determined according to the request_type returned. Only the following SIP messages are processed by the Bare PC SIP Server: Register Invite, 100 Trying, 180 Ringing, 200 OK, Ack, Bye, and Unsupported. When the siphandler function has decided what to do with the SIP request, processing is carried out to forward the SIP message, or a reply is sent to the SIP User Agent (UA) by utilizing the generate_sip_response() function. This function generates the SIP reply (or 100 Trying response) based on the values retrieved earlier by parsing the SIP request. It then calls the sipsenddata() function, which calls the relevant protocol handlers to format the headers in the SIP reply.

Register Message: To process a Register message, the bare PC SIP server parses the Via (IP address:port), From and To (usernames@domain/IP), and Contact tags. It then calls the function check_registered_users(). A process similar to that described earlier is used to determine if the user is already registered (i.e., is found in the Registered_Users_Database). If so, only the relevant information is updated; otherwise, the system stores all necessary information parsed from the SIP request including the username, IP address and port number. This information is used to generate replies back to the UA on future requests until the UA re-registers or one of the parameters is updated. After the information is stored or updated, the server generates a 200 OK message and sends the reply back to the SIP UA.

Invite Message: For an Invite message, the bare PC SIP server parses almost all of the same fields as for the Register message. The server then sends messages to the caller and callee. A 100 Trying message is sent back to the caller letting the UA know that the SIP Server is processing the request. To send this message, the server looks up the IP address of the caller using the process described earlier. It also looks up the registration information for the callee and forwards the Invite message to its UA.

SIP Authentication: The Message format for an Invite request with authentication is shown in Figure 4. SIP authentication is done by challenging the initial request (Invite or Register) sent by the SIP UA. SIP uses HTTP authentication techniques. The bare PC SIP Server is designed so that each request is not authorized unless it receives the proper response for a given challenge. The server can be configured at start-up to operate with or without authentication. An authorization flag indicates if a particular request is approved or denied based on authentication. The bare PC SIP server processes the initial request, and then sends a challenge response back to the requesting SIP UA. The SIP server generates a challenge response that depends on the values of realm and nonce. The realm is typically set to the domain of the SIP server (for example, barepc.towson.edu or the IP address). The nonce is a string that is randomly generated by the server. Once the server receives the reply to the challenge, the fields in the authorization request are parsed from the SIP packet. Then the response value is computed using the MD5 algorithm and matched against the response value sent by the SIP UA. The response value is a hash that depends on the concatenation of all values in the authorization request. If the computed response matches the response sent by the SIP UA, the request is approved (authorized) and normal SIP call flow processing is allowed.

```
INVITE sip:67890111@barepc.towson.edu:5060 SIP/2.0
Via:SIP/2.0/UDP192.168.1.56:5060;brach=0320
From:<sip:0123456@ barepc.towson.edu>;tag=0
To: <sip: 67890111@ barepc.towson.edu>
Max-Forwards: 70
Call-ID: 0010-0003-DA76506F-0@AAE2A42DF82D1D0AA
 CSeq: 297386 INVITE
Contact: <sip:123456@192.168.1.56:5060>

Content-Type: application/sdp
Proxy-Authorization:Digest
username="8000",realm="BAREPC",nonce="3bd76584",
uri="sip:123456@192.168.2.81",response="6e91de67ad976997
ff"
User-Agent: BarePC SIP UA v1.0
Content-Length: 276
v=0
 o=Vega400 4 1 IN IP4 192.168.1.56
 s=Bare PC Sip Call
 t=0 0
 m=audio 10006 RTP/AVP 4 18 8 0 96
 c=IN IP4 192.168.1.56
 a=rtpmap:8 PCMA/8000
 a=rtpmap:0 PCMU/8000
 a=rtpmap:96 telephone-event/8000
 a=fmtp:96 0-15,16
 a=sendrecv
```

Figure 4. SIP invite with authentication.

D. User Interface

The bare PC SIP Server has a simple user interface that displays its basic configuration and state information when the interface function sipserverstate() is called. The displayed information includes the number of users added to the username and password database, and the server's configuration mode (proxy, redirector, authentication, stateless, or stateful). The server can also show the username, ip address, and port for each user logged into the system. An administrator can toggle through the list of users, or configure the server so that the display is triggered every time a user is added or removed from the Registered_User_Database by calling sipserverstate() from the Main task.

E. SIP Server Internals

The objects needed by the SIP server application such as apptask (for task implementation), SIPS (for SIP processing), DHCP, TFTP, UDP, IP, and Ethernet (for network protocol processing) or MD5 (for authentication) are implemented as C++ classes with associated .cpp and .h files as usual. Each object contains the data structures and methods for the object. Some assembly code may be used at lower levels. We do not discuss the code common to all bare PC applications such as USB boot code, Ethernet driver code, interfaces to hardware, and code to support other functionality needed by applications. The IP object is used in all bare PC applications and servers requiring network communication. The MainTask (Main task), RcvTask (Rcv or Receive task), and SipsTask (SIP task) are implemented as methods within apptask, while SIP server functionality is provided by sipsobj.

The methods in SIPS include processSIPSRequest(), sipserverinit(), sipserverget_db(), parse_authorization(), authenticate_user(), generate_sip_response(), sipsenddata(), format_sip_response(), siphandler(), register_user(), and parse_headers() as well as many others needed to implement lean SIP server functionality. We have omitted method parameters and do not discuss the specific functionality of all these methods, as we have seen the use of some of these above, and since method names suggest their functionality.

When a UDP packet containing a SIP request arrives, apptask calls insertSIPSTask() to insert a SIP task into the task queue and calls sipsobj.processSIPSRequest(), which serves as an entry point to the task and links to an entry in a table (known as the TCB table) that points to the entire packet and headers. This method in turn invokes siphandler(), which passes the packet to parseheaders() to parse the SIP packet as discussed previously. After the packet is parsed, the request is processed according to the request type. For example, in case of a register request, methods to check and register the user are called by the SIP handler, followed by a call to generate_sip_response() to form the appropriate response packet as seen earlier.

V. PERFORMANCE

In this section, we present the results obtained from our performance studies. We compare throughput and latency for the bare PC and OS-based SIP servers using register, register update, register logout, invite, invite-not-found, and redirect operations. We also report internal timings for the bare PC SIP server for the register operation under maximum load.

A. Experimental Set Up

The test network consists of a 100 Mbps Ethernet to which each SIP server and the client machines running SIPp are connected. In addition to the bare PC SIP server, the details of the systems and software used are as follows: OS-based SIP servers: OpenSer SIP Server ver 1.3.2–notls (Linux) OpenSer (KAMILIO/OpenSIPS) [21] and Brekeke SIP Server ver 2.1.6.6 (Windows) utilizing the Jakarta Web Server and Java platform [22]; machines: Dell GX260's with Intel Pentium 4 (2.4 GHz), 1.0 GB of RAM and 3COM Ethernet 10/100 PCI network cards; OSs: Microsoft Windows XP Professional ver. 2002 Service Pack 2 and Linux Ubuntu 8.04 Kernel 2.6.24-16; workload generator: SIPp [23].

For register updates, the SIP Server searches its user database for a match and then updates the corresponding user's location data and registration expiration time; and in the register logout operation, it removes the user from the database. The invite operation requires the server to lookup the callee's contact details in its database, forward the request to the callee, and send the response back to the caller. The invite-not-found operation is similar to invite except that the callee is not found in the database. For redirect, the server receives an invite message, but instead of forwarding the response to the callee, it forwards a temporarily moved message back to the caller.

For the register, register update, and register logout operations, latency measures the delay at the user agent between sending the register message and receiving the "200 OK" message. Latency for the invite operation measures the sum of two delays: the time between the invite message and "200 OK" messages; and the time between the "bye" and "200 OK" messages. Each of these operations was also tested with authentication enabled, which adds processing overhead due to verifying the MD5 hash, and extra message overhead due to the "unauthorized" message for registration and "407 proxy authentication" message for invite (and their responses). Latency for registration with authentication measures the sum of two delays: the time between the register request and the "unauthorized message"; and the time between the new register message with authentication credentials and the "200 OK" message. Latency for invite with authentication measures the sum of three delays: the time between the invite and "407 proxy authentication" messages; the time between the "invite with authentication" message and the "200 OK" messages; and the time between the "bye" and "200 OK" messages. For invite-not-found and redirect operations, the latency is similarly measured using the "404 not found" and "302 moved temporarily" messages.

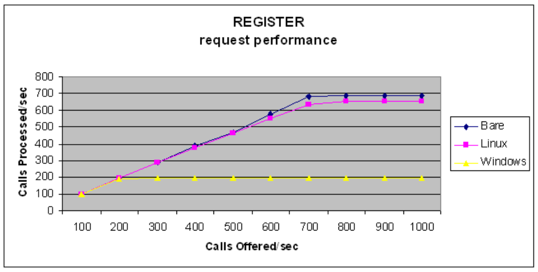

(a) Register

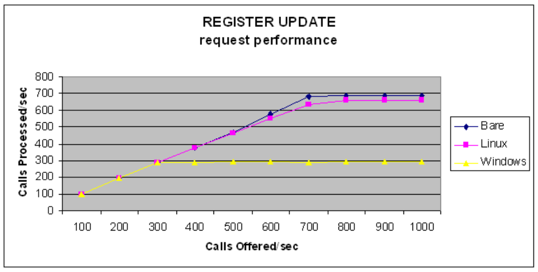

(b) Register update

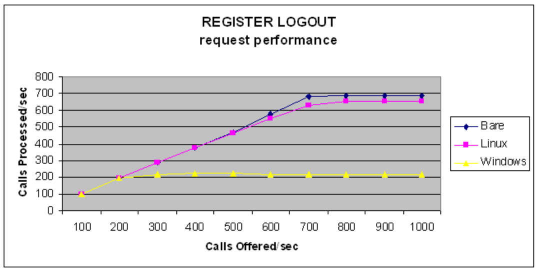

(c) Register logout

Figure 5. Throughput for register without authentication

We measured the throughput and latency of a server associated with each SIP call flow. The latency for a given operation is computed by adding the respective delays between sending the relevant messages to the server and receiving their responses as described above. The throughput is the number of calls per second successfully handled with respect to the offered load, which is the number of calls per second that are generated and sent to the server. The peak throughput is the highest throughput achieved under overload while the server remains stable (and produces consistent results). To conduct the experiments, the servers were configured to operate in three configuration modes with and without authentication: registrar, proxy, and redirector. In addition, internal timings were measured by inserting timing points within the bare SIP server. Each SIP server was pre-loaded with 10,000 unique SIP username and password pairs. The call flows for register, invite-not-found, and redirect were run for a maximum of 10000 unique users, measuring the performance of each call flow with rates varying from 10 to 1000 calls/sec. The invite test call flows were run for a maximum of 5000 users with rates varying from 50 to 100 calls/sec. Each experiment was repeated a minimum of three times to ensure that the results were consistent.

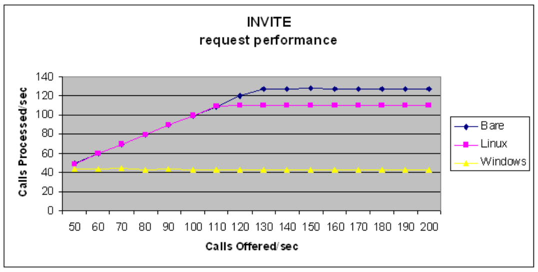

(a) Invite

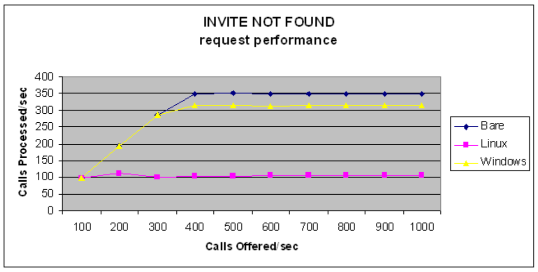

(b) Invite-not-found

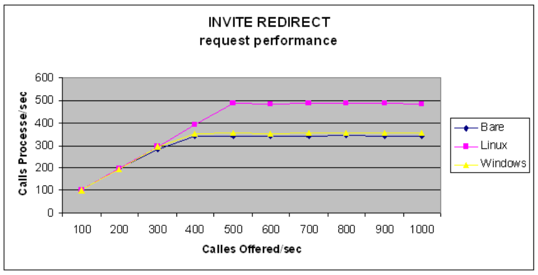

(c) Invite redirect

Figure 6. Throughput for invite without authentication

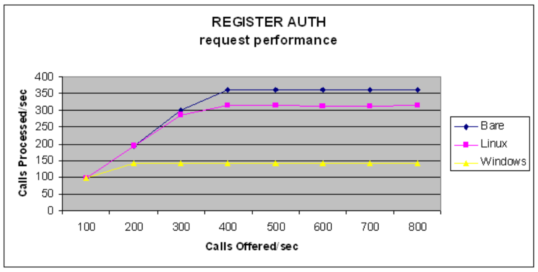

(a) Register

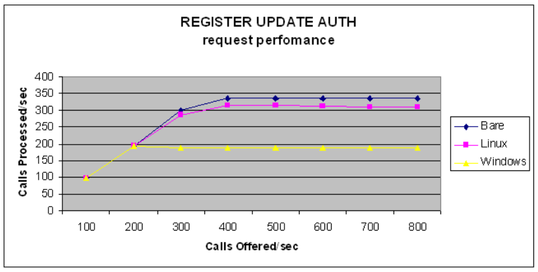

(b) Register update

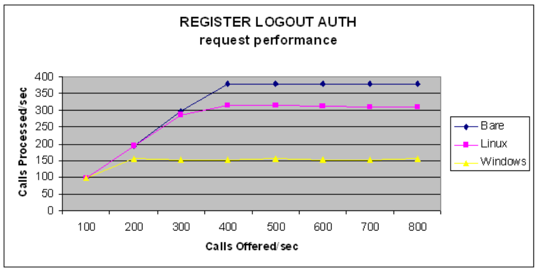

(c) Register logout

Figure 7. Throughput for register with authentication

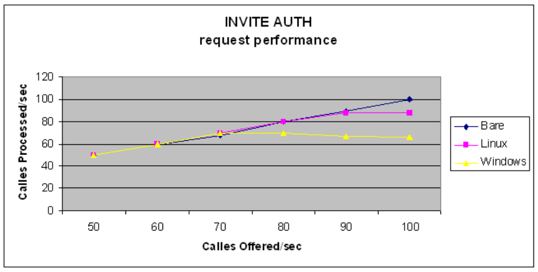

(a) Invite

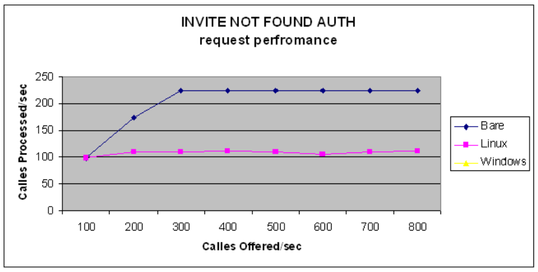

(b) Invite-not-found

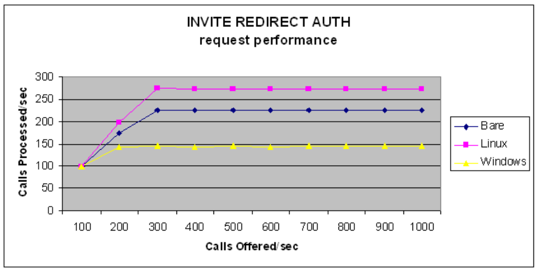

(c) Invite redirect

Figure 8. Throughput for invite with authentication

B. Throughput

The throughput for the register and invite operations respectively, without authentication, is shown in Figures 5 and 6. It can be seen that the peak throughput of the bare PC SIP server is always higher than that of the OS-based servers except in the case of invite redirect. The peak throughput of the bare PC server typically exceeds that of the Linux server by 50-125 calls/sec depending on the operation, although it is only 10 calls/sec more for invite and 150 calls/sec less than that of the Linux server for invite redirect. For example, the bare PC SIP server has a peak throughput of 700 calls/sec for register operations (without authentication), which is better than the peak throughput of Linux (650 calls/sec); the Windows server has a much lower peak throughput (around 200 calls/sec).

The peak throughput performance of the bare PC SIP server should be better than that of the OS-based servers, due to its simple design and the elimination of OS overhead. However, this performance advantage may be reduced or lost in certain cases due to inefficient algorithms or the lack of concurrency. The latter situation arises with the invite operation. The peak throughput of the bare PC server is only marginally higher than Linux in this case, but introducing a separate SIP task to handle an invite operation may improve performance. The apparent drop in performance of the bare PC server for invite redirect is due to a significant improvement in the performance of the Linux server in this case. Implementing Linux's search algorithm on the bare PC SIP server should improve its performance. A more efficient search algorithm should also improve the performance for the invite-not-found operation. The peak throughput of a given server does not vary much across the three register operations since the work performed in each case is essentially the same. The increase in the peak throughput of the Windows server for register update compared to that for the other two register operations is possibly due to caching.

The results in Figures 7 and 8 show that peak throughput of all servers is reduced as expected for both register and invite operations when authentication is added. This reduction in performance is due to the extra message overhead noted previously, and the overhead of computing and verifying the additional information needed for authentication with a message digest [8]. The negative impact of authentication on performance was also noted in [9]. There are no throughput values for the Windows server for invite-not-found with authentication since its message flow in this case could not be compared with that of the other two servers. It is evident that the peak throughput of the bare PC server with authentication shows a greater reduction versus its peak throughput without authentication compared to the OS-based servers. Adapting the approach used for authentication by Linux for the bare PC server could improve its performance.

C. Latency

Figures 9 and 10 compare the latencies for bare PC and OS-based SIP servers for the register and invite operations respectively, with and without authentication. In most cases, the bare PC server performs better than the OS-based servers. As seen in the figures, the highest latency percentages for the bare PC server are usually in the 0-30 ms range, and it rarely has latencies that exceed 150 ms.

For register and register logout without authentication in Figure 9, bare PC server latency performance is better than that of the Linux server, but for register update without authentication it is the same. For example, in case of register logout without authentication, the latency performance of the bare PC server is much better than that of the Linux server: bare PC server latencies are less than 60 ms and most are less than 30 ms, whereas some Linux server latencies are in the 121-150 ms range and only a few are in the 31-60 ms range (none are less than 30 ms). In contrast, the performance of the Windows server is far worse than both of them with a large percentage of latencies exceeding 150 ms. For all register operations with authentication, the latency performance of the bare PC and Linux servers is the same.

It can be seen in Figure 10 that the latency performance of the bare PC server is better than that of the Linux server for invite and redirect without authentication, but worse for invite-not-found without authentication. Latency performance for both servers in case of redirect with authentication is the same. For invite with authentication, the latency of the bare PC server sometimes exceeds 150 ms.

As noted above, improving concurrency and use of a more efficient search algorithm may help to improve bare PC server latency performance without authentication. Further studies are needed to determine if the techniques used to implement authentication in the Linux server will improve latency performance of the bare PC server with authentication.

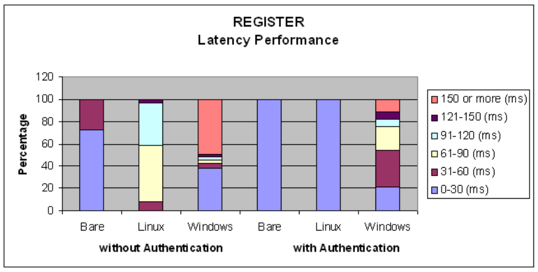

(a) Register

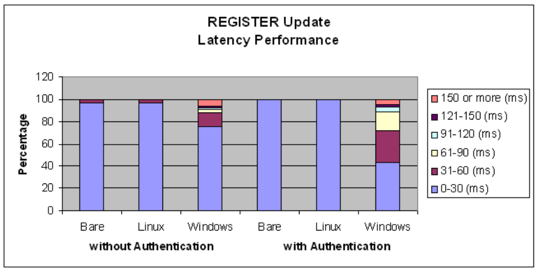

(b) Register update

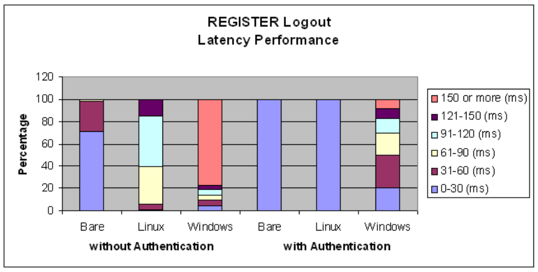

(c) Register logout

Figure 9. Latency for register with and without authentication

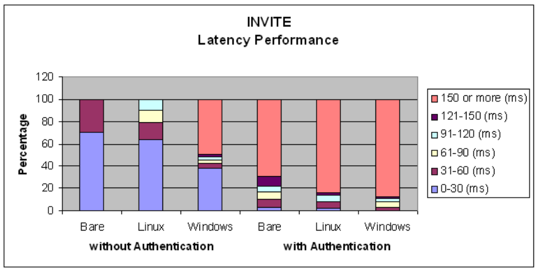

(a) Invite

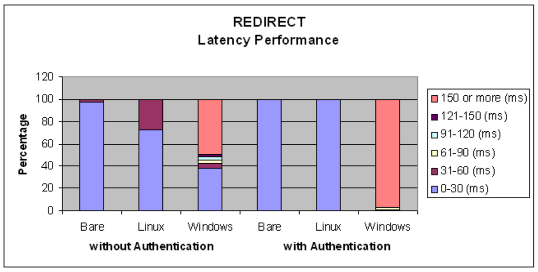

(b) Invite redirect

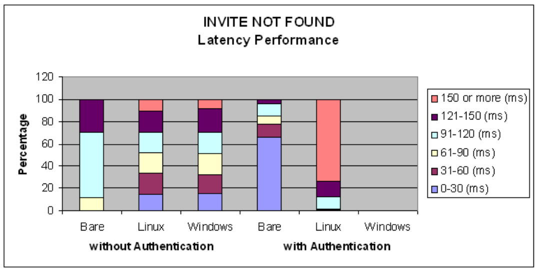

(c) Invite-not-found

Figure 10. Latency for invite with and without authentication

D. *Internal Timings*

Figure 11 compares average values of internal timings for the bare PC SIP server collected during the register operation under maximum load conditions. It is seen that FindUser, which searches for a given user, and ParseSIPHeaders, which processes the SIP header are the most expensive operations, although the former is twice as expensive as the latter. The least expensive operation is AddUser, which simply adds the information for a new user, and thus takes an insignificant amount of time as would be expected. The AuthenticateUser and FormatSIPResponse operations have approximately the same cost, which is about half that of ParseSIPHeaders. We conducted tests on the OpenSER server using OProfile 0.9.5 [24], which showed that the timings for the AddUser and ParseSIPHeaders operations exceed the corresponding timings on the bare PC by factors of 4 and 7 respectively.

We also used SIPp to increase the load on the server and obtain better estimates of internal timings when processing requests. Specifically, we varied the registration request rate from 100-800 requests/sec in increments of 100 requests/sec. We then measured the execution time spent in the siphandler() method that invokes all the other methods needed to process each request and generate the response as discussed previously. We also obtained the total internal processing time to register a user with authentication, which involved processing 2 packets sent to the server and processing two responses to be sent to the SIP UA. Thus, the total processing time includes the network delay and delay due to addition and removal of the various protocol headers.

The results are shown in Figure 12. It can be seen that the execution time spent in the siphandler() method is very small (approximately 180 microsecs) regardless of the registration request rate as would be expected due to its low overhead in processing SIP requests and responses. Likewise, while the total processing time spent per SIP request is larger due to network overheads, it drops in accordance with the increased request rate until the server reaches its capacity and then shows a slower rate of decrease. This is because the server has less ability to meet the offered load when its peak capacity is reached.

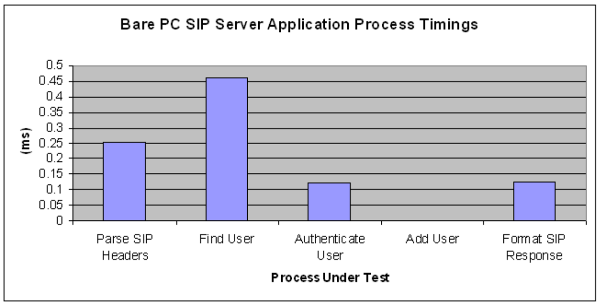

Figure 11. Internal timings for server operations

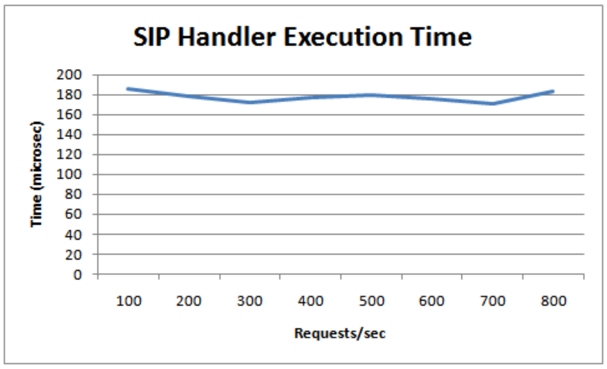

(a) Execution time spent in the SIP handler() method

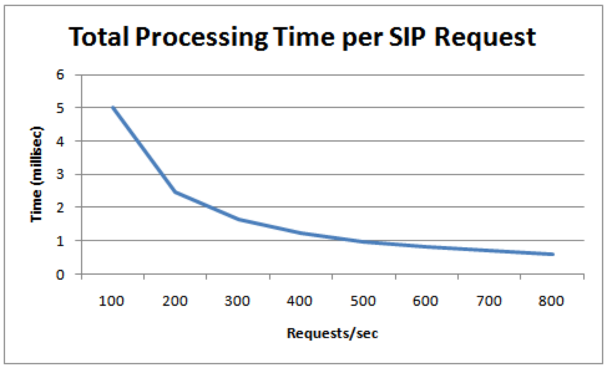

(b) Total processing time per SIP request

Figure 12. Internal timings under increasing load

E. *Throughput Analysis*

Further insight into the results on throughput may be obtained by considering sustainable throughput, which is defined as the maximum rate of calls for which the processed call rate matches the offered call rate. Sustainable throughput reflects the extent to which a server can cope with the offered load, and it can be determined from the preceding Figures 1-4.

For example, the sustainable throughput of the bare PC server for the register, register update, and register logout operations without authentication is respectively 400, 600, and 700 calls/sec (the peak throughput for all three register operations without authentication is 700 calls/sec). It can be seen that the sustainable throughput of the bare PC server exceeds that of the Linux server for all operations without authentication except for invite-not-found when it is the same. In contrast, the sustainable throughput for the two servers for all operations with authentication is the same (or differs by a small amount). As noted earlier, in the case of peak throughput with and without authentication, the bare PC server's values are higher than those for the Linux server except for invite redirect. Thus, both sustainable and peak throughput values should be used to estimate server capacity with and without authentication.

VI. CONCLUSION

We described the design, implementation, and performance of a bare PC SIP server. Design details provided included an overview of bare PC SIP server tasking, server operation, and protocol intertwining. We also gave internal implementation details to illustrate bare PC SIP server functionality. In particular, we described the boot sequence, user lookup and database tables, and SIP message processing. In addition, we examined the relationship between tasks and method invocation in the server when processing SIP requests and responses.

Performance of the server was studied by measuring its throughput and latency for registration, proxying and redirection, with and without authentication. We also compared bare PC SIP server performance with that of the OpenSER server running on Linux and the Brekeke server running on Windows. The results show that the bare PC server has better performance than the Windows server and better or equal performance to the Linux server in most cases. The exceptions are throughput performance for invite redirect with or without authentication, and latency performance for invite-not-found without authentication for which the Linux server is better. Latency performance for the invite operation with authentication was poor for all servers.

We also provided internal timings measured on the bare PC SIP server when processing registration requests with authentication under increasing server load. It was found that Find User is the most expensive operation, Parse SIP Headers is moderately expensive, whereas Format SIP Response and Authenticate User are less expensive.

The observed performance results reflect the simple server design, efficient tasking strategy, and low implementation overhead due to absence of an OS. It is expected that the performance of the bare PC server can be improved by improving concurrency and using more efficient algorithms. The bare PC SIP server implementation could also be modified based on internal timings to reduce the cost of the most expensive operations. Our results serve as a baseline to assess the minimal overhead associated with basic SIP server operations for both OS-based and bare PC servers, and to help improve the performance of bare PC SIP servers.

REFERENCES

[1] A. Alexander, A. L. Wijesinha, and R. Karne, "A Study of Bare PC SIP Server Performance," 5th International Conference on Systems and Network Communications (ICSNC), pp. 392-397, 2010.

[2] A. Alexander, A. L. Wijesinha, and R. Karne, "Implementing a VoIP SIP Server and User Agent on a Bare PC", 2nd International Conference on Future Computational Technologies and Applications (Future Computing), 2010.

[3] G. Ford, R. Karne, A. L. Wijesinha, and P. Appiah-Kubi, The Performance of a Bare Machine Email Server, 21st International Symposium on Computer Architecture and High Performance Computing (SBAC-PAD), pp. 143-150, 2009.

[4] L. He, R. Karne, and A. Wijesinha, "The Design and Performance of a Bare PC Web Server", International Journal of Computers and Their Applications, vol. 15, pp. 100-112, June 2008.

[5] A. L. Alexander, A. L. Wijesinha, and R. Karne, "An Evaluation of Secure Real-Time Transport Protocol (SRTP) Performance for VoIP," Third International Conference on Network and System Security (NSS), pp. 95-101, 2009.

[6] G. H. Khaksari, A. L. Wijesinha, R. K. Karne, L. He, and S. Girumala, "A Peer-to-Peer bare PC VoIP Application," Proceedings of the IEEE Consumer and Communications and Networking Conference (CCNC), pp. 803-807, IEEE Press, Las Vegas, NV, 2007.

[7] K. Ono and H. Schulzrinne, The Impact of SCTP on SIP Server Scalability and Performance, GLOBECOM, pp. 1421-1425, 2008.

[8] S. Salsano, L. Veltri, and D. Papalilo, SIP security issues: The SIP authentication procedure and its processing load, *IEEE Network*, pp. 38-44, 2002.

[9] E. M. Nahum, J. M. Tracey, and C. P. Wright, Evaluating SIP server performance, in: 17th International Workshop on Network and Operating System Support for Digital Audio and Video (NOSSDAV), Urbana-Champaign, Illinois, June 2007.

[10] M. Cortes, J. R. Ensor, and J. O. Esteban, On SIP Performance. *Bell Labs Technical Journal*, 9(3), pp. 155-173, 2004.

[11] C. Shen, H. Schulzrinne, and E. M. Nahum, Session Initiation Protocol (SIP) Server Overload Control: Design and Evaluation, IPTComm, pp. 149-173, 2008.

[12] V. A. Balasubramaniyan, A. Acharya, M. Ahamad, M. Srivatsa, I. Dacosta, and C. P. Wright, SERvartuka: Dynamic Distribution of State to Improve SIP Server Scalability, ICDCS, pp. 562-572, IEEE Computer Society, 2008.

[13] K. Ono and H. Schulzrinne, One Server Per City: Using TCP for Very Large SIP Servers, IPTComm, pp. 133-148, 2008.

[14] H. Jiang, A. Iyengar, E. M. Nahum, W. Segmuller, A. Tantawi, and C. P. Wright, Load Balancing for SIP Server Clusters, INFOCOM 2009.

[15] K. K. Ram, I. C. Fedeli, A. L. Cox, and S. Rixner, Explaining the Impact of Network Transport Protocols on SIP Proxy Performance, ISPASS, pp. 75-84, 2008.

[16] L. Chen, and C. Li, "Design and Implementation of the Network Server Based on SIP Communication Protocol," World Academy of Science, Engineering and Technology 31, pp. 138-141, 2007.

[17] S. Zeadally and F. Siddiqui, "Design and Implementation of a SIP-based VoIP Architecture," AINA 2004.

[18] R. K. Karne, K. V. Jaganathan, N. Rosa, and T. Ahmed, "DOSC: Dispersed Operating System Computing", OOPSLA '05, 20th Annual ACM Conference on Object Oriented Programming, Systems, Languages, and Applications, Onward Track, pp. 55-62, 2005.

[19] R. K. Karne, K. V. Jaganathan, and T. Ahmed, "How to Run C++ Applications on a Bare PC?" 6th International Conference on Software Engineering, Artificial Intelligence, Networking and Parallel/Distributed Computing (SNPD), pp. 50-55, 2005.

[20] G. Ford, R. Karne, A. L. Wijesinha, and P. Appiah-Kubi, The Design and Implementation of a Bare PC Email Server, 33rd Annual IEEE International Computer Software and Applications Conference (COMPSAC), pp. 480-485, 2009.

[21] Kamailio (OpenSER) SIP server, [Online]. Available: http://sourceforge.net/projects/openser Accessed: December 10, 2010.

[22] Brekeke SIP Server, [Online]. Available: http://www.brekeke.com/sip/ Accessed: May 28, 2010.

[23] SIPp, [Online]. Available: http://sipp.sourceforge.net/doc/reference.html Accessed: December 10, 2010.

[24] Oprofile-A System Profiler for Linux, [Online]. Available: http://oprofile.sourceforge.net/news/. Accessed: May 28, 2010.

Multicast TV Channels over Wireless Neutral Access Networks: Proof of Concept and Implementation

Lorenz Klopfenstein, Andrea Seraghiti, Alessandro Bogliolo
University of Urbino
Urbino, Italy 61029
Email: {lorenz.klopfenstein, andrea.seraghiti, alessandro.bogliolo}@uniurb.it
Stefano Bonino, Andrea Tarasconi
Essentia S.p.A
Reggio Emilia, Italy 42124
Email: {stefano.bonino, andrea.tarasconi}@essentia.it

***Abstract*—IP traffic trends and forecasts suggest that television over IP (IPTV) will be the killer application for next-generation networks (NGNs). There is, however, a chicken and egg situation between the deployment of broadband access networks and the diffusion of high quality multimedia services, such as high definition television, which actually impairs the development of NGNs. As a matter of fact, most existing access infrastructures are still under-provisioned and they provide no suitable support to the widespread diffusion of global Internet TV channels, while wireless access networks are sprouting worldwide to provide nomadic connectivity and to bridge digital divide in sparsely-populated regions. In this scenario, IPTV services are delivered only within the walled gardens of biggest wireline operators and they are far away from reaching the critical mass required to attract investments in NGNs. This paper proposes technological and architectural solutions which enable the widespread diffusion of Internet TV channels over existing wireless access networks, thus overcoming the deadlock between services and infrastructures and paving the way to NGNs. In particular, the paper addresses both technological and market issues and presents the results of laboratory tests and proof-of-concept experiments conducted within the wireless campus of the University of Urbino. Finally, the paper outlines the implementation of the key components of the proposed architecture as addins of *openBOXware*, an open source platform for the development of bandwidth-aware multimedia applications over IP.**

***Keywords*-Internet TV; IPTV; Multicast; Radio broadcast; Proxy.**

I. Introduction

Internet protocol television (IPTV) is expected to be the killer application for next-generation Internet [1], [2] for two main reasons. First, because it encompasses high-bandwidth multimedia services which cannot be delivered over today's network infrastructures with sufficient *quality of experience* (QoE) [3], thus prompting for the development of *next generation networks* (NGNs). Second, because IPTV is expected to inherit the popularity of traditional broadcast TV, thus driving the market penetration of NGNs and providing the business opportunities needed to motivate the investments they require.

This vision is further supported by IP traffic statistics [4] and video traffic forecasts [5], which predict that consumer IP traffic will account for 87% of the overall aggregate traffic in 2014 and almost 60% of this share will be taken by Internet video streaming and download. In 2011 IPTV services delivered within operators' networks are expected to account for more than 40% of the overall IP traffic [6].

In spite of the soundness of these arguments, the positive feedback loop between infrastructures and applications is hard to be triggered since none of the two elements can leap forward by itself. Hence, the broadband market suffers from a stagnation which is caused both by the lack of investments (access networks are under-provisioned and there are market-failure areas still affected by infrastructural digital divide) and by the lack of demand (users are aware that existing infrastructures are unsuitable to deliver high-quality multimedia services, so that such services do not create a new demand for network connectivity) [7], [8].

IPTV was born in a scenario characterized by insufficient access infrastructures managed according to monolithic business models and flat-fee access rates. In this context, wireline operators may offer high-value services (including IPTV) within their own walled gardens in order to increase their revenues, but they are not motivated to promote global high-bandwidth applications (such as Internet TV) which can be accessed by their customers through flat-fee connections without generating additional revenues [7].

Both the IPTV services delivered within the walled garden of some operator (literally called IPTV) and the Internet TV networks available worldwide are targeted only to Internet users. This trivial observation has two (less trivial) consequences: first, IPTV cannot be sold by itself to people who don't want to subscribe for an Internet connection [9], [8], second, IPTV users are assumed to be accustomed to Internet browsing. Hence, neither the commercial models nor the usage patterns of IPTV [10] resemble those of traditional television: while broadcast TV is a mass medium per excellence, IPTV is an interactive entertainment service which fully exploits the two-way unicast nature of IP networks to comply with Internet user's personal wishes.

Although the capability of supporting personal *on-demand services* (ODSs), such as video on demand and networked video recording, grants a competitive advantage to IPTV, ODSs raise scalability issues when the number of simultaneous users increases, while the significant difference in the usage experience slows down the convergence between broadcast television and IPTV.

A. The underlying network model

Starting from the observation that monolithic network models are inadequate to solve digital divide issues, to enable competition, and to promote innovation [7], regulations have been introduced in many countries to facilitate competition by forcing incumbent operators to allow new-entrants to use their infrastructures by means of local-loop unbundling, line sharing, bistream access, and convenient wholesale offers. Although such initiatives have contributed to increase broadband penetration [11], they haven't changed significantly the relationship between end-users and operators, since the new entrants have usually adopted the same market strategies of the incumbents. On the contrary, a drastic change in the value chain of broadband access could be induced by exploiting the separation between network connectivity and service provisioning which is inherent in the TCP/IP stack. The concepts of *open access network* (OAN) and *neutral access network* (NAN) have been recently introduced to this purpose.

OANs [12], [13] aim at enabling competition among service providers (SPs) on top of a shared infrastructure which acts as a transparent broker (Internet service providers are nothing but a special category of SPs). End-users connect to the shared infrastructure and register with the SP of choice, which has his/her own edge router directly connected to a common *operator-neutral* backbone [14].

NANs [15] are a special category of OANs conceived to trigger the positive externality which is a determinant of success and sustainability for a communication network: the larger the number of users in a network the greater the added value for each of them. According to the NAN model, a sizeable set of services have to be delivered within the access network and made available to the users before they register with any Internet SP. End-users establish commercial relationships with SPs, that in turn pay a share of their revenues to the NAN organization [12], [16] for the resources used by their customers.

NANs have the potential to reach higher penetration than traditional access networks because they are open to users who are not subscribers and who possibly pay only for the services they really benefit from. The larger the appeal, the popularity, and the usability of such services, the larger the diffusion and the penetration of the access network which makes them available. Mass media are the ideal services to be used as icebreakers for the diffusion of NANs.

The advent of wireless access technologies (WiFi, Hiperlan, WiMAX) and the allocation of significant public funding to address digital divide have prompted for the deployment of sustainable wireless access networks aimed at maximizing public utility. OAN and NAN models are particularly suited to this purpose. Although the feasibility of HD video streaming over wireless access networks has been recently assessed [17], [18], current wireless technologies are not ready to support high performance multicast services.

Based on the above arguments, this paper explores the feasibility of wireless NANs delivering IPTV services which retain the key features of free-on-air broadcast TV channels. Both architectural and technological issues are addressed and a working prototype is built to make a proof of concept. Section II presents the proposed architecture, Section III outlines the implementation details and the technical choices of the experiment conducted within the wireless campus of the University of Urbino [19], Section IV presents preliminary experimental results that demonstrate the feasibility of the proposed approach, Section V discusses its implementation on top of *openBOXware*, an open-source platform for the development of distributed multimedia applications [20]. Conclusions are drawn in Section VI.

II. Proposed architecture

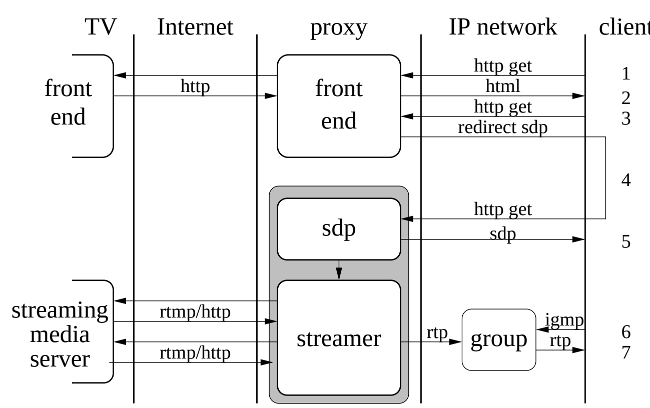

Figure 1. Schematic representation of the unicast-to-multicast proxy gateway.

The key components of the proposed architecture are the unicast-to-multicast TV proxy (hereafter called *proxy* for brevity) and the *base station* (BS), which grants wireless access to the *consumer premise equipment* (CPE).

A. Unicast-to-Multicast Conversion

The proxy acts as the TV head-end of an IPTV system, in that it receives, transforms and distributes TV contents to the subscribers. Its main functionalities can be described by referring to Figure 1, which provides a schematic representation of the overall software architecture used to make a live Internet TV channel available to a multicast group: the Internet TV platform is represented to the left, the client is represented to the right, and the proxy is in between.

The Internet TV platform (left-most side of Figure 1) is composed of a front-end (i.e., a web server allowing end-users to browse live TV channels and gain access to on-demand services by means of their own web browsers) and a content delivery network, CDN (i.e, a network of streaming media servers distributed worldwide to reduce latency, increase quality of service, and perform Internet traffic optimization by providing some form of multicast support). At the application level, the stream is usually transferred across the Internet either in HTTP or in RTMP over TCP. When the end-user selects a content on the front-end of the Internet TV network, the client is transparently redirected to the most convenient streaming server of the CDN. A live TV channel can either be viewed as a continuous single stream which uses the same encoding, or, in some cases, it can be viewed as a playlist of heterogeneous contents (possibly encoded in different formats) which are concatenated at run time. In some Internet TV platforms the transition between subsequent contents requires the client to issue a request for the new content. Such a request is automatically triggered by the client software at the end of each stream in order to be transparent to the end-user.

Similarly to the Internet TV platform, the proxy is divided into a front-end and one or more streamers. The front-end is composed of a set of web pages that allow the end-user to browse and to choose a multicast TV channel among the ones made available by the proxy. When the client issues an HTTP-get request to the front-end (step 1 in Figure 1), the web page is dynamically composed, by taking channel data directly from the Internet TV platforms they belong to, and returned to the client (step 2). When the user selects a channel, the request (step 3) is redirected (step 4) to the corresponding *session description protocol* (SDP) file, which contains information about the streaming protocol adopted, the format and encoding of the data, and the address and port of the multicast group associated with the channel. For load-balancing reasons, the SDP files of different channels can be hosted by different servers. At the same time, a *streamer* is started for the requested channel, producing a stream that matches the parameters contained in the SDP file. The server returns the SDP file (step 5) to the client, which issues an *internet group management protocol* (IGMP) request (step 6) to the corresponding multicast group. Finally, the client starts receiving the RTP audio/video streams (step 7) generated by a *streamer* and sent to the multicast group. The streamer is a process which runs on the proxy to perform the unicast-to-multicast transformation. To this purpose, it acts as a client for the streaming server of the Internet TV channel of choice, it possibly performs data transcoding when needed, and it generates the audio/video RTP streams. In case of a TV channel composed of multiple files to be concatenated at run time, this operation is transparently performed by the streamer, which produces a continuous stream. The streamer associated with a given channel is launched upon reception of the first request of the corresponding SDP file. Once the streamer is active, no further actions are required to serve subsequent requests to the same channel.

B. *Wireless Multicast*

In principle, multicast transmission is the most efficient solution for one-to-many communication over an IP network for four main reasons: i) the sender doesn't need to know the receivers, ii) the server sends each packet only once, iii) network nodes take care of replicating the packets only when it is striclty required to reach different users, iv) data packets are not delivered to receivers who don't want to receive them. Since each data packet is sent at most once across each link regardless of the number of receivers that will be reached through that link, bandwidth requirements become independent of the number of users. Due to the massive replication possibly required at the nodes, however, multicasting moves the bottleneck from bandwidth to computational requirements, which scale almost linearly with the number of users.

In principle, data replication issues could be locally overcome in a wireless network by exploiting the inherent broadcasting capabilities of a radio signal propagating over the air. By combining IP multicasting with radio broadcasting, both bandwidth and computational costs would become independent from the number of receivers.

Unfortunately, the radio multicast solutions available today within the IEEE 802.11 framework suffer from heavy limitations which come from the unicast-oriented standardization and implementation choices made over the years. In particular, most of the improvements introduced for enhancing the efficiency of unicast radio packets (such as *fast-frame*, *compression*, *Wireless Multimedia Extension*, and radio QoS) do not apply to broadcast/multicast radio packets, the only exceptions being the *raw rate* speed setting and the *no-ack* option introduced in IEEE 802.11e. Similarly, the strategies adopted by chipset vendors have sacrificed multicast/broadcast radio performance for the sake of unicast performance and cost reduction. For instance, top range chipsets provide four hardware queues for unicast traffic, while only one queue is available for broadcast/multicast traffic (one additional queue is usually dedicated to service packets). As a consequence, typical wireless point-to-multipoint base stations can provide limited performance and quality of service to multicast traffic, which competes with higher priority service radio packets.

The wireless equipment adopted in our setup have been specifically optimized at the *hardware abstraction level* (HAL) to overcome the above-mentioned limitations.

III. Implementation

This section outlines the implementation of a prototype of the architecture presented in Section 2.

A. Multicast proxy implementation

The proxy presents the list of available TV channels in a standard HTML webpage, served by ASP.NET (Mono) on an Apache server. The list is built by merging the lists of channels offered by remote Internet TV providers (retrieved by means of web service calls to their APIs) together with the list of possible local channels based upon media stored inside the proxy itself. The list is displayed and browsed by the client by means of any common web browser.

The client may request a specific TV channel by accessing a web URI using the browser. When such a request reaches the proxy, it checks whether the requested channel is already being streamed. This is done through a database that keeps tracks of the streaming processes, the channels they are handling, their parameters, and the streaming server they are running on. If no streamer is currently active, a new process is launched on a streaming server, which starts retrieving the desired channel and forwarding it to a multicast group picked by the proxy. Finally, the proxy server generates the SDP announcement containing the information required to retrieve the audio/video data streams and to decode them correctly.

Such an SDP announcement is served back to the requesting client using the ”application/sdp” MIME type, so that the client, if properly configured, will automatically start an application capable of decoding and playing back the streams as declared by the announcement (*VLC Media Player* is used to this purpose in our setup). An SDP announcement is a standard text file containing the full description of a “media streaming session”. At its most basic configuration, it can simply contain the IP address the stream is directed to and its components, which can be any number of video and audio streams, and their respective port numbers. Additionally, the announcement can also contain advanced details about each stream’s encoding, which will be used by the client-side decoder to decide on how to interpret the incoming data.

Each streamer running on a streaming server is an instance of a mixed-mode .NET assembly running on *Mono* and relying on a native streaming back-end implemented in C++ using the *GStreamer* multimedia framework. The streamer determines the URI of the original resource associated with the TV channel requested by the client. The URI may refer to a local file, to a HTTP resource (as used by *Youtube*), to an Adobe RTMP stream (used by *StreamIt.it*), to a Microsoft Media Server (MMS) stream (used by *Rai.tv*), or to any other supported stream. As soon as the original location of the resource is ascertained, the native streamer is launched. The streamer relies either on built-in functionalities of *GStreamer* or on custom elements integrated with it in order to retrieve the stream and decode it. For instance, streaming through the Adobe RTMP protocol is not currently built into any mainstream *GStreamer* distribution, so that the specific support was provided by an in-house plug in.

The original audio and video streams are demuxed and then processed independently: each stream is decoded and converted as needed and then re-encoded using the encoding of choice for its final delivery. In our implementation, video data is always decoded and re-encoded using MPEG4-AVC/H.264 compression at a constant bitrate. Audio data is mixed down to stereo (in case of multichannel audio), resampled at 44.1 kHz, and finally encoded using the *Advanced Audio Coding* (AAC) scheme. In our setup the *x264* encoder has been used for video data and the *faac* encoder for audio data, each used through their respective *GStreamer* elements.

Note that the video compression step during transcoding also inserts SPS/PPS headers (i.e., *sequence/picture parameter set*) in the raw H.264 data stream, in order to ease the synchronization of client-side players[1]. These additional parameter headers inside the data stream contain information about compression, resolution and other properties that can be used by the decoder to synchronize to the stream and to properly decode the contents. This is needed mainly because video formats can vary abruptly between TV channels and even between single files belonging to the same channel, possibly causing the video player to lose sync and display corrupted data. Sometimes an abrupt change in resolution, if not handled during transcoding, can even crash some less resilient decoders on the receiving end. In case of TV channels with varying compression schemes and resolutions, one or more scaling and resizing steps can be added to the media pipeline in order to provide a more uniform output stream at the cost of a loss in picture quality, in addition to SPS/PPS headers (this feature was not used in our proof of concept). On the other hand, transcoding at runtime can be entirely avoided when channels are based on streams with pixel resolutions and encoding known beforehand. In this case, encoding information can be directly added to the SDP announcement (this may be the case especially for local files streamed from the proxy itself, which can be adequately prepared before streaming).

It is also worth noting that compression levels can be adapted to the available wireless bandwidth, trading off picture and sound quality, and even video resolution, for the number of simultaneous TV channels. On the other hand, wireless interference can be compensated by using less aggressive compression modes. This can be done, for instance, by targeting a lower H.264 encoding profile level, which issues more I-frames and avoids complex prediction techniques, thus easing the player’s work to re-sync upon losing a packet. Those parameters can be either statically

[1] This option is known as “byte-stream” in the x264 encoding options.

configured in the proxy (as in our implementation) or dynamically adapted at runtime according to channel quality, number of channels or wireless traffic statistics.

B. Wireless equipment

The solution adopted for our experiments is based on the Essentia WFL R108F25x(B) radio module equipped with an Atheros AR5414 radio chipset. Hardware and protocol limitations have been overcome by means of multicast-oriented optimizations performed at the HAL, in the operating system (i.e., Essentia OpenWifless ESS OS), and in the device drivers. In particular, multiple multicast queues have been implemented and the IEEE 802.11e protocol has been extended in order to provide wireless multimedia extension (WMM) and QoS support to broadcast/multicast traffic.

As a result, the performance achieved by the current implementation of the radio module on multicast traffic over a point-to-point link equals that of unicast traffic. In addition, the radio protocol provides to multicast traffic full IEEE 802.1Q-2005 QoS support.

IV. Experimental results

A. Lab experiments

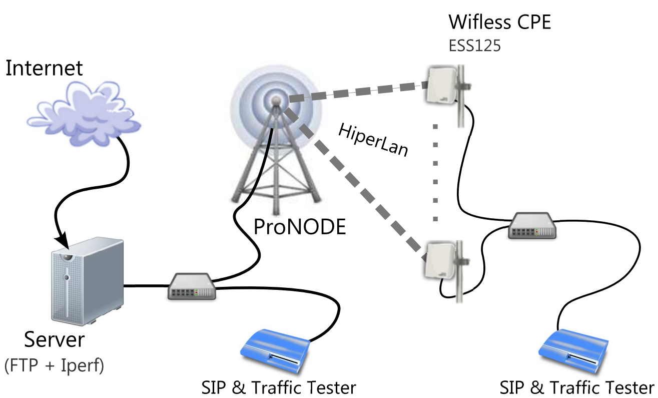

Figure 2. Schematic representation of the experimental setup described in Section IV-A.

Extensive experiments were performed to assess the multicast performance of the wireless equipment and its scalability with the number of clients in a point-to-multipoint setup typical of a metropolitan access network. To this purpose, both the BS (namely, an Essentia Wifless ESS 24562 base station) and the CPEs (namely, Essentia Wifless 125 CPEs) adopted the enhanced radio module described in the previous subsection. An Agilent N2X traffic tester was used for traffic generation and performance measurements. In particular, the tester was used to simulate both a server connected to the BS, and 50 clients connected to 50 CPEs (VLAN tagging was used to connect the 50 CPEs to the tester across the same ethernet link). Two types of traffic were simulated concurrently: a multicast downlink uncompressable stream from the server to all the clients and a unicast full-duplex UDP traffic between the server and each client. The experimental setup is depicted in Figure 2.

The aim of the experiment was to test the maximum achievable multicast bandwidth in presence of a background unicast traffic, and the scalability of the solution in terms of bandwidth and computational resources. Hence, a constant flow of 100kbps uplink and 100kbps downlink was generated for each client, summing up to 5Mbps uplink and 5Mbps downlink of unicast backgroud traffic across the BS. Then the multicast downlink traffic was increased while monitoring link quality and BS resource usage with 1 and 50 CPEs.

CPEs	Multicast traffic [Mbps]	Delay [ms]	Jitter [ms]	PLR %	CPU usage %
1	16.0	8	0.1	0	30
50	16.0	10	0.1	0	33
50	16.2	60	0.2	0	33
50	16.4	520	0.8	0	33
50	16.6	900	1.0	1	33

Table I
Performance achieved by a 24562 BS connected to 50 CPEs for different multicast traffic loads added to a background of full-duplex unicast traffic. Data refer to a radio channel of 20MHz at 5.5GHz, operated at a 24Mbps multicast raw speed.

The results reported in Table I show that the multicast performance of the BS does not depend on the number of CPEs connected. The marginal increase of CPU usage from 30% to 33% when connecting 50 CPEs is due to the additional 49 full-duplex unicast streams to be handled in our setup. Hence, as expected, multicast transmission does not suffer from scalability issues, the only physical limitation being the AR51414 HS encryption engine, which can handle up to 120 concurrent CPEs with no performance loss, and up to 512 CPEs per sector with performance degradation.

As for the limiting multicast bandwidth, no performance degradation occurs until 16Mbps of uncompressable traffic, while the degradation observed over this value is due to the limited computational resources of the CPEs. The maximum multicast traffic achieved by equipping CPEs with the same processor used in the BS was of 37Mbps per sector for a multicast raw speed of 54Mbps.

Additional tests were performed to determine the effect of modulation *raw speed* on the trade-off between multicast throughput and RF sensitivity of the Essentia WFL R108F25X(B) radio module. The experimental results are reported in Table II. Since the same modulation has to be imposed on all the CPEs associated with the same multicast group (or otherwise data replication would be necessary), the modulation raw speed can be used to span the trade off between the number of TV channels that can be delivered per sector (i.e., bandwidth or throupghput, column 4 in Table II) and the radius of the coverage area of the BS (i.e., sensitivity, column 2 in Table II). In particular, the coverage

Modulation Raw Speed	Sensitivity [dbm]	Mode HD/FD	Throughput [Mbps]	Jitter [ms]	Delay [ms]
54	-71	HD	37.0	0.5	3
		FD	19.5	0.5	4
48	-76	HD	34.0	0.1	5
		FD	18.2	0.1	5
36	-82	HD	27.2	0.1	4
		FD	14.5	0.1	6
24	-85	HD	19	0.1	5
		FD	10.0	0.1	7
18	-88	HD	15.0	0.1	6
		FD	7.5	0.1	4
12	-90	HD	10.5	0.1	7
		FD	5.1	0.1	8
9	-90	HD	7.4	0.1	7
		FD	3.8	0.1	6
6	-92	HD	5.2	0.1	9
		FD	2.5	0.1	5

Table II
EFFECT OF MODULATION ON THROUGHPUT AND SENSITIVITY OF THE ESSENTIA WFL R108F25X(B) RADIO MODULE.

radius of the radio link doubles every 6dB of system gain (or sensitivity) if the same antennas are used. Hence, a 10X extension of the coverage radius (which corresponds to a 100X extension of the coverage area) could be achieved by changing the modulation from 54Mbps to 6Mbps, at the cost of reducing the number of TV channels per sector.

As a final remark, it is worth noting that multicast/broadcast packets are usually not retransmissible because of the lack of acknowledge in the protocol. This is an advantage in terms of protocol overhead (which ultimately has a benefit in terms of throughput) and a disadvantage in terms of QoS (which ultimately impacts the limiting distance of the radio link). In order to overcome this possible limitation, the CPEs adopted in our setup implement the *no-ack* option which allows one or more of them to inform the BS of the loss of a multicast packet, asking for retransmission. The overhead of the *no-ack* option ranges from 5% to 20% in case of CPEs operated with poor SNR.

B. Proof-of-concept experiments

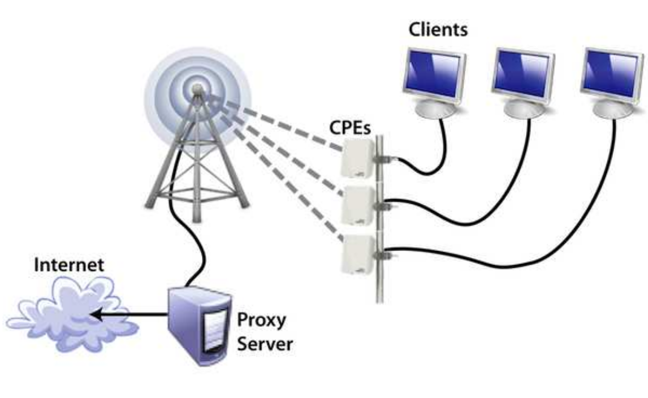

Figure 3. Schematic representation of the experimental setup described in Section IV-B.

A proof-on-concept experiment was conducted in Urbino (Italy) in May 2010 during a public event organized in the conference hall of the Ducal Palace. The setup is schematically represented in Figure 3.

Both the front-end and the streamer of the unicast-to-multicast proxy were executed on a 2.4GHz Intel Core 2 Quad with 4GB of RAM running Ubuntu 10.04. The proxy was installed within the intranet of the University of Urbino and connected to an Essentia Wifless ESS 24562 BS (belonging to the same LAN) installed on the roof of a building in front of the event site. Backhauling was granted by the Internet gateway of the University of Urbino, providing up to 150Mbps of Internet bandwidth. 10 PCs running *Opera Web Browser* and *VLC Media Player* on top of *Windows XP* were used as clients. Each of them was connected to an Essentia Wifless 125 CPE installed right outside the conference hall. Both *RAI Radiotelevisione Italiana* (http://www.rai.tv/) and *Streamit.it* (http://www.streamit.it/) were used as Internet TV providers. In addition, high-definition 1080p contents were streamed directly by the proxy. The performance of the BS (in terms of multicast and unicast throughput, packet loss, CPU, and memory usage) was monitored every 15s.

The experiment was used to demonstrate the feasibility of real-time transcoding and multicast transmission of HD Internet TV channels over a wireless link. In particular, it was clearly shown that bandwidth and computational resources increase linearly with the number of users watching unicast TV channels, while they are independent of the number of users watching a multicast TV channel.

A representative test was performed by comparing network behavior and device load when switching from watching the same TV channels through direct unicast connections to watching it as a shared multicast stream routed through the proxy server. As expected, the number of unicast connections has a linear impact on network traffic and device load, while the number of clients associated with the same multicast group deon't have any measurable effect neither on bandwidth occupation nor on CPU/memory usage on the BS. The same results were obtained both by streaming local resources from the proxy server and by transcoding live TV channels through the streamer.

The final stress test of the setup was executed in the following configuration: 2 clients watching the same multicast HD channel compressed at a constant rate of 5Mbps and streamed directly from the proxy, 2 clients watching the same *standard-definition* (SD) TV channel provided by *RAI Radiotelevisione Italiana* and transcoded at run time by the multicast proxy, 1 client watching a unicast SD channel provided by *Streamit.it*, 1 client watching a unicast HD channel provided by *Streamit.it*, 1 client watching the multicast version of a *Streamit.it* SD channel, 1 client watching the multicast version of a *Streamit.it* HD channel, and 2 clients watching a multicast HD content local to the proxy and compressed at a constant rate of 2Mbps. Figure 4 shows the 10 clients and the traffic/CPU/memory monitors as they appeared during the experiments.

Figure 4. Picture taken during the proof of concept experiment described in Section IV-B.

In summary, there were 2 unicast streams taken from the Internet, 3 Internet TV channels taken from the Internet and made available in multicast by the proxy, and 2 HD multicast streams directly generated by the proxy. Moreover, one of the clients watching a multicast TV channel was also connected to *YouTube* in order to generate unicast traffic across the same wireless link. The overall multicast traffic was of 12Mbps with a peak of unicast downlink traffic of 7Mbps. No packet loss was observed and the CPU of the BS was used only at 32%.

This final configuration also demonstrates that runtime transcoding of multiple standard and high definition video streams can be realistically done with consumer-grade hardware, without any quality degradation nor any noticeable delay for the clients.

V. Open Source Framework

The results of the proof-of-concept experiment prompted for the development of *openBOXware*, a portable, open-source framework providing a suitable abstraction for building bandwidth-aware client-server multimedia applications [20].

The final purpose of the framework is to offer a common development platform that can be adopted at various points of the scenario described in this paper, including content providers, proxy servers and receiving client end-points. Multimedia contents can be added and managed with ease at any stage by exploiting the abstraction and the flexibility offered by the plug-in system of *openBOXware*.

A. *OpenBOXware*

The software stack of *openBOXware* is similar to the one adopted in the original implementation of the unicast-to-multicast proxy described in Section III-A. Multimedia handling and streaming is based on the *GStreamer* framework, while the basic runtime support is offered by *Mono*, the open-source implementation of *.NET*, which provides the language runtime, the type system, and the virtual runtime environment where the framework runs independently of the underlying hardware (*Mono* runtime is currently able to be compiled and run on many different platforms, including the most common *x86* and *ARM* architectures). The hardware abstraction features of *Mono* also provide the support for a dynamic plug-in system whose components can be easily distributed and run across different devices without need for recompilation.

In addition to what was originally implemented for the proof of concept, the framework also provides: a graphical user interface based on *Qt* widget toolkit, which enables the implementation of client-side applications, a complete *HTTP web server*, which allows the creation of web pages or web services, and a *Universal Plug and Play* (UPnP) module, which enables seamless interactions with other UPnP devices possibly available on the same local network.

All components and services that the framework implements and supports are exposed through an abstract API. Multimedia functionalities are provided by *pipelines*, which can be instantiated both by the framework and by its add-ins. Each pipeline is responsible for streaming an incoming data source to a target data sink. Transcoding is automatically handled by the framework as long as the source and sink components are properly described. Users of the framework never have to directly interact with the underlying *GStreamer* implementation, dealing only with abstract high-level descriptions of incoming and outgoing streams.

The API and the add-in system enable third-party developers and end-users to create their own plug-ins (or *extension points*) which can exploit all the multimedia handling capabilities of *openBOXware*. The system provides for three kinds of extension points:

- *Application*, the most powerful kind of extension point. Like the others it can be individually started and terminated, but it is the only one capable of interacting directly with the end-user through a custom graphical user interface. The extension point obtains a graphical context in which it can render itself, providing a custom-tailored user experience while still being able to integrate and exploit any other *openBOXware* functionality.
- *MediaSource*, used to expose a collection of media elements to the rest of the framework. Examples of media elements include Internet TV channels, web radios, online multimedia contents, or directories of resources local to the device or made available by other UPnP devices. These elements are then shared with the framework and with other applications in such a way that they can be explored as a hierarchical tree of multimedia resources. Each media element contains an abstract description of the resource it rep-

resents, specifying how the stream must be retrieved and how it must be decoded by the framework. *OpenBOXware* provides built-in support to the most common resources, including HTTP, TCP and UDP streams. Common multimedia streaming protocols like Adobe RTMP, Microsoft MMS, and RTSP are supported as well. The actual contents of the multimedia stream can be detected automatically by the framework or can be defined explicitly by the MediaSource developer. Once the resource is fully described through the API, the framework can automatically handle all needed transcoding and the user has only to deal with the abstract media element object.

- *MediaTarget*, used to expose a local or remote endpoint, capable of receiving a multimedia stream (encoded in a certain format with specific properties) and playing it back. A single media target is composed of a video target, an audio target and a muxing target, which together define how the final stream must be encoded by the framework to match the specification. The muxing target determines how the audio and video sub-streams are combined together in a data stream that can be parsed by the receiving end (common supported container formats include Matroska, MP4 and FLV). Video and audio streams are encoded separatedly using the specification provided by the respective sub-targets: encoding format, bitrate, and any other property of the final data stream.

Any application can bind a MediaSource to a MediaTarget in a pipeline and start streaming data from the source to the target while the framework automatically takes care of the transcoding steps possibly required to adapt the stream to the target of choice.

B. Multicast TV on top of openBOXware

OpenBOXware is a general handler of multimedia flows streamed from heterogeneous sources to both local and remote targets. The capability of handling multiple simultaneous pipelines makes it suitable for *openBOXware* to be installed not only at the receiving end point, but also at the initial and intermediate nodes of a content delivery network. In particular, *openBOXware* provides a common framework for implementing all the software elements of the proof-of-concept outlined in Section IV-B: both the proxy server and the client-side application receiving the multicast stream could be implemented as *openBOXware* Applications, while the heterogeneous Internet TV sources could be implemented as independent MediaSources to be streamed to specific multicast groups, implemented as a MediaTargets.

A possible implementation of the proof of concept architecture on top of *openBOXware* is outlined in the rest of this section.

All the TV channels and media contents available are exposed as independent MediaSources to the instance of the framework running on the proxy server. The hierarchy of media elements is made available to the proxy front-end Application which makes use of the built-in web server in order to publish dynamic pages which allow end-users to browse the registered media sources by means of a simple web browser. The framework relies on an extensible list of content providers to make any new content available as soon as the corresponding add-in is installed on the proxy server.

Similarly to what happened in the original proof-of-concept implementation, when a play request reaches the web server (i.e., the front-end), the proxy application creates a pipeline for the selected media element and starts streaming it to a multicast group address. Clients may then receive the audio and video streams by interpreting the SDP descriptor file that is returned via HTTP by the proxy.

Although a standard web browser and a common media player can be used to select and receive contents from the proxy, specific client-side Applications can be developed on top of *openBOXware* to offer to the end-user custom interfaces and advanced features to browse and watch TV channels streamed through the proxy server. In our implementation, the server exposes an additional interface, other than the one dedicated to web browsers, in the form of a *REST* web service that responds with *JSON* encoded data. The JSON file is parsed and interpreted by the client application, which provides the user interface and the access control mechanisms. When a channel (or a media element) is selected, an HTTP request is issued that determine the web service running on the proxy to launch the stream and return the SDP file describing the streaming session the client can tune into. On the client side, the streams are received through a *GStreamer* pipeline and decoded locally.

VI. Conclusions

This paper has presented real-world experiments demonstrating the feasibility of multicast transmission of HD TV channels over the wireless point-to-multipoint connections often adopted in metro networks to bridge digital divide and to provide nomadic connectivity. The proposed solution makes use of two key components: a proxy, which acts as a client for the unicast TV channels available on the Internet and makes them locally available at specific multicast groups, and enhanced wireless equipment providing adequate support to multicast multimedia communication within the IEEE 802.11 framework.

The results of the proof-of-concept experiments outlined in this paper prompt for the development of new application-level solutions and market strategies aimed at enabling massive diffusion of Internet TV channels [21].

According to the neutral-access-network model [15], the diffusion of a popular and well understood application (such as television) over IP networks could play a fundamental role to enhance broadband penetration and to motivate investments in next-generation networks.

A suitable support for the development of advanced IPTV delivery systems over managed IP networks is provided by *openBOXware*, an extensible open-source multimedia framework specifically conceived to bridge the gap between the proof-of-concept presented in this paper and real-world multicast IPTV applications [20].

Acknowledgment

The research leading to these results has received funding from the EU IST Seventh Framework Programme ([FP7/2007-2013]) under grant agreement n 25741, project ULOOP (User-centric Wireless Local Loop).

References

[1] A. Seraghiti, L. Klopfenstein, S. Bonino, A. Tarasconi, and A. Bogliolo, "Multicast TV Channels over Wireless Neutral Access Networks," in *Proceedings of Conference on Evolving Internet (INTERNET-10)*, 2010, pp. 153–158.

[2] Y. Xiao, X. Du, J. Zhang, F. Hu, and S. Guizani, "Internet Protocol Television (IPTV): The Killer Application for the Next-Generation Internet," *IEEE Communications Magazine*, vol. 45, no. 11, pp. 126–134, 2007.

[3] R. Jain, "Quality of Experience," *IEEE Multimedia*, vol. 11, no. 1, pp. 95–96, 2004.

[4] Akamai, "The State of the Internet: 3rd Quarter, 2010 Report," *Akamai White Paper*, vol. 3, no. 3, 2011.

[5] Cisco, "Cisco Visual Networking Index: Forecast and Methodology, 2009-2014," *Cisco White Paper*, 2010.

[6] ——, "Global IP Traffic Forecast and Methodology," *Cisco White Paper*, 2008.

[7] Broadband Working Group, "The Broadband Incentive Problem," *MIT Communications Futures Program White Paper*, September 2005.

[8] J. E. Prieger and W.-M. Hu, "The broadband digital divide and the nexus of race, competition, and quality," *Information Economics and Policy*, vol. 20, no. 2, pp. 150 – 167, 2008.

[9] K. Flamm and A. Chaudhuri, "An analysis of the determinants of broadband access," *Telecommun. Policy*, vol. 31, no. 6-7, pp. 312–326, 2007.

[10] M. Cha, P. Rodriguez, J. Crowcroft, S. Moon, and X. Amatriain, "Watching Television Over an IP Network," in *Proceedings of IMC-08*, 2008, pp. 71–83.

[11] S. Turner, "Broadband Reality Check II: The Truth Behind America's Digital Decline," *Free Press*, 2006.

[12] R. Battiti, R. Lo Cigno, M. Sabel, F. Orava, and B. Pehrson, "Wireless LANs: From WarChalking to Open Acess Networks," *Mobile Networks and Applications*, vol. 10, pp. 175–287, 2005.

[13] J. Barcelo, J. Infante, and M. Oliver, "wireless Open Access Networks: State-of-the-Art and Technological Opportunities," in *Proceedings of INTERNET-09*, 2009.

[14] V. Kordas, E. Frankenberg, S. Grozev, B. L. N. Zhou, and B. Pehrson, "Who Should Own, Operate and Maintain an Opeartor Neutral Access Network?" in *LANMAN2002: IEEE Workshop on Local and Metropolitan Area Networks*, 2002.

[15] A. Bogliolo, "Introducing Neutral Access Networks," in *Proceedings of Int.l Conference on Next Generation Internet Networks (NGI 2009)*, 2009.

[16] J. C. Francis, N. Elnegaard, T. G. Eskedal, and R. Venturin, "Business Opportunities of Open Broadband Wireless Access Networks," in *Proceedings of Int.l Workshop on Broadband Wireless Access for Ubiquitous Networking*, 2006.

[17] M. Garcia, J. Lloret, M. Edo, and R. Lacuesta, "IPTV Distribution Network Access System Using WiMAX and WLAN Technologies," in *Proceedings of UPGRADE-CN*, 2009, pp. 35–44.

[18] L. Cai, Y. Luo, S. Xiang, and J. Pan, "Scalable modulation for scalable wireless videocast," in *Proceedings of IEEE Infocom-10*, 2010.

[19] A. Bogliolo, "Urbino Wireless Campus: A Wide-Area University Wireless Network to Bridge Digital Divide," in *Proceedings of AccessNets-07*, 2007, pp. 1–6.

[20] A. Bogliolo *et al.*, "The openBOXware project," http://www.openboxware.net/trac/, 2010.

[21] A. Bogliolo, "Video logs of Wireless Multicast TV experiments," http://www.youtube.com/view_play_list?p=824B2CA538D70C6E, 2010.

The Outage Probability of the Satellite Telecommunication System in the Presence of Fading with Switch and Stay Combining on Satellite and Earth Station

Dragana Krstić
Department of Telecommunications,
Faculty of Electronic Engineering,
University of Niš
Aleksandra Medvedeva 14
Niš, Serbia
dragana.krstic@elfak.ni.ac.rs

Petar Nikolić
Tigartyres, Pirot, Serbia
nik.petar@gmail.com

Mihajlo Stefanović
Faculty of Electronic Engineering
University of Niš
Niš, Serbia
mihajlo.stefanovic@elfak.ni.ac.rs

***Abstract*—In this paper, the satellite communication system consisting of the earth transmitting station and the satellite transponder was considered. Switch and Stay Combining (SSC) diversity technics are used on receiving satellite and receiving earth stations to reduce fading influence to the system performances. The presence of Nakagami-*m* and Rice fading on receiving satellite and receiving earth stations is observed. The probability density functions (PDFs) of the signal at the Earth receiver station output are determined for different parameters. The outage probability, as standard performance criterion of communication systems operating over fading channels, is calculated under upper conditions. The results are shown graphically in several figures and made to assess the influence of various parameters. This is very useful for mitigation the influence of fading in the design of satellite communication systems in the presence of fading**

Keywords- satellite telecommunication system; Nakagami-m fading; Rice fading; SSC combining; probability density function; the outage probability.

I. INTRODUCTION

Satellite communication systems are now a major part of most telecommunications networks as well as every-day lives through mobile personal communication systems and broadcast television [2]. A fundamental understanding of such systems is therefore important for a wide range of system designers, engineers and users.

The fading and shadow effect are factors which degrade the system performances in telecommunication systems at the most. They derogate the power of transmitted signal. When a received signal experiences shadow effect or fading during transmission, its envelope and phase fluctuate over time. The most often are Rayleigh, Rice, Nakagami, Weibull and log-normal fading, and they are considered in the literature [3], [4].

Rayleigh and Rice distributions can be used to model the envelope of fading channels in many cases of interest The Rice fading is present very often in wireless telecommunication systems with direct line of site. When the fading appeared in the channel because of signal propagation by more paths, and dominate component exists because of optical visibility from transmitter to receiver, signal amplitude is modeled by Rice distribution [5]. It has been found experimentally, that Nakagami distribution offers better fit for wider range of fading conditions in wireless communications [6].

In wireless communication systems, various techniques for reducing fading effect and influence of shadow effect are used. Such techniques are diversity reception, dynamic channel allocation and power control. Upgrading transmission reliability and increasing channel capacity without increasing transmission power and bandwidth is the main goal of diversity techniques.

Diversity reception, based on using multiple antennas at the receiver, space diversity, with two or more branches, is very efficient methods used for improving system's quality of service, so it provides efficient solution for reduction of signal level fluctuations in fading channels. Multiple received copies of signal could be combined on various ways.

Several principal types of combining techniques can be generally performed by their dependence on complexity restriction put on the communication system and amount of channel state information available at the receiver. Combining techniques like maximal ratio combining (MRC) and equal gain combining (EGC) require all or some of the amount of the channel state information of received signal. Second, MRC and EGC require separate receiver chain for each branch of the diversity system, which increase its complexity of system.

Maximal-Ratio Combining (MRC) is one of the most widely used diversity combining schemes whose SNR is the sum of the SNR's of each individual diversity branches. MRC is the optimal combining scheme, but its price and complexity are higher. Also, MRC requires cognition of all channel parameters and admit in the same phase all input signals, because it is the most complicated for realization [7]-[9].

Signal at the EGC diversity system output is equal to the sum of its' input signals. The input signals should be admitted in the same phase, but it is not necessary to know the channel parameters. Therefore, EGC provides comparable performances to MRC technique, but has lower implementation complexity; therefore, it is an intermediate solution [10].

One of the least complicated combining methods is selection combining (SC). In opposition to previous combining techniques, SC receiver processes only one of the diversity branches, and it is much simpler for practical realization. Generally, selection combining, selects the branch with the highest signal-to-noise ratio (SNR), that is the branch with the strongest signal [10], [11], assuming that noise power is equally distributed over branches. Abu-Dayya and Beaulieu in [12] consider switched diversity on microcellular Ricean channels.

Similarly to the previous approaches, there is type of selection combining that chooses the branch with highest signal and noise sum. In fading environments, where the level of the cochannel interference is sufficiently high comparing with the thermal noise, SC selects the branch with the highest signal-to-interference ratio (SIR-based selection diversity) [13].

Switch and stay combining (SSC) is an attempt at simplifying the complexity of the system but with loss in performance. In this case, rather than continually connecting the antenna with the best fading conditions, the receiver selects a particular antenna until its quality drops below a predetermined threshold. When this happens, the receiver switches to another antenna and stays with it for the next time slot, regardless of whether or not the channel quality of that antenna is above or below the predetermined threshold. The consideration of SSC systems in the literature has been restricted to low-complexity mobile units where the number of diversity antennas is typically limited to two [14], [15]. Furthermore, in all these publications, only predetection SSC has thus far been considered wherein the switching of the receiver between the two receiving antennas is based on a comparison of the instantaneous SNR of the connected antenna with a predetermined threshold. This results in a reduction in complexity relative to SC in that the simultaneous and continuous monitoring of both branches SNRs is no longer necessary.

II. Related Work

An analytical technique well suited to numerical analysis is presented for computing the average bit-error rate (BER) and outage probability of M-ary phase-shift keying (PSK) in the land-mobile satellite channel (LMSC) with microdiversity reception in [16]. The closed-form expressions are found for *L*-branch microdiversity using both selection diversity combining (SDC) and maximal ratio combining (MRC). These expressions are extended to include both M-ary coherent PSK (M-PSK) and differential PSK [M-differential PSK (DPSK)]. Following previous empirical studies, the LMSC is modeled as a weighted sum of Rice and Suzuki distributions. Numerical results are provided illustrating the achievable performance of both M-PSK and M-DPSK with diversity reception. Using measured channel parameters, the performance in various mobile environments for various satellite elevation angles is also found.

An exact analytical technique is presented for computing the average bit error rate (BER) and outage probability of differentially detected PSK in the land mobile satellite channel (LMSC) when L branch maximal ratio combining (MRC) is employed in [17]. Following empirical study, the LMSC is modeled as a weighted sum of Rice and Suzuki distributions.

Empirical studies confirm that the received radio signals in certain cellular systems are well modeled by Nakagami statistics. Therefore, performing relevant systems studies can be potentially useful to a system designer. A very useful statistical measure for characterizing the performance of a mobile radio system is the probability of outage, which describes the fraction of time that the signal-to-interference ratio (SIR) drops below some threshold. A more refined criterion for the outage is the failure to simultaneously obtain a sufficient SIR and a minimum power level for the desired signal. Thus, in [18] the authors derived new expressions for the probability of outage where a mobile unit receives a Nakagami desired signal and multiple, independent, cochannel Nakagami interferers. A salient feature of their results is that the outage expressions do not restrict the Nakagami fading parameter, *m*, to strictly integer values. Furthermore, since the received signals in mobile radio also experience log-normal shadowing, they analyzed the case where the received signals are modeled by a composite of Nakagami and log-normal distributions. The outage probabilities are computed and graphically presented for several cases. The effect of specifying a minimum signal requirement for adequate reception is found to introduce a floor on the outage probability. It is also found that shadowing in macrocellular systems severely degrades the desired quality of service by increasing the reuse distance necessary for a given outage level.

In this paper, the satellite communication system consisting of the earth transmitting station and the satellite transponder was considered. SSC diversity technics are used on receiving satellite and receiving earth stations to reduce fading influence to the system performances. The presence of Nakagami-*m* fading on receiving satellite and receiving earth stations is observed in [1], and the presence of Rice fading on both, receiving satellite and receiving earth stations is observed here. The probability density functions (PDFs) and the outage probability of the signal at the Earth receiver station output are given for different parameters.

Beside generally used first Section, introduction, and the last, conclusion, the paper has further four core sections. The second Section of the paper presents related works, the third one shows and interprets the system model. The statistics of the output SNR is given in the fourth Section and numerical results in the fifth one.

III. System Model

The use of SSC combiner with great number of branches can minimize the bit error rate (BER) [19]. We determined

SSC combiner with two inputs because the gain is the greatest when we use the SSC combiner with two inputs instead of one-channel system. When we enlarge the number of inputs (branches) the gain becomes less. Because of that it is more economic using SSC combiner with two inputs.

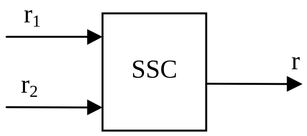

Figure 1. Model of the SSC combiner with two inputs

The model of this system is shown in Figure 1. The signals at the combiner input are r_1 and r_2, and r is the combiner output signal. Let see how the SSC combiner with two inputs works.

The probability of the event that the combiner first examines the signal at the first input is P_1, and for the second input is P_2. If the combiner examines first the signal at the first input and if the value of the signal at the first input is above the treshold, r_T, SSC combiner forwards this signal to the circuit for the decision. If the value of the signal at the first input is below the treshold r_T, SSC combiner forwards the signal from the other input to the circuit for the decision, regardless it is above or below the predetermined threshold. If the SSC combiner first examines the signal from the second combiner input it works in the similar way. The probability for the first input to be examined first is P_1 and for the second input to be examined first is P_2.

There are two diversity branches on satellite and on Earth receiver station. The SSC combining is used on both, receiver satellite and Earth station. System model is shown in Figure 2

Let Nakagami-*m* fading is present on both, receiver satellite and Earth station. The signals at the input are A_1 and A_2. In this case the probability density of signal A, at the satellite station output, is, for $0<A<A_T$:

$$p_A(A) = P_{1A} p_{A_2}(A) F_{A1}(A_T) + P_{2A} p_{A_1}(A) F_{A2}(A_T) \tag{1}$$

and for $A_T<A$

$$p_A(A) = P_{1A} p_{A_1}(A) + P_{1A} p_{A_2}(A) F_{A1}(A_T) + \\ + P_{2A} p_{A_2}(A) + P_{2A} p_{A_1}(A) F_{A2}(A_T) \tag{2}$$

A_T is the threshold of the decision.

The probability density of signal a, at the Earth receiver station output is, for $0<a<a_T$:

$$p_a(a) = P_{1a} p_{a_2}(a) F_{a1}(a_T) + P_{2a} p_{a_1}(a) F_{a2}(a_T) \tag{3}$$

and for $a_T<a$:

$$p_a(a) = P_{1a} p_{a_1}(a) + P_{1a} p_{a_2}(a) F_{a1}(a_T) + \\ + P_{2a} p_{a_2}(a) + P_{2a} p_{a_1}(a) F_{a2}(a_T) \tag{4}$$

The signals at the input are a_1 and a_2, a_T is the threshold of the decision.

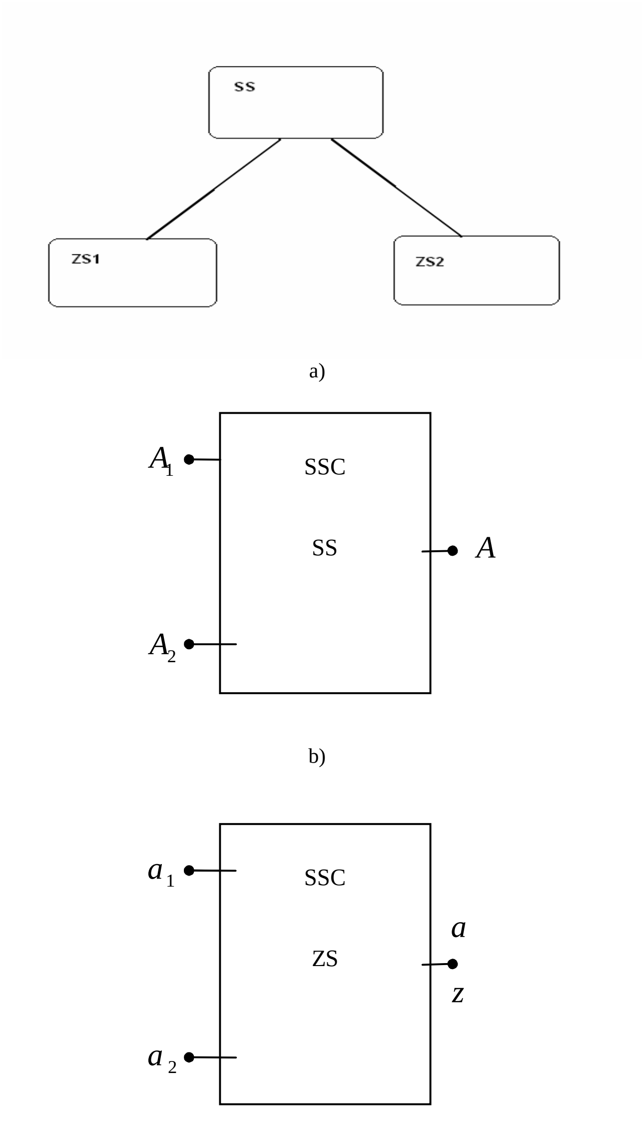

Figure 2. System model - a) entire system; b) Satellite Station (SS); c) Earth Station (ZS)

The signal z at the Earth receiver station output is [2]:

$$z = a\cos\varphi + y_1 = a\frac{A + x_1}{\sqrt{(A + x_1)^2 + y_1^2}} + y_1 \tag{5}$$

where x_1 and y_1 are the Gaussian components in phase and quadrature, respectively.

The conditional probability density of the signal z is:

$$p_z(z/x_1,y_1,A,a)=\frac{1}{\sqrt{2\pi}\sigma_2}e^{-\frac{\left[z-f_1(a,A,x_1,y_1)\right]^2}{2\sigma_2{}^2}} \tag{6}$$

where σ_i, i=1,2, are standard deviation of appropriate variables.

The probability density of the signal z is:

$$p_z(z)=\int dx_1\int dy_1\int da\int dA\frac{1}{\sqrt{2\pi}\sigma_2}e^{-\frac{\left[z-f_1(a,A,x_1,y_1)\right]^2}{2\sigma_2{}^2}}\cdot$$
$$\cdot p_A(A)\,p_a(a)\,p_{x_1y_1}(x_1,y_1) \tag{7}$$

The joint probability density of the Gaussian components x_1 and y_1 is:

$$p_{x_1y_1}(x_1,y_1)=\frac{1}{2\pi\sigma_1{}^2}e^{-\frac{x_1{}^2+y_1{}^2}{2\sigma_1{}^2}} \tag{8}$$

The function $f_1(a,A,x_1,y_1)$ is defined with:

$$f_1(a,A,x_1,y_1)=a\frac{A+x_1}{\sqrt{(A+x_1)^2+y_1{}^2}} \tag{9}$$

The probability density of output signal z, after some substitutions, is:

$$p_z(z)=\int_{-\infty}^{+\infty}dx_1\int_{-\infty}^{+\infty}dy_1\int_0^{+\infty}da\int_0^{+\infty}dA\frac{1}{\sqrt{2\pi}\sigma_2}\cdot$$
$$\cdot e^{-\frac{\left[z-f_1(a,A,x_1,y_1)\right]^2}{2\sigma_2{}^2}}\frac{1}{2\pi\sigma_1{}^2}e^{-\frac{x_1{}^2+y_1{}^2}{2\sigma_1{}^2}}p_a(a)p_A(A)=$$
$$=\int_{-\infty}^{+\infty}dx_1\int_{-\infty}^{+\infty}dy_1\int_0^{a_T}da\int_0^{A_T}dA\frac{1}{\sqrt{2\pi}\sigma_2}\cdot$$
$$\cdot e^{-\frac{\left[z-f_1(a,A,x_1,y_1)\right]^2}{2\sigma_2{}^2}}\frac{1}{2\pi\sigma_1{}^2}e^{-\frac{x_1{}^2+y_1{}^2}{2\sigma_1{}^2}}\cdot$$
$$\cdot[P_{1A}p_{A_2}(A)F_{A1}(A_T)+P_{2A}p_{A_1}(A)F_{A2}(A_T)]\cdot$$
$$\cdot[P_{1a}p_{a_2}(a)F_{a1}(a_T)+P_{2a}p_{a_1}(a)F_{a2}(a_T)]+$$
$$+\int_{-\infty}^{+\infty}dx_1\int_{-\infty}^{+\infty}dy_1\int_{a_T}^{+\infty}da\int_0^{A_T}dA\frac{1}{\sqrt{2\pi}\sigma_2}\cdot$$
$$\cdot e^{-\frac{\left[z-f_1(a,A,x_1,y_1)\right]^2}{2\sigma_2{}^2}}\frac{1}{2\pi\sigma_1{}^2}e^{-\frac{x_1{}^2+y_1{}^2}{2\sigma_1{}^2}}\cdot$$
$$\cdot[P_{1A}p_{A_2}(A)F_{A1}(A_T)+P_{2A}p_{A_1}(A)F_{A2}(A_T)]\cdot$$
$$\cdot[P_{1a}p_{a_1}(a)+P_{1a}p_{a_2}(a)F_{a1}(a_T)+$$
$$+P_{2a}p_{a_2}(a)+P_{2a}p_{a_1}(a)F_{a2}(a_T)]+$$
$$+\int_{-\infty}^{+\infty}dx_1\int_{-\infty}^{+\infty}dy_1\int_0^{a_T}da\int_{A_T}^{+\infty}dA\frac{1}{\sqrt{2\pi}\sigma_2}\cdot$$
$$\cdot e^{-\frac{\left[z-f_1(a,A,x_1,y_1)\right]^2}{2\sigma_2{}^2}}\frac{1}{2\pi\sigma_1{}^2}e^{-\frac{x_1{}^2+y_1{}^2}{2\sigma_1{}^2}}\cdot$$
$$\cdot[P_{1A}p_{A_1}(A)+P_{1A}p_{A_2}(A)F_{A1}(A_T)+$$
$$+P_{2A}p_{A_2}(A)+P_{2A}p_{A_1}(A)F_{A2}(A_T)]\cdot$$
$$\cdot[P_{1a}p_{a_2}(a)F_{a1}(a_T)+P_{2a}p_{a_1}(a)F_{a2}(a_T)]+$$
$$+\int_{-\infty}^{+\infty}dx_1\int_{-\infty}^{+\infty}dy_1\int_{a_T}^{+\infty}da\int_{A_T}^{+\infty}dA\frac{1}{\sqrt{2\pi}\sigma_2}\cdot$$
$$\cdot e^{-\frac{\left[z-f_1(a,A,x_1,y_1)\right]^2}{2\sigma_2{}^2}}\frac{1}{2\pi\sigma_1{}^2}e^{-\frac{x_1{}^2+y_1{}^2}{2\sigma_1{}^2}}\cdot$$
$$\cdot[P_{1A}p_{A_1}(A)+P_{1A}p_{A_2}(A)F_{A1}(A_T)+$$
$$+P_{2A}p_{A_2}(A)+P_{2A}p_{A_1}(A)F_{A2}(A_T)]\cdot$$
$$\cdot[P_{1a}p_{a_1}(a)+P_{1a}p_{a_2}(a)F_{a1}(a_T)+$$
$$+P_{2a}p_{a_2}(a)+P_{2a}p_{a_1}(a)F_{a2}(a_T)] \tag{10}$$

The signals A_1, A_2, a_1, a_2 have Nakagami-m distributions:

$$p_{A_1}(A_1)=\frac{2m_1{}^{m_1}A_1{}^{2m_1-1}}{\Omega_1{}^{m_1}\Gamma(m_1)}e^{-\frac{m_1A_1{}^2}{\Omega_1}} \tag{11}$$

$$p_{A_2}(A_2)=\frac{2m_2{}^{m_2}A_2{}^{2m_2-1}}{\Omega_2{}^{m_1}\Gamma(m_2)}e^{-\frac{m_2A_2{}^2}{\Omega_1}} \tag{12}$$

$$p_{a_1}(a_1) = \frac{2{m_3}^{m_3} {a_1}^{2m_3-1}}{{\Omega_3}^{m_3}\Gamma(m_3)} e^{-\frac{m_3 {a_1}^2}{\Omega_3}} \quad (13)$$

$$p_{a_2}(a_2) = \frac{2{m_4}^{m_4} {a_2}^{2m_4-1}}{{\Omega_4}^{m_4}\Gamma(m_4)} e^{-\frac{m_4 {a_2}^2}{\Omega_4}} \quad (14)$$

The signals for up and down links are not simetrical.

There is two parameters of Nakagami-*m* distribution: a shape parameter *m*, and a second parameter controlling spread, *Ω*.

The cumulative probability densities (CDFs) are given by:

$$F_{A_1}(A_1) = \gamma\left(\frac{m_1}{\Omega_1}{A_1}^2, m_1\right) \quad (15)$$

$$F_{A_2}(A_2) = \gamma\left(\frac{m_2}{\Omega_2}{A_2}^2, m_2\right) \quad (16)$$

$$F_{a_1}(a_1) = \gamma\left(\frac{m_3}{\Omega_3}{A_3}^2, m_3\right) \quad (17)$$

$$F_{a_2}(a_2) = \gamma\left(\frac{m_4}{\Omega_4}{A_4}^2, m_4\right) \quad (18)$$

where $\gamma\ (x,\ a)$ is incomplete gamma function defined by [20].

After putting the expressions (11) to (18) into (10) we obtain the probability density of the output signal *z* in the presence of Nakagami-*m* fading.. The other system performances could be calculated by means of the output signal probability density function.

When the signals A_1, A_2, a_1, a_2 have Rice distributions, probability density functions are [11]:

$$p_{A_1}(A_1) = \frac{A_1}{{\sigma_{A_1}}^2} e^{-\frac{{A_1}^2 + {\Omega_{A_1}}^2}{2{\sigma_{A_1}}^2}} I_0\left(\frac{A_1 \Omega_{A_1}}{{\sigma_{A_1}}^2}\right) \quad (19)$$

$$p_{A_2}(A_2) = \frac{A_2}{{\sigma_{A_2}}^2} e^{-\frac{{A_2}^2 + {\Omega_{A_2}}^2}{2{\sigma_{A_2}}^2}} I_0\left(\frac{A_2 \Omega_{A_2}}{{\sigma_{A_2}}^2}\right) \quad (20)$$

$$p_{a_1}(a_1) = \frac{a_1}{{\sigma_{a_1}}^2} e^{-\frac{{a_1}^2 + {\Omega_{a_1}}^2}{2{\sigma_{a_1}}^2}} I_0\left(\frac{a_1 \Omega_{a_1}}{{\sigma_{a_1}}^2}\right) \quad (21)$$

$$p_{a_2}(a_2) = \frac{a_2}{{\sigma_{a_2}}^2} e^{-\frac{{a_2}^2 + {\Omega_{a_2}}^2}{2{\sigma_{a_2}}^2}} I_0\left(\frac{a_2 \Omega_{a_2}}{{\sigma_{a_2}}^2}\right) \quad (22)$$

The parameters of Rice distribution are the signal amplitudes *Ω* and variances *σ*.

The cumulative probability densities (CDFs) for Rice distribution are given by:

$$F_{A_1}(A_1) = 1 - Q\left(\Omega_{A_1}/\sigma_{A_1}, A_1/\sigma_{A_1}\right) \quad (23)$$

$$F_{A_2}(A_2) = 1 - Q\left(\Omega_{A_2}/\sigma_{A_2}, A_2/\sigma_{A_2}\right) \quad (24)$$

$$F_{a_1}(a_1) = 1 - Q\left(\Omega_{a_1}/\sigma_{a_1}, a_1/\sigma_{a_1}\right) \quad (25)$$

$$F_{a_2}(a_2) = 1 - Q\left(\Omega_{a_2}/\sigma_{a_2}, a_2/\sigma_{a_2}\right) \quad (26)$$

Q(a,b) is the Marcum Q function defined as [21]:

$$Q(a,b) = \int_b^\infty t \exp\left[-\frac{t^2 + a^2}{2}\right] I_0(at)\,dt \quad (27)$$

After putting the expressions (19) to (28) into (10) we obtain the probability density of the output signal *z* in the presence of Rice fading.

IV. System Performances

The obtained expressions for the probability density function (PDF) of the output signal after diversity combining can be used to study the moments, the amount of fading, the outage probability and the average bit error rate of proposed system.

The outage probability P_{out} is standard performance criterion of communication systems operating over fading channels. This performance measure is commonly used to control the noise or cochannel interference level, helping the designers of wireless communications system's to meet the quality-of-service (QoS) and grade of service (GoS) demands.

In the interference-limited environment, the outage probability P_{out} is defined as the probability which combined SIR falls below a given outage threshold γ_T, also known as a protection ratio. Protection ratio depends on modulation technique and expected QoS.

The outage probability, $P_{out}(r_{th})$, is defined as:

$$P_{out}(z_{th}) = \int_0^{z_{th}} p_z(z)\,dz\ . \quad (28)$$

After putting $p_z(z)$ from (10), the outage probability can be expressed as

$$P_{out}(r_{th}) = \int_0^{r_{th}} dz \int_{-\infty}^{+\infty} dx_1 \int_{-\infty}^{+\infty} dy_1 \int_0^{+\infty} da \int_0^{+\infty} dA \frac{1}{\sqrt{2\pi}\sigma_2} \cdot$$

$$\cdot e^{-\frac{[z - f_1(a,A,x_1,y_1)]^2}{2\sigma_2^2}} \frac{1}{2\pi\sigma_1^2} e^{-\frac{x_1^2+y_1^2}{2\sigma_1^2}} p_a(a) p_A(A) =$$

$$= \int_0^{r_{th}} dz \int_{-\infty}^{+\infty} dx_1 \int_{-\infty}^{+\infty} dy_1 \int_0^{a_T} da \int_0^{A_T} dA \frac{1}{\sqrt{2\pi}\sigma_2} \cdot$$

$$\cdot e^{-\frac{[z - f_1(a,A,x_1,y_1)]^2}{2\sigma_2^2}} \frac{1}{2\pi\sigma_1^2} e^{-\frac{x_1^2+y_1^2}{2\sigma_1^2}} \cdot$$

$$\cdot [P_{1A} p_{A_2}(A) F_{A1}(A_T) + P_{2A} p_{A_1}(A) F_{A2}(A_T)] \cdot$$

$$\cdot [P_{1a} p_{a_2}(a) F_{a1}(a_T) + P_{2a} p_{a_1}(a) F_{a2}(a_T)] +$$

$$+ \int_0^{r_{th}} dz \int_{-\infty}^{+\infty} dx_1 \int_{-\infty}^{+\infty} dy_1 \int_{a_T}^{+\infty} da \int_0^{A_T} dA \frac{1}{\sqrt{2\pi}\sigma_2} \cdot$$

$$\cdot e^{-\frac{[z - f_1(a,A,x_1,y_1)]^2}{2\sigma_2^2}} \frac{1}{2\pi\sigma_1^2} e^{-\frac{x_1^2+y_1^2}{2\sigma_1^2}} \cdot$$

$$\cdot [P_{1A} p_{A_2}(A) F_{A1}(A_T) + P_{2A} p_{A_1}(A) F_{A2}(A_T)] \cdot$$

$$\cdot [P_{1a} p_{a_1}(a) + P_{1a} p_{a_2}(a) F_{a1}(a_T) +$$

$$+ P_{2a} p_{a_2}(a) + P_{2a} p_{a_1}(a) F_{a2}(a_T)] +$$

$$+ \int_0^{r_{th}} dz \int_{-\infty}^{+\infty} dx_1 \int_{-\infty}^{+\infty} dy_1 \int_0^{a_T} da \int_{A_T}^{+\infty} dA \frac{1}{\sqrt{2\pi}\sigma_2} \cdot$$

$$\cdot e^{-\frac{[z - f_1(a,A,x_1,y_1)]^2}{2\sigma_2^2}} \frac{1}{2\pi\sigma_1^2} e^{-\frac{x_1^2+y_1^2}{2\sigma_1^2}} \cdot$$

$$\cdot [P_{1A} p_{A_1}(A) + P_{1A} p_{A_2}(A) F_{A1}(A_T) +$$

$$+ P_{2A} p_{A_2}(A) + P_{2A} p_{A_1}(A) F_{A2}(A_T)] \cdot$$

$$\cdot [P_{1a} p_{a_2}(a) F_{a1}(a_T) + P_{2a} p_{a_1}(a) F_{a2}(a_T)] +$$

$$+ \int_0^{r_{th}} dz \int_{-\infty}^{+\infty} dx_1 \int_{-\infty}^{+\infty} dy_1 \int_{a_T}^{+\infty} da \int_{A_T}^{+\infty} dA \frac{1}{\sqrt{2\pi}\sigma_2} \cdot$$

$$\cdot e^{-\frac{[z - f_1(a,A,x_1,y_1)]^2}{2\sigma_2^2}} \frac{1}{2\pi\sigma_1^2} e^{-\frac{x_1^2+y_1^2}{2\sigma_1^2}} \cdot$$

$$\cdot [P_{1A} p_{A_1}(A) + P_{1A} p_{A_2}(A) F_{A1}(A_T) +$$

$$+ P_{2A} p_{A_2}(A) + P_{2A} p_{A_1}(A) F_{A2}(A_T)] \cdot$$

$$\cdot [P_{1a} p_{a_1}(a) + P_{1a} p_{a_2}(a) F_{a1}(a_T) +$$

$$+ P_{2a} p_{a_2}(a) + P_{2a} p_{a_1}(a) F_{a2}(a_T)] \qquad (29)$$

For binary phase shift keying (BPSK) modulation scheme, the bit error rate (BER) is given by

$$P_b(e) = \int_0^{\infty} P_b(e/\gamma) p_\gamma(\gamma) d\gamma \qquad (30)$$

where $P_b(e/\gamma)$ is conditional BER and $p(\gamma)$ is the PDF of the instantaneous SNR. $P_b(e/\gamma)$ can be expressed in terms of the Gaussian Q-function as

$$P_b(e/\gamma) = Q\left(\sqrt{2g\gamma}\right); \qquad (31)$$

Q is the one-dimensional Gaussian Q-function

$$Q(x) = \frac{1}{\sqrt{2\pi}} \int_x^{\infty} e^{-t^2/2} dt\,. \qquad (32)$$

Gaussian Q-function can be defined using alternative form as

$$Q(x) = \frac{1}{\pi} \int_0^{\pi/2} \exp\left(-\frac{x^2}{2\sin^2\phi}\right) d\phi \cdot \qquad (33)$$

For coherent BPSK modulation parameter g is determined as $g=1$ and $P_b(e/\gamma)$ is given by

$$P_b(e/\gamma) = Q\left(\sqrt{2\gamma}\right). \qquad (34)$$

V. NUMERICAL RESULTS

The probability density function curves (PDFs), $p(z)$, of the signal z at the Earth receiver station output, in the presence of Nakagami-m fading are given in Figures 3 to 6 for diferent parameters.

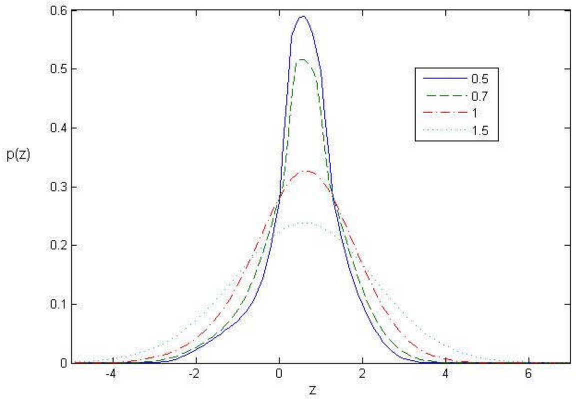

Figure 3. The probability density function $p(z)$ for Nakagami-m fading present on receiver satellite and Earth station, for different parameters: $\sigma_1 = 1, \sigma_2 = 0.5, 0.7, 1, 1.5,$
$m_1 = m_2 = 1, \Omega_1 = \Omega_2 = 1, m_3 = m_4 = 1, \Omega_3 = \Omega_4 = 1, a_t = 2, A_t = 2$

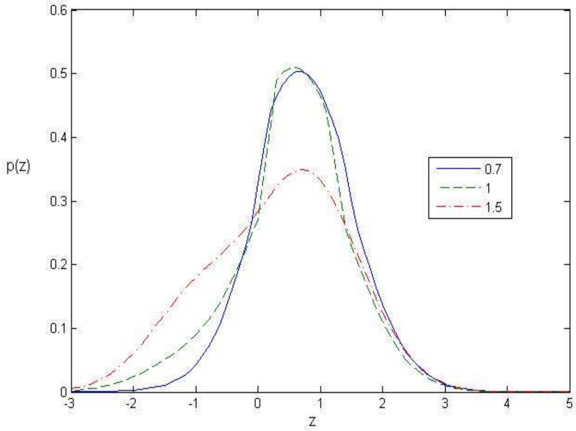

Figure 4. The probability density function $p(z)$ for Nakagami-m fading present on receiver satellite and Earth station, for different parameters:
$\sigma_1 = 0.7, 1, 1.5, \sigma_2 = 0.7, m_1 = m_2 = 1, \Omega_1 = \Omega_2 = 1, m_3 = m_4 = 1, \Omega_3 = \Omega_4 = 1,$
$\alpha_t = 1, A_t = 1$

We can see from these figures the influence of two parameters of Nakagami-m distribution, a shape parameter, m, and a second parameter, Ω, the standard deviations σ_i, and the signal amplitudes A_1, A_2, a_1 and a_2.

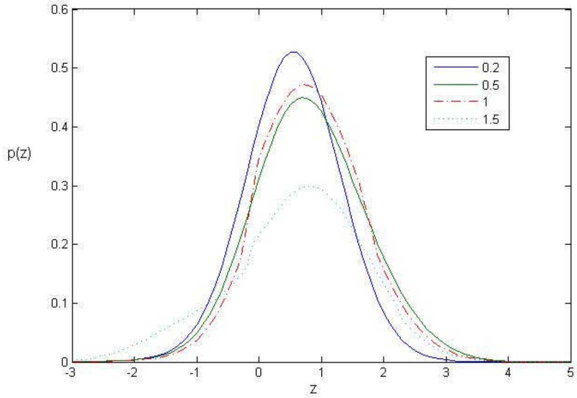

Figure 5. The probability density function $p(z)$ for Nakagami-m fading present on receiver satellite and Earth station, for different parameters: $\sigma_1 = 0.7, \sigma_2 = 0.7, , m_1 = m_2 = 1, \Omega_1 = \Omega_2 = 0.2, 0.5, 1, 1.5, m_3 = m_4 = 1,$
$\Omega_3 = \Omega_4 = 1, \alpha_t = 1, A_t = 1$

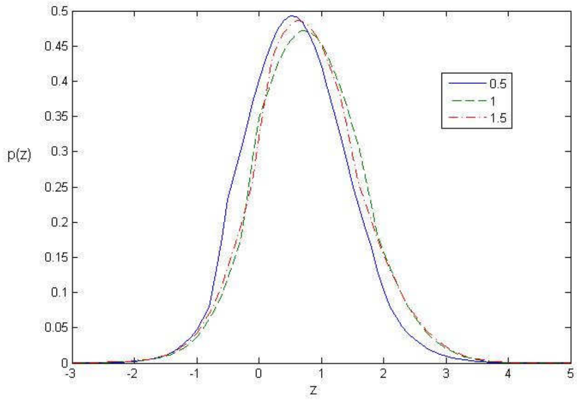

Figure 6. The probability density function $p(z)$ for Nakagami-m fading present on receiver satellite and Earth station, for different parameters: $\sigma_1 = 0.7, \sigma_2 = 0.7, , m_1 = m_2 = 1, \Omega_1 = \Omega_2 = 1, m_3 = m_4 = 1, \Omega_3 = \Omega_4 = 1, A_t = 1,$
$a_t = 0.5, 1, 1.5$

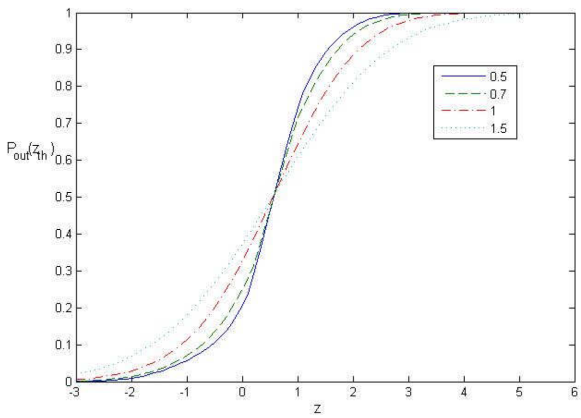

Figure 7. The outage probability $P_{out}(z)$ for Nakagami-m fading present on receiver satellite and Earth station, for different parameters:
$\sigma_1 = 1, \sigma_2 = 0.5, 0.7, 1, 1.5, m_1 = m_2 = 1, \Omega_1 = \Omega_2 = 1, m_3 = m_4 = 1, \Omega_3 = \Omega_4 = 1,$
$\alpha_t = 2, A_t = 2$

The outage probability curves $P_{out}(z)$, in the presence of Nakagami-*m* fading are given in Figures 7 and 8 for diferent parameters.

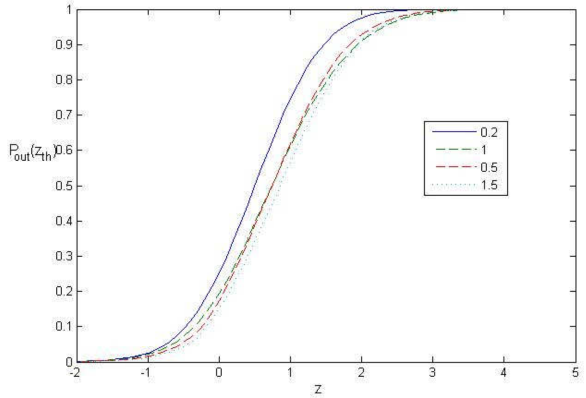

Figure 8. The outage probability $P_{out}(z)$ for Nakagami-*m* fading present on receiver satellite and Earth station, for different parameters: $\sigma_1=0.7$, $\sigma_2=0.7$, $m_1= m_2=1$, $\Omega_1= \Omega_2=0.2, 0.5, 1, 1.5$, $m_3= m_4=1$, $\Omega_3= \Omega_4=1$, $\alpha_t=1$, $A_t=1$

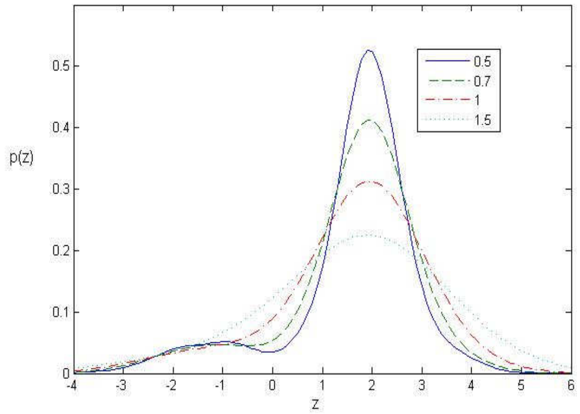

Figure 9. The probability density function $p(z)$ for Rice fading present on receiver satellite and Earth station, for different parameters: $\sigma_1 =1$, $\sigma_2 = 0.5, 0.7, 1, 1.5$, $\sigma_{A1} = \sigma_{A2} =1$, $\Omega_{A1} = \Omega_{A2} =1$, $\sigma_{a2} = \sigma_{a2} =1$, $\Omega_{a1}= \Omega_{a24}=1$, $a_t=2$, $A_t=2$

The probability density function curves (PDFs), $p(z)$, of the signal z at the Earth receiver station output, in the presence of Rice fading are given in Figures 9 to 12, for diferent parameters.

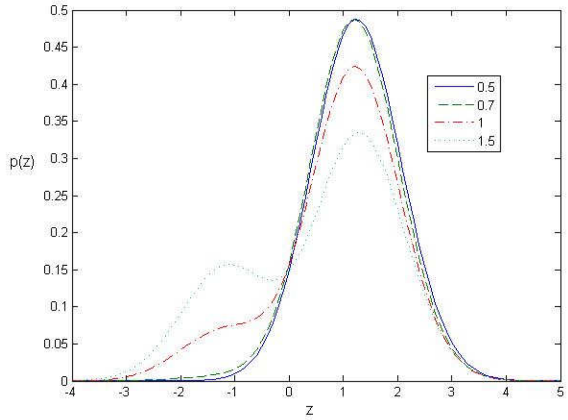

Figure 10. The probability density function $p(z)$ for Rice fading present on receiver satellite and Earth station, for different parameters: $\sigma_1= 0.7, 1, 1.5$, $\sigma_2=0.7$, $\sigma_{A1} =\sigma_{A2} =0.5$, $\Omega_{A1} = \Omega_{A2} =1$, $\sigma_{a2} = \sigma_{a2} =0.5$, $\Omega_{a1}= \Omega_{a24}=1$, $a_t=1$, $A_t=1$

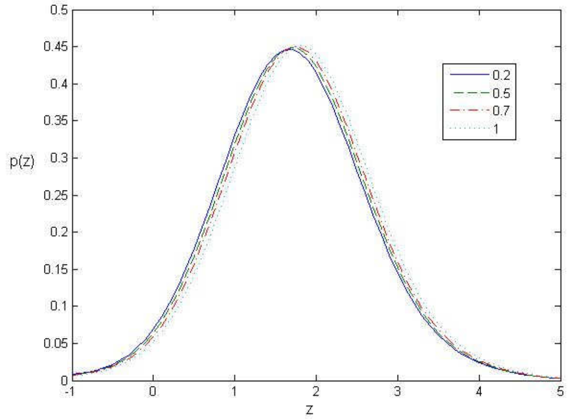

Figure 11. The probability density function $p(z)$ for Rice fading present on receiver satellite and Earth station, for different parameters: $\sigma_1= 0.7$, $\sigma_2=0.7$, $\sigma_{A1} = \sigma_{A2} =1$, $\Omega_{A1} = \Omega_{A2} =0.2, 0.5, 0.7, 1$, $\sigma_{a2} = \sigma_{a2} =1$, $\Omega_{a1}= \Omega_{a24}=1$, $a_t=1$, $A_t=1$

We can see from these figures the influence of two parameters of Rice distribution, the signal amplitudes Ω and variances σ, and the standard deviations σ_i, and the signal amplitudes A_1, A_2, a_1 and a_2.

The outage probability curves $P_{out}(z)$, in the presence of Rice fading are given in Figures 13 and 14 for diferent parameters.

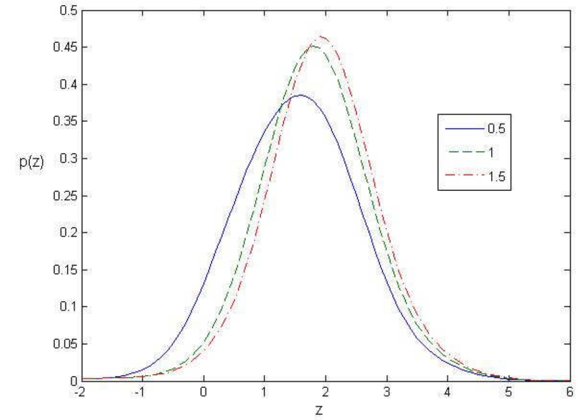

Figure 12. The probability density function $p(z)$ for Rice fading present on receiver satellite and Earth station, for different parameters: $\sigma_1 = 0.7$, $\sigma_2 = 0.7$, $\sigma_{A1} = \sigma_{A2} = 1$, $\Omega_{A1} = \Omega_{A2} = 1$, $\sigma_{a2} = \sigma_{a2} = 1$, $\Omega_{a1} = \Omega_{a24} = 1$, $a_t = 0.5, 1, 1.5, 2$, $A_t = 1$

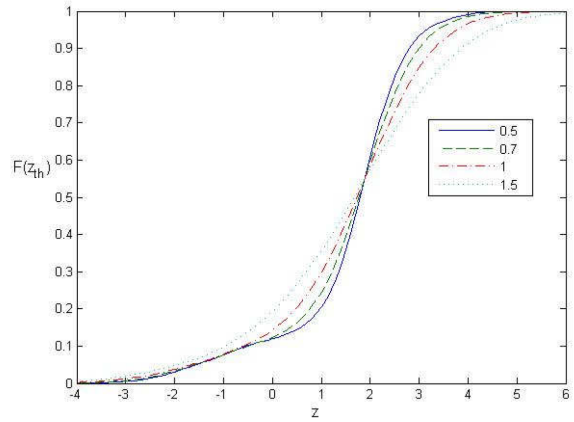

Figure 13. The outage probability $P_{out}(z)$ for Rice fading present on receiver satellite and Earth station, for different parameters: $\sigma_1 = 1$, $\sigma_2 = 0.5, 0.7, 1, 1.5$, $\sigma_{A1} = \sigma_{A2} = 1$, $\Omega_{A1} = \Omega_{A2} = 1$, $\sigma_{a2} = \sigma_{a2} = 1$, $\Omega_{a1} = \Omega_{a24} = 1$, $a_t = 2$, $A_t = 2$

The dependence of probability density functions, pdf $p(z)$, from z, the Earth receiver station output signal, are given in Figures 3 to 6 in the presence of Nakagami-*m* fading, and in Figures 9 to 12 in the presence of Rice fading, present on receiver satellite and Earth stations for some values of distribution parameters. In every graph one or several parameters are given by few values and one can see the variation of pdf versus values of selected parameters for constant other parameters.

The expression for probability density function (PDF) of the output signal after diversity combining is used to study the outage probability of proposed system. The outage probability is standard performance criterion of communication systems operating over fading channels.

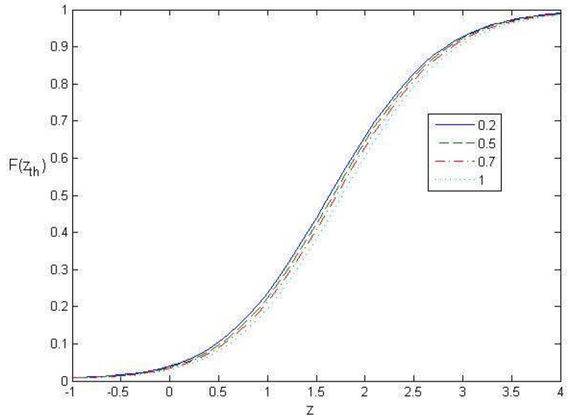

Figure 14. The outage probability $P_{out}(z)$ for Rice fading present on receiver satellite and Earth station, for different parameters: $\sigma_1 = 0.7$, $\sigma_2 = 0.7$, $\sigma_{A1} = \sigma_{A2} = 1$, $\Omega_{A1} = \Omega_{A2} = 0.2, 0.5, 0.7, 1$, $\sigma_{a2} = \sigma_{a2} = 1$, $\Omega_{a1} = \Omega_{a24} = 1$, $a_t = 1$, $A_t = 1$

The outage probability curves $P_{out}(z)$, are shown in Figures 7, 8, 13, 14 for determined values of distribution parameters: parameters of fadings on receiver satellite and Earth station, the standard deviations σ_i, and the signal values at the system inputs.

The values of $P_{out}(z)$ for some values of parameters σ_2, and constant other parameters, are shown in Figures 7 and 13. From this figure can be seen that $P_{out}(z)$ decreases with increase of parameter σ_2, for the same value of z, if z is bigger than threshold decision. From Figures 8 and 14, it can be seen that $P_{out}(z)$ decreases with increasing of spread parameters $\Omega_1 = \Omega_2$.

VI. CONCLUSION

In this paper the satellite communication system consisting of the earth transmitting station and the satellite transponder was considered. Switch and stay combining (SSC) diversity technics are used on receiving satellite and receiving Earth stations. SSC is used, as the simplest and the cheapest combining method, to reduce fading influence to the system performances. The presence of Nakagami-*m* and Rice fading on receiving satellite and receiving Earth stations is observed. Rice distribution is used to model the envelope of fading channels in wireless telecommunication systems with direct line of site, when dominate component exists. This type of the satellite communication system can be used for propagation channels consisting of one strong direct LOS (line of sight) component and many random weaker components for both, receiving satellite and receiving earth stations and for satellite propagation channels that obey a Nakagami *m* distribution. The fading is the limiting factor in both directions. Because it has been found experimentally that Nakagami distribution offers better fit for wider range of fading conditions in wireless communications, the influence of this kind of fading is analyzed also.

The probability density functions (PDFs) of the signal at the Earth receiver station output are represented for different parameter values. The other system performances, such as the system error probability and the outage probability, could be calculated by the output signal probability density function. In this paper, the outage probability, as standard performance criterion of communication systems operating over fading channels, is calculated and the curves are shown also.

In the future work the other combining techniques, such as Maximal Ratio Combining, (MRC), Equal Gain Combining, (EGC), and Selection Combining, (SC), could be investigated and the results compared with appropriate in this paper.

REFERENCES

[1] D. Krstić, P. Nikolić, M. Matović, A. Matović, M. Stefanović, "The Satellite Telecommunication System Performances in the Presence of Nakagami Fading on Satellite and Earth Station", The Sixth International Conference on Wireless and Mobile Communications ICWMC 2010, September 20-25, 2010, Valencia, Spain

[2] M. J. Ryan, Principles of Satellite Communications ISBN: 9780958023832, Argos Press, January 2004.

[3] M. K. Simon and M. S. Alouni, Digital Communication over Fading Channels, Second Edition, Wiley Interscience, New Jersey, p. 586, 2005.

[4] W. C. Jakes, Microwave Mobile Communication, 2nd ed. Piscataway, NJ: IEEE Press, 1994.

[5] S.O.Rice,"Statistical properties of a sine wave plus random noise" Bell Syst.Tech.J, vol.27, Jan.1948, pp109–157.

[6] M. Nakagami, The m-distribution- a general formula of intensity distribution of rapid fading. In: Hoffman WG, editor. Statistical methods of radio wave propagation. Oxford, UK: Pergamon; 1964.

[7] A. Annamalai and C. Tellambura, "Error rates for Nakagami-*m* Fading Multichannel Reception of Binary and *M*-ary Signals", IEEE Trans. On Commun., ISSN: 0090-6778, vol. 49, No. 1, January 2001, pp. 58-68.

[8] D. Krstić and M. Stefanović, "The statistical characteristics of the MRC diversity system output signal", Electronics and Electrical Engineering, No.1(73, January 2007), pp. 45-48.

[9] K. Noga, "The performance of binary transmission in slow Nakagami-fading channels with MRC diversity," IEEE Trans, Commun., vol. 46, July 1998, pp. 863-865.

[10] K. Sivanesan and N. C. Beaulieu, "Exact BER analysis of bandlimited BPSK with EGC and SC diversity in cochannel interference and Nakagami fading", IEEE Commun. Lett., vol. 8, Oct. 2004, pp. 623-625.

[11] H. Yang, M. S. Alouini, and M.K. Simon, "Average error rate of NCFSK with multi branch post-detection SSC diversity", Proc. 5th Nordic Signal Processing Symposium NORSIG-2002, Norway, Oct. 2002.

[12] A. Abu-Dayya and N. C. Beaulieu, "Switched diversity on microcellular Ricean channels", IEEE Trans. Veh. Technol., vol. 43, 1994, pp. 970-976.

[13] M. Stefanović, D. Krstić, J. Anastasov, S. Panić and A. Matović, "Analysis of SIR-based Triple SC System over Correlated α-μ Fading Channels", Proc. The Fifth Advanced International Conference on Telecommunications, AICT'09, Venice/Mestre, Italy, May 24-28, 2009.

[14] M. S. Alouini and M. K. Simon, "Postdetection Switched Combining- A simple Diversity Scheme with Improved BER Performance", IEEE Trans. on Commun., vol. 51, No 9, pp.1591-1602, September 2003.

[15] Y. C. Ko, M. S. Alouini and M. K. Simon, "Analysis and optimization of switched diversity systems", IEEE Trans. Veh. Technol., vol. 49, Issue 5, Sep 2000, pp.1813-1831.

[16] C. Tellambura, A. J. Mueller and V. K. Bhargava, "Analysis of M-ary Phase-Shift-Keying with Diversity Reception for Land-Mobile Satellite Channels," IEEE Trans. Vehicular Technology, Vol. 46, issue 4, November 1997, pp. 910–922.

[17] C. Tellambura, A. J. Mueller and V. K. Bhargava, "BER and Outage Probability for the Land Mobile Satellite Channel with Maximal Ratio Combining," IEE Electronics Letters, Vol. 31, Issue: 8, April 1995, pp. 606–608.

[18] C. Tellambura and V. K. Bhargava, "Outage Probability Analysis for Cellular Mobile Radio Systems Subject to Nakagami Fading and Shadowing", IEICE Trans. on Communications Vol.E78-B No.10, 1995, pp.1416-1423.

[19] B. Nikolic and G. Djordjevic, "Performance of SC and SSC Receivers in Hoyt Channel in the Presence of Imperfect Reference Signal Extraction", 9th International Conference on Applied Electromagnetics, August 31 - September 02, 2009, Niš, Serbia

[20] M.A. Blanco, Diversity receiver performance in Nakagami fading in Proc. IEEE Southeastern Conf. Orlando, 1983, pp. 529-532.

[21] J. I. Marcum, Table of Q Functions, U.S. Air Force Project RAND Research Memorandum -339, ASTIA Document AD 1165451, Rand Corporation, Santa Monica, CA, January 1, 1950.

Performance Model for Orthogonal Sub Channel in Noise-limited Environment

Jyrki T.J. Penttinen, Francesco D. Calabrese
Nokia Siemens Networks Innovation Center (NICE)
Madrid, Spain
jyrki.penttinen@nsn.com
francesco.calabrese@nsn.com

David Valerdi, Iñigo Güemes
Vodafone Center of Competence (CoC)
Madrid, Spain
david.valerdi1@vodafone.com
inigo.guemes@vodafone.com

Abstract—**OSC (Orthogonal Sub Channel) is an enhancement for the GSM voice service. It provides up to double capacity in the radio interface with the same hardware compared to the GSM Half Rate (HR) mode. This paper investigates the effects of OSC on the capacity utilization as a function of the OSC capable handset penetration. The variation of the radio network capacity is studied by taking into account the division of the time slot usage between HR and OSC capable terminals, which depends on the OSC capable handset penetration. The achievable capacity gain is studied by investigating the blocking rate behavior. In addition, a set of test cases was carried out in a GSM network in order to evaluate the radio performance of OSC in terms of the carrier per noise level. The tests were performed in a noise-limited indoor environment, and the quality and received power level distributions were analyzed. Based on the post-processing and analysis of the performance data as a function of the OSC penetration, a generic model to estimate the effect of OSC on the GSM capacity gain was developed. The model utilizes the network statistics and performance indicators of GSM, and provides an estimate of the possible OSC gains in the investigated regions before the OSC feature is actually activated.**

Keywords—OSC, GSM, 2G, SAIC, voice evolution, capacity enhancement, radio network planning, optimization, DHR.

I. INTRODUCTION

The capacity utilization is one of the most important optimization items of the GSM radio interface. The recently developed Dual Half Rate (DHR) functionality can be considered as a major step in the 2G evolution path. OSC (Orthogonal Sub Channel) is a solution for offering the pairing of two separate users into a single HR (Half Rate) time slot resource in such a way that no hardware enhancements are needed in the network side. OSC utilizes a SAIC (Single Antenna Interference Cancellation) functionality of the already existing handsets, which means that OSC provides a SAIC penetration dependent capacity gain as soon as it is activated via a software update of the Base Transceiver Stations (BTS) and Base Station Controllers (BSC) of the GSM radio network.

Based on [1], this paper presents an extended analysis of the OSC gain as a function of SAIC handset penetration, and complements the analysis by investigating further the radio performance analysis presented in [2]. These results are processed in order to form a complete OSC gain model that consists of the predicted effect on the capacity and radio performance of GSM voice calls.

During the evolution of the circuit switched (CS) domain of GSM, there have been various capacity enhancement methods applied in the networks like Dynamic Frequency and Channel Allocation [3], Adaptive Multi Rate codecs [4] and Frequency Hopping (FH) [5]. Also several other solutions have been proposed, although these are still under development, like multiple beam smart antennas [6]. At the moment, though, one of the most concrete ways that provide with a notable capacity effect is the SAIC concept. There are various studies available presenting the respective benefit in different environments [7][8][9][10].

The first DHR deployments are based on the OSC functionality that has been evaluated and standardized by 3GPP GERAN [11][12][13][14]. It utilizes SAIC and provide capacity enhancement without need for modifications to the already existing new mobile station generation.

Despite of the availability of various studies about the SAIC gain, the capacity behavior in a typical OSC network deployment is not clear. This paper presents thus an analysis of the effect of OSC on the offered capacity by investigating the benefits, e.g., in terms of the utilization and possibility for the reduction of the transceivers as a part of the frequency re-farming between GSM and other technologies such as HSPA (High Speed Packet Access) and LTE (Long Term Evolution). Based on realistic radio measurements in an indoor environment, this paper also investigates the effective proportion of the coverage area where OSC can be utilized.

The GSM HR mode is selected as a reference for the investigations as it is assumed to be available in a typical environment. The capacity gain of OSC is obviously lower in the cell edge where the network dependent algorithm switches the OSC first to the HR mode and eventually to the FR (Full Rate) mode assuming that Adaptive Multi Rate (AMR) functionality is utilized. This paper investigates the capacity effect of OSC together with the impacts on the radio quality, which together forms a complete prediction model for the OSC gain as a function of the OSC penetration.

First, a brief overview to the principles and functionality of OSC is given in Section II. Then, a theoretical analysis of the capacity behavior of OSC is presented in Section III. The analysis shows the mapping of the estimated OSC penetration value in the actual usage of the Time Slots (TSL) for OSC and GSM Half-Rate (HR) modes. Then, the effect of OSC is investigated on the variation of the offered traffic, which gives possibility to estimate either the reduction of the already deployed capacity (transceiver units, TRX) or, which gives time for the postponing of the future hardware capacity additions yet maintaining the original or lower blocking rate of the GSM cell. The effects of OSC on the radio performance are investigated in Section IV, which provides information about the usability of OSC within the coverage area. The field tests carried out in this section are based on the noise-limited indoor environment, but the results can be extended also to the outdoor. Based on Sections III and IV, the complete model is proposed in Section V. The input of the model is based on the Key Performance Indicators (KPI) of GSM. The output predicts the effect of OSC on the respective OSC coverage compared to the GSM HR (Half Rate) mode as a function of the OSC penetration. Finally, Section VI presents the conclusions of the work.

II. THE FUNCTIONALITY AND USABILITY OF OSC

GSM technology is globally most widely deployed cellular mobile communication system. In emerging markets, the increase trend of new-developed subscribers and consequent voice traffic explosion creates a great pressure on network operators, especially for those operators that need to provide service to a large population with only limited bandwidth. In mature markets, GSM frequencies are being re-farmed to UMTS and LTE in order to provide a national-wide mobile broadband service with a limited investment and better quality; this action will squeeze GSM bandwidth and increase demand over GSM technology to achieve higher capacity and spectrum efficiency, so as to maintain the current traffic volumes and user experience. Furthermore, considering that the Average Revenue per User (ARPU) continues decreasing, most operators are facing the challenge of improving their hardware utilization efficiency.

In order to cope with the scenarios outlined above, some possible solutions are brought up. Among them, one of the most promising proposals is the OSC feature, a voice capacity enhancement for the GSM networks. OSC is standardized in 3GPP, and the first live network OSC trials have been carried out in 2010. OSC is backwards compatible solution with the original TDMA frame structure of GSM, exploiting the single 200 kHz frame bandwidth by multiplexing more users to its 8 physical time slots. The OSC DHR (Dual Half Rate) mode utilizes a single physical TSL for up to four users compared to the HR mode that can multiplex two users within the same TSL, or only one user in the FR (Full Rate) mode.

In Downlink (DL), OSC DHR distinguishes between two independent GSM users sharing the same HR resource by interpreting the 8-level GMSK modulation as two separate QPSK (Quadrature Phase Shift Keying) modulation diagrams in such a way that the users form pairs within the HR TSL as presented in FIGURE 1.

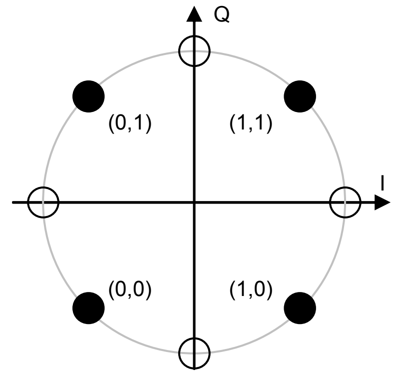

FIGURE 1. Two separate OSC DHR users can be multiplexed in DL via the pairing based on the QPSK constellation.

As presented in FIGURE 2, a MUD (Multi-User Detection) receiver is used in Uplink (UL) in order to identify two users sharing the same physical time slot, and the separation of the users is handled via different training sequences [11]. This requires antenna diversity in the GSM base station with MUD functionality [9]. The applied Multiple-Input, Multiple-Output (MIMO) concept gives benefits especially in Rayleigh fading channel [12]. A GMSK modulation is used in UL.

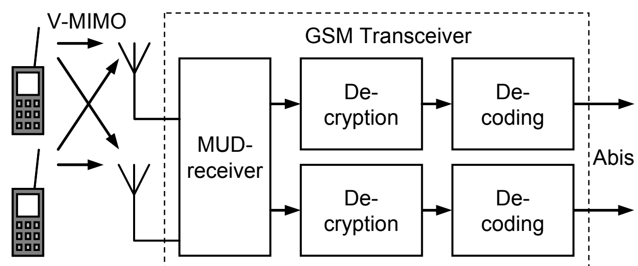

FIGURE 2. Two OSC DHR users can share the same HR resource in UL via the MIMO functionality of MUD.

FIGURE 3 shows an example about the average behavior of the OSC DHR and HR calls in a fully occupied 8-TSL TRX assuming that the OSC penetration is 50% and that the users are uniformly distributed over the investigated area.

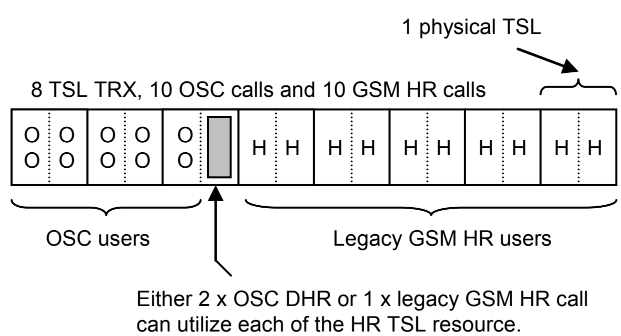

FIGURE 3. An example of the utilization of the TRX resources for OSC DHR and GSM HR calls with the same OSC (SAIC) terminal penetration.

As FIGURE 3 indicates, the TSL division for the OSC and HR calls can be estimated to be 1:2 in case of 50% OSC penetration, i.e., OSC utilizes 1/3 of the physical TSL resources in this case.

When the radio conditions are ideal, i.e., there are no restrictions from the radio network side in the usage of the TSL for OSC DHR, HR or FR calls, it is thus possible to fit 2 times more OSC DHR calls into the same TSL compared to HR calls.

The following analysis shows the more detailed division of the TSL utilization for the OSC DHR and HR users as a function of the OSC penetration, assuming that the network supports both modes in the normal operation.

III. EFFECT OF OSC ON CAPACITY

This analysis shows the behavior of the GSM cell capacity when both GSM HR and OSC DHR users are found in the area. More specifically, the distribution of the HR and OSC users in the same cell is studied as a function of the OSC capable SAIC mobile station penetration. The capacity enhancement is shown between the extreme values, i.e., when only HR users are found, and when the cell is populated with OSC users, in a fully loaded cell.

In the scenarios presented in this paper, it is assumed that the functionality of the OSC is ideal, i.e., it is transparent for the existing HR traffic, and that there is no impact of the feature on the previous functionality of the network. It should be noted that this analysis concentrates purely on the radio interface time slot capacity, and does not consider the effects of the feature on the radio link budget. The assumption of these calculations is thus the presence of a coverage area where the quality and received power levels are sufficiently high for the functioning of the OSC.

The benefit of OSC is obvious in a fully loaded network where major part of the GSM Mobile Stations (MS) is OSC capable. The presented investigations are divided into three scenarios: The effect of OSC DHR on the TSL distribution in a fully loaded cell, on the number of users per TSL, and on the blocking rate, which can result the possibility to reduce TRX units from the GSM sites.

A fully loaded cell can be taken as a basis for the study. The assumption is that both HR and OSC capable users are uniformly distributed over the investigated area. This means that the OSC capable MS penetration equals to the probability of the OSC MS entering to the cell, the rest of the MSs entering to the cell utilizing the HR mode. It should be noted that the term HR refers to a MS that is capable of utilizing both HR and FR modes.

When the OSC feature is activated in the GSM network, the total number of users, i.e., Mobile Stations that are distributed in the investigated area, is a mix of OSC DHR users and GSM HR users:

$$N_{MS}^{tot} = N_{MS}^{OSC} + N_{MS}^{HR} \tag{1}$$

The amount of the OSC users depends on the OSC capable MS penetration α with $\{\alpha \in \mathbb{R} | 0 \leq \alpha \leq 1\}$. The number of OSC capable users is thus:

$$N_{MS}^{OSC} = \alpha \cdot N_{MS}^{tot} \tag{2}$$

This means that the number of HR users is:

$$N_{MS}^{HR} = (1-\alpha) \cdot N_{MS}^{tot} \tag{3}$$

The total number of physical TSLs is divided to the TSLs utilized by the OSC users and the HR users. The expression for the TSLs occupied by the OSC and HR users is thus:

$$N_{TSL}^{tot} = N_{TSL}^{OSC} + N_{TSL}^{HR} \tag{4}$$

The formula contains physical TSLs for OSC and HR. As a single OSC TSL can be utilized by a total of 4 OSC users, we can present the relationship between the TSL and the number of the users in the following way:

$$N_{MS}^{OSC} = 4 \cdot N_{TSL}^{OSC} \tag{5}$$

Equally, a total of 2 HR users can utilize the TSL, which can be expressed as:

$$N_{MS}^{HR} = 2 \cdot N_{TSL}^{HR} \tag{6}$$

FIGURE 4 clarifies the idea of the notation. In this specific case, the OSC user penetration α is 12 / 22 = 55%, and the physical TSL utilization for OSC users is 3/8.

Assuming that the users are distributed uniformly in the coverage area, the utilization of the TSLs depends on the OSC penetration. The following analysis represents the best case scenario of a number of HR MSs, which is multiple of 2 and a number of OSC MSs, which is multiple of 4 so that no TSL is occupied by less than 4 OSC MSs or less that 2 HR MSs.

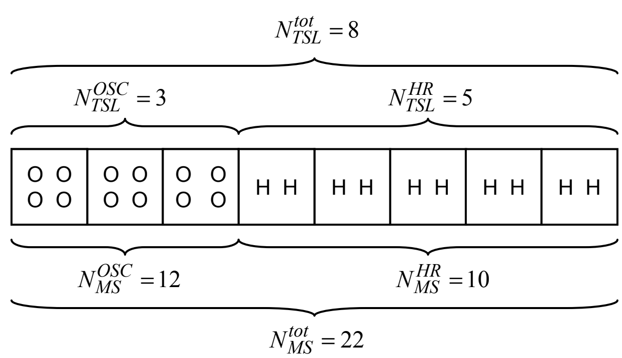

FIGURE 4. An example of the utilization of a single TRX by OSC (marked as O) and HR (marked as H) users.

By combining (4), (5) and (6), we can write:

$$N_{TSL}^{tot} = N_{TSL}^{OSC} + N_{TSL}^{HR} = \frac{N_{MS}^{OSC}}{4} + \frac{N_{MS}^{HR}}{2} \tag{7}$$

We can then introduce the dependency from the OSC penetration using (2) and (3):

$$N_{TSL}^{tot} = \frac{\alpha \cdot N_{MS}^{tot}}{4} + \frac{(1-\alpha)N_{MS}^{tot}}{2} \tag{8}$$

We have therefore expressed the total number of needed TSLs as a function of the total number of MSs and the OSC penetration coefficient.

A. The number of users as a function of α

Similarly, we can express the total number of MSs that can be served as a function of the total number of available TSLs and the OSC penetration coefficient.

Let's then introduce β with $\{\beta \in \mathbb{R} | 0 \leq \beta \leq 1\}$, which gives the percentage of the physical TSLs occupied for the OSC users. The analysis can be carried further and we can write:

$$\begin{aligned} N_{MS}^{tot} &= N_{MS}^{OSC} + N_{MS}^{HR} \\ &= \beta \cdot N_{TSL}^{tot} \cdot 4 + (1-\beta) \cdot N_{TSL}^{tot} \cdot 2 \\ &= 2 \cdot N_{TSL}^{tot} \cdot (2\beta + 1 - \beta) \\ N_{MS}^{tot} &= 2 \cdot (1+\beta) \cdot N_{TSL}^{tot} \end{aligned} \tag{9}$$

We can rearrange as follows:

$$\begin{aligned} N_{TSL}^{tot} &= \frac{\alpha \cdot N_{MS}^{tot}}{4} + \frac{(1-\alpha) \cdot N_{MS}^{tot}}{2} \\ &= \frac{\alpha \cdot N_{MS}^{tot} + 2 \cdot (1-\alpha) N_{MS}^{tot}}{4} \\ N_{TSL}^{tot} &= \frac{(2-\alpha)}{4} N_{MS}^{tot} \end{aligned} \tag{10}$$

The total number of users can then be expressed as a function of the TSLs:

$$N_{MS}^{tot} = \frac{4 \cdot N_{TSL}^{tot}}{2-\alpha} \tag{11}$$

By comparing (9) and (11) we obtain:

$$\frac{4 \cdot N_{TSL}^{tot}}{2-\alpha} = 2 \cdot (1+\beta) \cdot N_{TSL}^{tot} \tag{12}$$

Therefore the utilization of the TSLs by the OSC users can be expressed as a function of OSC user penetration:

$$\beta = \frac{\alpha}{2-\alpha} \tag{13}$$

FIGURE 5 shows the physical TSL utilization for the OSC and HR users as a function of the OSC penetration, i.e., the level of the TSL occupation as a function of the percentage of the SAIC capable handset of the all mobiles in the investigated area.

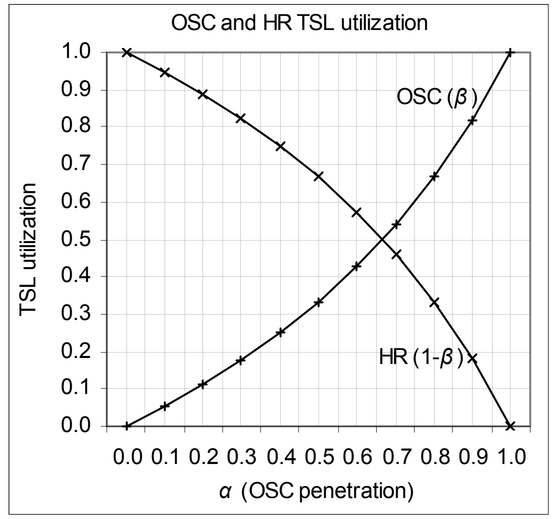

FIGURE 5. The TSL utilization for the OSC and HR calls as a function of the OSC penetration.

One point of interest of FIGURE 5 is the SAIC handset penetration of 50%, which indicates that the OSC paired connections utilize 33% of the physical TSL capacity of the cell, the rest being occupied by HR users. Another point of interest is the breaking point where both HR and OSC utilize the same amount of TSLs. The graph shows that it is found at 67% of OSC penetration.

It should be noted that the calculation is valid within the functional coverage area where OSC can be used, i.e., where the received power level is high enough. For the areas outside the OSC coverage, HR and FR modes are assumed to function normally with their respective ranges of received power levels indicated in [15].

B. The effect of OSC on the number of users per TSL

As the number of the OSC and HR users is known as a function of α, we can create a function that expresses the usage of a single TSL in terms of the number of users served. It is clear that the values of the served users oscillates within the range of [2, 4], lowest value indicating 100% HR, and highest value representing the 100% DHR OSC penetration.

The number of the users per TSL in a cell that contain mixed HR and OSC users can be obtained by utilizing (10) and (11):

$$\frac{N_{MS}^{tot}}{N_{TSL}^{tot}} = 2 \cdot \left(1 + \frac{\alpha}{2-\alpha}\right) \tag{14}$$

FIGURE 6 shows the number of users per TSL as a function of the OSC penetration α. As can be noted, the extreme value of 4 is a result of OSC penetration of 100%.

As an example, the 50% OSC penetration level provides an offered capacity for about 2.67 users (which is a mix of OSC and HR users in average) per timeslot. It is again assumed that the OSC functionality can be utilized over the whole investigated area, meaning that the cell border area of the GSM coverage is not considered in this analysis.

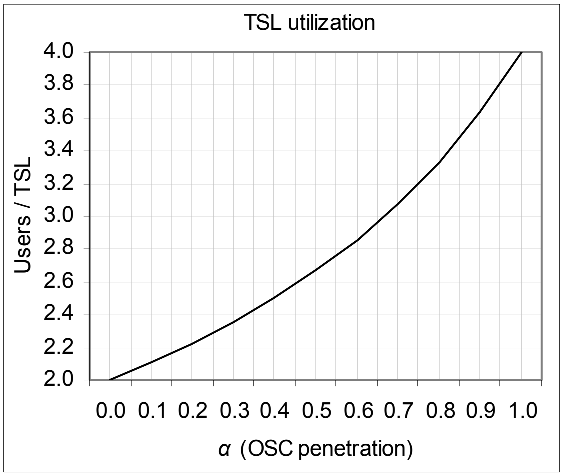

FIGURE 6. The number of users per TSL as a function of the OSC penetration.

C. *The effect of OSC on blocking rate*

The original situation of the fully occupied cell with only HR users present, i.e., when OSC is not activated, can be taken as a reference also for the following analysis. Assuming that the blocking rate of the GSM HR cell in busy hour is B, we can estimate its change via the well-known Erlang B [16] after OSC has been activated:

$$B(N) = \frac{\frac{A^N}{N!}}{\sum_{n=0}^{N} \frac{A^N}{n!}} \tag{15}$$

Term B is the blocking rate (% of the blocked calls compared to the number of whole attempts), N is the available amount of time slots, and A is the product of the average call density and average time of reservation, i.e., the offered load.

As it is not possible to solve the equation of offered traffic analytically, it can be utilized in a recursive format:

$$\begin{cases} B(0) = 1 \\ B(N) = \dfrac{AB(N-1)}{N + AB(N-1)} \end{cases} \tag{16}$$

Furthermore, the offered traffic (Erl) can be expressed as:

$$\bar{x} = A \cdot (1 - B) \tag{17}$$

We can establish a reference case with OSC 0% in the following way. The *B(N)*[OSC = 0%] can be set to 2%. This means that, e.g., in the case of 7 traffic TSLs for FR GSM, the respective offered load A = 2.94 Erl and the offered traffic is $\bar{x}$ = 2.88 Erl. The proportion of the offered traffic over the whole timeslot capacity $\bar{x}$ / TSL_{tot} = 0.41 Erl/TSL. If HR codec is utilized, there is double the amount of users served within the same TSL number. This can be expressed in Erlag B formula by marking the available radio resources as 14, which results A = 8.21 Erl and $\bar{x}$ = 8.04 Erl. The $\bar{x}$ / TSL_{tot} is now 1.15 Erl/TSL, i.e., FR TSL. The difference between these figures shows the Erlag B plus HR gain, i.e., the more there is available capacity, the more efficiently the calls can be delivered with the same blocking rate.

When the OSC functionality is activated and the same blocking rate is maintained, the available resources with the same hardware is now 4·7 = 28 for the *B(N)*[OSC = 100%], i.e., when $\alpha = 1$. The $\bar{x}$ is now 19.75, and the efficiency 2.82 Erl/TSL, i.e., FR TSL. This shows one of the benefits of OSC as it increases clearly the capacity efficiency via the Erlang B gain if the same amount of hardware is maintained.

If instead the amount of users is kept the same, the additional capacity that is liberated via the more efficient usage of TSLs via OSC can be removed partially or totally. This provides the basis for 3G re-farming if the operator has both 2G and 3G licenses.

With a lower amount of timeslots, the same number of users can still be served with the same or lower blocking rate like FIGURE 6 indicates. The blocking rate depends on the usage of the TSLs for OSC, i.e., on β, which can be expressed as a function of α as shown in (13).

D. *The effect of OSC on the TSL and TRX reduction*

It is possible to investigate the dependency of the number of users and Erlang B formula's offered traffic as a function of the OSC penetration. In order to carry out this part of the study, an Erlang B table was created by utilizing (15) and (16).

A case example with a blocking rate of 2.0% was selected. A table of 1–200 TSLs was created as a basis for the analysis. FIGURE 7 summarizes the behavior of the channel utilization. It can be seen that the performance of the cell increases due to the Erlang B gain, along with the OSC penetration growth compared to the original proportion of the HR capable users.

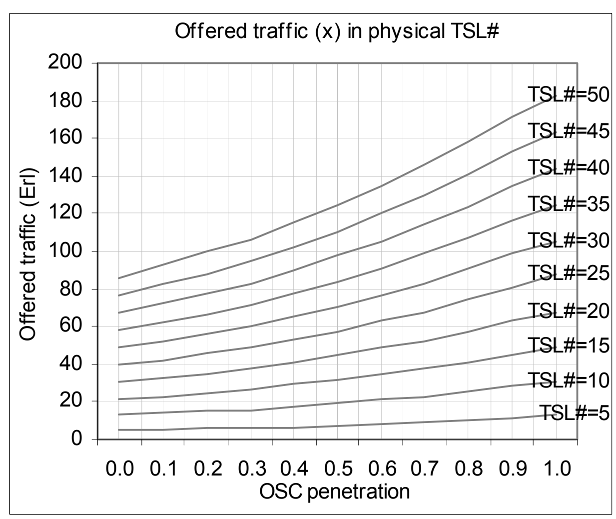

FIGURE 7. Offered traffic as a function of the OSC penetration, when the maximum number of the available time slots is 50 and B = 2%.

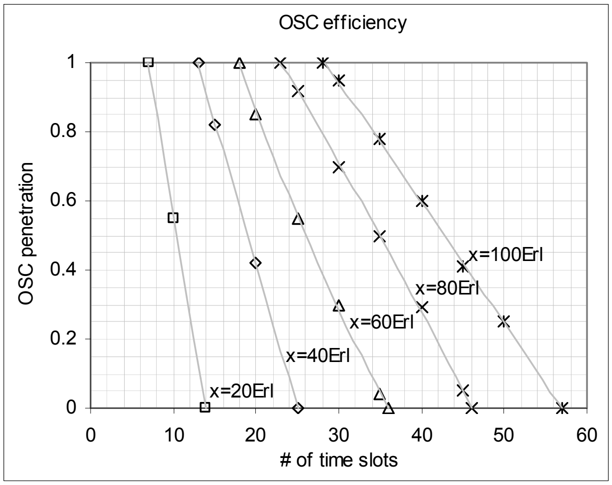

FIGURE 8. The required time slot number with B = 2% can be observed as a function of the OSC capable user penetration.

Next, an analysis of the effect of the SAIC handset penetration on the total reduction of the time slot number is presented. The calculation can be made by assuming that the offered traffic level $\bar{x}$ and the call blocking rate *B* are maintained in the original level.

FIGURE 8 summarizes the analysis carried out for 20–100 Erl of offered traffic. FIGURE 8 can be interpreted in such a way that when the OSC penetration grows, the needed number of TSLs with the same blocking rate (originally 2%) is now lower.

According to the basic behavior of the Erlang B model, the effect is logically strongest for the higher capacity cells. This can be noted especially from the highest investigated offered traffic class of 100 Erl, which requires only half of the timeslots when OSC penetration is 100%.

The effect of OSC can be seen in FIGURE 9, which shows the analysis for the required number of TRXs for a set of offered traffic classes (Erl) when the OSC capable SAIC handset penetration is known.

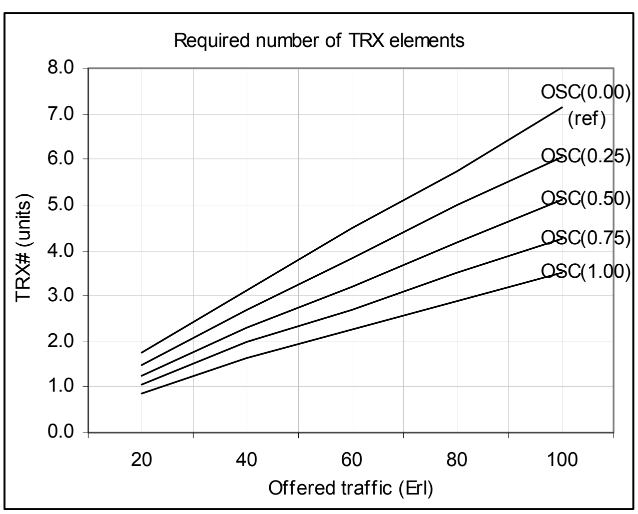

FIGURE 9. The effect of the OSC penetration on the required amount of TRXs when the blocking rate B is kept the same (2%).

The assumption in this case is that each TRX contains 8 traffic channels. It is now possible to interpret the benefit of OSC in terms of the transceiver units. Table I summarizes the calculation as a function of TRX number.

TABLE 1. The estimation of the needed TRX element number as a function of the OSC penetration, when the blocking probability *B*=2%.

$\bar{x}$ (Erl)	OSC penetration				
	0.00	0.25	0.50	0.75	1.00
20	1.8	1.5	1.3	1.1	0.9
40	3.1	2.7	2.3	2.0	1.6
60	4.5	3.8	3.2	2.7	2.3
80	5.8	5.0	4.2	3.5	2.9
100	7.1	6.1	5.1	4.3	3.5

TABLE 1 indicates that the benefit of OSC starts to be significant when the original BTS contains at least 4 TRX elements (per sector or in omni-radiating site). In that case, already a relatively low OSC penetration of 25% provides a possibility to remove a complete TRX element (i.e., one frequency block of 200 kHz) from the cell, yet still keeping the blocking rate below or the same as was observed originally, which is 2% in this example. If this capacity is removed, it can be utilized for the re-farming of 3G frequencies. Alternatively, if no TRX units are removed, the offered capacity can be utilized more efficiently for parallel packet data via the lower circuit switched call blocking rate. There are thus various different network evolution scenarios available due to OSC.

FIGURE 10 summarizes the amount of TRXs (assuming that each offers 8 physical traffic TSLs) that can be removed from the site depending on the OSC penetration and the offered traffic in such a way that the blocking rate would not change from the original 2 % figure. It should be noted that a small part of the TSLs are used also for signaling, and that each TRX unit is a physical 8-TSL equipment, so only integer values rounded up should be considered in the interpretation of the number of TRXs.

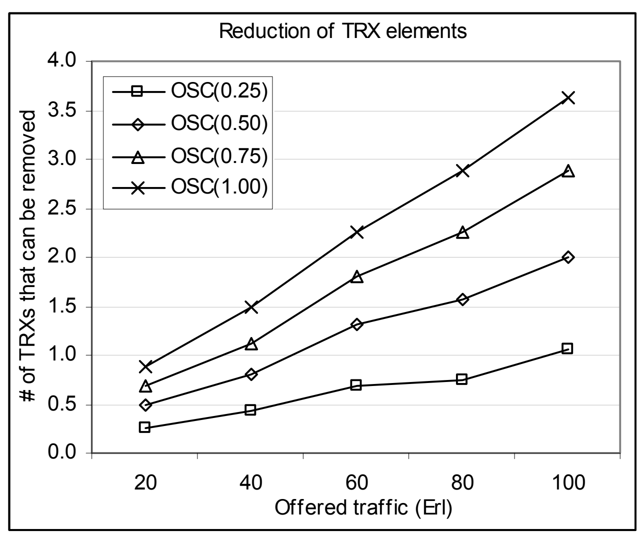

FIGURE 10. The effect of OSC on the reduction of TRX elements.

The presented analysis provide a base for the GSM network re-dimensioning in the following scenarios:

1) In the case of still growing GSM traffic, the estimation of the already existing penetration of SAIC terminals when the OSC feature is activated, as well as the prediction of the SAIC penetration development within the forthcoming years gives a possibility to adjust the radio capacity plans. This means that the otherwise required TRX extensions can be postponed or rejected as long as the blocking rate can be maintained in the allowed level with OSC.

2) In the case of stabilized or lower GSM traffic, the same blocking rate can be maintained with a lower amount of the TRX units. This liberated bandwidth can be reused for the delivery of the growing 3G traffic in the same frequency band, if available for the operator, which makes the frequency re-farming more fluent with OSC.

IV. OSC Radio Performance Analysis

A. *Methodology for the analysis*

The laboratory environment consisted of Base Station Sub system (BSS) and Network and Switching Sub-system (NSS) with functional elements (Base Transceiver Station BTS, Base station Controller BSC, Mobile Switching Centre MSC and Home Location Register HLR) as shown in Figure 11. The Abis interface was based on the IP emulation. The BTS was located in Madrid, Spain, and BSC in Finland. The voice calls were established only within the test network. Discontinuous Transmission (DTX) and Frequency Hopping (FH) were disabled during the measurement data collection.

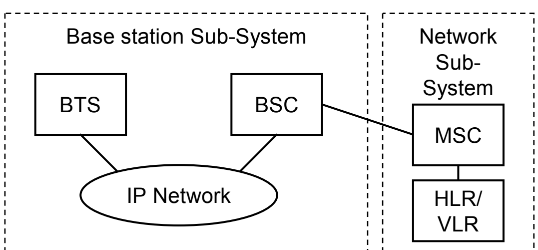

Figure 11. The laboratory setup consisted of a functional GSM network with a single radio cell.

The test network consisted of one cell in the indoors. The link budget was dimensioned by using adjustable attenuators and minimal TRX output power, which resulted in a cell radius of about 40 meters. The indoor radio propagation conditions provided nearly line of sight, with light wall obstacles. This setup represents a noise-limited environment within the whole functional received power level range of GSM.

For the evaluation of the radio performance, the quality level Q and received power level P_{RX} were correlated and stored in Slow Associated Control Channel (SACCH) frame intervals of 480 ms during the active voice calls. The correlated Q_n values with n = 0...7 and P_{RXm} categories with m = 0...5 were collected to a matrix. Table 2 presents the equivalence of the Q levels and bit error rate (BER), and Table 3 shows the P_{RX} categories in terms of dBm ranges [15].

The values for the Carrier-to-Noise ratio (C/N) are based on the thermal noise level and terminal's noise figure. The value for the noise floor can be estimated by applying the formula:

$$\begin{aligned} P_n &= 10\log_{10}\left(k_B TB \cdot 10^3\right) dBm \\ &= -174 dBm/Hz + 10\log_{10}(B) Hz \end{aligned} \tag{18}$$

where k_B is Boltzmann's constant ($1.38 \cdot 10^{-23}$ J/K), T is the temperature (290 K is assumed) and B is the bandwidth in Hz. For a single GSM frequency channel of 200 kHz, the thermal noise level is thus −120.98 dBm. The values of Table 3 contain also the receiver noise power of about 3 dB, resulting in total noise level N of −118 dBm.

The OSC functionality was set up to the BTS and BSC by utilizing non-commercial R&D software. DHR mode of OSC was utilized in a single TSL with minimally correlating training sequences.

Table 2. Mapping of quality categories (Q) and Bit Error Rates (BER).

Q_n category	BER (%)
n=0	[0.0, 0.2]
n=1	[0.2, 0.4]
n=2	[0.4, 0.8]
n=3	[0.8, 1.6]
n=4	[1.6, 3.2]
n=5	[3.2, 6.4]
n=6	[6.4, 12.8]
n=7	[12.8, 100]

Table 3. P_{RX} categories and respective Carrier-to-Noise ranges.

P_{RXm} category	P_{RX} (dBm)	C/N (dB)
m=5	[−38, −69]	[49, 80]
m=4	[−70, −79]	[39, 48]
m=3	[−80, −89]	[29, 38]
m=2	[−90, −94]	[24, 28]
m=1	[−95, −99]	[19, 23]
m=0	[−100, −110]	[8, 18]

B. *Laboratory tests with SAIC handsets*

The data collection was carried out over the functional coverage area by applying BSC measurement called RxLevel Statistics. SAIC terminals were used for the test calls. The collection was done in systematic manner by moving the terminals approximately 0.5 m/s with a test platform.

The correlated (Q, P_{RX}) matrix was collected for both OSC and reference GSM HR calls. It should be noted that the testing was done only for one physical TSL whilst the other traffic TSLs were blocked. As the environment was noise-limited and no inter-TSL interferences were present, this represents a fully loaded cell. The interval of the (Q, P_{RX}) matrices was 15 minutes.

Figure 12 shows the principle of the data collection, which was carried out in three different phases within high, medium and low ranges of received power levels. This method was applied to the investigations in order to collect the data over the P_{RX} categories in as uniform manner as possible.

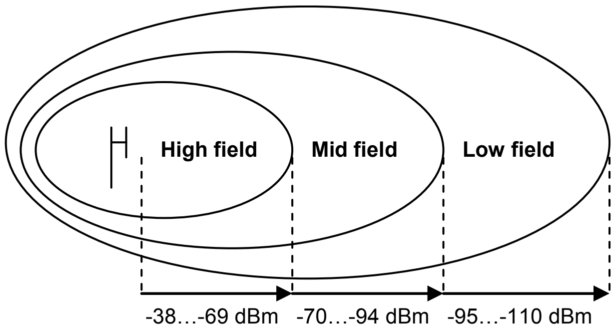

FIGURE 12. The measurement data were collected in three phases, within high, mid and low field (values of P_{RX} in dBm).

C. Laboratory results

The correlated (Q_n, P_{RXm}) results can be organized to a matrix format in such a way that the elements $v_{i,j}$ correspond to the number N of the samples of Q_{8-i}, where i=0,1,...,8, and P_{RXj-1}, with j=0,1,...,5, is indicated as $N(Q_n, P_{RXm})$. The result of (Q_0, P_{RX0}) represents thus the value of the matrix element $v_{8,1}$ and (Q_1, P_{RX1}) corresponds to the element $v_{7,1}$. The last result of (Q_7, P_{RX5}) is found in the element $v_{1,6}$. The following format clarifies the idea.

$$M = \begin{bmatrix} v_{1,1} & v_{1,2} & \cdots & v_{1,6} \\ v_{2,1} & \ddots & & \\ \vdots & & \ddots & \\ v_{8,1} & & & v_{8,6} \end{bmatrix} = \begin{bmatrix} N(Q_7,P_0) & \cdots & \cdots & N(Q_7,P_5) \\ N(Q_6,P_0) & \ddots & & \\ \vdots & & \ddots & \\ N(Q_0,P_0) & & & N(Q_0,P_5) \end{bmatrix}$$

The following matrices M_{GSM} and M_{OSC} presents the normalized results for GSM and OSC laboratory tests, respectively. Each matrix element represents the percentage of the number of samples for that Q and P_{RX} compared to the total number of samples.

$$M_{GSM} = \begin{bmatrix} 1.70 & 0.00 & 0.00 & 0.00 & 0.00 & 0.00 \\ 2.67 & 0.02 & 0.02 & 0.01 & 0.00 & 0.00 \\ 3.57 & 1.31 & 0.95 & 0.39 & 0.08 & 0.02 \\ 3.81 & 1.96 & 0.71 & 0.23 & 0.02 & 0.03 \\ 2.97 & 1.69 & 0.58 & 0.30 & 0.04 & 0.03 \\ 1.11 & 1.34 & 0.63 & 0.32 & 0.03 & 0.03 \\ 0.66 & 0.66 & 0.18 & 0.23 & 0.06 & 0.02 \\ 1.81 & 5.33 & 10.35 & 14.13 & 11.47 & 28.56 \end{bmatrix}$$

$$M_{OSC} = \begin{bmatrix} 4.44 & 0.03 & 0.00 & 0.00 & 0.00 & 0.00 \\ 2.85 & 5.09 & 0.01 & 0.01 & 0.00 & 0.00 \\ 0.00 & 5.36 & 1.93 & 0.16 & 0.00 & 0.03 \\ 0.00 & 0.80 & 6.95 & 0.70 & 0.00 & 0.05 \\ 0.00 & 0.07 & 6.53 & 1.42 & 0.02 & 0.04 \\ 0.00 & 0.00 & 4.19 & 0.99 & 0.07 & 0.05 \\ 0.00 & 0.00 & 1.97 & 1.19 & 0.05 & 0.07 \\ 0.02 & 0.00 & 2.07 & 18.65 & 24.24 & 9.92 \end{bmatrix}$$

In the original GSM mode and with full load of a single TSL, a total of two HR users consume the whole physical TSL. In the OSC mode, in turn, a total of 4 DHR users utilizes the physical TSL in the fully loaded TSL.

The Q_n and P_{RXm} results were collected in three phases, each lasting 15 minutes. One area is characterized as a strong field with main part of the results occurring in P_{RX} categories of P_{RX5} and P_{RX4}. The second represents medium field with values of P_{RX3} and P_{RX2}, and the third area represents low field with values belonging to P_{RX1} and P_{RX0}. The results were then combined in order to present the matrix of the complete field.

All the measurement data samples were collected as uniformly as possible by moving the platform in a constant speed. The data collection in the lowest field was done by observing the Radio Link Timer (RLT) parameter value directly in the mobile phone's engineering mode channel display. When the field reached the critical level, there occurred SACCH frame errors and the retransmission parameter value started to decrease from the original value of 20 towards 0. Before the zero-value was reached (which drops the call), the mobile was moved to the better field in order to raise the value back to 20 without breaking the connection.

There were a total of 20,383 and 19,399 samples collected during the GSM HR and OSC modes, respectively. In average, there is thus more than 400 samples per matrix element, which results in an average margin error Err[95%] = 0.98 / √(400) = 4.9% with 95% confidence level per each matrix element. Table III shows the Err[95%] for each P_{RX} category.

TABLE 4. The error margin in % of the samples of each P_{RXm} category with 95% confidence level.

Mode	P_{RX0}	P_{RX1}	P_{RX2}	P_{RX3}	P_{RX4}	P_{RX5}
HR	1.6	2.0	1.9	1.8	2.1	1.3
OSC	2.5	2.0	1.4	1.4	1.4	2.2

D. OSC Radio Performance Model

Based on the analysis presented previously, a comparison of the matrices can be now performed. GSM HR matrix M_{GSM} can be selected as a reference in order to produce a matrix M_{diff}, which indicates the difference or change of the original correlated (Q, P_{RX}) distribution in %-units due to the OSC mode. The matrix is:

$$M_{diff} = M_{GSM} - M_{OSC} \tag{19}$$

$$M_{diff} = \begin{bmatrix} -2.74 & -0.03 & 0.00 & 0.00 & 0.00 & 0.00 \\ -0.18 & -5.07 & 0.00 & -0.01 & 0.00 & 0.00 \\ +3.57 & -4.05 & -0.98 & +0.23 & +0.08 & -0.02 \\ +3.81 & +1.16 & -6.25 & -0.46 & +0.01 & -0.02 \\ +2.97 & +1.61 & -5.95 & -1.12 & +0.01 & -0.01 \\ +1.11 & +1.34 & -3.56 & -0.67 & -0.05 & -0.02 \\ +0.66 & +0.66 & -1.79 & -0.96 & +0.01 & -0.06 \\ +1.79 & +5.33 & +8.28 & -4.51 & +12.77 & +18.65 \end{bmatrix}$$

It can be noted that in the original M_{GSM}, there are all quality classes $Q_0...Q_7$ present in the lowest field, i.e., in P_{RX0} category, whilst M_{OSC} produces samples only to the quality classes Q_6 and Q_7 in the same field. It can be seen that the collection of samples for different P_{RX} levels is not uniform, indicating that the data collection happened slightly unequally in different fields, in addition to the fact that the ranges associated with each P_{RX} are different. This makes the comparison of the matrices challenging.

In order to cope with this issue, the result matrices can be normalized over each P_{RXm} category (that is by column) instead of the total number of the collected samples, in the following way:

$$M'_{GSM} = \begin{bmatrix} 9.29 & 0.00 & 0.00 & 0.00 & 0.00 & 0.00 \\ 14.6 & 0.13 & 0.12 & 0.03 & 0.00 & 0.00 \\ 19.5 & 10.7 & 7.07 & 2.48 & 0.71 & 0.05 \\ 20.8 & 16.0 & 5.27 & 1.49 & 0.13 & 0.09 \\ 16.2 & 13.7 & 4.34 & 1.92 & 0.31 & 0.11 \\ 6.08 & 10.9 & 4.69 & 2.05 & 0.22 & 0.09 \\ 3.63 & 5.40 & 1.35 & 1.45 & 0.49 & 0.05 \\ 9.88 & 43.3 & 77.16 & 90.6 & 98.2 & 99.6 \end{bmatrix}$$

$$M'_{OSC} = \begin{bmatrix} 60.7 & 0.26 & 0.00 & 0.00 & 0.00 & 0.00 \\ 39.0 & 44.8 & 0.06 & 0.06 & 0.00 & 0.00 \\ 0.00 & 47.2 & 8.15 & 0.68 & 0.02 & 0.34 \\ 0.00 & 7.04 & 29.4 & 3.01 & 0.02 & 0.48 \\ 0.00 & 0.65 & 27.6 & 6.13 & 0.10 & 0.43 \\ 0.00 & 0.04 & 17.7 & 4.29 & 0.30 & 0.48 \\ 0.00 & 0.00 & 8.32 & 5.14 & 0.20 & 0.72 \\ 0.27 & 0.00 & 8.75 & 80.7 & 99.36 & 97.5 \end{bmatrix}$$

Now, the difference can be calculated as:

$$M'_{diff} = M'_{GSM} - M'_{OSC} \tag{20}$$

The following matrix presents the result in %.

$$M'_{diff} = \begin{bmatrix} +51.5 & +0.26 & 0.00 & 0.00 & 0.00 & 0.00 \\ +24.4 & +44.7 & -0.05 & +0.03 & 0.00 & 0.00 \\ -19.5 & +36.5 & +1.08 & -1.80 & -0.69 & +0.28 \\ -20.8 & -8.91 & +24.1 & +1.53 & -0.11 & +0.39 \\ -16.2 & -13.1 & +23.3 & +4.22 & -0.21 & +0.33 \\ -6.08 & -10.8 & +13.0 & +2.24 & +0.08 & +0.39 \\ -3.63 & -5.40 & +6.97 & +3.68 & -0.28 & +0.67 \\ -9.61 & -43.3 & -68.4 & -9.90 & +1.21 & -2.07 \end{bmatrix}$$

It can be seen from the matrices that the proportion of quality classes Q_7 and Q_6 is higher in OSC than in GSM HR.

FIGURE 13 shows the impact of OSC on the quality level per each P_{RX} category. The most affected categories are P_{RX0}, P_{RX1} and P_{RX2} as they include more lower quality values.

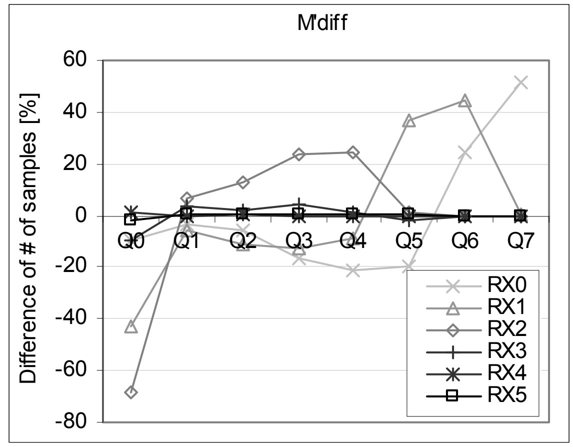

FIGURE 13. The M'diff presents the change in the distribution of the correlated Q and P_{RX} caused by OSC when HR is the reference.

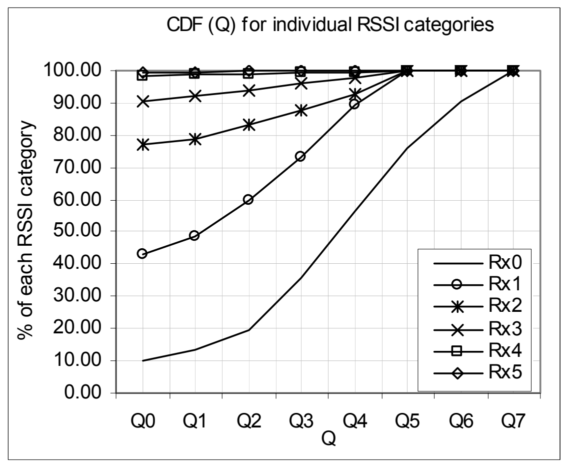

FIGURE 14. CDF of the GSM HR analysis, scaled individually for each P_{RX} category.

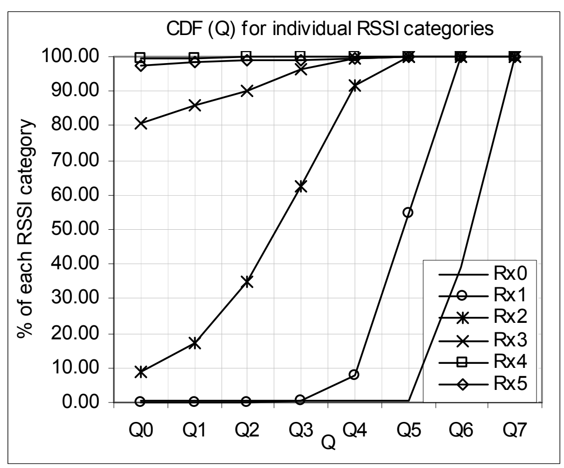

FIGURE 15. CDF of the OSC analysis, scaled individually for each P_{RX} category.

FIGURE 14 and FIGURE 15 show the difference in the Q class behavior. In GSM HR, the lowest P_{RX} has samples over all the Q classes whilst OSC only causes samples for Q_6 and Q_7.

The introduction of OSC feature causes each CDF to shift towards the higher Q classes corresponding to higher BER. This indicates that the useful coverage area produced via the OSC mode is smaller than the one produced by HR.

1) Scenario 1: Difference of the radio quality in a fully loaded GSM HR and OSC cell

TABLE 5 summarizes the laboratory test analysis in CDF, showing the differences between HR and OSC per P_{RX} category. As can be noted, the Q_5, i.e., BER in the interval [3.1%, 6.4%] can be reached with HR between P_{RX0} and P_{RX1} [−95, −110 dBm]. According to Table III, the OSC moves the C/N requirement higher, and the Q_5 can now be found between P_{RX1} and P_{RX2} [−90, −99 dBm].

TABLE 5. The 95 % Q criterion analysis for the GSM HR calls.
* Note: When the Q_0 value is achieved more than 95 % of the time, the corresponding %-value is shown in brackets.

P_{RX} category	Q value for GSM HR (reference)	Q value for OSC / difference with GSM HR (%-units)
P_{RX0}	6.5	6.9 / −0.4
P_{RX1}	4.5	5.9 / −1.4
P_{RX2}	4.3	4.4 / −0.1
P_{RX3}	2.5	2.8 / −0.3
P_{RX4}	0.0* (98.1 %)	0.0* (97.5 %) / 0.0 (−0.6 %-units)
P_{RX5}	0.0* (99.6 %)	0.0* (99.4 %) / 0.0 (−0.2 %-units)

It can be assumed that the practical threshold for the GSM call is at quality level of Q_4, corresponding to a BER in the range [1.6, 3.2]. FIGURE 16 shows the CDF of the combined P_{RX} classes as a function of the Q, indicating that the Q_4 is at 89.5% for GSM HR, and at 80.0% for OSC over the whole investigated area A_{GSM} in this specific case.

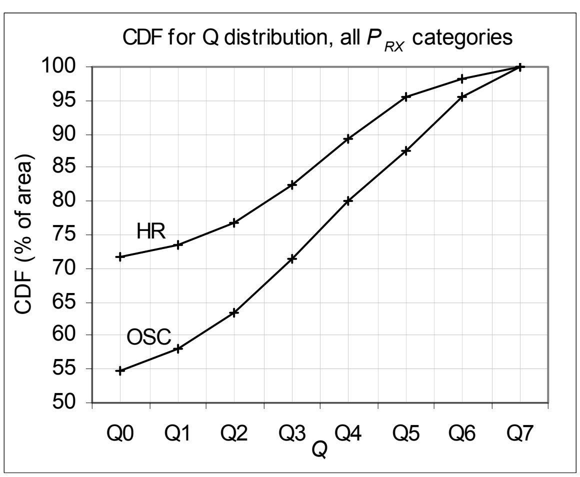

FIGURE 16. The HR and OSC coverage.

The CDF of HR and OSC indicates the presence of different Q classes during the measurement, which shows the percentage of Q classes in the investigated area. The effect of OSC can now be observed based on Q_4:

$$\begin{aligned} A_{change}[\%] &= 100\frac{A_{HR}-A_{OSC}}{A_{HR}} \\ &= 100\left(1-\frac{A_{OSC}}{A_{HR}}\right) \approx 10.6\% \end{aligned} \tag{21}$$

where A_{change} indicates how much the useful coverage area of OSC is smaller compared to the HR mode. The radius for the OSC mode is reduced from the HR mode by:

$$\begin{aligned} r_{change}[\%] &= 100\cdot\frac{r_{HR}-r_{OSC}}{r_{HR}} = 100\cdot\left(1-\frac{r_{OSC}}{r_{HR}}\right) \\ &= 100\cdot\left(1-\sqrt{\frac{A_{OSC}}{A_{HR}}}\right) \approx 5.5\% \end{aligned} \tag{22}$$

As the OSC brings up to 100% capacity enhancement compared to the GSM HR, the benefit of OSC is clear even with this level cell size reduction.

In practice, the original cell size remains as determined by the GSM FR and HR limits for the C/N and C/I levels. In other words, when the OSC feature is activated, the cell contains OSC, HR and FR coverage regions. The FR proportion remains the same also after the activation of OSC, but HR region is divided into OSC and HR regions. The final size of these depends mainly on the original overlapping portions of the neighboring cells and the criteria of the intra/inter-cell handover algorithms.

Furthermore, the OSC proportion depends also on the time slot usage by OSC, β, which in turn depends on the OSC capable handset penetration α.

2) Scenario 2: Only OSC (SAIC) handset penetration is known

In a practical GSM network, there is a certain penetration of OSC capable terminals in the investigated field. When OSC is activated, there are legacy terminals that are capable of functioning only with the previous GSM codecs (FR, HR, AMR), and SAIC terminals that are also capable to function in the DHR mode.

It is thus important to take the SAIC terminal penetration into account when modeling the effect of OSC in the field. The M'_{GSM} and M'_{OSC} presented previously show the correlated distribution of (Q, P_{RX}) in a fully loaded situation, i.e., when all the time slots are occupied either by GMS HR or OSC users. We can still utilize this assumption of fully loaded cell in order to find the limits of the effect. Let's assume the SAIC handset penetration is α of all the terminals in the investigated area. As the OSC DHR utilizes single TSL for a total of 4 users whilst GSM HR can multiplex two users in the same TSL, the TSL capacity related scaling factor is needed for the performance model.

In a typical case, there are 2 or more TRXs per cell in sub-urban areas, and 4 or more in dense city environment. The TSL utilization of the OSC vs. HR can be estimated by α. The TSL utilization factor β for the OSC TSL occupancy in a fully loaded cell as a function of the OSC mobile terminal penetration can be formulated as presented in [1]:

$$\beta = \frac{\alpha}{2-\alpha} \tag{23}$$

Now, when M'_{GSM}, M'_{diff} and OSC penetration α are known, the M'_{OSC} can be obtained by scaling the original GSM matrix element-wise. We can donate the elements of the matrix M'_{GSM} as $v_{m,n}^{GSM'}$ and the elements of the matrix M'_{OSC} as $v_{m,n}^{OSC'}$. The scaling between these corresponding elements can be assumed to be linear according to the principle of the linear interpolation function:

$$y = kx + b \quad , \tag{24}$$

where $\{k \in \mathbb{R} | 0 \leq k \leq 1\}$ and represents the coefficient in x-axis of the physical TSL usage, i.e.:

$$k = v_{m,n}^{OSC'} - v_{m,n}^{GSM'} \tag{25}$$

Term b is the value of y when $x = 0$, i.e., it equals to $v_{m,n}^{GSM'}$. Term x represents the usage of the TSLs for the OSC:

$$x = \beta \tag{26}$$

The scaling of each element for the partially loaded OSC cells can thus be done as follows:

$$y_{m,n} = \left(v_{m,n}^{OSC'} - v_{m,n}^{GSM'}\right) \cdot \beta + v_{m,n}^{GSM'} \tag{27}$$

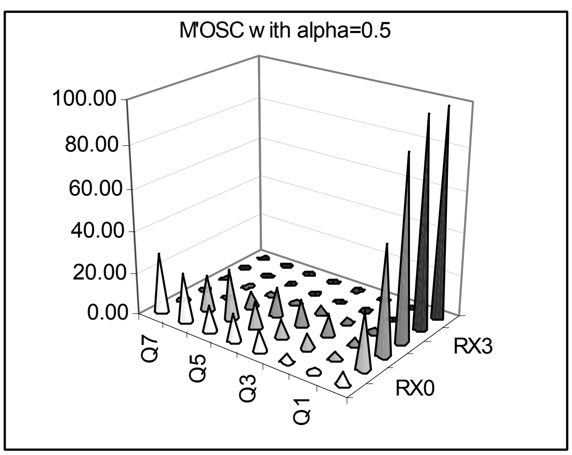

FIGURE 17. An example of the expected (Q, P_{RX}) distribution (normalized over each RXlevel category) when OSC user penetration α is 50% and the OSC TSL usage *B* is 37.5%.

M'_{GSM} and M'_{OSC} obtained from the laboratory can be utilized directly, and the estimate of the new M'_{OSC} (α) can be thus constructed by interpolating linearly the matrix values element-by element basis.

The usage of the laboratory results is most accurate in environment that contains approximately same type of radio channel, i.e., in noise-limited environment with almost line-of-sight and light proportion of Rayleigh fading. If the radio channel differs considerably from the laboratory, Scenario 3 should be considered instead. This means that the case results presented in this paper might vary depending, e.g., on the level of the co-channel and adjacent channel interferences as well as on the type of multi-path propagation characteristics in the investigated area.

3) Scenario 3: OSC (SAIC) handset penetration and new M'_{GSM} are known

When the new M'_{GSM} is known, showing the correlated (Q_n, P_{RXm}) matrix for HR calls, it can be assumed that the new M'_{OSC} is possible to construct by applying the M'_{diff} that was obtained from the laboratory. The assumption is that the OSC feature performance is independent of the radio conditions, i.e., the reference M'_{GSM} obtained from the laboratory already contains the radio channel related performance, whilst M'_{OSC} includes this same radio performance effect and an additional OSC performance specific performance. Assuming this is applicable in varying radio conditions, the new M'_{OSC} can be constructed by taking into account the OSC penetration:

$$M'_{OSC} = M'_{GSM} + \beta \cdot M'_{diff} \tag{28}$$

As explained in scenario 2, the activation of OSC is seen within the HR coverage area, the FR area staying unchanged. The utilization of the OSC compared to the original HR region can now be interpreted from the practical measurements or by taking again the Q_4 criterion as a basis. Also another value of the quality classes can be utilized, if that corresponds to the OSC pairing and un-pairing criteria of the OSC algorithm.

V. COMPLETE OSC MODEL

The strength of the developed model is that it requires only few and basic inputs, which are: 1) Rx Level Statistics tables before the OSC functionality is activated; 2) estimation of the OSC capable penetration in the initial phase of the OSC activation; and 3) optionally the percentage of the utilized HR and FR codecs.

A. OSC model process

FIGURE 18 shows the complete process of the model. The model processes the input data in such a way that the expected (Q,P_{RX}) matrix is formed based on the measured and correlated (Q, P_{RX}) table element-by-element according to (27). By default, the scaling of each element can be done by utilizing the already formed difference matrix. It should be noted that the presented difference matrix is valid for the noise-limited environment, so new difference matrix might be needed for the interference-limited environment.

The output of the model indicates the proportion of the OSC usage as a function of the OSC capable handset penetration, with the capacity gain that can be expressed in terms of increased offered load/traffic or of the possibility to reduce TRX elements. The radio performance result is based on the analysis of the changed *C/I* or *C/N* distributions.

When the complete model is applied in the investigation of a realistic GSM network, the steps described in FIGURE 18 can be taken into account for solving first the impact on the radio performance, i.e., on the changes of the quality.

The actual capacity gain depends on the radio performance, i.e., which proportion of the GSM call can be utilized for the OSC, and on the OSC penetration, i.e., what share of the handsets can take the advantage of the usable coverage area for the OSC. The estimate of the performance change due to the activation of OSC would be made based on the pre-formed difference matrices and the SAIC penetration.

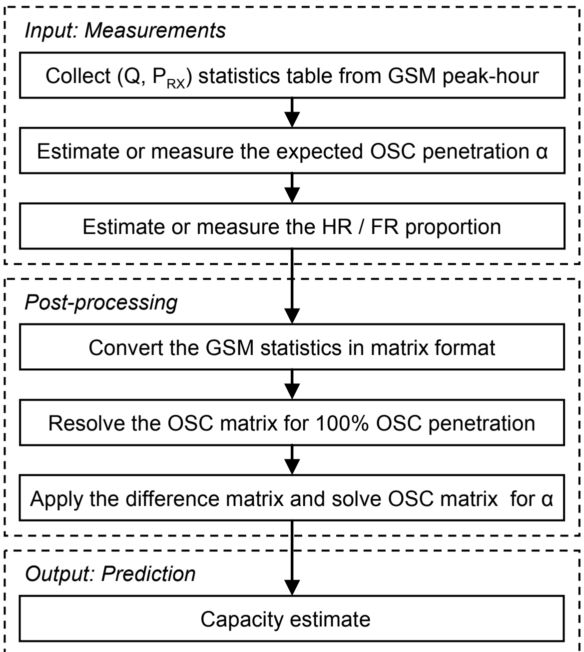

FIGURE 18. The process chart of the OSC model usage.

When the Rx level statistics table of GSM is measured from the field (i.e., the table without OSC feature activated), it can be assumed that the corresponding expected Rx level statistics table for the OSC is possible to construct by applying the correction curves that were obtained from the laboratory as shown in FIGURE 13. The assumption is that the OSC feature performance is independent of the radio conditions, i.e., the reference table of GSM obtained from the laboratory already contains the radio channel related performance, and that the OSC table includes this same radio performance effect and an additional OSC performance specific performance. Assuming this is applicable in varying radio conditions, the new OSC table can be constructed by taking into account the OSC penetration:

$$M'_{OSC} = M'_{GSM} + \beta \cdot M'_{diff} \quad , \tag{29}$$

where M'_{OSC} is the matrix format for the new OSC Rx level statistics table, M'_{GSM} is the matrix of the measured GSM Rx levels statistics table in the field, and M'_{diff} is the correction matrix obtained from the laboratory measurements. The practical way of constructing the OSC Rx level table is to utilize the β factor element-by-element basis for scaling first each of the difference matrix elements. Then, the difference matrix is utilized to scale the GSM Rx level statistics table element-by-element basis.

B. Process steps

The complete OSC model considers the radio performance, or changes of the performance due to the OSC activation, as well as the resulting capacity gain. The steps for the investigation of the OSC impact are:

Step 1: Storing of the Rx Level statistics measurement and codec utilization measurement via BSC. This gives the reference for the GSM performance without OSC.

From the codec utilization measurement, also the estimate of what is the utilization (percentage) of HR and FR codecs can be included. That information gives the equivalence of the original HR-FR division also area-wise as shown in FIGURE 19.

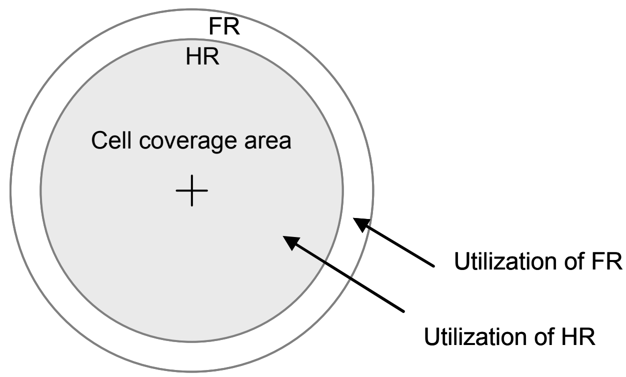

FIGURE 19. The original division of the FR and HR mode utilization before the OSC feature has been activated.

The investigation of the utilization of the codecs can be done for any time of the traffic, but the peak hour as criterion is recommended in order to collect as much data as possible in the given time window, and to make sure that the behavior of the effect of OSC on the capacity is done in the extreme conditions that represents the practical limit for the gain. In order to increase the accuracy of the estimate, the Rx level statistics measurement for the storing of the correlated Q and P_{RX} table can be done at the same time as the codec division.

Step 2: Estimation of the OSC capable SAIC handset proportion in the field, i.e., the factor α. The estimate can be carried out via the network statistics that is based on an IMEI (International Mobile Equipment Identity) analysis, which is correlated with the database of the models that support SAIC. The estimate can also be done based on the sales statistics, or other practical "best-effort" estimate. Based on this information, the average TSL utilization for the OSC capable handsets can be estimated by using (23).

Step 3: Estimation of the capacity regions assuming the OSC DHR functions within a part of the HR region. The FR region can be assumed to work unchanged, as the situation was before the OSC activation. The criterion for the OSC percentage can be selected as presented in FIGURE 16, i.e., based on the Q_4 level in CDF of the area. If the practical implementation of the OSC pairing and un-pairing is based on the other Q levels, that can be utilized instead.

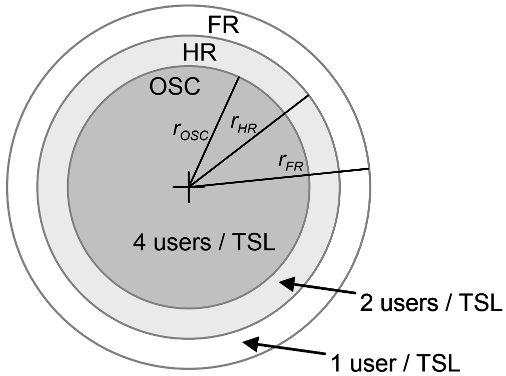

FIGURE 20. When OSC feature is activated, there will be functional areas for OSC DHR, HR and FR in the cell, each providing different capacity performance.

Step 4: Capacity estimate for the OSC and HR regions, and estimate of each region proportions. The division can be estimated by the HR and FR codec utilization statistics of BSC, U_{HR} indicating the utilization for HR (%) and U_{FR} indicating the utilization for FR (%). This division gives the first type of indicator for the capacity gain.

C. OSC utilization

During the laboratory measurements described above, the codec utilization measurement was not yet activated. In practice, the voice codec statistics measurement can be activated in BSC in the same manner as (Q, P_{RX}) statistics in order to obtain the realistic division of the HR and FR utilization. In this analysis, we can assume case values of U_{FR} = 10% and U_{HR} = 90%. The comparison is done by calculating first the reference situation, i.e., the total capacity utilization via HR and FR, by giving a weight of δ_{HR} = 2 (users / TSL) for HR (δ_{HR}) and 1 (users / TSL) for the FR (δ_{FR}):

$$\begin{aligned} U_{GSM}^{tot} &= \delta_{FR} \cdot U_{FR} + \delta_{HR} \cdot U_{HR} \\ &= 1 \cdot 10\% + 2 \cdot 90\% = 180\% \end{aligned} \tag{30}$$

The reference value is for full FR utilization, which results 100%. The HR mode as such gives thus 80% capacity gain in this specific example. When OSC is activated, the utilization of OSC and HR can be estimated accordingly, and the new capacity utilization can be thus calculated by:

$$U_{OSC}^{tot} = \delta_{FR} \cdot U_{FR} + \delta_{HR} \cdot U_{HR} + \delta_{OSC} \cdot U_{OSC} \quad , \tag{31}$$

where the weight for OSC users (δ_{OSC}) is 4 (users / TSL). Assuming the utilization is still 10% for FR, we get the new division between the HR and OSC utilization by observing the Q_4 criterion and CDF as shown in FIGURE 16. The respective division between the HR and OSC regions can be thus solved.

In this specific case of the laboratory results, by observing the FIGURE 16 and respective result via (30) and (31), the OSC utilization is 100–10.6 = 89.4 (%) compared to the original HR area. The remaining 10.6 (%) share of the area represents thus the new HR region. The total utilization of the capacity when OSC is activated is thus:

$$U_{OSC}^{tot} = 1 \cdot 10\% + 2 \cdot 10.6\% + 4 \cdot 79.4\% = 348.8\% \tag{32}$$

The original situation without OSC presenting a 100 % reference, this means that the capacity gain of Dual Half Rate OSC is 248.8% compared to the presence of only FR mode, and 348.8·100/180–100 = 93.8% compared to the presence of both, FR and HR modes.

It is possible to investigate further the dependency of the number of users and Erlang B formula's offered traffic as a function of the OSC penetration as shown in FIGURE 7, which shows the principle of the method with an example of 2% blocking rate. Other blocking rates are possible to be used as a basis for the calculations based on the statistics collected from the network. In order to estimate the capacity gain correctly, the investigation of the blocking rate of the network area of interest during the busy hour is thus needed.

FIGURE 7 summarizes the behavior of the channel utilization. It can be seen that the performance of the cell increases due to the Erlang B gain, along with the OSC penetration growth compared to the original proportion of the HR capable users.

D. TRX reduction gain

The calculation for the reduced GSM resources can be made by assuming that the offered traffic level and the call blocking rate are maintained in the original level. FIGURE 8 summarizes the analysis carried out for 20...100 Erl of offered traffic when the blocking rate is 2%.

As can be seen from FIGURE 8, along the growth of the OSC penetration, the needed number of TSLs with the same blocking rate (originally 2%) gets lower. According to the behavior of the Erlang B model, the effect is logically strongest for the higher capacity cells. This can be noted especially from the highest investigated offered traffic class of 100 Erl, which requires only half of the timeslots when OSC penetration is 100%.

Two cases can be constructed based on the offered traffic behavior of GSM as a function of OSC penetration. As a first case, the offered capacity can be maintained the same, which means that the blocking rate for the users will be lower (gain of lower blocking rate). This case applies also to the situation where future TRX expansions are planned they can be postponed until the original (or separately decided new) blocking rate is achieved.

If, instead, the offered capacity is lowered by keeping the blocking rate the same, we can estimate the OSC capacity gain in terms of the savings in the TRXs. This TRX reduction can be made based on TABLE 6, by taking into account that each TRX element should be informed as integer number that is rounded up (containing always 8 physical TSLs). Again, the blocking rate of 2% (or lower) is utilized as the criterion. The possibility to reduce the TRX elements can be utilized for the additional capacity for 3G and 4G.

TABLE 6. The estimation of the number of TRX elements that can be removed as a function of OSC penetration, when the blocking probability B=2%.

$\bar{x}$ (Erl)	OSC penetration				
	0.00	0.25	0.50	0.75	1.00
20	-	-	-	-	1
40	-	1	1	2	2
60	-	1	1	2	2
80	-	1	1	2	3
100	-	1	2	3	4

TABLE 6 indicates the capacity gain obtained as a function of the OSC penetration in terms of the TRX element reduction within the functional area of OSC. This case applies to the re-farming of the 2G, 3G and 4G frequencies.

The reduced need for the GSM bandwidth in order to still deliver the original 2G traffic with an unchanged quality of service level may provide the possibility to add a new UMTS carrier of 5 MHz [17] to the same band. As an example, if the original GSM band is of 10 MHz (50 channels of 200 kHz each), according to FIGURE 9, the 80 Erl traffic can be offered with half of the original amount of TRXs when the SAIC handset penetration is near 100%. This means that the original GSM traffic could be possible to deliver within 5 MHz band still maintaining approximately the same blocking rate, which leaves sufficiently space for adding a complete UMTS carrier as a parallel solution.

The benefit can also be seen with LTE, which provides more freedom to select the bandwidth, compared to the fixed 5 MHz band of UMTS. The narrowest LTE bands, i.e., 1.4, 3 and 5 MHz [18] can be utilized to the gradual increasing of LTE, when first, GSM traffic can be offered in smaller band by OSC, and when GSM traffic eventually lowers.

By applying the model and reference measurements for the quality effect of OSC in noise-limited environment, the optimal site configurations can be achieved. According to the results presented in this paper, the sites that contain at least 4 TRXs with approximately 2% blocking rate during the peak-hour, can benefit from the activation of OSC in such a scale that the 4-TRX cell with OSC penetration of about 25% would give possibility to remove one complete TRX, the blocking rate still being at the same or lower 2% level. Alternatively, if the SAIC penetration is relatively high, in order of 75%, one TRX element can be removed even from a 3-TRX cell without impacts on the blocking.

In the live network, the final effects of OSC depend on the proportion of the overlapping cells, co-channel interference levels, inter-cell handover algorithms and their parameter values. In any case, the presented analysis gives indication about the behavior of OSC when the OSC-paired HR calls, which can fit a maximum of four users to a single TSL, are switched back to HR mode that allows two users to a single TSL, or to FR mode that occupies the whole TSL for a single connection. The presented model shows how to estimate the proportion of these regions, and what the effect of OSC is on the final capacity compared to the network that supports only the basic mode of FR/HR.

VI. CONCLUSIONS

This paper shows the behavior of the OSC capacity and radio performance as a function of the OSC penetration by comparing it with the GSM HR/FR traffic. The presented analysis is based on theoretical studies of the capacity and traffic behavior, as well as on single cell indoor measurements in the non-interfering environment.

According to the analysis presented in this paper, the OSC might function in about 10% smaller coverage area than HR mode in a tightly dimensioned environment. This proportion depends on the network dimensioning, which should be taken into account in the interpretation of the presented results.

The results presented in this paper show that the OSC offers a SAIC capable MS penetration dependent capacity gain, which can be utilized for lowering the blocking rate of the GSM network. In this scenario, the OSC does not benefit only the voice capacity, but it also provides higher efficiency for the data calls as OSC leaves more time slots for the use of packet switched domain. As in this case, the OSC allows the circuit switched calls to be delivered via lower amount of TSLs, it also liberates TSLs for the PS calls resulting higher average data throughputs per data user. It also means that recently standardized DLDC (Downlink Dual Carrier) of GSM benefits from OSC as the probability to obtain TSLs from two separate carriers for DLDC users increases.

Alternatively, the OSC feature can be utilized for releasing a part of the TRXs still maintaining the same or lower blocking rate that is dimensioned for the GSM HR network. This scenario can be utilized for the frequency re-farming. Assuming that the renewal period of current GSM handsets is typically from 3 to 4 years, i.e., the OSC capable MS penetration grows relatively fast, the OSC functionality provides efficient parallel utilization of GSM and 3G/4G.

The presented method is based on the correlated received power level and quality measurements of BSC. It is shown that the matrix format, even if the utilized P_{RX} category ranges are relatively wide (from 5 to 10 dB resolution) due to the limitations of the statistics collection tool, can be utilized in the estimation of the OSC performance based on the quality measurements of the GSM network before the OSC is activated. The benefit of this method is that the statistics can be collected by activating the correlating data collection under the whole BSC area. The collected data is thus statistically considerably more accurate compared to a single mobile radio interface measurement results.

The results indicate the OSC performance in indoor radio channel that contains a relatively small proportion of fast fading components. The speed represents a typical slow-moving pedestrian type, and the cell is noise limited. The GSM HR codec was utilized for the reference. In case of other references (GSM FR and different AMR levels), and other radio conditions, additional measurements are needed for creating the M'_{diff} matrix, which would be a future work item. Assuming the effect of the environment is low on the M'_{diff}, the results presented in this paper may be used as a general estimate of the OSC. As a future work item, the model will be evaluated in the outdoor environment with interfering components present.

The model can be considered useful because only basic KPIs and statistics about the OSC capable handset penetration is required as input values. The result of the model indicates the effect of the OSC for the combination of the radio performance and capacity behavior.

ACKNOWLEDGMENT

This work is based on the analysis and laboratory tests carried out at Nokia Siemens Networks Innovation Center (NICE), Madrid, Spain and collaborated with Vodafone. The laboratory setup by Mr. Mikko Nurkka and comments given by Mr. Luis Maestro and Mr. Kari Niemelä are gratefully acknowledged.

REFERENCES

[1] J. Penttinen, F. Calabrese, K. Niemelä, D. Valerdi, and M. Molina. Performance Model for Orthogonal Sub Channel in Noise-limited Environment. Conference proceedings. International Academy, Research, and Industry Association (IARIA). The Sixth International Conference on Wireless and Mobile Communications, ICWMC 2010. September 20-25, 2010, Valencia, Spain. 6 p.

[2] J. Penttinen, F. Calabrese, L. Maestro, K. Niemelä, D. Valerdi, and M. Molina. Capacity Gain Estimation for Orthogonal Sub Channel. Conference proceedings. International Academy, Research, and Industry Association (IARIA). The Sixth International Conference on Wireless and Mobile Communications, ICWMC 2010. Valencia, Spain, September 20-25, 2010. 6 p.

[3] Jose Gimenez, Pablo Tapia, Matti Salmenkaita, and Mariano Fernandez-Navarro. Analysis of dynamic frequency and channel assignment in irregular network environment. The 5th International Symposium on Wireless Personal Multimedia Communications. Volume 2, 2002, Pp. 863-867.

[4] Mikko Säily, Guillaume Sébire, and Eddie Riddington. GSM/EDGE: Evolution and performance. ISBN 978-0-470-74685-1. Wiley, Oct. 2010. 504 p.

[5] A. N. Barreto and R. Pirhonen. Capacity Increase in GSM Networks Using Source-Adaptive AMR. Vehicular Technology Conference, 2006. VTC 2006-Spring. IEEE 63rd, Volume 2. Pp. 553-557.

[6] M. H. Ahmed, W. Wei, and S. A. Mahmoud. Downlink Capacity Enhancement in GSM Systems with Frequency Hopping and Multiple Beam Smart Antennas. IEEE International Conference on Communications (ICC 2000), 18-22 June, 2000. Volume 2. Pp. 1015-1019.

[7] R. Meyer, W. H. Gerstacker, R. Schober, and J. B. Huber. A Single Antenna Interference Cancellation for Increased GSM Capacity. IEEE Transactions on Wireless Communications, Vol. 5, Issue 7. July 2006. Pp. 1616-1621.

[8] A. Mostafa, R. Kobylinski, I. Konstanic, and M. Austin. Single Antenna Interference Cancellation (SAIC) for GSM Networks. IEEE 58th Vehicular Technology Conference, 2003. VTC 2003-Fall. Pp. 1089-1093.

[9] X. Chen, Z. Fei, J. Kuang, L. Liu, and G. Yang. A Scheme of multiuser reusing one slot on enhancing capacity of GSM/EDGE networks. 11th IEEE Singapore International Conference on Communications Systems, November 2008. Pp. 1574-1578.

[10] M. Moisio and S. Nikkarinen. Capacity Gains of Single Antenna Interference Cancellation in GSM. Symposium on 15th IEEE International Personal, Indoor and Mobile Radio Communications (PIMRC) 2004. Volume 4, 2004. Pp. 2700-2704.

[11] Meeting report GP-081309. New WID on Voice services over Adaptive Multiuser Orthogonal Subchannels (VAMOS). 3GPP GERAN #39.

[12] 3GPP TR 45.903. Feasibility study on Single Antenna Interference Cancellation (SAIC) for GSM networks, V 8.0.0. 18 December 2008.

[13] Meeting report GP-071792. Voice Capacity Evolution with Orthogonal Sub Channels. Nokia Siemens Networks, 3GPP GERAN #36. November 2007.

[14] Technical Specification Group GERAN. Meeting Report. Meeting #42, Shenzhen, P. R. of China, 11 - 15 May, 2009. 229 p.

[15] 3GPP TS 05.05 V8.20.0 (2005-11). Technical Specification Group GSM/EDGE. November 2005. 100 p.

[16] S. Qiao. A Robust and Efficient Algorithm for Evaluating Erlang B Formula. Dept. of Comuting and Software, McMaster University, Canada. October 17, 1998. 8 p.

[17] Harri Holma and Antti Toskala. WCDMA for UMTS; HSPA evolution and LTE. ISBN 978-0-470-31933-8. Wiley, 2008. 539 p.

[18] Harri Holma and Antti Toskala. LTE for UMTS; OFDMA and SC-FDMA based radio access. ISBN 978-0-470-99401-6. Wiley, 2009. 433 p.

BIOGRAPHIES

Mr. Jyrki T.J. Penttinen has worked in telecommunications industry since 1994, for Telecom Finland and it's successors until 2004, and after that, for Nokia and Nokia Siemens Networks. He has hold mobile networks research, design and technical management positions in Finland, Spain, Mexico and USA. His special interests areas are related to the radio interface of GSM/3G evolution, LTE and mobile TV. He currently works in Senior Solutions Architect position with NSN Innovation Center, Madrid, Spain. Mr. Penttinen obtained his M.Sc., Lic.Sc. and D.Sc. degrees from Helsinki University of Technology (currently known as Aalto University, School of Science and Technology), Finland, 1994, 1999, and 2011, respectively.

Mr. Francesco D. Calabrese Graduated with a degree in Mobile Communications in September 2005 from Aalborg University (Denmark) and in Telecommunication Engineering in October 2005 from L'Aquila University (Italy). From September 2005 to September 2006 he worked as a researcher at the Department of Electronic Systems at Aalborg University collaborating with Nokia Siemens Networks on the design of Radio Resource Management algorithms for LTE. From September 2006 on he continued his research in the same area while pursuing a PhD degree, which he completed in June 2009. He has been with the Nokia Siemens Networks Innovation Center in Madrid (Spain) since July 2009, and is currently in charge of WCDMA and HSPA+ investigations.

Mr. David Valerdi holds a technical product manager position at Vodafone Group PLC, one of the largest mobile telecommunications network company in the world. With an extensive international experience in telecom sector, he was previously senior system engineer working for Telefonica and Motorola. David obtained telecoms engineering qualifications and became MBA graduated with honors in 2009, at Instituto de Empresa.

Mr. Iñigo Güemes has worked in mobile industry since 1998, for Airtel Móvil, its successor Vodafone Spain and Vodafone Group PLC. He has hold mobile networks design, optimization, technical management and business integration analyst positions in Spain and Germany. He currently works in technical Product Manager position at Vodafone Group PLC in Madrid (Spain). Mr. Güemes graduated with a degree in Radio Telecommunication Engineering in November 1998 from Basque Country University (UPV /EHU, Spain) and became MBA in 2009, at Escuela de Organización Industrial (EOI, Spain).

CDMA-Based UHF-RFID System with Semi-Passive UHF Transponders

Andreas Loeffler, Ingo Altmann
Chair of Information Technologies
Friedrich-Alexander-University of Erlangen-Nuremberg
Erlangen, Germany
Email: {loeffler, altmann}@like.eei.uni-erlangen.de

Fabian Schuh
Chair for Information Transmission
Friedrich-Alexander-University of Erlangen-Nuremberg
Erlangen, Germany
Email: fabian.schuh@nt.eei.uni-erlangen.de

***Abstract*—RFID systems, in general, increase the efficiency of logistic systems, e.g., inventory of stocks. Unfortunately, present existing systems come fast to their limits if a certain number of RFID transponders must be *inventoried* in a limited period of time, as the channel access method of current RFID systems is based on Time Division Multiple Access. To shorten the inventory process, this work shows an implementation of an UHF RFID system based on semi-passive UHF transponders, using Code Division Multiple Access as anti-collision method. The work focuses on the uplink channel (tag to reader) that covers the transponders' backscattered signals. This channel access method enables simultaneous transfer of transponder data; i.e., all transponders in the field may respond at the same time within the same frequency band. The data transfer realized for the uplink channel uses a set of orthogonal spreading sequences (Gold codes) being different for every transponder. The RFID reader designed in this work despreads the backscattered signals and decodes the data of the different transponders. This work shows, in principle, the opportunity for a simultaneous data transfer on the uplink channel in RFID systems, which in turn may reduce the time needed for a complete inventory round. The entire system is build upon dedicated hardware, which is, also, a new aspect of this paper.**

Keywords-Radio frequency identification; cdma; uhf; transponder; digital signal processors.

I. Introduction

Nowadays, the RFID technology makes it possible to register all purchased goods of a customer at a checkout counter, but so far it was not possible to accomplish an entire stock inventory within a big warehouse, at once. If several transponders are located within the reading range of a reader, it may come, with a certain probability, to overlapping signals (collisions) between some of these transponders. This is the reason why anti-collision procedures are widely used, which in turn provide methods trying to prevent transponders from broadcasting their information simultaneously. Existing RFID solutions, which are qualified to cope with reading several transponder in one *inventory round*, are based on Time Division Multiple Access (TDMA, see Figure 1a), meaning that the transponder in the reader's field transmit their data at different moments. Loeffler et al. show in [1] that code division multiple access (CDMA)-based systems (Figure 1b) may improve the process of inventory rounds.

Regarding TDMA-based systems, basically, one differentiates between the time-independent principle of pure or unslotted ALOHA and the temporally subdivided principle of slotted ALOHA. By using unslotted ALOHA, data is sent at the time it is available, therefore it is fairly unorganized. In contrast to unslotted ALOHA, the principle of slotted ALOHA defines the points of time a broadcasting of data is permitted. For instance, data transmitted by two transponders using slotted ALOHA only experience a collision if both transponders begin to send their data at the same time slot.

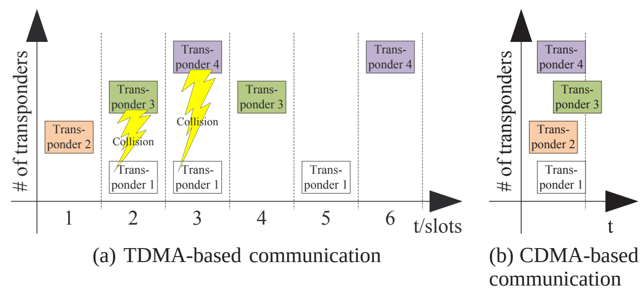

Figure 1. Different communication channel access techniques for RFID: TDMA, CDMA

The anti-collision procedure of the EPC Gen2 standard [2], [3] is based on slotted ALOHA. A so called *Q*-parameter controls the overall inventory process. The choice of *Q* is a typical trade-off. Choosing a high *Q* will lead in fact to a smaller number of collisions but on the other hand to an increased time needed for an inventory round. A smaller *Q* will lead to less acquisition time, but to more collisions, indeed. In addition, the usage of TDMA methods brings the systems to its limits when a certain number of transponders have to be *inventoried* in a very short time. For instance, fast working production lines could face that kind of problem.

The introduction of Code Division Multiple Access may find a remedy ([1], [4]). The transponders, each equipped with a unique orthogonal spreading code, may send their data at any given point in time. Overlapping signals will be sorted out by the process of despreading.

The objective of this work is the realization of a CDMA-based RFID system using semi-passive UHF transponders, whereby the recognition of the transponders shall be done quasi-simultaneously. This means that the transponders are transmitting data within the same time range and frequency band, in contrast to existing systems based on TDMA. For a first workaround this work concentrates on the uplink (i.e., tag to reader communication). The designed UHF transponders operate in semi-passive mode, meaning that the digital part of the transponders has an active power supply, whereas the radio frequency (RF) part works in passive mode (principle of backscatter [3]). The RFID reader, though, is separated into two parts. Part one, described as transmitting system, generates a sinusoidal wave at a certain UHF frequency. The frequency band for the usage of RFID within Europe is limited to a band between 865 MHz and 868 MHz. Part two, the receiving system, mixes down the backscattered signals, which are further processed analog, A/D converted and processed digital within a DSP. An overview of the complete system is given in Figure 3.

The paper is organized as follows. Following the introduction (Section I) and related work (Section II), Section III shows various anti-collision methods for RFID. This section focuses on ALOHA and slotted ALOHA as well as on some basic CDMA methods. Also, theoretical considerations are made to show the essential advantages of CDMA in RFID systems. Section IV goes into more detail regarding the combination of RFID and CDMA as channel access method. The proposed and realized CDMA-based RFID system is described in Section V. Within this section, the transmit stage, the transponder and the receiving stage are explained in detail. Section VI presents measurements regarding the system parts in the preceding section. Results are depicted in Section VII, whereas the article concludes with Section VIII.

II. Related Work

There is still ongoing research in the topic of combining classic RFID and CDMA methods. Mazurek [5]–[7] describes an approach where active RFID transponders are used to implement a direct-sequence (DS) CDMA RFID uplink transmission. The overall system design is described in [5]. It consists of several tags working in the 433 MHz ISM (industrial, scientific and medical) radio band. 127+1 Gold chips are applied at a stated chip rate of the RFID tags with 97.75 kHz. As the RFID tags are active, the output power level of the tags' transmitters is -10 dBm. Also, this paper shows theoretical, simulated and experimental results of the implementation. More results of this system are shown in [6]. Mazurek presents in [7] a performance analysis of the proposed active RFID system with the unslotted DS-CDMA transmission scheme. According to his paper, the active RFID system with DS-CDMA is able to successfully read out three times more tags per kilohertz bandwidth (RFID uplink channel) than an ALOHA-based RFID system. This shows the available potential of CDMA in RFID systems.

Other work related to this subject mainly consists of theoretical work and carried out simulations. The work done in [8] compares different approaches to overcome present limitations by simulating and evaluating slotted ALOHA, ID arbitration and direct-sequence CDMA. Lim and Mok [8] came to the result that the performance results of CDMA gives superior performance compared to the other two methods. Tseng and Lin [9] demonstrated (under usage of simulations) that the proposed Spreaded Partial-Q Slot Count algorithm outperforms existing anti-collision algorithms (such as common EPC Gen2) in terms of throughput. This algorithm is indeed a mixture of the commonly used EPC Gen2 anti-collision algorithm and a DS-CDMA approach.

A design of a CDMA-based transponder in HF-RFID (i.e., 13.56 MHz) is proposed by Fukumizu et al. [10]; the system is based on a PSK-like modulation scheme with a time hopping DS-CDMA multi-access, i.e., a combination of TDMA and CDMA. A SAW (surface acoustic wave) RFID tag is proposed in [11] and a prototype was tested at a frequency of 250 MHz.

The work from Rohatgi and Durgin [12] is in turn more closely related to this work. Nevertheless, basic differences are, e.g., the chosen chip rate, which is 1 kcps (chips per second), whereas this system operates with a minimum chip rate of 1.5 Mcps. Another difference is the underlying code sequence of the transponders. Rohatgi and Durgin [12] propose the usage of a PN-sequence (Pseudo Noise) in contrast to the Gold codes used in this work. The generation of orthogonal code sequences with different lengths is, e.g., described in [13] and will therefore not be part of this paper.

III. Basic Principles of Anti-Collision Methods for RFID

This section shall outline some basic issues regarding anti-collision methods within RFID. Basic and state-of-the-art anti-collision methods are shown in Subsection III-A. Subsection III-B presents theoretical performance issues regarding the throughput by comparing state-of-the-art TDMA methods with CDMA anti-collision methods.

A. ALOHA and slotted ALOHA

Before elucidating the state-of-the-art anti-collision method for UHF RFID systems, the principle of ALOHA and unslotted ALOHA [14] is illustrated. The ALOHA protocol (or pure ALOHA), first published by Abramson [15], is a very simple transmission protocol. The transmitter sends its data, no matter if the transmission channel is free or not. This means the transmitter does not care about collisions with other transmitters. The transmitter resends its data later, if the acknowledgment from the receiver is missing. RFID systems based on the principle of pure ALOHA are, e.g., based on the TTF principle, i.e., transponder-talks-first. The IPX protocol from IPICO [16] is an example for RFID systems using unslotted or pure ALOHA.

The extended ALOHA protocol, called slotted ALOHA [17], introduces time slots in which the transmitter must send its data at the beginning. Therefore, collisions only occur within a full time slot. This extension doubles the maximum throughput of the system. Most current RFID protocols are based on the principle of slotted ALOHA, as is also the very common used EPC standard UHF Class-1 Generation-2 air interface protocol V1.2.0 (ISO 18000-6C), commonly known as "Gen2". Basically, the "Gen2" standard works as follows. The standard defines, that every communication is triggered by the RFID reader, i.e., RTF (reader-talks-first). An inventory round, i.e., the process of detecting all available transponders, for instance, is started with the *Query*-command to acquire all transponders available in the read range. This command inherits a so called *Q*-parameter. Using this *Q*-parameter, every transponder generates a random number RN in the range $[0; 2^Q - 1]$ and initializes its internal slot counter with this random number. If, at a given moment, the value of the slot counter of one or more transponders equals 0, the transponders send a 16 bit random number called RN_{16}. After the acknowledgment of the RN_{16} through the reader, the electronic product code (EPC) is transmitted from the transponder to the reader and the transponder will be marked as *inventoried*. All the left-over (non-marked) transponders are prompted to decrement its slot counter by sending a *QueryRep*-command, and the procedure starts all over again. In the case of several transponders initializing their slot counters with the same random number RN, it will come sooner or later to a signal collision as the slot counters will reach zero at the same time slot. If the reader recognizes such a collision, another inventory round will be initiated to identify the left-over transponders. Therefore, a newly value of Q will be introduced and new random numbers will be calculated.

Lots of work has been done to improve the current EPC standard. Improving the current standard anti-collision method by choosing an appropriate value of Q, e.g., dynamically, is described in [18]–[20]. The right choice of Q is of great importance for the overall system performance, so that an accurate estimation would improve the time needed for an inventory round. Slightly new algorithms, based on the current EPC "Gen2" standard are outlined, e.g, in [21], [22]. New better performing algorithms for the slotted ALOHA protocol for RFID are described in [23]–[26]. A complete new system with time hopping on the communication link from tag to reader is outlined in [27].

B. Throughput in TDMA- and CDMA-based Systems

The throughput S in dependence of the traffic channel rate G describes the performance of a given transmission system regarding how many packets must be transmitted (statistically) until a successful transmission occurs. This statement is given with the term $\frac{G}{S}$ as described by Kleinrock and Tobagi [28]. The reciprocal of this term, i.e., $\frac{S}{G}$ defines accordingly the probability of a successful transmission. The channel capacity is determined by maximizing S with respect to G [28]. According to Abramson [15] the pure ALOHA transmission has a relation between S and G of

$$S = G\, e^{-G} \tag{1}$$

, whereas the throughput of the slotted ALOHA transmission is defined after Roberts [17] with

$$S = G\, e^{-2G} \tag{2}$$

. Accordingly, the maximum channel capacity is $\frac{1}{2e} \approx 18.4\%$ for pure ALOHA and $\frac{1}{e} \approx 36.8\%$ for slotted ALOHA.

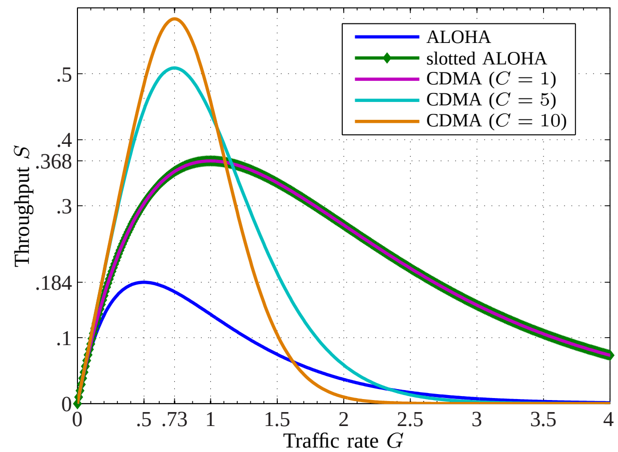

Figure 2. Various throughputs S over traffic rate G for ALOHA, slotted ALOHA and CDMA

For a fair comparison between CDMA-based systems and ALOHA systems, the total bandwidth has to be maintained the same for both systems. A CDMA system has a so called spreading factor C, which is proportional to the length of the spreading codes respectively the ratio between chip rate and bit rate (i.e., R_{chip}/R_{bit}) used. According to Linnartz and Vvedenskaya [29] the throughput S and the offered traffic rate G is

$$S = G\, e^{-CG} \sum_{k=0}^{C-1} \frac{(CG)^k}{k!} \tag{3}$$

. Setting $C = 1$ leads to the slotted ALOHA transmission scheme. Figure 2 shows various throughputs S over the traffic rate G. The figure shows the throughputs for ALOHA (channel capacity 18.4%), slotted ALOHA and CDMA with spreading factor $C = 1$ (channel capacity 36.8%), CDMA with $C = 5$ (channel capacity 50.87%) and CDMA with $C = 10$ (channel capacity 58.31%). This graph shows the basic difference between TDMA (ALOHA-based) and CDMA systems. In general, TDMA-based RFID systems can handle much more RFID transponders with a lower overall throughput. CDMA-based system, on the other hand, are able to handle a limited amount of RFID tags with higher overall throughput. For instance, assuming a limited amount of RFID transponders for a traffic rate $G = 0.73$. The throughput of unslotted ALOHA would be $S_{\text{ALOHA}} = 16.95\%$ and the throughput of slotted ALOHA $S_{\text{unslotted ALOHA}} = 35.18\%$. A CDMA-based system with a spreading factor C of 10 would have there its maximum throughput of $S_{\text{CDMA},C=10} = 58.31\%$. This scenario is shown in Figure 2.

Finally, it can be stated that CDMA-based RFID systems may be better for particular applications, in which the number of transponders is limited and the inventory process has to be made very fast, e.g., fast production lines and automation processes.

Particular slotted ALOHA CDMA systems and corresponding performances may be found in [30], [31]. Other works describe certain CDMA systems with error correction which really outperform the TDMA-based systems. Examples can be found in [32]–[36]. Also this list is not complete it gives a short overview of CDMA-based system performances.

IV. Basic Principles of CDMA for RFID

This section shows some basic work regarding UHF RFID systems in conjunction with CDMA.

An IC design for an experimental transponder is offered in [37]. The transponder uses time-hopping DS-CDMA, but operates within the RFID HF region (13.56 MHz). Therefore, the transponder cannot be compared directly with the proposed approach, but shows, that a fully integrated circuit for future releases of CDMA-based RFID UHF transponders is possible. Wang et al. [38] describes an anti-collision method based on CDMA. Gold codes are used as spreading sequences. Also, a first design of a transponder is outlined. Within this design, a field effect transistor (FET) is used as source for backscattering. A new transmission scheme for TTF transponders is presented in [39]. The uplink is based on asynchronous DS-CDMA. It is shown, by simulation, that the proposed CDMA method outperforms the classical RFID transmission in terms of channel capacity. Also, Gold codes are used to separate the various RFID transponders.

Mutti and Floerkemeier [40] explore the chances how CDMA methods can help to inventory large buildups of transponders. A combination of slotted ALOHA and CDMA is proposed to receive better inventory results. Therefore, the CDMA method is only used at the moments when the channel collides. Also, they show that Gold codes are very suitable for the usage within RFID systems. Simulation results show that Gold codes outperform Kasami codes.

A new anti-collision method is presented in [9] with the goal to achieve a fast inventory process. A so called spread partial-Q slot count algorithm which is based on slotted ALOHA CDMA increases the overall throughput at the cost of bandwidth and complexity.

Other algorithms are presented in [41], [42], where the throughput is increased by using dynamic slotted ALOHA CDMA algorithms with orthogonal variable spreading factors. Theoretic analysis and simulations show an increasing performance regarding the identification process. However, the proposed algorithms perform different, when the conditions of the RFID system changes. A better gain may only be achieved, if the system itself is involved into the design of the algorithms.

Another approach is described by Liu and Guo [4], that uses Huffman spreading sequences to improve the process of inventory. Therefore several performances have been compared. Simulation results show the increase in performance if proposed Huffman spreading sequences are used. Anyway, a direct hardware implementation has to consider the various states within the IQ constellation diagram to be imaged to the backscatter modulator.

A minimum mean-squared error single user adaptive receiver for the asynchronous DS-CDMA system, based on the least-mean-square (LMS) algorithm is presented in [43]. The article states that the proposed algorithm achieves a faster convergence rate than the transversal LMS algorithm.

Wuu et al. [44] presents a zero-collision scheme, that is based on CDMA and hash-chain mechanisms. The results of the paper show that with the applied techniques, not only a zero-collision scheme, but also a secure channel may be realized to outperform standard technologies. Anyway, the authors assume, that CDMA can be implemented into RFID systems, particularly RFID transponders.

Summing up, it can be stated, that the usage of CDMA for RFID not only provides better system performance, but also offers advanced security issues. Furthermore, very low effort was put into the realization of such a CDMA-based RFID system as such. Therefore, this missing piece is one of the subjects of this work.

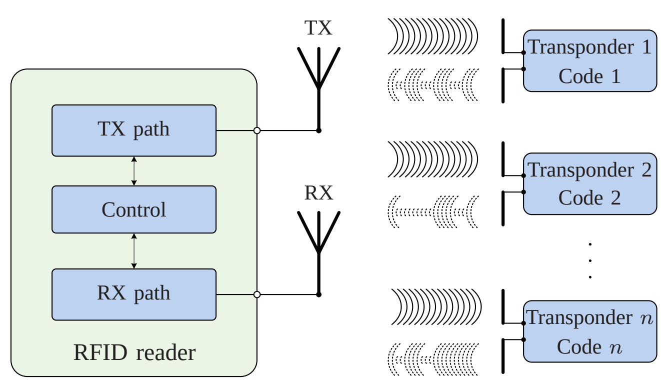

Figure 3. Basic architecture of RFID system

V. CDMA-BASED RFID SYSTEM

Within this section the basics of the proposed RFID system are presented. Going into more detail, subsection V-A shows the architecture of the *Transmitting System*, followed by subsection V-B presenting the proposed semi-passive RFID transponders and subsection V-C describing the *Receiving System*.

Figure 3 shows the basic architecture of the CDMA-based RFID system. Generally, it consists, as any other RFID system, too, of two major parts. First, the RFID reader itself and second, one or more transponders. The big difference between this system and other current systems is the channel access method in the uplink (transponder to reader communication) layer, in this case based on CDMA; this fact is illustrated in Figure 3 showing every transponder (Transponder 1 to Transponder n) with a unique spreading code (Code 1 to Code n).

The basic working principle is also indicted in Figure 3, showing the RFID reader with transmitting a sinusoidal wave over its transmit antenna TX, thus allowing the various transponders in the field to modulate and reflect (principle of backscatter) this incident wave back to the RFID reader. Therefore, the total backscattered signal consists of the additive superposition of n (if multipath is negligible) backscattered transponder signals with each transponder using its own unique spreading code. Receiving this superimposed signal over RX, the reader is, generally, able to separate the various transponder signals from each other (process of despreading) in order to restore the transponders' data.

Figure 3 and Figure 5, respectively, show the concept and the architecture of the realized RFID reader. The following paragraphs will refer to these figures.

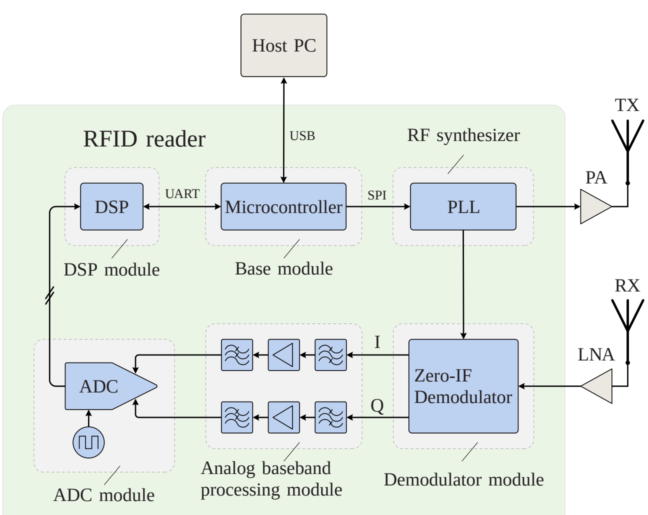

Figure 4. Basic concept of RFID reader

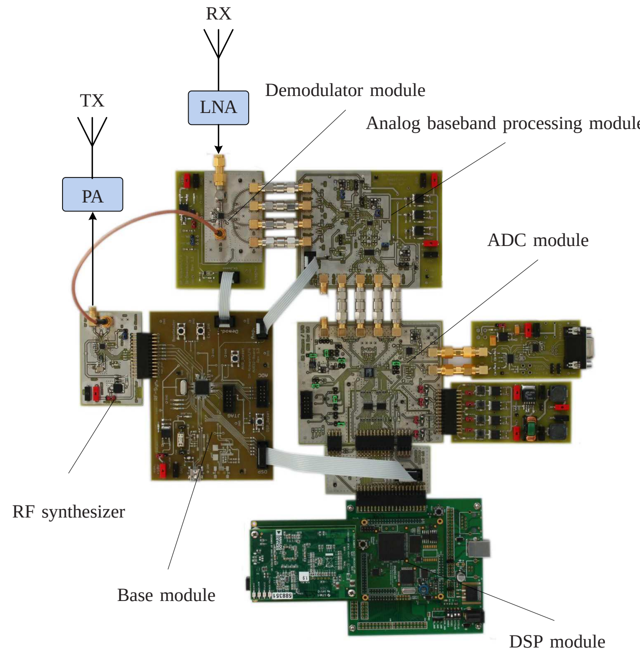

Figure 5. Architecture of CDMA-based RFID reader

A. *Transmitting System*

The proposed semi-passive UHF transponder works in accordance with the principle of backscattering. The incident wave to be backscattered is generated by the *Transmitting System*. Considering the RFID uplink channel (tag to reader), the introduced *Transmitting System* (see Figure 3 and Figure 5) consists of a PLL-based RF synthesizer (Figure 3 and Figure 5) , generating a sine wave (here with $f_{\text{carrier}} = 866.5\,\text{MHz}$, maximum output power $P_{out} = 1\,\text{dBm}$ at $50\,\Omega$), an upstream power amplifier (PA, Gain $G_{PA} = 20\,\text{dB}$, 1 dB compression point $= 24\,\text{dBm}$), and a linear polarized $50\,\Omega$ antenna (TX, Gain $G_{TX} \approx 7\,\text{dBi}$). The purpose of the transmitter is to generate an RF wave to be reflected (backscattered) by the UHF transponder whereby the reflected wave is received by the *Receiving System* further discussed in subsection V-C.

It has to be mentioned that the RF synthesizer not only generates a sine wave for the transmitting part, but also for the receiving part of the system. Indeed, it is used as local oscillator (LO) source for the downmixing part of the receiver. However, both synthesized RF waves inherit the same frequency as they are both created by the same PLL; the waves only differ of π in phase.

B. *Transponder*

The major tasks of the semi-passive UHF transponders are:

- Generate spreading code
- Create spreaded data

- Modulate and reflect incoming RF signal at $f_{\text{carrier}} = 866.5\,\text{MHz}$ (principle of backscatter)

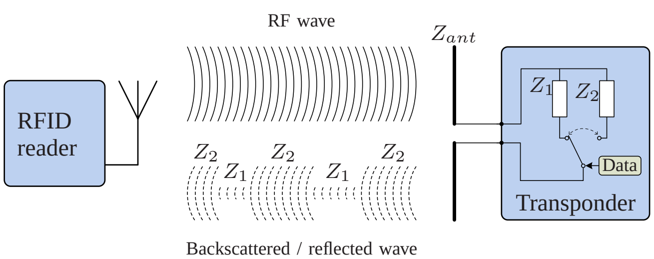

Figure 6. Basic function of RFID transponder

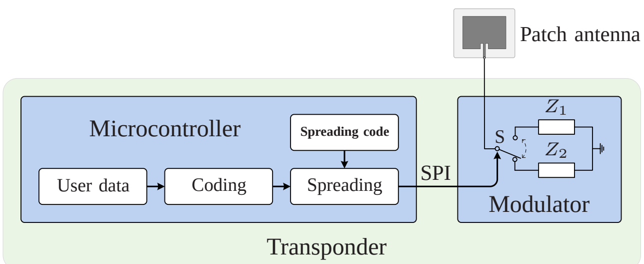

Figure 7. Concept of CDMA-based semi-passive UHF RFID transponder

Figure 6 shows the basic principle of an RFID transponder. An incident RF wave is reflected by the transponder. The phase and amplitude of the reflected wave is affected by three major issues: The first two issues are structural mode and antenna mode scattering [45], [46], the third issue is the multipath propagation. Multipath effects are a non-changeable fact, so they can be neglected at this point. The structural mode scattering of an antenna is dependent on the structure of the antenna itself (material, antenna geometry, etc.) and cannot be changed - therefore, the structural mode may not be used for a normal data transmission. The antenna mode scattering, on the other hand, describes the receiving and emitting effects of an antenna, which usually depend on the impedances used; particularly the impedance of the antenna Z_{ant} itself and the corresponding load impedance Z_{load} of the following transponder system. Assuming that Z_{load} can adopt two values being Z_1 and Z_2. According to Figure 6 the antenna mode scattering may be changed by altering the load impedance Z_{load} of the transponder's antenna according to the data the transponder wants to send. Binary data may be send by altering Z_{load} between Z_1 and Z_2, thus changing the reflection coefficient between Z_{ant} and Z_{load}, which in turn leads to an alteration of the reflection of the RF wave in phase and amplitude. Again, this only affects the antenna mode scattering. However, the total resulting backscattered signal is the superposition of the multipath signal, the structural mode scattering and antenna mode scattering effects. Measurements at the end of this paper will show this effects.

Figure 7 shows the basic concept of the CDMA-based semi-passive transponder. A central microcontroller generates the binary output data stream (i.e., the already coded and spreaded user data) to drive the fast RF switch 'S', that alters between two impedance states Z_1 and Z_2; according to the binary state of the output data stream, a logical '1' triggers Z_2, a logical '0' triggers Z_1 to be the corresponding load impedance. Therefore, the data stream directly affects the reflection coefficient. The performance of the uplink (tag to reader radio channel) depends very much on the modulation efficiency η_{mod} of the backscatter modulator [47]–[49], which basic calculation is subject of the following paragraph.

1) Determining Load Impedances: Assuming an antenna with complex antenna impedance

$$Z_{ant} = R_a + j\,X_a \tag{4}$$

with $R_a = R_r + R_l$ as the sum of radiation resistance R_r and real antenna losses R_l, and X_a as the imaginary part of the antenna impedance. The complex reflection coefficients $\Gamma_{1,2}$ between the antenna impedance and the load impedances $Z_{1,2}$ can be described as

$$\Gamma_{1,2} = \frac{Z_{1,2} - Z_{ant}^*}{Z_{1,2} + Z_{ant}} = \frac{Z_{1,2} - R_a + j\,X_a}{Z_{1,2} + R_a + j\,X_a} \tag{5}$$

According to Rembold [50] the modulation efficiency η_{mod} can be expressed as

$$\begin{aligned} \eta_{mod} &= \frac{P_{mod}}{P_{max}} = \frac{2}{\pi^2}\,|\Gamma_1 - \Gamma_2|^2 \qquad (6)\\ &= \frac{2}{\pi^2}\left|\frac{Z_1 - R_a + j\,X_a}{Z_1 + R_a + j\,X_a} - \frac{Z_2 - R_a + j\,X_a}{Z_2 + R_a + j\,X_a}\right|^2 \\ &= \frac{8R_a^2}{\pi^2}\left|\frac{Z_1 - Z_2}{(Z_1 + R_a + j\,X_a)\,(Z_2 + R_a + j\,X_a)}\right|^2 \end{aligned}$$

, whereby P_{max} (the maximum receivable power of the antenna) and P_{mod} (the entire power with the information carrying signals) are defined as

$$P_{max} = \frac{1}{8}\,\frac{|U_0^2|}{R_a} = \frac{1}{2}\,|a|^2 \tag{7}$$

$$P_{mod} = \frac{|a|^2}{\pi^2}\,|\Gamma_1 - \Gamma_2|^2 \tag{8}$$

with U_0 as the antenna's open circuit voltage and a being the wave from the antenna impedance to the load impedance (see Rembold [50] for details).

Maximum modulation efficiency η_{mod} is achieved when the difference of the complex reflections coefficients Γ_1 and Γ_2 is maximum. Supposing two vectors (Γ_1 and Γ_2) in a complex coordinate system, the maximum difference between both vectors is achieved at the point when the phase φ_Γ differs with π under the assumption that the maximum absolute value of any Γ is limited to 1. That determines the complex reflection coefficients $\Gamma_{1,2}$ to

$$\Gamma_1 = e^{j\varphi_{\Gamma,1}} \tag{9}$$

$$\Gamma_2 = e^{j\varphi_{\Gamma,1}+j\pi} \tag{10}$$

Setting $\varphi_{\Gamma,1}$ to 0 sets $\Gamma_{1,2}$ to ± 1. According to Equation (5) this will define the load impedances to

$$Z_{1,2} = \frac{Z^*_{ant} + \Gamma_{1,2}\, Z_{ant}}{1-\Gamma_{1,2}} \tag{11}$$

$$\rightarrow Z_1 = \frac{Z^*_{ant} + Z_{ant}}{0} = \pm\infty \tag{12}$$

$$\rightarrow Z_2 = \frac{Z^*_{ant} - Z_{ant}}{2} = \frac{-2jX_a}{2} = -jX_a \tag{13}$$

The antenna designed for the RFID transponders is a $50\,\Omega$ patch antenna (Figure 9). Therefore the imaginary part (within the specified frequency range) $X_a \approx 0$. This determines $Z_2 = -jX_a \approx 0$. A load impedance of $Z_1 = \infty$ corresponds to an open circuit wheres $Z_2 = 0$ corresponds to a short circuit. Choosing open and short circuit states as desired load impedances, the maximum achievable modulation efficiency is, according to Equation (7), determined to be

$$\eta_{mod} = \frac{2}{\pi^2}\ |+1+1|^2 = \frac{8}{\pi^2} \approx 81\% \tag{14}$$

. In order to have the maximum modulation efficiency for the CDMA-based RFID system, the load impedances of the realized semi-passive transponders are set to open and short circuit. By choosing these values as load impedances, one has to keep in mind, that this is only advisable for semi-passive UHF RFID transponders. If passive transponders are designed, one has to consider the power consumption into its calculations. Therefore, open and short circuit values are not suitable, as the backscattered power is, in fact, too high, as the transponder needs a large portion of the incoming power for supplying itself [51].

2) Transponder Basics: Figure 8 illustrates the concept of the transponder and Figure 9 shows one of the realized transponders to achieve the previously mentioned tasks. The microcontroller (µC) is powered by a power supply and may be user-controlled using USB or pushbuttons. The µC generates the unique spreading code and subsequently, the spreaded outgoing data. The data are forwarded to the SPI interface to drive the modulator of the transponder with different input voltages to adjust different load impedances respectively reflection coefficients of the modulator. The block diagram of the modulator (Figure 7) shows the principle of the proposed simple backscatter modulator. An example on how to design load modulators can be found in [52]. However, the incoming spreaded data stream is low-pass filtered to limit the outgoing bandwidth. As the modulator should be as simple as possible, an RF switch 'S' forms the interface between the logic data and the backscattered HF wave. The inputs of the switch are driven by the spreaded data stream with two voltage levels (0 and 2.75 V) given by a buffer driver. One connection of the switch is linked to the patch antenna's microstrip line ($50\,\Omega$); the ground connection is linked to the patch antennas ground plane. By triggering the switch's input with the spreaded data to be sent, either Z_1 or Z_2 is connected to the antenna. This modification changes in turn the reflection of an incident electromagnetic wave. The difference of phase and amplitude of the reflection is a direct indicator for the efficiency of a backscattering modulator. As mentioned above the modulators load impedances are set to open and short circuit to achieve maximum modulation efficiency. An exemplary spectral extract of the backscattered output of the transponder, measured at the receiving antenna, is given in Figure 16. On closer inspection, one can see the spreaded data (chip rate is 1.5 Mcps) around the carrier frequency (866.5 MHz). As these data signal levels ($P \approx$ -90 dBm $\pm$ 10 dB) are not very high, an accurate implementation of the receiving system becomes necessary.

For a limited downlink (reader to tag) capability the transponders are equipped with a module for measuring the field strength (RSSI) and a module for measuring the frequency (RF Divider) of the incident RF wave emitted by the reader. The *RF Divider* is currently used to indicate the transponder to send its data as soon as a carrier between 865 MHz and 868 MHz is detected. The RSSI module is used for statistical measurements. Anyway, both modules are not part of this work.

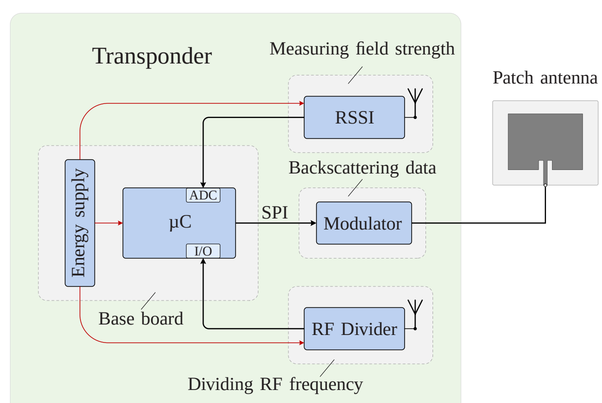

Figure 8. Block diagram of semi-passive UHF RFID transponder with limited downlink capabilities

3) Modulator: The transponder's modulator is one of the key components of the system. Usually, it effects the energy supply (only for passive working transponders) and the modulation efficiency (for passive and semi-passive working transponders) of transponders. Therefore, it has a direct effect for the maximum achievable range of such a system. The principle of the modulator has been already discussed above, so that this paragraph focuses primarily

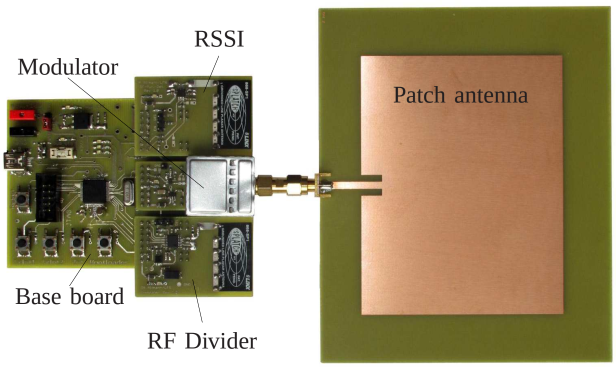

Figure 9. Prototype of semi-passive UHF RFID transponder

on the realization. Figure 10 shows the modulator, with and without RF shielding. The left part of the modulator is connected to the transponder's base board, the right SMA plug to the patch antenna as shown in Figure 9. The part within the RF shielding is responsible for the backscattering effects. A part of the incident RF wave is fed into the modulator. The part depends on the antenna (structural and antenna mode) and the reflection coefficient between antenna impedance Z_{ant} and the load impedance Z_{load} of the connected modulator. This part is fed into the RF switch and the load impedance (either Z_1 or Z_2), which corresponds to the current state of the switch. The state of the switch is defined by a buffered microcontroller output. which itself shows the current voltage of the binary data stream to be sent. In the case of Z_1 (open circuit state), the incident wave is entirely reflected with no phase shift. State Z_2 (short circuit) also corresponds to a total reflection, but with a phase shift of 180°.

Measuring the load impedances of the modulator show a very good accordance with the theoretical results. Figure 11 shows the reflection coefficients within a Smith chart. As one can see the phase difference is not exactly π. Z_2 (short circuit) has nearly short circuit properties; Z_2 (open circuit) has nearly open circuit properties. The frequency range of the measurement was between 852 MHz and 882 MHz.

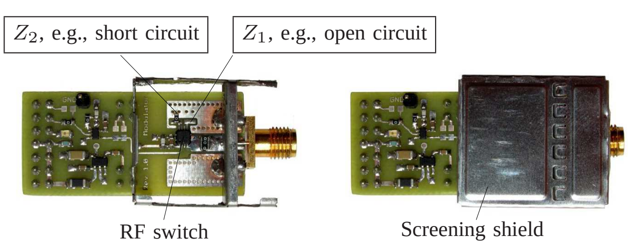

Figure 10. Backscatter modulator

4) Gold Codes: The choice of an appropriate set of spreading codes is a key issue when designing CDMA systems. Gold codes seem to be one of the best codes to be used in UHF RFID systems. Mutti and Floerkemeier [40], for instance, state that Gold codes outperform Kasami codes. Moreover, one Gold code family contains a large number of unique codes, which provides a high probability of finding a well-suited set of codes for a system to be designed.

Gold codes, first introduced by Robert Gold [53], are commonly used in spread spectrum systems, such as WLAN and UMTS as well as in GPS (C/A code). The generation of Gold codes is quite simple as only two linear feedback shift registers (LFSR) are necessary to create one set of codes.

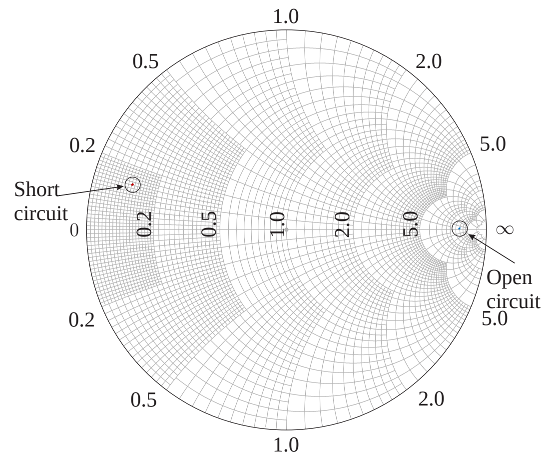

Figure 11. Smith chart of modulator

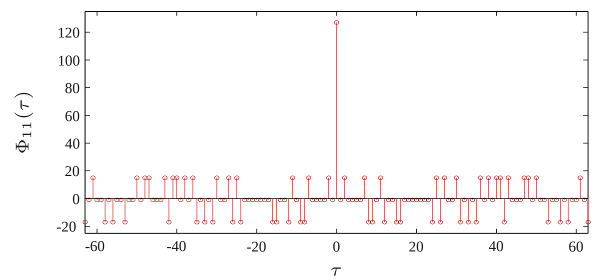

(a) ACF of Code 1

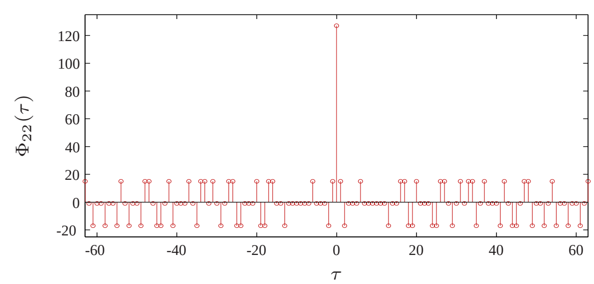

(b) ACF of Code 2

Figure 12. ACF of original Gold codes

Other advantages of Gold code are:

- Good balance between auto- and cross-correlation
- Flexibility in code length
- No user synchronization necessary, i.e. the transponders need not to be synchronized among each other

Because of above mentioned advantages, the proposed CDMA-based system uses Gold sequences.

However, Gold codes have a length of $2^m - 1$ with m being the order of each linear feedback shift register. For reasons of flexibility a Gold code generator has been implemented on the transponder's 32 bit µC. The choice fell upon a Gold code length of 127 ($m = 7$). The characteristic polynomial is 137_{dec} for the first LFSR and 143_{dec} for the second one. The initial value for the first LFSR is 85_{dec}. By choosing two Gold codes (Code 1 and Code 2) the second LFSR is initialized with 127_{dec} for the first and with 111_{dec} for the second code. Then, a small adjustment was made to the generated Gold codes to be more compatible to the µC. A succeeding binary '0' is added to each code to move it to a length of 128 bit. To show the effect of this '0', the auto-correlation function (ACF) and cross-correlation function (CCF) have been evaluated for both Codes. Figure 12 shows the ACF Φ_{cc} of the original 127 bit Gold codes. Figure 13 illustrates the ACF $\Phi_{cc}(\tau)$ of the adjusted (127+1 bit) Gold codes. The results are slightly higher values beyond the peak value at $\tau = 0$. As not only the auto-correlation counts, the corresponding cross-correlation $\Phi_{1_2}(\tau)$ between the two codes are presented in Figure 14. As expected the values of the adjusted codes are slightly higher compared to the original ones, but without loosing the typical noise-like character. This means, that the effect of the added '0' is negligible for further considerations. However, final system implementations have to consider that fact.

C. Receiving System

The major tasks of the *Receiving system* are:

- Receive incoming signals from several transponders, i.e., downmixing, analog baseband processing and A/D conversion
- Find separate data streams (transponders) by despreading, demodulating and decoding the signals

The *Receiving system* mainly consists of a hardware part that is needed to mix down the backscattered RF signal, centered at $f_c = 866.5\,\text{MHz}$, into baseband, despread, demodulate, and decode the baseband signal in order to determine the transponders' data. Figure 15 presents the structure of this receiving part of the RFID reader. The incoming RF signal is caught by a receiving antenna (RX) and amplified by a following low noise amplifier (LNA). A subsequent Zero-IF IQ-Demodulator mixes down the RF signal directly to baseband. The output of the demodulator consists of differential I- and Q-signals, which are band-pass filtered, twice

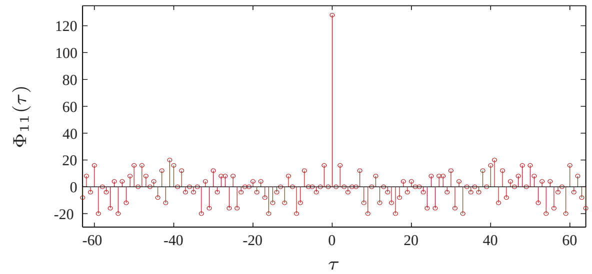

(a) ACF of Code 1

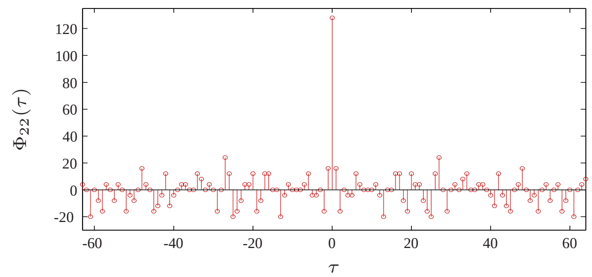

(b) ACF of Code 2

Figure 13. ACF of adjusted Gold codes

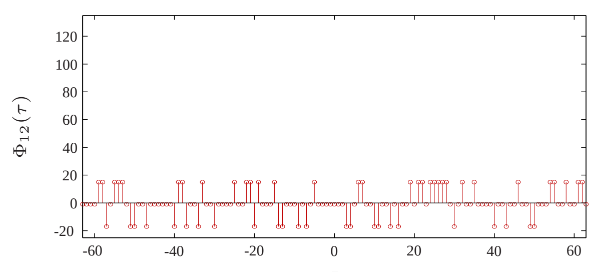

(a) CCF of original Code 1 and Code 2

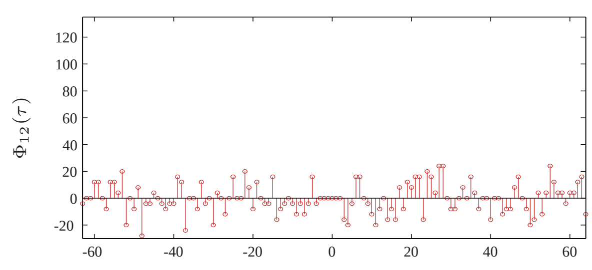

(b) CCF of adjusted Code 1 and Code 2

Figure 14. CCF of both, original and adjusted Gold codes

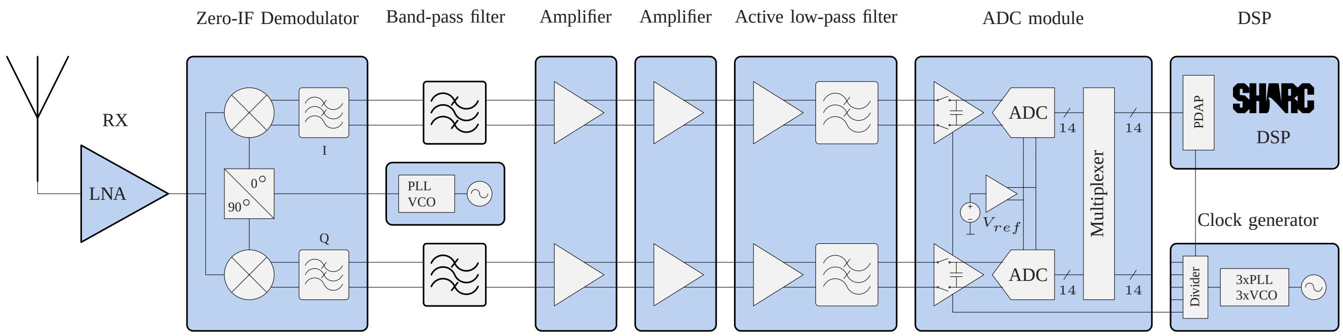

Figure 15. Architecture of receiving system

amplified and active low-pass filtered. It has to mentioned that the IQ signals are completely handled differentially throughout the amplifier and filter stages to keep the signal-to-noise ratio (SNR) at a high level. The succeeding Analog-to-Digital conversion (ADC) module samples both, the I- and Q-signal, simultaneously. The A/D converted signals are fed into a digital signal processor (DSP) block with a data rate of 450 Mbps (Sampling of 2 channels with each channel having a resolution of 15 bit (14 data + 1 status bit) including a sampling rate of 15 Msps). The DSP module despreads, demodulates and decodes this data stream. The results are the user data of each recognized transponder.

The following paragraphs focus on the details of the receiving system.

1) Demodulator: The incoming low-noise amplified signal is fed into the demodulator. The demodulator uses the second RF synthesizer signal (the first is used as RF signal source for the transmit path, see above) as local oscillator (LO) source, to mix down the RF signal directly into baseband (Zero-IF). The demodulator is based on the LT5575 chip [54] from Linear Technology and 50 Ω-matched between 865 MHz and 868 MHz. The output of the demodulator is differential with 2 I- and 2 Q-signals, respectively.

2) Band-Pass Filter: The differential working band-pass filter, which succeeds the demodulator, is used to suppress the DC-part of the baseband signal, i.e. mainly the non-information carrying down-mixed carrier signal, and high-frequency disturbing signals (from the internal mixer of the demodulator). Therefore the passband is set between 16 kHz and 20 MHz.

3) Amplifier Stage: The following amplifier stage is build upon two differential amplifiers (LTC6421-20 [55] and LTC6420-20 [56]), each with a differential voltage gain of 10 V/V.

4) Active Anti-Aliasing Filter: The last analog signal processing stage is an active anti-aliasing filter for the succeeding ADC module. The cut-off frequency of the 4th order low-pass filter (Chebyshev characteristic) is currently set to 2.5 MHz. This stage is based on LT6604-2.5 [57] from Linear Technology.

5) A/D Conversion: One very important part of the receiving system is a well-designed A/D conversion stage for the baseband signal. The subjective of the ADC module is a time synchron sampling of the differential I- and Q-signals. The module is based on a dual A/D converter of type AD9248 from Analog Devices [58]. Two channels may be sampled synchronously with a resolution of 14 bit per channel. Maximum sampling rate is 40 Msps. As the fast parallel input of the succeeding DSP module has only 20 bit the internal multiplexer of the A/D converter is used to transmit the I- and Q-data after each other. Therefore one status bit is used to indicate the current transmitted channel data. Here, the A/D converter is driven with 15 Msps per channel, which corresponds to an overall sampling clock rate of 30 MHz. The 14 bit per channel plus the status bit and the sampling rate, generate in total a data rate of 450 Mbps to be handled by the subsequent DSP module.

6) DSP Module: The purpose of the DSP is the handling of all calculations, necessary to evaluate the transponders' user data. Therefore, the following stages are necessary:

- Data acquisition (from ADC module)
- Despreading of baseband signals
- Demodulation of despreaded signals
- Decoding of demodulated data

The following paragraphs give a short introduction to these topics. The data acquisition phase has to be accomplished only once, against what the following stages have to be passed through by every transponder respectively spreading code available.

Data Acquisition: As the amount of data to handle is quit large (450 Mbps) the data streams are not handled in real time. However, through the usage of this DSP (ADSP-21469 from Analog Devices [59]) the processing speed is quite high. The A/D converted data signals are acquired through the DSP's PDAP (Parallel Data Aquisition Port) interface. From there, they are transfered to an internal 8x32 bit buffer. Finally, the data are passed via DMA access to an internal memory. As of limited memory capabilities the data is transferred block-wise to the external memory. As the sampled values are stored as 32 bit values (DWORD), the amount of data for one shot (duration is $T_{shot} \approx 188\,\mu s$) is 90112 samples per channel, so in total 720896 bytes or 704 kbytes.

Despreading: The process of despreading is the most calculation intensive operation the DSP has to handle. As this phase needs more time than the data acquisition process the system is, up-to-date not able to work real-time. Parallel processing would be a good solution. The DSP itself has a clock rate of 450 MHz.

Despreading data from the baseband signal has to be done for I- and Q-channel separately. The despreading operation is realized using the cross-correlation between I and Q signals and the origin codes used by every transponder in the field. If $s[k]$ is the I or Q signal and $c[k]$ one of the corresponding codes of one of the transponders, the cross-correlation $\Phi_{s,c}(\tau)$ between these signals is done by multiplying every time instance signal s with code c. Equation (15) shows the corresponding relationship between $c[k]$ and $s[k]$

$$[s \bigstar c][\tau] = \Phi_{s,c}(\tau) = \sum_{t=-\infty}^{+\infty} s^*[t] \cdot c[\tau + t] \qquad (15)$$

A code length of 128 chips corresponds to 1280 samples ($R_{chip} = 1.5$ Msps and $R_{sample} = 15$ Msps) and 90112 samples per channel for I and Q. This results into 230,686,720 multiplications and 180,224 additions.

One goal was to reduce this high amount of operations. This is realized through estimation of the time moments the chips appear within the IQ signals. This estimation method works as follows. The IQ baseband signal is sampled and correlated among the first $2 \cdot 1280 = 2560$ samples. This results in 6,553,600 multiplications and 5120 additions. The first maximum, corresponding to the first peak indicates the initial index i_0 to start the despreading process. The following peaks are estimated by jumping from i_0, 1280 samples ahead. As certain incertitudes (oscillators, etc.) will lead to synchronization errors, the correlation is not only made at sample index $i_0 + n \cdot 1280$, but at 5 samples before and after the estimated time index. That means, the second peak is determined by executing the cross-correlation $\Phi_{i,1}(\tau)$ as given in Equation (16).

$$\Phi_{i,1}(\tau) = \sum_{t=i_0+1280-5}^{i_0+1280+5} s^*[t] \cdot c[\tau + t] \qquad (16)$$

The result is 11 correlations per peak and a new synchronization index, as the new peak indicates the next starting point for the succeeding peak estimation. With 70 data peaks within one shot and 1 within the initial guess, the total number of correlations per channel is $2560 + 69 \cdot 11 = 3319$. This leads to 8,496,640 multiplications and 6,638 additions in total for both channels. This is only 3.6% of the full correlation.

Demodulation: The process of demodulation inherits the merge of the I and Q signals. According to their signal quality, estimated through the maximum correlation values, the signals are weighted and superimposed. This process of demodulation is beyond this paper's scope and not further described.

Decoding User Data: The demodulated signal stream is Manchester coded [1] and needs to be decoded accordingly. The resulting data stream corresponds to the transponder's respectively the user data.

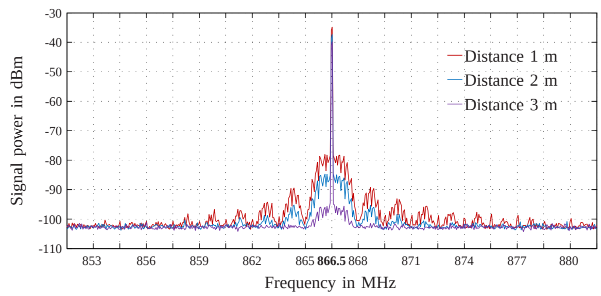

Figure 16. Spectrum of backscattered signal from transponder

VI. Measurements

This section presents measurements of various parts of the system, including transponder, analog baseband processing and DSP.

A. Transponder Measurements

Figure 16 shows the spectrum of the backscattered transponder signals. For this measurement an RF signal ($P_{TX} = 10$ dBm, $f_{\text{carrier}} = 866.5$ MHz) is fed into the linear polarized transmit antenna. One transponder is placed at a distance of 1, 2 and 3 m. The resulting reflected signal spectrum after the receiving antenna is shown in Figure 16. As expected, the backscattered signal parts drop with increasing distance from the reader's antennas.

The IQ constellation diagrams of the received RF signal are shown throughout Figure 17 to Figure 19. It can be shown that the backscattered signals show a mixture between ASK and PSK modulation. For instance, as in Figure 17, the mean of the data points (from the two states of the one transponder) is not the origin (0,0). This discrepancy is the effect of multipath and structural antenna mode scattering. Same applies for Figure 18 with 2 transponders, generating $2^2 = 4$ constellation points, and Figure 19 with 3 transponders, generating $2^3 = 8$ constellation points. The number of constellation points for n transponders is 2^n because all n transponders have 2 states sharing the same coherent RF signal from the reader.

However, as expected the transponders show a near exact

BPSK modulation (as configured in subsubsection V-B3), if the ASK part is neglected.

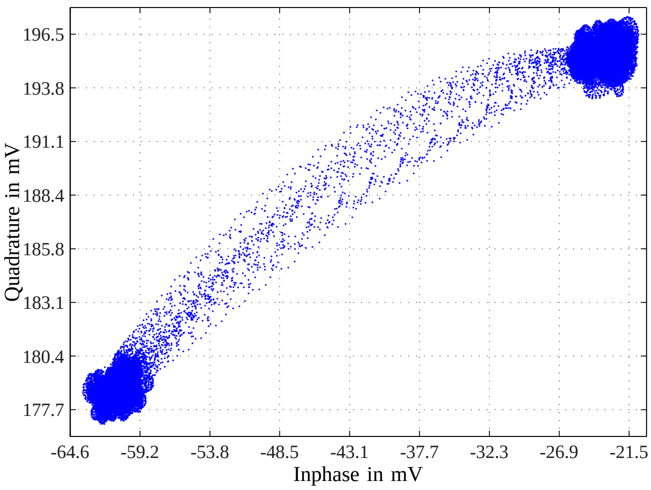

Figure 17. IQ constellation diagram for 1 transponder

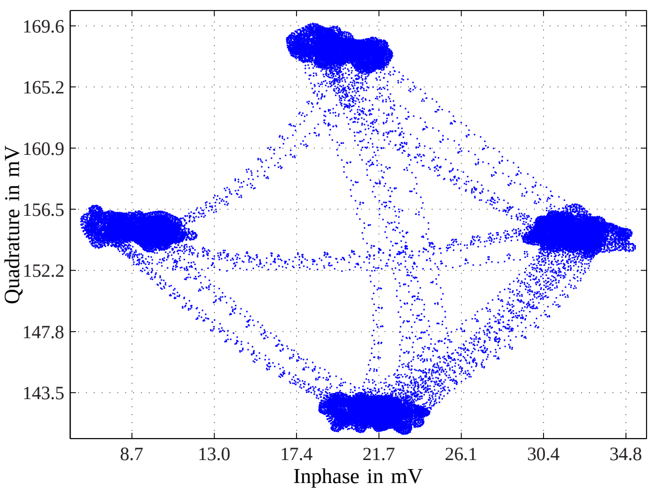

Figure 18. IQ constellation diagram for 2 transponders

B. RX Measurements

Two measurements have been carried out to show the basic working principle of the analog baseband processing module. The goal of this module is the signal conditioning for the succeeding ADC module. Figure 20 shows the output of the demodulator, i.e. the I- and Q-signals. As mentioned above these signals are handled differentially (I_+, I_-, Q_+ and Q_-). To simplify matters the differential signals have been put together ($I = I_+ - I_-$ and $Q = Q_+ - Q_-$) . The signals are amplified and filtered with a resulting signal as shown in Figure 21. The signals were recorded with 2 transponders in the field. As in the IQ measurements before, 2 transponders generate $2^2 = 4$ different signal levels (evaluated from Figure 21):

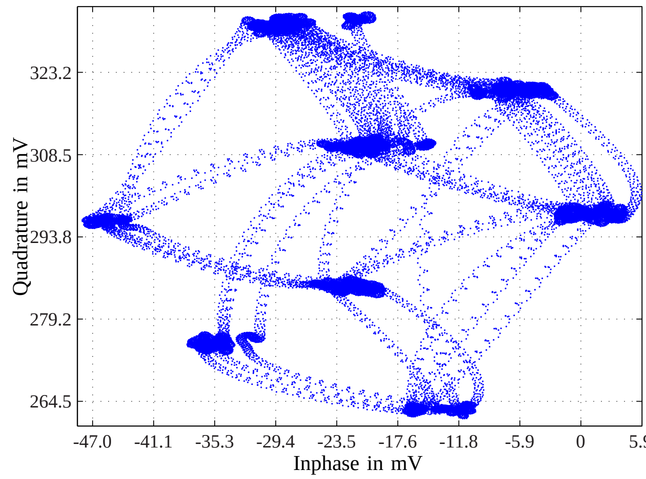

Figure 19. IQ constellation diagram for 3 transponders

1) $0.1\,\mathrm{V} + j0.2\,\mathrm{V}$
2) $0.3\,\mathrm{V} - j0.4\,\mathrm{V}$
3) $-0.2\,\mathrm{V} - j0.2\,\mathrm{V}$
4) $-0.4\,\mathrm{V} + j0.5\,\mathrm{V}$

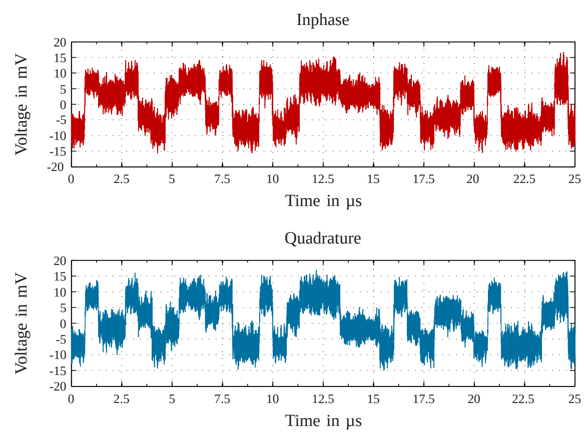

Figure 20. IQ signal after demodulator / 2 Transponders

C. DSP Measurements

The DSP module comes with some debugging functionalities. One of these functionalities is able to provide the DSP values, from its internal or external memories, via USB to a host PC. Figure 22 shows the results of a full cross-correlation. For simplicity the CCFs have been normalized to one. The values show the maximum number of samples (90112) and the peaks, with each peak describing a bit. The value of the bit may be positive $(+1)$ or negative (-1). The difference between the peaks and the noise floor is an indicator for the quality of the communication link.

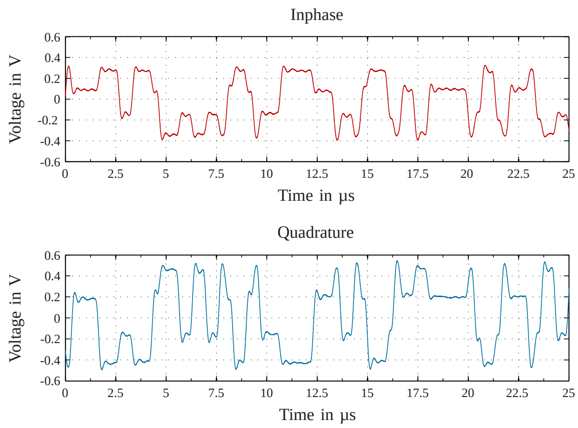

Figure 21. IQ signal after baseband processing / 2 Transponders

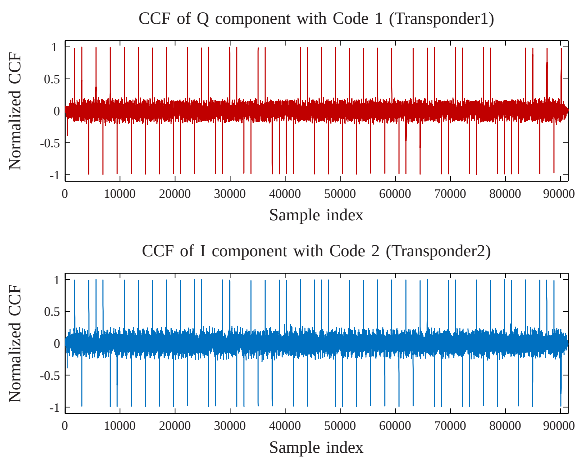

Figure 22. Cross-correlation of signals with origin spreading codes - Process of despreading / 2 Transponders

VII. Results

According to the measurements the proposed system worked as expected. It was proved that the UHF RFID system for broadcasting information data using a CDMA method worked out very good. During the experiments there was a maximum distance to the antennas being around 15 m. The transmitted RF-power at 866.5 MHz was 20 dBm. The introduced transponders are semi-passive, which means that the communication link is still passive, whereas the data generation (on the transponder's side) is active, driven by 3.3 V power supplies.

Smaller problems arose, when various transponder had a different path length to the antennas. In that case one transponder (the nearest) dominated the second transponder (more far away) which often occurred to a non-detection of transponder two. This problem is known in CDMA systems and is referred to as near-far problem [60]. One possibility to reduce the near-far effect is the usage of Huffman sequences [4]. But this approach asks for more than 2 states of the load impedance of the transponder's modulator. Nevertheless, carried out indoor experiments showed that the near-far effect of the proposed system is, in fact, very low.

Also, theoretical work, which states an advantage of CDMA-based RFID systems compared to state-of-the-art RFID systems based on TDMA methods, complies with the measured results of the proposed CDMA-based UHF RFID system.

VIII. Conclusion

This article presented a realization of a CDMA-based RFID system working in the UHF region. The system itself is build upon a *Transmitting system* providing a continuous electromagnetic wave. This emitted RF carrier is backscattered through one or more designed UHF tags. Each of these semi-passive operating transponders generate a unique spreading sequence. The proposed spreading sequences are Gold codes providing a good orthogonality. A simple modulator on the transponder generates the desired backscatter signal. The *Receiving system* captures this signal by down mixing the RF signal to baseband. Further analog signal processing and subsequent A/D conversion gives the DSP the chance to despread, demodulate and decode the desired transponder signals.

The significant advantage of such a structure compared to present systems lies in the ability to avoid particular TDMA-based anti-collision schemes. This, indeed, will lead to less time needed for *inventorizing* RFID tags, as this can be achieved within one time slot. Topics for future research are, regarding the receiver side, the need for much more computational resources (RAKE receiver, [61]) and the near-far problem, CDMA-based systems have to deal with.

References

[1] A. Loeffler, F. Schuh, and H. Gerhaeuser, "Realization of a CDMA-based RFID System Using a Semi-active UHF Transponder," in *Wireless and Mobile Communications (ICWMC), 2010 6th International Conference on*, Sep. 2010, pp. 5 –10.

[2] *Class 1 Generation 2 UHF Air Interface Protocol Standard "Gen 2"*, EPCglobal Inc. Std. UHF Class 1 Gen 2 Standard v. 1.2.0, 2008.

[3] K. Finkenzeller, *RFID handbook*. Wiley West Sussex, England, 2003.

[4] H. Liu and X. Guo, "A passive UHF RFID system with Huffman sequence spreading backscatter signals," in *Proceedings of the 1st international conference on The internet of things*. Springer-Verlag, 2008, pp. 184–195.

[5] G. Mazurek, "Design of RFID system with DS-CDMA transmission," in *Automation Science and Engineering, 2008. CASE 2008. IEEE International Conference on*, Aug. 2008, pp. 703 –708.

[6] ——, “Experimental RFID system with active tags,” in *Signals and Electronic Systems, 2008. ICSES ’08. International Conference on*, Sep. 2008, pp. 507 –510.

[7] ——, “Active RFID System With Spread-Spectrum Transmission,” *Automation Science and Engineering, IEEE Transactions on*, vol. 6, no. 1, pp. 25 –32, Jan. 2009.

[8] A. Lim and K. Mok, “A study on the design of large-scale mobile recording and tracking systems,” in *System Sciences, 1998., Proceedings of the Thirty-First Hawaii International Conference on*, vol. 7, Jan 1998, pp. 701–710 vol.7.

[9] D.-F. Tseng and Z.-C. Lin, “An Anti-Collision Algorithm in RFID Systems Based on Interference Cancellation and Tag Set Partitioning,” in *Vehicular Technology Conference, 2008. VTC Spring 2008. IEEE*, May 2008, pp. 1609 –1614.

[10] Y. Fukumizu, M. Nagata, S. Ohno, and K. Taki, “A Design of Transponder IC for Highly Collision Resistive RFID Systems,” in *Advanced System Integrated Circuits 2004. Proceedings of 2004 IEEE Asia-Pacific Conference on*, Aug. 2004, pp. 438–439.

[11] J. Pavlina, B. Santos, N. Kozlovski, and D. Malocha, “SAW wireless, passive sensor spread spectrum platforms,” in *Ultrasonics Symposium, 2008. IUS 2008. IEEE*, Nov. 2008, pp. 1112–1115.

[12] A. Rohatgi and G. Durgin, “Implementation of an Anti-Collision Differential-Offset Spread Spectrum RFID System,” in *IEEE Antennas and Propagation Society International Symposium 2006*, 2006, pp. 3501–3504.

[13] A. Hottinen and K. Pehkonen, “A flexible multirate cdma concept with multiuser detection,” in *Spread Spectrum Techniques and Applications Proceedings, 1996., IEEE 4th International Symposium on*, vol. 2, Sep 1996, pp. 556–560 vol.2.

[14] D. Bertsekas and R. Gallager, *Data networks (2nd ed.)*. Upper Saddle River, NJ, USA: Prentice-Hall, Inc., 1992.

[15] N. Abramson, “THE ALOHA SYSTEM: another alternative for computer communications,” in *Proceedings of the November 17-19, 1970, fall joint computer conference*, ser. AFIPS ’70 (Fall). New York, NY, USA: ACM, 1970, pp. 281–285. [Online]. Available: http://doi.acm.org/10.1145/1478462.1478502

[16] IPICO, “IPICO’s IP-X RFID Air-interface Protocol,” Mar. 2009. [Online]. Available: http://www.ipico.com/

[17] L. G. Roberts, “ALOHA packet system with and without slots and capture,” *SIGCOMM Comput. Commun. Rev.*, vol. 5, pp. 28–42, April 1975. [Online]. Available: http://doi.acm.org/10.1145/1024916.1024920

[18] L.-C. Wang and H.-C. Liu, “A Novel Anti-Collision Algorithm for EPC Gen2 RFID Systems,” in *Wireless Communication Systems, 2006. ISWCS ’06. 3rd International Symposium on*, Sep. 2006, pp. 761 –765.

[19] Y. Maguire and R. Pappu, “An Optimal Q-Algorithm for the ISO 18000-6C RFID Protocol,” *Automation Science and Engineering, IEEE Transactions on*, vol. 6, no. 1, pp. 16 –24, Jan. 2009.

[20] P. Pupunwiwat and B. Stantic, “A RFID Explicit Tag Estimation Scheme for Dynamic Framed-Slot ALOHA Anti-Collision,” in *Wireless Communications Networking and Mobile Computing (WiCOM), 2010 6th International Conference on*, Sep. 2010, pp. 1 –4.

[21] D. Lee, O. Bang, S. Im, and H. Lee, “Efficient dual bias Q-Algorithm and optimum weights for EPC Class 1 Generation 2 Protocol,” in *Wireless Conference, 2008. EW 2008. 14th European*, Jun. 2008, pp. 1 –5.

[22] Y. Cui and Y. Zhao, “A modified Q-parameter anti-collision scheme for RFID systems,” in *Ultra Modern Telecommunications Workshops, 2009. ICUMT ’09. International Conference on*, Oct. 2009, pp. 1 –4.

[23] J. H. Choi, D. Lee, and H. Lee, “Query tree-based reservation for efficient RFID tag anti-collision,” *Communications Letters, IEEE*, vol. 11, no. 1, pp. 85 –87, Jan. 2007.

[24] O. Bang, S. Kim, and H. Lee, “Identification of RFID tags in dynamic framed slotted Aloha,” in *Advanced Communication Technology, 2009. ICACT 2009. 11th International Conference on*, vol. 01, Feb. 2009, pp. 354 –357.

[25] D. Liu, Z. Wang, J. Tan, H. Min, and J. Wang, “ALOHA algorithm considering the slot duration difference in RFID system,” in *RFID, 2009 IEEE International Conference on*, Apr. 2009, pp. 56 –63.

[26] S. Makwimanloy, P. Kovintavewat, U. Ketprom, and C. Tantibundhit, “A novel anti-collision algorithm for high-density RFID tags,” in *Electrical Engineering/Electronics, Computer, Telecommunications and Information Technology, 2009. ECTI-CON 2009. 6th International Conference on*, vol. 02, May 2009, pp. 848 –851.

[27] Z. Zhang, Z. Lu, Z. Pang, X. Yan, Q. Chen, and L.-R. Zheng, “A Low Delay Multiple Reader Passive RFID System Using Orthogonal TH-PPM IR-UWB,” in *Computer Communications and Networks (ICCCN), 2010 Proceedings of 19th International Conference on*, Aug. 2010, pp. 1 –6.

[28] L. Kleinrock and F. Tobagi, “Packet Switching in Radio Channels: Part I–Carrier Sense Multiple-Access Modes and Their Throughput-Delay Characteristics,” *Communications, IEEE Transactions on*, vol. 23, no. 12, pp. 1400 – 1416, Dec. 1975.

[29] J.-P. M. Linnartz and N. D. Vvedenskaya, “DS-CDMA Packet Network with Random Access,” Dec. 2010. [Online]. Available: http://www.wirelesscommunication.nl/reference/chaptr06/stack/cdmastck.htm

[30] S. Gopalan, G. Karystinos, and D. Pados, “Capacity, throughput, and delay of slotted ALOHA DS-CDMA links with adaptive space-time auxiliary-vector receivers,” *Wireless Communications, IEEE Transactions on*, vol. 4, no. 1, pp. 79 – 92, Jan. 2005.

[31] A. Sakata, T. Yamazato, H. Okada, and M. KATAYAMAt, “Throughput Comparison of CSMA and CDMA slotted ALOHA in Inter-Vehicle Communication,” in *Telecommunications, 2007. ITST ’07. 7th International Conference on ITS*, Jun. 2007, pp. 1 –6.

[32] A. Sastry, "Effect of Acknowledgment Traffic on the Performance of Slotted ALOHA-Code Division Multiple Access Systems," *Communications, IEEE Transactions on*, vol. 32, no. 11, pp. 1219 – 1222, Nov. 1984.

[33] Z. Liu and M. El Zarki, "Performance analysis of DS-CDMA with slotted ALOHA random access for packet PCNs," in *Personal, Indoor and Mobile Radio Communications, 1994. Wireless Networks - Catching the Mobile Future., 5th IEEE International Symposium on*, vol. 4, Sep. 1994, pp. 1034 – 1039 vol.4.

[34] R. van Nee, R. van Wolfswinkel, and R. Prasad, "Slotted ALOHA and code division multiple access techniques for land-mobile satellite personal communications," *Selected Areas in Communications, IEEE Journal on*, vol. 13, no. 2, pp. 382 –388, Feb. 1995.

[35] F. L. Lo, T. S. Ng, and T. Yuk, "Performance analysis of a fully-connected, full-duplex CDMA ALOHA network with channel sensing and collision detection," *Selected Areas in Communications, IEEE Journal on*, vol. 14, no. 9, pp. 1708 –1716, Dec. 1996.

[36] Q. Liu, E.-H. Yang, and Z. Zhang, "Throughput analysis of CDMA systems using multiuser receivers," *Communications, IEEE Transactions on*, vol. 49, no. 7, pp. 1192 –1202, Jul. 2001.

[37] Y. Fukumizu, M. Nagata, S. Ohno, and K. Taki, "A design of transponder IC for highly collision resistive RFID systems," in *Advanced System Integrated Circuits 2004. Proceedings of 2004 IEEE Asia-Pacific Conference on*, Aug. 2004, pp. 438 – 439.

[38] P. Wang, A. Hu, and W. Pei, "The Design of Anti-collision Mechanism of UHF RFID System based on CDMA," in *Circuits and Systems, 2006. APCCAS 2006. IEEE Asia Pacific Conference on*, Dec. 2006, pp. 1703 –1708.

[39] G. Mazurek, "Collision-Resistant Transmission Scheme for Active RFID Systems," in *EUROCON, 2007. The International Conference on Computer as a Tool*, Sep. 2007, pp. 2517 –2520.

[40] C. Mutti and C. Floerkemeier, "CDMA-based RFID Systems in Dense Scenarios: Concepts and Challenges," in *RFID, 2008 IEEE International Conference on*, Apr. 2008, pp. 215–222.

[41] D. Yang, Y. Chen, and B. Wang, "RFID anti-collision algorithm in logistics service system," in *Service Operations and Logistics, and Informatics, 2008. IEEE/SOLI 2008. IEEE International Conference on*, vol. 2, Oct. 2008, pp. 1891 – 1896.

[42] W. Bisheng, Y. Dongkai, and Z. Qishan, "Efficient Identification UHF RFID system scheme based on combination of DFSA and OVSF-CDMA," *IEICE Electronics Express*, vol. 5, no. 22, pp. 954–961, 2008.

[43] C. Paleologu, C. Vlădeanu, and S. El Assad, "Fast Convergence Least-Mean-Square Algorithms for MMSE Receivers in DS-CDMA Systems," *International Journal On Advances in Networks and Services*, vol. 1, no. 1, 2008.

[44] L.-C. Wuu, Y.-J. Chen, C.-H. Hung, and W.-C. Kuo, "Zero-Collision RFID Tags Identification Based on CDMA," in *Information Assurance and Security, 2009. IAS '09. Fifth International Conference on*, vol. 1, Aug. 2009, pp. 513 – 516.

[45] R. Hansen, "Relationships between antennas as scatterers and as radiators," *Proceedings of the IEEE*, vol. 77, no. 5, pp. 659 –662, May 1989.

[46] K. Penttila, M. Keskilammi, L. Sydanheimo, and M. Kivikoski, "Radar cross-section analysis for passive RFID systems," *Microwaves, Antennas and Propagation, IEE Proceedings* -, vol. 153, no. 1, pp. 103 – 109, Feb. 2006.

[47] U. Karthaus and M. Fischer, "Fully integrated passive UHF RFID transponder IC with $16,7\mu W$ minimum RF input power," *IEEE*, vol. 38, no. 10, pp. 1602–1608, 2003.

[48] F. Fuschini, C. Piersanti, F. Paolazzi, and G. Falciasecca, "On the Efficiency of Load Modulation in RFID Systems Operating in Real Environment," *Antennas and Wireless Propagation Letters, IEEE*, vol. 7, pp. 243 –246, Mar. 2008.

[49] P. Nikitin and K. Rao, "Antennas and propagation in uhf rfid systems," in *RFID, 2008 IEEE International Conference on*, Apr. 2008, pp. 277 –288.

[50] B. Rembold, "Optimum modulation efficiency and sideband backscatter power response of RFID-tags," *Frequenz - Journal of RF-Engineering and Telecommunications*, vol. 63, no. 1 -2, pp. 9 –13, Jan. 2009.

[51] D. Dobkin, *The RF in RFID: passive UHF RFID in practice*. Newnes, 2008.

[52] D. Pardo, A. Vaz, S. Gil, J. Gomez, A. Ubarretxena, D. Puente, R. Morales-Ramos, A. Garcia-Alonso, and R. Berenguer, "Design criteria for full passive long range uhf rfid sensor for human body temperature monitoring," in *RFID, 2007. IEEE International Conference on*, March 2007, pp. 141–148.

[53] R. Gold, "Optimal binary sequences for spread spectrum multiplexing (Corresp.)," *Information Theory, IEEE Transactions on*, vol. 13, no. 4, pp. 619 – 621, Oct. 1967.

[54] Linear Technology, "LT5575 - 800MHz to 2.7GHz High Linearity Direct Conversion Quadrature Demodulator," Oct. 2010. [Online]. Available: http://www.linear.com/pc/productDetail.jsp?navId=H0,C1,C1011,C1725,P36240

[55] ——, "LTC6421-20 - Dual Matched 1.3GHz Differential Amplifiers/ADC Drivers," Oct. 2010. [Online]. Available: http://www.linear.com/pc/productDetail.jsp?navId=H0,C1,C1154,C1009,C1126,P80589

[56] ——, "LTC6420-20 - Dual Matched 1.8GHz Differential Amplifiers/ADC Drivers," Oct. 2010. [Online]. Available: http://www.linear.com/pc/productDetail.jsp?navId=H0,C1,C1154,C1009,C1126,P80614

[57] ——, "LT6604-2.5 - Dual Very Low Noise, Differential Ampli?er and 2.5MHz Lowpass Filter," Oct. 2010. [Online]. Available: http://www.linear.com/pc/productDetail.jsp?navId=H0,C1,C1154,C1008,C1148,P85251

[58] Analog Devices, “AD9248: Dual 14-Bit, 20/40/65 MSPS, 3 V Analog-to-Digital Converter,” Oct. 2010. [Online]. Available: http://www.analog.com/en/analog-to-digital-converters/ad-converters/ad9248/products/product.html

[59] ——, “ADSP-21469: High Performance Fourth Generation DSP,” Oct. 2010. [Online]. Available: http://www.analog.com/en/embedded-processing-dsp/sharc/adsp-21469/processors/product.html

[60] J. Andrews, “Interference cancellation for cellular systems: A contemporary overview,” *IEEE Wireless Communications*, vol. 12, no. 2, pp. 19–29, 2005.

[61] R. E. Ziemer and W. H. Tranter, *Principles of Communication: Systems, Modulation and Noise, 5th Edition*. Wiley, July 2001.

High Throughput and Low Power Enhancements for LDPC Decoders

Erick Amador and Raymond Knopp
EURECOM
06904 Sophia Antipolis, France
name.surname@eurecom.fr

Renaud Pacalet
TELECOM ParisTech
06904 Sophia Antipolis, France
renaud.pacalet@telecom-paristech.fr

Vincent Rezard
Infineon Technologies France
06560 Sophia Antipolis, France
vincent.rezard@infineon.com

***Abstract*—Modern VLSI decoders for low-density parity-check (LDPC) codes require high throughput performance while achieving high energy efficiency on the smallest possible footprint. In this paper, we present two optimizations to enhance the throughput and reduce the power consumption for these decoders. As a first optimization, we seek to speedup the decoding task by modifying the processing step known as *syndrome check*. We partition this task and perform it in *on-the-fly* fashion. As a second optimization, we address the topic of iteration control in order to save energy and time on unnecessary decoder operation when processing undecodable blocks. We propose an iteration control policy that is driven by the combination of two decision metrics. Furthermore, we show empirically how stopping criteria should be tuned as a function of false alarm and missed detection rates. Throughout this paper we use the codes defined in the IEEE 802.11n standard to show performance results of the proposed optimizations.**

***Keywords*—LDPC codes; iterative decoding; syndrome calculation; throughput enhancement; stopping criteria; iteration control; low power.**

I. Introduction

Low-density parity-check (LDPC) codes have gained a lot of interest because of their outstanding error-correction performance. Originally proposed by Gallager in 1962 [3] and rediscovered by Mackay [4] in the 1990s, these codes exhibit a performance that comes very close to the limits imposed by Shannon.

Several communication standards have already adopted these codes, ranging from Wireless Local/Metropolitan Area Networks (IEEE 802.11n [5] and 802.16e [6]) and high-speed wireless personal area networks (IEEE 802.15.3c [7]) to Digital Video Broadcast (DVB-S2 [8] and DTMB [9]) and 10Gbit Ethernet (10GBASE-T [10]). Furthermore, these codes are currently being proposed for next generation cellular and mobile broadband systems as defined by the ITU-R to comply with the IMT-Advanced radio interface requirements: IEEE 802.16m [11] and 3GPP LTE-Advanced [12].

In the case of mobile wireless terminals high throughput and low power operation are required. Nevertheless, these goals are often contradictory due mainly to the iterative nature of the decoding algorithms used. For a successful decoding task the fulfillment of all parity-check constraints is verified, but usually for an unsuccessful task a preset maximum number of iterations is completed.

In this paper, we propose to optimize one recurrent task that is performed within each decoding iteration. Syndrome check or verification is performed in order to confirm the validity of the obtained codeblock and hence decide whether to continue or halt the decoding process. This task corresponds to the evaluation of all the parity-check constraints imposed by the parity-check matrix. We propose to perform this task *on-the-fly* so that a partially unsatisfied parity-check constraint can disable a potential useless syndrome verification on the entire matrix. We identify as benefits from this technique the elimination of several hardware elements, a reduction on the overall task latency and an increase on system throughput.

One form of the proposed technique has been identified in [13] for the purpose of improving the energy-efficiency of a decoder. This technique, nevertheless, is sub-optimal in the error-correction sense as it introduces undetected codeblock errors. In this work, we show the assumptions for this technique and a performance analysis, along with a proposal to recover the performance loss.

As a second topic, we consider iteration control for avoiding unnecessary decoder operation. Early detection of an undecodable block not only saves energy on unnecessary iterations but may improve the overall latency when an automatic repeat-request (ARQ) strategy is also in use. Previously proposed iteration control policies [14][15][16][17] differ on the decision metrics used. These decision metrics are characterized by their dependence or not upon extraneous variables that must be estimated. The parameters used within the decision rule must be tuned to particular scenarios. In the previous art it has been shown how this tuning essentially trades off error-correction performance and the average number of iterations.

In this work, we identify a decision metric provided by a specific decoding algorithm, the Self-Corrected Min-Sum algorithm [18]. This algorithm has been shown to provide quasi-optimal error-correction performance at very low complexity. We propose to combine two decision metrics in order to control the iterative decoding task. We perform comparisons among the previous art and the proposed hybrid control policy in terms of error-correction performance, average number of iterations and false alarm rate. The main advantage our work shows is the energy efficiency of the proposed policy as it exhibits empirically very low missed detection rates. Furthermore, we argue that the tuning of parameters of a

$$H = \begin{bmatrix} 1\,1\,0\,1\,0\,1 \\ 1\,0\,1\,1\,1\,0 \\ 0\,1\,1\,0\,1\,1 \end{bmatrix}$$

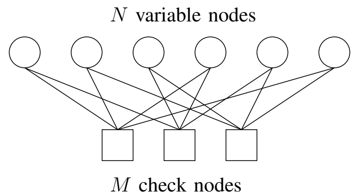

Fig. 1. LDPC code matrix and graph example.

Codeblock symbols

$$\begin{array}{c}
\begin{array}{cccccc} C_1 & C_2 & C_3 & C_4 & C_5 & C_6 \end{array} \\
\begin{bmatrix} 1 & 0 & 0 & 0 & 1 & 1 \\ 0 & 1 & 0 & 1 & 1 & 0 \\ 1 & 1 & 0 & 0 & 0 & 1 \\ 0 & 1 & 0 & 0 & 1 & 1 \end{bmatrix}
\end{array}
\begin{array}{l}
\\
\rightarrow \; C_1 \oplus C_5 \oplus C_6 \\
\rightarrow \; C_2 \oplus C_4 \oplus C_5 \\
\rightarrow \; C_1 \oplus C_2 \oplus C_6 \\
\rightarrow \; C_2 \oplus C_5 \oplus C_6
\end{array}$$

Parity−check matrix **Parity−check constraints**

Fig. 2. Example parity-check constraints.

stopping rule should be done based upon the false alarm and missed detection rates performance.

This paper merges and extends our previous work in [1][2]. The remainder of this paper is organized as follows. Section II presents LDPC codes and their iterative decoding. Section III outlines the proposed syndrome check method and its performance while Section IV shows the system level impact along with results for a VLSI architecture. In Section V, we show prior stopping criteria and the proposed iteration control policy while Section VI shows simulation results and the tuning of stopping criteria. Section VII concludes the paper.

II. Background

In this section, we introduce the target error-correction codes along with their iterative decoding algorithm and the type of messages used in the computation kernels.

A. LDPC Codes

Binary LDPC codes are linear block codes defined by a sparse parity-check matrix $\boldsymbol{H}_{M\times N}$ over GF(2). This matrix defines M parity-check constraints among N code symbols. The number of non-zero elements in $\boldsymbol{H}$ is relatively small compared to the dimensions $M \times N$ of $\boldsymbol{H}$.

A codeword $\boldsymbol{c}$ corresponds to the null space of $\boldsymbol{H}$:

$$\boldsymbol{H} \cdot \boldsymbol{c}^T = \boldsymbol{S} = \boldsymbol{0}\,, \tag{1}$$

where $\boldsymbol{S}$ is referred to as the *syndrome*. Indeed, the condition $\boldsymbol{S} = \boldsymbol{0}$ suggests that no further decoding iterations are necessary. Typically, a maximum number of iterations is set to define an unsuccessful decoding operation.

A quasi-cyclic (QC) LDPC code is obtained if $\boldsymbol{H}$ is formed by an array of sparse circulants of the same size, [19]. If $\boldsymbol{H}$ is a single sparse circulant or a column of sparse circulants this results in a cyclic LDPC code. *Architecture-aware* [20] and QC-LDPC codes are composed of several layers of non-overlapping rows, this enables the concurrent processing of subsets of rows without conflicts.

The code can also be represented by a bipartite graph in which rows of $\boldsymbol{H}$ are mapped to *check nodes* and columns to *variable nodes*. The non-zero elements in $\boldsymbol{H}$ define the connectivity between the nodes. Figure 1 shows an example matrix (non-sparse) and the corresponding code graph representation.

The rows in $\boldsymbol{H}$ establish the parity constraints of the code as a function of the code symbols with the location of the non-zero elements of the matrix. Figure 2 shows an example correspondance between the code symbols C_n, the parity-check matrix and the parity-check constraints.

The parity-check constraints are of even parity and the $\oplus$ operation corresponds to the modulo-2 addition.

B. Decoding Algorithm

LDPC codes are typically decoded iteratively using a two-phase message-passing algorithm commonly known as *sum-product* [21] or *belief propagation*. This algorithm exchanges code symbol extrinsic reliability values between check and variable nodes. Each decoding iteration consists of two phases: variable nodes update and send messages to the neighboring check nodes, and check nodes update and send back their corresponding messages. Node operations are in general independent and may be executed in parallel. This allows the possibility to use different scheduling techniques that may impact the convergence speed of the code and the storage elements requirements. The algorithm initializes with intrinsic channel reliability values and iterates until hard-decisions upon the accumulated resulting posterior messages satisfy equation (1). Otherwise, a maximum number of iterations is completed.

The computational complexity of the decoding task resides in the operation performed at the check nodes of the code graph, indeed it is in here where the tradeoff between error-correction performance and complexity takes place. Optimal message computation is performed by the Sum-Product algorithm [21] at the expense of high complexity. The Min-Sum (MS) algorithm [22] performs a sub-optimal message computation at reduced complexity. Several correction methods have been proposed to recover the performance loss of the MS algorithm by downscaling the messages computed using a normalization or an offset value, [22].

It has been argued in [18] that the sub-optimality of MS decoding is not due to the overestimation of the check node messages, but instead to the loss of the symmetric Gaussian distribution of these messages. This symmetry can be recovered by eliminating unreliable variable node messages or *cleaning* the inputs of the check node operation. In [18] the Self-Corrected MS (SCMS) decoding is introduced, which exhibits quasi-optimal error-correction performance. An input to the check node operation is identified as *unreliable* if it has changed its sign with respect to the previous iteration. Unreliable messages are *erased* and are no longer propagated along the code graph. In [23] a comparison is performed in terms of energy efficiency among the most prominent message computation kernels.

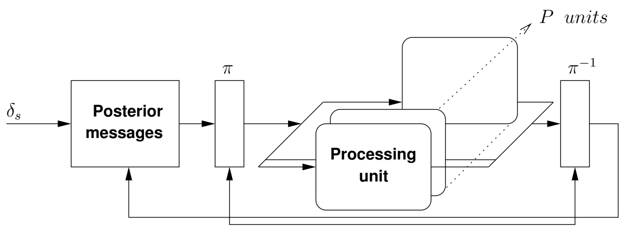

Fig. 3. General structure of an LDPC decoder.

Motivated by the outstanding error-correction performance and low complexity of the SCMS kernel, in Section V we look closely at the behavior of this kernel in order to assist the early detection of undecodable blocks.

The general structure of an LDPC decoder is shown in Figure 3. *Intrinsic* channel values δ_s are initially used to generate *extrinsic* messages, these are messages generated after processing each row in $\boldsymbol{H}$. The sum of all extrinsic messages generated constitutes the posterior messages that are used to perform a hard-decision and obtain the final decoded message. The posterior messages are distributed to and from P processing units by interleaving units (π and π^{-1}) that correspond to the code graph connectivity.

Log-likelihood (LLR) messages are commonly used since their arithmetic [24] exhibits very low complexity (e.g., additions instead of multiplications). For every received code symbol x the corresponding LLR is given by:

$$L(x) = \log \frac{P(x=0)}{P(x=1)} \,, \tag{2}$$

where $P(A = y)$ defines the probability that A takes the value y. LLR values with a positive sign would imply the presence of a logic 0 whereas a negative sign would imply a logic 1. The magnitude of the LLR provides a measure of reliability for the hypothesis regarding the presence of a logic 0 or 1. Considering the messages involved in the decoding process, the LLR of an information bit x is given by:

$$L(x) = L_c(x) + L_a(x) + L_e(x) \,, \tag{3}$$

where $L_c(x)$ is the intrinsic message received from the channel, $L_a(x)$ is the a-priori value and $L_e(x)$ is the extrinsic value estimated using the code characteristics and constraints. $L(x)$ is the *a posteriori* value and a hard-decision upon it (extraction of the mathematical sign) is used to deduce the binary decoded value. Figure 4 shows the evolution of the posterior messages LLRs for both a converging and a non-converging codeblock. These figures correspond to instances of decoding the LDPC code defined in [5] with block length of 648 and code rate 1/2 over the additive white Gaussian noise (AWGN) channel with quadrature phase-shift keying (QPSK) modulation at a signal-to-noise ratio (SNR) of $E_b/N_0 = 1dB$ with 60 maximum iterations. Works in [25][26] have shown how the LLR values evolve within the decoding process. Depending upon the operating signal-to-noise ratio (SNR) regime these values will initially fluctuate or enter right away a strictly monotonic behavior.

III. On-the-fly Syndrome Check

A hard-decision vector upon the posterior messages is required after each decoding iteration in order to calculate the syndrome. Syndrome calculation involves the product in equation (1), but this is equivalent to the evaluation of each parity constraint with the corresponding code symbols.

The arguments of each constraint correspond to the hard-decision of each LLR. A non-zero syndrome would correspond to any parity-check constraint resulting in odd parity. This condition suggests that a new decoding iteration must be triggered. The calculation of the syndrome in this way is synonymous to the verification of all parity-check constraints and we refer to this as *syndrome check*.

The typical syndrome check requires a separate memory for the hard-decision symbols and a separate unit for the syndrome calculation (or verification of parity-check constraints), this consumes time in which no decoding is involved. In this context, we use the word *typical* in two senses: one referring to the calculation of the syndrome with stable values and the other referring to the evaluation of the syndrome after the end of a decoding iteration.

A. Proposed Method

Based upon the behavior of the LLRs illustrated in Figure 4, we propose to perform the syndrome check *on-the-fly* in the following way: each parity-check constraint is verified right after each row is processed. Algorithm 1 outlines the proposed syndrome check within one decoding iteration for a parity-check matrix with M rows.

Algorithm 1 *On-the-fly* syndrome check

1. Decode each row i (or a plurality thereof for parallel architectures)
2. Evaluate each parity-check constraint PC_i by performing the $\oplus$ operation on the hard-decision values
3. Verification:

if $(PC_i = 1)$ **then**
  Disable further parity-checks verification
else
  if $(i = M)$ **then**
    Halt decoding: valid codeblock found
  end if
end if

For the proposed syndrome check there are two extreme cases regarding the latency between iterations. The worst-case scenario corresponds to the case when all individual parity-checks are satisfied but at least one from the last batch to process fails, in which case a new decoding iteration is triggered. The best-case scenario is when at least one of the first rows' parity-check fails, this disables further rows' parity-check verification and the next decoding iteration starts right after the end of the current one. The difference with the typical syndrome check is that it is always performed and it necessarily consumes more time as it involves the check of

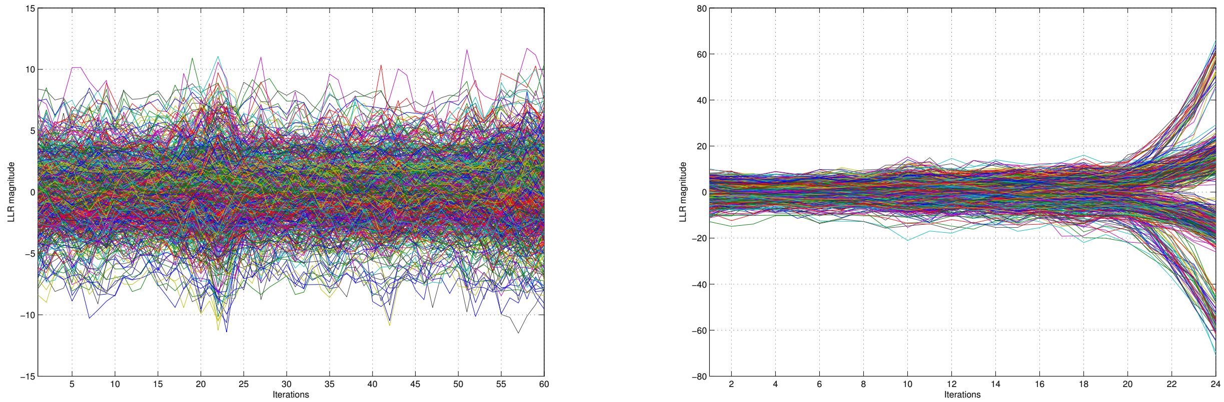

(a) LDPC non-converging codeblock

(b) LDPC converging codeblock

Fig. 4. Posterior messages LLRs magnitude evolution.

the entire $\boldsymbol{H}$. Figure 5 shows the timing visualization of these scenarios and the evident source for latency reduction of the decoding task.

The notion of *typical* syndrome check that we use might appear rather naive at first glance, but notice that among all the published works on decoder architectures the way the syndrome is verified is consistently neglected. It could be argued that the syndrome of an iteration can be verified concurrently with the decoding of the following iteration. This indeed would belittle our claim on task speedup (refer to Section IV) but nevertheless the *on-the-fly* syndrome check hardware would still be of considerable lower complexity than said alternative mainly due to the lack of memories to save the hard decisions of the previous iteration.

B. Performance Analysis

A closer examination of the proposed syndrome check reveals the possibility for special scenarios. Indeed, the proposed syndrome check does not correspond to equation (1) since the parity-check constraints are evaluated sequentially and their arguments (LLR sign) could change during the processing of the rows. Consequently, there is a possibility that the decision taken by the *on-the-fly* strategy might not be the correct one at the end of the decoding process. Table I shows the possible outcomes of the decision taken by the proposed strategy in contrast to the typical syndrome check. A *Pass* event is synonymous to the condition $\boldsymbol{S} = \boldsymbol{0}$. A *false alarm* outcome corresponds to the case when all parity-check constraints were satisfied, indeed halting the decoding task during any iteration as a valid codeblock has been identified (when in fact a final typical syndrome check would fail). On the other hand, a *miss* outcome takes place when during the last iteration (maximum iteration limit) a single parity-check constraint fails rendering the codeblock as invalid (when in fact the typical syndrome check would pass). Both outcomes are the result of at least one LLR sign change right before the last row processing.

From this set of possible outcomes the probability P_H for

TABLE I
DECISION OUTCOMES OF THE PROPOSED SYNDROME CHECK

On-the-fly syndrome check	Typical syndrome check	Outcome decision
Pass	Pass	Hit
Pass	Fail	False Alarm
Fail	Pass	Miss
Fail	Fail	Hit

the proposed syndrome check to be correct can be expressed by:

$$\begin{aligned} P_H &= 1 - (P_{FA} + P_M) \\ &= 1 - (P_P P_{CBE} + (1 - P_P)(1 - P_{CBE})) , \end{aligned} \quad (4)$$

where P_{FA} is the probability of a *false alarm*, P_M is the probability of a *miss* , P_{CBE} is the probability of a codeblock error and P_P is the probability of the proposed syndrome check to pass.

Based upon the analysis and observations in [25][26] the LLRs monotonic behavior is guaranteed for the high SNR regime, in this regime the outcome decision would be a *hit* with probability 1. Nevertheless, as the SNR degrades the inherent fluctuations of the LLRs at the beginning of the decoding process may cause the decision to be a *miss* or a *false alarm* with non-zero probability. In Figure 6, we show the outcome of the decoding of 10^5 codeblocks using the same simulation scenario as in Figure 4 with code length 1944 and two code rates in order to observe the rate at which a *miss* and a *false alarm* may occur on the low SNR regime.

Even though the *hit* rate is shown to be empirically greater than a *miss* or a *false alarm* it is important to address the occurrence of such anomalies. A *miss* result would trigger an unnecessary retransmission in the presence of an ARQ protocol, while a *false alarm* result would introduce undetected codeblock errors. This indeed represents some concerns that must be analyzed on an application-specific context, as for

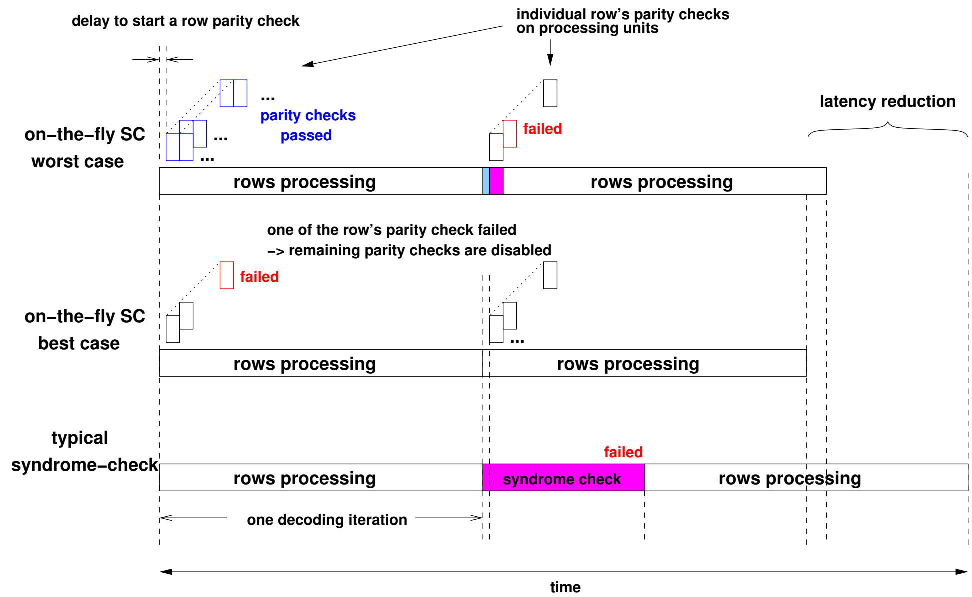

Fig. 5. Timing visualization for two consecutive decoding iterations.

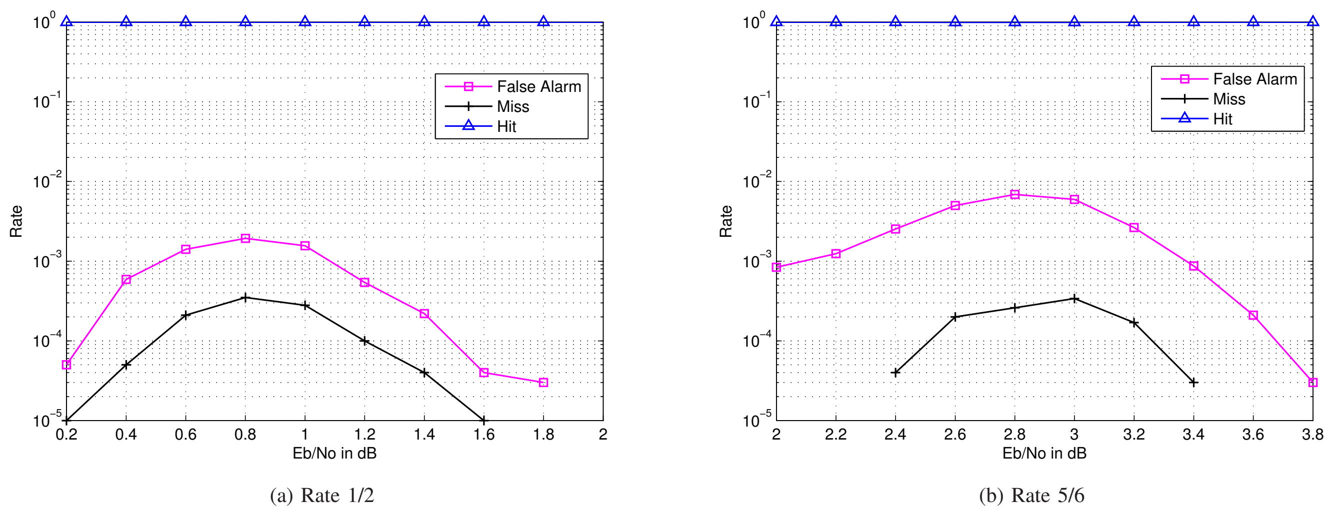

Fig. 6. Decision outcome rates from the proposed syndrome check for N=1944.

example a wireless modem for [5] is not likely to operate at such low SNR because of the required minimum packet-error rate performance.

The error-correction performance is affected by the *false alarm* outcomes. In Figure 7, we compare the simulated bit-error rate (BER, in solid lines) and frame-error rate (FER, in dashed lines) of the typical syndrome check and the proposed method, this corresponds to the same simulation scenario from Figure 6a. The performance loss is such that an error-floor becomes evident, therefore we address the ways in which this situation can be circumvented.

Detection of the *miss* and *false alarm* outcomes can be performed in two ways:

1) Validating the result provided by *on-the-fly* syndrome check by calculating the typical syndrome check.
2) Allowing an outer coding scheme to detect such conditions: e.g., a cyclic redundancy check (CRC) that typically follows a codeblock decoding.

We propose to detect both *miss* and *false alarm* outcomes by validating the final calculated syndrome (in *on-the-fly* fashion) while executing the first iteration of the following codeblock (CB). Figure 8 depicts both situations. In this way an ARQ protocol can react to a *false alarm* outcome and also avoid an unnecessary retransmission under the presence of a *miss* outcome. The performance is fully recovered, shown in Figure 7 as *validated on-the-fly* syndrome check.

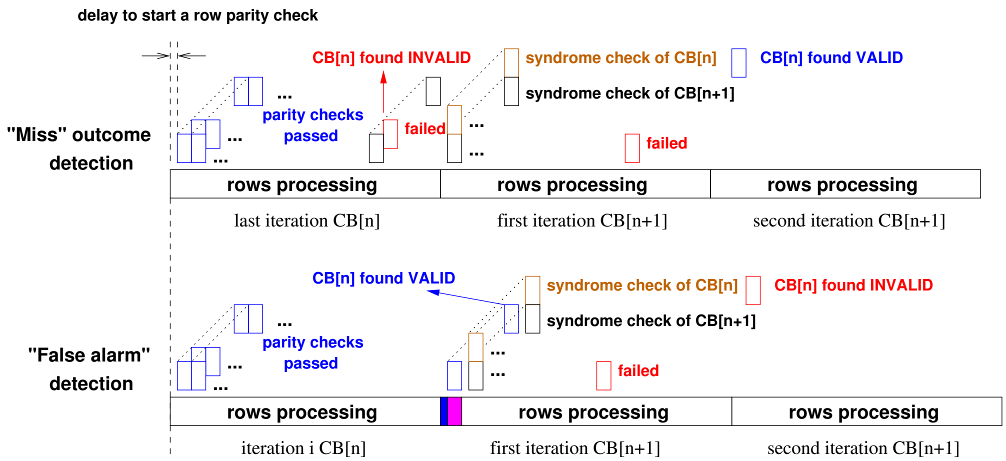

Fig. 8. *False alarm* and *miss* outcomes detection.

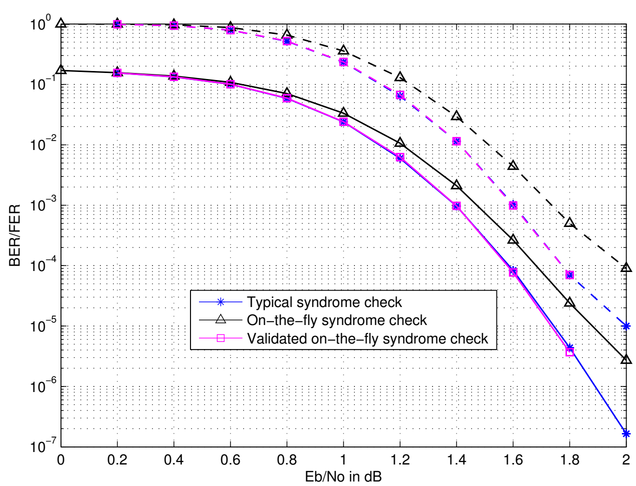

Fig. 7. Error-correction performance comparison.

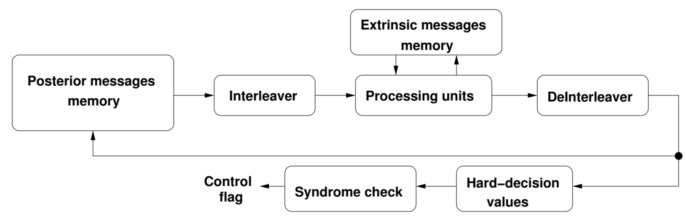

Fig. 9. Canonical decoder architecture.

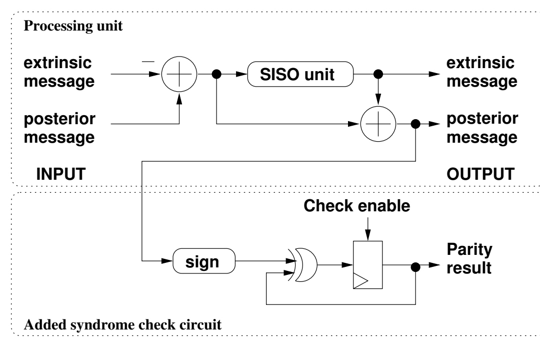

Fig. 10. Processing unit with syndrome check option.

IV. Decoding Task Speedup

In Figure 9, we show an LDPC decoder with the modules used to perform the typical syndrome check. From this it is evident that the proposed strategy does not require dedicated elements for the syndrome verification. In fact, in order to implement the syndrome check in *on-the-fly* fashion each processing unit is augmented by a marginal set of components. Figure 10 shows a serial processing unit driven by a SISO kernel and the added syndrome check capability. Synthesis results on CMOS $65nm$ technology showed that the area overhead due to the syndrome check capability is only 0.65% for a BCJR-based processing unit (the SISO kernel is the modified BCJR algorithm described in [27]).

If the *false alarm* and *miss* outcomes are to be detected by the proposed method in Section III-B, then the syndrome check circuitry must be replicated and the hard-decision memory in Figure 9 must be kept. Notice that the implementation of *on-the-fly* syndrome check must be evaluated on an application-specific context: decoder operating range, outer multilevel coding schemes and ARQ protocols, logic and memory overheads.

The main benefit of the proposed syndrome check is the speedup of the overall decoding task. The processing latency per decoding iteration for P processing units is given in number of cycles by:

$$\tau_c = m_b \times \frac{Z}{P} \times L_c \ , \tag{5}$$

where a QC-LDPC code defines $\boldsymbol{H}$ as an array of m_b block-rows of Z rows. In this case P rows are processed concurrently. L_c is the number of cycles consumed during the decoding task where decoding and syndrome verification take place. This value depends upon the number of arguments to process per row, memory access latencies and syndrome verification duration. It is in the latter time duration where our

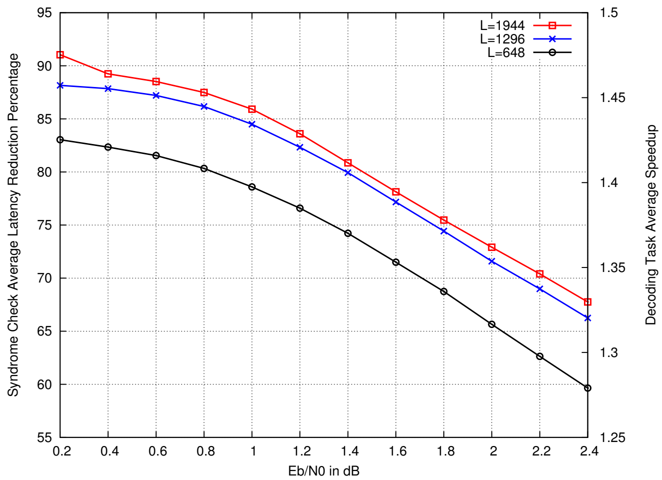

(a) Rate 1/2

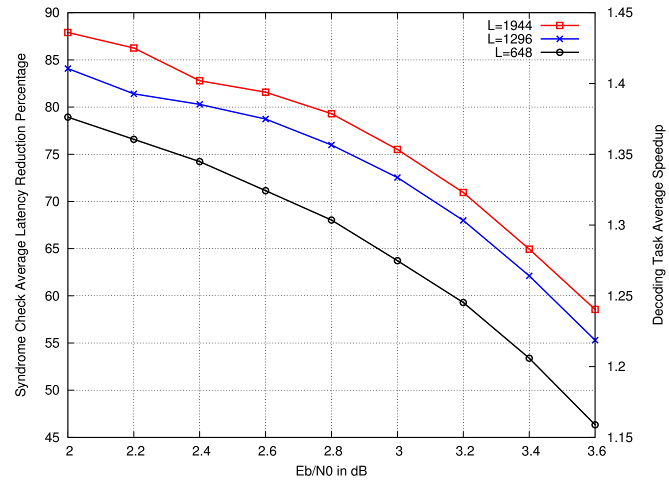

(b) Rate 5/6

Fig. 11. Average latency reduction for the syndrome check process and overall decoding task speedup.

proposal exhibits advantages in terms of speedup. A reduction in the overall task latency improves as well the decoder throughput assuming the arrival time of frames is high enough to provide a 100% decoder utilization:

$$\Gamma = \frac{N \times R \times f_{clk}}{I \times \tau_c} \,, \tag{6}$$

where I is the total number of iterations, R the coding rate of the N code symbols and f_{clk} the operating frequency.

The main benefit from the proposed strategy is the reduction in the time consumed during the syndrome check when the decoding process is far from reaching convergence. It could be argued that the syndrome check may very well be disabled during a preset number of initial iterations, but still this tuning must be done offline or shall depend upon extraneous variables like the SNR. Estimating these variables provides sensible overheads. Figure 11 shows the obtained average latency reduction of the syndrome check process compared to the typical one as a function of operating SNR. A total of three use cases with different code lengths L are shown, for a code rate of 1/2 in Figure 11a and code rate of 5/6 in Figure 11b. The low SNR region provides the best opportunities for syndrome check latency reduction since LLRs fluctuate quite often in this region, i.e., a higher decoding effort renders useless the initial syndrome verification.

Indeed, what this strategy is doing is speeding up a portion of the decoding task. With the use of Amdahl's law [28] it is possible to observe the overall speedup of the decoding task based upon the obtained latency reduction of the syndrome check. The overall speedup is a function of the fraction $P_{enhanced}$ of the task that is enhanced and the speedup $S_{enhanced}$ of such fraction of the task:

$$S_{overall} = \frac{1}{(1 - P_{enhanced}) + \frac{P_{enhanced}}{S_{enhanced}}} \,. \tag{7}$$

Figure 11 shows as well the average speedup obtained as a function of operating SNR for the same test cases, these results consider that the syndrome check process corresponds to 35% of the overall decoding task per iteration. Amdahl's law provides an upper bound for the achievable overall speedup, 1.53 for this setup. The average speedup is higher for the code rate 1/2 case since the parity-check matrix contains more rows than the code rate 5/6. For the former case the achieved speedup ranged from 84% to 96% of the maximum achievable bound, this corresponds to enhancing the decoder throughput by a factor of 1.28 and 1.48, respectively.

V. Iteration Control

Iterative decoding algorithms are inherently dynamic since the number of iterations depends upon several factors. Proper iteration control policies should identify decodable and undecodable blocks in order to improve on energy expenditure and overall task latency. Convergence of a codeword is detected by verifying equation (1) while non-convergence is usually detected by completing a preset maximum number of iterations.

A. Prior Art

Iteration control techniques (also known as *stopping criteria*) attempt to detect or predict the convergence or not of a codeblock[1]and decide whether to halt the decoding task. This decision is aided by so-called *hard* or *soft* decisions. Hard-decision aided (HDA) criteria are obtained as a function of binary-decision values from the decoding process; on the other hand, the soft-decision aided (SDA) criteria use a non-binary-decision parameter from the decoding process that is compared against threshold values.

The authors in [29] proposed a termination criterion that detects so-called *soft-word cycles*, where the decoder is trapped in a continuous repetition without concluding in a codeblock.

[1]We use the general term *codeblock* instead of *codeword* in order to address decodable and undecodable instances.

This is achieved by storing and comparing the soft-words generated after each decoding iteration. This is carried out by means of content-addressable memories. This criterion saves on average iterations but clearly introduces storage elements.

In [14] a stopping criterion was proposed based upon the monitoring of the variable node reliability (VNR), defined as the sum of the magnitudes of the variable node messages. This decision rule stops the decoding process if the VNR does not change or decreases within two successive iterations. This comes from the observation that a monotonic increasing behavior is expected from the VNR of a block achieving convergence. The criterion is switched off once the VNR passes a threshold value that is channel dependent.

The criterion proposed in [30] is similar to the one in [14], it monitors the convergence of the mean magnitude of the variable node reliabilities. The decision rule uses two parameters tuned by simulations that are claimed to be channel independent.

The authors in [15] proposed a criterion that uses the number of satisfied parity-check constraints as the decision metric. Given the syndrome $\boldsymbol{S} = [s_1, s_2, \ldots, s_M]^T$, the number of satisfied constraints at iteration l is:

$$N_{spc}^{l} = M - \sum_{m=1}^{M} s_m \ . \tag{8}$$

The decision rule monitors the behavior of this metric tracking the increments and their magnitudes as well as the persistence of such behavior. In this rule three threshold values are used, all claimed to be channel independent.

A similar scheme was presented in [16]. This criterion monitors the summation of the checksums of all parity-checks given by:

$$S_p = \sum_{m=1}^{M} P_m \ , \tag{9}$$

where P_m is the checksum of row m as follows:

$$P_m = \bigoplus_{n \in \mathcal{I}_m} c(n)\ , \text{ with } c(n) = \begin{cases} 0 & \text{if } sign(n) > 0 \\ 1 & \text{otherwise} \end{cases} \tag{10}$$

where $c(n)$ is the hard-decision mapping of a soft-input of a row and $\mathcal{I}_m$ is the set of non-zero elements in the mth row. This is indeed the complement of the decision metric used in [15]. The decision rule monitors this metric and uses two threshold values that are dependent upon signal-to-noise ratio to make a decision.

In [17] a channel-adaptive criterion was proposed by monitoring the *sign-changing rate* of the LLRs per iteration. The control rule uses two threshold values that are claimed to be channel independent.

The above control policies have been derived based upon the observation of the characteristic behavior shown by a particular decision metric within the decoding task. The decision metrics used by these control policies are characterized by their dependence or not upon extraneous variables. Estimating these variables (e.g., SNR) raises the implementation effort. In Section VI, we show empirically how the tuning of the parameters used for a decision rule essentially trades off the false alarm rate and missed detection rate of undecodable blocks.

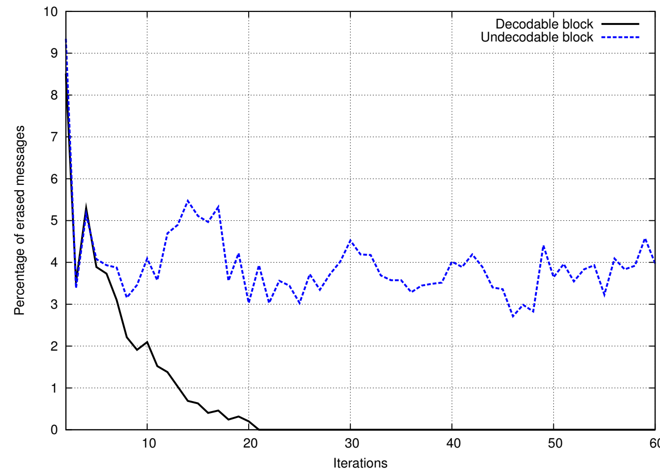

Fig. 12. Percentage of erased messages.

B. Proposed Control Policy

SCMS decoding introduces the concept of *erased messages*, messages which are deemed useless and are discarded after each decoding iteration. A formal treatment behind the concept of *erased messages* can be found in [18], but intuitively the number of messages erased per iteration provides some measure of the reliability (convergence) of the decoding task. For example, the fewer messages erased, the more reliable the decoding task is. Through simulations we observed the total number of erased messages per iteration to identify the possibility to detect earlier an unsuccesful decoding task and also convergence. In the case of an undecodable block the number of erased messages fluctuates around a mean value (dependent upon the SNR), whereas for a decodable block this metric approaches zero relatively fast. In Figure 12, we show how the percentage of erased messages evolves with each decoding iteration for an instance of a decodable and an undecodable block. This corresponds to the decoding of the code defined in [5] with block length 1944 and coding rate 1/2 over the AWGN channel with QPSK modulation, with a maximum of 60 decoding iterations at $E_b/N_0 = 1dB$.

By detecting the characteristic monotonic decreasing behavior of the total number of erased messages when the decoder enters a convergence state, it is possible to save energy on potential undecodable blocks. The *erased messages* metric follows the cumulative quality of the arguments for the parity-check constraints, allowing in fact to observe the dynamics and evolution of the decoding process with fine granularity.

In Figure 13, we show the average number of decoding iterations as a function of SNR for the same simulation scenario of Figure 12 for several stopping rules:

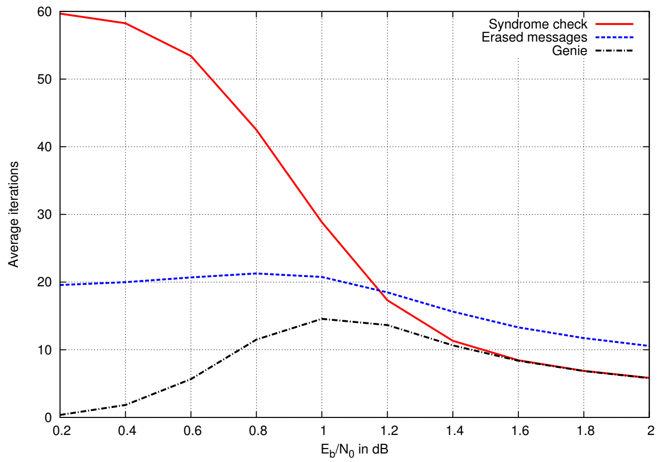

Fig. 13. Average iterations for stopping rules.

1) Syndrome check verification, this corresponds to equation (1).
2) Erased messages metric. Decoding is halted when either the number of erased messages equals zero or a non-convergence condition is satisfied. For non-convergence detection we allow only a fixed number of increments of this metric.
3) Genie. An ideal stopping rule with foreknowledge of the transmitted block, in this case decoding would not even start on an undecodable block.

The syndrome check and the genie criteria correspond to the empirical bounds of any valid stopping rule. From Figure 13 it is clear that the number of erased messages may be used as a decision metric to detect earlier undecodable blocks, but indeed it is not suitable for detecting early convergence since the absence of erased messages within an iteration is not a necessary condition for convergence.

From these observations we use the erased messages metric to detect an undecodable block and the syndrome check for decodable blocks. We devise a stopping rule that follows the evolution of the total number of erased messages by counting the increments of this metric and halting the decoding task once the number of increments exceeds a given threshold T. This threshold is a static parameter that essentially trades error-correction performance and the average number of iterations. Algorithm 2 outlines the proposed decision rule. After the decoding of a row m the number of erased messages ϵ_m is accumulated per iteration in S_ϵ^l. This sum is compared with the one from the previous iteration in order to detect the behavior of the metric as illustrated in Figure 12.

The objective of a stopping criterion can be formulated as the detection of an undecodable block. Thus the possible outcomes of such criterion may be a hit, a false alarm and a missed detection. A false alarm corresponds to the halting of the decoding task that would have been successful in the absence of such stopping rule. This indeed generates unnecessary retransmissions in ARQ protocols. On the other hand, a missed detection represents useless energy expenditure and an unnecessary delay to request a retransmission. Even though any stopping criteria can be tuned to make arbitrarily small the average number of iterations this has an impact on the false alarm rate. In [15] the authors showed empirically how the average number of iterations and the false alarm rate are complementary. We investigated further by looking at the missed detection rate since this indeed can provide hints into a criterion's efficiency. We compared the proposed criterion in Algorithm 2 to the works in [15] (Shin) and [14] (Kienle) along with the syndrome check and the genie rules. In Figure 14, we show the performance comparison in terms of average iterations, false alarm and missed detection rates. We observed that when tuning the stopping criteria to have a similar false alarm rate, as shown in Figure 14b, the missed detection rates exhibit different behaviors. In fact, the proposed criterion showed missed detection rates of several magnitudes of order smaller than the other criteria. The curves for $T = 10$ and $T = 12$ of the proposed criterion are below the value of 10^{-6}, not shown in the figure.

Algorithm 2 Stopping Criterion - SCMS

```
ε_m: number of erased messages in row m
M: set of check nodes
f_s: boolean function for syndrome check, equation (1)
count ← 0;  S^l_ε ← 0
for all iterations 1 < l ≤ iterations_max do
  for all rows m ∈ M do
    Decode row m
    S^l_ε ← S^l_ε + ε_m
  end for
  if (f_s) then
    Halt decoding (convergence)
  end if
  if (S^l_ε > S^{l-1}_ε) then
    count ← count + 1
  end if
  if (count > T) then
    Halt decoding (non-convergence)
  end if
end for
```

Since it is possible to monitor several decision metrics we investigated how a particular combination may impact the tuning and performance of the resulting *hybrid* control rule. By assisting the decision process with several metrics it is possible to tune the control policy to reach better performance in terms of false alarms, missed detections and average number of iterations. Nevertheless, it was possible to reduce the missed detections only by adding the rule in Algorithm 2. For this reason we propose to enhance the performance of the previous art by adding the number of erased messages per iteration as a second decision metric on an SCMS-based LDPC decoder. Figure 15 shows the proposed hybrid iteration control system.

We selected the number of parity-check constraints metric [15] as it offers less computational complexity than the VNR metric [14]. In Table II, we compare the cited stopping rules

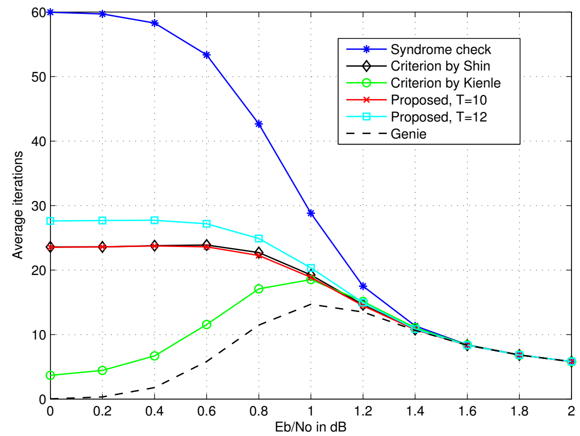

(a) Average iterations

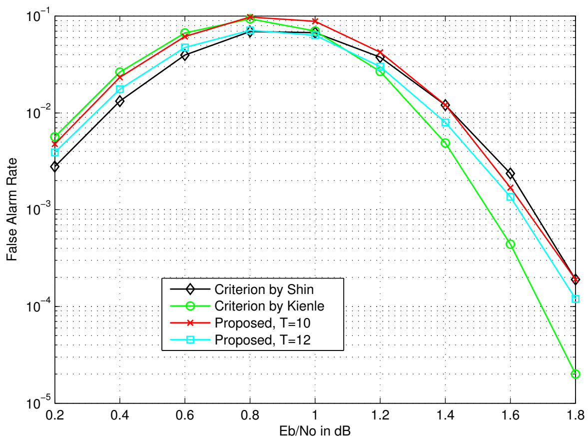

(b) False alarm rates

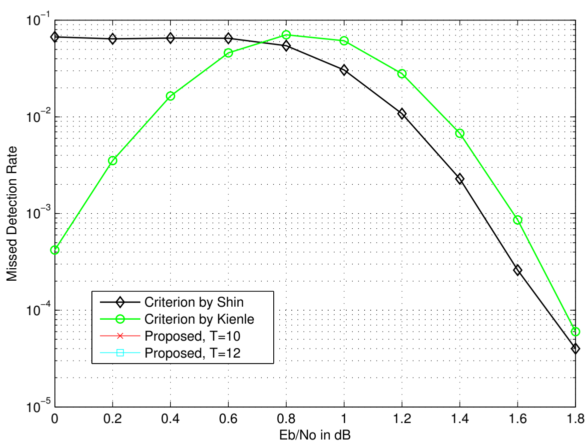

(c) Missed detection rates

Fig. 14. Performance of stopping criteria.

and the one proposed in [17] (Chen) along with Algorithm 2. The number of operations is given as a function of the dimensions of the parity-check matrix. N is usually much larger than M (e.g., twice for a rate 1/2 code), this means that on the number of calculations alone the criterion by Kienle is the most complex one. Furthermore, the type of data used by this criterion requires full resolution real quantities, this indeed imposes a more complex datapath (within a VLSI implementation) when compared to the other listed criteria.

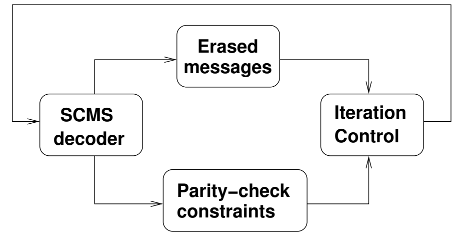

Fig. 15. Hybrid iteration control system.

TABLE II
COMPLEXITY OF DECISION RULES

Criterion	Operations		Tuning Parameters	Data Type
	Compare	Add		
Shin [15]	3	M+3	3	Integer
Kienle [14]	1	N	1	Real
Chen [17]	3	N	2	Integer
Algorithm 2	2	M+2	1	Integer

Therefore, by observing the performance (error-correction, average iterations, false alarm and missed detection rates) of the mentioned stopping criteria we propose the hybrid iteration control policy for SCMS-based LDPC decoders such that two decision metrics are monitored in order to detect decodable and undecodable blocks. Even though it is possible to monitor all previously proposed decision metrics we found out that the erased messages metric provides the most effective detection for undecodable blocks (in the sense of exhibiting the lowest missed detection rate). In the following, we provide results when utilizing the hybrid technique by using both Algorithm 2 and the criterion in [15] embodied as shown in Figure 15.

VI. STOPPING CRITERIA COMPARISON

All stopping criteria can reduce the average number of iterations depending upon the tuning of the decision parameters used within their control policy. This has consequences of different aspects that are worth investigating. In the following, we tune the stopping criteria in [14][15][17] along with the proposed hybrid control to be used in the SCMS decoding within the simulation scenario described in the previous section.

Figure 16 shows the simulated BER performance for the tested criteria. The stopping criteria can be tuned to be close in performance, for the case of the criterion in [15] (Shin) the parameters used were $\theta_d = 6, \theta_{max} = 4$ and $\theta_{spc} = 825$; for the criterion in [14] (Kienle) $MB = 16$ was used; and for the criterion in [17] (Chen) $lte = 6, thr = 9\%$ were used. The proposed hybrid criterion uses $T = 22$ and the same setup just mentioned for [15].

Figure 17 shows the average number of iterations for the stopping criteria. The syndrome check and the genie are once

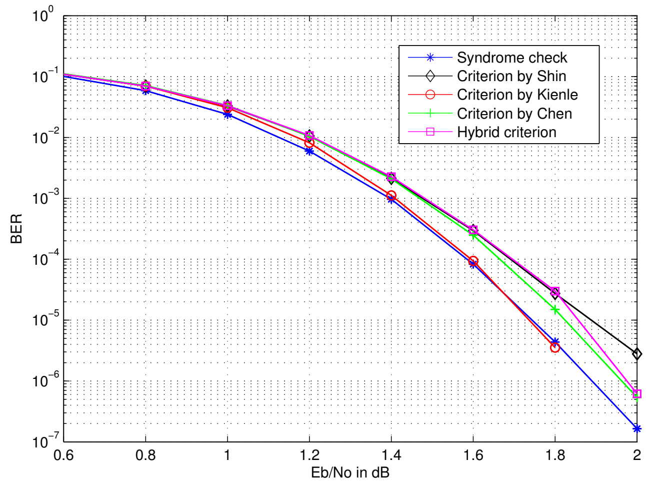

Fig. 16. Error-correction performance for stopping criteria.

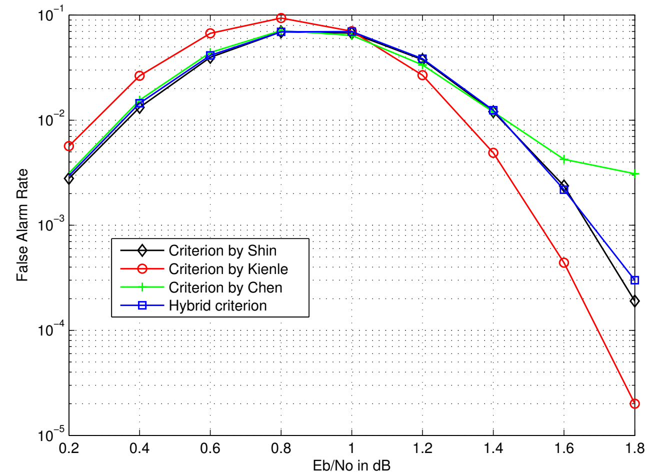

Fig. 18. False alarm rate of stopping criteria.

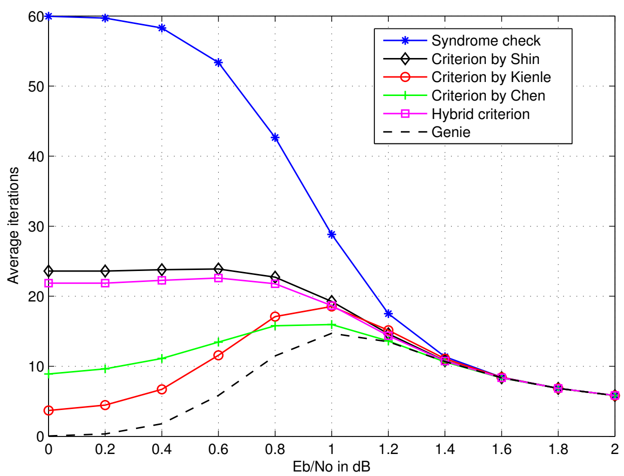

Fig. 17. Average iterations for stopping criteria.

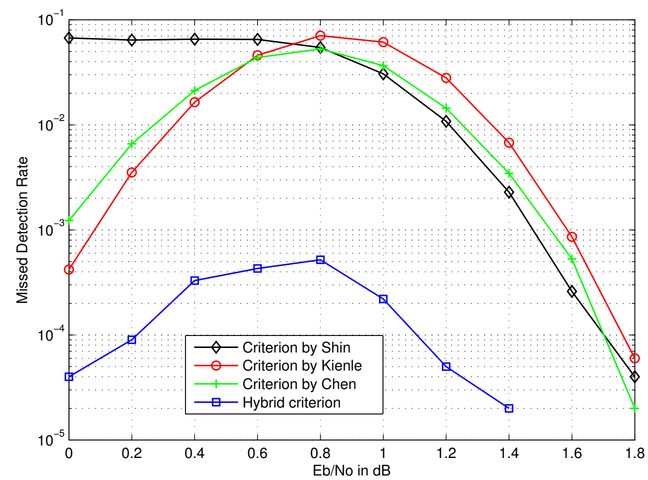

Fig. 19. Miss rate of stopping criteria.

again provided to observe the achievable empirical bounds. Here the tradeoff between average iterations and performance loss is evident. From these figures the criterion by Kienle shows an advantage for a fewer number of iterations in the low SNR region with the smallest performance loss, but this criterion shows the highest false alarm rate (FAR) on the same SNR region.

In Figure 18, we show the FAR of the simulated stopping criteria. This is a relevant figure of merit since the stopping mechanism on its own can be responsible for unnecessary retransmissions. We can observe how the criterion by Kienle shows a smaller number of false alarms on the high SNR region, this is due to the inherent threshold that is used within this criterion to disable the stopping rule, but on the other hand this criterion shows the highest false alarm rate for the low SNR region. The comparison between the proposed criterion and the one by Shin and Chen is much closer and indeed can be tuned to have a similar performance.

So far we can observe that the criterion by Kienle in the low SNR region exhibits the lowest average number of iterations but leads to the highest number of retransmissions. In general, the FAR of these criteria is relatively close, so we proceed to investigate their missed detection performance. Indeed, the missed detection rate (MDR) can provide further insights into which criterion is actually saving energy without incurring into any penalties. Figure 19 shows the MDR for the investigated criteria. The criterion by Kienle performs better than Shin for the low SNR region, but this no longer holds as the SNR increases. The criterion by Chen follows similarly the criterion by Shin. The most relevant result is that the proposed hybrid criterion achieved a MDR at least one order of magnitude below the best of the other ones.

Notice that on the high SNR regime all stopping criteria are irrelevant. A proper receiver design should guarantee the operation of the wireless modem to be within this regime so that a target BER/FER is provided. Nevertheless, in the

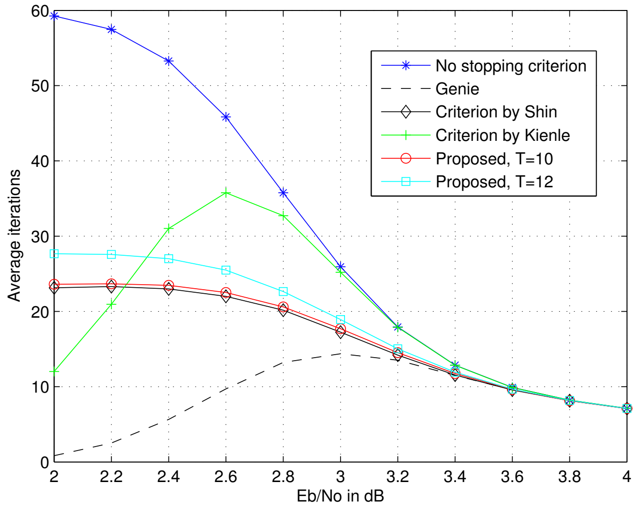

Fig. 20. Average iterations over a fading channel.

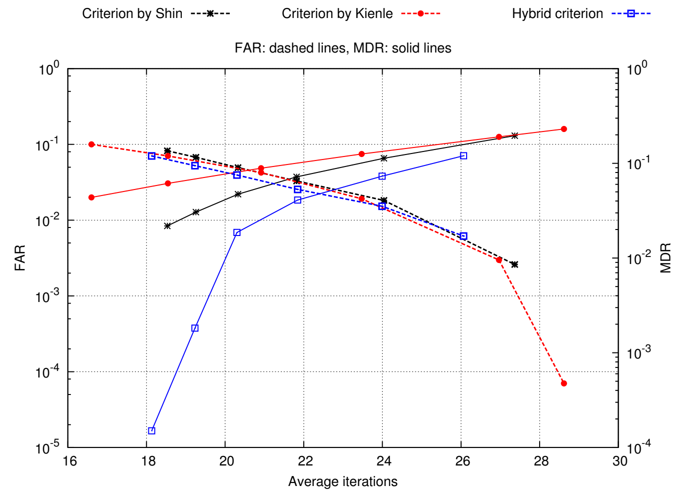

Fig. 21. FAR and MDR for stopping rules with different tuning of parameters.

eventuality that a particular application involves a highly fluctuating channel quality and battery-operated devices these stopping criteria would become relevant. Because of this reason we assert the importance of our study in order to assess the performance of such criteria.

We validated as well the independence of the proposed decision rule and the parameters in Algorithm 2 from the channel characteristics. We applied the criteria in [14][15] to the same LDPC code simulation scenario from Figure 14a on a fading channel where all symbols have independent channel gains that follow a Rayleigh distribution. Figure 20 shows the obtained average number of iterations. For the proposed hybrid policy two values of T were used. It can be observed how all the criteria follow the same behavior as in the AWGN case (refer to Figure 14a) but the criterion proposed by Kienle.

The performance for each stopping criterion depends upon the tuning of the decision-making parameters. In Figure 21, we show the FAR and MDR for different choices of tuning parameters that result in different average number of iterations. These results are from the same simulated scenario for $E_b/N_0 = 1dB$. From this we can observe the tradeoff involving FAR and the average number of iterations for all criteria. In general, the criteria can reduce the average number of iterations but this would result in a higher FAR, this tradeoff must be selected based upon the particular target application (required throughput and allowable retransmissions). Furthermore, we can observe the relationship between MDR and average number of iterations. In this respect the proposed criterion exhibits the best performance. From this figure we can see how a proper tuning of the parameters for a decision rule must consider the relationship between FAR and MDR. FAR refers to the penalty risk introduced by the stopping rule, whereas MDR refers to how effective the stopping rule is for detecting undecodable blocks.

VII. Conclusion

In this paper, we presented two valuable optimizations to enhance the decoding task from a speedup perspective along with low power considerations. The overall speedup in the task allows important throughput gains as well. As a first optimization we proposed an alternative method for performing the syndrome check. By partitioning the calculation among the rows of the parity-check matrix several advantages were identified. *On-the-fly* syndrome check reduces the number of hardware components on a VLSI architecture, offers a speedup in the overall decoding task and improves accordingly the decoding throughput. We analyzed the possible scenarios in which this technique may potentially provide erroneous outcomes regarding the validity of a codeblock and proposed how to handle these cases such that there is no error-correction performance loss. Results from a decoder for the codes defined in IEEE 802.11n provided a speedup of up to a factor of 1.48 at a cost of less than 1% in logic area overhead for a $65nm$ CMOS process.

The second proposed optimization considered the control of iterations. Even though iteration control is relevant only for the low SNR region of the performance curves it is an important technique studied for the purpose of avoiding useless decoder operation. We provided insights into the performance of several control rules in terms of the detection of undecodable blocks as false alarms and missed detections. We proposed a stopping criterion whose control law relies upon the combination of two decision metrics. Motivated by the quasi-optimal error-correction performance of the SCMS decoding kernel, we enhanced the performance of the previous art by adding the number of erased messages per iteration as a second decision metric for proper iteration control. We achieved a notorious decrease in the average number of missed detections for the iteration control policy, making it the best choice in terms of energy efficiency. Furthermore, we showed empirically how the proper tuning of stopping criteria should consider both FAR and MDR in order to accurately assess their performance.

REFERENCES

[1] E. Amador, R. Knopp, V. Rezard, and R. Pacalet, "Hybrid Iteration Control on LDPC Decoders," in *Proc. of 6th International Conference on Wireless and Mobile Communications*, September 2010, pp. 102–106.

[2] E. Amador, R. Knopp, R. Pacalet, and V. Rezard, "On-the-fly Syndrome Check for LDPC Decoders," in *Proc. of 6th International Conference on Wireless and Mobile Communications*, September 2010, pp. 33–37.

[3] R. Gallager, "Low-Density Parity-Check Codes," *IRE Trans. Inf. Theory*, vol. 7, pp. 21–28, January 1962.

[4] D. J. C. MacKay and R. M. Neal, "Good Codes Based on Very Sparse Matrices," in *Cryptography and Coding. 5th IMA Conf., Lecture Notes in Computer Science*, October 1995, vol. 1025, pp. 100–111.

[5] IEEE-802.11n, "Wireless LAN Medium Access Control and Physical Layer Specifications: Enhancements for Higher Throughput," *P802.11n-2009*, October 2009.

[6] IEEE-802.16e, "Air Interface for Fixed and Mobile Broadband Wireless Access Systems," *P802.16e-2005*, October 2005.

[7] IEEE-802.15.3c, "Amendment 2: Millimeter-wave-based Alternative Physical Layer Extension," *802.15.3c-2009*, 2009.

[8] ETSI DVB-S2, "Digital video broadcasting, second generation," *ETSI EN 302307*, vol. 1.1.1, 2005.

[9] DTMB-2006, "Framing Structure, Channel Coding and Modulation for Digital Television Terrestrial Broadcasting System," *Chinese National Standard GB 20600-2006*.

[10] IEEE-802.3an, "Amendment: Physical Layer and Management Parameters for 10Gb/s Operation," *P802.3an-2006*, 2006.

[11] IEEE-802m, "TGm System Requirements Documents (SRD)," *802.16m-10/0003r1*, 2010.

[12] 3GPP LTE-Advanced, "Requirements for Further Advancements for E-UTRA (LTE-Advanced)," *3GPP TSG RAN TR 36.913 v8.0.0*, 2009.

[13] C. Struder, N. Preyss, C. Roth, and A. Burg, "Configurable High-Throughput Decoder Architecture for Quasi-Cyclic LDPC Codes," in *Proceedings of the 42th Asilomar Conference on Signals, Systems and Computers*, October 2008.

[14] F. Kienle and N. Wehn, "Low Complexity Stopping Criterion for LDPC Code Decoders," in *Proc. of IEEE VTC 2005-Spring*, 2005, pp. 606–609.

[15] D. Shin, K. Heo, S. Oh, and J. Ha, "A Stopping Criterion for Low-Density Parity-Check Codes," in *Proc. of IEEE VTC 2007-Spring*, 2007, pp. 1529–1533.

[16] Z. Cui, L. Chen, and Z. Wang, "An Efficient Early Stopping Scheme for LDPC Decoding," in *13th NASA Symposium on VLSI Design*, 2007.

[17] Y.H Chen, Y.J. Chen, X.Y Shih, and A.Y Wu, "A Channel-Adaptive Early Termination Strategy for LDPC Decoders," in *IEEE Workshop on Signal Processing Systems*, 2009, pp. 226–231.

[18] V. Savin, "Self-Corrected Min-Sum Decoding of LDPC Codes," in *Proc. of IEEE International Symposium on Information Theory*, 2008, pp. 146–150.

[19] M. Fossorier, "Quasi-Cyclic Low-Density Parity-Check Codes from Circulant Permutation Matrices," in *IEEE Trans. Information Theory*, 2004, vol. 50, pp. 1788–1793.

[20] M. Mansour and N. Shanbhag, "High-Throughput LDPC Decoders," *IEEE Trans. on VLSI Systems*, vol. 11, no. 6, pp. 976–996, December 2003.

[21] F.R. Kschischang, B. Frey, and H.A. Loeliger, "Factor graphs and the sum-product algorithm," *IEEE Trans. Inf. Theory*, vol. 47, pp. 498–519, Febraury 2001.

[22] J. Chen and M. Fossorier, "Near Optimum Universal Belief Propagation based Decoding of LDPC Codes," in *IEEE Trans. on Comm.*, 2002, pp. 406–414.

[23] E. Amador, V. Rezard, and R. Pacalet, "Energy Efficiency of SISO Algorithms for Turbo-Decoding Message-Passing LDPC Decoders," in *Proc. of 17th IFIP/IEEE International Conference on Very Large Scale Integration*, October 2009.

[24] J. Hagenauer, E. Offer, and L. Papke, "Iterative Decoding of Binary Block and Convolutional Codes," *IEEE Trans. on Inf. Theory*, vol. 42, pp. 429–445, Mar. 1996.

[25] A. Heim and U. Sorger, "Turbo Decoding: Why Stopping-Criteria Do Work ," in *5th International Symposium on Turbo Codes and Related Topics*, 2008, pp. 255–259.

[26] G. Lechner and J. Sayir, "On the Convergence of Log-Likelihood Values in Iterative Decoding," in *Mini-Workshop on Topics in Information Theory, Essen, Germany*, September 2002.

[27] M. Mansour, "A Turbo-Decoding Message-Passing Algorithm for Sparse Parity-Check Matrix Codes," *IEEE Trans. on Signal Processing*, vol. 54, no. 11, pp. 4376–4392, November 2006.

[28] J. L. Hennessy and D. A. Patterson, *Computer Architecture: A Quantitative Approach*, Morgan Kaufmann Publishers, third edition, 2003.

[29] G. Glikiotis and V. Paliouras, "A Low-Power Termination Criterion for Iterative LDPC Code Decoders," *IEEE Workshop on Signal Processing Systems Design and Implementation*, pp. 122–127, November 2005.

[30] Jin Li, Xiao hu You, and Jing Li, "Early Stopping for LDPC Decoding: Convergence of Mean Magnitude (CMM)," in *IEEE Communications Letters*, 2006, number 9.

Pilot Pattern Design for PUSC MIMO WiMAX-like Filter Banks Multicarrier System

Faouzi Bader and Musbah Shaat
Centre Tecnològic de Telecomunicacions de Catalunya-CTTC
PMT, av. Canal Olimpic s/n. 08860 Castelldefels-Barcelona, Spain
Email: {faouzi.bader, mshaat}@cttc.es

***Abstract*—In this paper, we analyze different designed pilot patterns adapted to the DL-PUSC pilot grid for filter banks multi-carrier (FBMC) system. Different scheme have been proposed (pair of pilots, auxiliary pilot scheme, interference approximation method, and Scattered pilot method) and their performance evaluated and compared when using conventional cyclic prefix orthognal frequency division multiplaxing (CP-OFDM) system. We shown that by applying certain designed patterns especially for filter banks multi-carrier, the bite error rate can outperforms in certain cases that achieved by the CP-OFDM system. The performance evaluations are done in hypothetical WiMAX scenario on which the FBMC system will substitute the CP-OFDM by maintaining as much as possible the physical layer (PHY) compatibilities.**

***Keywords*-WiMAX, Pilot pattern, Filter banks multicarrier system, OQAM, MIMO, pilot pattern.**

I. Introduction

Wireless multicarrier (MC) communication scheme has proven its effectiveness in many of new communication standards (WiMAX, LTE, DVB-S, WiFi, etc.) [1]. This is not a fortuity, as multicarrier schemes offer many advantages as their robustness in frequency selective channels, their simplicity during the equalization and synchronization processes, besides, their high degree of flexibility and scalability in offering best solutions in scarcity radio resource scenarios. One of the most extended multicarrier schemes is the orthogonal frequency division multiplexing (OFDM), which encompass the advantages cited above, besides is one of the schemes always considered and tested in emerging wide band communication standards. A cyclic prefix (CP) is often used in OFDM which acts as a buffer region where delayed information from the previous symbols can be stored. The OFDM receiver has to exclude samples from the cyclic prefix which got corrupted by the previous symbol. The OFDM scheme is actually used in several communication systems as in e.g., WiFi, WiMAX, DVB-S2, and LTE [1].

Filters bank multiple carrier (FBMC) scheme is actually appearing as an alternative scheme to the conventional OFDM scheme, mainly in cognitive based environments [2] [3] [5] [6]. There are several advantages in using the FBMC than the OFDM, and one of them is the proper use of the CP to cope with the channel impulse response which results in a loss of capacity, which is not the case in FBMC, added requirements for block processing to maintain orthogonality among all the subcarriers. In OFDM systems, the leakage among frequency sub-bands has a serious impact on the performance of the FFT-based spectrum sensing in cognitive radio (CR) environment. Moreover, to combat the leakage problem in OFDM netwok a very tight and hard implementation for synchronization has to be imposed among the nodes. Another advantage of using the FBMC scheme, is that the subchannels can be optimally designed in the frequency domain to have a desired or specific spectral containment.

Filter bank MC system (FBMC) with offset quadrature amplitude modulation (OQAM) (named also OQAM-OFDM) can achieve smaller intersymbol interference (ISI) and intercarrier interference (ICI) without using the CP, by using well designed pulse shapes that satisfy the perfect reconstruction conditions. Moreover, the problem of the spectral leakage can be solved by minimizing the side-lobes of each subcarrier which leads to high efficiency (in terms of spectrum and interference) [4]-[7].

So far, some attempts have been made to introduce the FBMC in the radio communications arena, through proprietary schemes, in particular the IOTA technique (see: TIA-902.BBAB, Wideband air interface Isotropic Orthogonal Transform Algorithm (IOTA) physical layer specification , document of the Telecommunications Industry Association [8] [9], and in 3GPP TSG-RAN WG1. TR25.892, Feasibility study of OFDM for UTRAN enhancement. V1.1.0, June 2004). However, the full exploitation of FBMC techniques and their optimization in the context of radio evolution, such as dynamic access, as well as their combination with MIMO techniques, have not been considered. Physical Layer for Dynamic Spectrum Access (PHYDYAS) FP7 European project with code ICT-211887 [2], is one of the pioneer research projects at the European level that tried to resolve pending technical challenges for a real exploitation of the FBMC scheme.

In this paper, the authors present a FBMC system that aims to maintain a certain degree of compatibility with the OFDM based WiMAX specifications described in IEEE 802.16e standard [11]. Several pilot patterns for channel estimation are here proposed and analyzed for FBMC following the MIMO downlink (DL) partial usage of subcarriers (PUSC) frame structure of WiMAX, but due to the nature of the FBMC system, the pilots cannot be as straightforwardly applied as in OFDM. The main reason is that, every FBMC pilot symbol besides suffering the traditional effect of the additive white Gaussian noise (AWGN) a new interference component from frequency-time surrounding subchannels is added, what will affect the well acquisition of the pilot information at the receiver, therefore, results a degradation on the system capacity.

This paper is an extension of the analysis presented by the authors in [10], where the pilot pattern adaptation for FBMC included only the interference "*approximation method*" (IAM) and the "*auxiliary pilot*" scheme for channel estimation. In this paper, besides results presented in [10], the authors proposed new pilot patterns as the "*pair of pilots*" and the "*scattered pilots*" methods. Note that, the added pilot schemes are always designed considering the specificity of the FBMC scheme and the mitigation of the surrounding interference effect.

The paper is structured as follow: a brief overview on pilot allocation structures in WiMAX system is presented in Section II. The structure of the FBMC communication system and its adaption to the downlink partial usage of subcarriers (PUSC) specifications using MIMO with different proposed pilot patterns structures are presented in Section III. Section IV, introduces the simulation setup, and presents achieved performances. Finally, in Section V, the main conclusions on obtained results are drawn.

II. Brief Overview of Pilot Allocation Structures in WiMAX Systems

The general statement and frame structure of WiMAX system for the time division duplex (TDD) mode can be found in [11]. To ensure the compatibility of FBMC system with WiMAX (at least within the context of pilot allocation) these statements have to be considered as basis within the ICT-PHYDYAS project [2] [3]. WiMAX offers three different subcarrier permutation schemes [11]. The first, is the Full Usage of the Subchannels (FUSC) scheme allocates first the pilots on fixed positions, and the remaining subcarriers are used to transmit the data. The second and the third scheems are the Partial Usage of the Subcarriers (PUSC), and the Band Adaptive Modulation and Coding schemes (later referred as AMC) respectively, which divide the whole frame (excluding the Preamble, the PCH and DL/UL-MAPs) into minimal data units (named slots), where dedicated pilots and data are jointly allocated. Each slot is defined as a two dimensional units which spans in both frequency and time directions.

A. Pilot and data allocation for the PUSC, AMC and FUSC modes

1) PUSC mode: The shape of one slot in the PUSC scheme is two clusters in frequency direction and two OFDM symbols in the time direction. Hence, the number of data subcarriers is 48. Due to subchannel permutation the clusters are transmitted at distant positions in the spectrum, although each cluster is transmitted as a whole in adjacent subcarriers. Consequently, the PUSC permutation scheme increases the frequency diversity.

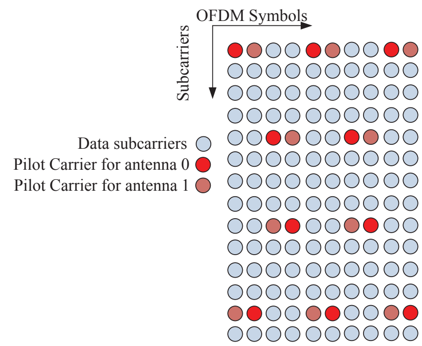

Figure 1. Cluster structure for STC downlink PUSC using 2 antennas.

2) AMC mode: The AMC permutation scheme is characterized by mapping adjacent subcarriers to each slot. By doing so, although frequency diversity is minimized. The use of adaptive modulation and coding may lead to great benefits by transmitting for each user on those bands where the channel experiences favorable conditions. For this permutation scheme, a smaller resource unit defined by nine contiguous subcarriers is used. This basic allocation unit is referred to as a 'bin'. Each bin contains one pilot subcarrier (whose position is changed every OFDM symbol) and eight data subcarriers. There are four types of AMC slots. The first is given by the collection of six consecutive bins (hence a 6×1 structure), the second has a 2×3 structure, and the third and the fourth are given by the 3×2 and the 1×6 structures respectively.

3) FUSC mode: For the FUSC permutation scheme, the symbol structure is constructed using pilot, data and empty subcarriers. Pilots and empty subcarriers are first allocated. The remaining subcarriers are then used as data subcarriers. 48 data subcarriers are later mapped to each subchannel. The subcarriers from each subchannel is mapped to physical subcarriers and placed equidistantly in the spectrum. For the FUSC scheme, one slot is defined as one subchannel per one OFDM symbol, thus giving a total of 48 data subcarriers. Figure 2, shows an example of the location of the pilots within one cluster for two transmit antennas. It can be observed that the position of the pilot symbols from the variable set change each two OFDM symbols. Designed pilot patters for FBMC will focus mainly on the downlink PUSC scheme.

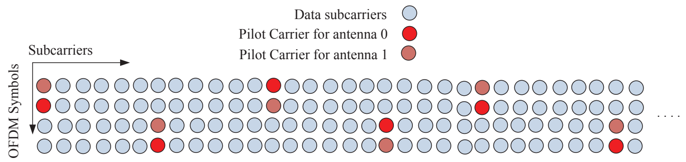

Figure 2. Cluster structure for STC FUSC using 2 antennas.

III. FBMC Scheme and pilot allocation

The hereafter subsections describe the transmission and reception structures of the FBMC scheme, the specificity operation of allocating pilots within a FBMC frame compared with conventional OFDM, and the different designed pilot pattern schemes considering the specificity of the FBMC.

A. Filter Bank based multicarrier structure

In FBMC, the filters bank are used in the transmultiplexer configuration using the synthesis filter bank (SFB) at the transmitter side, and the analysis filter banks (AFB) at the receiver side [11][12] (see Figure (3)). In FBMC systems, the use of critically sampled filter banks would be problematic, since the aliasing effects would make it difficult to compensate imperfections of the channel by processing the subchannel signals after the AFB only. Therefore, a factor of two oversampling is commonly applied in the subchannel at the AFB (see Figure (3b)).

In this paper the authors focused on uniform modulated filters bank with a prototype filter $g[m]$ of length L which is shifted to cover the whole of the system bandwidth. The output signal from the synthesis filter bank is given by

$$S[m] = \sum_{k=0}^{M-1}\sum_{n\in Z} d_{k,n}\, g[m-n\frac{M}{2}]\, e^{j2/Mm(m-\frac{D}{2})} e^{j\varphi_{k,n}} \quad (1)$$

where D is the delay term which depends on the length of the prototype filter $g[m]$, and $\varphi_{k,n}$ is an additional phase term. The transmitted symbols $d_{k,n}$ are real-valued symbols. Equation (1) can be written in a more compact form such that

$$S[m] = \sum_{k=0}^{M-1}\sum_{n\in Z} d_{k_p,n_p}\, g_{k,n}[m] \quad (2)$$

where M is the number of subcarriers (M=IFFT/FFT size) and also the number of active subcarriers, $d_{k,n}$ denotes the real-valued symbol at the k-th subcarrier during the n-th symbol interval, modulated at rate 2/*T*. The signalling interval T is defined as the inverse of the subcarrier spacing, i.e., $T = 1/\Delta f$. The symbols $d_{k,n}$ and $d_{k,n+1}$ can be

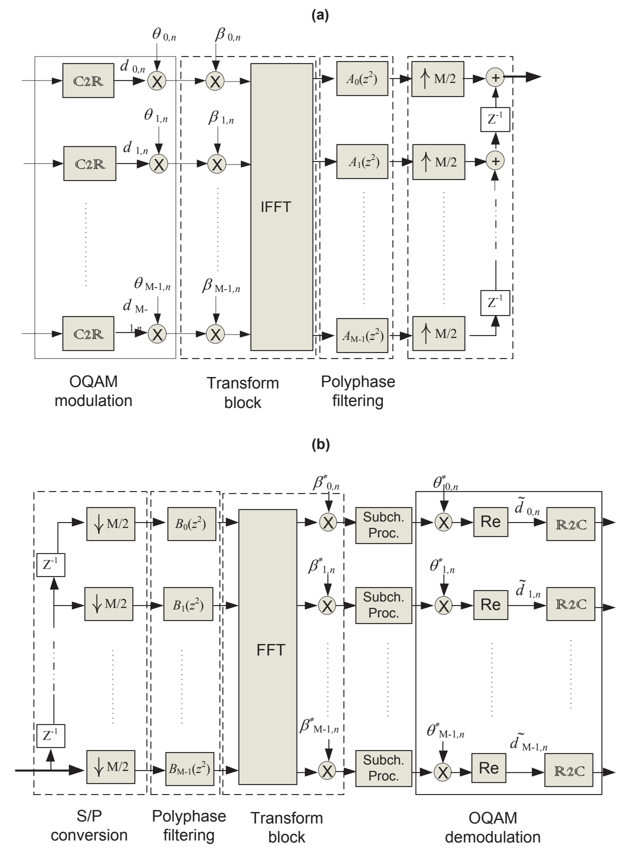

Figure 3. Multicarrier polyphase filter bank for SISO case, (a) Synthesis filter bank, (b) Analysis filter banks.

interpreted as the in phase and quadrature (I/Q) components respectively of the complex-valued symbol $c_{k,l}$ (of rate 1/*T*) from a QAM-alphabet. The phase term $\varphi_{k,n}$ in equation (1) guaranty and holds the real orthogonality condition [18] by having,

$$\Re \sum_{m=-\infty}^{+\infty} g_{\acute{k},\acute{n}}[m]\, g^*_{n,k}[m] = \delta_{k,\acute{k}}\delta_{n,\acute{n}} \quad (3)$$

The synthesized signal burst is therefore a composite of multiple subchannel signals each of which consists of a linear combination of time-shifted (by multiples of *T*/2) and overlapping impulse responses of the prototype filter, weighted by the respective symbol values $d_{k,n}$. L is the length of the filter prototype $p[m]$ and depends on the size of the filter bank and the overlapping factor K by having $L = KM$ [12][13]. The "$C2R$" and the "$R2C$" blocks in Figure 3, indicate the conversion of the data from complex into real form, and the inverse operation respectively. Note that each sub-carrier is modulated with an Offset Quadrature Amplitude Modulation (OQAM) which consists in transmitting the real and the imaginary parts of a complex data symbol with a shift of half the symbol period between them [13] [14].

B. Pilot allocation in FBMC

In FBMC system, either real or imaginary parts of the complex symbols are used for data transmission in a staggered manner. When a real (imaginary) part of a subcarrier symbol is used, the unused imaginary (real) part is at the receiver a fairly complicated function of surrounding data symbols. Usually in OFDM systems recovering the channel state information (CSI) is first proceed from known time and frequency pilot locations within certain intervals. The whole signal is recovered by means of different interpolation techniques [15]. Therefore, the channel state information (CSI) recovery process in OFDM is simple. However, this is not the case in filters bank systems, here every FBMC time-frequency pilot position is contaminated or suffered interference from the neighboring subchannels (see descriptive scheme in Figure 4) [16]. With ideal channel this interference is only located on the imaginary part of the subchannel signal. Thus, the real part yields the originally transmitted symbol $d_{k,n}$. Note that this interference depends on the real (imaginary) data around the pilot frequency-time position (k, n), and has a random variable behavior sometime close to zero. Therefore, sending a known symbol at a known time-frequency location is not enough, since at the receiver side the interference part will depends on the surrounding data [2] [16] values.

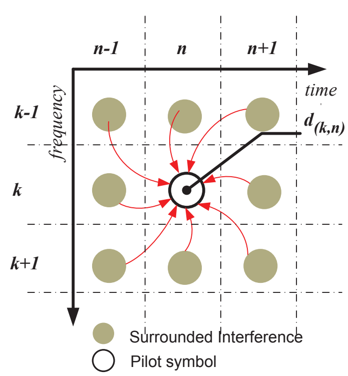

Figure 4. Time-frequancy pilot location in a FBMC system with surrounded interferes.

The contribution weights on the interference of the data surrounding a certain symbol closely coincide with the response of the filter banks and depend on the design of the prototype filter. Table I, shows the filter banks weights used in this paper [2] [14] [18]. As a resume, the nature of FBMC systems makes it impossible to construct pilot symbols for channel estimation in the same way as in OFDM.

Table I

REPRESENTATION OF THE TIME-FREQUENCY RESPONSE OF THE FBMC SYSTEM CONSIDERED IN THIS WORK. DUE TO THE EMPLOYED OFFSET QAM MODULATION, THE EFFECTIVE TIME-FREQUENCY RESPONSE WILL BE REDUCED TO ONLY BOLD VALUES IN [2].

0.0006	0.0001	0	0	0	0.0001	0.0006
-j0.00429	0.1250	j **0.2058**	**0.2393**	j **0.2058**	0.1250	j0.049
-j0668	0.0002	**0.5644**	**1.000**	**0.5644**	0.0002.	0.0668
j0.00429	0.1250	j **0.2058**	**0.2393**	j **0.2058**	0.1250	j0.049
0.0006	0.0001	0	0	0	0.0001	0.0006

C. Pilot pattern adaptation for FBMC downlink PUSC scheme: the MIMO context

Using the PUSC permutation, the set of active subcarriers is divided into clusters. The Pilots and the data subcarriers are allocated within each cluster [11], each one formed by 14 adjacent carriers, where two of them are dedicated to pilot symbols. In case of single antenna transmission, the pilots' positions are changing between each odd and even symbols. In case of two transmitting antennas, the pilots are placed following the scheme in Figure 5a. Specific pilot locations are reserved and exclusively used by each antenna. A proposed pilot pattern for a 2×2 FBMC system is shown in Figure 5b. This structure is built considering a time oversampling equal to *T*/2. That means that the relative pilot overhead using this structure is the same as that considering an OFDM system, i.e., for each pilot one offset quadrature amplitude modulation is used in FBMC. Therefore, one QAM symbol will be used in OFDM. At the AFB side, the received output signal samples of the interest pilot symbol at the frequency-time position (k_p, n_p) can be expressed as:

$$r_{k_p,n_p} \simeq h_{kp,np}(d_{k_p,n_p} + j\, t_{kp,n_p}) + z_{k_p,n_p} \tag{4}$$

where h_{k_p,n_p} and z_{k_p,n_p} are the channel coefficient and the noise term respectively at pilot subcarrier k_p and time index n_p. According to the values depicted in Table I, we note that most part of the energy is localized in a restricted set (shown in bold) around the considered symbol. Consequently, we assumed in (4) that the intrinsic interference term depends only on this restricted set (denoted by (k, n) in (5)). Moreover, we assume that the channel is quasi-static at least over all this zone. The value $t_{k,n}$ is defined as an intrinsic interference and is equal to,

$$t_{k_p,n_p} = \sum_{(k,n)\neq(k_p,n_p)} h_{k_p,n_p} d_{k,n} \sum_{m=-\infty}^{+\infty} g_{k,n}[m]\, g^*_{n_p,k_p}[m] \tag{5}$$

In case having a MIMO system with N_t transmit antennas and N_r receive antennas, the real (imaginary) pilot symbol $d^{(i)}_{k,n}$ is transmitted at the frequency-time position $(k_p; n_p)$ over the transmit antenna $i(i \in \{1, ..., N_t\})$. So, after transmitting through the radio channel, we demodulated at

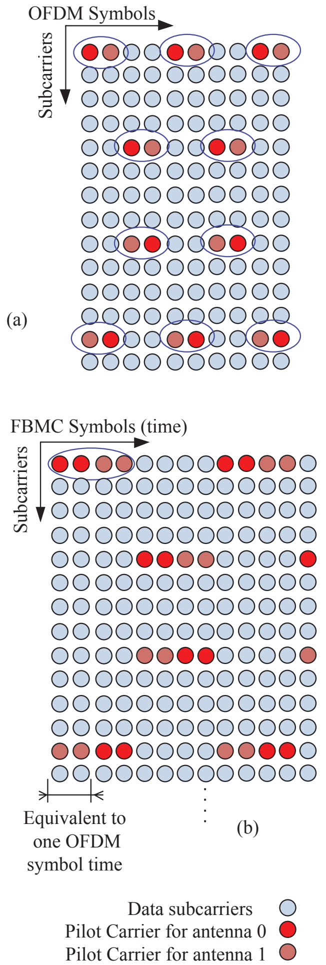

Figure 5. Pilot pattern for 2×2 antennas, (a) cluster structure for STC downlink PUSC in WiMAX, (b) STC PUSC adapted to FBMC.

the $j-th$ received antenna [17], and the received signal is,

$$r^{(j)}_{k_p,n_p} = \sum_{i=1}^{N_t} h^{(j\,i)}_{k_p,n_p}(d^{(i)}_{k_p,n_p} +_j t^{(i)}_{k_p,n_p}) + z^{(j)}_{k_p,n_p} \qquad (6)$$

where $h^{(j,i)}_{k_p,n_p}$ is the channel coefficient between transmit antenna "i" and receive antenna "j". If the prototype filter is designed with good frequency selectivity and a roll-off factor $\alpha \leq 1$, the range includes k_p with both adjacent subcarriers $(k_p - 1)$ and $(k_p + 1)$ in the frequency direction.

D. FBMC adaptation using auxiliary pilot scheme

C. Lélé et al. used in [18] the "auxiliary pilot" concept in OQAM-OFDM preamble for channel estimation. This concept, was in this paper used and adapted to deal with the channel estimation process in a FBMC MIMO system. In Figure 6, a modified scheme from that depicted in Figure 5b is presented to use auxiliary pilot scheme in a MIMO-FBMC system. As it can be shown in Figure 6, two types of pilots per antenna are used, each one allocated in a predefined position within the FBMC frame. As described in [2] [3] and [19], the main goal of the auxiliary pilot (named also as *'help pilot'*) position located adjacently to the pilot position (k_a, n_a) is to cancel the extra interference effect appeared in (5).

In other words, the interference part that affects the pilot must become equal zero, or small enough to be neglected. The main reason by introducing a spacing between both pair of pilots (one per each antenna) in Figure 6, is to avoid to have an auxiliary pilot in the window of another auxiliary pilot as recursive calculation of auxiliary pilots would be required (see the filter weights values in Table I), which may be somewhat inconvenient. However, using this slightly modified pilot pattern scheme this difficulty can be avoided, and each of the auxiliary pilots can be calculated independently. For MIMO case, this can be achieved by choosing the value of the auxiliary pilot equal to

$$d^i_{k_a,n_a} = \frac{\sum_{\substack{(k,n)\in\Omega_{k_p n_p} \\ (k,n)\neq(k_p,n_p)(k,n)\neq(k_a,n_a)}} d^i_{k,n}\,\hat{u}_{k-k_p,n-n_p}}{\hat{u}_{k_p-k_a,n_p-n_a}} \qquad (7)$$

Note that it is preferable to choose the auxiliary pilot in such a way that the magnitude of the denominator is maximized.

E. FBMC using Interference Approximation Method (IAM)

The interference approximation method (IAM) was presented by C. Lele et al. in [18] for preamble-based channel estimation using the Isotropic Orthogonal Transform Algorithm (IOTA) scheme [9].

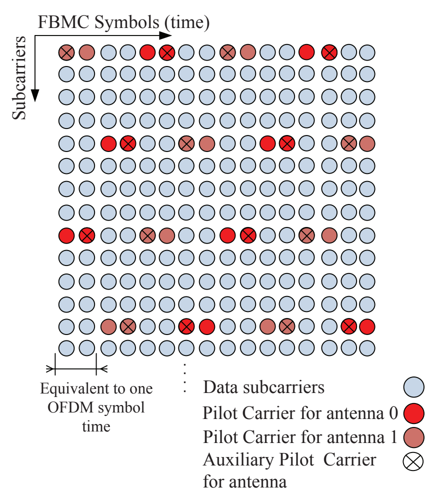

Figure 6. Pilot and auxiliary pilot pattern structure for 2×2 MIMO FBMC system.

The method is based on the assumption that the contributions come only from the first frequency-time order neighboring positions. The authors, extended this concept to the MIMO mode using two antennas at the transmitter. The pilot pattern structures proposed is depicted in Figure 7. In Figure 7a, a set of three pilot positions are reserved for each antenna i. The pilot symbol $d^i_{k_p,n_p}$ is first located in the center position of this set, the remained pilots $d^i_{k_p,n_{p-1}}$ and $d^i_{k_p,n_{p+1}}$ are here named as "Aided Pilot Carrier" (APC), as their main function is to aid the pilot $d^i_{k_p,n_p}$ to obtain an approximation of the interference generated by the filter banks. Note that, in both depicted structures in Figure 7 (7a, and 7b), we dealt with partial interference as the amount of interference of Ω_{k_p,n_p} that affects the pilot $d^i_{k_p,n_p}$ could not be here estimated. In Figure 7b, we confined with the information from the $(k_p, n_p - 1)$, $(k_p, n_p + 1)$, $(k_p - 1, n_p)$, and $(k_p + 1, n_p)$ APCs frequency-time positions. We focused on the case where the pilots' positions $(k_p, n_p - 1)$, $(k_p, n_p + 1)$ of each antenna are forced to zero. Therefore, forcing the largest interference weights caused by the filter bank contributions (see values in Table I) (i. e., $|u_{k,n+1}| = |u_{k,n-1}| = 0.5644$) to zero. The interference weight at the frequency-time positions $(k_p - 1, n_p)$, and $(k_p + 1, n_p)$ is $|u_{k-1,n}| = |u_{k+1,n}|$=0.2393, which have relatively lowest interference weights. This approach allows to maximize the modulus of the resulting pilot, and hence to minimize the noise effect.

F. FBMC using pair of pilots (POP) scheme

As previously mentioned, in FBMC the channel estimation issues is different of that in conventional cyclic prefix OFDM. The reason is that,as already point out, the sought channel frequency response values are complex whereas the training input is real. Moreover, the AFB output samples also contain imaginary contributions from neighboring times and frequencies directions. Under the assumption of having a good time-frequency localization with the employed filter prototype, and a relatively low channel frequency selectivity, J. P. Javaudin et al. proposed in [19] the POP method for coming up with the channel acquisition in a QAM-OFDM system using two preamble symbols. The authors modified proposed POP scheme in [19] to deal with channel estimation in a MIMO FBMC system using modified PUSC pilot pattern scheme depicted in Figure 5b. Here the pais of pilots relies on simple algebraic relations for the input/output samples in two time slots, and aims at computing a channel estimate operation by using (4) in two different (in practice consecutive) time slots $\{n, n + 1\}$ to construct a system of equations using the real and imaginary parts of a channel gain $H^{(c)}_{k,n}$ (*c, means complex value*). Note that $H^{(c)}_{k,n} = H^R_{k,n} + jH^I_{k,n}$ R and I refer to the "Real" and "Imaginary" parts. The pilot pattern proposed in Figure 5b, preserves the orthogonality between each antenna's pilots. To describe the *POP*'s channel information acquisition, we denote by

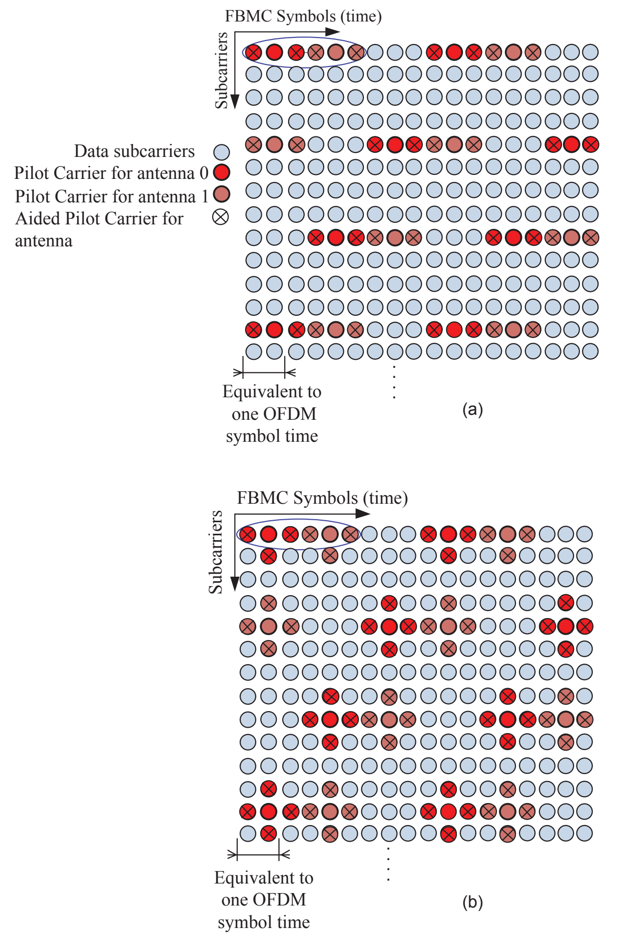

Figure 7. Pilot and pilot support using IAM concept for FBMC in DL-PUSC mode for 2 antennas: (a) reserved allocation for pilots, (b) pilot and aided pilot carrier (APC) positions.

(k_p, n_p) and (k_p, n_{p+1}) the frequency-time positions of the two pilots $d^i_{k_p,n_p}$ and $d^i_{k_p,n_p+1}$ respectively *(i refers to the antenna index)*. The value $W^{(c)}_{k_p,n_p} = \frac{1}{H^{(c)}_{k_p,n_p}}$ correspond to the zero forcing *(ZF)* equalization coefficient. By neglecting the noise part in (4), once can have for each even k a received signal at the $j - th$ antenna as,

$$\begin{cases} r^{(j)}_{k_p,n_p} W^{(j,i)}_{k_p,n_p} = & d^{(i)}_{k_p,n_p} + j\, t^{(i)}_{k_p,n_p} \\ r^{(j)}_{k_p,n_p+1} W^{(j,i)}_{k_p,n_p+1} = & d^{(i)}_{k_p,n_p+1} + j\, t^{(i)}_{k_p,n_p+1} \end{cases} \tag{8}$$

Then

$$\begin{cases} r^{R,(j)}_{k_p,n_p} W^{R,(j,i)}_{k_p,n_p} - r^{I,(i)}_{k_p,n_p} W^{I,(j,i)}_{k_p,n_p} = & d^{(i)}_{k_p,n_p} \\ r^{I,(j)}_{k_p,n_p} W^{R,(j,i)}_{k_p,n_p} + r^{R,(i)}_{k_p,n_p} W^{I,(j,i)}_{k_p,n_p} = & d^{(i)}_{k_p,n_p+1} \end{cases} \tag{9}$$

having $W^{(j,i)}_{k_p,n_p} \simeq W^{(j,i)}_{k_p,n_p+1}$ hence

$$\begin{pmatrix} r^{R,(i)}_{k_p,n_p} & -r^{I,(i,j)}_{k_p,n_p} \\ r^{I,(j)}_{k_p,n_p+1} & r^{R,(j,i)}_{k_p,n_p+1} \end{pmatrix} \begin{pmatrix} W^{R,(j,i)}_{k_p,n_p} \\ W^{I,(j,i)}_{k_p,n_p} \end{pmatrix} = \begin{pmatrix} d^{(i)}_{k_p,n_p} \\ d^{(i)}_{k_p,n_p+1} \end{pmatrix} \tag{10}$$

$$\begin{pmatrix} W^{R,(i,j)}_{k_p,n_p} \\ W^{I,(j,i)}_{k_p,n_p} \end{pmatrix} = \frac{1}{r^{R,(j)}_{k_p,n_p} r^{R,(j)}_{k_p,n_p+1} + r^{I,(j)}_{k_p,n_p} r^{R,(j)}_{k_p,n_p+1}} \times \begin{pmatrix} W^{R,(j,i)}_{k_p,n_p} \\ W^{I,(j,i)}_{k_p,n_p} \end{pmatrix}$$

More compactly

$$W^{(j,i)}_{k_p,n_p} = \frac{d^{(i)}_{k_p,n_p} r^{*(j)}_{k_p,n_p+1} + j\, d^{(i)}_{k_p,n_p+1} r^{*(j)}_{k_p,n_p}}{\Re(r^{(j)}_{k_p,n_p} r^{*(j)}_{k_p,n_p+1})} \tag{11}$$

We set for each antenna the value of each pair of pilots such that; $d^{(i)}_{k_p,n_p+1} = 0$ and $d^{(i)}_{k_p,n_p} = 1$ with $i \in \{1, \ldots, N_t\}$. Thus,

$$W^{(j,i)}_{k_p,n_p} = \frac{r^{*\,(i)}_{k_p,n_p+1}}{\Re(r^{(i)}_{k_p,n_p} r^{*\,(j)}_{k_p,n_p+1})} \tag{12}$$

One of the advantages of the *POP* scheme, besides its simplicity is that, it doesn't explicitly depends on the employed prototype filter. However, it must be emphasized that the above derivation only holds when noise is negligible. One can see that in the presence of noise, the method can have unpredictable performance since the degree of the noise enhancement in general also depends on unknown (hence uncontrollable) data.

G. FBMC using scattered pilots

Scattered or orthogonal pilot sequences are usually used to transmit over N_t antennas in CP-OFDM systems [20]. Using such pilot sequences it is possible to recover the channel coefficients for each pair of receive and transmit antennas. As for MIMO CP-OFDM system it is possible to choose the value of the pilot in the form; for instance, $[P_1, P_2]$ for antenna "1", and $[\acute{P}_1, \acute{P}_2]$ for antenna "2" (see references in [20]). The assumption of constant channel over 2 consecutive symbols is fulfilled in OQAM-OFDM (FBMC) system. Adapting the orthogonal pilot sequences to PHYDYAS's FBMC specifications, we start from the equivalent D-PUSC pilot structure for two antennas at the transmitter as depicted in Figure 1, and we propose an adapted pilot structure version for MIMO FBMC as in Figure 8a. Using proposed scattered pilots in Figure 8, with PHYDYAS filter parameters [3] depicted in Table I, we assume that the channel is quasi-static at least over four consecutive FBMC time symbols. As in previous pilot allocation schemes, the main objective is always to cancel the interference caused by the neighboring symbols (see Figure 4). First, orthogonality between the pilot sequences over the antennas could be preserved by setting one of the pilots to zero. Secondly, the interference is compensated by setting the value of one of the neighbors to the total of the intrinsic interference.

The cancelation of the intrinsic interference is performed in two steps too. First, the $d^i_{k,n-1}$ ($i \in \{1,2\}$ *refers to transmit antenna index*) symbol is determined to cancel the interference over (k,n) position. Then $d^2_{k,n+2}$ and $d^1_{k,n-1}$ symbols are determined to cancel the interference over the $(k,n+1)$ and (k,n) respectively. It can be seen in Figure 8, that $d^i_{k,n+2}$ is placed at position $(k,n+2)$, so by modifying the $d^i_{k,n+2}$ value it doesn't generate interference on the symbol located at position (k,n). As a consequence, this allows to cancel intrinsic FBMC interference in both (k,n) and $(k,n+1)$ time-frequency positions. The values of $d^2_{k,n}$ and $d^1_{k,n+1}$ are here fixed to zero. Note that proposed scattered pilot scheme in Figure 8, could be considered as a special case of the auxiliary pilot scheme depicted in Figure 6.

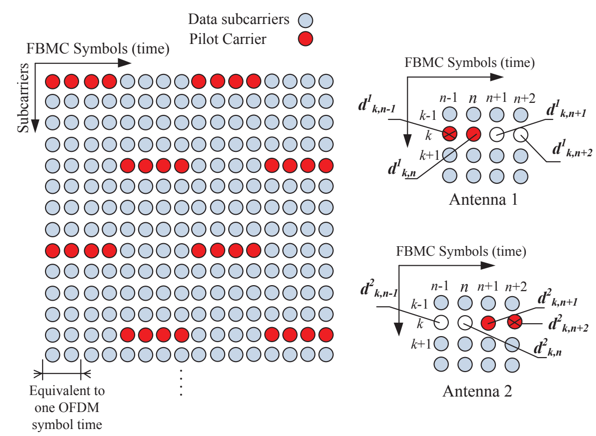

Figure 8. Simplified orthogonal pilot sequences in FBMC MIMO system with 2 transmit antennas: (a) general structure, (b) pilot allocation for each transmitted antenna.

IV. Simulations results

The pilot pattern structures were tested using the reference filter bank parameters in PHYDYAS project [2][3], with an overlapping factor K =4 and WiMAX-physical layer like basic parameters with: FFT-size and M equal to 1024, a bandwidth of 10 MHz, and subcarrier spacing of 10.94 kHz. This allows a transmission of 53 OQAM symbols. Note that due to the effect of the cyclic prefix in an OFDM based WiMAX system only 47 symbols can be used. During all the simulations the evaluated link is the downlink PUSC (DL-PUSC) structure [11].

In all the simulations received signals are assumed perfectly synchronized in time and frequency domain. The interpolation process is carried out using two dimensional linear surface interpolations within the areas limited by the carriers and the symbols with pilot supports. Simulations have been run over 600 channel realizations. Note that a weak spatial correlation is assumed for both transmit and receive antennas. The CP-OFDM transmitted signal was again scaled in each experiment so it has to be of the same power with the channel input in the corresponding FBMC/OQAM system. Note that there is no channel coding scheme used during the simulation process.

It can be seen in Figure 9, that the POP scheme adapted for MIMO FBMC exhibited a performance worse than the CP-OFDM schemes for both channels; Veh-A, and Veh-B. A similar strategy for the pair values of $(0, \pm 1)$ for pilots have been adopted as in [19] for each antenna pilot pattern. Although a performance degradation is experienced by the CP-OFDM scheme in the Veh-B channel, the POP scheme still yields worse results in the Veh-A channel. Therefore, it can be concluded that the POP scheme is unsuitable for filter bank multicarrier system due to its poor performance compared with the CP-OFDM scheme.

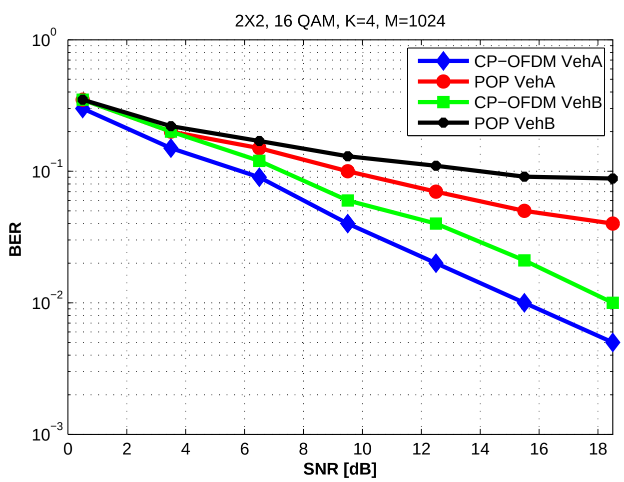

Figure 9. A 2×2 MIMO scheme performances using FBMC and CP-OFDM for Veh-A and Veh-B at 60 Km/h, using adapted POP method to downlink PUSC. Filter bank references: M=1024, K=4, and 16 QAM modulation with ZF equalization.

In Figure 10 and Figure 11, the use of the two variants of the adapted IAM-R (depicted in Figure 7a, and Figure 7b respectively) are analyzed. In Figure 10, two APC carriers are used to estimate the interference effects of the used filter. Here we dealt with a partial interference approximation as not all the interference $(\Omega_{k_p,n_p} = \Omega_{1,1})$ that affects the pilot $d^i_{k_p,n_p}$ could be estimated. The real values used in $[d^i_{k_p,n_{p-1}} d^i_{k_p,n_p} d^i_{k_p,n_{p+1}}]$ are $[\,0\; d^i_{k_p,n_p}\; 0\,]$ respectively, with the centered value $d^i_{k_p,n_p} = \pm 1$. It can be also observed that the "IAM-Ra" scheme in Figure (10) performs similarly as the CP-OFDM for SNRs lower than 8 dB for Veh-A channel environment, and for SNRs lower than 5 dB in case of Veh-B channel environment. An error floor is observed when the IAM is used at high SNRs due to the unavoidable intrinsic interference which is shows up at weak noise regimes.

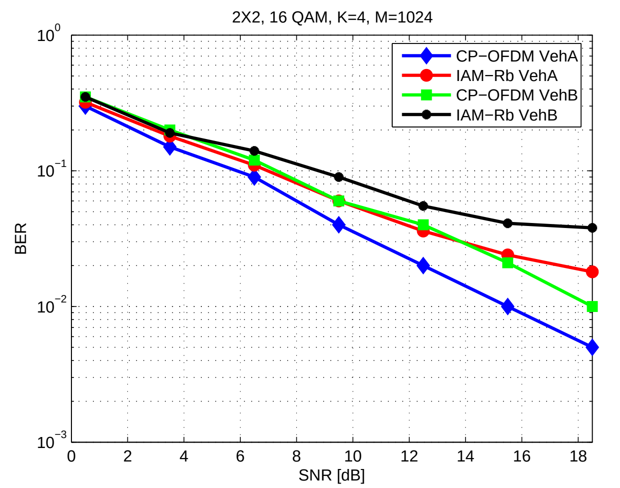

Figure 10. A 2×2 MIMO scheme performances using FBMC and CP-OFDM for Veh-A and Veh-B channels at 60 km/h, using adapted IAM method in DL-PUSC: (a) IAM-Ra refer to scheme in 7a for 2 antennas.

However, a better result is achieved in Figure 11 "IAM-Rb" due to the use of several APC carriers, more exactly four "aided" pilots. In Veh-A channel environment very similar performance in terms of BER is achieved using the FBMC and/or the CP-OFDM scheme. The CP-OFDM performs around 1/2 dB better than the FBMC. In channels with higher frequency selectivity as in Veh-B channel environment, the FBMC system performs similarly as the CP-OFDM up to SNR= 12 dB. For higher values of SNRs the CP-OFDM clearly outperforms the FBMC system. Here the value of $d^i_{k_p,n_p-1}$,and $d^i_{k_p,n_{p+1}}$ is zero, and $[d^i_{k_{p-1},n_p} d^i_{k_p,n_p} d^i_{k_{p+1},n_p}]$ use ± 1 values in alternation. The main reason for such alternation is to alleviate the risk of hight peaks power [18]. Note that, still not all the interference that affects the pilot $d^i_{k_p,n_p}$ could be estimated but only almost the largest ones.

Figure 12, shows that the use of auxiliary pilots in FBMC system outperforms the conventional CP-OFDM system. In Veh-A channel with 60Km/h of velocity moving the FBMC with Minimum Mean Square Error (MMSE) equalization achieves better performs than the CP-OFDM. Even using the zero forcing (ZF) equalization the performances are lightly better than the CP-OFDM with ZF.

Figure 13, depicts obtained performance with scattered pilots for CP-OFDM and FBMC using non iterative MMSE receiver. It can be observed that for pedestrian channel (type A at 3 km/h of mobility) FBMC performance is very similar to that obtained with a CP-OFDM system. Due to the very

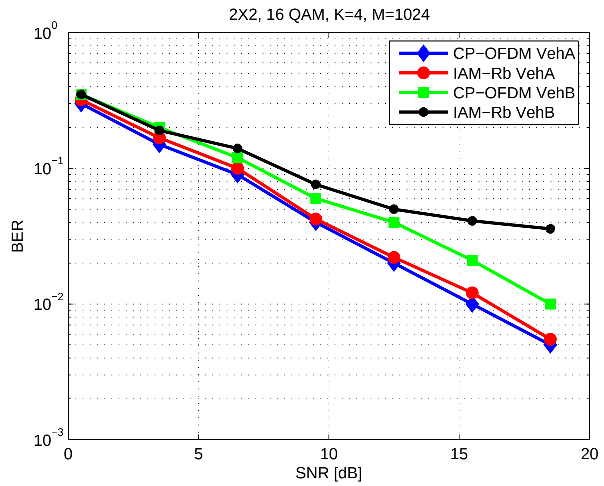

Figure 11. A 2 × 2 MIMO scheme performances using FBMC and CP-OFDM for Veh-A and Veh-B channels at 60 km/h, using adapted IAM method in DL-PUSC. IAM-Rb (describes scheme in Figure 7b) for 2 antennas. M=1024, K=4, and 16 QAM with ZF equalization.

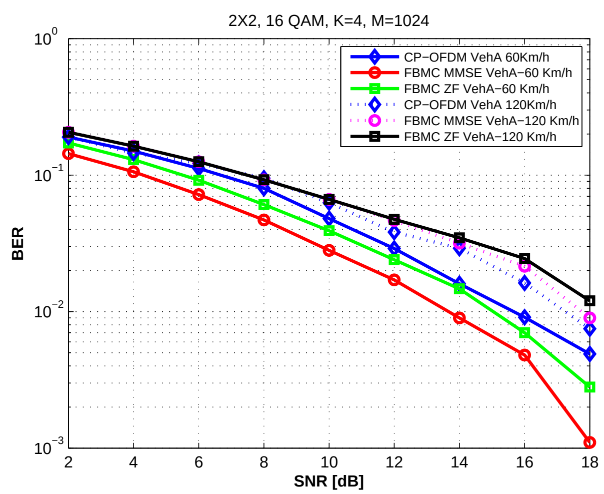

Figure 12. A 2 × 2 MIMO scheme performances using FBMC and CP-OFDM for Veh-A at different MS velocities (60 Km/h and 120 Km/h), using adapted auxiliary pilot method (see fig. 6) vs. conventional CP-OFDM. M=1024, K=4, DL-PUSC mode, and 16 QAM using MMSE [17] and ZF equalizations.

low variability of this channel, the assumption of having four FBMC time symbols (equivalent to two OFDM time slots) makes sense as the channel is quasi invariant. In the case of higher frequency selectivity channels, as the Veh-A/B, additional degradation in MIMO can occur in FBMC due the assumption of a constant channel over the symbols besides the interference effect of the first order neighbors.

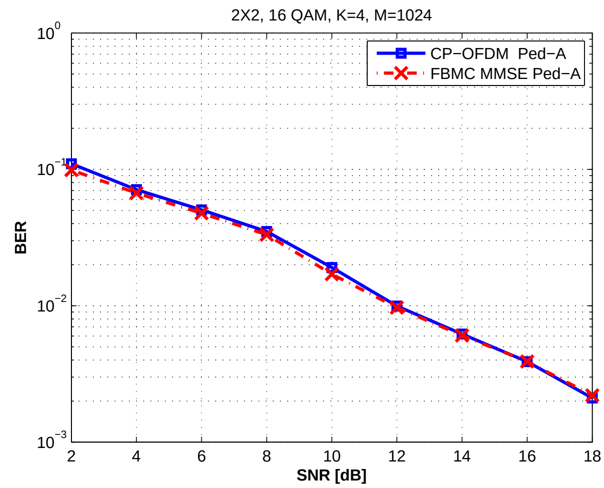

Figure 13. CP-OFDM and FBMC comparison with 2 × 2 SDM, over Ped-A channel with non iterative MMSE receiver.

V. Conclusion

In this paper the authors studied the possibility to adapt the pilot pattern of the DL-PUSC MIMO WiMAX scheme to MIMO FBMC system. Different scheme have been proposed and their performance evaluated and compared with CP-OFDM system (POP, auxiliary pilot scheme, IAM-Ra,IAM-Rb, and Scattered pilots). Proposed auxiliary pilot scheme seems able to eliminate the secondary interference from the neighboring symbols into the pilots antenna using both the ZF and the MMSE receivers, and to achieve better BER performances than CP-OFDM. Besides, the proposed scheme has the same pilot overhead as in OFDM. The use of scattered pilot for MIMO based on combined auxiliary pilots will be further investigated such that the antennas pilot positions doesn't suffer the effect of the surrounding interference due to the largest weights of the filter banks.

Acknowledgment

The authors would like to thank all the partners of the European ICT 2008-211887 project PHYDYAS.

References

[1] K. Baum, B. Classon, and P. Sartori, *"Principles of Broadband OFDM Cellular System Design"*. Wiley-Blackwell. March 2009.

[2] ICT-211887 PHYDYAS European project, www.ict-phydyas.org. (visited 31^{st} January 2011).

[3] ICT-PHYDYAS Deliverable 3.1 "Equalization and demodulation in the receiver (single antenna)", Section: Channel estimation. 2008.

[4] B. Farhang-Boroujeny, *"Filter bank spectrum sensing for cognitive radios," IEEE Trans. on Signal Processing,"* vol. 56, no. 5, pp. 1801-1811. May 2008.

[5] M. Shaat and F. Bader, *"Low Complexity Power Loading Scheme in Cognitive Radio Networks: FBMC Capability"*, in Proceeding of 20^{th} IEEE International Symposium on Personal, Indoor and Mobile Radio Communications (IEEE PIMRC'2009), pp. 2597-2602. Tokyo, Japan. September 2009.

[6] B. Farhang-Boroujeny and R. Kempter, *"Multicarrier communication techniques for spectrum sensing and communication in cognitive radios,"* IEEE Communications Magazine (Special Issue: on Cognitive Radios for Dynamic Spectrum Access), vol. 48, no. 4, pp. 80-85, Apr. 2008.

[7] H. Zhang, D. L. Ruyet, and M. Terre,*"Spectral efficiency analysis in OFDM and OFDM/OQAM based cognitive radio networks,"* in Proc. of the IEEE Vehicular Technology Conference (IEEE VTC-Spring'09), pp.1-5, Barcelona, Spain. April 2009.

[8] J. P. Javaudin and D. Lacroix,*"Technical description of OFDM/IOTA modulation, 3GPP TSG-RAN-1 meeting no. 31,"* Tokyo, Japan. Feb 18-21, 2003.

[9] "Wideband air interface isotropic orthogonal transform algorithm (IOTA) - public safety wideband data standards project - digital radio technical standards TR-8.5 subcommittee," TIA902.BBAB (Physical Layer Specification, March 2003).

[10] F. Bader and M. Shaat, *"Pilot Pattern Adaptation and Channel Estimation in MIMO WIMAX-Like FBMC System,"* in Proc. of Sixth International Conference on Wireless and Mobile Communications (ICWMC'2010). pp. 111-116. September 2010. Valencia, Spain.

[11] Part 16: Air Interface for Fixed and Mobile Broadband Wireless Access Systems Amendment 2: Physical and Medium Access Control Layers for Combined Fixed and Mobile Operation in Licensed Bands and Corrigendum 1, IEEE Std. 802.16e, 2006.

[12] M. Bellanger,*"Filter Banks Digital Processing and Signals: Theory and Practice,"* John Wiley and Sons, New York, NY-USA, 3^{rd} edition 2000.

[13] M. Bellanger, *"Transmit diversity in multicarrier transmission using OQAM modulation,"* in Proc. of the International Symposium on Wireless Pervasive Computing (ISWPC'2008), Santorini (Greece), May 2008

[14] M. Bellanger, *"Specification and design of a prototype filter for filter bank based multicarrier transmission,"* Proc. of the IEEE International Conference on Acoustics, Speech, and Signal Processing, (IEEE ICASSP'2001). Vol 4. pp. 2417-2420. Salt Lake City, USA. May 2001.

[15] R. V. Nee,*"OFDM Wireless Multimedia Communications."* Artech House. January 2000.

[16] P. Siohan, C. Siclet, and N. Lacaille,*"Analysis and design of OFDM/OQAM systems based on filterbank theory,"* IEEE Transactions on Signal Processing, vol. 50, no. 5, pp. 1170-1183, 2002.

[17] J. P. Javaudin and Y. Jiang, *"Channel estimation in MIMO OFDM/OQAM,"* in Proc. of the IEEE International Workshop on Signal Processing Advances for Wireless Communications (IEEE SPAWC'2008). pp. 266-270. Recife, Pernambuco, Brazil, July, 2008.

[18] C. Lélé, J.-P. Javaudin, R. Legouable, A. Skrzypczak, and P. Siohan, *"Channel estimation methods for preamble-based OFDM/OQAM modulations,"* European Transactions on Telecommunications (ETT), Vol 19, Issue 7, pp. 741-750. November 2008.

[19] J. P. Javaudin, D. Lacroix, and A. Rouxel, *"Pilot-aided channel estimation for OFDM/OQAM,"* in Proc. of the IEEE Vehicular Technology Conference (VTC-spring 2003), pp. 1581-1585, April 2003.

[20] N. Chen, M. Tanaka, and R. Heaton,*"Channel Equalisation for OFDM using scattered pilots,"* in Proc. of the IEEE Vehicular Technology Conference (IEEE VTC-Spring'2002). pp. 1040-1044. Birmingham, Alabama-USA. May 2002.

Field Tests and Comparison of the Channel Properties for the DRM+ System in the VHF-Bands II (87.5 MHz-108.0 MHz) and III (174-230 MHz)

Friederike Maier, Andrej Tissen
Institute of Communications Technology
Appelstr. 9A
Leibniz University of Hannover
Hannover, Germany
Email: maier@ikt.uni-hannover.de,
tissen@ikt.uni-hannover.de

Albert Waal
RFmondial GmbH
Appelstr. 9A
Hannover, Germany
Email: waal@rfmondial.de

Abstract - **This paper presents a comparison of the channel properties for the DRM+ (Digital Radio Mondiale, Mode E) radio system in the frequency Bands II and III for mobile reception. The impact of different transmitting frequencies and receiver velocities is analyzed by simulations of the system performance with different channel profiles. A closer view is taken on the upper bounds of receiver velocities as this is the main problem for proper reception at higher frequencies. Additionally, measurements of the DRM+ system in the VHF-Bands II and III are presented to analyze and compare the performance in the real-world. The theoretical work show that reception is possible up to receiver velocities of around 200 km/h in Band III in a worst case scenario. The measurements show comparable results for Band II and III.**

Keywords* - *Digital Radio Mondiale; DRM+ ; mobile reception; Doppler spread; digital broadcasting; channel properties; COFDM

I. INTRODUCTION

DRM+ is an extension of the long, medium and short-wave DRM standard up to the upper VHF band. Field trials with DRM+ were conducted in Hannover [1] and Kaiserslautern [2] in Band II and in Paris in Band I. It has been approved in the ETSI (European Telecommunications Standards Institute) DRM standard [3] for frequencies up to 174 MHz. In Germany and other countries the VHF-Band II (87,5-108 MHz) is fully occupied by FM-radio, which will not be switched off in the next years. At the same time, in Band III, which allocates the frequencies from 174 to 230 MHz, there is a lot of free spectrum intended for audio broadcast, therefore evaluations about the use of DRM+ in Band III were started. In Band III DRM+ can coexist with the multiplex radio system DAB (Digital Audio Broadcast), offering local radios a cheap and flexible possibility to digitize their signals, which is hardly possible with DAB due to its multiplexed structure [4].

Section II in this paper gives a short introduction to the DRM+ system parameters. Evaluations of the channel properties, simulations of the effects of mobile reception for different receiver velocities at different frequencies are presented in Section III and Section IV gives a comparison of measurement results in Band II and III. Section V gives a conclusion of the possibilities and limitations of the DRM+ system in the VHF-Band III from 174-230 MHz.

Table I
DRM+ SYSTEM PARAMETERS

Subcarrier modulation	4-/16-QAM
Signal bandwith	96 kHz
Subcarrier spread	444.444 Hz
Number of subcarriers	213
Symbol duration	2.25 ms
Guard interval duration	0.25 ms
Transmission frame duration	100 ms

II. DRM+ SYSTEM PARAMETERS

The DRM+ system uses Coded Orthogonal Frequency-Division Multiplex (COFDM) modulation with different Quadrature Amplitude Modulation (QAM) constellations as subcarrier modulation. The additional use of different code rates result in data rates from 37 to 186 kbps with up to 4 audio streams or data channels. A signal with a low data rate is more robust and needs a lower signal level for proper reception. Table I shows the system parameters in an overview.

In order to improve the robustness of the bit stream against burst errors, bit interleaving and multilevel coding is carried out over one transmission frame (100 ms) and cell interleaving over 6 transmission frames (600 ms).

In the simulations and the measurements 16-QAM subcarrier modulation with a code rate of $R_0 = 0.5$ (protection level 2) resulting in a bit rate of 149 kbps was used.

III. IMPACT OF THE MOBILE CHANNEL

The following Section gives an overview of the channel properties at different frequencies and receiver velocities and how they can effect the reception.

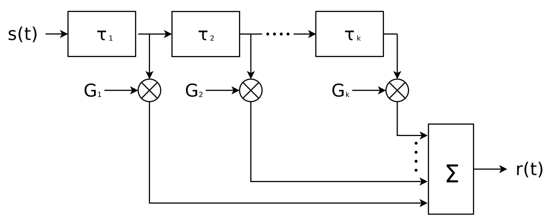

Figure 1. Tapped delay filter

A. Channel properties

To analyze the performance of the system at different frequencies and receiver velocities, simulations were conducted with a rural channel, implemented as a tapped delay filter as described in [5] and shown in Figure 1. The complex output signal $r(t)$ is generated as shown in Equation 1.

$$r(t) = \sum_{k=1}^{N_T} G_k(t)m(t-\tau_k). \tag{1}$$

With the complex input signal $m(t)$, the relative path delays τ_k and the path process $G_k(t)$. $|G_k(t)|$ follows a Rayleigh distribution, the phase follows a uniform distribution, every path is characterized by a Doppler spectrum and a certain attenuation. In case that all waves are arriving from all directions at the receiving antenna with approximately the same power the real Doppler spectrum can be approximated by the Jakes spectrum:

$$P_d(f) = \frac{A}{\sqrt{1-(\frac{f}{f_d})^2}} \qquad \text{for} \qquad |f| \leq f_d \tag{2}$$

For propagation paths with large delay times for example the 'Single Frequency Network' used in Section III-D, the Gaussian spectra are used. They are defined with the help of the Gaussian function:

$$G(f, A, f_1, f_2) = Ae^{-\frac{(f-f_1)^2}{2f_2^2}} \tag{3}$$

The spectra denoted by 'Gauss1' and 'Gauss2' consist of a single Gaussian function and are defined as [3]:

Table II
CHANNEL PROFILE 'RURAL'

Path Nr.	Delay in μs	Powerlevel in dB	Doppler-spectrum
1	0	-4	JAKES
2	0.3	-8	JAKES
3	0.5	0	JAKES
4	0.9	-5	JAKES
5	1.2	-16	JAKES
6	1.9	-18	JAKES
7	2.1	-14	JAKES
8	2.5	-20	JAKES
9	3.0	-25	JAKES

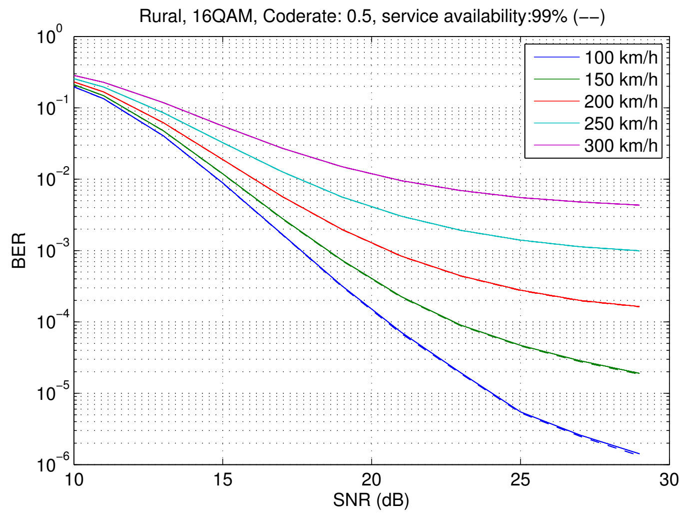

Figure 2. Performance in Band III

$$P_d(f) = G(f, A, \pm 0.7f_d, 0.1f_d) \tag{4}$$

where the '+' sign is valid for 'Gauss1' and the '-' sign for 'Gauss2'

Table II shows the properties of the tapped delay filter for a 'rural' channel. A set of other channels is given in the DRM ETSI Standard [3].

B. Inter-Carrier-Interference

A moving receiver causes Doppler shifts of the OFDM carriers. If this is combined with multipath propagation, paths from different directions can cause frequency dependent Doppler shifts, which results in Inter-Carrier-Interference (ICI). This interference can be handled as additional near-Gaussian noise [6]. In [7] upper bounds of the normalized interference power for a classical (Jakes) channel model depending on the maximum Doppler shifts (f_d) and the symbol duration (T_s) are given as

$$P_{ICI} \leq \frac{1}{12}(2\pi f_d T_s)^2. \tag{5}$$

The Doppler shift increases with increasing carrier frequencies f_0 and receiver velocities v as $f_d = f_0 \cdot \frac{v}{c} \cdot cos(\alpha)$, with the speed of light c and the angle between the direction of arrival and the direction of motion α.

The effect of ICI power was added as an additional noise relative to the signal amplitude in function of the receiver velocity for an angle $\alpha = 0$ as the worst caste scenario when the receiver is moving directly towards or away from the transmitter on a radial route.

Additionally to the averaged Bit Error Rate (BER) the BER with a service availability of 99 % was plotted. In [8] a 'good' mobile reception is defined as having a coverage of 99 % of the locations. The simulation was conducted with 100 channel calls. Every call loads a random set of

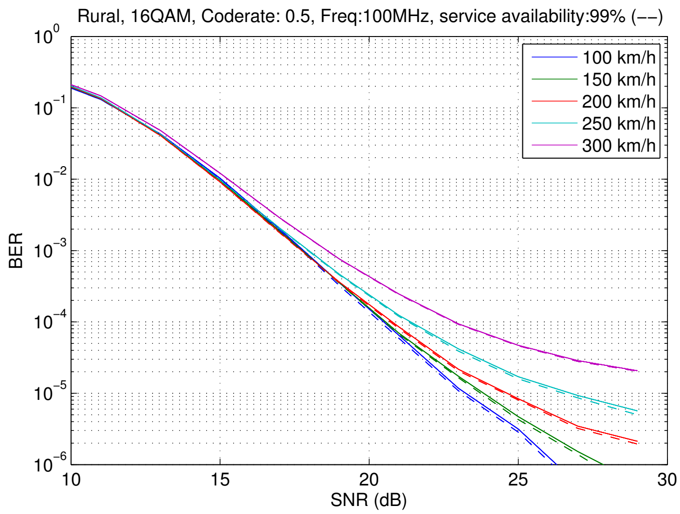

Figure 3. Performance in Band II

path processes, which stands for a different set of multipath components, that can be seen as different locations. An approximation of the 99 % coverage probability can be calculated as the average of the (in this case) 99 simulation calls, having the lowest BER. With every call 120 frames (12 sec. of data) containing a pseudo-random bit sequence were filtered by the tapped delay filter, decoded and the BER was calculated.

C. ICI in a 'rural' channel

Simulations were conducted with a 'rural' channel profile for receiver velocities from 100 - 300 km/h. It's parameters are given in Table II.

Figure 2 shows the simulation of the performance of a DRM+ system in Band III (200 MHz). For comparison Figure 3 shows the results for Band II (100 MHz). The BER for a coverage probability of 99 % is plotted together with the values for 100 % for receiver velocities from 100 to 300 km/h. In [9] a BER of 10^{-4} is given as a value where a proper reception is still possible in a DRM system. The simulation results show that at 100 MHz a signal to noise ratio (SNR) of 20 dB is necessary to reach this value at a

Table III
CHANNEL PROFILE 'SFN'

Path Nr.	Delay in μs	Powerlevel in dB	Doppler-spectrum
1	0	0	JAKES
2	100	-13	GAUSS1
3	220	-18	GAUSS2
4	290	-22	GAUSS1
5	385	-26	GAUSS2
6	480	-31	GAUSS1
7	600	-32	GAUSS2

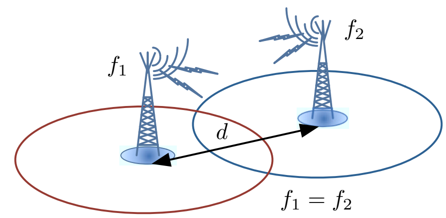

Figure 4. A 'Single Frequency Network' of two transmitters

velocity of 100 km/h. For 300 km/h a SNR of 22.5 dB is necessary. At 200 MHz and 100 km/h the necessary SNR stays the same as at 100 MHz. Stepping up the receiver velocity, the impact of the ICI increases faster. In Band III at 150 km/h a SNR of 22.5 dB is necessary, at 200 km/h the BER of 10^{-4} is hardly achieved with around 30 dB. At higher velocities this scenario doesn't achive a bit error rate of 10^{-4}.

The coverage probability has no big effect on the system performance within the analyzed velocities. At a frequency of 100 MHz and the lowest velocity, small differences can be seen at high SNR values, at 200 MHz there are no differences between the full coverage and a coverage probability of 99 %. This shows that the coherence time of the channel at these frequencies is short enough (for 150 km/h it is 0.072 sec. at 100 MHz and 0.036 sec. at 200 MHz) that the average over the simulation time stays nearly the same. The deep fades are short enough that the cell- and bitinterleaver can handle them. Simulations carried out with low receiver velocities as shown in Section III-E showed more differences between the full coverage and a certain coverage probability.

D. ICI in a 'Single Frequency Network' channel

A special case of propagation occurs in a 'Single Frequency Network' (SFN) as shown in Figure 4. It represents a network of transmitters sharing the same radio frequency to achieve a large area coverage. As shown in Table III the delays are in the range of several hundreds micro seconds representing signals arriving from the different transmitter stations in the overlapping area.

Simulation were conducted with a 'Single Frequency Network' (SFN) channel profile for receiver velocities from 50 - 200 km/h. Figure 5 shows the worst case performance of a 'Single Frequency Network' at a frequency of 200 MHz. It can be seen that for a receiver velocity of 150 km/h a slightly higher SNR is needed as for 100 km/h to get a bit error rate below 10^{-4}. For 200 km/h it is still possible to get a proper reception, but more field strength is needed.

E. Slow and flat fading

For low receiver velocities in Band II slow fading over the whole signal bandwidth can lead to deep fades, lasting

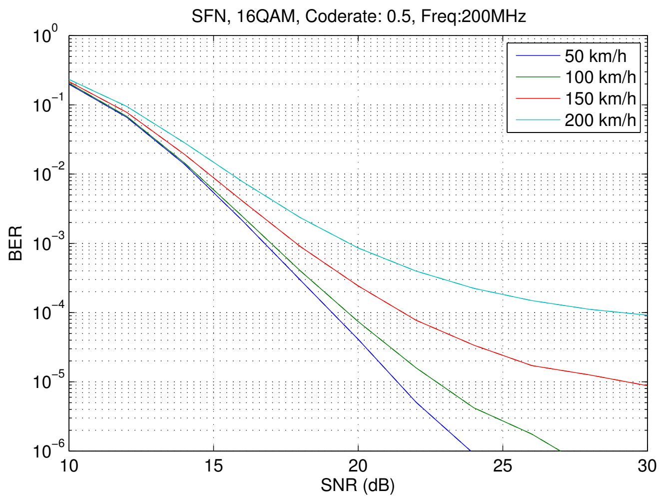

Figure 5. Performance in a 'Single Frequency Network' in Band III

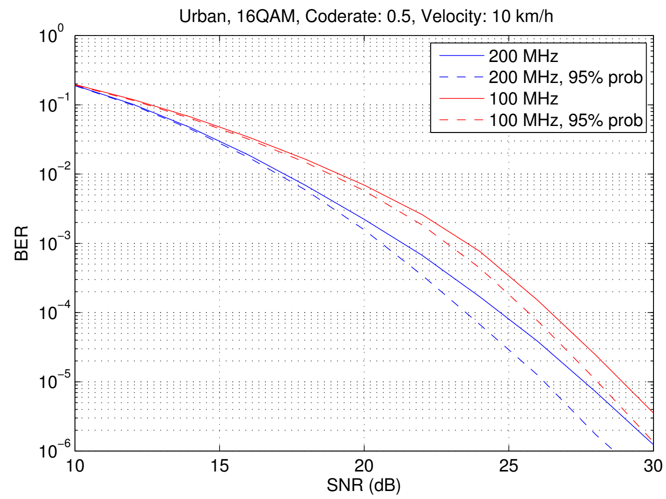

Figure 6. Comparison of the performance in a slow and flat fading environment

longer than the cell interleavers time (600 ms). This can result in signal dropouts as there is no chance to recover the signal by the following error correction. As a shorter wavelength results in a higher spatial resolution of the interference pattern in the air, the coherence time becomes smaller, which results in less dropouts due to slow fading.

Figure 6 shows a comparison of the system performance with a slowly moving receiver at 10 km/h for frequencies of 100 and 200 MHz. The performance is enhanced by the higher frequency. Additionally an error probability of 95 %, calculated as described in Section III-B, is plotted. The differences between full 'coverage' and a coverage probability of 95 % in this slow channel exceed the differences in the fast channel clearly, especially for the lower frequency. The reason for this are the higher spatial resolution of the interference patterns of the field strength in the air. Moving through this interference patterns, the resulting signal dropouts are shorter with higher frequencies, the interleaver and error correction can work.

F. The pilot grid

For channel estimation DRM+ uses pilots, that are distributed diagonally over the frames [10]. As shown in Figure 7 the pilots are inserted on every fourth subcarrier and every four symbols. As described in [11], the maximum Doppler frequency a system can handle depends on the pilot grid in time direction.

Considering the symbol duration of T_s=2.5 ms, in time direction, the channel is measured every $4 * T_s$=10 ms resulting in a sampling frequency of 100 Hz. To satisfy the sampling theorem the maximum Doppler frequency f_d, which is the reciprocal of the channels coherence time, has to fulfill the condition: $f_d < 50$ Hz. At 100 MHz this value is achieved at a velocity of 540 km/h, at 200 MHz at 270 km/h.

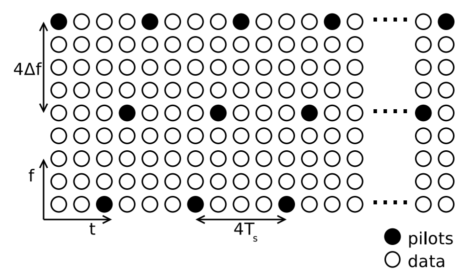

Figure 7. Pilot grid

IV. Measurements in Band II and III

In winter/spring 2010 DRM+ measurements were conducted at 95.2 MHz (Band II) and 176.64 MHz (Band III) in the city of Hannover and its surroundings. The transmitter was located at the roof of the university building at a height of 70 m over the ground. Both in Band II and III an ERP (Effective Radiated Power) of 30 W was transmitted with directive yagi antennas with nearly the same radiation pattern, so that in the main beam the results of the coverage measurements are comparable. The transmission content was generated with a Fraunhofer Content Server and consisted of an audio stream with a bit rate of 103.6 kbps and a pseudo-random bit sequence with 45.4 kbps, to measure the Bit Error Rate (BER). The transmitter equipment consisted of a modulator from RFmondial, an amplifier from Nautel for Band II and a Thomson linear amplifier for Band III. The measurements included the field strength, which was recorded with an Rhode & Schwarz test receiver (ESVB), the audio status and BER of the receiver (RFmondial software receiver) and the Signal to Noise Ratio (SNR), calculated via the time correlation/synchronization.

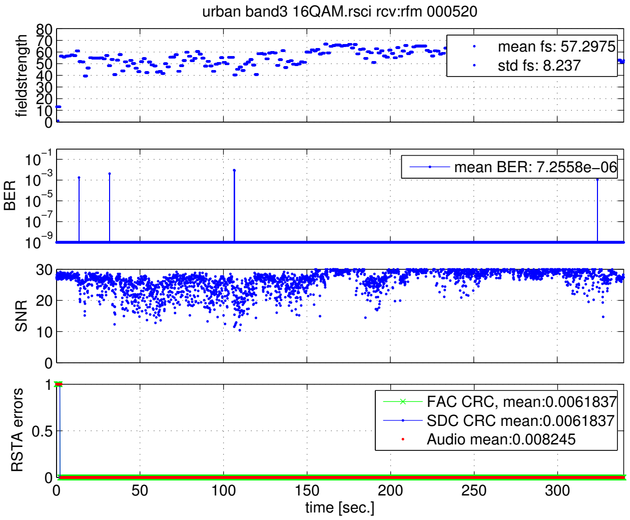

Figure 8. Measurement results in Band III

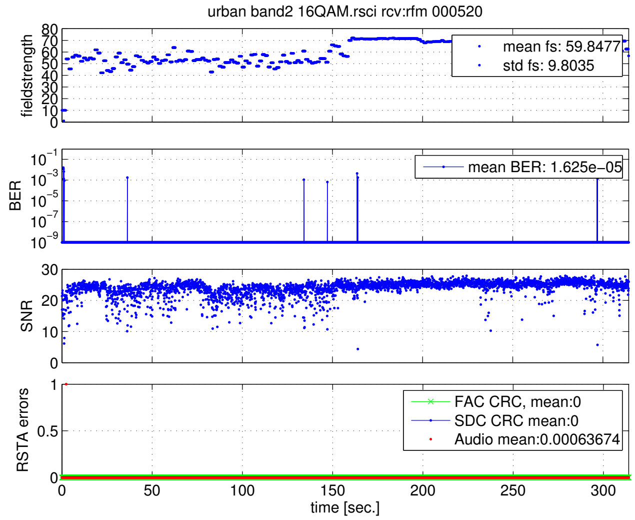

Figure 9. Measurement results in Band II

A. *Measurements in an urban environment*

To test the reception in an urban environment measurements were conducted in the inner city of Hannover. As this area is located in the main beam of the transmission the results for Band II and III are comparable. The measurements were conducted at a velocity of around 15 km/h on the same route.

In Figures 8 and 9, the results are shown over the time. In the first row the field strength is plotted. Additionally the mean field strength (mean fs) and the standard deviation of the field strength (std fs) are inserted in the Figures. This shows that the field strength in Band II is slightly higher than in Band III, the standard deviation is a bit lower in Band III which can be caused by differences in slow and flat fading. The second row shows the BER, which is slightly lower in Band III than in Band II. The third one shows the calculated SNR which is higher in Band III. As at the time of the measurement in Band III only block 12A (around 223 MHz) is used for DAB in the region of Hannover, this could be caused by less interferences. In Band II interferences from other FM transmitters can effect the reception and degrade the SNR. The last row shows the status of the Cyclic Redundancy Check (CRC) of the Fast Access Channel (FAC), the CRC of the Service Description Channel (SDC) and the audio decoder errors (0: errorfree, 1: one or more CRC/audio frames corrupted). Here some more errors show up in Band III. On the whole at both frequencies the reception was nearly the same.

B. *Measurements of the coverage limit*

Additional measurements of the coverage limit were conducted on a highway leaving the city in the main beam and passing rural area and some villages. In the maps in Figure 10 and 11 the audio status is plotted.

While the reception in the open (flat) environment is still good, errors came up passing villages. Compared to Band III, in Band II some more errors occurred while leaving the city of Hannover and in the village before Sehnde. Here due to a four-lane road velocities up to 100 km/h could be driven. This could be caused again by higher interferences with FM in Band II.

V. Conclusion

Evaluations of the channel properties in Band III for a DRM+ system show that the main problems using the system at higher frequencies are the Inter-Carrier-Interference and the density of pilots needed for the channel estimation.

Simulations of the systems performance in a 'rural' channel, including the effects of ICI as noise in function of the receiver velocities, show no differences between Band II and III for a velocity of 100 km/h. At velocities up to 200 km/h the reception was effected by the ICI but still suffice the bit error rate necessary for proper reception. In Band II reception was still possible at 300 km/h, in Band III with velocities higher than 200 km/h, the BER exceeds the value necessary for proper reception in the evaluated worst case scenario.

The simulations of a 'Single Frequency Network' at a frequency of 200 MHz show a similar result. Reception is possible up to receiver velocities of 200 km/h.

To fulfill the sampling theorem for the pilots that have to be sampled for the channel estimation, in Band III a Doppler shift corresponding to a receiver velocity of 270 km/h should not be exceeded.

Regarding slow and flat fading, which appear at low receiver velocities in a multipath environment, the shorter wavelength in Band III can reduce the problem as the interference pattern has a higher spatial resolution. As a

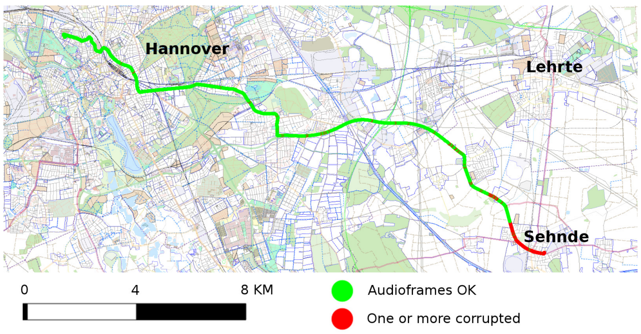

Figure 10. Audio status in Band III (mapdata (c) OpenStreetMap and contributors, CC-BY-SA, http://www.openstreetmap.org)

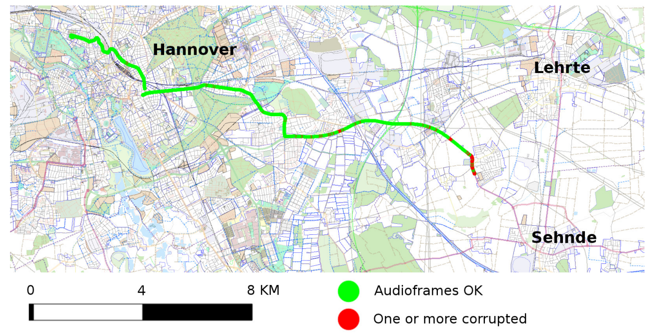

Figure 11. Audio status in Band II (mapdata (c) OpenStreetMap and contributors, CC-BY-SA, http://www.openstreetmap.org)

result, a receiver is passing the deep fades in a shorter time and the interleaver and error correction can work.

The measurements conducted in Band II and III show no big differences. While measuring the coverage limit, less errors were recorded in Band III, which can be caused by less interferences in Band III in Hannover.

A real speed test could not be conducted due to speed limits. As the ICI only becomes a problem when different carriers are effected by different Doppler shifts due to multipath propagation, this tests should be made in a region with obstacles in the countryside. The region of Hannover is a quite flat area.

Acknowledgment

The authors would like to thank the NLM (State Media Authority Lower Saxony), RFmondial, Thomson, Nautel, BNetzA (Federal Network Agency), the DRM Consortium, Fraunhofer IIS and others for their support and good advice.

References

[1] F. Maier, A. Tissen, and A. Waal. Evaluation of the Channel Properties for a DRM+ System and Field Tests in the VHF-Band III (174-230 MHz). In *Wireless and Mobile Communications (ICWMC), 2010 6th International Conference on*, pages 160 –163, 2010.

[2] A. Steil, F. Schad, M. Feilen, M. Kohler, J. Lehnert, E. Hedrich, and G. Kilian. Digitising VHF FM sound broadcasting with DRM+ (DRM mode E). In *Proc. IEEE Symposium on Broadband Multimedia Systems and Broadcasting (BMSB '09)*, 2009.

[3] ETSI. ES 201 980, Rev.3.1.1., Digital Radio Mondiale (DRM), System Specification. 2009.

[4] A. Steil and J. Lehnert. DRM+, a perfect complement to DAB/DAB+ in VHF band III - Technical results, planning aspects, and regulatory work -. In *11th Workshop Digital Broadcasting, Fraunhofer IIS Erlangen*, 2010.

[5] F. Hofmann. *Multilevel-Codierung und Kanalschätzung für OFDM in der Lang, Mittel- und Kurzwelle*. Shaker Verlag, 2003.

[6] P. Robertson and S. Kaiser. The effects of Doppler spreads in OFDM(A) mobile radio systems. In *Proc. IEEE Vehicular Technology Conference (VTC '99)*, pages 329–333, 1999.

[7] Y. Li and L. Cimini. Bound on the interchannel interference of OFDM in time-varying impairments. *IEEE Trans. Commun.*, 49:401–404, 2001.

[8] ITU-R. P.1546-3, Method for point-to-area predictions for terrestrial services in the frequency range 30 MHz to 3000 MHz. 2007.

[9] M. Kühn. *Der digitale terrestrische Rundfunk*. ISBN 978-3-7785-4008-4. Hüthig, 2008.

[10] A. Waal. *Konzeption und Realisierung eines digitalen Hörfunksystems mit Mehrwertdiensten zur lokalen Versorgung*. ISBN 978-3-8322-9422-9. Shaker Verlag, Aachen, Hannoversche Beiträge zur Nachrichtentechnik, 2010.

[11] H. Schulze and C. Lüders. *Theory and Applications of OFDM and CDMA Wideband Wireless Communications*. Wiley, 2005.

Selfish Flow Games in Non-Cooperative Multi-Radio Multi-Channel Wireless Mesh Networks With Interference Constraint Topology

Ibrah Shah, Sadaqat Jan
School of Engineering and Design
Brunel University
West London, UK
(Ibrar.Shah,Sadaqat.Jan)@brunel.ac.uk

Kok-Keong Loo, C. Campbell
School of Engineering and Information Sciences
Middlesex University, UK
J.Loo @mdx.ac.uk

***Abstract*—Due to the advancement in technology, routers of Wireless Mesh Networks can be equipped with multiple interfaces to achieve parallel communication sessions among nodes. Assigning distinct non-overlapping channels to each set of communicating radios increases network connectivity and throughput. On the other hand, the performance of wireless networks is always limited by the interference phenomena among the concurrent transmission sessions. Combined with interference constraint topology due to limited available orthogonal channels, selfishness of end users further degrades individual fairness and affects overall network performance due to their protocol deviation in a non-cooperative environment. In this paper, we have proposed a non-cooperative game theoretical model in a multi-radio multi-channel Wireless Mesh Network based on the end users flows in an interference constrained topology. Necessary conditions for the existence of Nash Equilibrium have been derived. Our simulation results show that our distributed algorithm converges to a stable state in finite time where each node gets fair end to end throughput across multiple-collision domains at the end of the game. Further, the Price of Anarchy of the system was measured for several runs which is always near to one; showing the strength and stability of our proposed scheme.**

Keywords-Multi-Radio Multi-Channel; Game Theory; Wireless Mesh Networks; Network Flows; Interference Constraint Topology; Price of Anarchy.

I. INTRODUCTION

In Non-Cooperative Networks, nodes behave selfishly to maximize their own benefit by deviating from the defined protocol [2], which leads to system-wide performance degradation, instability and individual unfairness. In Mobile Adhoc Networks (MANETs) [3], for example, each node acts as user of the network as well as rely data for others. A non-cooperative node can misbehave by dropping others packets to save its battery life while sending its own packets to be forwarded by other nodes. This selfish behavior of free riders leads to limited connectivity of the network and affects individual as well as network-wide performance. If all nodes behave selfishly in the same manner, the network will end up with each entity in isolation, as shown in Fig. 1, nodes c and g drop the incoming packets from other nodes

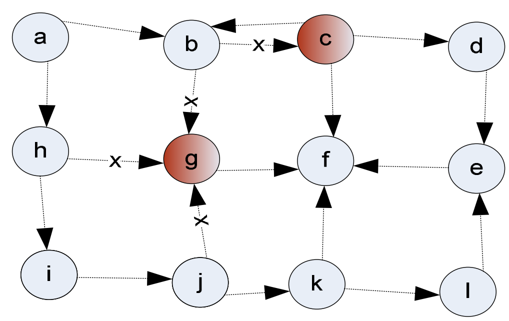

Figure 1. Non-Cooperative behaviour in MANETs

while send their packets to be forwarded by other nodes in the network. To cope up with these similar behaviors, multiple techniques have been used to enforce cooperation among the nodes for the stability of overall system [4]. Viewing this behavior from game theoretic prospective, a conflicting situation where each entity is self interested in the network resources or service leads to a non-cooperative game.

Like MANETs, Wireless Mesh Networks (WMNs) [5] have multi-hop topology spanning multiple collision domains. The inherited advantages of self configuration, self healing and self organization along with static nature of its backhaul routers make it a prime candidate for wireless broadband provisioning in users premises. However, unlike MANETs, WMNs routers can be equipped with multiple radios due to their static nature and the existence of permanent power supplies. Since multiple channels are available in the free Industrial, Scientific and Medical (ISM) band, multiple radios can be tuned simultaneously to exploit the free non-overlapping channels and hence increase the overall capacity, connectivity and resilience of the wireless mesh backhaul. Due to these characteristics, WMNs is a prime candidate to be deployed as a broadband wireless access network in the user premises. In WMNs, backhaul routers are divided into three types: Gateways, Access Points (APs) and core backbone routers. The Gateways have direct connection to the Internet while APs provide network access to the mesh backhaul users. The core backbone routers have the responsibilities of forwarding users traffic to/from the Internet via mesh gateways as shown in Fig. 2.

Due to the capabilities of meshing, IEEE has established subgroups in their existing network standards like IEEE 802.11s for WLAN based mesh networks, IEEE802.16e for Metropolitan Area Mesh Networks and IEEE 802.15 for Personal Area Mesh Networks. Since WMNs have the potential to be widely deployed as a broadband multi-hop wireless network [6], many vendors have invested in it and have deployed practical mesh topologies, e.g., Nortel [7], Motorola [8] and TroposNetworks [9].

Multi-Radio Multi-Channel (MRMC) in WMNs has gained a lot of research attention in the recent years [10]. Since wireless networks are always bandwidth constrained due to the shared wireless medium, interference from other transmissions, high bit error rates and retransmissions limit the capacity of wireless networks; multi radios tuned to multiple non-overlapping channels improve the overall capacity by decreasing the interference as the same channel can be reused multiple times in the same backhaul away from its transmission and interference range. Since designing a good MRMC algorithm is crucial for the WMNs performance, therefore a considerable amount of research has been done in this specific area.

Although, selfish routing and forwarding problems in MANETs have been well researched by providing solutions from Game Theory and considering all nodes as players of the game [11,12,13], the static infrastructure of WMNs shifts the set of players to the end users premises. Since forwarding nodes have no incentive to behave selfishly and there is no point to consider them in the set of players [14].

Game theory is a mathematical tool which is used in a situation when multiple entities interact with each other in a strategic setup. Formally, a game can be defined [15] as consisting of a non-empty finite set of $N=\{N_1,N_2,\ldots,N_{|N|}\}$ players, a complete set of actions/strategies $A_i=\{a_1,a_2,\ldots a_{|Ai|}\}$ for each $N_i \in N$. A set of all strategies space of all players, represented by the matrix $A=A_1xA_2x\ldots xA_{|N|}$. $A(a_i,a_{-i})$ is a strategy profile when a player $N_i \in N$ selects an action a_i from its action set Ai against the

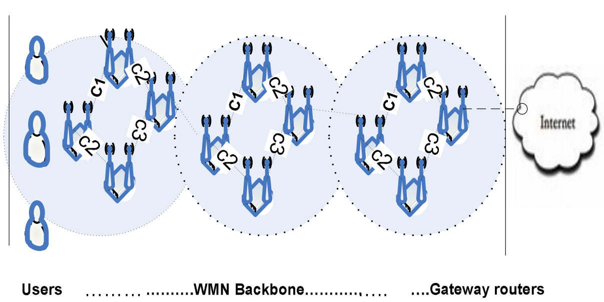

Figure 2. WMNs Components

actions of all other players N_{-i}. The notation $-i$ is a convenient way to represent a set of entities or set of events excluding a specific entity or event in a strategic setup. For example N_{-i} means set of all players excluding N_i and a_{-i} means set of actions of all players excluding action of N_i during a strategic interaction. At the end of the game, each player $N_i \in N$ gets benefit in the form of a real number (R) called outcome or payoff of the player which is determined by the utility function U_i as: $U_i=A_i \rightarrow R$.

Depending on the player's knowledge about each other's strategies, payoffs, and past histories; games can be subdivided into different categories. When players have complete information about each other's strategies and payoffs, such type of game is called a game with complete information. In games of incomplete information, players have partial or no information about each other strategies and payoffs. Games can be simultaneous or sequential depending upon the occurrence of individual players actions. When players interact with each other and take their decisions simultaneously, such games are called simultaneous move games. When the players take decision one after the other, such type of games are called sequential. When all players have information about each other past moves and actions, such type of games are called games with perfect information. All the simultaneous move games are games with imperfect information. Games where cooperation is enforced among players outside the pre-defined rules of the game are called cooperative games. In non-cooperative games, players cannot communicate with each other through some enforceable agreement other than the rules of the game [16].

In this paper, which is the extension of our previous work [1], we address end users flow game across non-cooperative multi-radio multi-channel WMNs in a selfish environment by considering and interference constrained topology. We prove analytically the existence of Nash Equilibrium (NE) under certain conditions.

The rest of our paper is organized as follows. In Section II, related research work is presented. Section III provides an introduction to our game theoretical model along with some essential concepts. In Section IV, we present our analytical results and necessary condition for the existence of Nash Equilibrium. In Section V, we discuss the convergence algorithm. In Section VI, we present our simulation results and conclude our paper in Section VII with future directions and recommendations.

II. RELATED WORK

Application of game theory to networks is not new and a huge amount of literature can be found at different layers of the protocol stack. In [17], for example, congestion control has been analyzed using game theory while [18, 19, 20] have addressed routing games. Power control games have been extensively studied in [21, 22] while Medium Access Control has been analyzed by using game theoretical analysis in [23, 24]. A detailed survey targeting the telecommunication problems using game theory can be found in [25], while game theory applications in wireless networks can be specifically found in [26].

Due to the practical importance of WMNs, considerable research efforts have been put in the designing of an intelligent MRMC technique. In [27], authors have addressed MRMC with a graph theoretic approach while A. Raniwala *et al.* [28] have presented MRMC models based on flows. The work of M. Alicherry *et al.* [29] addresses routing and channel assignment as a combined problem. Although all of the above research work have tackled MRMC from different aspects but they consider that all the nodes cooperate with each other for system wide throughput optimization and selfish behavior has been explicitly ignored.

In one of their pioneering work, Felegyhazi *et al*. [30] have proven the existence of Nash Equilibrium in a non-cooperative multi radio multi channel assignment. They have formulated channel assignment as a game where nodes, equipped with multiple radios, compete for shared multiple channels in a conflict situation and the result shows that the system converges to a stable Nash Equilibrium where each player gets equal and fair share of the channel resources. The work of Chen et *al.* [31] is an extension of [30] where perfect fairness has been provided to all players by improving the max-min fairness. Despite the interesting results, their work is limited to single collision domain while multi-hop networks like WMNs span multiple collision domains and hence all the above cited work cannot be applied to this specific scenario as discussed. In one of the recent study Gao *et al.* [32] have provided a more practical approach by extending the number of hops in the mesh backbone. They have proved that allowing coalition among players can lead to node level throughput improvement. They have provided a coalition-proof Nash Equilibrium and algorithms to reduce the computational complexity of equilibrium convergence; their solution considers cooperation among the nodes inside the coalition and hence cannot be applied to a fully non-cooperative WMNs environment. More importantly, it will be more apposite to consider end users generating flows as players of the game [31] because of their competition for the common channel resource across the wireless mesh backhaul. In such a situation, channel assignment and flow routing may be tackled simultaneously. A class of game theoretical model for routing in transportation networks has been presented by Rosenthal [33]. The author have considered *n* players in a competitive environment, each wanted to ship one unit from source to destination while minimizing its transportation cost. They have proven the existence of pure strategy Nash Equilibrium. In [34, 35], authors have provided game theoretic solutions based on end users flows to control congestion inside the communication network. Routing in general wired networks has been studied as a non-cooperative game in [36, 37, 38, 39, 40], where the conditions for the existence of Nash Equilibrium has been derived. Banner *et al.* [41] have extensively studied the non-cooperative routing problem in wireless networks based on splittable and unsplittable flows. Although, they have proven the existence of Nash Equilibrium for both classes of flow problems; their solution is not applicable to MRMC WMNs. In [14], selfish routing and channel assignment in wireless mesh networks is formulated as a Strong Transmission Game where it is assumed that selfish nodes at the user premises assign channels, in a strategic setup, to their end to end paths. While they have solved channel assignment and routing problem in a non-cooperative environment from the end users selfish prospective, the strong assumption of non-interference among channels need a large set of orthogonal frequencies which is limited by the fewer channels available in the IEEE 802.11 a/b/g/n standards [33, 34, 35, 36]. In practice, channel assignment is always an interference constrained phenomena due to the availability of fewer channels in the orthogonal frequency set of ISM band [46] and large backbone size of WMNs. In one of our recent work [1], a single stage selfish flow game was formulated in a MRMC multiple collision domain and fairness of individual nodes was investigated with the assumption of an interference free topology. In this paper, we extend our previous work by considering channel interference during game formulation. To the best of our knowledge, this is the first work in the area of competitive flow routing in a MRMC WMNs with interference constrained topology.

III. SYSTEM MODEL AND CONCEPTS

As shown in Fig. 2, mesh routers having multi radio capabilities reside in multiple collision domains. We assume that there is always a chance of channel usage conflict across the mesh backbone.

A. Network Model

We represent multi-hope WMNs spanning multiple collision domains with a Unit Disk Graph (UDG) G (V, E) [47], where the sets V and E represent mesh backhaul routers and their associated links accordingly in the graph G. We assume that each mesh router uses same transmission power as in IEEE 802.11 a/b/g/n [42, 43, 44, 45] standards. Any two mesh routers v_i and v_j can communicate with each other successfully, if the Euclidian Distance between them is less than the sum of their radii i-e for any two routers $(v_i, v_j) \in V$:

$$d(v_i, v_j) < r_{v_i} + r_{v_j} \tag{1}$$

where r_{vi} and r_{vj} are the radii of vertices v_i and v_j respectively. In other words, they are in the transmission range of each other as shown in Fig. 3 by smaller circles around the vertices. Let the interference range of a node is represented by the outer circle, whose radii is twice that of smaller circle, then two set of nodes (v_1,u_1), (v_2,u_2) cannot communicate with each other if either:

$$d(u_1,v_2)<2(r_{u1}+r_{v2}) \parallel d(v_1,v_2)<2(r_{v1}+r_{v2}) \parallel d(u_1,u_2)<2(r_{u1}+r_{u2}) \parallel d(v_1,u_2)<2(r_{v1}+r_{u2}) \tag{2}$$

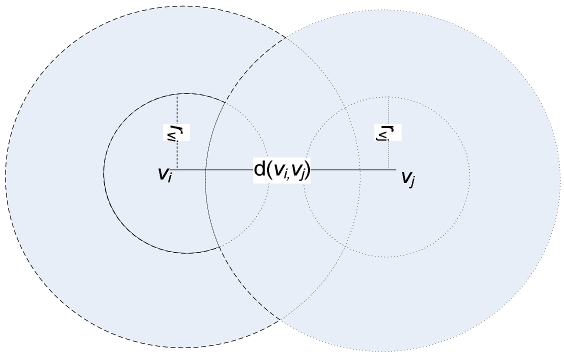

Figure 3. Transmission and Interference Range

Channel assignment to nodes links is essentially same as colouring the edges of UDG with appropriate colours such that two edges e_i, e_j belonging to any two pair of nodes (u_i,v_i), (u_j,v_j) satisfying any of the condition in (2) get distinct colours. Refer to Fig. 3, where colouring of UDG means assigning distinct colours to interfering edges. However, due to the multi-radio nature of mesh routers, interference constraint and limited available non-overlapping channels; we assume relaxation in the colouring assignment where two interfering edges can be assigned with same colour. We will discuss it in more detail in section B.

B. Game Theoritic Model

We formulate our game theoretic model by considering selfish end users as players of the game with imperfect information in non-cooperative multi-collision domain mesh network as follows. We divide the core of the mesh network in a set of multiple collision domains D={1, 2, 3,…, |d|} and the set of non-overlapping orthogonal channels, as present in IEEE 802.11a/b [33, 34, 35, 36], are represented by C={C_1,C_2,C_3,….$C_{|C|}$} as shown in Fig. 4. We refer to any channel C_i in a specific collision domain as C_{ij} where C_i∈C and $j \in$ D , respectively. The maximum achievable data rate on a channel $C_i \in$ C is represented by R_{Ci}. We assume that the maximum achievable capacity on all the channels is the same, i-e:

$$R_{Ci} = R_{Cj}\,,\ \forall\ C_i,\ C_j \in \mathrm{C} \tag{3}$$

We assume that channels set is limited according to the IEEE 802.11 a/b/g/n [31, 32, 33, 34] standards and there is a chance that a channel reused can interfere according to the condition given in (2). We define the degree of interference of a channel C_k ∈C as Φ_{Ck} , showing the number of links which have been assigned the same channel C_k in the same collision domain *j.* In the UDG, it is the number of incident edges having same colours as defined in (2).

Nodes originating flows from the user premises are the players of the game represented by a finite non-empty set $\mathrm{N} = \{N_1, N_2, N_3, \ldots .N_{|\mathrm{N}|}\}$, where N_n is any player belonging to the set N. The set of flows generated by any

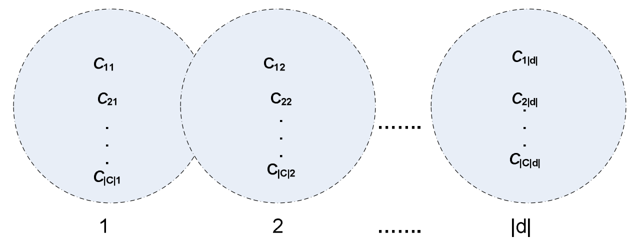

Figure 4. Channel distribution in multiple collision domains

player Nn∈ N is represented by a non-empty set f={f_1, f_2, …, $f_{|f|}$}, where f_n ∈ f represents any flow generated by player N_n∈ N. We define the strategy of a player N_n∈ N as the channel selection vector for each of its flow across the multiple collision domains. i.e,:

$$A_n = \left\{ f_{1,Ci}\,,\ f_{2,Ci}\,,\ \ldots..,\ f_{|f|,Ci} \right\} \tag{4}$$

where $f_1, f_2,\ldots f_{|f|}$ ∈ f are the flows of player N_n and C_i ∈C is the arbitrary channel in the channel set across collision domains 1, 2, …., |d| ∈D.

Accordingly, the strategy profile of all players is represented by:

$$\mathrm{A} = \left(A_1, A_2, \ldots ., A_{|\mathrm{N}|}\right)^T \tag{5}$$

The n^{th} row of the vector in (5) shows the strategy of player N_n, i-e, A_n as in (4). Each player N_n ∈ N takes a rational decision by selecting an end to end path across the core of the network towards the gateway of the mesh by maximizing its utility function. We formulate the utility function of players N_n as:

$$U_n = \sum_{f_n \in \mathrm{f}\,,C_i \in C\,,\,j=1}^{|d|} \left(\frac{1}{\Phi_{C_{ij}}} \left(\frac{f_n}{F_{ij}} \right) R_{C_{ij}} \right) \tag{6}$$

where C_{ij} denotes the channel C_i selected by player N_n ∈ N for its flow f_n ∈ f in j^{th} collision domain and F_{ij} is the total number of flows on channel C_{ij} as defined in (7). R_{Cij} is the maximum achievable data rate on channel C_i ∈C in collision domain j∈D, which is equal for all channels as in (3). We assume that all users generate CBR flows and define the parameter, F_{ij}, representing the number of flows on a specific channel, C_i∈C, in any collision domain, j∈D, as:

$$F_{ij} = \frac{Q(C_{ij})}{\tau(CBR)} \tag{7}$$

where $Q(C_{ij})$ is the queue length associated with the link which has assigned channel C_{ij} and τ (CBR) is the constant bit rate of any flow. Ideally, F_{ij} determines the number of flows or load on a specific channel. Naturally, a rational player strategy will be to select an end-to-end path having channels which are least loaded by other flows and the channels are least interfered. We define the term Φ_{Ci} as the degree of interference on a specific link to which channel C_i has been assigned. In such a selfish environment, game theory provides a realistic solution towards the stability of the system by reaching a point where no flow can move to any other channel across the whole end to end path unilaterally. This stable point is called Nash Equilibrium (NE) and is defined below [15].

A strategy profile A^* is called Nash Equilibrium if for each player $N_n \in$ N:

$$U_n\left(A_n^*, A_{-n}\right) \geq U_n\left(A_n, A_{-n}\right), \ \forall A_n \in \mathrm{A} \qquad (8)$$

where $U_n(A_n^*, A_{-n})$ is the payoff, according to the utility function defined in (6), of player N_n by selecting the strategy A_n^* against the strategies of all other players A_{-n} as in (5). In other words, in NE, everyone is playing its best response to everyone else in a game. It is the point where no player can get any benefit by unilaterally deviating from its strategy.

IV. Existence of Nash Equilibrium

To check the existence of Nash equilibrium in our proposed model, we assume two types of channels in any collision domain. Channels having maximum number of flows are represented by C_{max} and the category of channels having minimum number of flows as C_{min}. We define a parameter ℓ_{ik} which is the difference of number of flows on any two channels C_i, $C_k \in$ C within a specific collision domain $j \in$ D i-e:

$$\ell_{ik} = F_{ij\,(max)} - F_{kj\,(min)} \qquad (9)$$

where $F_{ij(max)}$ and $F_{ij(min)}$ are the number of flows on C_{max} and C_{min}, respectively.

We define another term $\psi(C_i, C_k)$, which defines the difference in degree of interference between two channels C_i, $C_k \in$C within a specific collision domain $j \in$ D as:

$$\psi_{(Ci,\, Ck)} = \Phi_{Ci} - \Phi_{Ck} \qquad (10)$$

Where Φ_{Ci} and Φ_{Ck} are the degrees of interference on channel C_i and C_k, respectively as defined in section III.

Being rational, the objective of each player is to maximize its utility by selecting an end to end path with channels having minimum number of load and minimum interference on it. We define some necessary conditions for such a selfish environment and prove the existence of Nash Equilibrium.

Lemma 1: For a MRMC multi-collision domain mesh network, for $\psi(C_i,C_k)$=0, if $\left(\frac{nf_n}{F_{ij}}\right).R_{C_{ij}} = 1 \ \forall f_n \in \mathrm{N}_n$ AND $\forall f_m \neq f_n \in \mathrm{N}_m, \left(\frac{f_m}{F_{ij}}\right).R_{C_{ij}} = 0$ with $\ell_{ik} \geq 1 \ \forall C_i \in \mathrm{C}_{\max}, C_k \in \mathrm{C}_{\min}$ for any $j \in$ D, then the strategy profile A^* is not a Nash Equilibrium.

If all the flows of any player N_n selects any channel $C_i \in C_{max}$ in any collision domain while flows of all other users N_m put their flows on $C_m \in C_{min}$, then player N_n will have an incentive to unilaterally deviate from her strategy and this can no longer be a Nash Equilibrium. As shown in Fig. 5, player N_1 selects Channel 1 for all its four flows in collision domain j. Its utility can be increased if one of the flow is transferred to other channels (C_2, C_3 or C_4).

Proof: Let α_n be the gain of player N_n deviating from its current strategy which has defined all its flows $n.f_n$ on one of channel $C_{ij} \in C_{max}$. Let F_{ij} be the total flows on $C_{ij} \in C_{max}$ and F_{kj} be the total flows on $C_{kj} \in C_{min}$.

then:

$\alpha_n = U_n' - U_n$, where U_n' is the new payoff of player N_n after deviating from its current strategy.

Let $\theta \in N_n$ is one of the flow, which player N_n redirect to another channel $C_k \in C_{min}$ in any collision domain $j \in$D and calculate the benefit of change along the path as follows.

$$\alpha_n = \sum_{f_n \in \mathrm{f},\, C_i \in \mathrm{C},\, j=1}^{|j-1|} \left(\frac{1}{\Phi_{C_{ij}}}\left(\frac{f_n}{F_{ij}}\right) R_{C_{ij}}\right) + \left(\frac{1}{\Phi_{C_{ij}}} . \frac{(n-\theta) f_n}{(F_{ij}-\theta) f_n}\right) R_{C_{ij}}$$

$$+ \left(\frac{1}{\Phi_{C_{kj}}} . \frac{\theta f_n}{(F_{kj}+\theta)}\right) R_{C_{kj}} - \left(\frac{1}{\Phi_{C_{ij}}} . \frac{n f_n}{F_{ij}}\right) R_{C_{ij}}$$

$$+ \sum_{f_n \in \mathrm{f},\, C_i \in \mathrm{C},\, j=j+1}^{|d|} \frac{1}{\Phi_{C_{ij}}}\left(\frac{f_n}{F_{ij}}\right) R_{C_{ij}}$$

(11)

By considering only $j \in$D collision domain:

$$= \frac{1}{\Phi_{C_{ij}}} . \left(\frac{(n-\theta) f_n}{\left(F_{ij}-\theta\right)}\right) R_{C_{ij}} + \frac{1}{\Phi_{C_{kj}}} . \left(\frac{\theta f_n}{\left(F_{kj}+\theta\right)}\right) R_{C_{kj}}$$

$$- \frac{1}{\Phi_{C_{ij}}} . \left(\frac{n f_n}{F_{ij}}\right) R_{C_{ij}}$$

Since R_{Cij}=R_{Ckj}, $F_{kj}+\theta$=F_{ij} and $\Phi_{Cij} = \Phi_{Ckj}$ as $\psi(C_i,C_k)$=0,

Therefore:

$$= \frac{1}{\Phi_{C_{ij}}}\left[\left(\frac{(n-\theta) f_n}{\left(F_{ij}-\theta\right)}\right) R_{C_{ij}} + \left(\frac{\theta f_n}{F_{ij}}\right) R_{C_{ij}} - \left(\frac{n f_n}{F_{ij}}\right) R_{C_{ij}}\right]$$

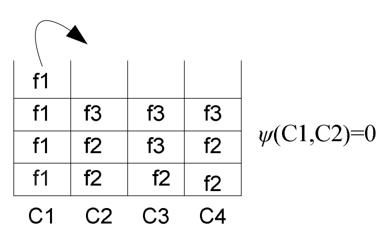

Figure 5. Example of homogenous flows on one channel

After simplification:

$$\alpha_n = \frac{1}{\Phi_{C_{ij}}}\left[\left(\frac{\theta f_n(n-\theta}{F_{ij}(F_{ij}-\theta)}\right)R_{C_{ij}}\right] \qquad (12)$$

> 0 as $(n-\theta)$ and (F_{ij}- θ) are positive.

Hence the strategy profile A* cannot be a Nash Equilibrium.

Lemma 2: In a MRMC multiple-collision domain mesh network, for $\psi(C_i,C_k)$=0, in any collision domain j ∈D along the end to end path of flows, if ℓ_{ik}>1for any $C_i \in C_{max}, C_k \in C_{min}$ then the strategy profile A* is not a Nash Equilibrium.

Let ℓ_{ik}>1in any collision domain j ∈D along the end to end path of flows then it essentially means that there exists a channel $C_{kj} \in C_{min}$ in j ∈D for which $\frac{Q(Cij)}{\tau\,(CBR)} - \frac{Q(C_{kj})}{\tau\,(CBR)} > 1$, and hence at least one of the flow $f_n \in N_n$ on $C_{ij} \in C_{max}$ has incentive to change for her benefit. As shown in Fig. 6, N_2 can unilaterally switch one of its flows to C_1, C_2 or C_4.

Proof: Let a user N_n changes its flow, f_n, from $C_{ij} \in C_{max}$ to $C_{kj} \in C_{min}$ in j∈D collision domain along the end to end path. The gain of change is calculated as follows:

$$\alpha_n = \sum_{f_n\in f,\, Ci\in C,\, j=1}^{|j-1|}\left(\frac{1}{\Phi_{C_{ij}}}.\left(\frac{f_n}{F_{ij}}\right)R_{C_{ij}}\right)+\frac{1}{\Phi_{C_{kj}}}.\left(\frac{f_n}{\frac{Q(C_{kj})}{\tau(CBR)}+1}\right)R_{C_{kj}}$$

$$-\frac{1}{\Phi_{C_{ij}}}\left(\frac{f_n}{\frac{Q(C_{ij})}{\tau(CBR)}}\right)R_{C_{ij}}+\sum_{f_n\in f,\, Ci\in C,\, j=j+1}^{|d|}\frac{1}{\Phi_{C_{ij}}}\left(\frac{f_n}{F_{ij}}\right)R_{C_{ij}} \qquad (13)$$

By considering the j^{th} collision domain only, the first and last summation terms become irrelevant and hence by simplification, we get:

$$= \frac{1}{\phi Ckj}\left(\frac{f_n}{\left(\frac{Q(Ckj)}{\tau\,(CBR)}+1\right)}\right)RC_{kj} - \frac{1}{\phi Cij}\left(\frac{f_n}{\frac{Q(Cij)}{\tau\,(CBR)}}\right)R_{C_{ij}}$$

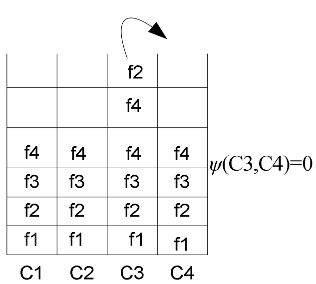

Figure 6. Flow distribution on channels where ℓ>1

Since $\Phi_{Cij} = \Phi_{Ckj}$ as $\psi(C_i,C_k)$=0, therefore:

$$= \frac{1}{\phi Cij}\left[\left(\frac{f_n}{\left(\frac{Q(Ckj)}{\tau\,(CBR)}+1\right)}\right)R_{C_{kj}} - \left(\frac{f_n}{\frac{Q(Ckj)}{\tau\,(CBR)}+\ell}\right)R_{C_{kj}}\right]$$

$$\alpha_n = \frac{1}{\phi Cij}\left[\left(\frac{\ell*\ \tau\,(\mathrm{CBR})-\tau\,(\mathrm{CBR})}{\tau(Ckj)+\tau(\mathrm{CBR})*(\tau(Ckj)+\ell*\tau(\mathrm{CBR}))}\right)f_nR_{C_{kj}}\right] \qquad (14)$$

>0, as ℓ>1

Since player N_n has an incentive to change from its current strategy to the new one, and hence the current strategy profile A* cannot be a Nash Equilibrium.

Lemma 3: In a MRMC Multiple-Collision domain mesh network, for $\psi(C_i,C_k)$=0, for any player N_n if $\forall f_nC_{ij}$-$\forall f_nC_{kj}$>2 and ℓ_{ik}≥1 in any collision domain j ∈D, $\forall C_{ij} \in C_{max}$, $\forall C_{kj} \in C_{min}$, then the strategy profile A* is not a Nash Equilibrium.

As shown in Fig. 7, difference of flows of N_2 on C_2 and C_3>2, although it does not deviate from lemma2, player N_2 has incentive to switch one of its flow from C_2 to C_3.

Proof: Let θ_1, $\theta_2 \in N_n$ are the number of flows of player N_n on C_{max} and C_{min} respectively. We define $\Delta\theta_{1,2} = \theta_1 - \theta_2$ as the flow difference of any player on two *max*, *min* channels. Let N_n redirects one of its flow from C_{max} to C_{min} in any collision domain j ∈D along the end to end path. Then the gain of change is given by:

$$\alpha_n = \sum_{f_n\in f,\, Ci\in C,\, j=1}^{|j-1|}\frac{1}{\Phi_{C_{ij}}}.\left(\left(\frac{f_n}{F_{ij}}\right)R_{C_{ij}}\right)+\frac{1}{\Phi_{C_{ij}}}.\left(\frac{(\theta_1-1)f_n}{(F_{ij}-1)}\right)R_{C_{ij}}$$

$$+\frac{1}{\Phi_{C_{kj}}}\left(\frac{(\theta_2+1)f_n}{(F_{kj}+1)}\right)R_{C_{kj}}-\frac{1}{\Phi_{C_{ij}}}\left(\frac{\theta_1 f_n}{F_{ij}}\right)R_{C_{ij}}-\frac{1}{\Phi_{C_{kj}}}\left(\frac{\theta_2 f_n}{F_{kj}}\right)R_{C_{kj}}$$

$$+\sum_{f_n\in f,\, Ci\in C,\, j=j+1}^{|d|}\frac{1}{\Phi_{C_{ij}}}\left(\frac{f_n}{F_{ij}}\right)R_{C_{ij}} \qquad (15)$$

We suppose the change of end to end path for N_n accurse in the j^{th} collision domain only and hence by eliminating the first and last summation terms. Since $F_{kj}=F_{ij}- \ell$ before flow switch from C_{ij} to C_{kj} and $F_{kj}+1=F_{ij}$ after flow switch by assuming $\ell = 1$, by substituting appropriate terms:

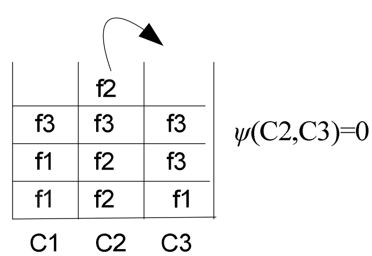

Figure 7. Homogenous flows difference on two channels>2

$$\alpha_n = \frac{1}{\Phi_{C_{ij}}}\left(\frac{(\theta_1-1)f_n}{\left(F_{ij}-1\right)}\right)R_{Cij} - \frac{1}{\Phi_{C_{ij}}}\left(\frac{\theta_1 f_n}{F_{ij}}\right)R_{Cij}$$
$$+\frac{1}{\Phi_{C_{ij}}}\left(\frac{(\theta_2+1)f_n}{F_{ij}}\right)R_{Cij} - \frac{1}{\Phi_{C_{ij}}}\left(\frac{\theta_2 f_n}{\left(F_{ij}-\ell\right)}\right)R_{Cij}$$

Since $\phi C_{ij}=\phi C_{kj}$ as $\psi(C_i,C_k)=0$ and by further simplification:

$$\alpha_n = \frac{1}{\Phi_{C_{ij}}}\left(\frac{\theta_1-(\theta_2+1)f_n}{F_{ij}\left(F_{ij}-1\right)}\right)R_{Cij} \tag{16}$$

The term $\theta_1-(\theta_2+1)$ and $F_{ij}-1>0$ as $\Delta\theta_{1,2}>2$ $\therefore$ $\alpha_n>0$ and A^* cannot be a Nash Equilibrium under such condition.

Lemma 4: In a MRMC Multiple-Collision domain mesh network, for $\psi(C_i,C_k)\geq 1$, for any player N_n if $\forall f_n C_{ij}-\forall f_n C_{kj}=1$ and $\ell_{ik}\geq 1$ in any collision domain $j\in D$, $\forall C_{ij}\in C_{max}$, $\forall C_{kj}\in C_{min}$, then the strategy profile A^* is not a Nash Equilibrium.

As shown in Fig. 8, difference of flows of N_2 on C_2 and $C_3>2$, although it does not deviate from lemma 2, player N_2 has incentive to switch one of its flow from C_2 to C_3.

Proof: The proof of this lemma is straightforward. Let $f_n\in$ f be the only flow of player $N_n\in$ N on C_{max}. It essentially means that there are no flows defined by player N_n on channel C_{min} in any collision domain $j\in$D along the end to end path. The gain of change is given by:

$$\alpha_n = \sum_{f_n\in \mathrm{f},\, Ci\in \mathrm{C},\, j=1}^{|j-1|} \frac{1}{\Phi_{C_{ij}}}.\left(\left(\frac{f_n}{F_{ij}}\right)R_{C_{ij}}\right) + \frac{1}{\Phi_{C_{kj}}}.\left(\frac{f_n}{\left(F_{ij}+1\right)}\right)R_{C_{kj}}$$
$$-\frac{1}{\Phi_{C_{ij}}}\left(\frac{f_n}{F_{ij}}\right)R_{C_{kj}} + \sum_{f_n\in \mathrm{f},\, Ci\in \mathrm{C},\, j=j+1}^{|d|} \frac{1}{\Phi_{C_{ij}}}\left(\frac{f_n}{F_{ij}}\right)R_{C_{ij}} \tag{17}$$

We suppose the change of end to end path for N_n accurse in the j^{th} collision domain only and hence by eliminating the first and last summation terms.

$$=\frac{1}{\Phi_{C_{kj}}}\left(\frac{f_n}{F_{kj}+1}\right)R_{C_{kj}} - \frac{1}{\Phi_{C_{ij}}}\left(\frac{f_n}{F_{ij}}\right)R_{C_{ij}}$$

Since $F_{kj}+1\leq F_{ij}$ and $R_{Cij}=R_{Ckj}$, by substituting the appropriate terms and further simplification:

$$=\frac{1}{\Phi_{C_{kj}}}\left(\frac{f_n}{F_{ij}}\right)R_{C_{ij}} - \frac{1}{\Phi_{C_{ij}}}\left(\frac{f_n}{F_{ij}}\right)R_{C_{ij}}$$
$$=\left(\frac{\Phi_{C_{ij}}-\Phi_{C_{kj}}}{\Phi_{C_{kj}}.\Phi_{C_{ij}}}\right)\left(\frac{f_n}{F_{ij}}\right)R_{C_{ij}}$$
$$\alpha_n = \left(\frac{\psi(C_{ij},C_{kj})}{\Phi_{C_{kj}}.\Phi_{C_{ij}}}\right)\left(\frac{f_n}{F_{ij}}\right)R_{C_{ij}} \tag{18}$$

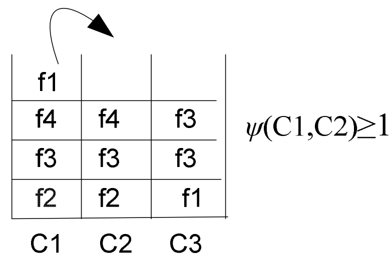

Figure 8. An interfarence difference

Here we only consider the case $F_{kj}+1==F_{ij}$ for simplicity, we can prove that $F_{kj}+1<F_{ij}$ have the same results.

The term $\psi(C_{ij},C_{kj})\geq 1$, therefore:
$\alpha_n>0$ and A^* cannot be a Nash Equilibrium under such a condition.

Proof of NE existence: In a MRMC Multiple-Collision domain mesh network, if $\ell<=1$ for all $j\in$D and Lemma 1 and 3 do not hold then the strategy profile A^* is a Nash Equilibrium. From (14) of lemma 2, let $\ell=1$ and we assume that lemma1 and 3 do not hold, then:

$$\alpha_n = \left(\frac{\tau(CBR)-\tau(CBR)}{\left(Q(C_{kj})+\tau(CBR)\right)*\left(Q(C_{kj})+\ell*\tau(CBR)\right)}\right)f_n.R_{Ckj}=0 \tag{19}$$

Also for $\ell=0$:

$$\alpha_n = \left(\frac{-\tau(CBR)}{\left(Q(C_{kj})+\tau(CBR)\right)*\left(Q(C_{kj})\right)}\right)f_n.R_{Ckj}<0 \tag{20}$$

Also from (18) of lemma4, let $\psi(C_{ij},C_{kj})\geq 1$:

$$\alpha_n = \left(\frac{-\psi(C_{ij},C_{kj})}{\Phi_{C_{kj}}.\Phi_{C_{ij}}}\right)\left(\frac{f_n}{F_{ij}}\right)R_{C_{ij}}<0 \tag{21}$$

Both the negative sign and zero result show that each player has no incentive to deviate from its current strategy and hence the current strategy profile is a Nash Equilibrium.

Theorem 1: A strategy profile A^* is Nash Equilibrium, if:

1) $\forall f_n\in N_n, \left(\frac{nf_n}{F_{ij}}\right)RC_{max}<1, \exists\left(\frac{f_m}{F_{ij}}\right)R_{C_{max}}>0\ for\ \ell\geq 1, \forall j, \forall C_{max}, C_{min}, \psi(C_{max},C_{min})=0$
2) $\forall C_{max}, C_{min}, 1\geq\ell\geq 0, \forall j\in D, \psi(C_{max},C_{min})=0$
3) $\Delta\theta_{C_{max},C_{min}}\leq 2$ for $\ell\geq 1, \forall f_n\in N_n, \forall N_n\in$ N $, \forall j\in D, \psi(C_{max},C_{min})=0$
4) $\psi(C_{max},C_{min})<1, \forall C_{max},C_{min}, if\ \ell\geq 1,\ if\ \theta 1 f_n-\theta 2 f_n\geq 1$ for θ_1 on C_{max}, θ_2 on C_{min} for any player $N_n\in$ N.

V. Convergence to Nash Equilibrium

In the previous section, we have proven that NE exists in a multi-radio multi-channel flow game with interference constraint in a non-cooperative environment. In this section we present a distributed algorithm running on each end node with imperfect information. As shown in Fig. 9, each player has information about each channel usage inside all collision domains but no player knows the strategy of her opponent players, thus a game of imperfect information.

Using Algorithm 1, each player $N_n \in \mathrm{N}$ selects channels for all its flows $f_n \in \mathrm{f}$ in each collision domain across the end to end path in a distributed manner. Lines 5, 9, 13 and 17 of the algorithm are sufficient conditions where it converges and ends up with an NE. Furthermore, each node keeps a record of its channel usage, $C_{ij}\_f_{nCount}$, in each collision domain for a necessary check at lines 9 and 14. Players in this game move simultaneously without having information about other players past histories. With this imperfect information, the game converges to stable NE in a non-cooperative environment.

Algorithm 1: Nash Equilibrium in MRMC multiple-collision domain game with interference constraint.

1. for each $N_n \in \mathrm{N}$
2.   for each $f_n \in \mathrm{f}$ (do)
3.   for j=1 to |d|
4.   for i=1 to $C_{|c|}$
5.   if $Q(C_{ij}) \leq Q(C_{min(j)})$ & $\phi_{Cij} \leq \phi_{Cmin(j)}$
6.   Select channel C_i for flow f_n
7. $C_{ij}\_f_{nCount}$=$C_{ij}\_f_{nCount}$+1
8.   exit;
9.   elseif$(C_{ij}_f_{nCount}$ - $C_{(rem)}\_f_{nCount}) \leq 2$ & $(\frac{nf_n}{F_{ij}})R_{Cij} \neq 1$ & C_{ij}-$C_{(rem)j} \leq 1$
10.   Select channel C_i for flow f_n
11. $C_{ij}\_f_{n\mathrm{Count}}$= $C_{ij}\_f_{n\mathrm{Count}}$ +1
12.   exit;
13.   elseif$(Q(C_{rem(j)})$-$Q(C_{ij}) \geq 1$ & $\psi(C_{rem(j)}, C_{ij}) \geq 1$
14.   Select channel C_i for flow f_n
15. $C_{ij}\_f_{n\mathrm{Count}}$= $C_{ij}\_f_{n\mathrm{Count}}$ +1
16.   exit;
17.   else
18.   next i
19.   next j
20.   while(f_n)

Figure 9. Algorithm for Nash Equilibrium convergence using imperfect information

VI. Performance Evaluation

In this section, we evaluate our proposed algorithm and show its results in terms of individual fairness and price of anarchy. In the second subsection, we investigate and compare the throughput difference of our scheme with a random channel selection scheme by varying the number of players. All the experiments were conducted in MATLAB to test the performance and effectiveness of the proposed scheme.

A. Price of Anarchy and Individual Fairness

In this subsection, we investigate the Individual fairness of end user nodes and Price of Anarchy (*PoA*). We formulate the *PoA* as the ratio of throughput achieved by individual players in case of worst NE and best NE i-e

$$PoA = \frac{\Gamma_n(NE_{worst})}{\Gamma_n(NE_{best})}, n = 1, 2..., N_{|N|} \tag{22}$$

where Γ_n is the end-to-end throughput of player $N_n \in \mathrm{N}$.

In the simulation, 40 nodes are deployed randomly in a rectangular area of 600X600 units. The transmission range is considered 50 units and interference range is taken as twice of the transmission range. We configure 12 nodes on the left hand side of topology as players of the game. At the right hand side of the topology, 3 nodes are configured as the gateways. Each node generates 10 CBR flows of 64Kbps during each run of the game. Simulation was carried out by considering IEEE 802.11a [31], where 8 non-overlapping channels were selected for parameter C across 5 collision domains. Each node is configured with two radios, each for transmission and reception. All players move simultaneously having no information of one another past histories. With this imperfect information, we investigate the performance of the proposed scheme in terms of *PoA*. Since multiple NEs exist for this game, the mechanism for selecting the best NE by players is beyond the scope of this paper. We aim to solve this problem in a separate study. As shown in Fig. 10, the *PoA* is in the range of 0.71 and 1 for all the players. This shows a very strong indication that the individual throughput is not degraded even if the system converges to a worst NE.

Fairness among players was measured at the end of the game. As shown in Fig. 11, individual players achieve end to end data rate with a standard deviation of 2.19Mbps, with imperfect information, at the end of the game. This shows that using our algorithm, players achieve fair end to end data rate across multiple collision domains when game converges to NE. The reason is that when the game ends up with NE, each player is playing its best response as its strategy to every other player of the game and hence has no incentive to deviate individually from its current strategy. We carried out simulation by considering the same set of parameters, where nodes deviate from the proposed algorithm with selfish behavior. As shown in Fig. 12, although some nodes perform better comparatively to our scheme by achieving high end to end throughput; the standard deviation is

3.74Mbps. This shows that some of the selfish nodes get access to less interfered channels while leaving the crowded channels for others. This selfish behavior leads to individual unfairness of the system as compared to the proposed scheme.

B. Standard Deviation and Max-Min throughput Difference

In second scenario, 100 nodes are deployed in a rectangular area of 1000X1000 units. The transmission range is taken 25 units and the interference range as twice of the transmission range. Variance among players throughputs was measured by varying the set of players, N, from 5 to 40 in 5 steps. Since the previous work done in this area is either on selfish routing in wired networks or in wireless networks without considering multiple radio multiple channels in the core network. Therefore, we compared our proposed scheme with random channel selection where flows select channels across multiple collision domains arbitrarily. Fig. 13 compares max-min throughput difference by using our scheme with random channel selection. Max-min throughput difference is the difference between the flow which gets maximum throughput and flow that gets minimum throughput, as in Chen *et al.* [31]. It can be observed that our scheme outperforms random channel selection for each set of players by having minimum max-min throughput difference. The max-min difference is higher for both systems at beginning but as the number of players increases max-min throughput difference of our proposed system either decreases or remains constant when the game ends up with NE. This shows the stability of our scheme at NE. The max-min throughput difference for random selection does not remain stable with varying number of players, as shown in Fig. 8. This is because some of the selfish end nodes, being rational, select less crowded channels across multiple collision domains and thus increase their end to end throughput while leaving more crowded channels for other nodes.

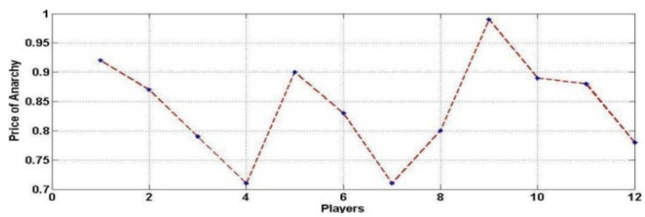

Figure 10. Price of Anarchy with D=5,C=8, N=12, f=10 and CBR=64Kbps

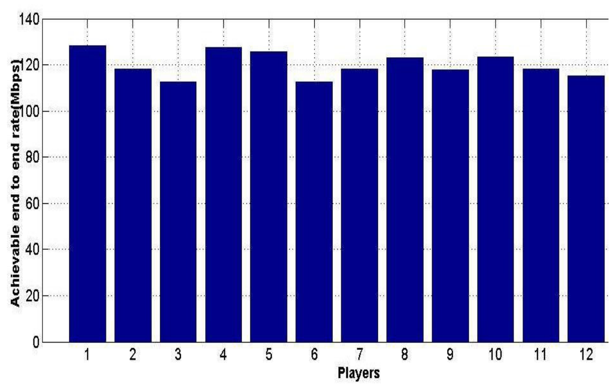

Figure 11. Total End to End rate of individual players with imperfect information with D=5,C=8, N=12, f=10 and CBR=64Kbps

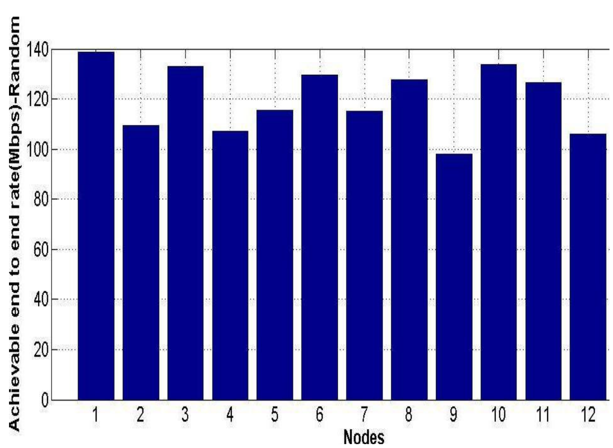

Figure 12. Total End to End rate of individual players with imperfect information with D=5,C=8, N=12, f=10 and CBR=64Kbps

Fig. 14 shows the standard deviation comparison of players throughputs in our proposed scheme against that of random selection. The values for collision domains (D), Channels (C), number of flows per node and CBR were kept same in both schemes while number of players/nodes was varied from 5 to 40 in step 5. Results in Fig. 14 suggest that our proposed scheme always performed better than random selection irrespective of the number of players. When number of nodes is low, some selfish players have always incentive to select less crowded channels across multiple collision domains and hence variance among players throughputs is high leading to high standard deviation. With increase in number of players, our proposed system shows a constant and predictable decrease in standard deviation while random selection scheme is unpredictable. This means that our proposed system achieves good fairness in long run when the system converges to NE.

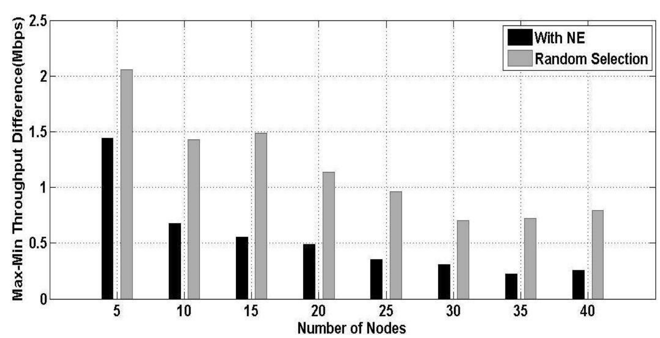

Figure 13. Max-Min Throughput Difference by varying number of players with imperfect information. D=5,C=8,N=5:5:40, f=10,CBR=64Kbps

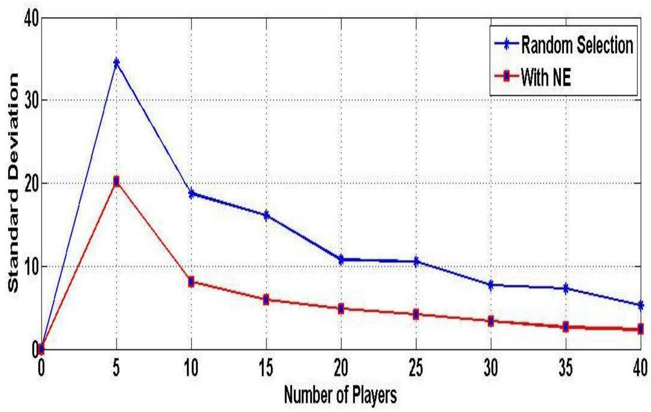

Figure 14. Standard Deviation among players throughput with D=5,C=8,N=5:5:40, f=10,CBR=64Kbps

VII. CONCLUSION

In this paper, we have developed a multiple-collision domain MRMC game theoretic model based on end user flows in a non-cooperative environment. An interference constrained topology was considered due to the limited available orthogonal channels. Our analytical results have proven that Nash Equilibrium exists with proposed necessary conditions in a game of imperfect information. Based on a distributed algorithm, our game theoretic model converges to stable state in finite time and all channels are perfectly load-balanced at the end of the game. Simulation results show that standard deviation of players throughputs is less than that of random channel selection scheme in long run. Furthermore, the Price of Anarchy of the system is close to one showing the efficiency of the proposed scheme.

We have considered single stage static game where players move simultaneously and once NE is established there is no incentive for any player to deviate from its current strategy, individually.

The work done in this paper can be extended to incorporate routing along with channel assignment in a non-cooperative environment by considering co-channel interference in the game formulation. It can be an interesting future research direction to investigate the effect of the coalition of flows on the overall fairness of players in repeated games.

In future, we are working to extend our proposed model to investigate the different mechanisms for selecting the best NE among the players. Further, we are working on coalition resistance game theoretic models for joint selfish routing and MRMC in multi-collision domain WMNs in an interference constraint non-cooperative environment.

REFERENCES

[1] I. Shah, S. Jan, and K-K. Loo, "Selfish Flow Games in Non-cooperative Multi-radio Multi-channel Wireless Mesh Networks with Imperfect Information", 6th International Conference on Wireless and Mobile Communications(ICWMC), Valencia , Spain, pp. 219-225, 2010

[2] L. Santhanam, B. Xie, and D. Agrawal, "Selfishness in mesh networks: wired multihop MANETs," IEEE Wireless Communications, vol. 15, pp. 16-23, 2008.

[3] S. Basagni, M. Conti, S. Giordano, and I. Stojmenović, Mobile Ad Hoc Networking. Wiley-IEEE Press, 2004.

[4] P. Michiardi and R. Molva, "A game theoretical approach to evaluate cooperation enforcement mechanisms in mobile ad hoc networks," in Modeling and Optimization in Mobile, Ad Hoc and Wireless Networks (WiOpt), Sophia Antipolis , France , pp. 3-5, 2003.

[5] I. F. Akyildiz, X. Wang, and W. Wang, "Wireless mesh networks: a survey," Computer Networks, vol. 47, pp. 445-487, 2005.

[6] R. Bruno, M. Conti, and E. Gregori, "Mesh networks: commodity multihop ad hoc networks," IEEE Communications Magazine, vol. 43, pp. 123-131, 2005.

[7] S. Roch, "Nortel's Wireless Mesh Network solution: Pushing the boundaries of traditional WLAN technology," Nortel Technical Journal, vol. 2, 2005.

[8] S. Cass, "Viva mesh vegas," IEEE Spectrum, vol. 42, pp. 48-53, 2005.

[9] http://www.tropos.com/index1.php , last accessed: 14/06/2011.

[10] H. Skalli, S. Ghosh, S. Das, L. Lenzini, and M. Conti, "Channel assignment strategies for multiradio wireless mesh networks: issues and solutions," IEEE Communications Magazine, vol. 45, pp. 86-95, 2007.

[11] W. Z. Wang and X. Y. Li, "Truthful low-cost unicast in selfish wireless networks" in 18th International Parallel and Distributed Processing Symposium, Santa Fe, New Mexico, pp. 219-226, 2004.

[12] L. Anderegg and S. Eidenbenz, "Ad hoc-VCG: A truthful and cost-efficient routing protocol for mobile ad hoc networks with selfish agents," Proceedings of the 9th Annual International Conference on Mobile Computing and Networking,, San Diego, California, pp. 245-259, 2003.

[13] S. Zhong, L. E. Li, Y. G. Liu, and Y. R. Yang, "On designing incentive-compatible routing and forwarding protocols in wireless ad-hoc networks: an integrated approach using game theoretic and cryptographic techniques," Wireless Networks, vol. 13, pp. 799-816, 2007.

[14] J. Xiao, N. Xiong, L. T. Yang, and Y. He, "A joint selfish routing and channel assignment game in wireless mesh networks," Comput. Commun., vol. 31, pp. 1447-1459, 2008.

[15] M. J. Osborne and A. Rubinstein, A Course in Game Theory. The MIT press, 1994.

[16] M. Sáiz, Game Theory at Work: OR Models and Algorithms to Solve Multi-Actor Heterogeneous Decision Problems PhD thesis, 2007 - library.wur.nl.

[17] T. Alpcan and T. Basar, "A game-theoretic framework for congestion control in general topology networks (I)," IEEE Conference On Decision and Control, Maui, USA, pp. 1218-1224, 2002.

[18] A. A. Economides and J. A. Silvester, "A game theory approach to cooperative and non-cooperative routing problems," in Proc. IEEE International Telecommunications Symposium, pp. 597-601.

[19] A. Blum, E. Even-Dar, and K. Ligett, "Routing without regret: On convergence to Nash equilibria of regret-minimizing algorithms in routing games," in Proceedings of the Twenty-Fifth Annual ACM Symposium on Principles of Distributed Computing, Denver, Colorado, USA , pp. 45 – 52, 2006.

[20] D. Fotakis, S. Kontogiannis, E. Koutsoupias, M. Mavronicolas, and P. Spirakis, "The structure and complexity of Nash equilibria for a selfish routing game," Automata, Languages and Programming, pp. 785-785.

[21] C. U. Saraydar, N. B. Mandayam, and D. J. Goodman, "Efficient power control via pricing in wireless data networks," IEEE Trans. Commun., vol. 50, pp. 291-303, 2002.

[22] C. W. Sung and W. S. Wong, "A noncooperative power control game for multirate CDMA data networks," IEEE Transactions on Wireless Communications, vol. 2, pp. 186-194, 2003.

[23] Cui, L. Chen and S. Low, "A game-theoretic framework for medium access control," Selected Areas in Communications, IEEE Journal on, vol. 26, pp. 1116-1127, 2008.

[24] L. Chen, S. H. Low, and J. C. Doyle, "Random access game and medium access control design," IEEE/ACM Transactions on Networking, , vol. 18, pp. 1303-1316, 2010.

[25] E. Altman, T. Boulogne, R. El-Azouzi, T. Jimenez, and L. Wynter, "A survey on networking games in telecommunications," Comput. Oper. Res., vol. 33, pp. 286-311, 2006.

[26] M. Felegyhazi and J. P. Hubaux, "Game theory in wireless networks: A tutorial," Submitted to ACM Computing Surveys, 2006.

[27] K. Marina, S. R. Das, and A. P. Subramanian, "A topology control approach for utilizing multiple channels in multi-radio wireless mesh networks," Computer Networks, vol. 54, pp. 241-256, 2010.

[28] A. Raniwala and T. Chiueh, "Architecture and algorithms for an IEEE 802.11-based multi-channel wireless mesh network," in Proceedings IEEE INFOCOM 2005. 24th Annual Joint Conference of the IEEE Computer and Communications Societies, Miami USA, pp. 2223-2234, 2005.

[29] M. Alicherry, R. Bhatia, and L. E. Li, "Joint channel assignment and routing for throughput optimization in multi-radio wireless mesh networks," in Proceedings of the 11th Annual International Conference on Mobile Computing and Networking, Cologne, Germany , pp. 58 - 72 . 2005.

[30] M. Felegyhazi, M. Cagalj, S. Bidokhti, J. P. Hubaux, and L. EPFL, "Non-cooperative multi-radio channel allocation in wireless networks," in IEEE INFOCOM 2007. 26th IEEE International Conference on Computer Communications, Alaska, USA, pp. 1442-1450, 2007.

[31] T. Chen and S. Zhong, "Perfectly fair channel assignment in non-cooperative multi-radio multi-channel wireless networks," Comput. Commun., vol. 32, pp. 1058-1061, 2009.

[32] L. Gao and X. Wang, "A game approach for multi-channel allocation in multi-hop wireless networks," in Proceedings of the 9th ACM International Symposium on Mobile Ad Hoc Networking and Computing, Hong Kong, China, pp. 303-312, 2008.

[33] R. W. Rosenthal, "A class of games possessing pure-strategy Nash equilibria," International Journal of Game Theory, vol. 2, pp. 65-67, 1973.

[34] E. Altman, "Flow control using the theory of zero sum Markov games," IEEE Transactions on Automatic Control, vol. 39, no. 4, pp. 814-818, 1994.

[35] Y. A. Korilis and A. A. Lazar, "On the existence of equilibria in noncooperative optimal flow control," Journal of the ACM (JACM), vol. 42, pp. 584-613, 1995.

[36] R. J. La and V. Anantharam, "Optimal routing control: Repeated game approach," IEEE Transactions on Automatic Control, vol. 47, pp. 437-450, 2002.

[37] A. Orda, R. Rom and N. Shimkin, "Competitive routing in multiuser communication networks," IEEE/ACM Transactions on Networking (ToN), vol. 1, pp. 510-521, 1993.

[38] H. Kameda, "How harmful the paradox can be in the Braess/Cohen-kelly-jeffries networks," in Proc INFOCOM., pp. 437-445, 2002.

[39] E. Altman, T. Basar, T. Jimenez, and N. Shimkin, "Competitive routing in networks with polynomial costs," IEEE Transactions on Automatic Control, vol. 47, pp. 92-96, 2002.

[40] T. Roughgarden and É. Tardos, "How bad is selfish routing?" Journal of the ACM (JACM), vol. 49, pp. 236-259, 2002.

[41] R. Banner and A. Orda, "Bottleneck routing games in communication networks," IEEE Journal on Selected Areas in Communications, vol. 25, pp. 1173-1179, 2007.

[42] “IEEE 802.11a Standard”; standards.ieee.org/, last accessed: 14/06/2011

[43] “IEEE 802.11b Standard”; standards.ieee.org/, last accessed: 14/06/2011

[44] “IEEE 802.11g Standard”; standards.ieee.org/, last accessed: 14/06/2011

[45] “IEEE 802.11n Standard”; standards.ieee.org/, last accessed: 14/06/2011

[46] M. Biggs, A. Henley, and T. Clarkson, "Occupancy analysis of the 2.4 GHz ISM band," IEE Proceedings Communications, vol. 153, issue 6 , pp. 481-488, 2004.

[47] B. N. Clark, S. Colbourn David and J. Charles, "Unit disk graphs," Discrete Mathematics, vol. 86, pp. 165-177, 1990.

Extended Mobile WiMAX Signal Transmission over RoF viaTriple Symmetrical Dispersion System SMF, DCF and CFBG

Mazin Al-Noor, Jonathan Loo, Richard Comley
School of Engineering and Information Sciences,
Middlesex University, Hendon, NW4 4BT
LONDON, UK
M.Al-Noor@mdx.ac.uk, J.Loo@mdx.ac.uk, R.Comley@mdx.ac.uk

Abstract— **The main impediments for long distance signal transmission in the fibre optic system, especially the radio over fibre (RoF) system, are the chromatic dispersion and signal power attenuation. Additionally, the power consumption in the laser diode and optical amplifiers affect the signal transmission costs; however, it is lower than in a wireless system. Therefore, decreasing the power consumption and chromatic dispersion and increasing the data bit rate in RoF are the demands for present and future fibre optic system technology. In order to increase the signal transmission distance and improve the frequency spectrum, we study in this paper a mobile Worldwide Interoperability for Microwave Access (WiMAX) signal transmission over RoF via a triple symmetrical dispersion system. The combination of three different fibres - single mode fibre (SMF), dispersion compensating fibre (DCF) and chirped fibre Bragg grating (CFBG) - is used to transmit a 120Mbps mobile WiMAX scalable Orthogonal Frequency Division Multiple Access (OFDMA) signal with 3.5GHz carrier frequency and 20MHz bandwidth over a RoF system. To compensate the dispersion, the SMF and DCF are employed and specifically the high reflector CFBG is applied to reduce signal power loss. In our study, the WIMAX signal is transmitted through a triple symmetrical dispersion system consisting of 2xDCF (20 km) and 2xSMF (100 km) connected to SMF (24 km) and CFBG. Simulation results clearly indicate that the limited signal transmission length and data bit rate in the RoF system, caused by fibre attenuation and chromatic dispersion, can be overcome by the combination of SMF, DCF and CFBG. The transmission distance in the fibre is extended to 792 Km, SNR and OSNR are highly satisfactory; simultaneously the power consumption is decreased.**

Keywords- Worldwide Interoperability for Microwave Access (WiMAX); Radio over Fibre (RoF); Dispersion Compensating Fibre (DCF); Chirped Fibre Bragg Grating (CFBG); Single Mode Fibre (SMF).

I. INTRODUCTION

The communication systems such as wireless broadband and mobile broadband systems offer better client service, by enhancing mobility, accessibility and simplicity of communication between people. Therefore, there has been growing interest in WiMAX systems, WiMAX IEEE 802.16 and 802.16e-2005 mobile [1]. In comparison to Universal Mobile Telecommunication System (UMTS) and Global System for Mobile communications (GSM), WiMAX offers an enlarged significant bandwidth by using the channel bandwidth of 20 MHz and an improved modulation technique (64-QAM).

When equipments are operating with low-level modulation and high-power amplifiers, WiMAX systems are capable to serve larger geographic coverage areas, and they support the different modulation technique constellations, such as BPSK, QPSK, 16-QAM and 64-QAM[2][3]. WiMAX physical layer consist of OFDM, which offers resistance to multipath. It permits WiMAX to operate in non-line-of-sight environments (NLOS) and is highly understood for alleviating multipath for wireless broadband. WiMAX provides modulation and forward error correction (FEC) coding schemes adapting to channel conditions; it may be changed per user and per frame [2].

The electrical distribution of high-frequency microwave signals through either free space or transmission lines causes difficulties and costs. Losses increase with frequency in free space, due to absorption and reflection; and in transmission lines impedance rises with frequency, which leads to very high losses. Therefore, expensive regenerating equipment is required to distribute high-frequency radio signals electrically over long distances. The alternative would be to distribute baseband signals, radio frequency (RF) signals or signals at low intermediate frequencies (IF) from the control station (CS) to the base station (BS) and subsequently to the user. The RF or baseband signals are down-converted to the required microwave or mm-wave frequency at each BS, amplified and transmitted. Reverse, from user to the BS, the signals would be up-converted [4].

The radio in millimeter-wave (mm-wave) band is the promising media to transmit the ultra-broadband signal in the wireless telecommunication system and, since the recent ten years, has been developing to a favorite research topic. By optics method the mm-wave signal is readily generated and can be transmitted through a long fiber distance. In the RoF system, the generation of the optical mm-wave is one of the key techniques. Several techniques to generate the optical mm-wave at around 60 to 120GHz have been reported, including direct modulation of laser diode (LD), heterodyne technique with optical phase locking, electrical sub-harmonic injection and external modulation. Of all these techniques, the optical external modulation is an appropriate option to generate the optical mm-wave signal with high spectral purity [5].

RoF systems are analogue fibre optic links, which are used to transmit demodulation signal carrier of radio frequency (RF) directly or indirectly from a CS to a BS through a remote unit antenna (RAU) or radio accesses antenna (RAP) to the client [6].

In order to find leading techniques for the WiMAX network deployment, RoF has been studied extensively in recent years. Many studies have been focused on the fibre [7][8][9][10], the low attenuation (0.2 dB/km), and high performance solution for high-speed fibre based on wireless access.

The utilization of millimeter-wave (MMW) frequency for high-speed wireless access, in future RoF systems, would meet the requirement of high bandwidth and overcome the spectral congestion at low frequency. Surely, the RoF system is the future network technology, which has on one hand the capacity to satisfy the demands for decreasing electromagnetic smoking, wireless traffic, power, noise, cost, and antenna size and, on the other hand, to increase frequency, bandwidth, data rate and capacity also eventually improves the spectral efficiency.

So far, the investigations have been narrowed to resolve the dispersion effect and to control the chromatic dispersion, which is explained in Section II, the signal distortion also reduce the power and increase the transmission distance [11]. In our study, the compensators methods are used to equalize the dispersion slope in a fibre and have been demonstrated in the form of DCF and CFBG. DCF has proved to be effective to overcome chromatic dispersion in high velocity light; with a special design, consisting of a fibre and a negative dispersion slope, it compensates the positive dispersion in SMF. We also use an optical amplifier and a CFBG, due to the high insertion loss of DCF, which is discussed in Section III and IV.

CFBG is a high Bragg reflector placed in a short segment of an optical fibre, used to correct chromatic dispersion. It can be used as a wavelength-specific reflector or as an inline optical fibre. CFBGs are extensively employed for functions such as dispersion compensation, stabilizing laser diodes, and add/drop multiplexing in optical fibre systems. The CFBGs comply with environmental requirements by increased stability and durability (free from rust), they can be highly multiplexed (many sensing points in a single fibre cable), and have the advantage of low power attenuation through transmission over several kilometers [12].

This paper studies methods to increase the WiMAX signal transmission distance through utilizing a RoF system with the aim to reduce power consumption and to obtain satisfactory OSNR, SNR and high quality signal transmission spectrums. The work focuses on WiMAX signals transmitted over RoF by applying SMF, DCF and CFBG. The paper is organized as follows. In Section II, we focus on related work; in Section III, we describe the theory of light dispersion in the fibre optic cable for SMF, DCF and for CFBG. In Section IV, we introduce the system description of WiMAX and RoF system and describe the design of the complete system. We discuss the simulation results in Section V and finally, conclusions are drawn in Section VI.

II. RELATED WORK

As mentioned in Section I, RoF technology as a means to deliver WIMAX signals has been studied by a number of researchers. Based on the IEEE 802.16d-2004 specification in the 3.5 GHz band, [13] reported about measured spectra and Error Vector Magnitude (EVM) for different single mode fiber spans up to 5 km.

Also, [14] investigated EVM for RoF WiMAX signal transmission. In this approach, fiber lengths between 0km and 5km for both uplink and downlink instances were investigated. The results show, on the downlink, the EVM measured was better than 3.1% between -3dBm and 10dBm. Lowest EVM was measured at 3dBm.

A hybrid radio on dense-wavelength-division-multiplexing (DWDM) transport system for WiMAX applications is proposed in [15]. The researchers were able to improve the bit error rate (BER) over a large, effective area fiber (LEAF) of 100km.

In [16], a WiMAX-RoF transport system is proposed and achieved satisfactory BER performance over a 120 km SMF length for both, down and up links.

Osadchiy et al [17] proposed a bi-directional WiMAX-over-fiber signal transmission system. The scheme supports signal transmission on a 2.4 GHz carrier at a bit rate of 100 Mb/s downlink and 64 Mb/s uplink for an 80km access fiber link. They also demonstrated a successful transport of 100 Mb/s WiMAX-compliant signals with a 5.8 GHz RF carrier over a 78.8km deployed SMF and a 40km distribution SMF. The results show that the WiMAX signal stayed within 5% RMS EVM after 118.8-km fiber link transmission and air transmission.

III. THEORY AND ANALYSES

Dispersion is a highly important factor due to the effect on the bit rate. There are three types of dispersions: material dispersion, also known as chromatic dispersion, is caused by the fact that the refractive index of the fibre medium varies as a function of wavelengths, waveguide dispersion depends on geometrical characteristics like shape, design and chemical composition of the fibre core and finally, intermodal dispersion, which is related to the fact that the light is not transmitted as a single beam [18].

Accordingly, chromatic dispersion emerges because of variable frequency components and also signals at differing wavelengths move at different velocities due to the refractive index. It has the following units of measurement: ps/nm/km, where nm is the spectral width of the pulse, ps refers to the time spread of the pulse and km refers to the fibre length. The chromatic dispersion of SMF is 16 ps/ nm/km at 1550 nm and 17ps/nm/km at 1552nm, and can be expressed as follows [19]:

$$D_{chr} = -\frac{1}{L}\frac{dt_g}{d\lambda} \tag{1}$$

where L is the fibre length and t_g is the time to dispread the distance. For externally modulated sources, transmission distance limited by chromatic dispersion can also be expressed as follows [19]:

$$L < \frac{2\pi c}{16|D|\lambda^2 B^2} \quad (2)$$

where B is the bandwidth; λ is the wavelength and c is the light velocity. Eq. (1) and (2) show the transmission distance of the signal is limited due to the chromatic dispersion in the SMF. To abolish the limitation of signal transmission in the SMF, techniques like DCF and CFBG have been demonstrated to be useful to compensate the accumulated dispersion in the fibre. DCF has a dispersion characteristic that is contrary to that of the transmission fibre. Dispersion compensation is achieved by inserting an open loop of DCF into the transmission path. The total dispersion in the DCF open loop needs to be equal and opposite of the accumulated dispersion in the SMF. This means that, if the SMF has a low positive dispersion, the DCF will have a large negative dispersion. With this technique, the absolute dispersion per length is nonzero at all points along the fibre, whereas the total accumulated dispersion is zero after some distance. The length of the DCF should be minimized as the special fibre used has a higher attenuation than the transmission fibre. The attenuation is around 0.6dB/km at 1550nm compared to 0.2dB/km for SMF [20].

Because of the high power loss in DCF, the CFBG is applied to control and tune the difference in arrival times of the multiple frequency components resulting from a typical dispersion. It has been shown that strong, long, and highly reflective gratings can be used for dispersion in communication links in transmission with negligible loss aspersion, by proper design of the grating. For high-bit-rate systems, higher- order dispersion effects become important, dissipating the advantage of the grating used in transmission. The rules utilized for the design of the grating to compress pulses in a near ideal technique are a compromise between the reduction of higher-order dispersion and pulse recompression. Bandwidths are limited with this configuration by the strength of the coupling constant and length of a realizable uniform period grating.

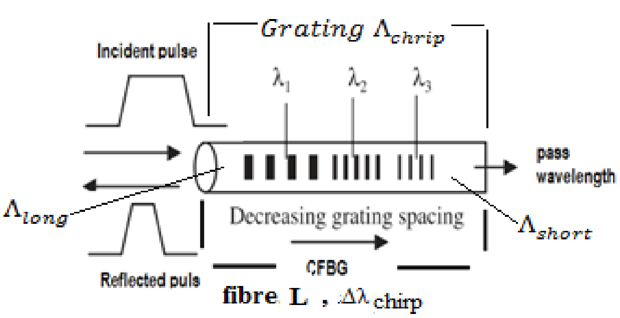

Figure 1. The wavelength reflected in CFBG by the Bragg grating referred to Bragg wave is λ1. λ2, λ3 and the unwanted wavelength passes; the spacing decreases along the fibre; accordingly, the Bragg wavelength decreases with distance along the grating length.

The reflected wavelength in CFBG amends with the grating period, because the spacing of the grating varies and is designed for a desired wavelength. The different wavelengths reflected from the grating will be subject to different delays; if the injected light wavelength differs from the grating resonant wavelength, the light is not reflected. As shown in Figure 1 , the chirp in the period can be related to the chirped bandwidth λ_{chirp} of the fibre grating which is presented in the following equation [11]:

$$\Delta\lambda_{chirp} = 2n_{eff}\left(\Lambda_{long} - \Lambda_{short}\right) = 2n_{eff}\Delta\Lambda_{chirp} \quad (3)$$

The reflection from a chirped grating is a function of wavelength, and therefore, light entering into a positively chirped grating (increasing period from input end) suffers a delay in reflection that is approximately [11].

$$\tau(\lambda) \approx \frac{(\lambda_0 - \lambda)}{\Delta\lambda_{chirp}} \frac{2L_g}{v_g},$$

$$for\ 2n_{eff}\Lambda_{short} < \lambda < 2n_{eff}\,\Lambda_{long} \quad (4)$$

where λ_0 is the Bragg wavelength at the center of the chirped bandwidth of the grating, and vg is the average group velocity of light in the fibre. By introducing a maximum delay of 2Lg/vg between the shortest and the longest reflected wavelengths, the effect of the chirped grating is that it disperses light. This dispersion is of importance since it can be used to compensate for chromatic dispersion in optical fibre transmission systems. The figure of merit is a high-length grating with a bandwidth important feature of a dispersion-compensating device as at 1550 nm, the group delay τ in reflection is ~10 nsec/m. Several parameters affect the performance of the CFBGs for dispersion compensation: the insertion loss due to reflectivity < 100%, dispersion, bandwidth, and polarization mode-dispersion, deviations from linearity of the group delay also group delay ripple. Ignoring the first and the last two parameters momentarily, we consider the performance of a chirped grating with linear delay characteristics, over a bandwidth of Δλ chirp.

The dispersion coefficient D_g [ps/nm/km] for the linear CFBG is given by the following simple expression [8]:

$$D_g = \frac{2n}{c\,\Delta\lambda_{\text{chirp}}} \quad (5)$$

where *n* is the average mode index, *c* is the light velocity, Δλ is the difference in the Bragg wavelengths at the two ends of the grating. Eq. (5) represents that D_g of a chirped grating is ultimately limited by the bandwidth Δλ; the increase in the transmission distance will be possible only, if the signal bandwidth is reduced.

IV. SYSTEM DISCRIPTION OF WIMAX OVER ROF

An important difference between fixed and mobile WiMAX is the physical layer. Mobile WiMAX uses OFDMA as its physical layer transmission scheme instead of plain Orthogonal Frequency Division Multiplexing (OFDM). OFDMA can also be used as a multiple access mechanism when groups of data subcarriers, called sub channels, are allocated to different users. Mobile WiMAX also introduces more scalability into the actual physical layer parameters. Cyclic prefix durations and channel bandwidths in multiple OFDMAs, which have different amounts of subcarriers, are utilized to allow the wireless link design to be optimized according to the environment where the system is deployed.

Figure 2 illustrates the schematic simulation setup of WiMAX over RoF, including the dispersion model techniques SMF, DCF and CFBG. In this simulation, the BS deployed the data of mobile WiMAX IEEE 802.16e-2005 to the fibre system as a RF signal; firstly, to the RAU antenna as an electrical signal; subsequently, converted to the fibre optic signal by modulating the RF to the laser beam, which a laser diode has injected into the SMF; this modulation operation arises in the Mach Zehnder Modulator (MZM).

In future work, it would be possible to use a WiMAX Femtocell instead of a BS because it has several advantages. It can be use in microcell, pico-cell area and indoor; the typical cell radius ranges between 50-100m[17]. The proposed scheme would not require to be changed, because, at the end of fibre, the optical signal is converted to the electrical RF signal, which would radiate via Femtocell to micro or pico-cell. The WiMAX transmission signal is centered at 3.5 GHz; comprising 128 subcarriers and 64QAM (6 bit-per-symbol) modulates each; the bandwidth is 20MHz, and the transmitted bit rate is 120Mbps. The important component in WiMAX is the scalable orthogonal frequency division multiplexing (S-OFDMA). In the basic version of OFDMA, one sub-carrier is assigned to each user. The spectrum of each user is quite narrow, which makes OFDMA more sensitive to narrowband interference. The core of an orthogonal multi-carrier transmission is the Fast Fourier transform (FFT) respectively, inverse FFT (IFFT) operation; synchronization and channel estimation process together with the channel decoding play an important role. To ensure a low cost receiver (low cost local oscillator and RF components) and to enable a high spectral efficiency, robust digital synchronization and channel estimation mechanisms are needed. The throughput of an OFDM system does not only depend on the used modulation constellation and Forward Error Correction (FEC) scheme, but also on the amount of reference and pilot symbols spent to guarantee reliable synchronization and channel estimation [23].

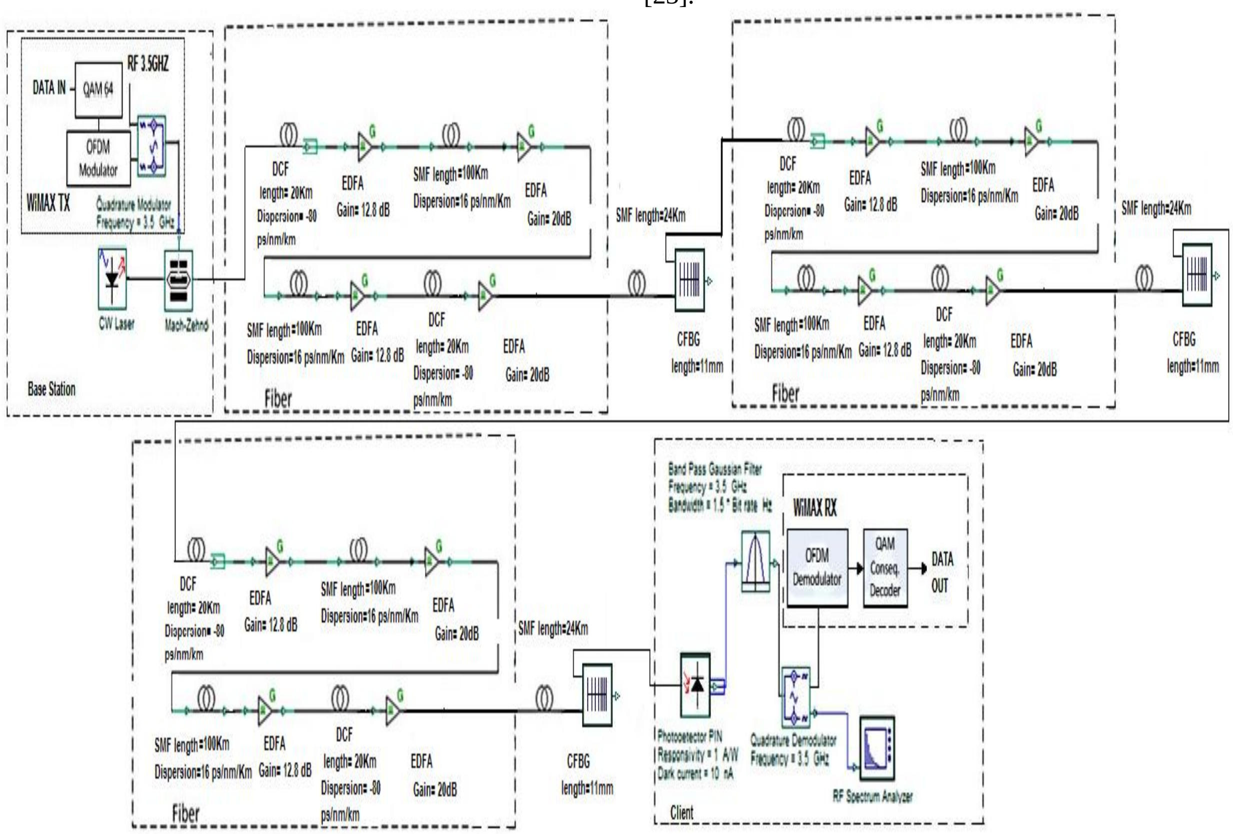

Figure 2. Schematic shows the setup of WiMAX downlink integrated in the RoF system which consist of SMF, DCF and CFBG for the increased fibre length of 792km.

OFDMA utilized in mobile WiMAX is scalable in the ability that by flexibly adjusting FFT sizes and channel bandwidths with fixed symbol duration and subcarrier spacing, it can address wide spectrum needs in different area regulations in a cost competitive approach. The S-OFDMA consists of a flexible and large fast Fourier transform (FFT) size changes from 128 to 2048, and it is used in IEEE802.16e-2005 [3].

The transmitter's (TX) source data in the WiMAX are encoded, and then modulated by QAM64, buffered and manipulated through serial to parallel (S/P) mechanism so as to make an appropriate vector for IFFT. The signal is transmitted to the fibre as a RF signal; subsequently, converted to an optical signal by the RAU antenna by being indirectly modulated through the MZM. Intensity modulators are important components for high bit rate light wave systems operating at a wavelength of 1552nm.

The MZM structure is composed of an input optical branch, where the incoming light is split into two arms, and two independent optical arms, which are subsequently recombined by the output optical branch. As shown in Figure 3, the continuous wave (CW) laser diode (LD) emits a light wave into an optical input of the MZM; the WiMAX_RF radiates into two electrical inputs of MZM. The bias voltage of V1, 2_{bias} = Vπ/2 controls the degree of interference at the output optical branch and accordingly the output intensity. The MZM is based on an electro-optic effect, the effect that in certain materials, e.g., LiNbO3, the refractive index n changes with respect to the voltage V applied across electrodes. The optical field at the output of the modulator is given by following equation [24]:

$$E_{out}(t) = \frac{1}{2}\left[exp\left(\frac{\pi}{V_\pi}V_1(t)\right) + exp\left(j\frac{\pi}{V_\pi}V_2(t)\right)\right] E_{in} \qquad (6)$$

where V_π is the modulation voltage, which is the differential drive voltage (V1-V2=V_π) resulting in differential phase shift of π rad between two waveguides. E_{in} (t) is the optical field applied to the input of the modulator. The MZM modulated electrical signal refers to WiMAX–RF; optical beam

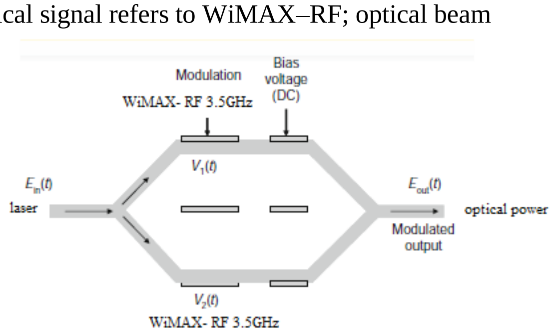

Figure 3. Schematic shows Mach- Zehnder LiNbO3 (MZM) optical input from laser diode CW and two electrical inputs from WiMAX_Tx

refers to the CW laser and is injected in the output as an optical power signal over fibre. The CW LD technology is at the standard telecommunications wavelength of 1552.52 nm. The CW LD output power is too low and would require additional amplification. The CW LD has an average output power of 3 dBm for laser frequency 193.1 THz with a linewidth of 10 MHz and relative noise dynamic of 3dB and a noise threshold of
-100dB .

Subsequently, the optical signal is transmitted over the RoF system, which is composed of a triple symmetrical dispersion system: each consisting of DCF (20 km), SMF (100 km) SMF (100 km) and DCF (20 km), connected to the SMF (24 km) and to the CFBG, which is added after every 264 km. This setup allows a compensation of the positve dispersion signal in SMF; therefore, the signal transmission is increased to 264km fibre length.

The SMF dispersion parameter is 16 ps/nm/km and the SMF length is set up to 100km; the SMF signal attenuation is 0.2dB/km; therefore, total accumulated dispersion is 16×100=1600 ps/nm. The dispersion slope will be sharper with the increment of the transmitting fibre length L as expressed in Eq. (2). DCF is configured to negative dispersion -80ps/nm/km at 1552nm to compensate the positive signal dispersion in SMF, considered in Eq. (7). It is proved to be effective to reverse chromatic dispersion in high-velocity light and it is highly important to increase the signal transmission distance and bit rate by a DCF function to keep the wavelength at a zero dispersion, which is called the "zero-dispersion wavelength" (λ_0).

$$(D_{smf} \times L_{smf}) + (D_{DCF} \times L_{DCF}) = 0 \qquad (7)$$

where D_{smf} is the dispersion factor in the SMF , L_{smf} is the fibre length of the SMF , D_{DCF} is the dispersion factor in the DCF and the L_{DCF} is the length of the DCF.

$$\left(\frac{16ps}{nm}/km \times 100km\right) + \left(-\frac{80ps}{nm}/km \times 20km\right) = 0 \qquad (8)$$

Eq. (8) shows the result of the accumulated dispersion in combined DCF and SMF. SMF is configured to a fibre length of 100km and DCF is configured to the negative dispersion of -80ps/nm and used over a 20km fibre length to reduce the chromatic dispersion and, as explained before, DCF is added to keep the transmission signal of zerodispersion for a long distance.

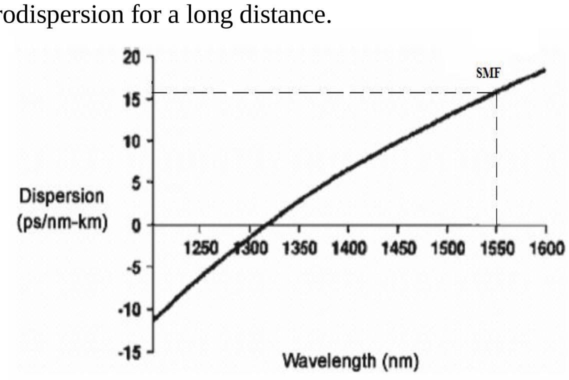

Figure 4. Illustrates the dispersion character for the wavelength

As shown in Figure 4, the dispersion of the light signal in fibre optic is zero by 1330nm and 16 ps/nm/km by 1550 nm wavelength. The advantage of using a wavelength of 1552nm compared to a wavelength of 1330nm lies in low power attenuation. The devices working with the 1330 nm wavelength are able to transmit a high amount of power but the modulation constraints of the laser source can make the design more complicated. The wavelength of 1550nm is the most used in terrestrial communication systems and a wide range of devices are available[25]; the Doppler Effect is lower than at other frequencies and for this carrier it is possible to carry out DPSK (Differential Phase Shift Keying) and QAM modulation schemes.

Figure 5 illustrates the affected DCF of the signal dispersion in SMF; the signal transmitter TX injects the WiMAX RF in the fibre after modulation through the laser diode and MZM. In the fibre system the SMF is configured for a fibre length of 100km because of the SMF's dispersion character of 17ps/nm/km at 1552nm, the 20km DCF is added and configured to the negative dispersion of -80nm/ps/km to keep the transmission signal of zero dispersion.

As described in Section III, the DCF has a high-power attenuation and cannot be used in this system for a distance longer than 20 km; therefore, the EDFA is employed after 100Km of SMF, being configured to 12.8 dB. The CFBG

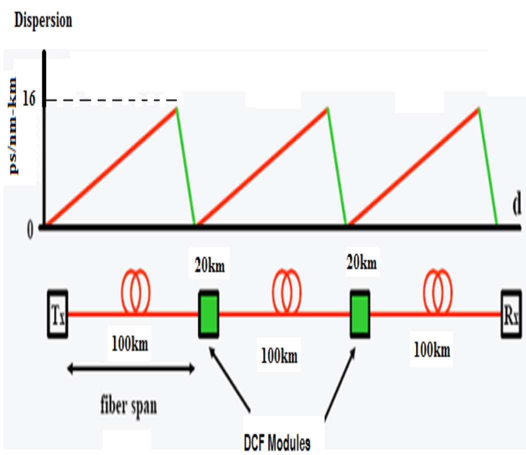

Figure 5. Illustrates that for every 100km SMF fibre length there are 20 km long DCF modules to compensate the accumulation dispersion in the SMF.

chirped bandwidth is $\Delta\lambda$=2 nm; n=0.0006 and lengths of 110 mm. The optical power is converted to the current electrical signal by a photo detector diode (PIN for dark current 10nA and centre frequency 193.1 THz). The electrical bandpass Gaussian filter is used to minimize the electrical signal noise and group delay becomes constant for all frequencies. In a receiver, a bandpass Gaussian filter allows signals within a selected range of frequencies to be heard or decoded, while preventing signals at unwanted frequencies from getting through the centre frequency (f_0). As mentioned before, f_0 is set up to 3.5GHz for a bandwidth of 20MHz.

The applied RAU antenna can offer a small antenna size for broadband operation. The RAU can convert the incoming RF signal to the fibre and subsequently to an electrical signal. The incoming optical signal is detected by a photodiode (PD) and converted to the RF signal, then amplified and transmitted over the wireless path for 300m to the BS antenna and to the WiMAX RX. At the WiMAX receiver the RF signal is demodulated by the Quadrature demodulator, which implements an analog demodulator using a carrier generator for Q and I Quadrature components; it consist of two low pass filter. 7GHz cutoff frequency of low pass filter is configured; the OFDM demodulator is implemented by a complex point 1024 FFT; in OFDM the FFT is used to realize multi-carrier modulation, which reduces the complexity of OFDM systems greatly. Generating OFDM symbols with high data rate requires a high-speed FFT processor. Moreover, an FFT processor with low area and low power consumption is needed by the portable feature of OFDM systems. In the QAM sequence decoder, the bit sequence is split into two parallel subsequences; each can be transmitted in two quadrature carriers when building a QAM modulator. This is achieved by using a serial to parallel converter.

V. RESULT AND DISCUSSION

The simulation results clearly show that the fibre attenuation and the chromatic dispersion, which are the main cause for a limited signal transmission length and data bit rate in the RoF, can be controlled by transmitting the WiMAX-OFDMA for 120 Mbps bit rate via a combination of different fibers, namely SMF, DCF and CFBG. The results indicate that the use of a accumulated dispersion compensation method, which consist of a triple symmetrical compensator system and, in addition, a CFBG for each system, is the means to control the chromatic dispersion, keep the transmission signal of zero dispersion and to increase the transmission distance to 792 km.

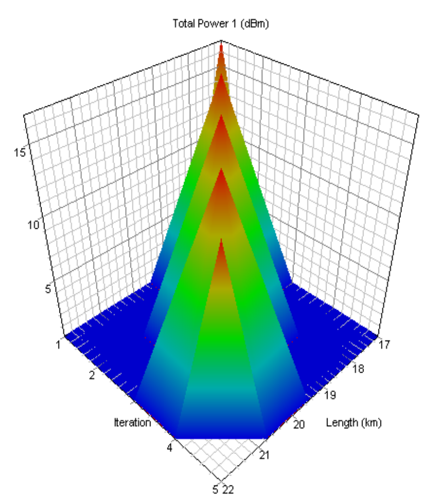

Figure 6. Illustrates the total power dBm in the DCF for a DCF length from 17 to 22km and the wavelength is 1552nm

Figure 6 shows the total of the signal power in dBm according to the DCF length from 17km to 22km. At 17km, the signal power is 16.2dBm; at 22km, the signal power is 8dBm, due to the high signal power loss the CFBG and the EDFA are used. The red colour refers to the optical power, the power is focused in the centre of the fibre and the green colour refers to the noise in the DCF, which is caused by the laser diode.

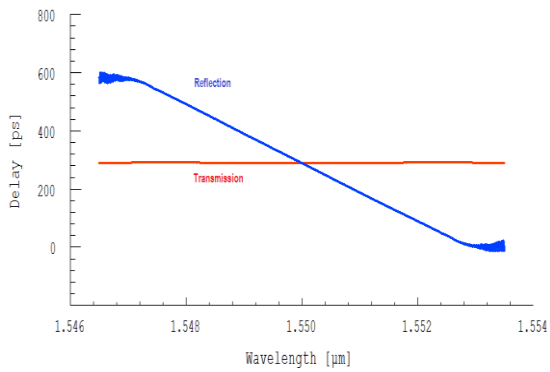

Figure 7. Illustrates the delay in the CFBG for the wavelength from1546 nm(1.546um) to 1554 nm (1.554um); the delay is measured in ps.

Apart from the combination in the order of DCF-SMF-SMF-DCF-SMF with a fibre length of 20-100-100-20-24 km, a 55mm long CFBG is added at every 264 km to compensate the chromatic dispersion. Figure 7 shows the reflectivity and delay characteristics of the chirped gratings operating in 10-55mm grating length. It is noted that the reflection wavelength of 1548 to 1552 nm has the delay time of 50ps; respectively the delay in the CFBG is important to balance the wavelength and to control the chromatic dispersion, due to the different frequency velocities in the fibre.

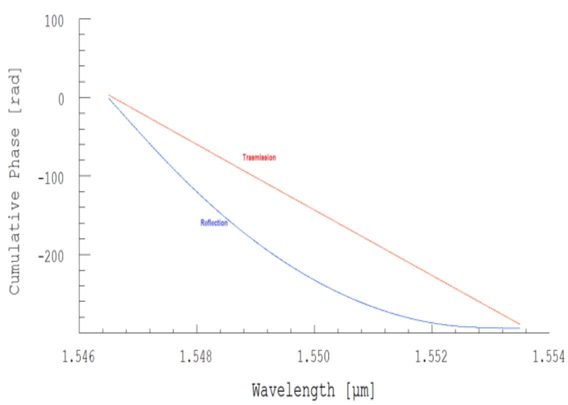

Figure 8. Shows the cumulative phase of the transmission and reflection wavelength.

The control of the chromatic dispersion is essential in the fibre optic system network, due to the increase of the signal transmission distance, as well as the data bit rate. The CFBG can be implemented in DWDM and in this research is used as signal tuneable. The cumulative phase difference between transmitted and reflected wavelength is shown in Figure 8. The blue line refers to the reflective wavelength in the CFBG and the red line represents the forward wavelength transmission. Any delay in the wavelength in the CFBG refers to phase delay 75ps at wavelength 1552nm.

TABLE I. OSNR INPUT AND OUTPUT

	Input Signal dB	***Input OSNR (dB)***	***Output Signal (dB)***	***Output OSNR(dB)***
CFPG 10mm	-0.06141464	99.9856	-8.5112	26.63
CFBG 32mm	-0.0141464	99.9856	--11.2111	23.62
CFBG 55mm	-0.06141464	99.9856	-13.4115	19.62621
	(nm)	***(nm)***	***(nm)***	***(nm)***
Wavelength	1552.5244	1552.524	1552.52	1552.524

As mentioned in Sections I and III, the wave delay in the CFBG is important because the light spectrum in SMF and DCF travels with different velocity, which means that it consists of different wavelength, which reaches the end of a fibre optic cable delayed. Therefore, the CFBG is used to control the chromatic dispersion and power attenuation, as well.

Table (I) shows the input parameter at transmitter after MZM and the output parameter after 792km. The WiMAX-RF modulated to laser for frequency 193.1THz for a wavelength of 1552.5244nm. The difference between the input OSNR and output OSNR ranges at ~ -74dB; if the chirped gratings are set up to 10mm, the input signal power is at -0.0614 dBm and the output signal power is at -8.5112 dB. The difference between input and output power is -8.4498 dB, when the chirped grating of CFBG is 10mm for a fibre length of 792km. The result is highly satisfying because the optical amplifier only used 192 dB for the fibre length of 792km.

As shown in Figure 9, the configuration of the CFBG chirp length has an influence on the OSNR: the shorter the chirp length the higher OSNR. The higher output OSNR after 792km is 26.63dBm, when the chirp grating is set up to 10mm length, and lower OSNR, when the chirped grating is set up to 55mm. Additionally, the figure shows that the OSNR has decreased linearly, which is an important result because it let the signal in a stable condition and the signal quality is affected positively. This means, that the configuration of the CFBG can improve the signal quality in the RoF system and can be used as a band pass filter and tuneable component, as well.

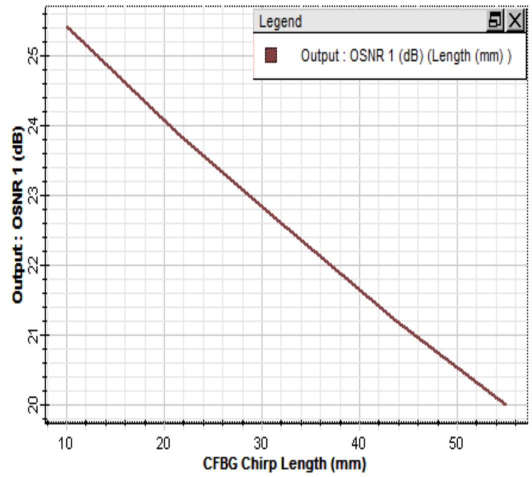

Figure 9. OSNR measurement at the Chirped Grating length from 10mm to 55mm in CFBG

As shown in Figure 10, the total gain power measured at CFBG chirp length from 10mm to 55mm at wavelength 1552nm decreases linearly. At a chirp length of 10mm the power is -8.5112dB, at 32mm -11.2111dB and at 55mm, the power is 13.4115 dB.

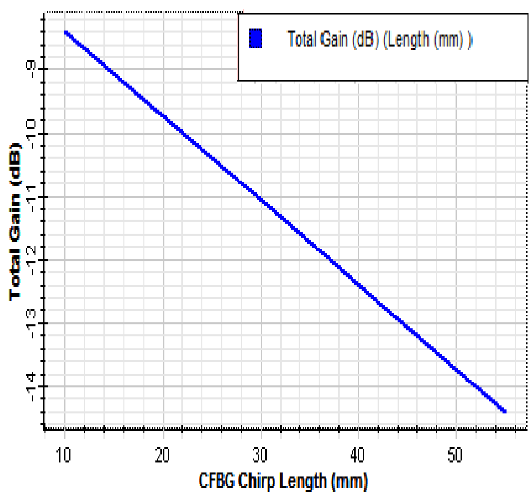

Figure 10. Total power measurement at the chirped Grating length from 10-55mm in CFBG

Figure 11 (A) shows the optical bandwidths for a fibre length of 264 and 792km at a wavelength of 1552nm. At all fibre lengths, the optical bandwidth is 300nm. There is a minor change in the optical signal power after the signal has travelled for 528 km: at 264 km, the signal power is -5 dBm, at 792 km the signal power is -14 dBm; however, a limited optical amplifier was used. The green area refers to the noise, which is produced by the laser diode, and the red area refers to the optical bandwidth, which is expressed in terms of wavelength rather than frequency, using the following equation [26]:

$$B_\lambda = \frac{\lambda^2}{c} B_0 \quad (9)$$

where B_o optical bandwidth is for wavelength 1552nm; c is light speed; λ^2 is the wavelength square.

Figure 11 (B) shows the optical bandwidths for a fibre length of 792km at a wavelength of 1552nm. At all fibre lengths, the optical bandwidth is 300nm. The intensive green colour at 1552nm (1.55um) refers to the noise intensity in the bandwidth. The red colour refers to the signal power at -25dBm.

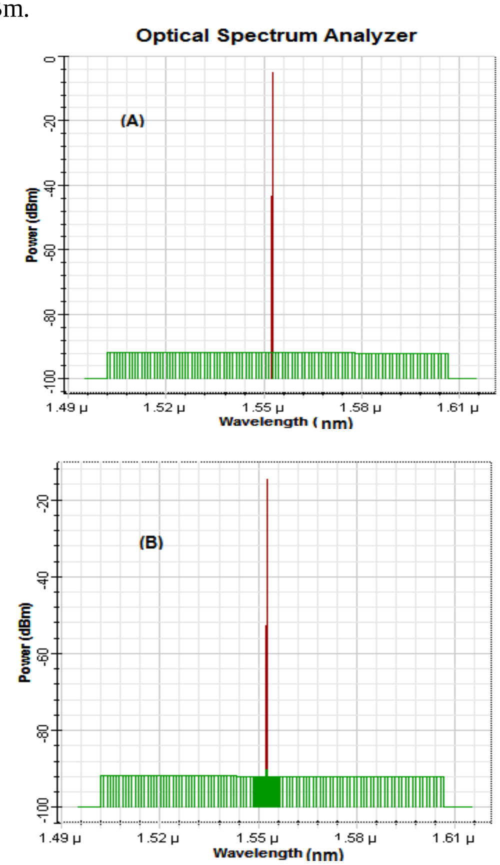

Figure 11. (A) optical bandwidth for fibre length after 264km (B) optical bandwidth after 792km fibre legnth

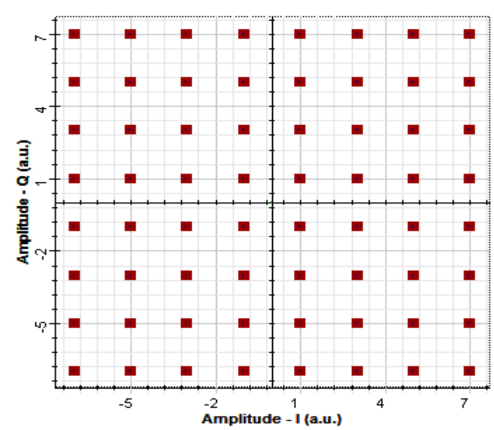

Figure 12. Constellation diagram of 120–Mbit/s WiMAX QAM-64 transmission downlink for fibre length 792Km

Figure 12 shows a constellation diagram, which is a representation of a signal modulated by a digital modulation scheme It clearly shows the electrical constellation at the WiMAX transmitter which is a representation of 6 bit-data per symbol of the 64-QAM modulator, of WiMAX TX for OFDM 1024 and modulator 64- QAM 8 bit by SNR 116.78 dB; the signal is clear and noise free.

Figure 13 shows the electrical constellation diagram at WiMAX-TX receiver. The signal at the receiver is transmitted over RoF via the combined SMF and DCF for a length of 528km. The DCF length is 4x20km and the SMF length is 4x100km, respectively 2x24km. Compared to Figure 11, a change in the 6 bit QAM 64 can be recognized because of noise and power attenuation, which are added to the signal through the wavelength deployed over a distance of 528km in the fibre. The black colour refers to the noise and the red colour refers to the total signal.

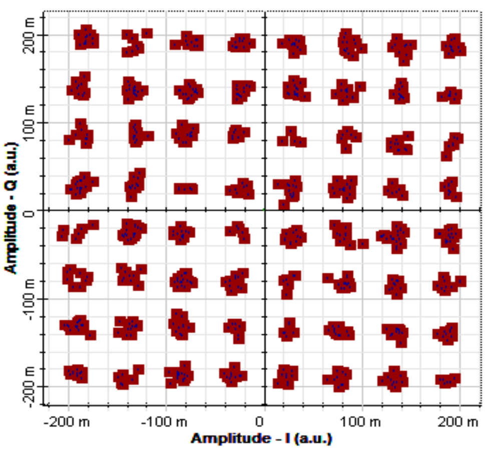

Figure 13. Constellation diagram of 120–Mbit/s WiMAX QAM-64 receiver downlink for fibre length 528Km

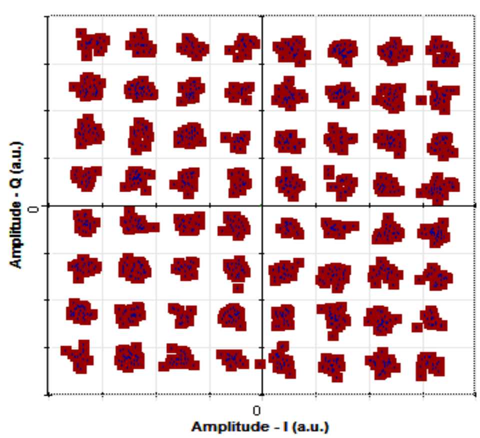

Figure 14. Constellation diagram of 120–Mbit/s WiMAX QAM-64 received downlink for fibre length 792Km

Figure 14 illustrates the electrical constellation diagram 64QAM for 6 bit at the receiver after the WiMAX transmission signal travelled over a fibre length of 792km and was converted to an electrical signal by the photo detector diode. The signal has a noise, which is shown in blue, due to the laser diode noise; the red colour refers to the WiMAX signal total signal. The comparison of Figure 12 and Figure 13 shows that the noise has slightly increased by the extended signal transmission distance from 528km to 792km. The reason for this is the long transmission distance; the signal power becomes weak due to the laser noise and the DCF attenuation. To reduce these effects, an increase of the optical power amplifier is needed. This result shows the maximum signal transmission distance for a limited fixed power amplifier.

Figure 15 shows the RF spectrum of WiMAX 3.5 GHz carrier frequency for bandwidth 20 MHz at the WiMAX transmitter before transmitting over fibre, the bandwidth is in the frequency range of f_0-f_L,f_0,f_0+f_H (3.5-3.49, 3.5, 3.5+3.51) GHz, the spectrum of the signal power, displayed in blue, measured at 100 dBm and the green colour refers to the noise, which is measured as 22 dBm.

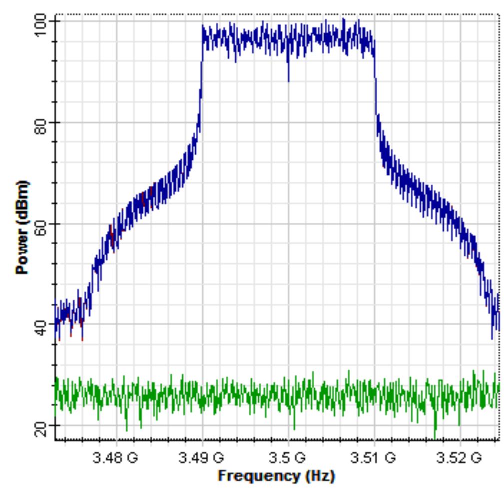

Figure 15. 3.5GHz WiMAX-TX for bandwidth 20MHz and FFT 1024 before transmitting over RoF .

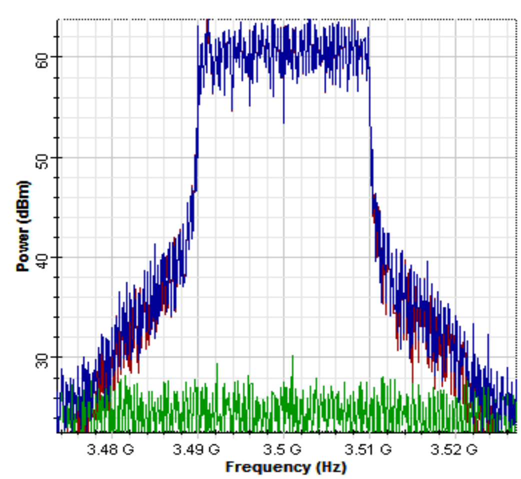

Figure 16. WiMAX carrier frequency 3.5GHz for bandwidth 20MHz at WiMAX-RX after tranmission over RoF for fibre length of 792km.

Figure 16 shows the 20MHz bandwidth after a fibre length of 792 km for an output power of 60dBm; the noise is measured as 26 dBm. The spectrum consistes of the signal and noise, which is illustrated in blue and the red area refers to the signal without noise.

The power loss between the transmitter and receiver is 30dBm. The signal is deployed over SMF, DCF and tuned by a CFBG filter for fibre length 792km. At the end of the 792 km fibre length, the optical to noise ratio (OSNR) is 26.64 dB. Typically, the larger the OSNR value, the lower the receiver sensitivity.

Table (II) shows the parameter at the electrical transmitter at electrical input of MZM; the maximum value of SNR is 116.78512 dB for WiMAX_RF 3.5GHz; the total power is 16.785116 dBm.

TABLE II. TOTAL POWER AND SNR AT TRANSMITTER

	Total Power (dBm)	Signal Power (dBm)	Noise Power (dBm)	SNR (dB)
Min value	-100	-100	-100	0
Max Value	16.785116	16.785116	-100	116.78512
Ratio max/min	116.78512	116.78512	0	116.78512
	(Hz)	(Hz)	(Hz)	(Hz)
Frequency at min	0	0	0	0
Frequency at max	3.5e+009	3.5e+009	3.5e+009	3.5e+009

Table (III) shows the parameter of the electrical signal after having been converted from optical at the photo detector diode; the SNR is 31.318564 dB; the diffrence between input and output is 85.466556 dB; considering the WiMAX signal has been transmitted over a fibre length of 792km , this result is highly satisfactory

TABLE III. TOTAL POWER AND SNR AT THE RECEIVER

	Total Power (W)	Signal Power (W)	Noise Power (W)	SNR (dB)
Min value	23.26439e-015	0.39134784e-024	23.26439e-015	0
Max Value	0.13552317e-009	0.13547414e-009	49.022992e-015	31.318564
Ratio max/min	5825.3479	346.17323e+012	0.47456081	31.318564
	(Hz)	(Hz)	(Hz)	(Hz)
Frequency at min	50e+006	50e+006	50e+006	50e+006
Frequency at max	3.5e+009	3.5e+009	3.5e+009	3.5e+009

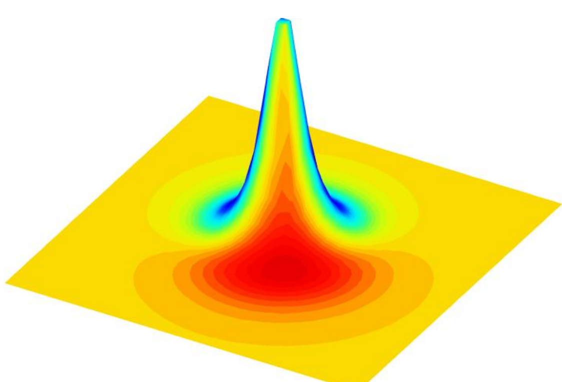

Figure 17. Signal transmitted in SMF for fibre length of 264km

Figure17 shows an optical signal transmitted over SMF fibre; the red colour refers to the optical power, which is to be seen clearly in the centre of the SMF after 264km fibre length.

The SNR is measured as 31.31856 dB at the receiver in comparison to the SNR of a WiMAX transmission signal over air, which is typically 21dB for a code rate of ¾ [20]. The BS-TX propagation loss via air according to the Egli calculator[26] ranges at 167.57 dB for 5km. Compared to the transmission of the signal over fibre, which has travelled 792 km, using a laser diode of 5 dBm for fibre attenuation 180dB per 792km (SMF+DCF) attenuation, the result is highly satisfactory.

VI. CONCLUSION

This paper proposed a method for transmitting RF signals over fibre, using a WiMAX system downlink deployed via SMF/DCF and CFBG over a RoF system. The system is able to carry a WiMAX S-OFDMA signal of 128 subcarriers with an FFT of 1024 for a 3.5GHz carrier frequency and bandwidth of 20MHz. The bit rate for WiMAX increased to 120Mbps with 64-QAM over a RoF system for a fibre length of 792km. We compared the chirp length 10mm to 55mm in CFBG with OSNR and proved the best OSNR result with 10mm chirp. The results show that by using SMF with a DCF setup for dispersion of -80 and a CFBG setup for a length of 10 to 55mm, we achieved an increase in the WiMAX transmission over fibre distance to 792km. This method is able to control the chromatic dispersion affected in the fibre. This means that the power budget of the WiMAX downlink signal can be improved compared to the energy consumed in a WiMAX transmission BS antenna 167.57dB for 5 km; the data bit rate increased to 120Mbps. Finally, the bandwidth spectrum stayed relatively constant over the long fibre distance, and the result of SNR and OSNR are highly satisfactory; the power consumption is very low between the input and output of the fibre.

In summary, with the described setup, we reached the aim to increase the transmission distance, to improve the frequency spectrum and to reduce the power consumption. Additionally, as future work, it is possible to further increase the signal transmission distance for various mobile and fixed broadband systems, such as the WiMAX and UWB system by utilizing more than three circuits, consisting of the triple symmetrical dispersion system SMF, DCF and CFBG.

REFERENCES

[1] M. Al-Noor, K.-keong J. Loo, and R. and Comley, "120 Mbps Mobile WiMAX Scalable OFDMA Signal Transmission over RoF with SMF , DCF and Chirped FBG for Fibre Length of 792 km," *ICWMC, 2010 6th International Conference*, IEEE Computer Society, 2010, pp. 373-377.

[2] D. Pareek, The Business of WiMAX, Southern Gate, Chichester, west sussex: John Wiley & Sons, Ltd, 2006.

[3] WiMAX Forum," Mobile WiMAX, Part I: A technical overview and performance evaluation," June 2006.

[4] A.N. oma Ng, Radio-over-Fibre Technology for BroadBand. Wireless Communication Systems door, Eindoven: CIP-data Library Technische Universiteit Eindhoven, 2005.

[5] J. Ma, J. Yu, X. Xin, C. Yu, and L. Rao, "Optical Fiber Technology A novel scheme to implement duplex 60-GHz radio-over-fiber link with 20-GHz double-sideband optical millimeter-wave transmitted along the fiber," Optical Fiber Technology, vol. 15, 2009, pp. 125-130.

[6] I. Harjula, et al., "Practical issues in the combining of MIMO techniques and RoF in OFDM/A Systems," 7th WSEAS Int. Conf. on Electronics, Hardware, Wireless and Optical Communications, Cambridge, pp. 244-248, 2008.

[7] D. Wake, N.J.G. Anthony Nkansah, C. Lethien, C. Sion, and J.-P. Vilcot, "Optically Powered Remote Units for Radio-Over-Fiber Systems," Lightwave Technology, vol. 26, 2008, pp. 2484-2491.

[8] J. Ma, J. Yu, X. Xin, C. Yu, and L. Rao, "Optical Fiber Technology A novel scheme to implement duplex 60-GHz radio-over-fiber link with 20-GHz double-sideband optical millimeter-wave transmitted along the fiber," Optical Fiber Technology, vol. 15, 2009, pp. 125-130.

[9] L. Chen, J. Lu, J. He, Z. Dong, and J. Yu, "A radio-over-fiber system with photonic generated 16QAM OFDM signals and wavelength reuse for upstream data connection," Optical Fiber Technology, vol. 15, Jun. 2009, pp. 222-225.

[10] X. Jin-ling, H. Xu-guang, and T. Jin, "A full-duplex radio-over-fiber system based on a novel double-sideband modulation and frequency quadrupling," Optics Communications, vol. 283, 2010, pp. 874-878.

[11] Y. Chaba and R.S. Kaler, "Comparison of various dispersion compensation techniques at high bit rates using CSRZ format," in Optik - International Journal for Light and Electron Optics,vol.121, 2010, pp. 813-817.

[12] H. Yin and D.J. Richardson," Optical Code Division Multiple Access Communication Networks Theory and Applications," Tsinghua University Press, Beijing and Springer-Verlag GmbH Berlin Heidelberg, 2007.

[13] F. Martínez, J. Campos, A. Ramírez, V. Polo, A. Martínez, D. Zorrilla, and J. Martí, "Transmission of IEEE802 . 16d WiMAX signals over radio-over-fibre IMDD links," Project TEIDE FIT-330210-2006-86 and European Network of Excellence ISIS, pp. 1-9.

[14] M.-li Yee, A. Ng, and M. Sauer, "Performance Analysis of IEEE 802 . 16e WiMAX Radio-over-fiber Distributed Antenna System," Power, 2009, pp. 197-200.

[15] S.-J. Tzeng, H.-H. Lu, W.-I. Lin, H.-C. Peng, S.-S. Hsu, and H.-W. Wang, "A hybrid radio-on-DWDM transport system for PHS/LAN/ITS/WiMAX applications," Optical Fiber Technology, vol. 15, Mar. 2009, pp. 119-124.

[16] H.-han Lu, C.-yi Li, S.-jye Tzeng, H.-chun Peng, and W.-i Lin, "Optical Fiber Technology Full-duplex radio-on-fiber transport systems based on main and multiple side modes injection-locked DFB laser diode," Optical Fiber Technology, vol. 15, 2009, pp. 251-257.

[17] A.V. Osadchiy, K. Prince, and I. Tafur Monroy, "Converged delivery of WiMAX and wireline services over an extended reach passive optical access network," Optical Fiber Technology, vol. 16, Jun. 2010, pp. 182-186.

[18] R. Kashyap, Fiber Bragg Gratings, Academic Press, San Diego, 1999.

[19] G.P. Agrawal, Fiber- Optic Communication Systems, New York , USA: John Wiley & Sons, Inc., 2001.

[20] Marcos D. Katz VTT, Frank H.P. Fitzek "WiMAX Evolution Emerging Technologies and Applications" Chichester,West Sussex, P Wiley & Sons 2009. Pp. 115-127.

[21] M.D. Katz and F. H.P.Fitzek, WiMAX Evolution, west Sussex, UK: John Wiley & Sons, Inc., 2009.

[22] Fazel, K, and S Kaiser. Multi-carrier and spread spectrum systems. John Wiley & Sons, 2003

[23] S. Han, W. Yue, and S. Smith, "FTTx and xDSL: A Business Case Study of GPON versus Copper for BroadBand Access Networks," submitted to FTTH Conference paper to be published, 2006.

[24] B.Chomycz, plannig Fiber Optical Network,New York,USA: MG Graw-Hill,2009.

[25] I.P.Kaminow and T. LI, Optical Fiber Telecommunications IVa Components, Jamestown Road,London: AP Academic Press, 2002.

[26] http://www.radius.net/egli--free-space-calculator.html ,17.05.2011.

System Level Simulation of E-MBMS Transmissions in LTE-A

Paulo Gomes, José Seguro and Américo Correia
Instituto de Telecomunicações (IT-IUL/ISCTE-IUL)
Lisbon, Portugal

paulo.sousa.gomes@gmail.com,
zemiguelseguro@hotmail.com,
americo.correia@iscte.pt

***Abstract*–Interference coordination methods for Evolved-Multimedia Broadcast/Multicast Service (E-MBMS) in Long-Term Evolution Advanced (LTE-A) are presented. In this paper, OFDM/OFDMA signals based on LTE parameters are combined with Multipoint MIMO, Turbo codes and signal space diversity methods. Different interference coordination techniques, such as, Multipoint MIMO coordination, Fixed Relay stations, adaptive frequency reuse and schedulers are considered to evaluate the E-MBMS spectral efficiency at the cell borders.**

The system level coverage and throughput gains of Multipoint MIMO system with hierarchical constellations and Turbo-codes are simulated associated to the presence or not of fixed relays and measuring the maximum spectral efficiencies at cell borders of single cell point-to-multipoint or single frequency network topologies. The influence of the relay transmission power and cell radius in the performance of the previous cellular topologies is also evaluated.

Keywords – OFDM; multiple antennas; diversity; Turbo-codes; MIMO; Interference; Relays.

I. Introduction

Long Term Evolution Advanced (LTE-A) considers a series of new transmission technologies, such as, coordinated multipoint transmission and reception or relay and carrier aggregation, in order to meet the high technical and service requirements of IMT-Advanced standards. Those requirements include amongst others, peak data rate up to 100Mbps in high speed mobility environment and 1 Gbps in a pedestrian environment, using increased spectral flexibility that allows bandwidth allocation between 20MHz and 100MHz. The LTE standard is the basic standard that paves the way for the future 4th Generation (4G) wireless networks, as stated in [1].

The Evolved - Multimedia Broadcast/Multicast Service (E-MBMS) framework [2] is envisaged to play an essential role for the LTE-A proliferation in mobile environments. E-MBMS constitutes the evolutionary successor of MBMS, which was introduced in the Release 6 of Universal Mobile Telecommunication System (UMTS). With E-MBMS the mass provision of multimedia applications to mobile users will be a reality.

Point-to-Multipoint (PTM) transmission does not employ feedback and therefore need to be statically configured to provide desired coverage in the cell since, transmitted signal is lowest at the cell border. However, when close to cell borders, the PTM bearer can greatly benefit from exploiting also the signals from adjacent cells transmitting the same service, i.e., from soft-combining.

Two types of Evolved-MBMS transmission scenarios exist:

1) Multi-cell transmission (MBSFN: Multi-Media Broadcast over a Single Frequency Network) on a dedicated frequency layer or on a shared frequency layer

2) Single-cell transmission (SCPTM: Single Cell Point to Multipoint) on a shared frequency layer.

Inter-cell interference co-ordination is one method here considered which is expected to improve coverage and increase cell-edge bitrate [3]. Inter-cell interference co-ordination techniques, such as reuse schemes and channel allocation, has been studied thoroughly for circuit switched services in second generation accesses [4].

Cooperative multiple input multiple output (MIMO) and Fixed Relays are other emerging techniques to combat inter-cell interference and improve cell edge performance [5].

Sharing data and channel state information among neighboring base stations (BSs) allows them to coordinate their transmissions in the downlink and jointly process the received signals in the uplink. Cooperative MIMO techniques can effectively turn inter-cell interference into useful signals, allowing significant power and diversity gains to be exploited. The architecture of the high-speed backbone enables the exchange of information (data and control information) between the BSs. Cooperative MIMO systems are only concerned with the BS to mobile station (MS) channel which are PTM channels.

We consider Orthogonal Frequency Division Multiplexing / Orthogonal Frequency Division Multiple Access (OFDM/OFDMA) where the use of Turbo codes in combination with Multipoint MIMO and Complex Rotation Matrices (CRM) [6][7] are applied to OFDM/OFDMA and exploited to achieve spatial and frequency diversity gains in LTE-A networks.

The work of this paper is based on previous work carried out by the authors. In chapter 6 of [8] the authors have considered multi-resolution techniques for MBMS considering both WCDMA and OFDMA. In chapter 16 of [9] the authors have considered the capacity and inter-site gains of LTE E-MBMS. In this paper we have extended that work including MIMO, CRM and Relays in the LTE E-MBMS network and have evaluated by system simulations the coverage and throughput performance. To the best of the authors' knowledge, up to now there are no work in the literature that investigated the performance and benefits of such cellular OFDMA system that incorporates multi-point coordinated MIMO, turbo codes, CRM, hierarchical constellations and low power fixed relay stations.

Section II introduces the coordinated MIMO and coordinated interference schemes. In Section III, the performance curves of system level simulations are presented. Conclusions are drawn in Section IV.

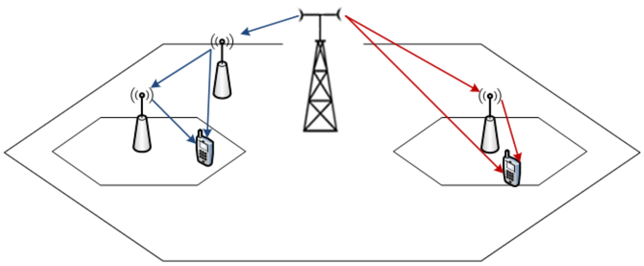

Figure 1. Fixed Relays system.

II. Coordinated MIMO and Interference Schemes

With MIMO cooperative systems [10][11] there is an important reduction of inter-cell interference in the area where the SISO/MIMO cooperative system exists. In LTE the BS is denoted as evolved-NodeB (eNB) and concentrates in it functionalities like radio resource managing, radio link control, interference coordination, mobility control, etc. The communication between eNBs is made through the X2 interface, and each adjacent eNB is interconnected to each other (mesh network). This feature eases the implementation of MIMO cooperative systems by reducing the interference as the same content can be transmitted to mobiles from different antennas (eNBs) at the same physical resource block.

Figure 1 illustrates the Fixed Relays stations (RSs). RSs are low cost fixed radio infrastructures without wired backhaul connections. They store data received from BS and forward to the MSs, and vice-versa. Fixed relay stations (RSs) typically have smaller transmission powers and coverage areas than BSs. They enhance the capacity at specific regions, namely, cell borders, improving signal reception. By combining the signals from RSs and BSs, the MS is able to exploit the inherent diversity of the relay channel (see Figure 1). The disadvantages of RSs are the additional delays introduced in the relaying process and the potentially increased levels of interference due to frequency reuse.

Without any inter-cell interference co-ordination each sector of the cell has unlimited access to the whole bandwidth; this is reuse 1. Any inter-cell interference co-ordination scheme will restrict the resources available for scheduling. By limiting the (maximum) output power as a function of frequency and/or time, $P_{\max}(f,t)$. We will limit the power $P_{\max}$ both in time (sub-frame duration) and on frequencies f in a planned scheme on sectors of cells. A pure fractional frequency reuse 1/3 is achieved by dividing the frequencies into three subsets f_1, f_2 and f_3 and limiting the power by setting

$$\begin{aligned} P_{\max}(f,t) &= P, \quad f \in f_n \\ P_{\max}(f,t) &= 0, \quad f \notin f_n \end{aligned} \tag{1}$$

for each sector of the cell. With reuse partitioning [12] the spectrum is first divided into partitions and then each partition into the desired number of reuse subsets. The scheduler can then utilize the partitions depending on mobile radio position, based on path loss measurements. A reuse partition with a mixture of reuse 1 and 1/3 is achieved by dividing the frequencies into two partitions, f_A and f_B, where f_B further is divided into three resulting in four subsets, f_A, f_{B1}, f_{B2} and f_{B3}. The power limitation for the fractional reuse subsets f_{Bn} is set as above described.

Soft reuse [13] (hybrid reuse partitioning) is a variant of reuse partitioning where a tighter reuse is achieved by using the same frequencies in more than one partition (f_A=f_B) but with different power levels. If we apply to the fractional 1/3 reuse example, then we limit the power by setting

$$\begin{aligned} P_{\max}(f,t) &= P, \quad f \in f_n \\ P_{\max}(f,t) &= p < P, \quad f \notin f_n \end{aligned} \tag{2}$$

Figure 2 illustrates the cellular layout (tri-sectored antenna pattern) indicating the fractional frequency reuse of 1/3 considered in the system level simulations. 1/3 of the available bandwidth was used in each sector to reduce the multi-cell interference. As indicated in Figure 2, the identification of the sources of multi-cell interference, i.e., the use of the same adjacent sub-carriers (named physical resource blocks) is given by the sectors with the same colour, green, yellow and pink. The small blue hexagons refer to the area where reuse 1 co-exists with the fractional reuse of 1/3 as an example of soft reuse.

In the analysis of the scenario Single-Cell Point-to-Multipoint (SC-PTM) there is one radio link between the mobile and the closest base station. It does not assume any time synchronism between the transmissions from different base stations with the same colour resulting in interference from all cells without the same colour. However, an adaptation of this scenario can include macro-diversity to help reduce interference levels. This can be accomplished by combining the two best radio links from surrounding BSs. In this case, time synchronization between the two closest base station sites with the same colour (i.e. transmitting in the same frequency) is assumed in order to combine them at the receiver using soft-combining techniques. Multi-cell interference is reduced because only the other base station sites with the same colour remain un-synchronous and capable to interfere.

In the MBSFN scenario there are at least three radio links, one for each of the three closest base stations to the mobile. Time synchronism is assumed between the transmissions from the closest base stations with the same colour resulting in much less interference from the cellular environment. This results in macro-diversity combining of the three best radio links.

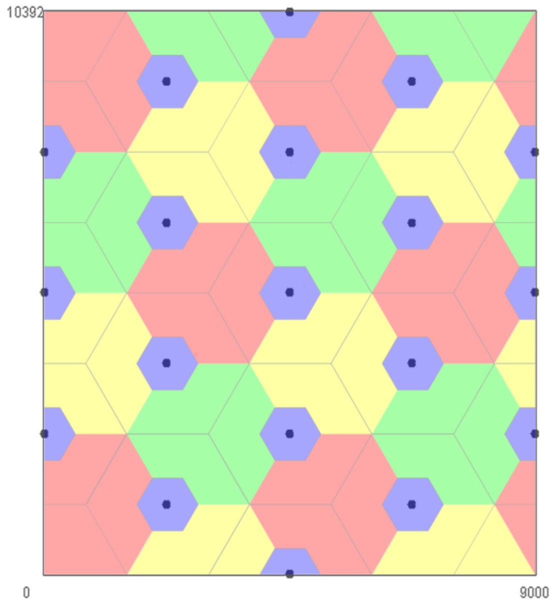

Figure 2. Cellular Layout with mixed fractional frequency reuse, R=1500m

III. NUMERICAL RESULTS

To study the behavior of the proposed scheme, several Monte Carlo simulations were performed in the link level simulation. This study is valid for any OFDM system and it was performed using the LTE parameters mentioned 3GPP documents [14] for a 10MHz bandwidth, which are shown in Table I. The reference link level parameter for all simulation results (SISO and MIMO) presented in this paper is BLER=0.01. This reference applies to near real time services where retransmissions are not allowed. Two different coding rates 1/2 and 3/4 where chosen to check which one would offer the highest average spectral efficiency for the analyzed SC-PTM and MBSFN topologies. The path loss uses 3GPP distance attenuation formula in Table I, and the distance d, is the distance between the actual geographic location of the user and the BS to which it has a radio link established with the best signal to interference plus noise ratio (SINR) as the selection criteria. Small and large scale fading are also included in the system level simulator, according to the parameters of Table I.

Transmission BW	10 MHz
Distance attenuation (*d* = distance in kilometers)	L=122.23+34.88log(d)
Base station power (40 W)	46dBm
Cell Radius (m)	1500, 2250
Cell Layout (hexagonal grid)	3 sectors/site
Shadow fading Log-normal	σ=8dB
User Mobility	Random walk
Multipath fading 3GPP	TypU, MBSFN
Max antenna gain (Angular spread model from SCM, including feeder loss)	15dBi

TABLE I. SIMULATION PARAMETERS FOR 10MHZ.

Coverage Results

In the system level simulations mobile users receive blocks of bits transmitted from base stations and each block undergoes small and large scale fading and multi-cell interference. In terms of coverage or throughput the SINR of each block is computed taking into account all the above impairments and based on the comparison between the reference SINR at a BLER of 1%, and the evaluated SINR it is decided whether the block is or not correctly received.

Figure 3 presents the coverage vs. the fraction of the total transmitted power (denoted as Ec/Ior), for hierarchical 64QAM (64-HQAM), coding rate 1/2 and SC-PTM scenario where different frequency reuse, namely, 1/3, 1 and hybrid 1+1/3 consisting of reuse 1 for users inside DR and reuse 1/3 for users outside DR (see Figure 2) is evaluated. All interfering sites transmit with the maximum power of 90% according to the parameters indicated in Table I. The cell radius R is 2250m, and strong blocks (H1) are separated from medium blocks (H2) and weak blocks (H3) without macro-diversity combining, denoted as 1RL. In addition, fixed relay with two different transmission powers, 10W and 2.5W are also illustrated (TD in the legend).

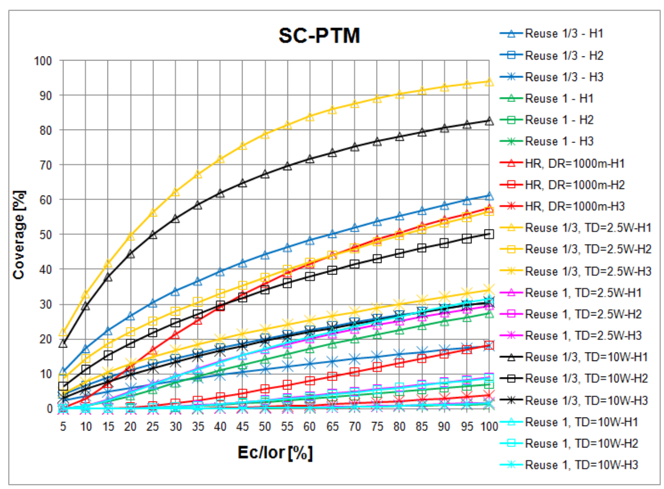

Figure 3. Coverage vs Ec/Ior SC-PTM (1RL) scenario, 64-HQAM, coding rate ½, R=2250m

With reuse 1/3, the base stations of the topology including fixed relays (FR) with TD=2.5W, provide the highest coverage (considering the coverage provided by BSs and RSs) followed by the topology with FR of TD=10W, the smallest coverage belongs to reuse 1. However, only reuse 1/3 with TD=2.5W is close to the reference value of 95% coverage. This is explained because the use of RSs allows the system to extend the coverage of BSs (especially at cell borders, see figure 7) without significant increase in intercell interference since RSs transmit with only 2.5W compared to 40W used by BSs. Depending on the value of transmitted power a cell area with different radius was considered. For TD=10W, the radius is R_relay=1500m and if TD=2.5W, R_relay=1000m. The results of Figures include the two R-relay values and show about the same normalized coverage independently of the transmitted power (TD). In this sense, smaller TD is preferable to get higher power saving reduction and coverage gain.

Reuse 1 schemes have the worst overall performance as expected, since intercell interference in these is very high.

Figure 4 presents results for the same scenario in Figure 3, but using coding rate 3/4. In these case the performance of all schemes is greatly reduced due to higher coding rate used combined with 64QAM modulation and cell radius of 2250m. The same analysis done to Figure 3 can be applied, as we can see that reuse 1/3 with FRs provide the best coverage results and the smallest coverage belonging to reuse 1 scheme.

Figure 5 and Figure 6, present the results for the same scenarios but using hierarchical 16QAM (16-HQAM) instead. We can observe that with 16-HQAM there is a generalized gain in terms of coverage when compared to 64-HQAM. This is due to 16-HQAM being a lower level modulation, thus being more robust to fading and multi-cell interference. There is not a single 64-HQAM based scheme that is capable of achieving 95% coverage, therefore the use of lower coding rate (Figure 3), MIMO/SISO coordination with macro-diversity combining 2 radio links and hierarchical 16QAM is advised, to achieve the reference value.

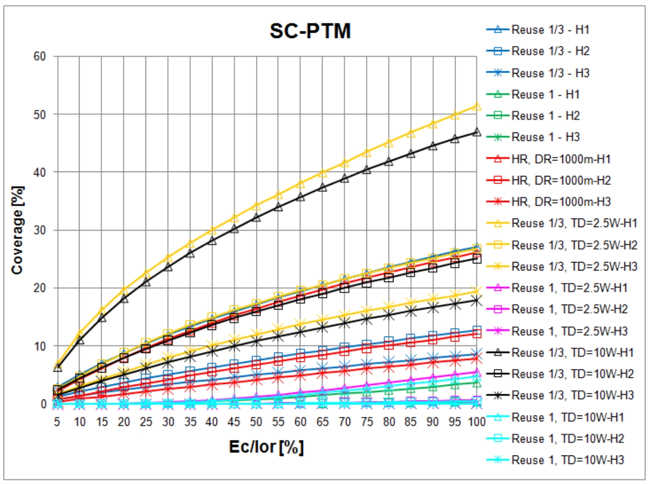

Figure 4. Coverage vs Ec/Ior SC-PTM (1RL) scenario, 64-HQAM, coding rate ¾, R=2250m

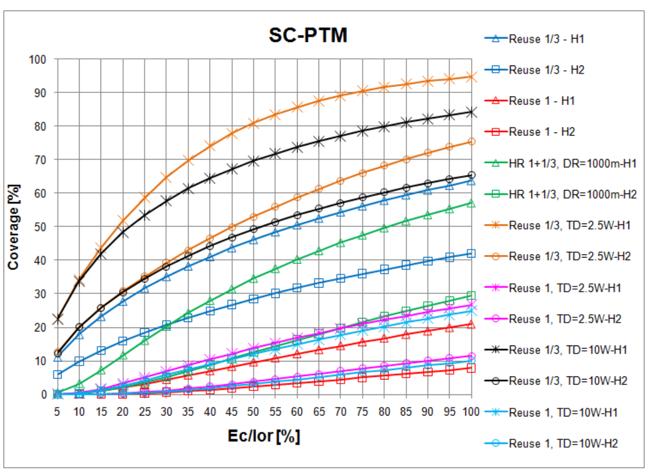

Figure 5. Coverage vs Ec/Ior SC-PTM (1RL) scenario, 16-HQAM, coding rate ½, R=2250m

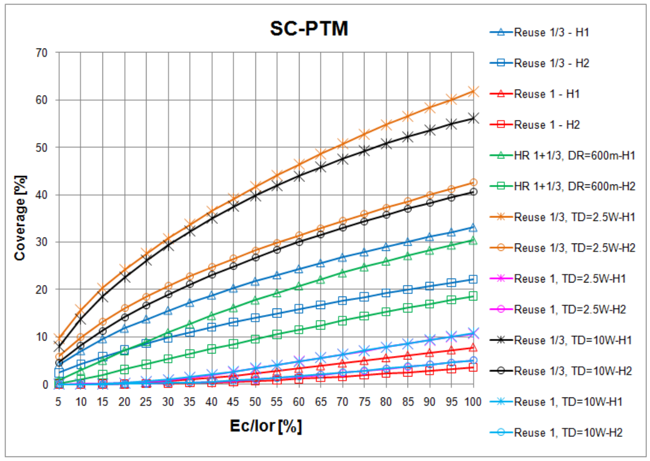

Figure 6. Coverage vs Ec/Ior SC-PTM (1RL) scenario, 16-HQAM, coding rate ¾, R=2250m

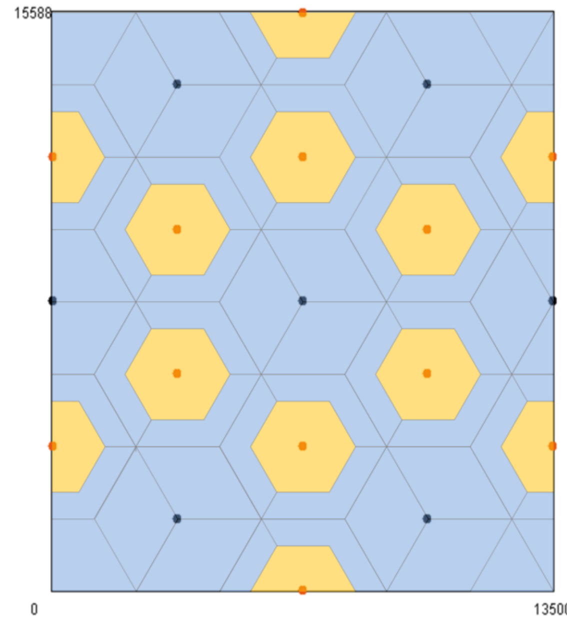

Figure 7. Coverage of Fixed Relays, and Base Stations, R=2250m.

The best results for 16-HQAM are achieved with reuse 1/3 with TD = 2.5W and reuse 1/3 with TD =10W.

In Figure 8, the coverage performance curves for MBSFN scenario, versus Ec/Ior, are presented for cell radius of 2250m and should be compared to the corresponding results of Figure 3 for the SCPTM scenario. As expected there is a difference in the coverage between the two scenarios where MBSFN takes advantage of its lower inter-cell interference. The coverage values for reuse 1/3 H1 and H2 blocks is above 95% followed by reuse 1/3 with FR with TD=2.5W. The coverage of reuse 1 is the lowest. Reuse 1/3 can also introduce some energy saving advantage over other schemes since with just only 15% of Ec/Ior it can achieve coverage for H1 blocks over 95%, and furthermore, with just 50% of Ec/Ior the coverage for H1 and H2 blocks surpasses 95%.

There is no significant advantage in terms of coverage from using relay stations (RSs), since reuse 1/3 is better. This is due to the small amount of inter-cell interference in MBFSN scenario. However, as (RSs) have smaller transmission powers the comparison should take into account the reduction of the transmitted power in all the area. There are 12 RSs and 7 BSs in all area resulting in power saving advantage with RSs, especially with TD=2.5W.

Hybrid reuse with DR=1350m also achieves coverage values around 95%, and because it can use reuse 1 (for higher throughputs) and reuse 1/3 (for higher coverage) simultaneously it can be a good compromise between throughput vs. coverage. The coverage of reuse 1 is the lowest.

Figure 9 corresponds to Figure 8, but considering coding rate 3/4. In this case there is a reduction in coverage achieved for all schemes, and only reuse 1/3 and hybrid reuse can achieve 95% coverage. Reuse 1 has the worst coverage.

When we move to 16-HQAM (Figure 10 and Figure 11), we see that the coverage values improve slightly for all schemes, especially for reuse 1 based schemes. We also observe that with the same Ec/Ior, 16-HQAM modulation achieves higher coverage values than those of 64-HQAM, showing that using lower modulation schemes can improve coverage values and achieve power transmission savings.

Another important technique is the use of spatial multiplexing (MIMO) associated to signal space diversity (SSD) provided by CRM to enhance the capacity. The spectral efficiency of QPSK, 2x2MIMO is equivalent to H16QAM with SISO. Figure 12 and Figure 13 present the coverage vs. the fraction of the total transmitted power, for different coding rates considering the SC-PTM and MBSFN scenarios, respectively. Instead of H1 and H2 blocks now we have Antenna 1 (A1) and Antenna 2 (A2) blocks, where the coverage of each antenna is about the same. In the MBSFN scenario, we consider the existence of coordinated MIMO transmission, i.e., with macro-diversity combining the three best radio links. In addition to reuse 1/3, reuse 1 is also evaluated. As expected the coverage of reuse 1/3 is higher than the reuse 1 due to less inter-cell interference. With reuse 1/3 both coding rates assure the 95% coverage. The MBSFN scenario is preferable than SC-PTM because MBSFN takes advantage of its lower inter-cell interference.

Figure 16 and Figure 17 present the coverage vs. the fraction of the total transmitted power, for coding rate 1/2 and 3/4 respectively, considering the SC-PTM scenario and 4x4MIMO. Figures 11 and 12 correspond to the Figure 14 and Figure 15 but considering the MBSFN scenario.

The results are similar to the ones obtained to 2x2 MIMO. The coverage of reuse 1/3 is higher than the reuse 1 due to less inter-cell interference and the MBSFN scenario is better than SC-PTM because MBSFN takes advantage of its lower inter-cell interference. As expected, the code rate ½ presents better coverage than ¾.

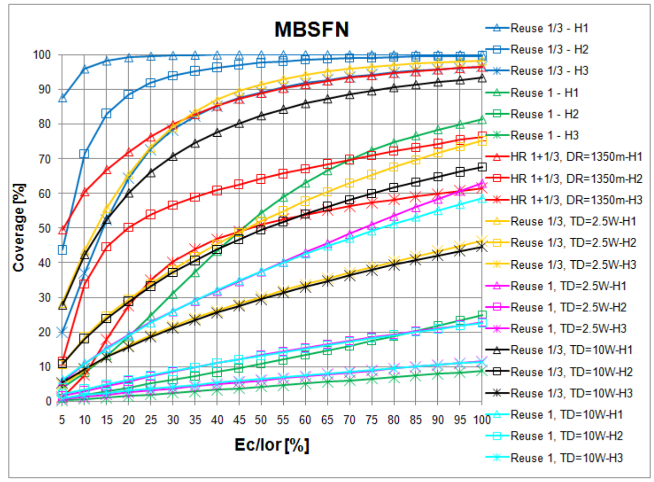

Figure 8. Coverage vs Ec/Ior for MBSFN scenario, 64-HQAM, coding rate ½, R=2250m

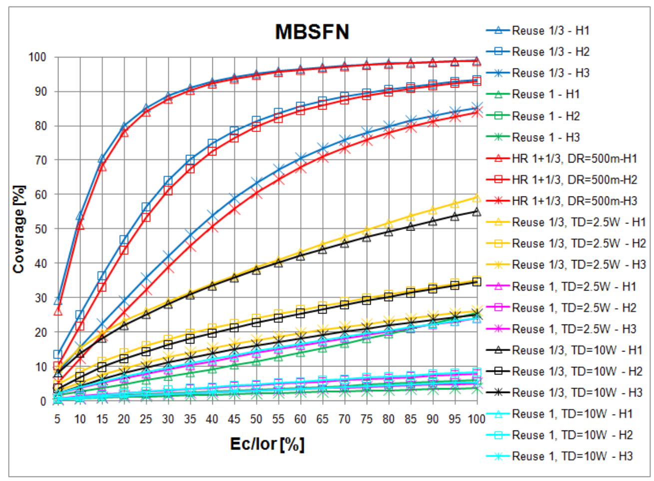

Figure 9. Coverage vs Ec/Ior for MBSFN scenario, 64-HQAM, coding rate ¾, R=2250m

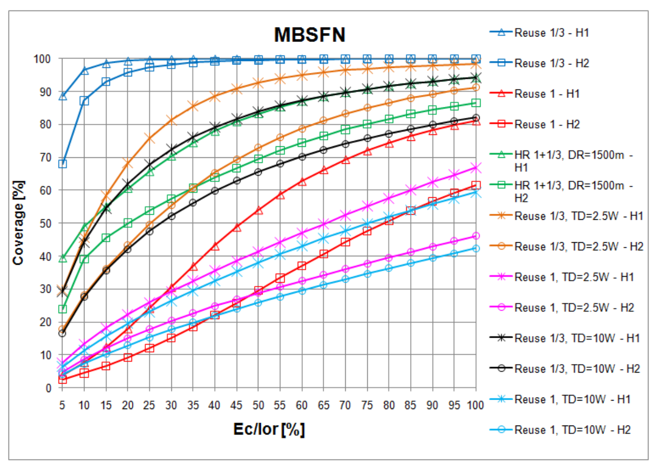

Figure 10. Coverage vs Ec/Ior for MBSFN scenario, 16-HQAM, coding rate ½, R=2250m

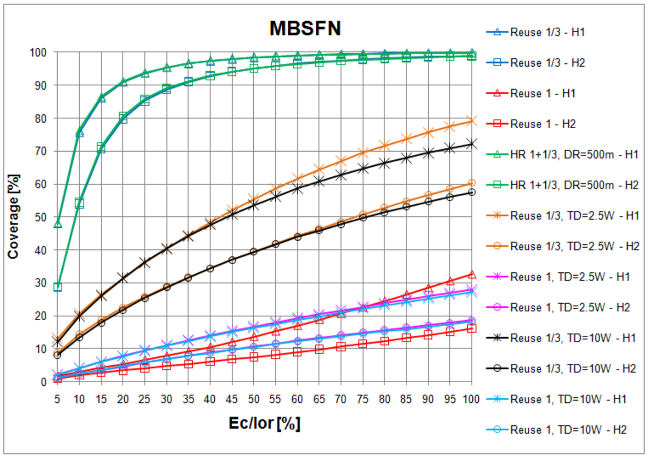

Figure 11. Coverage vs Ec/Ior for MBSFN scenario, 16-HQAM, coding rate ¾, R=2250m

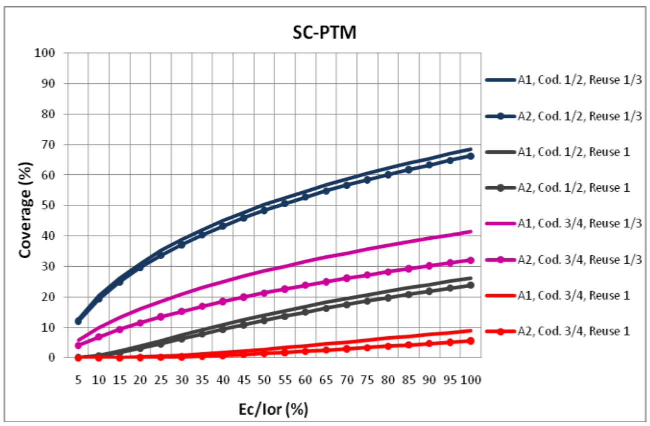

Figure 12. 2x2MIMO coverage (%) vs. Ec/Ior (%), for SC-PTM scenario, R=2250m

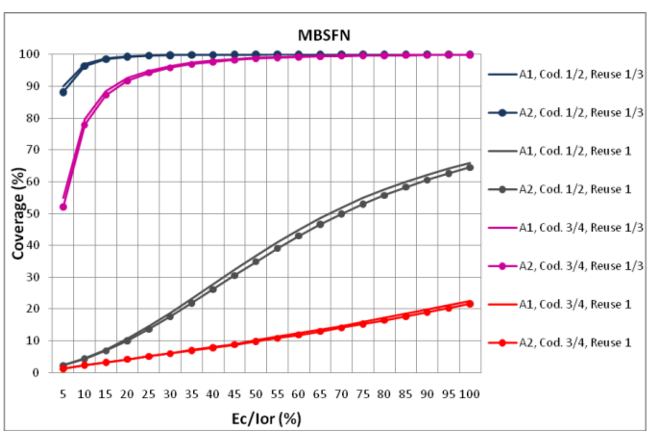

Figure 13. 2x2MIMO coverage (%) vs. Ec/Ior (%), for MBSFN scenario, R=2250m

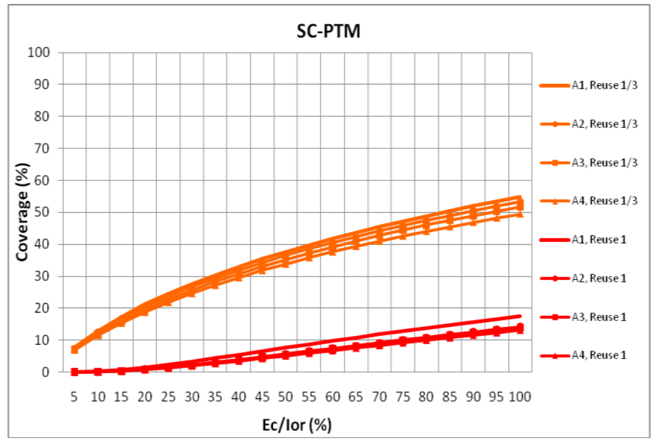

Figure 14. 4x4MIMO coverage (%) vs. Ec/Ior (%), for SC-PTM scenario, coding rate ½, R=2250m

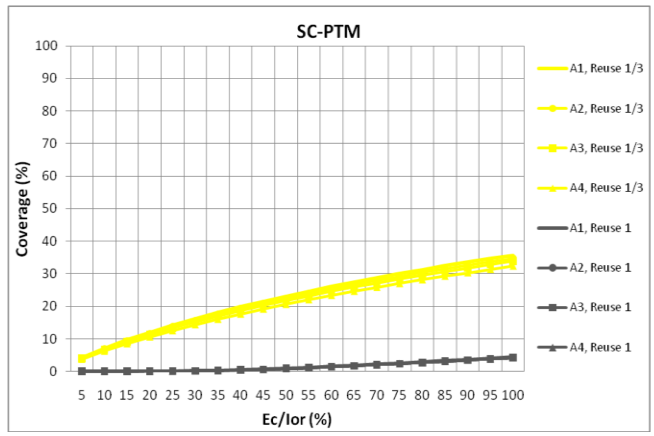

Figure 15. 4x4MIMO coverage (%) vs. Ec/Ior (%), for SC-PTM scenario, coding rate ¾, R=2250m

Throughput Results

Figure 18 presents the average throughput distribution as function of Ec/Ior for H64QAM, coding rate 1/2 and the SC-PTM scenario without macro-diversity combining (1RL) for R=2250m and different reuse schemes. Here the results for schemes using BSs and RSs represent the joint throughput of those. We observe that the maximum throughput is achieved in the reuse 1/3 topology and RSs with TD=2.5W, as expected from the corresponding

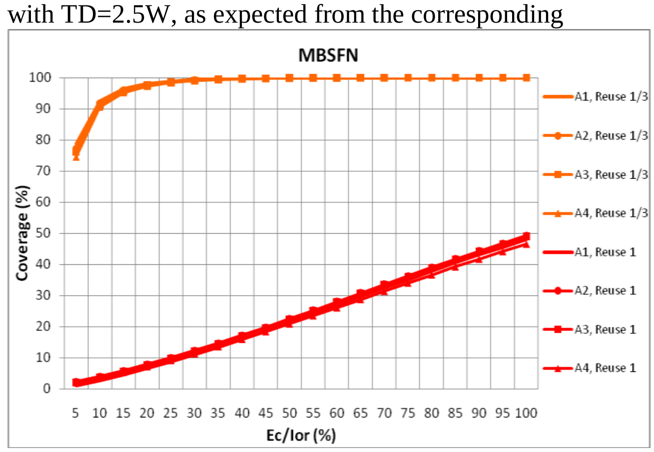

Figure 16. 4x4MIMO coverage (%) vs. Ec/Ior (%), for MBSFN scenario, coding rate ½, R=2250m

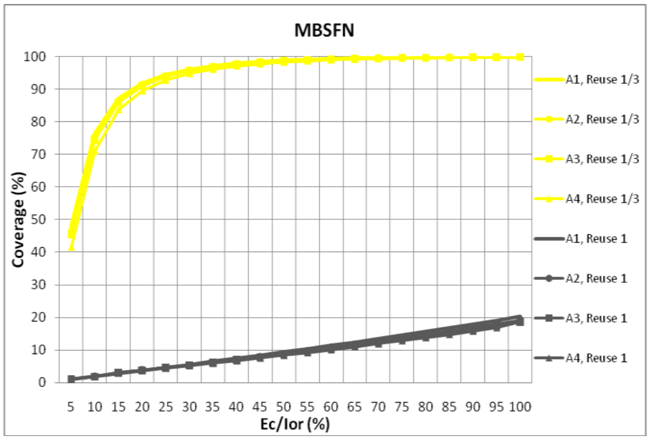

Figure 17. 4x4MIMO coverage (%) vs. Ec/Ior (%), for MBSFN scenario, coding rate ¾, R=2250m

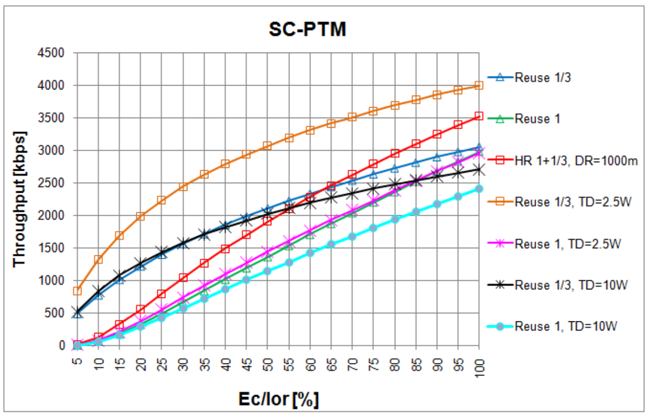

Figure 18. Throughput vs Ec/Ior for SC-PTM 64-HQAM, coding rate ½, Base Stations.

coverage values presented in Figure 3. HR is the second best, since it combines the coverage values achieved by using reuse 1/3 with the higher throughput achieved in the zones where users can use reuse 1.

With reuse 1/3 and RSs it was possible to increase the throughput compared to the single reuse 1/3, confirming the importance of having RSs in the cell area. Due to the smaller coverage, reuse 1 achieves the smallest throughput in spite of its higher inherent throughput. Users located closer to the base station have smaller inter-cell interference and higher throughput when reuse 1 is employed.

Figure 19 shows the respective throughput achieved only by RSs in Figure 18. As we can see, RSs have lower throughputs when compared to BSs, due to having transmission gaps where no information is transmitted and reduced power output. However, as we saw in Figure 18, the overall throughput when using a combination of BSs and RSs for SC-PTM is higher than those achieved by reuse 1 or 1/3, because BSs achieve significant higher throughputs when exists interfering RSs instead of BSs.

Figure 20 corresponds to previous Figure 18 but considering coding rate 3/4. We observe that the maximum throughput is achieved for reuse 1/3 and RS with TD=2.5W, followed by reuse 1/3 and RS with TD=10W. This was already expected due to higher coverage associated to less inter-cell interference provided when reuse 1/3 schemes are used. We also denote that increasing the RS power output, from TD=2.5W to TD=10W slightly decreases maximum throughput, since RS transmitting with higher power will increase inter-cell interference, and reduce overall coverage as illustrated in Figure4. The results for RSs are presented in Figure 21. Again, RSs have lower throughput than BSs, but their reduced power output and transmission gaps greatly reduce intercell interference in neighbor cells, improving signal conditions and throughput in those.

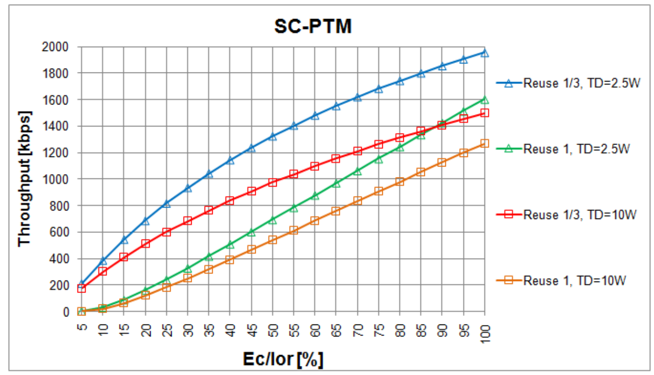

Figure 19. Throughput vs Ec/Ior for SC-PTM, 64-HQAM, coding rate ½, Relay Stations.

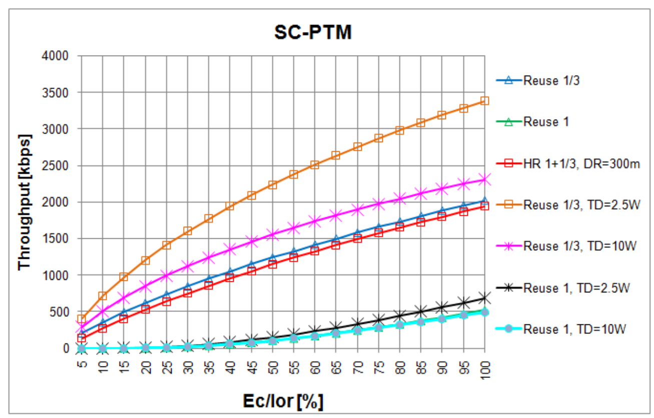

Figure 20. Throughput vs Ec/Ior for SC-PTM 64-HQAM, coding rate ¾, Base Stations.

Figure 22 corresponds to Figure 18 but for MBSFN network. Hybrid reuse 1+1/3 achieves maximum throughput, followed by reuse 1 and reuse 1/3. This was already expected due to its higher coverage associated to less inter-cell interference provided by the SISO coordination of the MBSFN network. For this scenario, using RS is not essential due to the SISO coordination that increases both coverage and throughput, in particular, users located at the cell borders. Figure 24 and Figure 25 present the results considering coding rate 3/4. For this scenario the best results are achieved for hybrid reuse 1+1/3 and reuse 1/3. Reuse 1 and RS throughput results are almost three times lower than reuse 1/3, denoting the lack of robustness of the signal when higher coding rates are used. Reuse 1/3 and hybrid reuse are a better choice since they employ interference coordination.

For 16-HQAM and SC-PTM (Figure 26 to Figure 29) the maximum throughput achieved for all transmission schemes is slightly lower than 64-HQAM (due to lower modulation). Reuse schemes where BSs and RSs, namely reuse 1/3 with TD=2.5W, hybrid reuse 1+1/3 and reuse 1/3 achieve the best results like 64-HQAM. Also increasing coding rate (from 1/2 to 3/4) reduces the maximum throughput of all schemes, reducing signal robustness to transmission errors and interference and reducing overall coverage of cell area.

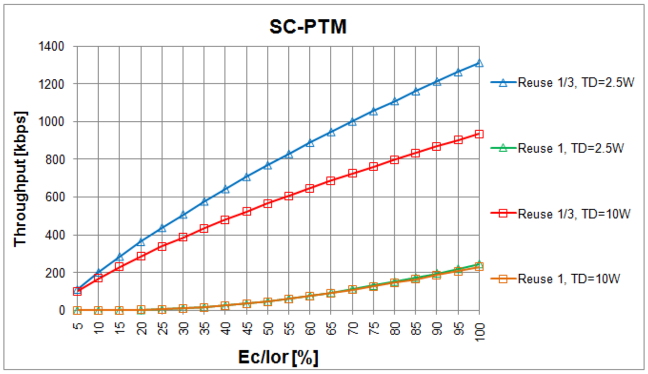

Figure 21. Throughput vs Ec/Ior for SC-PTM, 64-HQAM, coding rate ¾, Relay Stations.

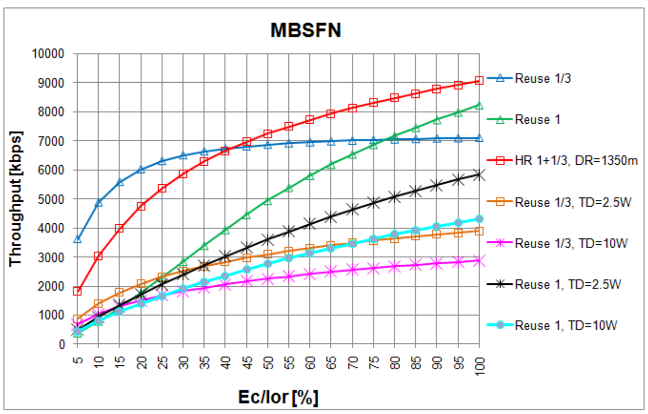

Figure 22. Throughput vs Ec/Ior for MBSFN 64-HQAM, coding rate ½, Base Stations.

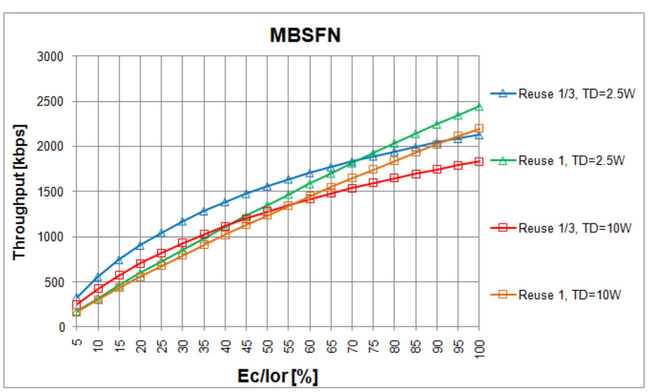

Figure 23. Throughput vs Ec/Ior for MBSFN, 64-HQAM, coding rate ½, Relay Stations.

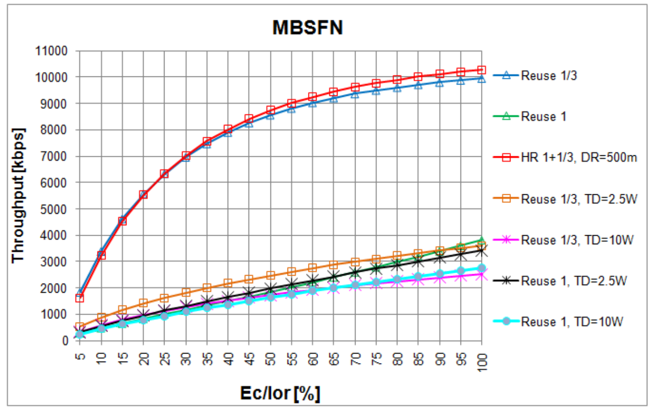

Figure 24. Throughput vs Ec/Ior for MBSFN 64-HQAM, coding rate ¾, Base Stations.

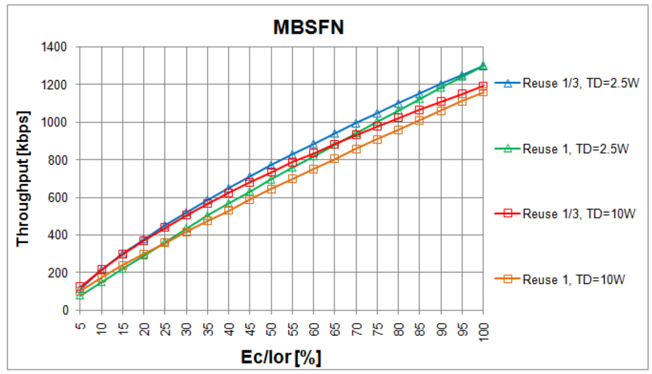

Figure 25. Throughput vs Ec/Ior for MBSFN, 64-HQAM, coding rate ¾, Relay Stations.

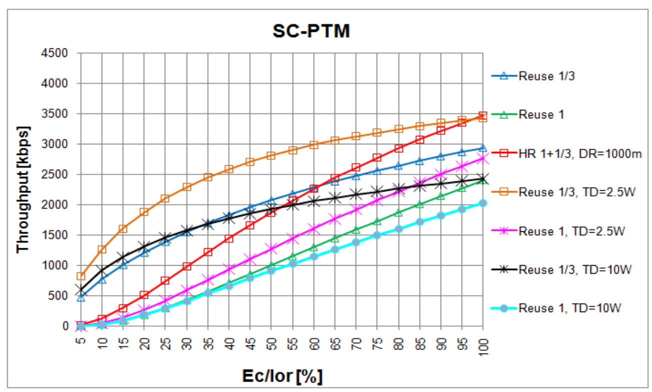

Figure 26. Throughput vs Ec/Ior for SC-PTM 16-HQAM, coding rate ½, Base Stations.

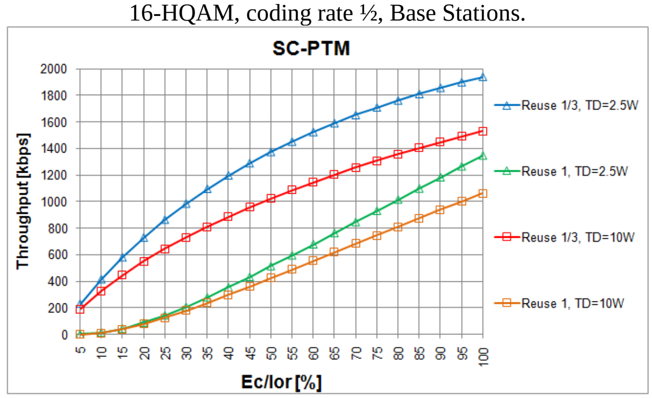

Figure 27. Throughput vs Ec/Ior for SC-PTM, 16-HQAM, coding rate ½, Relay Stations.

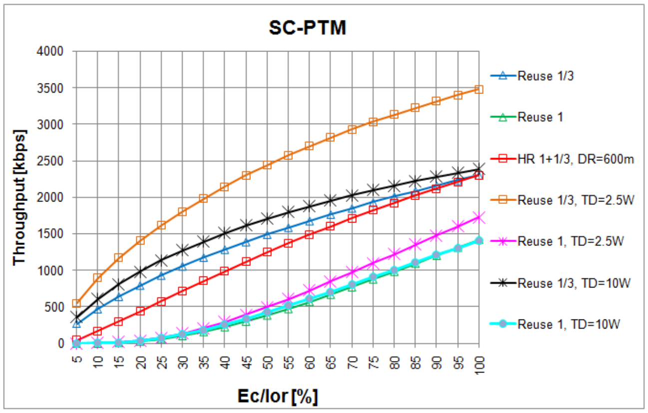

Figure 28. Throughput vs Ec/Ior for SC-PTM 16-HQAM, coding rate ¾, Base Stations.

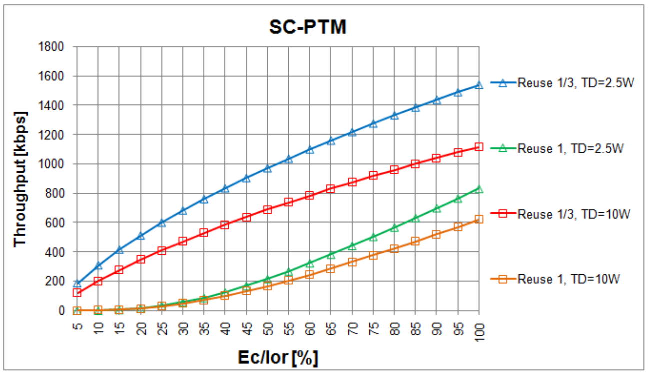

Figure 29. Throughput vs Ec/Ior for SC-PTM, 16-HQAM, coding rate ¾, Relay Stations.

Figure 30 to Figure 33 present the results for 16-HQAM and MBSFN network. When comparing the results for 16-HQAM (Figure 30) to 64-HQAM (Figure 22) when see that reuse 1 is now the reuse scheme that achieves higher spectral efficiency with around 10Mbps of throughput using all the transmission power available. This is happens because 16-HQAM is a modulation more robust and together with macro-diversity combining existing in MBSFN network allowing, this allows reuse one to take full advantage of using the total transmission bandwidth available.

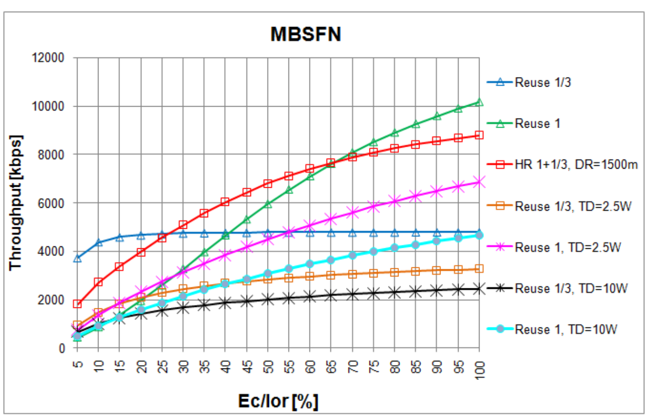

Figure 30. Throughput vs Ec/Ior for MBSFN 16-HQAM, coding rate ½, Base Stations.

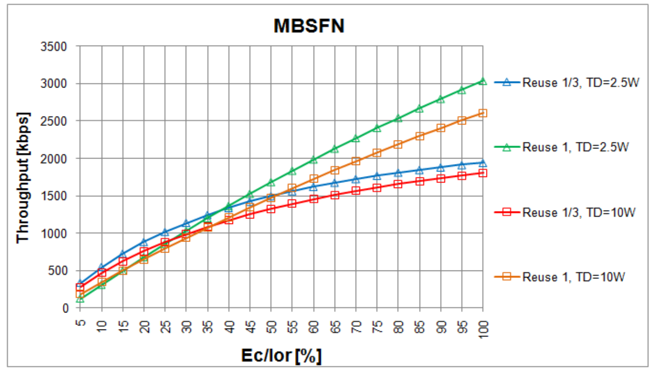

Figure 31. Throughput vs Ec/Ior for MBSFN, 16-HQAM, coding rate ½, Relay Stations.

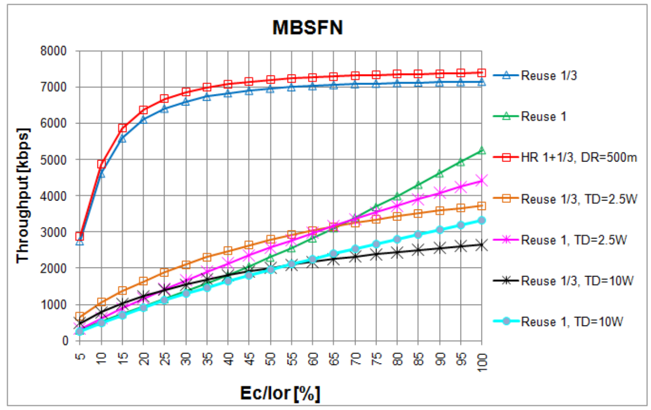

Figure 32. Throughput vs Ec/Ior for MBSFN 16-HQAM, coding rate ¾, Base Stations.

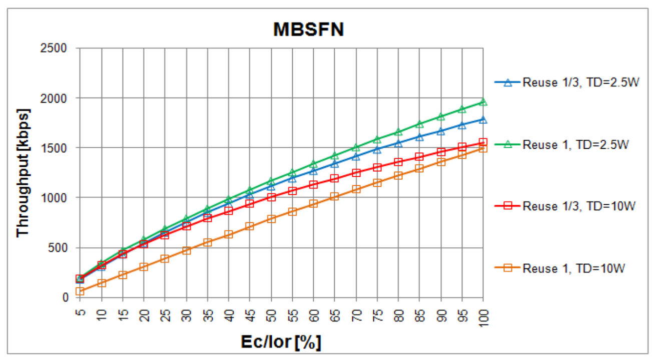

Figure 33. Throughput vs Ec/Ior for MBSFN, 16-HQAM, coding rate ¾, Relay Stations.

To increase the spectral efficiency at the cell borders we will check the use of 2x2 and 4x4 MIMO associated with QPSK modulation and SSD provided by CRM. Figures 34 and Figure 35 presents the average throughput vs Ec/Ior for both coding rates 1/2 and 3/4, for the SC-PTM and MBSFN scenarios using MIMO 2x2. Figures 36 and 37 correspond to the Figures 21 and 22 but considering 4x4 MIMO. Table II shows a comparison between the system spectral efficiency. We observe that the maximum throughput is achieved for coding rate 1/2, reuse 1 and reaches more than 1.7bps/Hz/cell, or 1.4bps/. The existence of coordinated MIMO transmission in a scenario as MBSFN, with macro-diversity combining the three best radio link, provides higher values of throughput.

Please note that E-MBMS services use dedicated carriers, and because of this, all the available transmission power can be used to achieve the results we present. This confirms the higher spectral efficiency of MIMO compared to 64-HQAM (presented in Figure 24) independently of the chosen reuse scheme. There is no advantage in using coding rate ¾ due to its lower coverage, in spite of higher maximum throughput.

IV. Conclusions

In this work, we have analyzed interference coordination methods for Evolved-Multimedia Broadcast/Multicast Service (E-MBMS) in Long-Term Evolution Advanced (LTE-A).

Based on the average coverage and throughput simulation results, for the SCPTM scenario it is recommended the use of reuse 1/3 and Relay Stations to increase the coverage and throughput of users located at cell borders.

For the MBSFN scenario we also recommend the use of reuse 1/3 or the hybrid reuse 1+1/3 due to their best compromise between coverage and maximum achieved throughput. Relay Stations are not necessary due to the availability of SISO coordination in the MBSFN scenario.

The introduction of signal space diversity, converted to frequency diversity in multi-path Rayleigh channels with OFDMA transmission and spatial multiplexing 4x4 and 2x2 MIMO enables enhancing the spectral efficiency at the cell borders of MBSFN. The coding rate 1/2, reuse 1 provides the highest spectral efficiency. It is not recommended to increase the coding rate within the MBSFN network to not decrease the throughput at the cell borders.

Acknowledgment

This work was supported by the internal Instituto de Telecomunicações (IT) project designated as COILS.

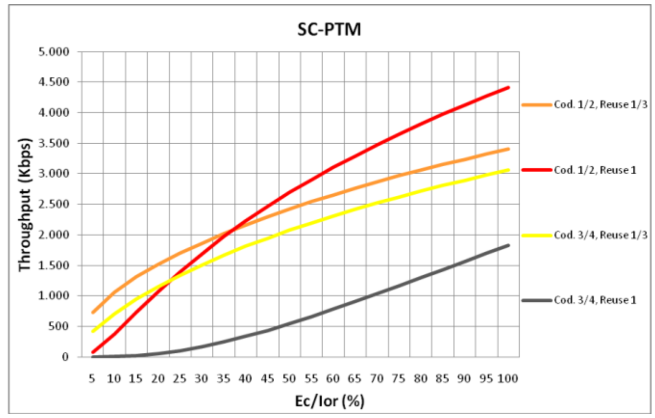

Figure 34. 2x2MIMO Throughput vs Ec/Ior for SC-PTM scenario

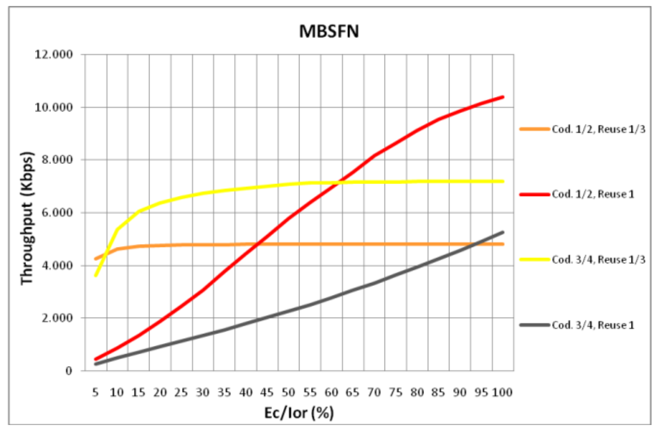

Figure 35. 2x2MIMO Throughput vs Ec/Ior for MBSFN scenario

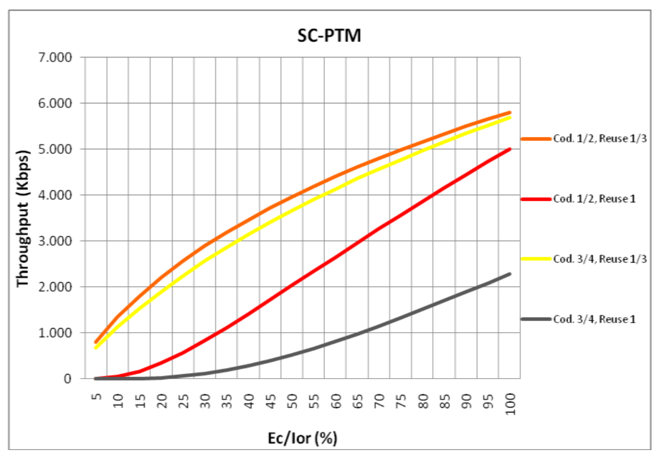

Figure 36. 4x4MIMO Throughput vs Ec/Ior for SC-PTM scenario

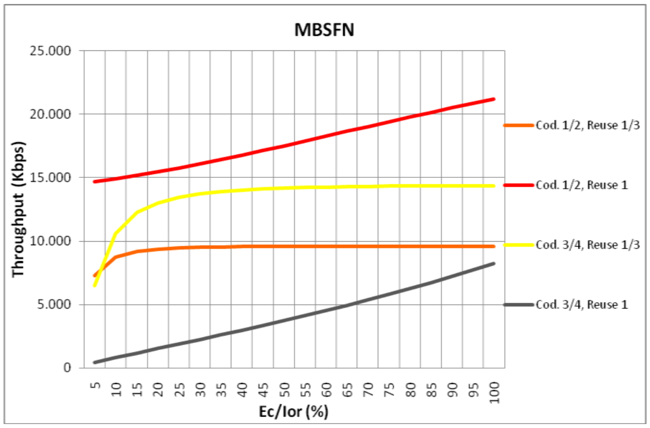

Figure 37. 4x4MIMO Throughput vs Ec/Ior for MBSFN scenario

Reuse Type	*Scenario*	*Coding*	*Fixed Relay Power (W)*	*System spectral efficiency ((bit/s)/Hz per site)*
Reuse 1/3	SCPTM	3/4	*N.A.*	0.125
			2.5	0.310
			10	0.345
	MBSFN	3/4	*N.A.*	0.760
			2.5	0.302
			10	0.310
	MBSFN – MIMO 2x2	1/2	*N.A.*	0.540
		3/4	*N.A.*	0.720
	MBSFN – MIMO 4x4		*N.A.*	0.920
			N.A.	1.480
Reuse 1	SCPTM	3/4	*N.A.*	0.010
			2.5	0.025
			10	0.022
	MBSFN	3/4	*N.A.*	0.140
			2.5	0.240
			10	0.245
	MBSFN – MIMO 2x2	1/2	*N.A.*	1.100
		3/4	*N.A.*	0.530
	MBSFN – MIMO 4x4	1/2	*N.A.*	2.080
		3/4	*N.A.*	0.830
Hybrid (1+1/3)	SCPTM	1/2	*N.A.*	0.350
	MBSFN	3/4	*N.A.*	1.000

TABLE II. SYSTEM SPECTRAL EFFICIENCY FOR 64-HQAM AND MIMO

References

[1] P. Gomes, J. Seguro, A. Correia, "MIMO Coordnation for E-MBMS Transmissions in LTE-A", 6th International Conference on Wireless and Mobile Communications (ICWMC'2010), Valencia, Spain, pp. 291-296, September 2010.

[2] 3GPP, "Feasibility Study on Improvement of the Multimedia Broadcast Multicast Service (MBMS); (Release 7)", TR 25.905 v7.2.0 (2009-12). http://www.3gpp.org [last access; June 24, 2010]

[3] 3GPP, "Physical Layer Aspects for Evolved UTRA; (Release 7)", TR 25.814 v7.1.0 (2009-12). http://www.3gpp.org [last access; June 24, 2010]

[4] I. Katzela and M. Naghshineh, "Channel Assignment Schemes for Cellular Mobile Telecommunication Systems: A Comprehensive Survey", *IEEE Personal Communications*, vol. 3, pp. 10-31, June 1996.

[5] C. X. Wang et al. "Cooperative MIMO Channel Models: A Survey", *IEEE Communications Magazine*, vol. 48, pp. 80-87, February 2010.

[6] J. Seguro, P. Gomes, N. Souto, A. Correia, R. Dinis,"Rotation Matrices for OFDM Transmission", IEEE EUROCON'2011, Lisbon, Portugal, April 2011.

[7] A. Correia, "Optimised Complex Constellations for Transmitter Diversity, WPC Journal, Kluwer Pub., pp. 267-284, 2002

[8] M. Silva, A. Correia, R. Dinis, N. Souto, J. Silva, "Transmission Techniques for Emergent Multicast and Broadcast Systems", CRC Press, 2010

[9] L. Song, J. Shen, "Evolved Cellular Optimisation for UMTS and LTE", CRC Press, 2010

[10] CX Wang et. Al. "Cooperative MIMO Channels: A Survey", IEEE Communications Magazine, Feb. 2010, pp. 81-87

[11] S. Ma, Y. Yang & H. Sharif "Distributed MIMO Technologies in Cooperative Wireless Networks", IEEE Communications Magazine, May 2011, pp. 78-82

[12] T. Salvalaggio, "On the Application of Reuse Partitioning", in *IEEE 38th Vehicular Technology Conference*, Philadelphia, pp. 182-185, June 1988.

[13] G. Fodor, "Performance Analysis of a Reuse Partitioning Technique for OFDM Based Evolved UTRA", in *IEEE 14th International Workshop on QoS*, New Haven, pp. 112-120, June 2006.

[14] 3GPP, "Evolved-UTRA Radio Frequency (RF) System Scenarios; (Release 9)" TR 36.942 v9.2.0 (2009-12). http://www.3gpp.org [last access; June 24, 2010]

Transformation of any Adding Signal Technique in Tone Reservation Technique for PAPR Mitigation thanks to Frequency Domain Filtering

Désiré Guel, Jacques Palicot
SUPELEC/IETR
Avenue de la Boulaie CS 47601
F-35576 Cesson-Sévigné cedex, France
{desire.guel, jacques.palicot}@supelec.fr

***Abstract*—Orthogonal Frequency Division Multiplexing (OFDM) suffers from a high Peak-to-Average Power Ratio (PAPR). Tone Reservation (TR) is a popular PAPR reduction technique that uses a set of reserved subcarriers to carry the peak reducing signal. The major advantages of TR technique include no transmission performance degradation, no transmission of Side Information (SI) and downward compatibility. Because of all these benefits, TR seems to be promising for use in commercial standards such as Digital Video Broadcasting-Terrestrial (DVB-T2). Thanks to a frequency domain filtering , in this paper, which is an extension of [1], we propose Classical Transformation (CT) and Adaptive Transformation (AT) algorithms to transform Adding Signal techniques (like clipping techniques) to TR techniques in order to benefit of the TR advantages. As the transformation is a low-complexity process (about the FFT/IFFT complexity), the obtained technique results in a low-complexity TR technique. However, the transformation generates a loss of performance in PAPR reduction, which can be improved by iterating the process of transformation. Later in the paper, several Adding Signal techniques (as well-known clipping techniques) are transformed to TR techniques. Performance comparisons are done based on Complementary Cumulative Distribution Function (CCDF), Bit Error Rate (BER) and Power Spectral Density (PSD) metrics. The simulation results showed that, at the same PAPR reduction gain, CT algorithm is 2 times more complex than AT algorithm.**

***Keywords*-Orthogonal Frequency Division Multiplexing (OFDM), Peak-to-Average Power Ratio (PAPR), Frequency Domain Filtering, Clipping Techniques.**

I. Introduction

Orthogonal Frequency Division Multiplexing (OFDM), although used in standards such as IEEE 802.11a/g, IEEE 802.16, HIPERLAN/2 and Digital Video Broadcasting (DVB) [2], suffers from high Peak-to-Average Power Ratio (PAPR). Large PAPR requires a linear High Power Amplifier (HPA), which is inefficient. Moreover, the combination of an insufficiently linear HPA range and large PAPR leads to in-band and out-of-band distortion [3]. Several PAPR reduction techniques have been proposed [4–7]. The simplest way to reduce PAPR is to deliberately clip and filter the OFDM signal before amplification. However, clipping is a nonlinear process and may cause significant distortion that degrades the Bit Error Rate (BER) and increase adjacent out-of-band carriers [8].

Some techniques use coding, in which a data sequence is embedded in a larger sequence and only a subset of all the possible sequences is used to exclude patterns with high PAPR [9]. These techniques require receiver modifications to decode the received signal. Also, multiple signal representation techniques have been proposed. These include Partial Transmit Sequence (PTS) technique [10], Selected Mapping technique (SLM) [11] and interleaving technique [12]. Theses methods reduce the PAPR by controlling the phase of the data subcarriers, which provides an effective solution. However, they are computationally expensive due to multiple IFFTs and exhaustive search to find optimal phase sequences; also they require transmitting continuous SI to the receiver, which degrades the capacity of the system. The overall BER performance may also be degraded if there are errors in the SI [5].

PAPR can be reduced by the Adding Signal techniques [13], which are very simple techniques to implement and have become very attractive. Tone Reservation (TR) [14], which is a particular Adding Signal technique is a popular PAPR reduction technique that uses a set of reserved subcarriers to design a peak reducing signal. TR technique does not distort data-bearing subcarriers. Also, it not only eliminates the need for SI, but also prevents the BER degradation, as occurs with other techniques. However, TR technique requires an efficient generation of the peak-reducing signal. The optimal peak-reducing signal generation is obtained by solving a Quadratically Constrained Quadratic Program (QCQP), which is a type of convex optimization problem [14]. Although the optimum of a QCQP exists, it is shown in [14] that the solution requires a high computational cost of $\mathcal{O}\left(N_r N^2 L\right)$, where N_r is the number of the reserved subcarriers, N is the number of subcarriers and L is the oversampling factor. The authors of [15] propose an optimal peak-reducing signal based on Second Order Cone programming (SOCP) formulation of QCQP problem. Since finding the optimal solution to QCQP problem is computationally demanding, an iterative way to reduce PAPR was also proposed [14, 16].

In [1], we proposed a tranformation algorithm to transform Classical clipping in TR clipping. This paper is an extension of [1], in which we propose two transformation algorithms the classical algorithm (algorithm from [1]) and an adaptative algorithm. Moreover, we apply these two transformations on several Adding Signal techniques like Geometrical method [17] and several types of clipping [18].

The remainder of this paper is organized as follows: Section II introduces the OFDM systems. Section III briefly reviews the Adding Signal techniques principle, gives some examples of these techniques and focuses on the TR techniques, which are specific Adding Signal techniques. Section IV describes the principle of the digital filter based on FFT/IFFT pair and derives the CT and AT algorithms. In Section V CT and AT algorithms are applied for PAPR reduction in a Wireless Local-Area-Network (WLAN) system, to two Adding Signal techniques and simulation results are provided, while in Section VI a conclusion is drawn.

II. OFDM Systems and PAPR issue

The basic idea underlying OFDM systems is the division of the available frequency spectrum into several subcarriers. To obtain a high spectral efficiency, the frequency responses of the subcarriers are overlapping and orthogonal, hence the name OFDM. This orthogonality can be completely maintained with a small price in a loss in SNR, even though the signal passes through a time dispersive fading channel, by introducing a cyclic prefix (CP).

The continuous-time baseband representation of an OFDM symbol is given by

$$x(t) = \frac{1}{\sqrt{N}} \sum_{k=0}^{N-1} X_k e^{j2\pi f_k t}, \quad 0 \le t \le T_s \ , \qquad (1)$$

where N data symbols X_k form an OFDM symbol $\mathbf{X} = [X_0, \cdots, X_{N-1}]$, $f_k = \frac{k}{T_s}$ and T_s is the time duration of the OFDM symbol.

In practice, OFDM signals are typically generated by using an Inverse Discrete Fourier Transform (IDFT) as described by the block diagram in Fig. 1.

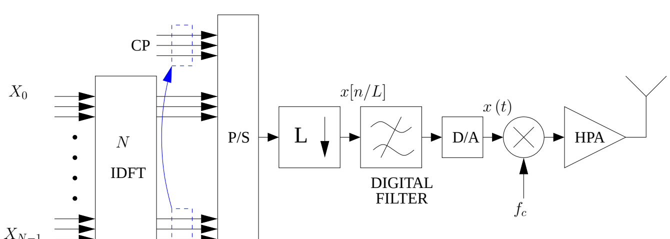

Figure 1: OFDM Transmitter Block Diagram.

The OFDM symbol represented by the vector $\mathbf{X} = [X_0 \cdots X_{N-1}]^T$ is transformed via IDFT into T_s/N-spaced discrete-time vector $\mathbf{x} = x[n] = [x_0 \cdots x_{N-1}]^T$, i.e.

$$x_n = \frac{1}{\sqrt{N}} \sum_{k=0}^{N-1} X_k e^{j2\pi \frac{n}{N} k}, \quad 0 \le n \le N-1 \ . \qquad (2)$$

In this paper, the discrete-time indexing $[n]$ denotes Nyquist Rate samples. Since oversampling may be needed in practical designs, we will introduce the notation $x[n/L]$ to denote oversampling by L. Several different oversampling strategies of $x[n/L]$ can be defined. From now on, the oversampled IDFT output will refer to oversample of (2), which is expressed as follows:

$$x[n/L] \ = \frac{1}{\sqrt{N}} \sum_{k=0}^{NL-1} X_k e^{j2\pi \frac{n}{NL} k}, \ 0 \le n \le NL-1 \ . \qquad (3)$$

The above expression (3) can be implemented by using a length-(NL) IDFT operation with the input vector

$$\mathbf{X}^{(\mathrm{L})} = \left[\ X_0, \cdots, X_{\frac{N}{2}-1}, \quad \underbrace{0, \cdots, 0}_{(L-1)N \ \text{zeros}} \quad X_{\frac{N}{2}}, \cdots, X_{N-1} \ \right].$$

Thus, $\mathbf{X}^{(\mathrm{L})}$ is extended from $\mathbf{X}$ by using the so-called zero-padding scheme, i.e., by inserting $(L-1)N$ zeros in the middle of $\mathbf{X}$, i.e.,

$$X_k^{(\mathrm{L})} = \begin{cases} X_k, & k \in \mathcal{S}_1 \\ 0, & k \in \mathcal{S}_2 \end{cases} ,$$

where $\mathcal{S}_1$ and $\mathcal{S}_2$ are the set of in-band (IB) indices and out-of-band (OOB) indices respectively.

The cost of transceiver components depends on the dynamic range of the signals. In the literature, the envelope variations are often described in terms of the crest-factor (CF), peak-to-mean envelope power ratio (PMEPR) or simply peak-to-average power ratio (PAPR). In this paper, we adopt the terms PAPR to quantify the envelope excursions of the signal. The PAPR of the signal $x(t)$ may be defined as

$$\mathrm{PAPR}_{[x]} \triangleq \frac{\max\limits_{t \in [0,T_s]} |x(t)|^2}{\mathcal{P}_x}, \qquad (4)$$

where $\mathcal{P}_x = E\left\{|x(t)|^2\right\}$ is the average signal power and $E\{.\}$ is the statistical expectation operator. Note that, in order to avoid aliasing the out-of-band distortion into the data bearing subcarriers and in order to accurately describe the PAPR, an oversampling factor $L \ge 4$ is required.

In the literature, it is customary to use the Complementary Cumulative Distribution Function (CCDF) of the PAPR as a performance criterion. It is denoted as

$$\mathrm{CCDF}_{[x]}(\psi) \triangleq \Pr\left\{\mathrm{PAPR}_{[x]} \ge \psi\right\}.$$

If N is large enough, based on the central limit theorem, the real and imaginary parts of OFDM $x(t)$ have Gaussian distribution and its envelope will follow a Rayleigh distribution. This implies a large PAPR. In [19], it is shown that the mean of the PAPR, which is a random variable, can be approximated to

$$E\,[\mathrm{PAPR}] \simeq \mathrm{C}_{(\mathrm{Euler})} + \ln[N], \tag{5}$$

where $\mathrm{C}_{(\mathrm{Euler})}$ is the Euler's constant defined bellow

$$\mathrm{C}_{(\mathrm{Euler})} = \lim_{N\to\infty}\left[\sum_{k=1}^{N}\frac{1}{k} - \ln[N]\right] \simeq 0.57721.$$

III. Adding Signal Techniques for PAPR Reduction

There are several different techniques for PAPR reduction, in this section, we present the Adding Signal techniques principle and then we focus on the TR techniques, which are specific Adding Signal techniques for PAPR reduction.

A. Adding Signal Techniques Principle

In Adding Signal context, the PAPR is reduced by adding a signal called sometimes "peak reducing signal" or "peak canceling signal". Many well known PAPR reduction techniques of the literature such us Tone Reservation (TR) [14], Tone Injection (TI) [14, 20], Geometric Approach for PAPR reduction method [17] are known as Adding Signal techniques. In [13], it is shown that any form of clipping can be formulated as an Adding Signal technique. The Adding Signal techniques consist of reducing the envelope of OFDM signal by adding a peak-reducing signal just before the HPA as shown in Fig. 2.

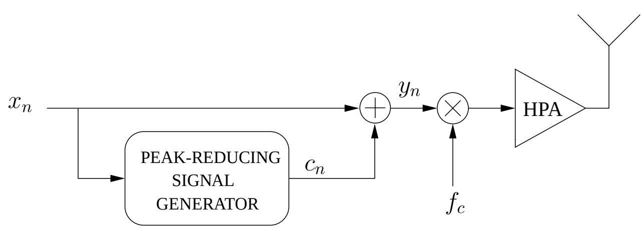

Figure 2: Adding Signal scheme for PAPR reduction.

Let $x_n, \quad n = 0, \cdots, NL-1$ be the L-times oversampled time-domain OFDM signal, where N is the number of subcarriers. The PAPR reduced signal is therefore expressed by

$$y_n = x_n + c_n, \quad n = 0, \cdots, NL-1. \tag{6}$$

The peak reducing signal c_n is computed according to PAPR reduction techniques. In [15], c_n is computed based on an optimization algorithm (SOCP) in frequency domain, while in [17], c_n is computed in time domain based on a Geometric approach. *S. Janaaththanan* et *al.* propose, in [16], to compute c_n in frequency domain with the Gradient algorithm, which is a low-complexity algorithm. In [13], the reducing signal c_n is computed in time domain based on a nonlinear function $f(.)$ called "function for PAPR reduction". Using $f(.)$ to reduce the PAPR of $x[n/L]$, the peak reducing signal c_n is written as

$$c_n = f(|x_n|)\, e^{j\varphi_n} - x_n, \tag{7}$$

where φ_n is the x_n phase.

B. Some Examples of Adding Signal Techniques

As préviously mentioned, depending on the way to generate the Adding Signal c_n, we obtain many different methods. In this section, we present the clipping techniques family [18], which could be easily seen as adding method and the geometrical method of [17].

1) Clipping techniques family: In the first subsection we formulate the classical clipping as an Adding Signal technique as described in Fig. 2, then in the second subsection we describe briefly four clipping techniques.

clipping technique formulated as an Adding Signal technique: Using the conventional clipping technique [8] to reduce OFDM PAPR, the output signal y_n, in terms of the input signal x_n is given as follows:

$$y_n = f(|x_n|)\, e^{j\varphi_n},$$

where φ_n is the x_n phase and $f(.)$ is the clipping function. As $f(.)$ is nonlinear function; according to Bussgang theorem [21], the output signal y_n can be written as

$$y_n = \alpha x_n + d_n, \quad \text{where} \quad \alpha = \frac{\mathcal{R}_{yx}(0)}{\mathcal{R}_{xx}(0)}. \tag{8}$$

$\mathcal{R}_{xx}(\tau)$ and $\mathcal{R}_{xy}(\tau)$ are autocorrelation and cross-correlation functions of the input signal and output signal. It is shown that the distortion term d_n is uncorrelated with the input signal x_n, i.e., $\mathcal{R}_{xd}(\tau) = 0$.

From (6) and (8), the peak-reducing signal c_n is expressed as

$$c_n = (\alpha - 1)\, x_n + d_n. \tag{9}$$

We see from (9) that, the peak-reducing signal depends on the distortion term resulting in the nonlinear process of the OFDM envelope.

several clipping techniques: It is obvious that in Eq. 9, the nonlinear clipping function is included in the α parameter. In this paragraph, we give some possible nonlinear function therefore some clipping techniques.

1) Classical Clipping (CC) technique
   The Classical Clipping (CC) proposed in [8] is one of the most popular clipping technique for PAPR reduction known in the literature [8, 22]. It is sometimes

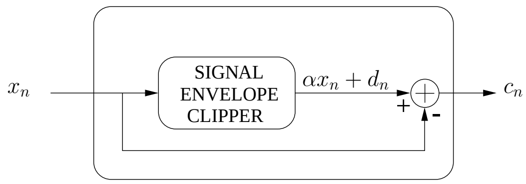

Figure 3: Peak-reducing signal generator block for clipping technique.

called hard clipping or soft clipping, to avoid any confusion, it is called Classical Clipping (CC) in this paper. In [8], its effects on the performance of OFDM, including the power spectral density, the PAPR and BER are evaluated. The function-based clipping used for CC technique is defined below and depicted in Fig. 5 (a).

$$f(r) = \begin{cases} r, & r \leq \mathrm{A} \\ A, & r > \mathrm{A} \end{cases} . \tag{10}$$

Where A is the clipping threshold. We derive now, a bound for the α parameter depending on the clipping threshold. This derivation, could be performed for every type of clipping function, but we restrict here it to the classical clipping function Let us consider the coefficient α defined in (8).

$$\begin{aligned} \alpha &= \frac{\mathcal{R}_{yx}(0)}{\mathcal{R}_{xx}(0)} \\ &= \frac{E\{rf(r)\}}{\mathcal{P}_x} = \frac{1}{\mathcal{P}_x}\int_0^{\infty} rf(r)\,p(r)\,dr, \end{aligned} \tag{11}$$

where $f(r)$ is the clipping function, $\mathcal{P}_x$ is the OFDM signal power, $p(r)$ is the probability density function (PDF) of the OFDM envelope and $E\{.\}$ is the statistical expectation operator. It can be shown that, for a large number of subcarriers, the OFDM envelope converges to Rayleigh envelope distribution. Therefore,

$$p(r) = \tfrac{2r}{\mathcal{P}_x} e^{-\frac{r^2}{\mathcal{P}_x}}, \quad r \geq 0 . \tag{12}$$

Substituting the expressions of $f(r)$ and $p(r)$ given by (10) and (12) into (11), we show that

$$\begin{aligned} \alpha &= \frac{1}{\mathcal{P}_x}\int_0^{A} r^2 \frac{2r}{\mathcal{P}_x} e^{-\frac{r^2}{\mathcal{P}_x}} dr + \frac{1}{\mathcal{P}_x}\int_0^{A} Ar\frac{2r}{\mathcal{P}_x} e^{-\frac{r^2}{\mathcal{P}_x}} dr \\ &= 1 - \left(1 + \frac{A^2}{\mathcal{P}_x}\right) e^{-\frac{A^2}{\mathcal{P}_x}} + \frac{A^2}{\mathcal{P}_x} e^{-\frac{A^2}{\mathcal{P}_x}} + \frac{A}{\sqrt{\mathcal{P}_x}}\sqrt{\pi}\,Q\left(\frac{A\sqrt{2}}{\sqrt{\mathcal{P}_x}}\right) \\ &= 1 - e^{-\frac{A^2}{\mathcal{P}_x}} + \frac{A}{\sqrt{\mathcal{P}_x}}\sqrt{\pi}\,Q\left(\frac{A}{\sqrt{\mathcal{P}_x}}\sqrt{2}\right), \end{aligned} \tag{13}$$

where $\frac{A}{\sqrt{\mathcal{P}_x}}$ is the clipping ratio (CR) and $Q(.)$ is the Q-function defined as

$$Q(x) \triangleq \frac{1}{\sqrt{2\pi}} \int_x^{\infty} e^{-\frac{\tau^2}{2}} d\tau .$$

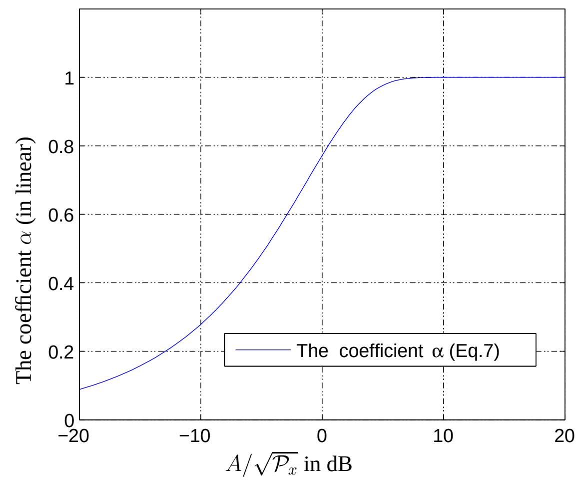

Figure 4: The coefficient α as a function of $\frac{A}{\sqrt{\mathcal{P}_x}}$.

Fig. 4 shows that the coefficient α expressed in (13) is an increasing function of $\frac{A}{\sqrt{\mathcal{P}_x}}$ and converges to 1 for $\frac{A}{\sqrt{\mathcal{P}_x}} \geq 5$ dB.

Now, let us consider the clipping threshold A sufficiently large such as $\alpha \approx 1$ but not very large, otherwise any peak will be reduced, i.e., $\frac{A}{\sqrt{\mathcal{P}_x}}$ approaches 5 dB. In this context, (9) becomes,

$$\begin{aligned} c_n &= (\alpha - 1)\,x_n + d_n \\ &\approx d_n . \end{aligned} \tag{14}$$

From (14), it can be concluded that, for $\frac{A}{\sqrt{\mathcal{P}_x}}$ approaches 5 dB, the peak-reducing signal is approximately equal to the distortion term resulting in the clipping of the OFDM envelope.

2) Heavyside Clipping (HC) technique: Often called hard clipping, HC is used in [23] as a baseband nonlinear transformation technique to improve the overall communication system performance. The heavyside function is expressed below and depicted in Fig. 5 (b).

$$f(r) = \mathrm{A}, \quad \forall r \geq 0 .$$

The HC technique is a case of school, it is widely used in theory but very rarely in practice. In [18] it is demonstrated, that HC has the worse performances of these four clipping techniques.

3) Deep Clipping (DC) technique

Deep Clipping has been proposed in [24] to solve the peaks regrowth problem due to the out-of-band filtering of the classical clipping and filtering method. So, in DC technique, the clipping function is modified in order to "deeply" clip the high amplitude peaks. A parameter called clipping depth factor has been introduced in order to control the depth of the clipping. The function-based clipping used for DC technique is defined below and depicted in Fig. 5 (c).

$$f(r) = \begin{cases} r & , \quad r \leq \mathrm{A} \\ \mathrm{A} - \beta (r - \mathrm{A}) & , \quad \mathrm{A} < r \leq \frac{1+\beta}{\beta}\mathrm{A} \\ 0 & , \quad r > \frac{1+\beta}{\beta}\mathrm{A} \end{cases},$$

where β is called the clipping depth factor.

4) Smooth Clipping (SC) technique
In [25], a Smooth Clipping technique is used to reduce the OFDM PAPR. In this paper, the function based-clipping for SC technique is defined below and depicted in Fig. 5 (d).

$$f(r) = \begin{cases} r - \frac{1}{b} r^3, & r \leq \frac{3}{2}\mathrm{A} \\ \mathrm{A}, & r > \frac{3}{2}\mathrm{A} \end{cases},$$

where $b = \frac{27}{4}\mathrm{A}^2$.

These four clipping functions are drawn on Fig. 5 and have been completely studied and compared in [18]. In the litterature it exists other clipping function, among them we may cite the 'invertible clipping' of [26]. All these clipping techniques could be formulated as Adding Signal technique (as previously done in Section III-B1 and therefore could be transformed in TR techniques (see following sections).

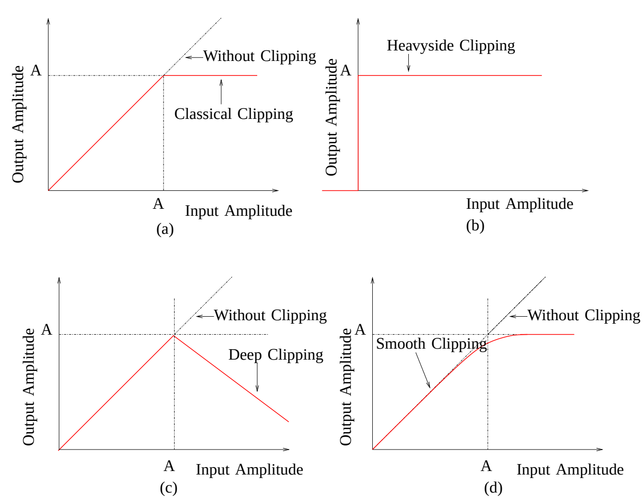

Figure 5: Functions-based clipping for PAPR reduction

C. Geometric Method for PAPR Reduction

The Geometric Method (GM) is an Adding Signal technique that was proposed for the first time in [17]. The GM technique is a backward-compatible technique, which means it does not require any additional information at the reception and the receiver should not be changed.

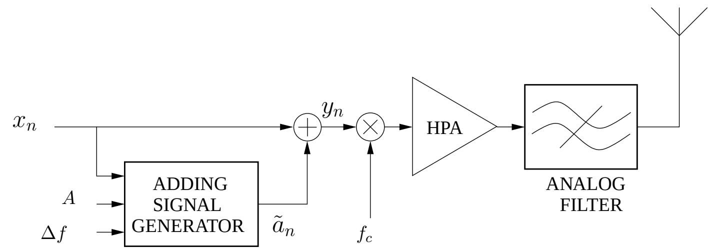

Figure 6: Principle of GM technique for OFDM PAPR reduction.

The principle of the technique is to first generate an "artificial signal" $a(t)$, which is then modulated into intermediate frequency Δf for give rise to an "adding signal" $c(t)$, which is in principle outside the useful band of the OFDM signal $x(t)$. The reduced signal $y(t) = x(t) + c(t)$ is modulated into RF frequency and then amplified. Immediately after amplification, the adding signal is removed by a bandpass analog filtering placed in the transmitter side. Fig. 6 shows the diagram of GM technique.

In [17], the "adding signal" $c(t)$ is determined using a geometric approach. It is expressed by the below equation

$$c(t) = \begin{cases} 0, & |x(t)| \leq A \\ \left[Ae^{j\varphi(t)} - x(t)\right] e^{j\Delta f t}, & |x(t)| > A \end{cases}$$

The mechanism of GM technique for PAPR reduction is described in Fig. 7.

D. Distortion Reduction in Adding Signal Techniques

Some of Adding Signal techniques can create the peak reducing signal without any in-band and out-of band distortion; this is the case of TR technique; we will go back to the details of this technique. However, when the peak reducing signal is generated based on nonlinear functions, some distortion are also generated. The well-know Adding Signal technique, in which some distortion are created is the clipping [8].

In [27], it is shown that, the peak reducing signal c_n calculated based on nonlinear functions, can be decomposed as follow

$$c_n = c_n^{(\mathrm{IB})} + c_n^{(\mathrm{OOB})}, \tag{15}$$

where, $c_n^{(\mathrm{IB})}$ is the peak reducing signal component created in the in-band of the OFDM signal, while $c_n^{(\mathrm{OOB})}$ is the peak reducing signal component created in the out-of-band of the OFDM signal.

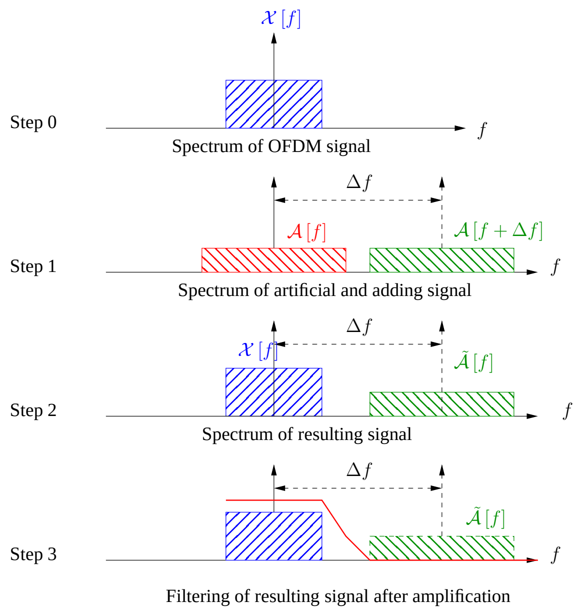

Figure 7: Mechanism of PAPR reduction.

Note that, $c_n^{(\mathrm{IB})}$ is responsible to in-band distortion that causes degradation of the BER whereas $c_n^{(\mathrm{OOB})}$ is responsible to out-of-band radiation that causes adjacent channel interference (ACI) and affects systems working in the neighbor bands.

In [8], the out-of-band distortion is mitigated by suppressing the out-of-band component $c_n^{(\mathrm{OOB})}$ of the peak reducing signal c_n. This distortion mitigation is done by a digital filter based on FFT/IFFT. But the in-band component $c_n^{(\mathrm{IB})}$ is kept, reason why in clipping and filtering technique of [8], the BER of the system is degraded.

The process of the suppression of the out-of-band distortion in Adding Signal is shown in Fig. 8 in frequency domain.

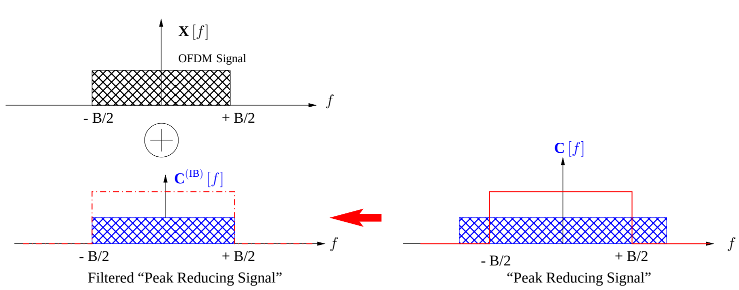

Figure 8: Out-of band distortion mitigation structure based on FFT/IFFT digital filter.

One drawback of out-of-band distortion suppression in Adding Signal techniques is peak regrowth due to the filtering of the peak reduction signal. Indeed, the digital filter based on FFT/IFFT truncates some of the information that is used to reduce PAPR and create some peak regrowth.

Some peak regrowth reduction methods have been proposed in the literature [22, 28]. A straightforward way of peak regrowth reduction is the repeated of Adding Signal and out-of-band distortion filtering. This method is proposed in [22] in the case of clipping and filtering. In [28], a peak regrowth reduction method based on the "deeply" clip the high amplitude peaks of the signal.

E. Overview of TR Techniques

The TR technique [14–16] is an Adding Signal technique. This technique has been studied mainly on the OFDM signal, without specification of a particular standard and can be generalized to all types of multicarrier systems. TR technique is a pioneering method, particularly since it was the first to be modeled as a convex optimization problem. The precursor of this technique is *J. Tellado* [14].

The principal idea of TR technique is to reserve N_r subcarriers in the OFDM symbol on which will be added a relevant information in order to change the time signal, so as to reduce the dynamics of the signal envelope. In this technique, the transmitter and receiver agree on the number and the positions of subcarriers, which are reserved to carry the corrective signal for decrease the PAPR.

It should be understood that at the beginning, TR technique is not backward compatible. Indeed when it was introduced for the first time by *J. Tellado* in [14], the positions of so-called "reserved subcarriers" are not fixed (known in advance), it assumes that the receiver must be informed by the transmitter on the positions dedicated subcarriers used to bring the "signal PAPR reduction".

In this paper, the TR technique will be implemented using the "unused subcarriers" so-called "null subcarriers" of the standards in order to make the technique backward compatible. The schematic diagram of the method is given in Fig. 9.

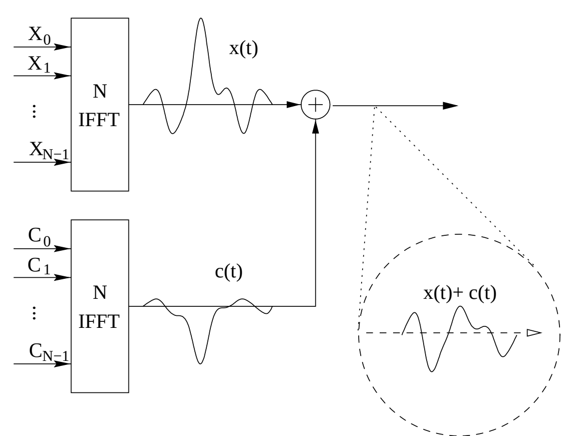

Figure 9: Illustration of Tone Reservation Structure.

The peak reducing signal c_n is carried by the reserved subcarriers and the peak-reduced signal is given by

$$y_n = x_n + c_n = \frac{1}{\sqrt{N}} \sum_{k=0}^{NL-1} (X_k + C_k)\, e^{2j\pi \frac{n}{NL}}, \quad (16)$$

where $0 \leq n \leq NL-1$ and $\mathbf{C} = [C_0, \cdots C_{NL-1}]$ is the set of peak-reducing subcarriers.

Let $\mathcal{R} = \{i_0, \cdots, i_{N_r-1}\}$ be the locations of the reserved subcarriers and let $\mathcal{R}^c$ be the complement of $\mathcal{R}$ in $\mathcal{S}_1$. In TR technique, the constraint on c_n is that $\mathbf{C}$ must satisfy $C_k \equiv 0$ for $k \in (\mathcal{R}^c \cup \mathcal{S}_2)$. On the other hand, $\mathbf{X}$ must satisfy $X_k \equiv 0$ for $k \in \mathcal{R}$. $\mathbf{X}$ and $\mathbf{C}$ are not allowed to be nonzero on the same subcarriers, i.e.,

$$X_k + C_k = \begin{cases} X_k, & k \in \mathcal{R}^c \\ C_k, & k \in \mathcal{R} \end{cases} . \quad (17)$$

Because of $\mathcal{R} \cap \mathcal{R}^c = \emptyset$, the BER of the system is not degraded. Because of $C_k = 0$ for $k \in \mathcal{S}_2$, there is not out-of-band radiation.

The only drawback of TR technique is the loss of troughput due to the reserved carriers to carry out the "peak reducing signal"(which is the case, for example, in the DVBT2 standard [2]). To minimize this loss, we propose to use unused or nulls carriers of the standards as reserved carriers (see Section V).

IV. From Adding Signal techniques for PAPR Reduction to TR techniques

In this section, we first describe the principle of the digital filter based on FFT/IFFT pair, which is used for the transformation of Adding Signal techniques in TR techniques. Then we derive the algorithms of classical and adaptive transformation of Adding Signal techniques in TR techniques. Finally, we evaluate their computational complexities.

Using the same principle of out-of band distortion suppression based on FFT/IFFT digital filtering, we have proposed in [1] for the first time the idea of the transformation of PAPR reduction techniques into TR techniques based on FFT/IFFT digital filtering. In [1], the classical clipping technique is transformed in TR technique for WLAN (IEEE 802.11 a/g) PAPR reduction. In this paper we propose an improvement of the classical transformation algorithm initially described in [1] by adaptively transform Adding Signal techniques to TR techniques. The new algorithm will be called adaptive transformation algorithm. Both algorithms are very similar and are both based on FFT/IFFT digital filtering.

A. The Digital Filter Based on FFT/IFFT Principle

Let $\tilde{c}_n$, the signal at the output of the IFFT/FFT pair based filter as shown in Fig. 10.

The FFT/IFFT pair-based filter consists of a FFT operation followed by an IFFT operation. The forward FFT transforms c_n back to the frequency-domain. The discrete frequency components of c_n on the reserved subcarriers are

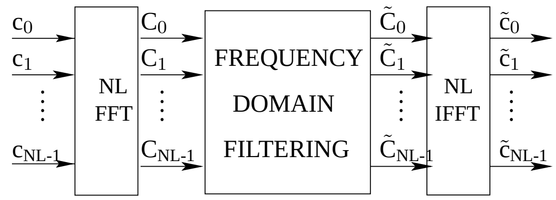

Figure 10: Digital filtering-based FFT/IFFT.

passed unchanged while the data subcarriers and the OOB components are setted to zero, i.e,

$$\tilde{C}_k = \mathcal{H}[C_k] = \begin{cases} C_k, & k \in \mathcal{R} \\ 0, & k \in (\mathcal{R}^c \cup \mathcal{S}_2) \end{cases} . \quad (18)$$

The IFFT operation transforms $\tilde{C}_k$, back to the time domain. This results in the filtered peak-reducing signal $\tilde{c}_n$ at the output of the filter-based FFT/IFFT.

The relation between the input and the output of the FFT/IFFT pair-based filter is written as:

$$\tilde{c}_n = \mathcal{F}^{-1}(\mathcal{H}[\mathcal{F}(c_n)]), \quad (19)$$

where $\mathcal{F}$ represents the FFT function, $\mathcal{F}^{-1}$ is the IFFT function and $\mathcal{H}$ is the digital filter response in frequency domain.

According to (18), only the components of c_n on the reserved subcarriers ($\mathcal{R}$) are used for OFDM PAPR reduction; that is why, the resulting PAPR reduction technique is a TR technique.

The FFT/IFFT pair-based filter complexity as well defined, depends only on the complexity of utilizing the FFT/IFFT pair and is approximated as $\mathcal{O}(NL \log_2 NL)$.

The principle of FFT/IFFT pair-based filter for transformation of Adding Signal techniques in TR techniques is shown in Fig. 11.

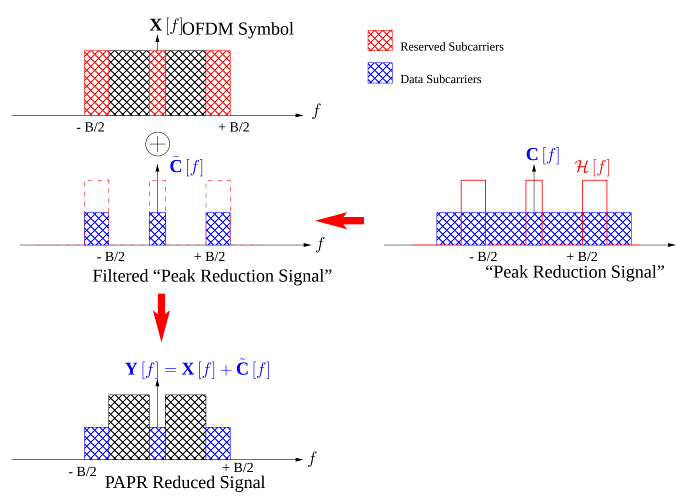

Figure 11: FFT/IFFT pair-based filter for transformation to TR technique.

In the same way as the out-of band distortion mitigation, the digital filter based on FFT/IFFT remove a part of the information, which is used for PAPR reduction and create some peak regrowth. For both classical and adaptive transformation algorithms, the repeated adding and filtering signal for PAPR reduction is used to reduce the peak regrowth phenomena.

Now let go to the details of classical and adaptive transformation algorithms.

B. Classical Transformation (CT) Algorithm

In this subsection, we describe the classical transformation algorithm of Adding Signal techniques for PAPR reduction to the TR techniques, which is based on the FFT/IFFT digital filter.

In order to reduce as much as possible the PAPR, the CT algorithm is based on an iterative algorithm, which the principle is as follow:

- Set up the locations of the reserved subcarriers $\mathcal{R}$ and the maximum iteration number $\mathcal{N}_{iter}$, and choose the function for PAPR reduction $f(.)$.
- Set up $i = 0$, where $x_n^{(0)} = x_n$ is the time-domain OFDM signal.
- Compute the (i)-iteration PAPR reduction signal as:

$$\tilde{c}_n^{(i)} = f_\Delta \left[f\left(x_n^{(i)}\right) - x_n^{(i)} \right], \tag{20}$$

  where $f_\Delta = \mathcal{F}^{-1} \circ \mathcal{H} \circ \mathcal{F}$ is the FFT/IFFT based digital filter response in time domain.
- Compute the $(i+1)$-iteration PAPR reduced signal as:

$$x_n^{(i+1)} = x_n^{(i)} + \tilde{c}_n^{(i)} \tag{21}$$

It must bear in mind that, the system complexity grows linearly with the number of iterations. The data processed by this algorithm in this paper are L over-sampled OFDM symbols. The complexity of computationnal of $\tilde{c}_n^{(i)}$ for each iteration is $\mathcal{O}(NL\log_2 NL)$ because f_Δ, which is the digital filter response is based on a backword FFT followed by a foreward IFFT. Assuming that $\mathcal{N}_{iter}$ is the maximum number of iterations, the CT-algorithm complexity can be approximated to $\mathcal{O}(\mathcal{N}_{iter} NL\log_2 NL)$.

C. Adaptive Transformation (AT)-Algorithm

The AT-algorithm for the transformation of Adding Signal techniques to TR techniques is based on the CT-algorithm. In distinction of the CT-algorithm, the AT-algorithm scales the PAPR reduction signal $\tilde{c}_n^{(i)}$ by an optimal scaling factor $\beta_{opt}^{(i)}$ in order to outperform the PAPR reduction performance. Whereby the PAPR reduced signal for AT-algorithm, at $(i+1)$-iteration, is written as:

$$x_n^{(i+1)} = x_n^{(i)} + \beta_{opt}^{(i)} \tilde{c}_n^{(i)} \tag{22}$$

The scaling factor $\beta_{opt}^{(i)}$ is the solution of the optimization problem, which is formulated as

$$\beta_{opt}^{(i)} = \arg\min_{\beta} \left[\max_{n} \left| x_n^{(i)} + \beta \tilde{c}_n^{(i)} \right| \right]. \tag{23}$$

An exact solution of Eq. (23) exists but leads to a high computation complexity. An alternative solution to Eq. (23) is a low computation complexity suboptimal solution. In [29], it is shown that, a suboptimal solution of Eq. (23) is given by minimizing the total power of the samples with $\left| x_n^{(i)} + \tilde{c}_n^{(i)} \right| > A$, where A is the magnitude threshold. Solving Eq. (23) leads to

$$\beta_{opt}^{(i)} = \arg\min_{\beta} \left[\sum_{n \in \mathcal{S}_p^{(i)}} \left| x_n^{(i)} + \beta \tilde{c}_n^{(i)} \right| \right], \tag{24}$$

where, $\mathcal{S}_p^{(i)} = \left\{ n : \left| x_n^{(i)} + \tilde{c}_n^{(i)} \right| > A \right\}$. The above minimization problem is a linear least-squares problem and the solution is given by

$$\beta_{opt}^{(i)} = -\frac{\sum\limits_{n \in \mathcal{S}_p^{(i)}} x_n^{(i)} \tilde{c}_n^{*(i)}}{\sum\limits_{n \in \mathcal{S}_p^{(i)}} \left| c_n^{(i)} \right|^2}, \tag{25}$$

where $(.)^*$ is the mathematical conjugate function.

The complexity of calculating $\beta_{opt}^{(i)}$ is $\mathcal{O}(\mathcal{N}_p)$, where $\mathcal{N}_p$ is the size of $\mathcal{S}_p^{(i)}$. After $\mathcal{N}_{iter}$ iterations, the AT-algorithm complexity can be approximated to $\mathcal{N}_{iter}\left[\mathcal{O}(NL\log_2 NL) + \mathcal{O}(\mathcal{N}_p)\right] \simeq \mathcal{O}(\mathcal{N}_{iter} NL\log_2 NL)$.

V. Transformation of Adding Signal techniques for PAPR reduction to TR techniques in a WLAN System context

In this section, based on the above analysis, using the CT and AT algorithms, we propose to transform the classical clipping technique [8] and the Geometric PAPR reduction technique [17] into TR techniques for PAPR reduction of the Wireless Local-Area-Networks (WLAN) system based on IEEE 802.11a/g standards. In the first subsection we provide the caracteristics of the IEEE 802.11a/g standards.Then using the two CT and AT algoritms in the second subsection, we give the obtained results .

A. The IEEE 802.11a/g standards based WLAN system

In WLAN IEEE 802.11a/g standard IFFT size (N) is 64. Out of these 64 subcarriers, 48 subcarriers are used for data, while 4 subcarriers are used for pilots. The rest 12 subcarriers are unused (null) subcarriers located at the positions $\mathcal{R} = \{0, 27, \cdots, 37\}$ of the IFFT input.

The IEEE 802.11a/g Standard specifications are given in [30] and the transmit spectral mask requirements is shown in Fig. 12.

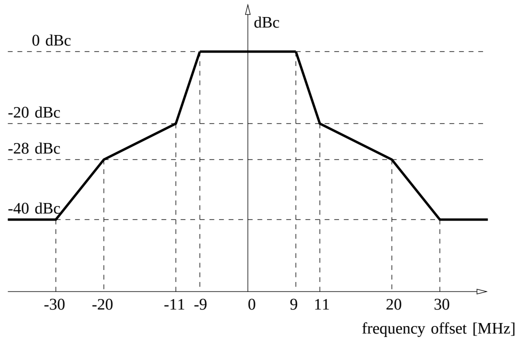

Figure 12: Spectral power mask of OFDM based WLAN.

B. Simulation results

- "Classical-TR-CC" and "Adaptive-TR-CC" are the TR techniques resulting of the transformation of classical clipping technique based on the CT and AT algorithms respectively.
- "Classical-TR-GM" and "Adaptive-TR-GM" are the TR techniques resulting of the transformation of Geometric PAPR reduction technique on the CT and AT algorithms respectively.

In this section, we evaluate the performance of the four TR techniques in a WLAN PAPR reduction context. For simulation results, only the unused subcarriers of the WLAN standard shall be utilized for PAPR reduction. The configuration, which is used for the simulations shown in Tab.I.

System Parameter	Parameter Value
Modulation Scheme	16-QAM
Number subcarriers	$\mathrm{N} = 64$
Number of data subcarriers	48
Number of pilot subcarriers	4
Oversampling Factor	$\mathrm{L} = 4$
Channel Model	AWGN
Clipping Ratio (CR)	$\frac{A}{\sqrt{\mathcal{P}_x}} = 5$ dB

Table I: Simulation Environment

The distribution based on the CCDF is used to evaluate the performance in terms of PAPR reduction of the system, the BER metric is used to evaluate the transmission performance of the system over an AWGN channel and the Power Spectral Density (PSD) of signals will be evaluated.

We evaluate also the high signal fluctuations of the PAPR by determining the performance in terms of PAPR reduction defined as

$$\Delta\mathrm{PAPR} = \mathrm{PAPR}_{[y]} - \mathrm{PAPR}_{[x]}, \quad [\text{in dB}]$$

where $\mathrm{PAPR}_{[y]}$ is the required PAPR of the signal $y(t)$ to obtain a specific value of the CCDF, while $\mathrm{PAPR}_{[x]}$ is the required PAPR of the signal $x(t)$ to obtain a specific value of the CCDF. Another aspect of performance evaluated in this paper is the average power variation denoted $\Delta\mathrm{E}$ and expressed as

$$\Delta\mathrm{E} = 10\log_{10}\left(\frac{\mathcal{P}_y}{\mathcal{P}_x}\right), \quad [\text{in dB}]$$

where $\mathcal{P}_y$ is the average power of the signal $y(t)$, while $\mathcal{P}_x$ is the average power of the signal $x(t)$.

We also draw PSD of the signal in order to check if, after the TR mitigation method, the PSD still respects the WLAN mask of Fig. 12.

Fig. 13 shows the peak power reduction results of Classical-TR-CC technique for different iterations. Simulation results from Fig. 13 shows that the reduction in PAPR increases with the iterations number. For example, at 10^{-2} of the CCDF, the reduction in PAPR for Classical-TR-CC technique is about 0.75 dB, 1.75 dB and 2.75 dB for $\mathcal{N}_{iter} = 1, 3$ and 5 respectively.

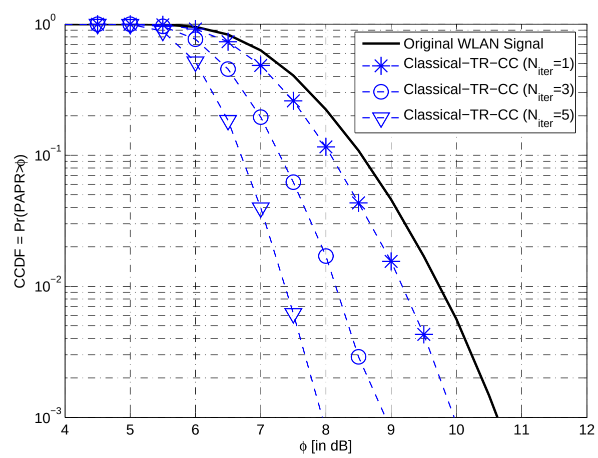

Figure 13: PAPR reduction performance for Classical-TR-CC technique for different iterations.

The reduction PAPR performance of the Adaptive-TR-CC technique for iterations number $\mathcal{N}_{iter} = 1, 3$ and 5 are plotted in Fig. 14 based on the CCDF curve. This figure provides the same conclusion as Fig. 13, i.e., the reduction in PAPR increases with the iterations number.

From Figs. 13 and 14, it is shown that the performance in PAPR reduction from CT algorithm as well from AT algorithm increases with the number of total iterations $\mathcal{N}_{iter}$.

Simulation results also shows that, for a given $\mathcal{N}_{iter}$, Adaptive-TR-CC technique is better than Classical-TR-CC technique in terms of PAPR reduction and Adaptive-TR-CC technique with $\mathcal{N}_{iter} = 3$ gives the same PAPR reduction performance as Classical-TR-CC technique with $\mathcal{N}_{iter} = 5$. It must bear in mind that, the system complexity grows linearly with the number of iterations.

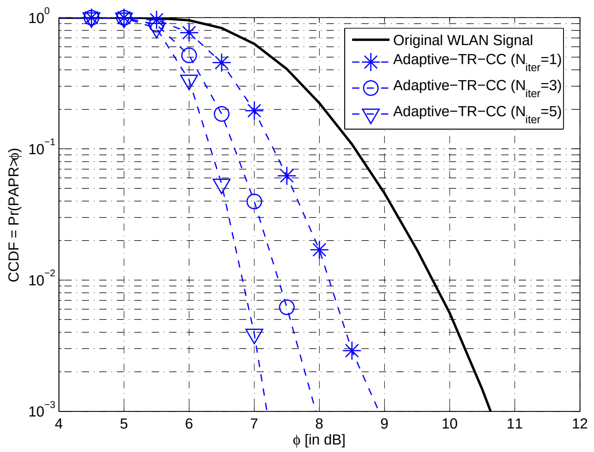

Figure 14: PAPR reduction performance for Adaptive-TR-CC technique for different iterations.

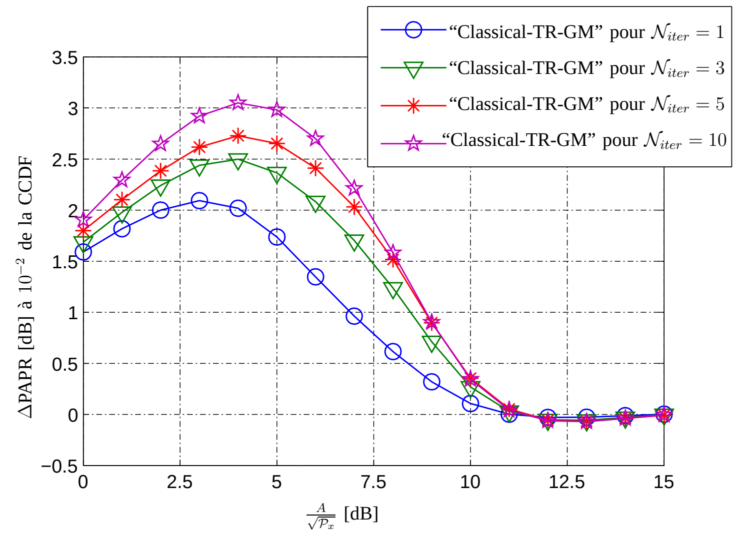

Figure 15: PAPR reduction performance of the Classical-TR-GM technique for different iterations number $\mathcal{N}_{iter}$.

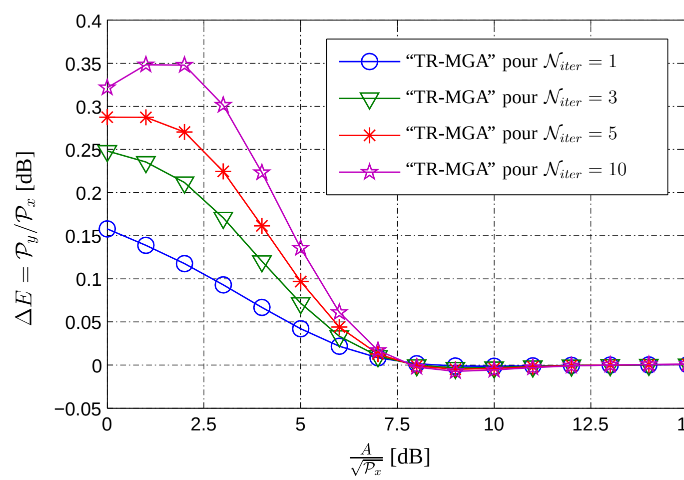

Figure 16: Average power ratio of the Classical-TR-GM technique for different iterations number $\mathcal{N}_{iter}$..

AT algorithm provides significant reduction in PAPR than CT algorithm at the same number of iterations; and AT algorithm with $\mathcal{N}_{iter} = 3$ provides the same PAPR reduction performance as the CT algorithm with $\mathcal{N}_{iter} = 5$. This means that at the same PAPR reduction gain, CT algorithm is $5/3 \sim 2$ times more complex than AT algorithm.

Fig. 15 shows the PAPR reduction performance according to A for different iterations. It shows that the reduction in PAPR increases with the number $\mathcal{N}_{iter}$ of iterations. It also shows that, for a given $\mathcal{N}_{iter}$, the maximum in PAPR reduction is achieved for $\frac{A}{\sqrt{\mathcal{P}_x}} \simeq 4$ dB and drops to 0 dB from $\frac{A}{\sqrt{\mathcal{P}_x}} \geq 11$ dB. The maximum PAPR reduction of the Classical-TR-GM technique at the value of 10^{-2} of the CCDF is 2 dB, 2.5 dB, 2.75 dB and 3 dB for $\mathcal{N}_{iter} = 1$, 3, 5 et 10 respectively.

The reduction in PAPR decreases when $\frac{A}{\sqrt{\mathcal{P}_x}}$ increases for the simple reason that, when the " threshold" A increases (i.e when $\frac{A}{\sqrt{\mathcal{P}_x}}$ increases), there are fewer and fewer samples of the multicarrier signal that satisfy the condition $|x_n| > A$. Therefore, there will be fewer and fewer PAPR reduction.

The study of variation in the average power in the Classical-TR-GM technique (refer to Fig. 16) shows that the average power of the transmitted signal increases with the reduction of PAPR. It is clear that for $\mathcal{N}_{iter} = 10$ where the PAPR reduction is most significant, the increasing of the average power is the most important.

Fig. 17 shows the transmission performance for Classical-TR-CC and Adaptive-TR-CC techniques over an AWGN channel. Fig. 18 is the BER performance for Classical-TR-GM and Adaptive-TR-GM techniques,

These simulation results show that the BER performance of the system using the different PAPR reduction techniques matches with the conventional BER; this means that the BER of the system is not degraded by the different techniques. Indeed, the different techniques used for PAPR reduction are TR techniques, as in TR techniques the data subcarriers and the PAPR reduction subcarriers are orthogonal, so the BER of the system is not corrupted.

Fig. 19 and Fig. 20 show the PSD of signals after investigating the PAPR-reduction algorithms. All the spectrums respect the WLAN spectral specifications. However, the level of spectrum under the PAPR reduction subcarriers with AT algorithm is higher than the level of spectrum with CT algorithm. Indeed at the same level of iteration, the power of the PAPR reduction signal with AT algorithm is higher than the PAPR reduction signal power with CT algorithm, that is why the performance in PAPR reduction with AT algorithm is better than whose with CT algorithm at the same number

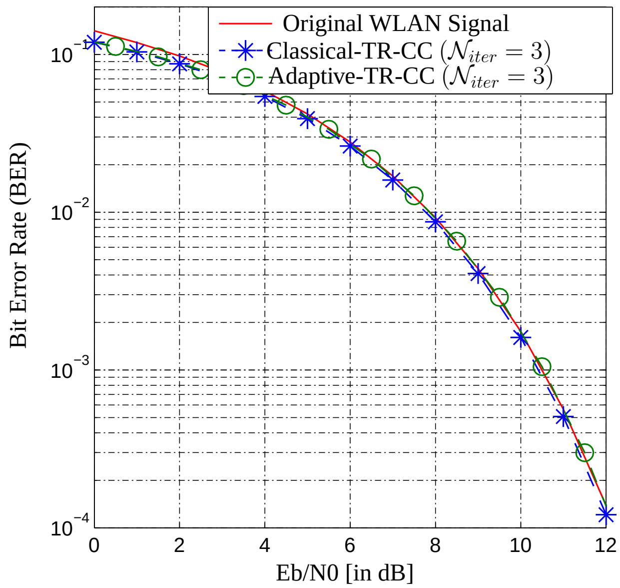

Figure 17: BER performance for Classical-TR-CC and Adaptive-TR-CC techniques over an AWGN channel.

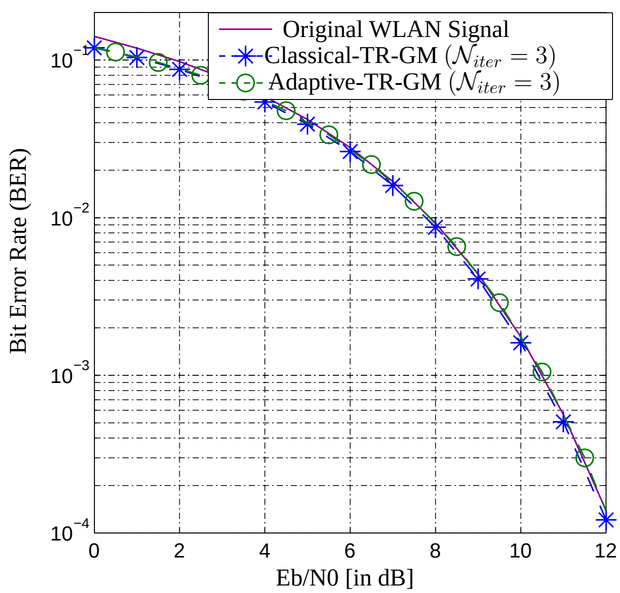

Figure 18: BER performance for Classical-TR-GM and Adaptive-TR-GM techniques over an AWGN channel.

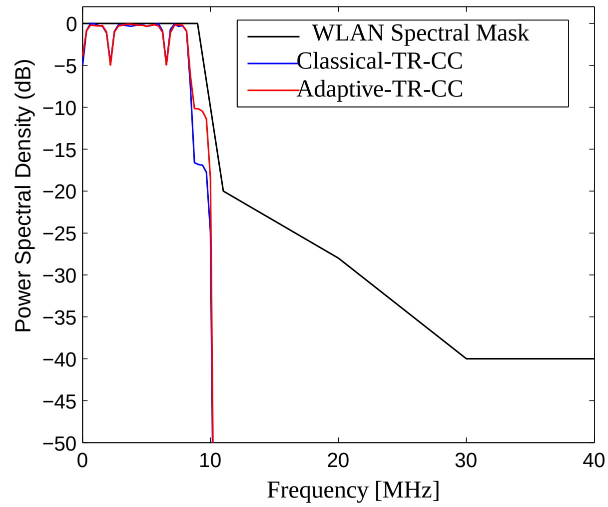

Figure 19: PSD of signals using "CT-CC" and "AT-CC" PAPR reduction technique ($\mathcal{N}_{iter} = 3$).

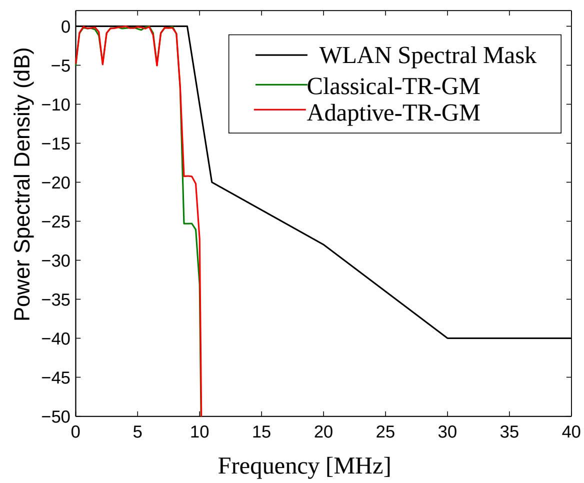

Figure 20: PSD of signals using "CT-MC" and "AT-MC" PAPR reduction technique ($\mathcal{N}_{iter} = 3$).

of iterations.

Despite the high level of the PAPR reduction signal spectrum resulting to AT algorithm, the WLAN spectral specifications are respected.

VI. Conclusion

TR is a popular PAPR reduction technique that uses a set of reserved subcarriers to carry the peak reducing signal. Because of its many advantages, TR seems to be promising for use in commercial systems.

In this paper, thanks to a Frequency Domain filtering, we have proposed two transformation algorithms to transform any Adding Signal techniques into TR techniques in order to benefit of the TR advantages. As the transformation in TR technique is a low-complexity process (about the FFT/IFFT complexity), the obtained technique results in a low-complexity TR technique. In order to increase the performance in PAPR of the obtained TR technique, the process of the peak reducing signal computation followed by filtering must be repeated several times.

Later in the paper, the classical clipping technique [8] and the Geometric PAPR reduction technique [17] are transformed into TR techniques for PAPR reduction. CT and AT algorithms proposed in this paper are applied and the performances of these two techniques are evaluated through the BER, PAPR reduction, as well as DSP of resulting signals, in the WLAN context.

From simulation results, it is shown that, AT algorithm provides more reduction in PAPR than CT algorithm at the same computational complexity; but leads to an increase in the level of the PAPR reduction signal spectrum that nevertheless respects the standard spectral specifications.

We can conclude that: to transform any Adding Signal technique into TR technique, AT transformation algorithm should be preferably used.

References

[1] D. Guel and J. Palicot, *FFT-IFFT Pair Based Digital Filtering for the Transformation of Adding Signal PAPR Reduction Techniques in Tone Reservation Techniques*, in International Conference on Wireless and Mobile Communications (ICWMC), August 2009.

[2] *DVB: Frame structure channel coding and modulation for a second generation digital terrestrial television broadcasting system (DVB-T2)*, Jun 2008.

[3] R. van Nee and R. Prasad, *OFDM for Wireless Multimedia Communications*, Boston: Artech House Publishers, March 2000.

[4] H. Ochiai and H. Imai, *Peak power reduction schemes on OFDM systems: a review*, in Proc. 11th Wireless Personal Multimedia Communications Symposium, pp. 247–252, 8–11 Sept. 1998.

[5] S. H. Han and J. H. Lee, *An overview of peak-to-average power ratio reduction techniques for multicarrier transmission*, IEEE Transactions on Wireless Communications, vol. 12, pp. 56–65, April 2005.

[6] T. Jiang and Y. Wu, *An Overview: Peak-to-Average Power Ratio Reduction Techniques for OFDM Signals*, IEEE Transactions on Broadcasting, vol. 54, pp. 257–268, June 2008.

[7] Y. Louet and J. Palicot, *A classification of methods for efficient power amplification of signals*, Annals of Telecommunications, vol. Volume 63, pp. 351–368, 2008.

[8] X. Li and J. L. J. Cimini, *Effects of clipping and filtering on the performance of OFDM*, IEEE Communication Letters, vol. 2, pp. 131–133, May 1998.

[9] A. E. Jones, T. A. Wilkinson, and S. K. Barton, *Block coding scheme for reduction of peak to mean envelope power ratio of multicarrier transmission schemes*, Electronics Letters, vol. 30, pp. 2098–2099, 8 Dec. 1994.

[10] S. H. Müller and J. Huber, *OFDM with reduce peak to average power ratio by optimum combination of partial transmit sequences*, Electronics Letters, vol. 33, pp. 368–369, Feb. 1998.

[11] R. W. Bauml, R. F. H. Fischer, and J. B. Huber, *Reducing the peak-to-average power ratio of multicarrier modulation by selected mapping*, Electronics Letters, vol. 32, no. 22, pp. 2056–2057, 1996.

[12] A. D. S. Jayalath and C. Tellambura, *Reducing the peak-to-average power ratio of orthogonal frequency division multiplexing signal through bit or symbol interleaving*, Electronics Letters, vol. 36, pp. 1161–1163, 22 June 2000.

[13] D. Guel and J. Palicot, *Clipping formulated as an adding signal technique for OFDM Peak Power Reduction*, in Proc. 69th Vehicular Technology Conference: VTC2009-Spring, 26–29 April 2009. Barcelona, Spain.

[14] J. Tellado-Mourelo, *Peak to Average Power Reduction for Multicarrier Modulation*. Ph.D, Stanford University, Sept 1999.

[15] S. Zabre, J. Palicot, Y. Louet, and C. Lereau, *SOCP Approach for OFDM Peak-to-Average Power Ratio Reduction in the Signal Adding Context*, in Proc. IEEE International Symposium on Signal Processing and Information Technology, pp. 834–839, 2006.

[16] S. Janaaththanan, C. Kasparis, and B. G. Evans, *A Gradient Based Algorithm for PAPR Reduction of OFDM using Tone Reservation Technique*, in Proc. IEEE Vehicular Technology Conference VTC Spring 2008, pp. 2977–2980, 11–14 May 2008.

[17] D. Guel, Y. Louet, and J. Palicot, *A Geometric Method for PAPR Reduction in a Signal Adding Context for OFDM Signals*, in Proc. 15th International Conference on Digital Signal Processing, pp. 347–350, 1–4 July 2007.

[18] D. Guel and J. Palicot, *Analysis and Comparison of Clipping techniques for OFDM Peak-to-Average Power Ratio Reduction*, in International Conference on DSP, July 2009.

[19] H. Ochiai and H. Imai, *Peak-Power Reduction Schemes in OFDM Systems: A Review*, in WPMC, pp. 247–252, 1998.

[20] S. H. Han, J. M. Cioffi, and J. H. Lee, *Tone injection with hexagonal constellation for peak-to-average power ratio reduction in OFDM*, IEEE Communication Letters, vol. 10, pp. 646–648, September 2006.

[21] J. Bussgang, *Crosscorrelation function of amplitude-distorted Gaussian signals*, Tech. Rep. 216, Research laboratory of electronics, Massachusetts Institute of Technology, Cambridge, 1952. Technical Report.

[22] J. Armstrong, *Peak-to-average power reduction for OFDM by repeated clipping and frequency domain filtering*, Electronics Letters, vol. 38, pp. 246–247, 28 Feb. 2002.

[23] Q. Hua, R. Raich, and G. Zhou, *On the benefits of deliberately introduced baseband nonlinearities in communication systems*, International Conference on Acoustics, Speech, and Signal Processing (ICASSP '04), vol. 2, pp. 905–908, May 2004.

[24] S. Kimura, T. Nakamura, M. Saito, and M. Okada, *PAR reduction for OFDM signals based on deep Clipping*, 3rd International Symposium on Communications, Control and Signal Processing, vol. 2, pp. 911–916, March 2008.

[25] P. Boonsrimuang, E. Puttawong, H. Kobayashi, and T. Paungma, *PAPR Reduction Using Smooth Clipping in OFDM System*, The 3rd Information and Computer Engineering Postgraduate Workshop 2003 (ICEP'2003), vol. 2, pp. 158–161, Jabuary 2003.

[26] S. Ragusa, J. Palicot, Y. Louet, and C. Lereau, *Invertible Clipping for Increasing the Power Efficiency of OFDM Amplification*, in IEEE International Conference on Telecommunications,, May 2006.

[27] D. Guel and J. Palicot, *OFDM PAPR Reduction Based on Nonlinear Functions without BER Degradation and Out-Of-Band Emission*, in Proc. International Conference on Signal Processing Systems (icSPS), 15–17 May 2009. Singapore.

[28] S. Kimura, T. Nakamura, M. Saito, and M. Okada, *PAR reduction for OFDM signals based on deep Clipping*, in 3rd International Symposium on Communications, Control and Signal Processing, pp. 911–916, March 2008.

[29] L. Wang and C. Tellambura, *An Adaptive-Scaling Algorithm for OFDM PAR Reduction Using Active Constellation Extension*, in IEEE 64th VTC-2006 Fall Vehicular Technology Conference, pp. 1–5, 25–28 Sept. 2006.

[30] *Wireless LAN Medium Access Control (MAC) and Physical Layer (PHY) specifications*, 2000.

www.iariajournals.org

International Journal On Advances in Intelligent Systems
ICAS, ACHI, ICCGI, UBICOMM, ADVCOMP, CENTRIC, GEOProcessing, SEMAPRO, BIOSYSCOM, BIOINFO, BIOTECHNO, FUTURE COMPUTING, SERVICE COMPUTATION, COGNITIVE, ADAPTIVE, CONTENT, PATTERNS, CLOUD COMPUTING, COMPUTATION TOOLS
issn: 1942-2679

International Journal On Advances in Internet Technology
ICDS, ICIW, CTRQ, UBICOMM, ICSNC, AFIN, INTERNET, AP2PS, EMERGING
issn: 1942-2652

International Journal On Advances in Life Sciences
eTELEMED, eKNOW, eL&mL, BIODIV, BIOENVIRONMENT, BIOGREEN, BIOSYSCOM, BIOINFO, BIOTECHNO
issn: 1942-2660

International Journal On Advances in Networks and Services
ICN, ICNS, ICIW, ICWMC, SENSORCOMM, MESH, CENTRIC, MMEDIA, SERVICE COMPUTATION
issn: 1942-2644

International Journal On Advances in Security
ICQNM, SECURWARE, MESH, DEPEND, INTERNET, CYBERLAWS
issn: 1942-2636

International Journal On Advances in Software
ICSEA, ICCGI, ADVCOMP, GEOProcessing, DBKDA, INTENSIVE, VALID, SIMUL, FUTURE COMPUTING, SERVICE COMPUTATION, COGNITIVE, ADAPTIVE, CONTENT, PATTERNS, CLOUD COMPUTING, COMPUTATION TOOLS
issn: 1942-2628

International Journal On Advances in Systems and Measurements
ICQNM, ICONS, ICIMP, SENSORCOMM, CENICS, VALID, SIMUL
issn: 1942-261x

International Journal On Advances in Telecommunications
AICT, ICDT, ICWMC, ICSNC, CTRQ, SPACOMM, MMEDIA
issn: 1942-2601